FRIEDRICH-SCHILLER-
UNIVERSITÄT
JENA

Supramolekulare Assemblierung amphiphiler Thiazole zur Realisierung selbstheilender photoelektrischer Aktivschichten

Dissertation
(kumulativ)

Zur Erlangung des akademischen Grades doctor rerum naturalium
(Dr. rer. nat)

vorgelegt dem Rat
der Chemisch-Geowissenschaftlichen Fakultät
der Friedrich-Schiller-Universität Jena

von Master of Science Maximilian Lutz Hupfer
geboren am 10.04.1990 in Schmölln

Gutachter:

1. Prof. Dr. Benjamin Dietzek, Friedrich-Schiller-Universität Jena

2. Prof. Dr. Volker Deckert, Friedrich-Schiller-Universität Jena

3. Prof. Dr. Andreas Fery, Technische Universität Dresden

Tag der Verteidigung: 02.10.2019

„Es gibt keine Landstraße für die Wissenschaft, und nur diejenigen haben Aussicht, ihre lichten Höhen zu erreichen, die die Mühe nicht scheuen, ihre steilen Pfade zu erklimmen“

Karl Marx – „Das Kapital“, Bd. 1, Vor- und Nachwort zur französischen Ausgabe

Inhaltsverzeichnis

1 Einleitung

In den letzten Jahrzehnten gewann die auf organischen Halbleitern basierende (Opto)Elektronik, wie zum Beispiel Solarzellen (OSZ)[1], Feld-Effekt Transistoren[2] (OFET), Sensoren[3] (OS) und Leuchtdioden[4] (OLED), gegenüber ihren anorganischen Pendants immer deutlicher an Bedeutung.[5] Neben den Vorteilen der kostengünstigen, flexiblen und transparenten Bauweise übertrafen in den letzten Jahren auch vereinzelt bestimmte Parameter, wie Wirkungsgrad[6], Feld-Effekt Mobilität[2], Betriebsspannung[7] und Lumineszenz[8], die der anorganischen Bauteile. Ein vollständiges Ersetzen jener anorganischen Elektronik wird dabei vordergründig durch die niedrige Stabilität organisch aktiver Schichten gegenüber der Umgebung und unter Betriebsbedingungen verhindert.[9] Dabei spielen die Degradation der organischen Moleküle, ihres Kontakts zum Metall sowie Reorientierung oder Entmischung durch Wärme und damit verbundenen Erzeugung von Defektzuständen eine wesentliche Rolle.[10-12]

Trotz zuvor erwähnter einzelner Rekordwerte ist eine Vielzahl an Parametern der Aktivschichten organischer Molekülen für (opto)elektronische Bauteile schlechter im Vergleich zu ihren anorganischen Pendants. Ein vielversprechender und für die organische Elektronik spezifischer Ansatz zur Verbesserung jener Eigenschaften ist neben der Steuerung der molekularen Merkmale[13-16] die der supramolekularen Struktur. Diese bestimmt wichtige Dünnschicht- und Bauteileigenschaften, wie Absorption[17-19]- und Emissionspektren[20-22], Abstrahlverhalten[23-25], Quanteneffizienz[26-30], offene Klemmspannung[31-33], Leitfähigkeit[34-36], Dynamiken des angeregten Zustandes[37-38], elektrochemisches Potential[39-40] und thermodynamische Stabilität[41-42], wesentlich. Neben der spezifischen Verbesserung optoelektronischer Eigenschaften durch die Einführung und Steuerung von supramolekularer Ordnung, bietet der Einsatz organischer Moleküle für Aktivschichten, im Gegensatz zu ihren anorganischen Gegenstücken, die Möglichkeit der Implementierung von Selbstheilungsmechanismen. Jene Mechanismen können dann wiederum dem Nachteil der geringen Stabilität und Lebensdauer von Aktivschichten organischer Moleküle entgegenwirken.

Diese Selbstheilungsmechanismen können in intrinsisch oder extrinsisch induzierten Stimulus zur (Selbst)Heilung zusammengefasst werden. Zusätzlich zu deren fortgeschrittenen Ansätzen zur (Selbst)Heilung mechanischer Eigenschaften von Polymeren, wie sie zum Beispiel von Yang *et al.*[43] and Ahner *et al.*[44] zusammengefasst wurden, sind kürzlich auch Konzepte zur

Wiederherstellung optischer[45] und elektronischer[46] Eigenschaften von Bulkmaterialien auf Polymerbasis vorgestellt wurden. Die Lebenszeit dieser (opto)elektronischen Bauteile hängt aber im Wesentlichen von der Unversehrtheit der Grenzflächen, bzw. der supramolekularen Struktur und der daraus resultierenden Parameter der Aktivschicht ab. Eine solche Selbstheilung der Grenzfläche im supramolekularen Maßstab[31-32, 47-48] wurde bisher in der Literatur noch nicht behandelt. Der Mechanismus zur Wiederherstellung der ursprünglichen supramolekularen Grenzflächenstruktur kann wiederum auf der thermodynamischen Stabilität und dem natürlich bedingten Wechsel zurück in jene, thermodynamisch bevorzugte, supramolekulare Strukturen nach einer Störung beruhen. Eine Methode die naturgemäß solche thermodynamisch stabilen supramolekularen Strukturen hervorbringt ist neben der klassischen Kristallisation[49] die der Selbstanordnung[50].

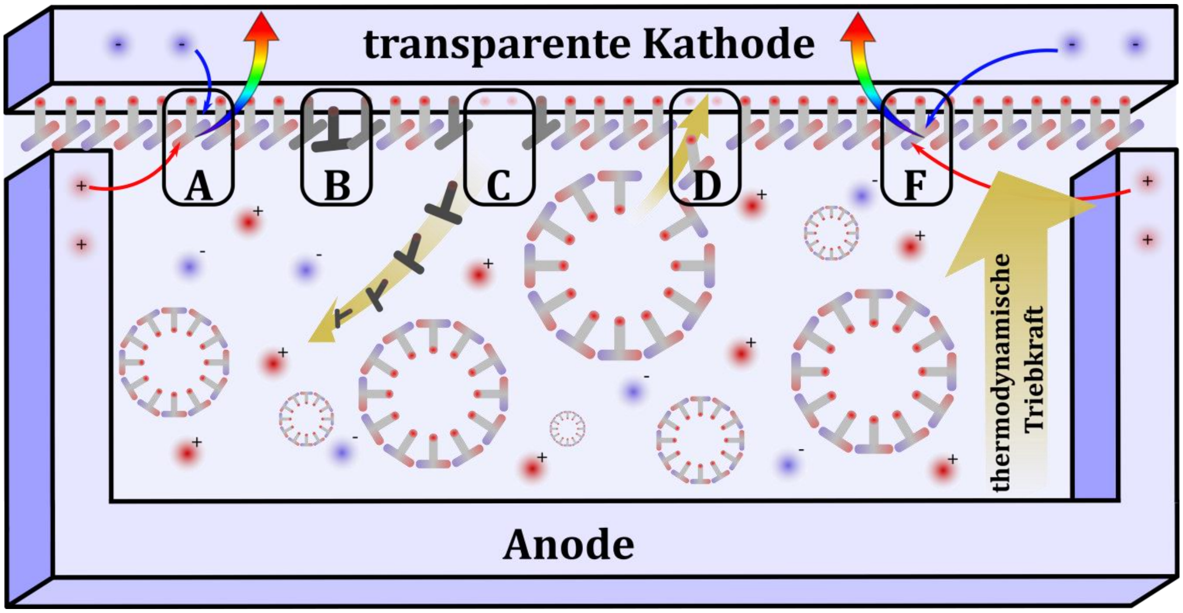

Abbildung 1.1: Konzept eines selbstheilenden, organischen, optoelektronischen Bauteils. Elektrolumineszenz der organischen Aktivschicht (A), lokale Photodegradation (B), Diffusion des Photodegradationsproduktes in die Lösung (C), Diffusion von Austauschmolekülen in die Aktivschicht (D), Wiederherstellung der Struktur und Funktion der Aktivschicht (F).

Im Rahmen dieser Arbeit wurde ein Konzept, welches die Selbstanordnung thermodynamisch stabiler, supramolekularer Strukturen in organischen Schichten und deren Selbstheilung durch eine thermodynamische Triebkraft beinhaltet, dargestellt Abbildung 1.1, entwickelt und untersucht. Bei diesem Konzept eines selbstheilenden Bauteils wird zwischen Elektroden ein Mikrovolumen mit einer elektrisch leitenden Lösung, gesättigt mit amphiphilen Austauschmolekülen, implementiert. Die unter Normalbetrieb thermodynamisch stabile organische Aktivschicht (A) kann lokal degradieren (B). Durch den Wechsel der Polarität des Degradationsproduktes gegenüber den in der Aktivschicht und im Austauschvolumen befindlichen Molekülen, ändert sich lokal das thermodynamische Gleichgewicht, wodurch das Degradationsprodukt in Lösung geht (C). Wiederum gesteuert durch die thermodynamische Triebkraft kann nun vom Austauschvolumen ein neues Molekül in die Aktivschicht diffundieren (D) und die Funktionalität der Schicht wiederherstellen (F). Die Basis dieses Konzepts bildet somit das thermodynamische Gleichgewicht zwischen Aktivschicht und Austauschmolekülen.

Ein Ansatz zur Steuerung des thermodynamischen Gleichgewichtes geht aus dem Erreichen von hoher supramolekularer, also übergeordneter, langreichweitiger Ordnung durch die thermodynamische Stabilität der Schicht hervor. Die für die Herstellung von organischen Schichten üblichen Beschichtungstechniken wie Verdampfen[51], Schleudern[52], Sprühen[53] oder Rakeln[54] erzeugen zwar reproduzierbare homogene Schichten, diese besitzen jedoch nur eine niedere und vor allem kurzreichweitige, lokale supramolekulare Ordnung. Zur Kontrolle der supramolekularen Struktur und dem Erreichen einer hoch- und ferngeordneten Schicht wurden verschiedene Techniken, wie das antiparallele Anordnen von bipolaren Donor-Akzeptor Farbstoffen[55], Ko-Selbstorganisation[56], Schicht-für-Schicht Verfahren [57-58] und (Selbst)Assemblierung amphiphiler Moleküle an Heterogrenzflächen entwickelt. Letzteres beinhaltet die Selbstorganisation von Mono- und Multilagen an der fest-flüssig-Grenzfläche[59-60], Assemblierung an der flüssig-flüssig-Grenzfläche[61], oder die Filmbildung an der flüssig-gasförmig-Grenzfläche, wie es zum Beispiel bei der Langmuir-(L)-Blodgett-(B)-Technik[62-66] angewendet wird.

Entwickelt von Langmuir[67] und Blodgett[68] erlaubt die LB-Technik eine kontrollierte Bildung supramolekularer Strukturen amphiphiler Moleküle auf dem dafür geeigneten LB-Trog und somit die Abscheidung anhand von molekulare Wechselwirkungen der Amphiphile mit einem Substrat. Dabei wird eine Lösung von Monomeren mit einer niedrigen Oberflächenkonzentration auf die Wasseroberfläche des LB-Troges getropft. Anschließend verteilen sich diese Moleküle nach dem Verdampfen des Lösungsmittels auf der Wasseroberfläche und richten sich, mit der polaren Gruppe zum Wasser und der unpolaren Gruppe zur Luft, an der Grenzfläche aus. Mittels beweglicher Barrieren kann die Oberfläche des LB-Troges und damit verbunden die Oberflächenkonzentration der Amphiphile systematisch variiert werden. Damit können supramolekulare Strukturen mit verschiedensten Wechselwirkungen der Amphiphile forciert werden. Diese supramolekularen Strukturen werden aus der sogenannten Π(A)-Isotherme bestimmt, welche die Abhängigkeit des Oberflächendrucks (Π) von der durchschnittlichen Fläche eines Moleküls (A) angibt.

Neben der fundamentalen Erforschung von Filmbildung, Orientierung und Dynamik von Monolagen oder Membranen von Peptiden[69-73], Phospholipiden[74-78] und Fettsäuren[79-80] mittels LB-Technik, gewann die Assemblierung amphiphiler Farbstoffe und deren Mischungen in Matrizen in letzter Zeit mehr an Bedeutung. Ziel der Forschung bildet dabei ein fundamentales Verständnis von (supra)molekularer Orientierung[81-82], Aggregation bzw. inter- und intramolekularer Wechselwirkungen[83-85] bezüglich der Verwendung für Aktivschichten in organischer (Opto)Elektronik. Die Assemblierung amphiphiler Farbstoffe, deren supramolekulare Struktur in L- und LB-Filmen und die sich daraus ergebenden (opto)elektronischen Eigenschaften hängen dabei stark von molekularen Parametern ab, wie der Art des Chromophors[86-87], die chemische Natur[88], Zahl und Lage der polaren und unpolaren Komponenten der Amphiphile[89-90]. Dabei wurden bisher verschiedenste Farbstoffklassen unter Variation der auxochromen Gruppen, Seitenketten und Ankergruppen, eingesetzt. Die geringfügig amphiphil funktionalisierbaren Oxazine[91-92] und Benzidine[93] finden, neben den stark zur Aggregation neigenden Azobenzenen[84, 94], Helicenen[95] und Spyropyranen[96], nur vereinzelt Einsatz in der LB-Forschung. Hingegen häufig verwendet werden die im Strukturmotiv variablen Cyanin-basierten Farbstoffklassen (Mero-[97-98], Phthalo[99-101]-, Hemi[102-105]-, Indocarbo[106-107]-, Thiacyanine[108-109]) sowie vielseitig funktionalisierbare und optoelektronisch stabile Porphyrine[110-111], Metallkomplexe[112-113], Corrole[114-115], Napthaline[116-117] und Perylene[118-119]. Die vollständige Integration der daraus assemblierten LB-Filme in optoelektronische Bauteile bildet, aufgrund der geringen thermodynamischen Stabilität und Homogenität mehrlagiger Schichten, die Ausnahme und bedarf weiterer Forschung.[120-129]

Eine hinsichtlich dessen vielversprechende und dabei nur geringfügig erforschte Farbstoffklasse wird durch die 4-Hydroxy-1,3-Thiazole (4-Hydroxythiazole) gebildet, siehe Abbildung 1.2. Die in ihrem Strukturmotiv dem körpereigenen Vitamin B1 ähnelnden Thiazole wurden von Grummt *et al.* 2007[130], am Beispiel des Pyridyl-Thiazols, zum ersten Mal erforscht und zeigten die für 4-Hydroxythiazole typische intensive Fluoreszenz. Diese Farbstoffklasse ist an ihrem Strukturmotiv vielseitig modifizierbar[131] und kann sowohl in Polymeren[132-136] als auch Metallkomplexen[137-139] als Ligand ihren Einsatz finden. In den letzten Jahren wurden vor allem grundlegende Struktur-Eigenschaft-Beziehungen dieser Farbstoffklasse untersucht. Habenicht *et al.*[140] zeigte die Regioisomerie zweier mit Nitrophenyl substituierten Derivate sowie deren, für elektronenziehend und -schiebend substituierten Farbstoffe, herausragender Fluoreszenzquantenausbeute. Des Weiteren konnte quantenchemisch und spektroskopisch die Erhöhung der Oszillatorstärke des *HOMO-LUMO*[1] Übergangs durch Erweiterung des π-Elektronensystems gezeigt werden.[141] Eine LB-Tauglichkeit der Farbstoffklasse sowie die Auswirkung von supramolekularer Assemblierung mittels LB-Technik auf die optischen Eigenschaften wurde erstmals an Pyridyl- und Pyrazinyl-Thiazolen und deren Substitution mit Sulfonamiden untersucht. Es konnte gezeigt werden, dass diese Derivate hochkomprimierbare stabile L- und LB-Filmen erzeugen. Gampe *et al.*[142-144] entwickelte Thiazolfarbstoffe mit mehreren π-Systemen gekoppelter Benzothiadiazole-Donor- und Tetraazaacene-Akzeptor-Systemen als vielversprechende Farbstoffe für die (Opto)Elektronik.

Im Rahmen dieser Arbeit und der dazu parallel laufenden, auf Synthese fokussierten Dissertation von Kaufmann[145], sollen neuartige zentral alkylisch funktionalisierte, T-förmige, amphiphile 4-Hydroxythiazole, zentral in Abbildung 1.2 dargestellt, hinsichtlich ihrer supramolekularen Struktur, der sich daraus ergebenden thermodynamischen Stabilität und optoelektronischen Eigenschaften von L- und LB-Filmen, entwickelt werden. Ziel ist es Filme jener Moleküle hinsichtlich ihres Einsatzes in der oben beschriebenen neuartigen Methode zur Selbstheilung eines optoelektronischen Bauteils zu optimieren. Hierbei wurde bisher grundsätzlich deren Fähigkeit zur Bildung stabiler L- und LB-Filme[146] gezeigt, jedoch noch nicht die supramolekulare Orientierung derer und dessen Auswirkung auf optoelektronische Eigenschaften untersucht. Der Hauptteil dieser Dissertation beschäftigt sich also mit der Filmbildung und der supramolekularen Orientierung amphiphiler 4-Hydroxythiazole, die eine Donor-, Akzeptor oder Donor-Akzeptor Substitution an der 2- und 5-Position besitzen (R1 und R2 in Abbildung 1.2). Zusätzlich wurde an der 4-Hydroxy-Position (R3) eine alkylische oder arylische Kette mit carboxylischem Anker substituiert. Bisherig literaturbekannte T-förmige Amphiphile neigen bei Kompression an der Wasser-Luft-Grenzfläche zum monomolekularen Kollaps und dem Ausbilden von homogenen doppellagigen Filmen.[147-148] Die wiederum in der LB-Technik bevorzugt verwendeten Strukturen weisen eine I-förmige molekulare Geometrie und eine klare Trennung von polaren (Chromophor) und unpolaren (alkyische Kette) Teilen auf.[66] Diese Trennung kann in einer aufrechten supramolekularen Anordnung durch den Verbund der unpolaren Teile zweier I-förmiger Moleküle eine LB-Doppellage beide

---

[1] Typen von Molekülorbitalen. *HOMO* gibt das höchste besetzte (*highest occupied*) und *LUMO* das niedrigste unbesetzte (*lowest unoccupied*) Molekülorbital an.

optoelektronisch aktiven Chromophore voneinander elektrisch isolieren.[74, 149-150] Daher sind, anders als bei I-förmigen Strukturen oder den zumeist zweifach alkylisch und einfach mit Ethylenoxid substituierten, literaturbekannten T-förmigen Molekülen[147-148, 151], die in dieser Arbeit verwendeten 4-Hydroxythiazole mit einem carboxylischen Anker über eine unpolaren Kette verbunden. Zusammen mit den am Chromophor verwendeten funktionellen polaren Gruppen an der 2- und 5-Position, kann das Molekül durch die sich daraus ergebenden, 1 bis 3-fach verankerte, Geometrien unterschiedliche supramolekulare Strukturen ausbilden. Intra- und intermolekularen Wechselwirkungen in den resultierenden supramolekularen Strukturen können diese als Einfach- oder Mehrfachlagen stabilisieren und somit ihren Einsatz in der selbstheilenden (Opto)Elektronik verbessern.

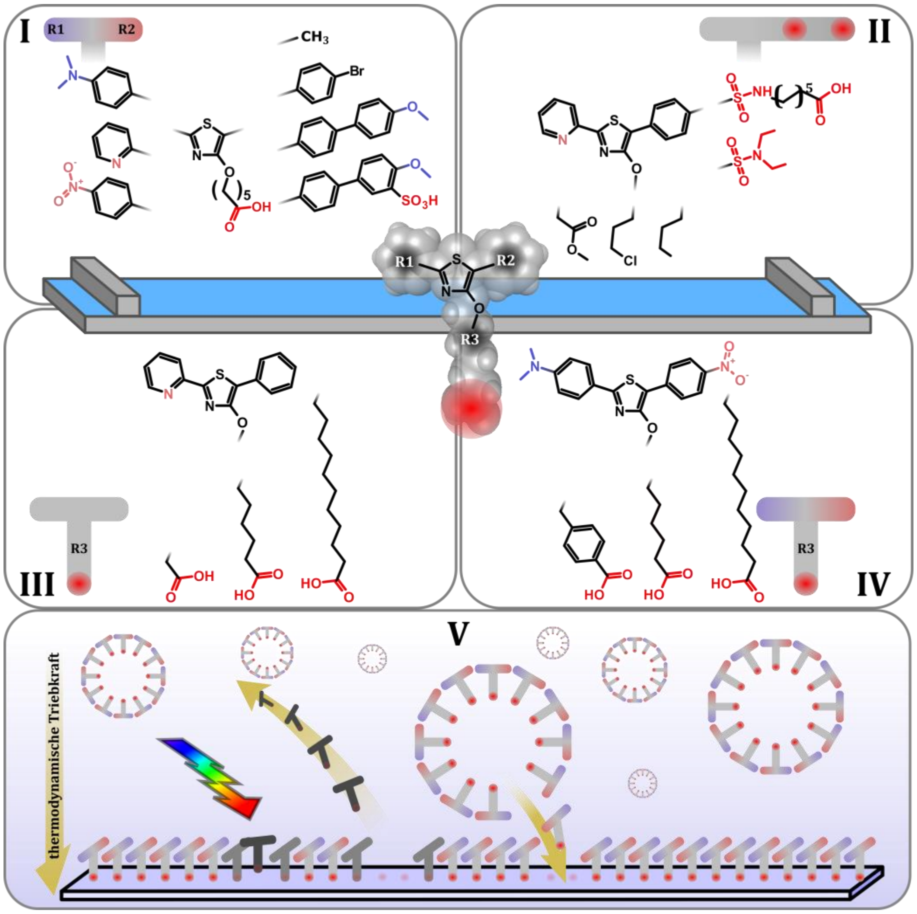

Abbildung 1.2: Schematische Darstellung, der in dieser Dissertation behandelten Kapitel. Die Variation auxochromer Gruppen an der 2- und 5-Position des Strukturmotives (I), die Variation in Art, Anzahl und Position polarer Ankergruppen (II), die Variation der Länge (III) sowie Art (IV) zentral unpolar funktionalisierten Zwischenketten. Der Einsatz des aus I-IV abgeleiteten Strukturmotivs im Model eines selbstheilenden Bauteils (V).

Das Ziel dieser Arbeit bildet daher das grundlegende Verständnis und die Kontrolle der gerade beschriebenen komplexen Filmbildungseigenschaften der T-förmigen, substituierten 4-Hydroxythiazole. Dafür wurden die Farbstoffe in Lösung, L- und LB-Filmen mit Absorption- und Emissionsspektroskopie, hinsichtlich inter- und intramolekularen Wechselwirkungen sowie Filmbildungseigenschaften, supramolekulare Orientierung und thermodynamische Stabilität mittels Π(A)-Isotherme, Π(A)-Hysterese, (polarisationsabhängiger) Emissionsspektroskopie und Rasterkraftmikroskopie untersucht. Für die Erforschung der thermodynamischen Stabilität und der sich daraus ergebenden supramolekularen Geometrie ist es notwendig Art und Länge der molekularen Substitutionen an der 2-, 5- und 4-Hydroxy-Position des Thiazols schrittweise zu variieren. Diese Variation ist in der Reihenfolge nach Kapiteln der Dissertation in Abbildung 1.2 mit R1, R2 und R3 dargestellt und wird wie folgt kurz beschrieben:

I. Den Ausgangspunkt bildet dabei die Variation der Substitutionen an der 2- und 5-Position des 4-Hydroxythiazols. Hierdurch werden grundlegende Filmbildungseigenschaften, intra-, bzw. inter-molekularen Wechselwirkungen und Einflussfaktoren als mögliche Ankergruppen analysiert.
II. Jene Ankergruppen für die Wassersubphase bilden einen bedeutenden Einflussfaktor auf die Filmbildung und sollen in Art, Position und Anzahl variiert werden. Sie bestimmen die Ausrichtung an der Wasser-Luft-Grenzfläche und die Stabilität des Transfers auf die Substratgrenzfläche ohne Reorientierung.
III. Ein weiterer Einflussfaktor auf die supramolekulare Orientierung amphiphiler, T-förmiger Moleküle ist die Länge der zentral funktionalisierten unpolaren Seitenkette. Deren Variation ermöglicht Geometrien unterschiedlicher thermodynamischer Stabilitäten, sowohl in L- als auch in LB-Filmen.
IV. Durch die Variation der Art der zentral funktionalisierten unpolaren Seitenkette können optoelektronische Parameter wie Absorptions- und Emissionsspektren, sowie die Leitfähigkeit der Aktivschicht gezielt gesteuert werden.

Darüber hinaus soll das abgeleitete Strukturmotiv hinsichtlich des Einsatzes in einem selbstheilenden optoelektronischen Bauteil untersucht werden.

V. Daher soll zuletzt die thermodynamische Stabilität und darauf folgend die Selbstheilung einer monomolekularen Schicht durch Selbstassemblierung an der Flüssig-Fest-Grenzfläche *in situ* in einem Modelschema eines selbstheilenden Bauteils bewiesen werden.

2 Einfluss der Substitution am Chromophor

Teile des Kapitels sind publiziert in [MLH1] Hupfer, M. L.; Kaufmann, M.; Preiß, L.; Weiß, D.; Beckert, R.; Dietzek, B.; Presselt, M., *Langmuir*, **2019**, *35* (7), 2587-2600

Zum besseren Verständnis zur Wahl des Ansatzpunktes für die Charakterisierung der intra- und intermolekularen Wechselwirkungen im L-Film und der daraus resultierenden supramolekularen Struktur und thermodynamischen Stabilität soll zunächst einleitend die LB-Technik erläutert werden. Den Kern einer jeden auf LB-Technik basierenden Studie bildet die supramolekulare Assemblierung von Molekülen an der Wasser-Luft-Grenzfläche und das Bestimmen der daraus resultierenden supramolekularer Geometrie mittels der Π(A)-Isotherme. Die hierzu von Davies und Rideal[152] erarbeitete Einteilung der unterschiedlichen Phasen eines L-Films langkettiger Fettsäuren, gemessen in seiner Π(A)-Isotherme, werden hier vereinfacht am Beispiel eines T-förmigen Thiazols in Abbildung 2.1 (A) dargestellt. Dabei gibt die Π(A)-Isotherme die Abhängigkeit des Oberflächendrucks (Π) von der durchschnittlichen Fläche eines Moleküls (A) an. Der Π wird mittels Plattenmethode nach Wilhelmy[153] (siehe Abbildung 2.1 (B)) bestimmt. Bei dieser Methode wird die Differenz der Grenzflächenspannungen ($\Delta\gamma = \Pi$) der reinen Wassersubphase gegenüber der Subphase in Präsenz eines L-Films gemessen. Diese Reduktion der Grenzflächenspannung wird durch die Präsenz von amphiphilen Molekülen an der Grenzfläche von Wasser und Luft erreicht, welches wiederum eine Reduktion eines an einem Platinplättchen ziehenden Meniskus zur Folge hat. Die durchschnittliche Fläche, die jedem Molekül zur Verfügung steht, wird aus der Fläche des Troges und der Anzahl der darauf assemblierten Moleküle errechnet.

Der Ausgangspunkt der Π(A)-Isotherme bildet dabei das Aufbringen einer Lösung amphiphiler Monomere in einer niedrigen Oberflächenkonzentration auf den LB-Trog. Bei jener niedrigen Oberflächenkonzentration grenzflächenaktiver Amphiphile beträgt die Differenz der Grenzflächenspannungen $\Pi = \gamma_{\mathrm{rein}} - \gamma_{\mathrm{Langmuir}} \approx 0$ mN/m. Aufgrund der nicht, bzw. kaum ausgeprägten molekularen Wechselwirkungen wird diese Phase der Π(A)-Isotherme auch „Quasi 2D Gasphase“[154] (blau in Abbildung 2.1 (A)) genannt. Die fortlaufende Kompression der Monolage führt zur systematischen Steigerung der Oberflächenkonzentration der Amphiphile, und der damit verbundenen Reduktion der Grenzflächenspannung. Die in dieser Phase (Flüssigphase[154], lila in Abbildung 2.1 (A)) wahrscheinlicher werdenden molekularen Wechselwirkungen richten die Moleküle zum einem aneinander aus, erlauben aber zum anderen noch

Diffusion. Weitere Kompression verringert die Wahrscheinlichkeit der Reorientierung und Diffusion, bei gleichzeitiger Maximierung der Wechselwirkung der Moleküle. Ab einer charakteristischen Oberflächenkonzentration kommt es zu einer deutlicheren Reduktion der Grenzflächenspannung, die sich durch den steilen Anstieg in der Π(A)-Isotherme äußert. Diese sogenannte „kondensierte Phase“[154] (rot in Abbildung 2.1 (A)) gibt durch Extrapolation des Anstiegs zu $\Pi = 0$ mN/m die maximale Fläche eines Moleküls (A_0)[154-155] in jener Phase an. Zusammen mit der, durch quantenchemische Berechnungen bestimmten, relaxierten molekularen Geometrie lässt sich die supramolekulare Geometrie des Moleküls in dieser kondensierten Phase ermitteln. Diese supramolekularen Geometrien können durch ihren möglichen intra- und intermolekularen Wechselwirkungen (ππ, bipolar) erste Hinweise über die thermodynamische Stabilität einer Monolage geben.

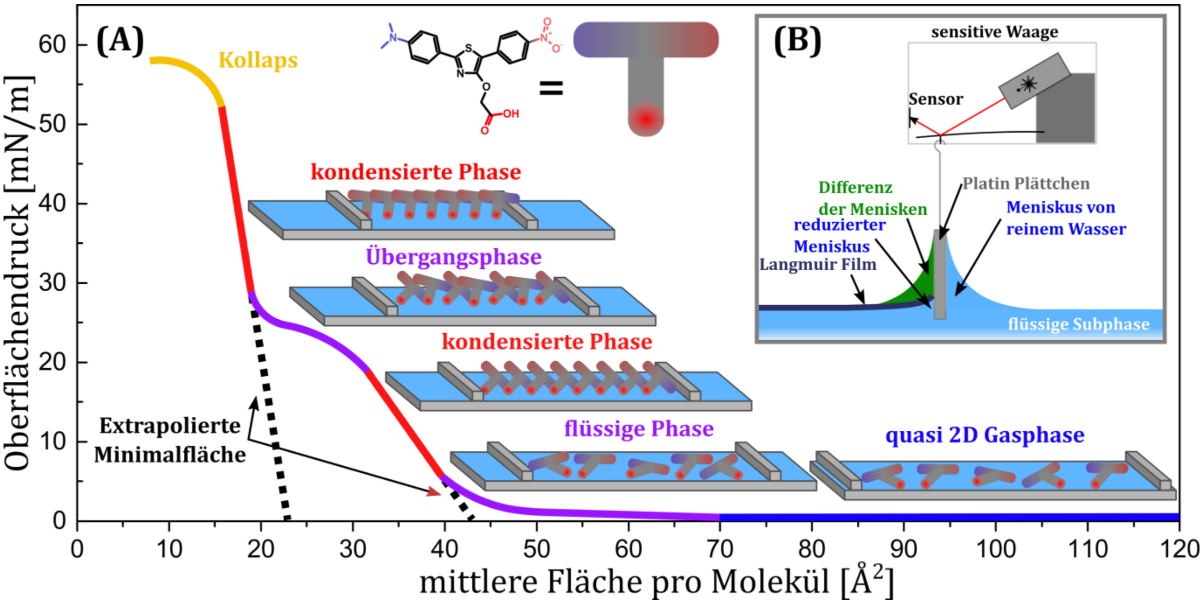

Abbildung 2.1: A) Schematische Darstellung einer Π(A)-Isotherme mit den verschiedenen Phasen (quasi-2D Gas-, quasi-2D Flüssig-, kondensierte und Übergangs-Phasen sowie Kollaps) die eine Monolage amphiphiler Moleküle bei Kompression an der Wasser-Luft-Grenzfläche durchläuft. Die supramolekulare Orientierung der jeweiligen kondensierten Phasen wird dabei für die extrapolierte Minimalfläche bestimmt. (B) Schematische Darstellung der Plattenmethode nach Wilhelmy[153].

Je nach molekularer Geometrie und Polarität möglicher Substitutionsmuster erlaubt diese (erzwungene) Assemblierung amphiphiler Moleküle verschiedene supramolekulare Geometrien, welche teilweise ohne den Einsatz der LB-Technik unzugänglich sind. Daher kann der L-Film bei vorhandener Stabilität der monomolekularen Assemblierung, gegebenenfalls mit

Durchlaufen einer Übergangsphase[156-158], von einer in eine weitere supramolekulare Geometrie wechseln. In dieser neuen, zweiten kondensierten Phase kann durch geänderte intra- und intermolekulare Wechselwirkungen eine andere thermodynamische Stabilität erreicht werden.

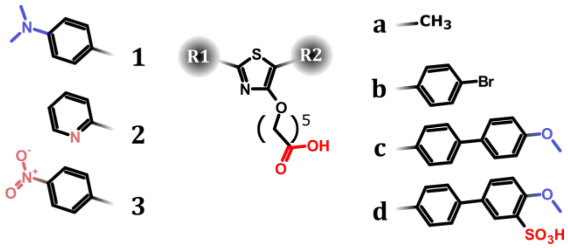

Abbildung 2.2: Schematische Übersicht der systematischen Variation des 2-R1-4-Hydroxy-5-R2-1,3 Thiazol-Kerns mit den 4-N,N-Dimethylaminophenyl- (**1**); 2-2-Pyridyl (**2**); 4-Nitrophenyl (**3**) R1- und Methyl- (**a**), Phenyl-4-Bromo- (**b**), Phenyl-4-Methoxyphenyl- (**c**) und 3-Phenyl-4-Methoxyphenyl-3-Sulfonsäure (**d**) R2-Substitutionen.

Um ein detailliertes Bild der supramolekularen Struktur amphiphiler T-förmiger 4-Hydroxythiazole zu erlangen, müssen sowohl die Seitenketten, Ankergruppen und chromophoren Substitutionen in Art (polar, unpolar) und Position (2, 4, 5-Position) systematisch variiert werden. Für einen thematischen Zugang in die Analyse von molekularer und supramolekularer Struktur wird in erster Abschätzung der notwendigen Amphiphilie eine $(CH_2)_5$ Kette (detaillierte Untersuchungen in folgenden Kapitel 3 und 4) mit Carbonsäure-(COOH)-Ankergruppe gewählt und im Rahmen der Dissertation von Kaufmann[145] synthetisiert. Im Folgenden wird der Einfluss der funktionalen Substitution des Chromophors (siehe Abbildung 2.2), mit 4-N,N-Dimethylaminophenyl (**1**), 2-Pyridyl (**2**), 4-Nitrophenyl (**3**) an der 2-Position, sowie Methyl (**a**), 4-Bromophenyl (**b**), 4-Methoxybiphenyl (**c**), 4-Methoxyphenyl-3-Sulfonsäure (**d**) an der 5-Position, auf die Filmbildung an der Wasser-Luft-Grenzfläche durch Analyse der $\Pi(A)$-Isotherme charakterisiert. Diese Studie des Einflusses von elektronenarmen, elektronenreichen und neutralen chromophoren Substituenten, bei gleichzeitiger Verlängerung des π-Systems und Einführung von Bipolarität, auf die supramolekulare Struktur des L-Films hebt sich damit deutlich gegenüber der in der Literatur üblichen Variation von Art und Länge unpolarer Seitenketten[86, 89-90] ab. Eine Analyse der spektralen Eigenschaften der Amphiphile in Lösung bzw. im L-Film soll weiteren Aufschluss auf mögliche intra- und intermolekulare Wechselwirkungen und damit auf die resultierende supramolekulare Struktur nach Kompression an der Luft-Wasser-Grenzfläche geben.[159-161] Die Ergebnisse dieser Analyse stellen einen entscheidenden Ausgangspunkt bei der Wahl der molekularen Funktionalisierung für weitere thermodynamische und optoelektronische Untersuchungen von L- und LB-Filmen amphiphiler 4-Hydroxythiazole, hinsichtlich der späteren Anwendung in einem selbstheilenden (opto)elektronischen Bauteil, dar.

2.1 Wechselwirkung in Lösung

Der Vergleich von Absorptions- und Emissionsspektren der drei verschiedenen Thiazol-Derivate in Lösung unterschiedlich polarer Lösungsmittel (Toluol, $CHCl_3$, CH_3OH) ermöglicht einen ersten Eindruck hinsichtlich möglicher intra- und intermolekularer Wechselwirkung an der polaren-unpolaren-(Wasser-Luft)-Grenzfläche und der aus ihnen resultierenden Assemblierung. Hierbei stellt die genaue Identifikation der Voraussetzungen molekularer Aggregation (Substitutionsmuster, Lösungsmittelpolarität, Konzentration) der Farbstoffe und deren spektrale Eigenschaften einen ersten Schritt zur Untersuchung supramolekularer Wechselwirkung im L-Film dar.[162] Die Interpretation der experimentell ermittelten Daten wird durch quantenchemische Analyse gestützt.

Abbildung 2.3 zeigt die exemplarisch für die drei Thiazol-Derivate stehenden Extinktion (ε) und Emission Aufgetragen über die Wellenlänge (λ) des 4-Nitrophenyl-(**3**)-substituierten Thiazol-Kerns. Die ε(λ)-Spektren weisen eine für die 4-Hydroxythiazole typische einzelne Absorptionsbande[140, 163] im sichtbaren Bereich ($S_0 \rightarrow S_1$ – Übergang) mit einem Anstieg von ε und einer leicht bathochromen Verschiebung durch Ausdehnung des π-Elektronensystems[141] von **a** zu **c** auf, siehe Tabelle 1. Das Einführen einer Sulfonsäure-(SO_3H)-Gruppe (**d**), welche als starker Anker für eine spätere Assemblierung auf der Wassersubphase gilt, lässt die Löslichkeit in unpolaren bzw. schwach polaren Lösungsmitteln drastisch sinken und erschwert das Bestimmen von ε. Die jedoch gemessenen (CH_3OH) und errechneten Absorptionsspektren zeigen keine weitere spektrale Verlagerung von λ_{abs} im Vergleich zu **c**.

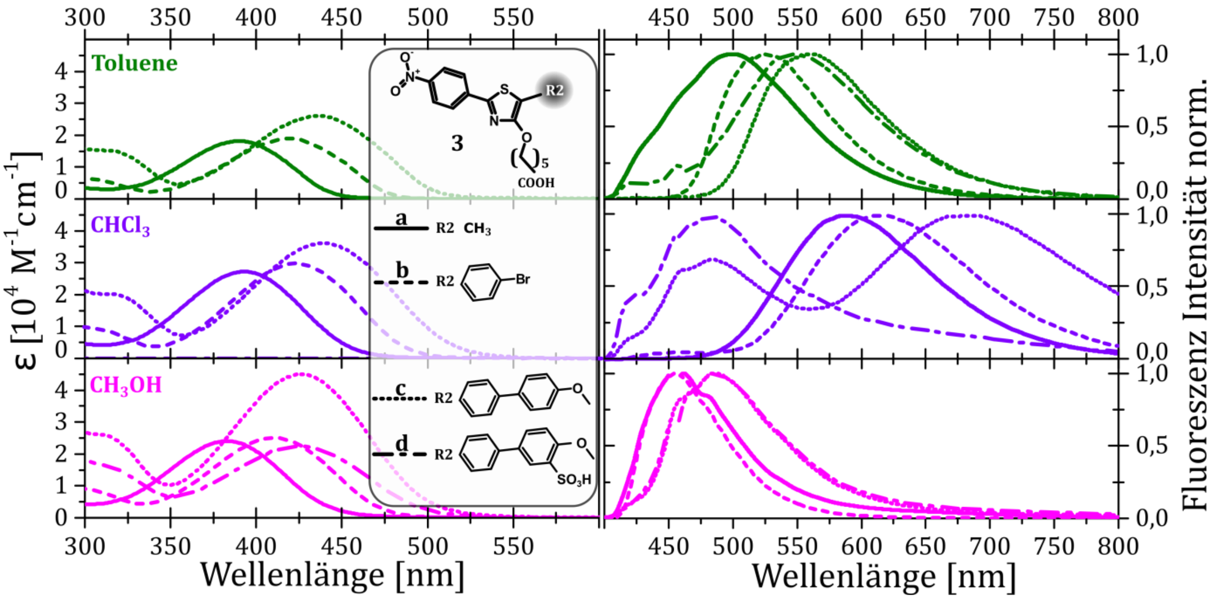

Abbildung 2.3: Extinktionskoeffizient (ε) (links) und normierte Emission ($\lambda_{Anregung}$ = 405 nm) (rechts) von dem 2-(4-Nitrophenyl)-4-Hydroxy-5-R2-1,3 Thiazol-Kern und einer Methyl- (durchgezogen), Phenyl-4-Bromo- (gepunktet), Phenyl-4-Methoxyphenyl- (gestrichelt) und 3-Phenyl-4-Methoxyphenyl-3-Sulfonsäure (gepunktet gestrichelt) R2-Substitution in Toluol (Dunkelgrün, obere Reihe), $CHCl_3$ (Violett, mittlere Reihe), CH_3OH (pink, untere Reihe).

		Toluol			**$CHCl_3$**			**CH_3OH**		
R1	R2	ε_{max} [$M^{-1}cm^{-1}$]	$\lambda_{max,abs}$ [nm]	$\lambda_{max,em}$ [nm]	ε_{max} [$M^{-1}cm^{-1}$]	λ_{max} [nm]	λ_{max} [nm]	ε_{max} [$M^{-1}cm^{-1}$]]	λ_{max} [nm]	λ_{max} [nm]
1	**a**	/	/	/	/	/	/	/	/	/
	b	40.724	396	483	39.204	394	485	43.611	391	485
	c	51.712	400	494	48.833	400	497	75.764	396	496
	d	/	/	458	/	400	469	/	397	496
2	**a**	12.512	347	420	9.127	345	420	11.145	342	422
	b	12.274	376	452	22.696	375	454	27.882	375	455
	c	43.656	393	479	36.612	392	482	28.652	386	492
	d	/	/	/	/	/	478	/	386	484
3	**a**	18.524	391	500	27.348	393	588	23.944	383	450
	b	19.525	419	525	30.201	423	615	24.965	411	450
	c	26.037	436	562	36.091	439	689	44.795	426	484
	d	/	432	546	/	430	669	/	425	485

Tabelle 1: Extinktionskoeffizient ($\varepsilon(\lambda_{max})$) (bestimmt *via* linearer Regression von c = 10^{-4} M to 10^{-7} M) und spektrale Position von Extinktions- und Emissionsmaximum (c < 10^{-6}M) ($\lambda_{Anregung}$ = 405 nm) des 2-R1-4-Hydroxy-5-R2-1,3 Thiazol-Kerns mit den 4-N,N-Dimethylaminophenyl- (**1**); 2-2-Pyridyl (**2**); 4-Nitrophenyl (**3**) R1- und Methyl- (**a**), Phenyl-4-Bromo- (**b**), Phenyl-4-Methoxyphenyl- (**c**) und 3-Phenyl-4-Methoxyphenyl-3-Sulfonsäure (**d**) R2-Substitutionen

Während die Emissionsspektren der 4-N,N-Dimethylaminophenyl-(**1**) und 2-Pyridyl-(**2**)-Derivate für alle Lösungsmittel eine literaturbekannte[163] positive Solvatochromie der Monomere, also eine spektrale Rotverschiebung bei steigender Lösungsmittelpolarität zeigen[164], konnte für die 4-Nitrophenyl-Derivate teilweise eine Blauverschiebung gemessen werden, siehe Tabelle 1. Anders als für die Methoxy-(CH_3O)-Thiazole bekannte negative Solvatochromie[165-166] handelt es sich hierbei um Aggregationseffekte, im Speziellen H-Aggregation nach Scheibe[167]. So werden die Emissionsspektren der Derivate von **3** vollständig von Aggregationseffekten in polaren Lösungsmitteln (CH_3OH) überlagert. Unter Berücksichtigung von Emissions-Anregungsspektren, kann die blauverschobene Emissionsbande einer ebenfalls blauverschobenen, in den Absorptionsspektren unsichtbaren Absorptionsbande zugeordnet werden. Bei der späteren Assemblierung von **3** an der Wasser-Luft-Grenzfläche können somit jene Wechselwirkungen dominieren und eine monomolekulare Filmbildung maßgeblich beeinflussen.

2.2 Supramolekulare Struktur im Langmuir-Film

Bei der Bestimmung der supramolekularen Geometrien eines amphiphilen Moleküls in einem L-Film mittels Π(A)-Isotherme, muss diese in Bezug auf die molekulare Dimension und mögliche elektrostatische Wechselwirkungen betrachtet werden. Die Diskussion dieser erlaubt die Identifikation LB-ungeeigneter Derivate und den Ausschluss bestimmter Orientierungen, bei denen ein größerer Flächenbedarf als der Gemessene nötig wäre. Die Isothermen von **3a**, **b**, **c**, **d** zeigen eine maximale A_0-Fläche der verschiedenen kondensierte Phasen (***I***, ***II***) kleiner als 50 $Å^2$, welche zu klein sind, um sie mittels einer flach, horizontal zur Oberfläche angeordneten supramolekularen Struktur (vergleiche Abbildung 2.4 (B), molekulare Geometrie **3c**: $22\ Å \cdot 15\ Å = 330\ Å^2$) erklären zu können. Daher wird erwartet, dass Teile des Chromophors bzw. dessen Substitutionen in der Wassersubphase gelöst sind und dabei vertikale, gekippte oder zur Wasseroberfläche geneigte L-Monolagen bilden. Die kleine A_0-Fläche des mit Methyl an der 5-Position substituierten **3a** (Abbildung 2.4 (A)) weist auf eine eventuelle Wasserlöslichkeit aufgrund von geringer Amphiphilie oder starker Tendenz zur Bildung von 3D Aggregaten hin. Damit ist es ähnlich wie für **2a** (siehe Abbildung 2.5 (B)) untauglich für den Einsatz in der LB-Technik.

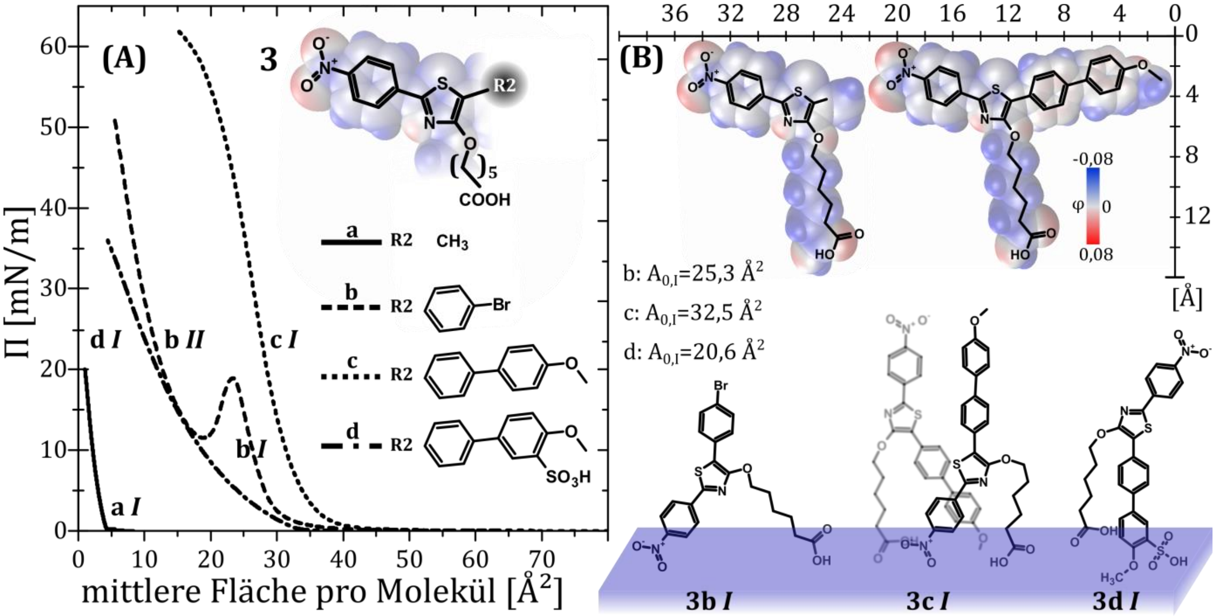

Abbildung 2.4: (A) Gemittelte Π(A)-Isothermen von 2-4-Nitrophenyl-4-Hydroxy-5-R1-1,3 Thiazolen (**3**) für Methyl- (**a**) (durchgezogen), Phenyl-4-Bromo- (**b**) (gepunktet), Phenyl-4-Methoxyphenyl- (**c**) (gestrichelt) und 3-Phenyl-4-Methoxyphenyl-3-Sulfonsäure- (**d**) (gepunktet gestrichelt) R2-Substitution. (B) Die aus der Π(A)-Isotherme bestimmten möglichen supramolekularen Geometrien der Moleküle in den jeweiligen kondensierten Phasen sind zusammen mit der molekularen Geometrie (exemplarisch für **c**), deren Dimension und dem elektrostatischen Potential über der Van-der-Waals Oberfläche dargestellt.

Verglichen zu den Dimethylamin-($N(CH_3)_2$)- und Pyridyl-(Py)-Gruppen von **1** und **2**, welche eine hohe Basizität (N,N-Dimethylanilin, $pK_a = 5.1$[168]; Pyridin, $pK_a = 5.14$[169]) aufweisen und anschließend näher betrachtet werden, verliert das mit 4-Nitrophenyl substituierte **3** einen zusätzlichen, im Falle der vorgenannten Derivate aus der Basizität resultierenden, Anker zur Wassersubphase. Die dadurch beeinflussten Π(A)-Isothermen von **3b** und **3d** weisen eine deutlich ausgeprägte Flüssigphase auf, wie in Abbildung 2.4 zwischen 0 und 7,5 mN/m zu sehen ist. Dabei deutet die fortwährende Kompression zu mittleren Molekülflächen kleiner als 20 Å, mit Ausbleiben eines steilen Anstieg des Oberflächendrucks, auf eine mögliche 3D-Aggregation des mit der SO_3H-Gruppe (**d**) substituierte und dadurch theoretisch fest in der Wassersubphase verankerten, 4-Nitrophenyl-Thiazol (siehe **3d *I*** in Abbildung 2.4 (B)) hin. Gleichwohl weist der Verlauf der in Abbildung 2.4 (A) dargestellten, Maxima und Minima durchlaufenden Π(A)-Isotherme von **3b** auf eine Verstärkung intermolekularer repulsiver Wechselwirkung (**3b *I***) mit anschließendem Kollabieren des L-Films hin. Dieses Phänomen des Durchlaufens eines lokalen Π(A)-Maximums wurde in der Literatur sowohl bei Molekülen mit Fettsäuren[170-172] als auch bei Flüssigkristallen[65, 148, 173-174] beobachtet und wird typischerweise, ohne weiterer

Untersuchungen, einer Kristallisationen sowie Multilagenbildung zugeordnet. Mit der Einführung eines ausgeprägten π-Elektronensystems und der angehängten CH_3O-Gruppe (**c**) wird der L-Film von **3** durch ππ- sowie bipolare Wechselwirkungen stabilisiert (**3c** ***I***) und somit der für die Thiazolderivate größte gemessene, literaturbekannte Oberflächendruck erreicht.

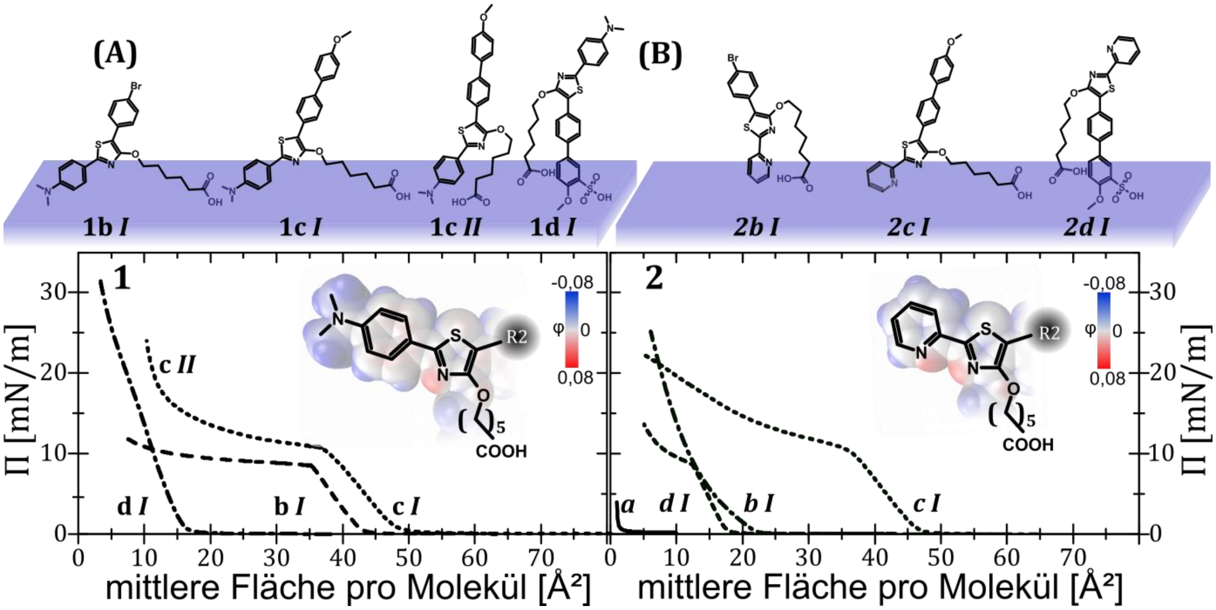

Abbildung 2.5: Gemittelte Π(A)-Isotherme des (A) 2-(4-N,N-Dimethylaminophenyl- (**1**) und (B) 2-Pyridyl (**2**)-4-Hydroxy-5-R1-1,3 Thiazols mit einer Methyl- (**a**) (durchgezogen), Phenyl-4-Bromo- (**b**) (gepunktet), Phenyl-4-Methoxyphenyl- (**c**) (gestrichelt) und 3-Phenyl-4-Methoxyphenyl-3-Sulfonsäure- (**d**) (gepunktet gestrichelt) R2-Substitution. Die aus der Π(A)-Isotherme bestimmten möglichen supramolekularen Geometrien der Moleküle in den jeweiligen kondensierten Phasen zusammen mit der molekularen Geometrie (exemplarisch für **c**), deren Dimension und dem elektrostatischen Potential über der Van-der-Waals Oberfläche.

Wie bereits erwähnt, konnte bestätigt werden, dass die $N(CH_3)_2$- und Py-Gruppe von **1** und **2** jeweils als zusätzlicher polarer Anker zur Wassersubphase wirken.[88, 150, 175] Die supramolekulare Struktur von **1b** ***I*** und **1c** ***I*** beginnt somit in einer vertikal gekippten Anordnung und unterscheidet sich nur durch die verdrehte Biphenyl-(bPh)-Substitution, welche die A_0-Flächen von **1c** vergrößert (Abbildung 2.5 (A)). Nur durch die Stabilisation der supramolekularen Struktur anhand des ausgeprägten π-Elektronensystems (**1c**) wird eine zweite kondensierte Phase (**1c** ***II***), mit stark verringerter molekularer Fläche, ermöglicht.

Die geringe Ausdehnung der molekularen Geometrie des Chromophors von **2** ermöglicht die für die Substitution **b** geringste A_0-Flächen bei gleichzeitig ähnlich zu **1b** gekippter supramolekularer Struktur (**2b** ***I*** in Abbildung 2.5 (B)). Ähnlich wie für **1c** ***I*** wird in **2c** ***I*** durch die bPh-Substitution die molekulare Geometrie verdreht und zusammen mit ausgeprägten ππ-Wechselwirkung kippt **2c** in der ersten kondensierten Phase deutlicher an, dies vergrößert die A_0-Fläche (vergleiche molekulare Struktur in Abbildung 2.5 (B)).

2.3 Spektrale Eigenschaften des Langmuir-Films

Abschließend soll durch Analyse der Signaturen im Emissionsspektrum, wie zum Beispiel mögliche spektrale Verschiebungen durch H- oder J-Aggregation oder Schwingungsprogression durch Packung- und Planarisierungseffekte[176], Aufschluss über die supramolekulare Struktur erhalten werden. Daher wurden die supramolekularen Strukturen der L-Filme der verschiedenen 4-Hydroxythiazole *in situ* bei Kompression mittels Emissionsspektroskopie untersucht. Nichtsdestotrotz wurden die folgenden, repräsentativen Emissionsspektren der bildgebenden supramolekularen Strukturen der Thiazol-Derivate in ihrer Gas-, Flüssig- (schwache molekulare Wechselwirkung) und kondensierten Phase (starke molekulare Wechselwirkung) mit den Emissionsspektren in Lösung verglichen. Anders als das in Lösung vollständig von Lösungsmittel umgebende Amphiphile kann es im L-Film mit sich, mit einem, oder beiden der Grenzflächen bestimmenden Medien (Wasser, Luft) interagieren. Mögliche spektrale Änderungen, hervorgehend durch die Stabilisierung niederenergetischer Zustände, bipolarer sowie ππ-Wechselwirkungen und Protonierung des Chromophor, kennzeichnen so einen Anstieg in der molekularen Ordnung durch Kompression.

Die L-Filme von **3a** und **b** (Abbildung 2.6) zeigen eine Blauverschiebung der Emission, also eine Stabilisierung hochenergetischer Zustände, bei verringerter Reorganisation durch Kompression. Im Falle von **3b** konnte gezeigt werden, dass derselbe Effekt selbstständig auch ohne Reduktion der Oberfläche eintritt und es sich damit um Aggregation eines LB-untauglichen Moleküls handelt. Dies bestätigt damit die, durch den Vergleich mit den Emissionsspektren in Lösung, die von der Π(A)-Isothermen vermutete Tendenz zur Aggregation des Chromophors im L-Film. Wiederum die Stabilisierung der supramolekularen Struktur des L-Films von **3c** durch bipolare sowie ππ-Wechselwirkungen und der damit verbundenen hohen Kompression bewirkt ein Stabilisieren niederenergetischer Zustände. Dies äußert sich durch eine bathochrome Verschiebung des Emissionsspektrums. Ähnlich starke intermolekulare Wechselwirkungen, gekennzeichnet durch schwingungsaufgelöste Emission der Monomere oder rotverschobene Emission von photoaggregierten Dimeren (Excimere), konnten für die jeweils zweiten kondensierten Phasen von **1c** und **2c** nachgewiesen werden. Die Emission von Excimeren wurde bereits in diesem Zusammenhang von Habenicht *et al.*[141] für die L-Filme von Pyridyl- und Pyrazinyl-4-Hydroxythiazol gezeigt. Eine Einführung einer SO$_3$H-Gruppe (**d**) für dieses Chromophor zeigte jedoch keinen spektralen Hinweis auf Erhöhung der supramolekularen Ordnung, obwohl dieses durch die zusätzliche Verankerung bei gleichzeitig hoher Kompression erwartet wurde.

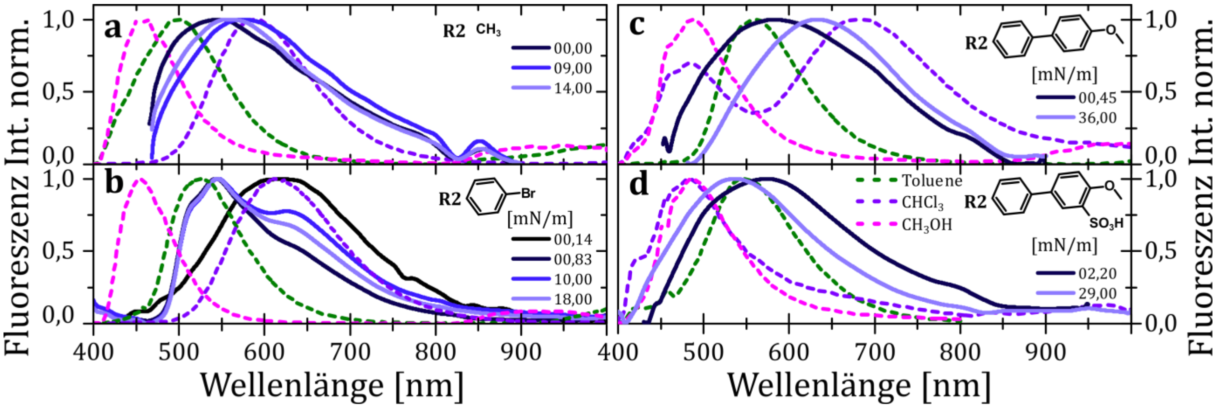

Abbildung 2.6: Normalisierte Emissionsspektren ($\lambda_{Anregung} = 405$ nm) von L-Filmen des 2-4-Nitrophenyl-4-Hydroxy-5-R2-1,3 Thiazols und einer Methyl (**a**), Phenyl-4-Bromo (**b**), Phenyl-4-Methoxyphenyl (**c**) und 3-Phenyl-4-Methoxyphenyl-3-Sulfonsäure (**d**) R2 Substitution und den jeweiligen Emissionsspektren der Moleküle in Lösung mit Toluol (Dunkelgrün), CHCl$_3$ (Violett) CH$_3$OH (Pink).

Mittels der Variation der Substituenten an der 2- und 5-Position des 4-Hydroxythiazols konnte, hier ausführlich am Beispiel von **3** dargestellt, ein Bild der supramolekularen Assemblierung mit intermolekularen Wechselwirkungen an der Wasser-Luft-Grenzfläche gezeigt werden. Dabei konnte vor allem durch den Vergleich zwischen spektralen Eigenschaften gelöster Amphiphile, deren L-Film sowie dessen $\Pi(A)$-Isothermen abschließend Aufschluss über dessen Assemblierung gewonnen werden. Damit wurde erfolgreich die Notwendigkeit der hier verwendeten ganzheitlichen Betrachtung von Emission in Lösung und im L-Film noch vor dem Abscheiden auf den LB-Film nachgewiesen. Während alle drei Thiazol-Derivate mit der Phenyl-4-Methoxyphenyl-Substitution Hinweise auf stabile L-Filme durch ππ- und bipolare

Wechselwirkungen zeigen (nähere Betrachtung in Kapitel 4 und 5), ist für die Phenyl-4-Bromo-Substitution jeweils nur durch eine zusätzliche Verankerung des Chromophors wie in **1** und **2** möglich. Die Verankerung der Chromophore weist unabhängig von der Substitution an der 2-Position keinen Hinweis auf zusätzliche Stabilität und Erhöhung der supramolekularen Struktur des L-Films auf. So wurde in diesem Kapitel mit der Untersuchung der spektralen Eigenschaften der Lösungen und Langmuir-Filme, der verschiedenen Variationen der funktionalen Substitution am 4-Hydroxythiazol Chromophors, eine Grundlage für weitere Betrachtungen hinsichtlich Filmbildung und deren thermodynamischer Stabilität geschaffen.

3 Einfluss der Anzahl, Art und Position der polaren Ankergruppen

Teile des Kapitels sind publiziert in [MLH2] Kaufmann, M.; Hupfer, M. L.; Sachse, T.; Herrmann-Westendorf, F.; Weiß, D.; Dietzek, B.; Beckert, R.; Presselt, M., *Journal of Colloids and Interface Science*, **2018**, 526:410-418.

Der nächste Schritt zur Aufklärung der Beziehung von molekularer Form und supramolekularer Struktur amphiphiler 4-Hydroxythiazole ist die Variation der Anzahl, Art und Position polarer Ankergruppen. Um den möglichen, durch die Gruppe in 2-Position des Thiazols induzierten, starken Wechselwirkungen mit der Subphase vorzubeugen, wurde das im vorrangegangenen Kapitel beschriebene Py-Derivat (**2**) gewählt und dessen Amphiphilie, bzw. polare Funktionalisierung an der 4-Hydroxy und 5-Position im Rahmen der Dissertation von Kaufmann[145] synthetisch variiert (siehe Abbildung 3.1). Dabei wurde die zentrale amphiphile Funktionalisierung durch eine terminale ersetzt (**4**). Dieses mit Sulfonamid (SO_2NH_2) und COOH polar funktionalisierte Molekül wird mit dem vereinfachten, unpolaren Chromophor und einer literaturbekannten[146] (**4a**, **b**) einfach polaren Variation, hinsichtlich Filmbildung und supramolekularen Orientierung des L- und LB-Films, verglichen. Das aus der Literatur bekannte Py-Thiazol ist dabei durch eine Methylacetat (**4a**) und Chloropropyl Seitenkette (**4b**)[146] zentral unpolar funktionalisiert. Mit diesen Thiazolen konnte bereits gezeigt werden, dass die Filmbildung dieser steifen, doppelt polaren Thiazole mit einer hohen Bandbreite der Kompressibilität einhergeht und damit unterschiedliche Abscheidebedingungen ermöglicht.

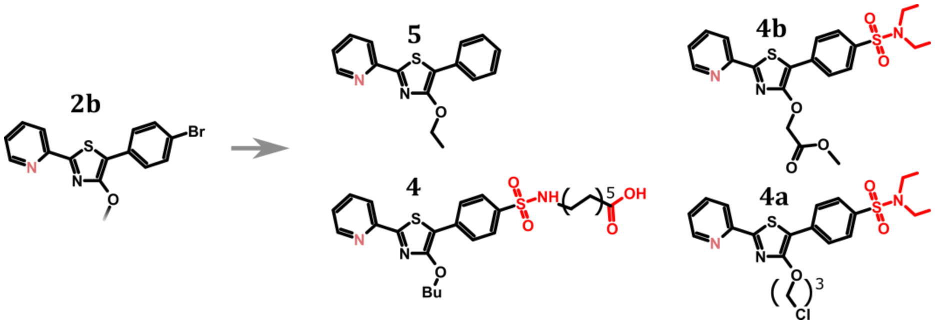

Abbildung 3.1: Schematische Übersicht der systematischen Variation in Art, Anzahl und Position polarer Ankergruppen des in Kapitel 2 verwendeten 2-Pyridyl Thiazoles zur 5-Phenyl-4-Alkoxythiazole Konfiguration mit (**5**) und ohne (**4**) Sulfonamid-Gruppe und den jeweils literaturbekannten einfach polar funktionalisierten Derivaten (**4a**, **4b**).

3.1 Supramolekulare Struktur im Langmuir-Film

Ausgangspunkt der Charakterisierung der supramolekularen Struktur des L-Films bildet die Π(A)-Isotherme (Abbildung 3.2 (A)), welche unter Zuhilfenahme der Kompressibilität (C_S) bzw. des Kompressibilitätsmodulus ($C_S^{-1} = -A\, d\Pi/dA$)[177-179] näher betrachtet wird. Wie bereits im vorrangegangen Kapitel gezeigt, kann die Py-Gruppe, der hierbei verwendeten Chromophore, als zusätzliche Ankergruppe fungieren und diese bei der supramolekularen Assemblierung an der Wasser-Luft-Grenzfläche unterstützen. Das unpolare und ohne klassische Ankergruppe versehene Referenzmolekül (**5**) weist eine nahezu homogene Verteilung des elektrostatischen Potentials (Abbildung 3.2 (B)) auf, was die fehlende Amphiphilie verdeutlicht. Der sich daraus ergebende L-Film lässt sich, aufgrund von 3D-Aggregation des komplanaren Chromophors, ohne erkennbare, kondensiert Phase komprimieren. Im Gegensatz dazu zeigen die steilen Anstiege der Π(A)-Isothermen von mit SO_2NH_2 funktionalisierten Py-Thiazole (**4a**, **4b**) deutliche kondensierte Phasen an, welche sich jeweils in C_S und kritischem Oberflächendruck (Π_K) unterschieden. Während C_S ein Maß der Komprimierbarkeit des L-Films ist und im Folgenden durch den C_S^{-1} dargestellt wird[152], gibt Π_K den Punkt des monomolekularen Kollapses an.[154]

Die Π(A)-Isothermen verdeutlichen, dass ein direkter Zusammenhang zwischen Steifheit der molekularen Form der amphiphilen Thiazole (**4 → 4a → 4b**) und des C_S^{-1} (Abbildung 3.2 (A)) der daraus resultierenden L-Film besteht. Der Vergleich zwischen der, mittels quantenchemischer Berechnungen bestimmten relaxierten, molekularen Geometrie und der aus der Π(A)-Isotherme errechneten A_0-Fläche verdeutlicht eine flache horizontale Anordnung des Moleküls zur Wasseroberfläche. Damit wird, anders als bei den einfach zentral an einer $(CH_2)_5$-Kette polar funktionalisierten Molekülen des vorrangengen Kapitels, das Chromophor durch die SO_2NH_2-, Py- und COOH-Gruppe zur Haftung an der Wasseroberfläche gezwungen. Nichtsdestoweniger konnte von Ahmida *et al.* in Bezug auf ein vierfach verankertes Porphyrin gezeigt werden, dass sich, bei Verlängerung der unpolaren, flexiblen Zwischenkette, dieses verankerte Moleküle vertikal aufrichten kann. Wegen der zusätzlichen langen $(CH_2)_{10}$-Kette startet die Π(A)-Isotherme von **4** bei deutlich größeren Flächen und weist einen geringeren Anstieg, also hohe Komprimierbarkeit im Vergleich zu **4a** und **b** auf. Besonders der steile Anstieg der Isotherme des molekular steifen **4b** zeigt den geringen Freiheitsgrad der supramolekularen Packung des L-Films bei gleichzeitig hoher Packungsdichte. **4** weist hingegen einen ähnlichen großen Wert für C_S^{-1} wie **4a** auf. Dieser wird aber über einen größeren Bereich molekularer Fläche erreicht. Somit ermöglicht das Separieren der zweiten polaren Gruppe vom Chromophor, mittels der zwischengeschalteten $(CH_2)_{10}$-Kette, eine langsame Filmbildung, welche wiederum eine geringere Tendenz zur lokalen Aggregatbildung aufweist. Zusätzlich kann diese molekulare Geometrie bei flacher supramolekularer Assemblierung ein leichtes Kippen des Chromophors durch Kompression (Vergleich supramolekulare Struktur Abbildung 3.2 (A)) ermöglichen.

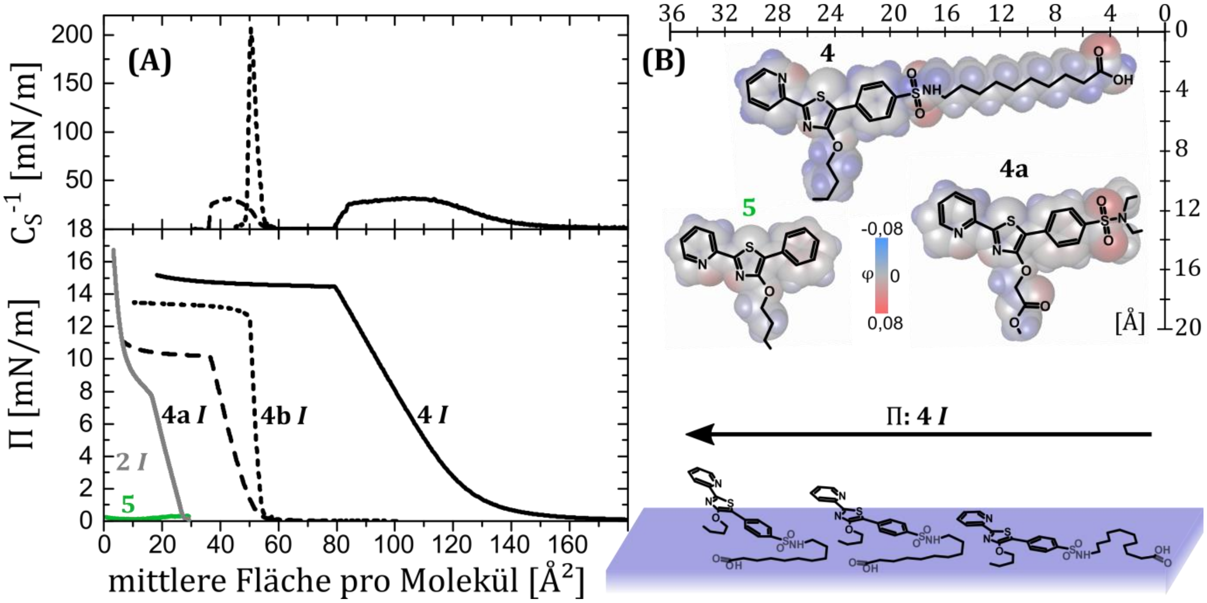

Abbildung 3.2: (A) Gemittelte Π(A)-Isotherme und Kompressibilität Modulus (C_S^{-1}) der 2-Pyridyl-5-Phenyl-4-Hydroxy-1.3 Thiazole ohne (**5**) (grün) und mit Sulfonamid-Gruppe (schwarz): **4** (durchgezogen), **4a** (gepunktet), **4b** (gestrichelt).

3.2 Supramolekulare Orientierung im Langmuir-Blodgett-Film

Es konnte gezeigt werden, dass sich die molekulare Orientierung des L-Films der verschiedenen polar verankerten Thiazole **4**, **4a** und **4b** unterscheidet. Damit variiert auch die Orientierung der Übergangsdipolmomente (*engl. transition dipole vector; TDV*) dieser Thiazole-Chromophore im L-Film[180-181]. Um die möglichen unterschiedlichen *TDV* von **4**, **4a** und **4b** zu untersuchen und auf die Orientierung der Chromophore rückschließen zu können, wurden die

L-Filme dieser Derivate *via* LB-Technik auf Quarzglas, bei verschiedenen Oberflächendrucken (Π_{LB}) der kondensierten Phase, abgeschieden. Aufgrund der hohen Fluoreszenzquantenausbeute bei gleichzeitig geringem Extinktionskoeffizienten wurden die LB-Filme mittels polarisationsabhängiger Fluoreszenzspektroskopie, anstelle der in der Literatur üblichen polarisationsabhängigen Absorptionsspektroskopie[100, 182-184], vermessen. Dafür wurde sowohl die Polarisation des anregenden als auch des emittierten Lichtes, wie in Abbildung 3.3 (A) abgebildet, variiert. Die Resultate dieser Messungen sind in den Spalten „I(α)“, „I(β) bei I(α)=max“ und „I(β) bei I(α)=min“ in Abbildung 3.3 (B) zusammengefasst. Jeder der LB-Filme zeigt eine ausgeprägte Abhängigkeit der Fluoreszenz von der Polarisation des eingestrahlten Lichtes. Damit unterscheidet diese sich von der jeweiligen, als isotrop angenommenen und durch Tropfbeschichtung hergestellten, Referenzprobe des Moleküls. Dieses ist dabei in einer Matrix aus Polymethylmethacrylat (PMMA, siehe graue Kreuze in Abbildung 3.3 (B)) eingebettet. Die Polarisationsabhängigkeit der Emission ist dabei ein grundsätzlicher Beweis einer Vorzugsorientierung der Moleküle in den hier verwendeten LB-Filmen.

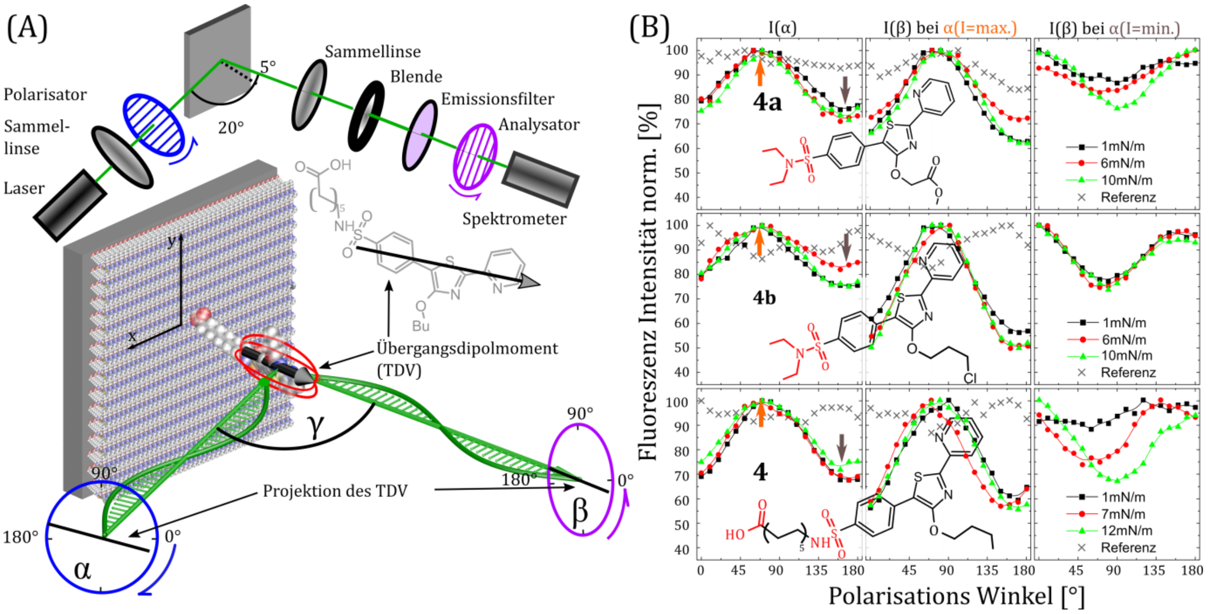

Abbildung 3.3: (A) Schematische Darstellung des Aufbaus zur Messung von Anisotropie mittels stationärer, polarisationsabhängiger Fluoreszenz und dessen Ergebnisse (B) von LB-Filmen bei verschiedenen Abscheidedrücken der kondensierten Phase von **4a, 4b, 4**.

Diese molekülunabhängige Vorzugsorientierung entspricht einem Polarisationswinkel von $\alpha = 70°$ ($I(\alpha)$=max). Unter der Annahme, dass die Moleküle wegen der Abscheidegeometrie (siehe Abbildung 3.3) entlang der Hauptachsen des Substrates orientiert sind, kann daraus eine um 20° von der Substratoberfläche geneigte Orientierung abgeleitet werden. Die geringe Abhängigkeit der Orientierung ($I(\alpha)_{max}$ - $I(\alpha)_{min} \approx 30\%$, $\alpha_{max} = 70°$) von dem verwendeten Π_{LB} lässt darauf schließen, dass durch Abscheidung mittels LB-Technik, eine Form von Umorientierung durch Molekül-Substrat-Wechselwirkungen stattfindet[185]. Die in einem perfekt orientierten, einheitlichen LB-Film ausgerichteten Moleküle müssten eine Fluoreszenzintensität bei senkrecht zum *TDV* polarisiertem eingestrahlten Licht von 0% aufzeigen, da durch diesen Polarisationswinkel kein Licht in der Schicht absorbiert wird. Jedoch lässt das Abweichen des Minimums von 0% darauf schließen, dass neben einer vorherrschenden Orientierung ein oder mehrere Domänen existieren. Dies wiederum steht im Einklang mit dem Modell kondensierter Phasen von L-Filmen gemäß Davies[152].

Um die jeweiligen supramolekularen Orientierungen des Chromophors innerhalb der Domänen zu charakterisieren, wurde der Polarisator im Maximum und Minimum der Fluoreszenzintensität fixiert und die Polarisation des emittierten Lichtes mit einem Analysator ($I(\beta)$) untersucht. Während $I(\beta)$ in der Phase der vorherrschenden Orientierung ($I(\alpha)$=max) für alle drei Moleküle keine Abhängigkeit von Π_{LB} aufweist, konnte für die Phase einer möglichen zweiten Domäne ein molekülabhängiges Ausrichten und ein Anstieg der supramolekularen Ordnung mit steigenden Π_{LB} nachgewiesen werden.

Somit zeigen die Moleküle des molekular steifen **4b** keine Abhängigkeit der molekularen Ordnung, also ihrer Anisotropie, von Π_{LB}. Hingegen konnte für **4**, welches eine hohe Flexibilität der molekularen Struktur besitzt und eine hohe C_S^{-1} aufweist, eine isotrope Orientierung am Anfang und eine anisotrope Orientierung am Ende der kondensierten Phase gezeigt werden. Damit kann durch die Einführung einer doppelt polaren Struktur, separiert durch eine $(CH_2)_{10}$-Kette, die supramolekulare Orientierung einer Nebendomäne durch Π_{LB} gesteuert werden. Der Einfluss dieser Substrat-Molekül-Wechselwirkungen auf die thermodynamische Stabilität wird im Vergleich zu den Molekül-Molekül-Wechselwirkungen im folgenden Kapitel 4 näher beleuchtet.

4 Einfluss der Länge der unpolaren Seitenkette

Teile des Kapitels sind publiziert in [MLH3] Hupfer, M. L.; Kaufmann, M.; Herrmann-Westendorf, F.; Sachse, T.; Roussille, L.; Feller, K.; Weiß, D.; Deckert, V.; Beckert, R.; Dietzek, B.; Presselt, M., *ACS Applied Materials and Interfaces*, **2017**, 9: 44181-44191

In Kapitel 2 wurde zunächst der Einfluss photoaktiver Funktionalisierungen durch Substitution an 2- und 5-Position der Thiazole **1**, **2** und **3** auf die Filmbildung und supramolekulare Struktur des L- und LB-Films untersucht. Dabei wurde der Einfluss der zentral substituierten (CH$_2$)$_5$-Kette mit COOH-Gruppe auf die Filmbildung vernachlässigt. Im folgenden Kapitel 3 konnte gezeigt werden, dass sich die Filmbildung durch eine (CH$_2$)$_{10}$-Kette eingeleitete molekulare Flexibilität gezielt steuern lässt.

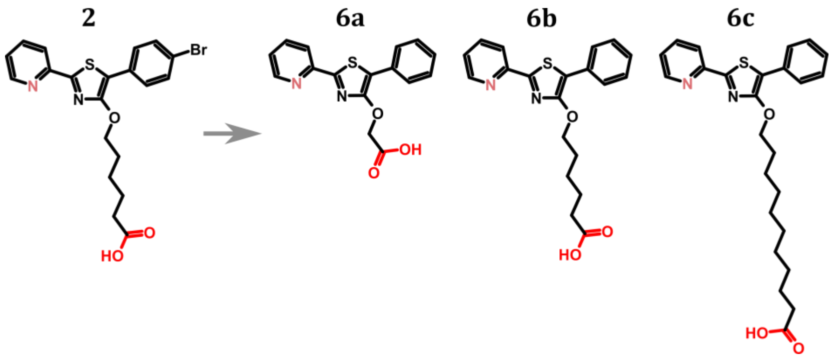

Abbildung 4.1: Schematische Übersicht der systematischen Variation der Länge der Alkylkette, welche das 2-Pyridyl-4-Hydroxy-5-Phenyl-1,3-Thiazol von der polaren Carbonsäure-Ankergruppe separiert.

In diesem Kapitel soll der Fokus auf der systematischen Variation der Länge der an der 4-Hydroxy-Position zentral funktionalisierten (CH$_2$)$_n$-Kette des Py-Ph-Derivates (**2**) liegen. Es soll hierbei die Filmbildung des L-Films und dessen supramolekulare Struktur untersucht werden. Dafür wurde die Anzahl der (CH$_2$)$_n$-Gruppen mit 1 (**6a**), 5 (**6b**) und 10 (**6c**) (siehe Abbildung 4.1) im Rahmen der Dissertation von Kaufmann[145] systematisch erhöht. Die dadurch ermöglichten supramolekularen Geometrien sollen sowohl im L- als auch im LB-Film hinsichtlich ihrer thermodynamischen Stabilität untersucht werden. Diese thermodynamische Stabilität der Moleküle im L- und LB-Film kann durch das zu starken ππ-Wechselwirkungen neigende Chromophor[186], abhängig von der supramolekularen Struktur, ermöglicht werden.[187]

So konnte Rong *et al.*[188] zeigen, dass ein stark verankertes (COOH-Ankergruppe) Porphyrin durch starke ππ-Wechselwirkung supramolekulare Keimstrukturen bildet, welche sich durch anschließendes thermisches Tempern im LB-Film zu ausgedehnten supramolekularen Strukturen umwandeln. Zur Untersuchung der Wechselwirkungen und der damit verbundenen thermodynamischen Stabilität wurden Kompressions- und Expansions-Π(A)-Isothermen[189-192] des L-Films sowie Absorptions- und polarisationsabhängige Fluoreszenzspektren der LB-Filme analysiert. Mit Letzterem soll untersucht werden, ob die supramolekularen Strukturen in einer thermodynamisch bevorzugten Geometrie direkt nach LB-Abscheidung vorliegen oder stattdessen durch Tempern in jene Geometrie überführt werden.

4.1 Supramolekulare Orientierung im Langmuir-Film

Die molekulare Geometrie des mit der kürzesten $(CH_2)_n$-Kette versehenen Moleküls **6a** ähnelt dem bereits im vorangegangenen Kapitel beschriebenen Thiazols **5**. Zugleich zeigt die Π(A)-Isotherme von **6a** (Abbildung 4.2 (A)) keine Abhängigkeit des Oberflächendrucks von der Kompression des L-Films. Das elektrostatische Potential wiederum verdeutlicht, dass die Trennung von Chromophor und COOH-Gruppe durch die kurze CH_2-Kette zu einem zu polaren Molekül führt, das aufgrund der damit verbundenen Wasserlöslichkeit für die LB-Technik ungeeignet scheint.

Die Π(A)-Isotherme von **6b** zeigt einen ähnlichen Verlauf wie das bereits in Kapitel 2 beschriebene Molekül **2b**. Beide unterscheiden sich nur durch das scheinbar grenzflächen-inaktive Brom an der 5-Phenyl-4-Position. Für die supramolekulare Struktur von **2b** wurde angenommen, dass die Py-Gruppe zunächst als zusätzlicher Anker zur Wassersubphase fungiert und das Molekül bei der aufrecht gekippten Assemblierung (vergleiche Abbildung 4.2 (B)) im L-Film unterstützt.

Die Π(A)-Isotherme des L-Films des mit dem längsten Abstandshalter (**6c**) funktionalisierten Moleküls zeigt, wie in Abbildung 4.2 dargestellt, ein deutlich mehrphasiges Verhalten an. Die erste kondensierte Phase (**6c *I***), die eine deutlich größere $A_{0,I}$-Fläche als **6b** aufweist, wird unter Betrachtung der molekularen Dimension einer flachen supramolekularen Struktur zugeordnet. Dieser ersten kondensierten Phase folgt ein Bereich großer Flächenreduktion bei gleichzeitig geringem Anstieg des Oberflächendrucks. Anders als das in der

Literatur angeführte Aufschieben von Multilagen der T-förmigen Flüssigkristalle[147-148, 151] mündet dieser als Übergangsphase (siehe Kapitel 2) beschriebene Teil der Π(A)-Isotherme in einer zweiten kondensierten Phase (**6c *II***) ($A_{0,I}/A_{0,II} \neq 2$ oder 3) des monomolekularen Films mit geänderter supramolekularer Struktur. Durch die Flächenreduktion des L-Films entsteht ein Kippen des Chromophors um die 4-Hydroxy-Gruppe (vgl. **6c *I*** *zu* **6c *II*** Abbildung 4.2 (B)). Die durchschnittliche Fläche pro Molekül wird also durch die locker auf der Wasseroberfläche schwimmende $(CH_2)_n$-Kette und der Länge des Chromophors bestimmt. Zudem konnte nachgewiesen werden, dass nach einer zweiten, kürzeren Übergangsphase eine dritte kondensierte Phase (mit weiter erhöhten Packungsdichten) (**6c *III***) folgt (siehe zusammengesetzte, gestrichelte Isotherme in Abbildung 4.2: (A)). Die hierbei erreichte, sehr kleine $A_{0,III}$-Fläche lässt sich nur schwer monomolekular begründen, da der Umfang des 4-Hydroxy-thiazol-Kerns größer als dem mittels Isotherme bestimmten Flächenbedarfes ist. Eine eventuell monomolekulare Struktur kann nur auf einer ausgestreckten $(CH_2)_{10}$-Kette, ähnlich der in **6b *I*** basieren, oder wie von Hawlik und Anderen[193-194] (für Fullerene ähnlichen Strukturmotivs) angeführten Anordnung in Zwischengitterplätzen beruhen.

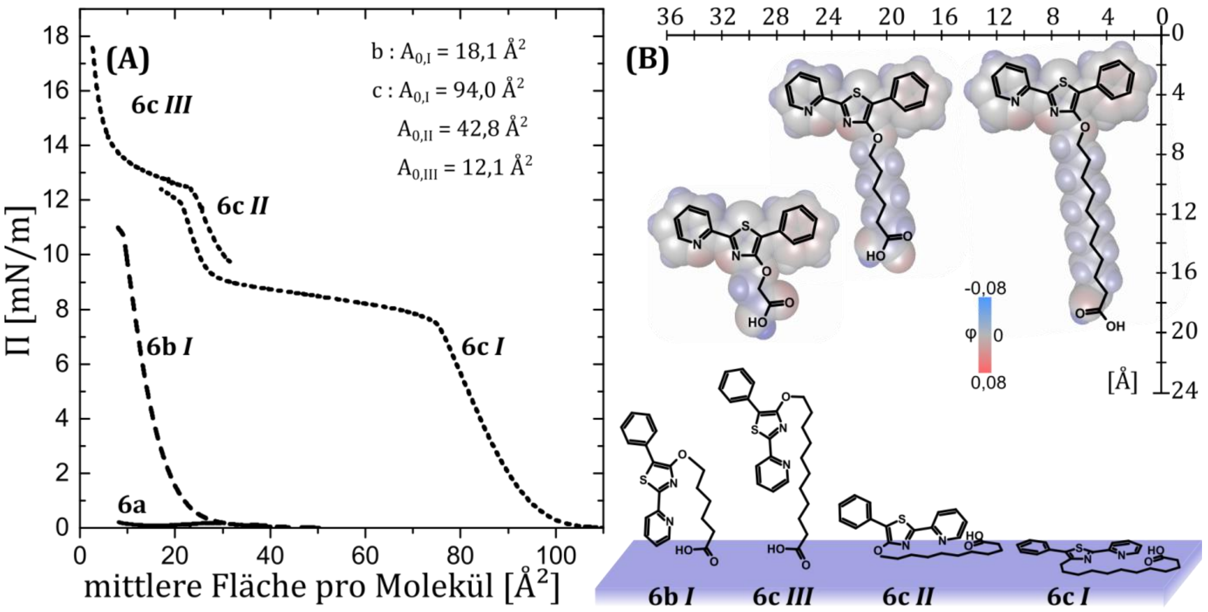

Abbildung 4.2: (A) Gemittelte Π(A)-Isotherme des zentral mit CH_2- (**6a**, durchgezogen), $(CH_2)_5$-(**6b**, gestrichelt), $(CH_2)_{10}$-COOH (**6c**, gepunktet) substituierten 2-Pyridyl-5-Phenyl-4-Hydroxy-1.3 Thiazols (B) Die aus der Π(A)-Isotherme bestimmten möglichen molekularen Orientierung, zusammen mit der molekularen Geometrie (exemplarisch für **6c**), deren Dimension und den elektrostatischem Potential über der Van-der-Waals Oberfläche.

4.2 Thermodynamische Stabilität des Langmuir-Films

Die oben erläuterten supramolekularen Strukturen der Py-Derivate **6b** und **6c** repräsentieren unterschiedliche Arten und Ausprägungen intermolekularer Wechselwirkungen. Diese können durch gezieltes Ansteuern des für die jeweilige kondensierte Phase charakteristischen Oberflächendrucks untersucht werden. Durch die Bildung der bei Raumtemperatur (RT) (25.18 - 25.44 meV) thermodynamisch stabilen Strukturen bzw. Aggregate bei Kompression (K) des L-Films kann bei nachfolgende Expansion (E) und weiterer K-E-Zyklen eine Hysterese der Π(A)-Isotherme auftreten.[195] Dabei kann die Energie (Gibbs'sche Energie G), die über Kompression in den L-Film überführt wird, direkt durch die Flächenänderung zwischen zwei aufeinander folgenden Π(A)-Isothermen gemäß der aus LB-Mischbarkeitsexperimenten[155] bekannten Formel $G = \int_0^{\Pi} A d\Pi$ bestimmt werden.

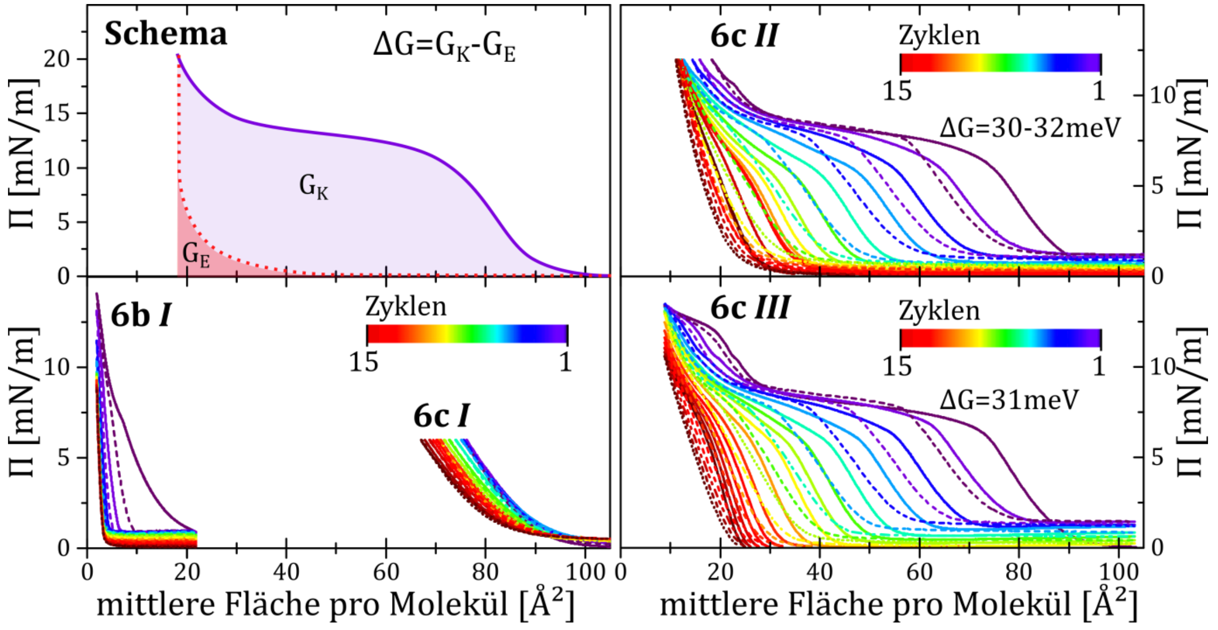

Abbildung 4.3: Schematische Darstellung zur Bestimmung der Gibb´schen Energie von Kompression (G_K) und Expansion (G_E) über das Integral der Π(A)-Isotherme sowie der Bestimmung der Bindungsenergie (ΔG); Gemessene Kompressions (K) (durchgezogen) - und Expansionszyklen (E) (gestrichelt) (15) des Langmuir-Films von **6b** und **c** für die individuellen kondensierten Phasen (***I***, ***II***, ***III***) der jeweiligen Π(A)-Isotherme.

Im Falle von **6b** verringert sich die $A_{0,I}$-Fläche innerhalb des ersten K-E-Zyklus von 18.1 Å² zu 4 Å² und konvergiert bei ungefähr 3 Å (vgl. Abbildung 4.3). Diese sehr kleinen Flächen können, vor allem im Vergleich zur molekularen Dimension, keiner monomolekularen Anordnung eines 2D-Films zugeordnet werden. Daher ist anzunehmen, dass durch Kompression des L-Films 3D-Aggregate, wie zum Beispiel Mizellen, ausgebildet werden. Der damit thermodynamisch instabile L-Film von **6b *I*** wird daher im Folgenden nicht weiter betrachtet.

Im Falle von **6c *I*** werden aufgrund der horizontalen supramolekularen Anordnung (Kannte zu Kannte) nur geringe molekulare Wechselwirkungen erwartet. Nichtsdestotrotz konnte eine geringe Reduktion der $A_{0,I}$-Fläche (von 95 zu 85 Å² bei 15 KE-Zyklen) beobachtet werden. Im starken Kontrast dazu wird beim Ansteuern der zweiten kondensierten Phase (Π_{Ziel} = 12 mN/m) eine deutliche Reduktion der $A_{0,I}$- und $A_{0,II}$-Fläche erreicht. Daraus lässt sich ableiten, dass, innerhalb eines K-Zyklus zu **6c *II*** bei RT, stabile Aggregate geformt werden. Diese Aggregate sind zum einem durch starke ππ-Wechselwirkungen zweier Chromophore gebunden und zum anderen steigt deren Anzahl pro K-E-Zyklus bis hin zum vollständigen Verschwinden der Phase **6c *I***. Daher ist anzunehmen, dass die im L-Film gespeicherte Energie der Bindungsenergie von Dimeren des Moleküls entspricht. Diese kann somit durch die Differenz zwischen erster und letzter Kompression des L-Films und dessen Integration über den Oberflächendruck mit ΔG_{II}=30 - 32 meV ermittelt werden. Beim gezielten Ansteuern der dritten kondensierten Phase konnten sehr ähnliche Verläufe der K-E-Zyklen gezeigt werden. Die daraus abgeleitete Energie der Dimerisierung (ΔG_{III}=31.25 meV) unterscheidet sich zu der aus der zweiten kondensierten Phase kaum. Anders als für **6b** erlaubt im Falle von **6c *II*** und **6c *III*** die längere CH_2-Kette supramolekulare Strukturen, die thermodynamisch stabile L-Filme bilden.

4.3 Supramolekulare Orientierung im Langmuir-Blodgett-Film

Schlussendlich soll die thermodynamische Stabilität der aus den individuellen Phasen des L-Films abgeschiedenen supramolekularen Strukturen der LB-Filme von **6c** bestimmt werden. Dafür wird die supramolekulare Geometrie des LB-Films mittels der im vorangegangenen Kapitel 3 beschriebenen Polarisationsabhängigkeit der Fluoreszenz bei RT und deren mögliche Änderung durch thermisches Tempern untersucht. Wie bereits beschrieben hätte eine isotrope Verteilung der Moleküle eine fehlende Variation der Fluoreszenzintensität mit systematischer Variation des Polarisationswinkels von 0° bis 180° zur Folge. Entgegen dieser Vorstellung zeigt die, mittels Tropfbeschichtung hergestellte, isotrope Referenz des Farbstoffes in einer PMMA-Matrix (siehe graue Linie in Abbildung 4.4 (A)) ein deutliches Absinken der Fluoreszenzintensität. Dieses nicht alternierende Verhalten des Fluoreszenzsignals wird auf die Umorientierung der Moleküle bei gleichzeitigem Verstärken von statischer Fluoreszenzlöschung zurückgeführt. Jene Umorientierung von zufällig orientierten Molekülen in energetisch bevorzugtere supramolekulare Strukturen wird durch eine Art photo-induziertes Tempern, also durch thermalisierte absorbierte Energie, induziert und überlagert in abgeschwächter Form auch die Messungen der LB-Filme. Diese LB-Filme zeigen ein ausgeprägtes Maximum der Fluoreszenzintensität zwischen 75° und 95° Polarisation. Der durch die Differenz zwischen $I(\alpha)_{max}$ und $I(\alpha)_{min}$ definierte Fluoreszenzkontrast ΔI[2], welcher nahezu unabhängig vom Abscheidedruck Π_{LB} ist, beträgt zwischen 25 und 30% und weicht damit erneut stark von dem für einheitliche Orientierung idealen 100% ab. Ähnlich wie die bereits in Kapitel 3 beschriebenen Moleküle **4**, **4a** und **b** wird daher angenommen, dass sich die Signale mehrerer supramolekularer Geometrien überlagern. Dieses Model der Superposition konnte durch die Oberflächenanalyse, mittels Rasterkraftmikroskopie und der damit entdeckten Präsenz verschiedener Domänen (Unterschied in Höhe und Phasenwinkel) von LB-Filmen desselben Π_{LB}, bestätigt werden.

Die Domänen verschiedener supramolekularer Geometrien wurden durch einen fixierten Polarisator (90°, 180°) angesteuert und deren Emission bei Rotation des Analysators vermessen. Die Fluoreszenzintensität der Hauptdomäne ((B) $I(\beta,\alpha=90°)$ in Abbildung 4.4) zeigt sich, ähnlich wie für **4**, **4a** und **4b**, unabhängig von Π_{LB}. Jedoch weißt das Molekül **6c** einen deutlich verstärkten Kontrast (ΔI=55 und 65%) bei ähnlicher Verschiebung des Maximums, wie für α in Abbildung 4.4 (A), mit Erhöhung des Π_{LB} zu größeren β auf. Die Vorzugsorientierung der Moleküle verläuft also, wie in Kapitel 3 postuliert, nahe der Hauptachse y (siehe Abbildung 3.3) und wird durch die LB-Abscheidung bestimmt. Deren supramolekulare Ordnung wird, wie aus den geringen Unterschieden in ΔI ersichtlich, im Wesentlichen durch Selbstassemblierung und nicht durch Kompression des L-Films bestimmt. Im Gegensatz dazu zeigt die durch $I(\beta,\alpha=180°)$ angesteuerte Nebendomäne einen deutlichen Anstieg in ΔI mit Π_{LB} bei gleichzeitigem Wechsel des Maximums (150 zu 180°) von **6c *I*** zu **6c *II*.** Diese in x- oder z-Achse der Substratebene liegende supramolekulare Struktur wird, wie bereits zuvor für **4 *I***, **4a *I*** und

---

[2] Mit Bezug auf das polarisationswinkelabhänige Maximum normierter Fluoreszenzintensitäten

b *I* beobachtet, durch Druck verdreht. Die leichte Reduktion des ΔI für I(β,α=90, 180°) von Π_{LB} = 12 zu 14 mN/m weist darauf hin, dass die 2D geordnete supramolekulare Struktur beim Wechsel von der zweiten in die dritte kondensiert Phase zerstört wird.

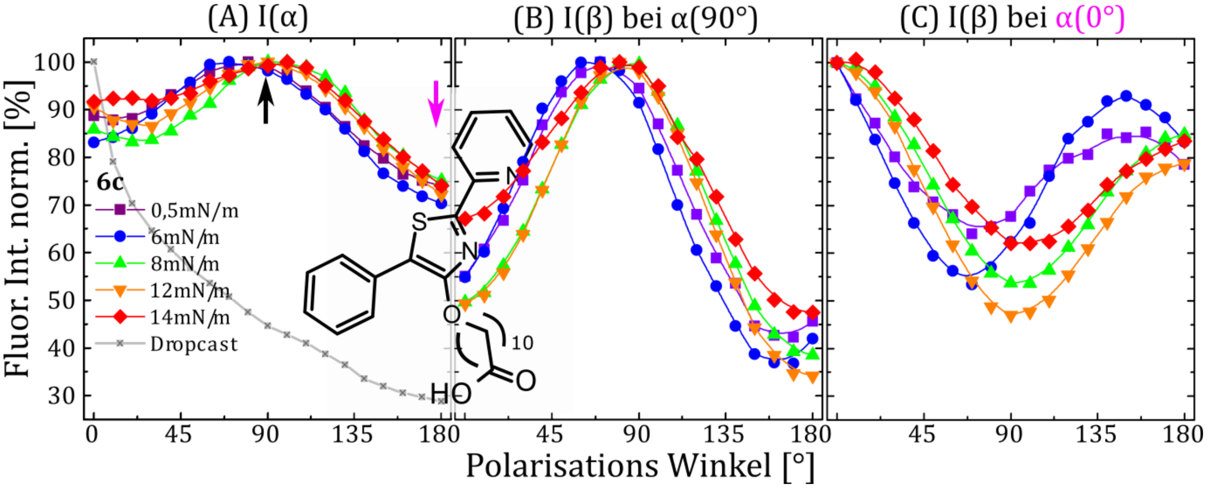

Abbildung 4.4: Stationäre, polarisationsabhängige Fluoreszenz von LB-Filmen von **6c** bei 5 unterschiedlichen Abscheidedrücken Π_{LB} (0,5, 6, 8, 12, 14 mN/m) im Vergleich mit einer durch Tropf-Beschichtung (**6c** in PMMA Matrix, graue Linien) hergestellten isotropen Referenz. Die Messungen (schematische Darstellung des Versuchsaufbaus in Abbildung 3.3) wurden ausgeführt ohne Analysator (A), Anregung bei 90° (B) und 0° (C) Polarisation und Rotation eines Analysators (B und C).

4.4 Thermodynamische Stabilität des Langmuir-Blodgett-Films

Nachfolgend gilt es nun die thermodynamische Stabilität der identifizierten zwei-, oder mehrdomänigen LB-Filme von **6c** zu untersucht. Dafür wurde die Fluoreszenzintensität I(β), fixiert bei α (90°, 180°) vor und nach einem kurzen Temperschritt (50°C, 15 min) verglichen. Die Variation von I(β) nach thermischem Tempern weist somit auf mögliche Umorientierung zu thermodynamisch bevorzugten supramolekularen Geometrien hin.

Wie in Abbildung 4.5 ersichtlich ändert sich der Verlauf von I(β) durch das thermische Tempern kaum. Allerdings konnte gezeigt werden, dass sich das photo-induzierte Tempern der Schichten reduziert. Für die aus der Flüssigphase (**6c *liq***) abgeschiedenen Moleküle, mit supramolekularen Geometrien geringer molekularer Wechselwirkungen, reduziert das thermische Tempern das photo-induzierte Tempern nur für die Nebendomäne (α = 180°). Wiederum für die zusammengebrochene supramolekulare 2D-Struktur von **6c *III*** wird dieser Effekt sowohl in der Haupt- als auch in der Nebendomäne beobachtet. Für die relativ hochgeordneten Filme von **6c *II*** beeinflusst das thermische Tempern nur die Nebendomäne. Unter den gegebenen Parametern des Temperns zeigte sich der aus **6c *I*** abgeschiedene LB-Film am stabilsten. Das photo-induzierte Tempern dieses Films ist nahezu vernachlässigbar, während zusätzlich I(β) keine Veränderung durch thermisches Tempern zeigt. Die aus dieser ersten kondensierten Phase der Π(A)-Isotherme abgeschiedenen Moleküle weisen eine supramolekulare Struktur mit starken Wechselwirkungen zur Substratoberfläche, bei gleichzeitiger dichter molekularer Packung, auf. Diese führt zu stabilen Filmen nach Abscheidung.

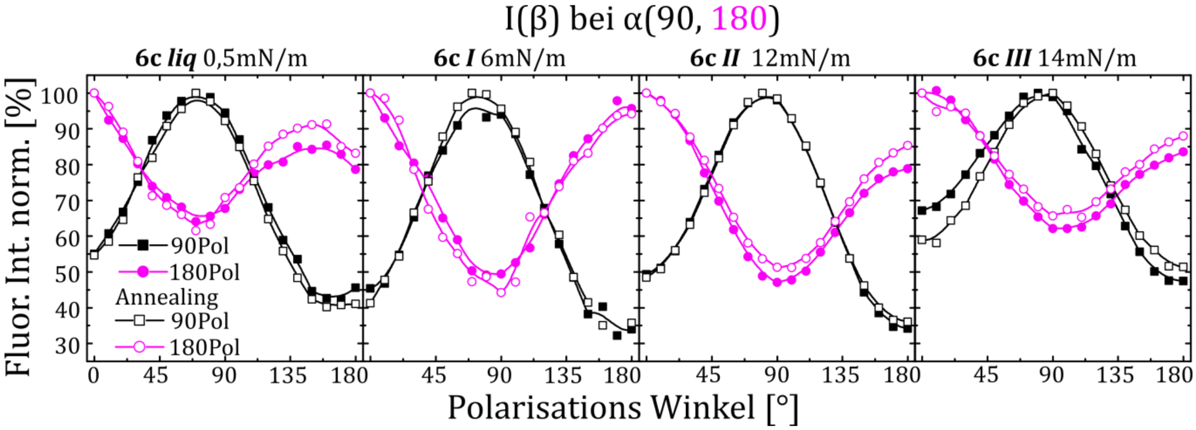

Abbildung 4.5: Stationäre polarisationsabhängige Fluoreszenz I(β) von LB-Filmen von **6c** bei 4 unterschiedlichen Abscheidedrücken Π_{LB} (0,5, 6, 12, 14 mN/m) bei α=90° (schwarz) und 180° (pink) vor (geschlossene Symbole) und nach(offene Symbole) Tempern (50°C, 15 min.).

Im Zuge der Untersuchungen dieses Kapitels wurden zum ersten Mal sowohl die thermodynamische Stabilität des L- als auch LB-Films desselben Amphiphils verglichen. So konnte **6c,** mittels Ansteuern verschiedener kondensierten Phasen des L-Films, die Abhängigkeit der Π(A)-Hysterese von den unterschiedlichen intermolekularen Wechselwirkungen[196-198] (ππ und London-Dispersion) gezeigt werden. Es wurde mittels Π(A)-Hysterese somit demonstriert, dass sich unter RT stabile Aggregate durch Ansteuern von **6c *II*** und ***III*** (ππ-Wechselwirkung) bilden. Die Untersuchung der supramolekularen Geometrie der LB-Filme von **6c** offenbarte eine eventuelle Umorientierung bzw. das Erhöhen der supramolekularen Ordnung gemäß Rong *et al.*[188]. Es zeigte aber auch ein Zusammenbrechen der 2D Ordnung durch Ansteuern von **6c *III***. Gerade intermolekulare Wechselwirkungen der Moleküle mit dem

Substrat in LB-Filmen von **6c *I*** zeigen, sowohl in der Haupt- als auch Nebenphase, thermodynamische Stabilität.

5 Einfluss der Art der unpolaren Seitenkette

Teile des Kapitels sind zur Publikation eingereicht in [MLH4] Hupfer, M. L.; Kaufmann, M.; May, S.; Preiß, J.; Weiß, D.; Dietzek, B.; Beckert, R.; Presselt, M., *Physical Chemistry Chemical Physics*, submitted , **2019**, und publiziert in [MHL5] Hupfer, M. L.; Kaufmann, M.; Roussille, L.; Preiß, J.; Weiß, D.; Hinrichs, K.; Deckert, V.; Dietzek, B.; Beckert, R.; Presselt, M., *Langmuir* **2019**, 35 (7), 2561-2570

Wie in Kapitel 2 gezeigt, unterstützt die Einführung einer Elektronen-schiebenden $N(CH_3)_2$-Gruppe (**1**) (*engl. Push*) (siehe Abbildung 5.1) die supramolekulare Assemblierung von L-Filmen des 4-Hydroxythiazoles und dient als polare Ankergruppe zur Wassersubphase. Wiederum eine bipolare Substitution mit einer Elektronen-ziehenden (*engl. Pull*) NO_2-Gruppe an der 2- und -schiebenden bPh-CH_3O Gruppe an der 5-Position (**3c**) (siehe Abbildung 5.1) zeigte, dass diese Kombination den L-Film bei hohen Kompressionen stärker stabilisiert. Im nachfolgenden Kapitel 4 wurde der Einfluss der Länge der unpolaren $(CH_2)_n$-Kette zwischen dem nahezu unpolaren Py-substituierten Chromophor (**6**) und polarem COOH-Anker auf die supramolekulare Struktur und thermodynamische Stabilität von L- und LB-Film gezeigt. Diese unpolare Kette, welche bisher nur der Amphiphilie diente, kann je nach supramolekularer Geometrie (vgl. **6c *I*, *II*, *III***) in einem LB-Film elektrisch isolierend wirken. So kann bei ausgestreckter $(CH_2)_{10}$-Kette durch deren isolierende Wirkung der Ladungsträgertransfer vom Chromophore über die Ankergruppe in das Substrat geblockt werden. Neben der sich aus der supramolekularen Struktur ergebenden thermodynamischen Stabilität, sind jedoch die (opto)elektronischen Eigenschaften wie Absorption, Emission und elektrische Leitfähigkeit maßgeblich für den Einsatz eines Farbstoffes in einem (opto)elektronischen Bauteil.

In diesem Kapitel sollen jene (opto)elektronischen Eigenschaften, allen voran die Leitfähigkeit, und deren Abhängigkeit von der molekularen sowie supramolekularen Geometrie, untersucht werden. Dafür wurden die oben genannten Erkenntnisse über supramolekulare Assemblierung aus Kapitel 2 durch die Verwendung eines bipolaren $N(CH_3)_2$- und NO_2-substituierten Thiazols kombiniert (siehe Abbildung 5.1). Die supramolekulare Assemblierung bipolarer Farbstoffe ist wiederum ein etabliertes Themengebiet in den grundlegenden Arbeiten von Kasha[176], in welcher die spektralen Verschiebungen verschiedenster Aggregate (H-, J-Aggregation) erarbeitet wurden. Würthner und andere[49, 59-60] machen sich diese bipolaren Wechselwirkungen zu Nutze um 3D supramolekulare Strukturen durch Selbstassemblierung zu bilden. Somit sollen sowohl optische als auch elektronische Eigenschaften von organischen Halbleitern kontrolliert werden. Das in diesem Kapitel angewandte bipolare Strukturmotiv soll wiederum durch damit verbundene intermolekulare Wechselwirkungen zur Stabilisierung des L-Films beitragen. Grundlegende Auswirkungen von nicht-kovalenten Wechselwirkungen (ππ, bipolar) auf die supramolekulare Struktur wurden von Tang *et al.*[187] in Bezug auf ein I-förmiges Strukturmotiv von Azobenzenen erforscht. Diese Azobenzene neigten bei Erhöhung der Bipolarität zur Verringerung der ππ-Wechselwirkung und der damit verbundenen Destabilisierung des L-Films. Das in diesem Kapitel verwendete und von Kaufmann[145] synthetisierte bipolare T-förmige *Push-Pull* Chromophor soll des Weiteren zentral sowohl mit einer alkylischen ($(CH_2)_{5,10}$) als auch arylischen (Ph) unpolaren Zwischenkette funktionalisiert werden. In einer supramolekularen Assemblierung kann somit zum einen die Anbindung durch die Substituenten des Chromophors und zum anderen auch die Anbindung über die Ankergruppen (COOH) mit leitfähiger Ph-Gruppe (konjugiertes π-System) an das Substrat, eine elektrische Leitfähigkeit durch die supramolekulare Struktur gewährleistet werden.

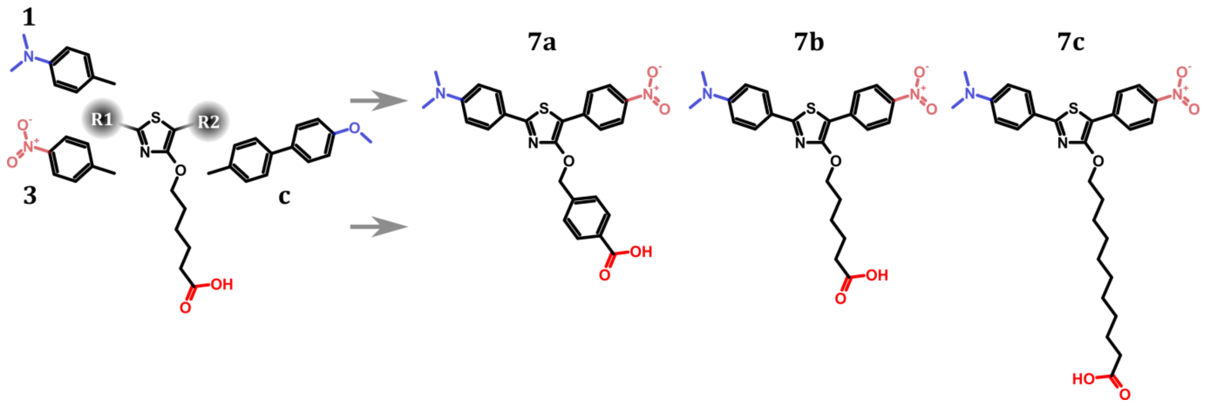

Abbildung 5.1: Schematische Übersicht der im Kapitel verwendeten Moleküle und systematischer Variation der Länge und Art der unpolaren Kette, welche das 2-4-N,N-Dimethylaminophenyl-4-Hydroxy-5-2-Nitrophenyl-1,3-Thiazole von der polaren Carbonsäure-Ankergruppe separiert.

5.1 Wechselwirkungen in Lösung

Wie bereits in Kapitel 2 gezeigt, kann der Vergleich von Absorptions- und Emissionsspektren der bipolaren Moleküle in Lösung verschiedener polarer Lösungsmittel einen entscheidenden Einblick in mögliche intra- und intermolekularer Wechselwirkungen geben. Anders als für die flexiblen $(CH_2)_n$-Ketten, ermöglicht sowohl die Interaktion der

Ph-Gruppe mit dem π-System des Chromophors als auch die dadurch entstehende Biegung der Chromophorstruktur eine intramolekulare Störung des π-System. Diese Störung kann starke spektrale Veränderungen in Absorption und Emission hervorrufen. Daher wurden die spektralen Eigenschaften von **7a** und **b** in Lösung (Toluol, Tetrahydrofuran, Ethylacetat, Dimethylsulfoxid) untersucht und wiederum mit quantenchemischen Rechnungen verglichen.

Die in Abbildung 5.2 gezeigten Extinktionskoeffizienten-(ε(λ))-Spektren von **7b** weisen das für 4-Hydroxythiazole mit *Push-Pull*-Charakter[140-142] typische einfache Absorptionsmaximum (~450 nm) auf. Verglichen zu den einzelnen *Push*- und *Pull*-substituierten Thiazolen **1** und **3** aus Kapitel 2, zeigt *Push-Pull*-Thiazol **7b** ein ähnlich hohes ε. Im Gegensatz zu der für die 4-Hydroxythiazole üblichen positiven Solvatochromie[163] der Emission zeigt die Lösungsmittelpolarität kaum Einfluss auf die Absorption.

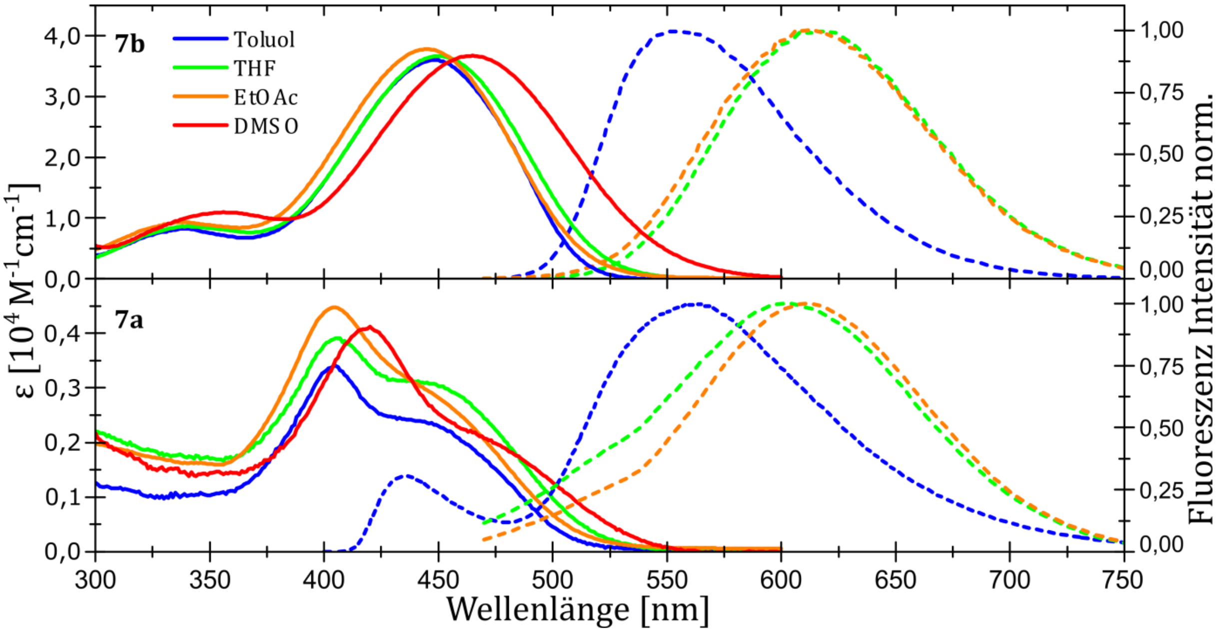

Abbildung 5.2: Extinktionskoeffizient- (ε) (durchgezogen) und normierte Emissionspektren ($\lambda_{\text{Anregung}}$ = 405; 450 nm) (gestrichelt) von 7b und a in Cyclohexan (Lila), Toluol (Blau), Tetrahydrofuran (THF, grün), Ethylazetat (EtOAc, orange), Dimethylsulfoxid (DMSO, rot).

Hingegen weisen die ε(λ)-Spektren von **7a**, neben dem für **7b** gezeigten typischen Absorptionsmaximum zum einen ein zusätzliches blauverschobenes (~405 nm) Fluoreszenzmaximum und zum anderen eine deutliche Reduktion des Extinktionskoeffizienten auf. Diese Effekte können durch verschiedene Konformere entstehen und neben dem energetisch günstigen Konformer koexistieren, wobei deren chromophores System durch Wechselwirkungen mit der Ph- oder COOH-Gruppe beeinflusst wird. Weiterhin wird der Einfluss zwischenmolekularer Wechselwirkungen als Ursache für die spektralen Unterschiede zwischen **7a** und **7b** untersucht. Zur vollständigen Aufklärung des Ursprungs beider Effekte werden jedoch zunächst die quantenchemischen Berechnungen[3] betrachtet.

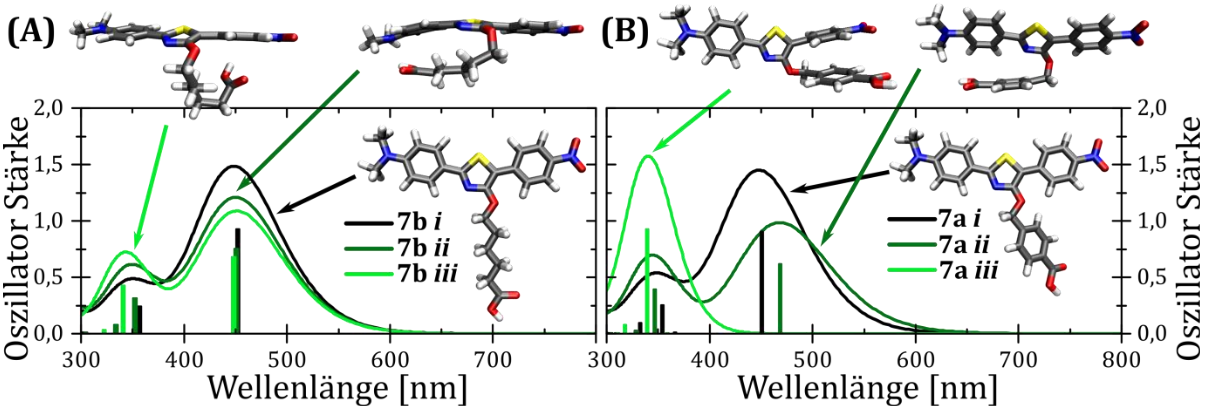

Abbildung 5.3: TD-DFT errechnete Absorptionsspektren der verschiedenen Konformere von **7a** und **b**.

Aus diesen Berechnungen, dargestellt in Abbildung 5.3, ergaben sich drei verschiedene Arten von Konformeren, bei der entweder keine (***i***), Ph-COOH—N(CH_3)$_2$-Ph Säure-Base (***ii***), oder Ph-COOH—NO_2-Ph bzw. Ph—Ph (***iii***) Wechselwirkungen (Störung des π-Systems) auftraten. Im Falle von ***i*** wird ersichtlich, dass die vom π-System elektronisch entkoppelten Seitenketten von **7a *i*** und **7b *i*** die Absorption des *Push-Pull*-Thiazols nicht beeinflussen. Die Säure-Base-Wechselwirkungen haben für **7a *ii*** und **7b *ii***, zusammen mit den damit verbundenen ππ-Wechselwirkungen, nur eine geringe Reduktion der Elektronendichte der N(CH_3)$_2$-Gruppe und Oszillatorstärke zur Folge. Es zeigte sich, dass die Interaktion der Seitenkette und des COOH-Ankers mit dem Chromophor für **7b *iii*** nur geringfügige spektrale Verschiebungen bzw. eine weitere Reduktion der Oszillatorstärke einzelner Übergänge hervorruft. Dieser Effekt wird allerdings deutlich durch die Präsenz der Ph-Gruppe und den daraus resultierenden ππ-Wechselwirkung in **7a *iii*** verstärkt.

---

[3] Es wurden dafür selbstständig Skripte ausgeführt, welche Martin Presselt entwickelte.

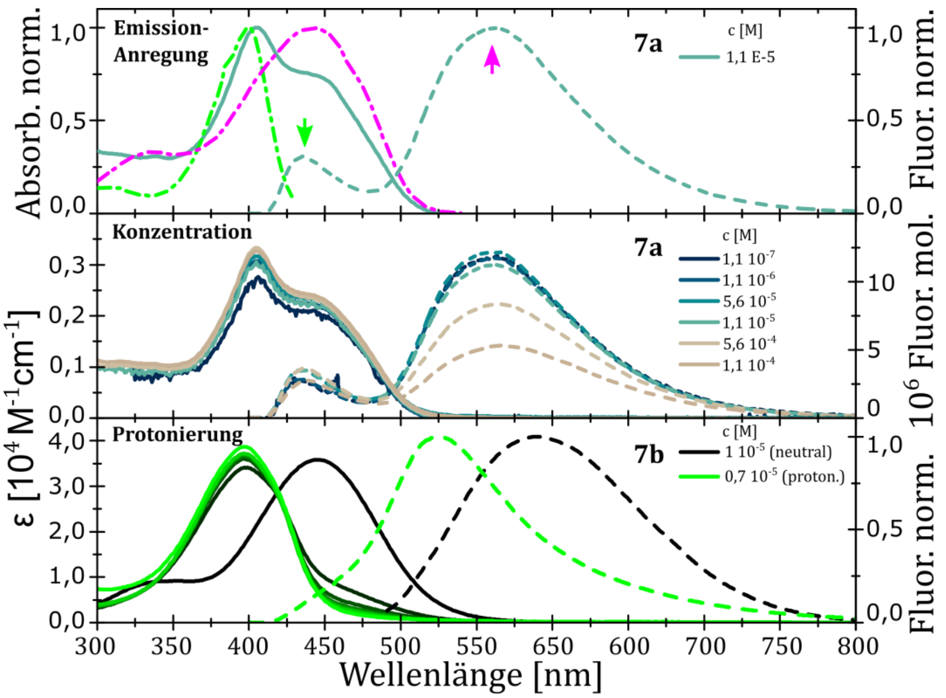

Abbildung 5.4: (oben) Normiertes Emissions-Anregungsspektrum von **7a** bei $\lambda_{em} = 430$ (grün) und 560 nm (pink) mit der jeweiligen normierten Absorption und Emission in Toluol (c = 1.1 10-5M). (mittig) Spektren des Extinktionskoeffizient (ε) und der molaren Emission in Abhängigkeit der Konzentration von c = 1.1 10-4 (dunkelblau) bis 1.1 10-7M (grau) von **7a**. (unten) Der Übergang der Spektren des Extinktionskoeffizient (ε) und der normierten Fluoreszenz der neutralen (schwarz) zur protonierten (grün) Spezies von **7b** und den jeweiligen Zwischenschritten.

Einen abschließenden Hinweis des Ursprungs der spektralen Unterschiede von **7a** und **b** geben die Emissionsspektren beider Moleküle (Abbildung 5.2). Diese zeigen unter Anregung der gemeinsamen Spezies (λ_{exc} = 450 nm) dasselbe spektrale Verhalten, wie eines der positiven Solvatochromie folgendem Emissionsmaximums (λ_{em} = 550-620 nm) des relaxierten *Push-Pull*-Monomers (*i*). Wiederum eine Anregung der zusätzlichen blauverschobenen Spezies von **7a** erzeugt zusätzlich eine, im Vergleich zur *Push-Pull*-Spezies, ebenfalls blauverschobene (430 nm), deutlich separierte Fluoreszenzbande geringerer konzentrationsunabhängiger Intensität. Durch Emissions-Anregungsspektroskopie (siehe Abbildung 5.4 (A)) konnte das Modell zweier vorhandener Spezies bestätigt werden. Aufgrund der konzentrationsunabhängigen Absorption und Emission der zusätzlichen Spezies (λ_{exc} = 400 nm, λ_{em} = 435 nm, siehe Abbildung 5.4 (B)) wird eine eventuelle H-Aggregation ausgeschlossen. Durch gezielte Protonierung der $N(CH_3)_2$-Gruppe des Chromophors (siehe Abbildung 5.4 (C)) konnte, am Beispiel von **7b**, ein ähnliches spektrales Verhalten wie bei der zusätzlichen Spezies von **7a** gezeigt werden. Daraus folgt, dass für **7a** neben der für **7b** bekannten Spezies *i* eine zusätzliche konformere Spezies existiert. In dieser Spezies sind über intramolekulare ππ-Wechselwirkungen der Ph-Zwischenkette und dem π-System die Säure-Base-Wechselwirkungen der $N(CH_3)_2$- und COOH-Gruppe stabilisiert und protonieren die $N(CH_3)_2$-Gruppe des Chromophors.

5.2 Supramolekulare Orientierung im Langmuir-Film

Aus dem Vergleich der experimentell und theoretisch ermittelten Absorption- und Emissionsspektren wird deutlich, dass bereits in Lösung eine intramolekulare Wechselwirkung in **7a** im Gegensatz zu **7b**, unabhängig von der Polarität des Lösungsmittels, stattfindet. Um den Einfluss dieser Wechselwirkungen und des bipolaren Strukturmotivs auf die Assemblierung und supramolekulare Struktur an der Wasser-Luft-Grenzfläche zu untersuchen, wurden die Π(A)-Isothermen der drei *Push-Pull*-Thiazole (**7a**, **b**, **c**) aufgenommen. Dabei wurde, wie bereits in den vorangegangen Kapiteln, zur Ermittlung der supramolekularen Struktur die A_0-Fläche der individuellen kondensierten Phasen der Π(A)-Isothermen mit der durch quantenchemische Berechnungen bestimmten relaxierten, molekularen Geometrie und dem elektrostatischen Potential verglichen. Ziel ist es eine für **7a**, **b**, **c** ähnliche supramolekulare Struktur des L-Films zu finden, deren elektrische Eigenschaften in abgeschiedenen LB-Filmen untersucht werden können.

Die in Abbildung 5.5 (A) dargestellte Π(A)-Isotherme von **7b** zeigt**,** wie bereits in Kapitel 2 (vergleiche Isotherme **1b**, **2b** und **3b**) berichtet, einen Anstieg des Oberflächendrucks bei einer durchschnittlichen Molekülfläche unter 50 Å². Eine so kleine Fläche weist darauf hin, dass sich das T-förmige, dreifach polare Molekül nicht mit einer horizontal zur Oberfläche liegenden flachen (vergleiche **6c *I***), sondern vertikal gekippten supramolekularen Struktur in der ersten kondensierten Phase assembliert (vergleiche **1b *I***). In dieser zweifach verankerten supramolekularen Struktur wirkt die $N(CH_3)_2$-Gruppe, ähnlich wie für **1b**, neben der COOHGruppe als zweiter Anker (vergleiche supramolekulare Struktur in Abbildung 5.5 (A) **7b *I***) zur Wassersubphase. Anders als für **1b** wird durch die bipolaren Wechselwirkungen von den $N(CH_3)_2$- und NO_2-Gruppen zweier *Push-Pull*-Thiazole jene supramolekulare Struktur des L-Films stabilisiert und durch Kompression eine zweite kondensierte Phase (**7b *II***) der Π(A)-Isotherme ermöglicht. Die kleine A_0-Fläche jener kondensierten Phase deutet darauf hin, dass durch die flexible Zwischenkette begünstigt eine versetzte Anordnung der *Push-Pull*-Thiazol vorherrscht, welche eine J-Typ bipolare Anordnung erzeugt. Π(A)-Hysterese Experimente zeigen wiederum im Vergleich zu **6b**, dass diese bipolaren Wechselwirkungen die thermodynamische Stabilität des 2D-Films gewährleisten. Anders als in dem von Tang *et al.*[187] angeführten bipolaren I-förmigen Strukturmotiv verschiedener Azobenzene konnte durch die Einführung der Bipolarität am Querbalken des T-förmigen Strukturmotivs unterschiedliche supramolekulare Strukturen mit verstärkter thermodynamischer Stabilität im L-Film erreicht werden.

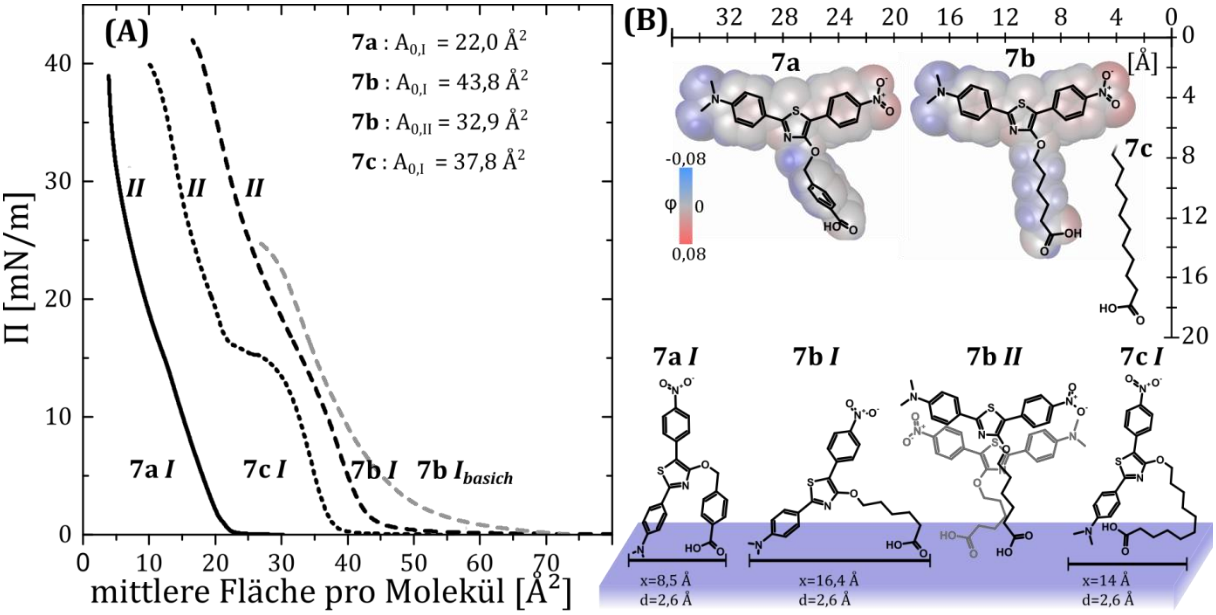

Abbildung 5.5: Gemittelte Π(A)-Isotherme des zentral mit arylisch (**7a**, durchgezogen), alkylisch $(CH_2)_5$- (**7b**, gestrichelt), $(CH_2)_{10}$-COOH (**7c**, gepunktet) substituierten 2-(4-N,N-Dimethylaminophenyl)-4-Hydroxy-5-Nitrophenyl-1,3Thiazoles (B). Die aus der Π(A)-Isotherme bestimmten möglichen molekularen Orientierungen der Moleküle in den jeweiligen kondensierten Phasen zusammen mit der molekularen Geometrie, deren Dimension und dem elektrostatischen Potential über der Van-der-Waals Oberfläche (exemplarisch für **7a** und **b**).

Im Vergleich zu **7b** weist die Π(A)-Isotherme von **7c** zum einen eine kleinere Fläche sowie zum anderen zwei, deutlich durch eine Übergangsphase (siehe Kapitel 2) getrennte, kondensierte Phasen auf. Die erste kondensierte Phase ist wiederum durch eine zweifach verankerte supramolekulare Struktur geprägt, bei der aber, anders als bei **7b**, durch die längere $(CH_2)_n$-Kette eine direkte COOH—$N(CH_3)_2$-Wechselwirkung ermöglich wird. Die kleine

$A_{0,II}$-Flächen der zweiten kondensierten Phase deutet auf eine, ähnlich wie bei **7b**, bipolare Anordnung des J-Typs hin.

Die starken intramolekularen Wechselwirkungen und die steife arylische Zwischenkette ermöglichen die kleinsten mittleren Molekülflächen der Π(A)-Isothermen aller *Push-Pull*-Thiazole. Während die ermittelte $A_{0,I}$-Fläche der ersten kondensierten Phase durch eine sehr dichte Anordnung der COOH- und $N(CH_3)_2$-Gruppen noch monomolekular erklärt werden kann (siehe **7a *I*** Abbildung 5.5 (B)), weist die $A_{0,II}$-Fläche der möglichen zweiten kondensierten Phase auf ein teilweises Herausdrücken einzelner Moleküle und den Kollaps des L-Films hin.

5.3 Spektrale Eigenschaften des Langmuir-Blodgett-Films

In den vorangegangenen Kapiteln konnten deutliche Unterschiede hinsichtlich optischer Eigenschaften der Lösung sowie Filmbildungseigenschaften des L-Films in Abhängigkeit der verwendeten Zwischenkette aufgezeigt werden. Nun sollen die aus dem L-Film abgeschiedenen supramolekularen Strukturen (LB-Film) hinsichtlich ihrer Absorptions- und Emissionseigenschaften untersucht werden, um die in Kapitel 5.2 erarbeiteten Strukturvorschläge zu spezifizieren.

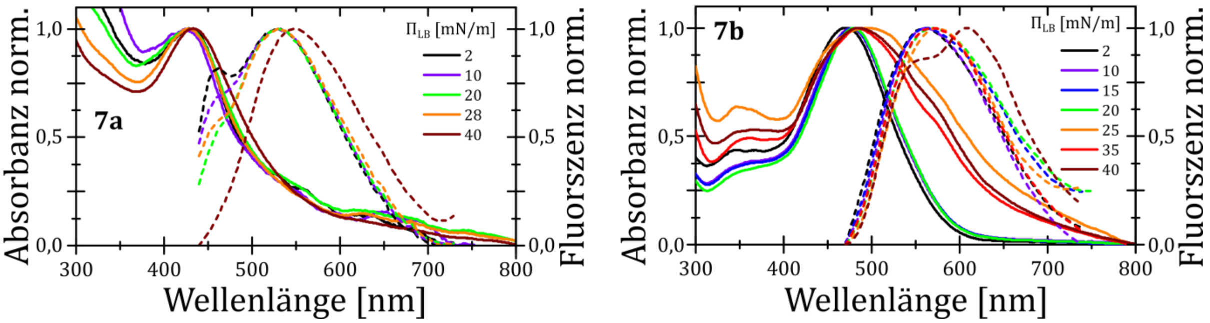

Abbildung 5.6: Absorptions- und Emissionsspektren von **7a** (Anregung 420 nm) und **7b** (Anregung 450 nm) bei bestimmten LB-Abscheidedrücken Π_{LB}.

Die in Abbildung 5.6 dargestellten Absorptionsspektren der LB-Filme von **7a** zeigen keine klar ausgeprägte Doppelmaxima-Struktur. Das der intramolekularen Störung des π-Systems (**7** ***iii***) zugeordnete Absorptionsmaximum (~405 nm) der Lösung ist in den LB-Filmen nicht ausgeprägt. Die Emissionsspektren zeigen jedoch, ähnlich wie die der Lösung, ein doppeltes Emissionsmaximum. Wenngleich dieses einerseits eine geringere Stokes-Verschiebung, also die eine kleine Differenz zwischen Absorptions- und Emissionsmaximum (λ_{max}(Abs)=400 nm, λ_{max}(Em)=430 nm), sowie andererseits ein stückweises Verschwinden jenes doppelten Emissionsmaximums durch vergrößern des Π_{LB} aufweist. Daraus folgt, dass durch fortlaufende Kompression die durch intramolekulare Wechselwirkung dicht gepackten Moleküle (<20 Å^2) von **7a** stückweise aus der Schicht herausgedrückt werden und relaxieren. Diese weisen wiederum das Emissionsspektrum des energetisch günstigsten Konformers auf (vgl. **7b** in Abbildung 5.2).

Die LB-Filme von **7b**, abgeschieden aus der ersten kondensierten und Übergangsphase des L-Films, zeigen eine identische, dem Lösungsmittelspektrum ähnelnde, spektrale Form. Erst durch den Wechsel der supramolekularen Struktur in die oben beschriebene bipolare Anordnung weist das Absorptionsspektrum eine Superposition[96] von Monomeren und J-Aggregaten auf, was in der zusätzlichen, deutlich rotverschobenen Absorptionsflanke zu erkennen ist. Die Emissionsspektren hingegen zeigen, bis auf den höchsten verwendeten Π_{LB}, nur die Monomer-Emission. Erst die aus der monomolekularen dichtesten Packung unterhalb des Kollaps abgeschiedenen LB-Filme (Π_{LB} = 40mN/m) zeigen eine, den J-Aggregaten zuzuordnende, Fluoreszenz.

5.4 Elektronische Eigenschaften des Langmuir-Blodgett-Films

Aus der optischen Charakterisierung der LB-Filme wurde deutlich, dass das Modell der supramolekularen Struktur der L-Filme von **7a** und **b** auch nach der Abscheidung auf Quarzglas Bestand hat. Es wurde damit eine supramolekulare Geometrie in der jeweils ersten kondensierten Phase (vergleiche **7a** ***I*** und **b** ***I***) beider *Push-Pull*-Thiazole bestätigt, bei dieser die elektrische Leitfähigkeit in Abhängigkeit der Art der Zwischenkette von **7** verglichen werden kann. Diese supramolekulare Geometrie soll zusätzlich mit der bipolaren J-Typ Struktur von **7b** ***II*** hinsichtlich des Einflusses der Packungsdichte der supramolekularen Strukturen des Moleküls auf die elektrische Leitfähigkeit untersucht werden. Zur Messung der Leitfähigkeit wurden die LB-Filme auf einer Goldoberfläche abgeschieden und mittels Leitfähigkeits-

Rasterkraftmikroskopie vermessen. Dabei ist jedoch bekannt, dass die vorhanden Ankergruppen (COOH und $N(CH_3)_2$) von **7** nur eine geringfügige Affinität zur Goldoberfläche aufweisen.

Die aufgenommen Strom-Spannungs-(I-V)-Kennlinien der jeweiligen supramolekularen Strukturen der LB-Filme zeigen ein deutliches Abweichen vom linearen Verlauf eines ohmschen Widerstandes, welches durch die von der organischen Schicht induzierten Potentialbarriere hervorgerufen wird.[199] Dabei deutet der lineare Verlauf der Ableitungen dI/dV in Abhängigkeit von dI auf einen Tunnelprozess der Elektronen durch die organische Schicht hin.[200] So stellen die hier verwendeten LB-Filme im vorhandenen Aufbau Schichten geringer Leitfähigkeit dar. Diese Leitfähigkeit der Schichten beider Moleküle zeigt sich unabhängig von der jeweiligen supramolekularen Struktur. Die LB-Filme von **7a *I***, bei der die doppelt verankerte supramolekulare Geometrie mit der größten Packungsdichte (Fläche pro Molekül <20 Å^2) vorliegt, zeigen im verwendeten Spannungsbereich einen maximal fließenden Strom von ~± 40 pA. Verglichen zu **7a *I*** steigt der Strom innerhalb dieses Spannungsbereiches für **7b *I*** um 3·103 pA an. Ein Wechsel der supramolekularen Struktur zur zweiten kondensierten Phase (**7b *II***) des Moleküls beeinflusst die Leitfähigkeit nicht maßgeblich.

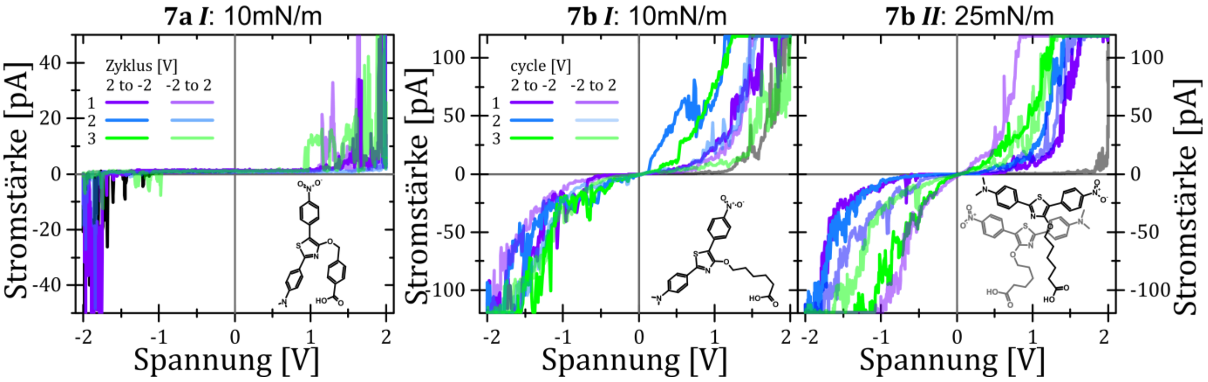

Abbildung 5.7: I-V-Kennlinien der Punktkontaktmessungen des Leitfähigkeits-Rasterkraftmikroskopie an LB-Filmen von **7a** (**I**) und **b** (**I**, **II**) mit drei vollen (Lila, Blau, Grün) Zyklen eingeteilt in 2 zu -2V (durchgezogen) und -2 zu 2 V (transparent) und einen Startzyklus (schwarz) von 0 zu 2 V.

Innerhalb der kontinuierlichen Messung der Leitfähigkeit durch aufeinanderfolgende Spannungszyklen einer supramolekularen Geometrie desselben Punkte auf der Probe weisen die I-V-Kennlinien von **7b *I*** und ***II*** geringe Unterschiede im Verlauf auf. Diese Unterschiede, welche sowohl zwischen den drei Zyklen (-2…2…-2 V) als auch zwischen den einzelnen Hin- (2 zu -2 V) und Rückzyklen (-2 zu 2 V) auftreten, deuten auf eine unterschiedliche Ausrichtung der Moleküle zu den Elektroden hin. Diese zwei verschiedenen supramolekularen Geometrien werden innerhalb der drei Spannungszyklen, aufgrund von Ausrichtung der bipolaren Moleküle im elektrischen Feld und des zusätzlichen Freiheitsgrads durch eine flexible $(CH_2)_n$-Kette, einander angenähert. Eine Erhöhung der molekularen Packung in **7a *I*** (vergleiche A_0-Flächen in Abbildung 5.5) verhindert diese Art von Reorientierung des LB-Films, aber wirkt dadurch elektrisch isolierender im Vergleich zur abgeschieden Monolage von **7b *I*** und ***II***.

Damit konnte in diesem Kapitel gezeigt werden, dass die Art der unpolaren Zwischenkette deutlichen Einfluss auf intramolekulare Wechselwirkungen und auf das spektrale Verhalten in Lösung hat. Durch die Funktionalisierung mit einer arylischen Ph-Kette wird eine zusätzliche, spektral blauverschobene und für Thiazole bisher einzigartige Spezies ausgebildet, bei der zusätzlich der Extinktionskoeffizient verringert ist. Bei einer Assemblierung an der Wasser-Luft-Grenzfläche ermöglichen diese intramolekularen Wechselwirkungen eine deutlich dichtere molekulare Packung, bei gleichzeitigem geringerem Freiheitsgrad durch die steife Ph-Kette. Die alkylische $(CH_2)_5$-Kette bildet neben der mit **7a *I*** vergleichbaren **7b *I*** eine zusätzliche kondensierte Phase **7b *II***. Grundsätzlich ermöglicht die Einführung der Bipolarität am Querbalken des T-förmigen Strukturmotiv, im Vergleich zu dem im Kapitel beschriebenen **6b *I*** oder dem literaturbekannten I-förmigen Strukturmotiv des Azobenzenes[187], eine Stabilisierung der supramolekularen Struktur und einer damit einhergehenden thermodynamischen Stabilität des L-Films. Durch spektroskopische Charakterisierung konnte nachgewiesen werden, dass alle supramolekularen Geometrien des L-Films erfolgreich auf die Substratoberfläche im LB-Film überführt werden konnten. Die anschließende elektrische Charakterisierung zeigte wiederum, dass Anstelle des Anteils an π-konjugierten Moleküleinheiten die molekulare Packungsdichte ausschlaggebend für die elektrische Leitfähigkeit durch den LB-Film ist.

6 Selbstassemblierung und Selbstheilung

Teile des Kapitels sind zur Publikation eingereicht in [MLH6] Hupfer, M. L.; Herrmann-Westendorf, F.; Kaufmann, M.; Weiß, D.; Dietzek, B.; Beckert, R.; Presselt, M., *Chemistry - A European Journal* **2019**, submitted

In den vorangegangenen Kapiteln wurde durch den Einsatz der LB-Technik an vielseitig funktionalisierten 4-Hydroxythiazolen, neben den optoelektronischen Eigenschaften, die thermodynamische Stabilität jener Schichten gezielt gesteuert. In Kapitel 3 wurde deutlich, dass durch das Forcieren verschiedener supramolekularer Geometrien mittels LB-Technik thermodynamisch stabile L-Filme der Py-Thiazole (**6**) gebildet werden können. Diese Stabilität ist für supramolekulare Strukturen ausgeprägter intermolekularer Wechselwirkungen am höchsten. Es zeigte sich, dass vor allem jene supramolekularen Strukturen der dazugehörigen LB-Filme, welche starke Wechselwirkungen mit dem Substrat ermöglichen, auch an der Festkörper-Luft-Grenzfläche thermodynamisch stabil sind.

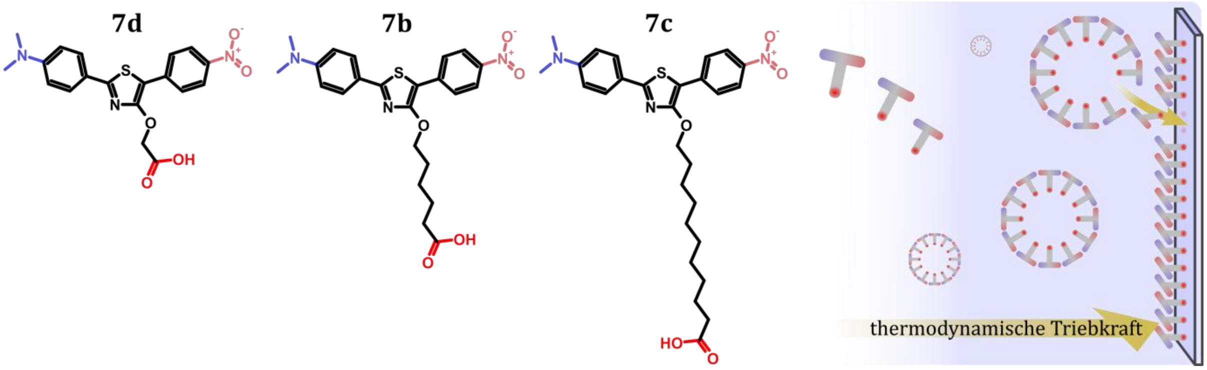

Abbildung 6.1: Schematische Übersicht der im Kapitel verwendeten 2-4-N,N-Dimethylaminophenyl-4-Hydroxy-5-2-Nitrophenyl-1,3-Thiazole mit systematischer Variation der Länge der unpolaren alkylischen Zwischenkette, welches Chromophor und polaren Carbonsäure-Ankergruppe separiert.

Durch die Einführung der starken bipolaren intermolekularen Wechselwirkung der *Push-Pull*-Thiazole (**7**) in Kapitel 5 wurden stabile supramolekulare Strukturen bis hin zu hohen Kompressionen ermöglicht. Diese wiesen, transferiert auf das Substrat, im LB-Film deutliche spektrale Verschiebungen in Abhängigkeit der supramolekularen Struktur auf. Jene erzwungenen supramolekularen Strukturen des LB-Films neigen allerdings zur Reorientierung innerhalb eines elektrischen Feldes. So kann der Einsatz der LB-Technik zwar einerseits das Forcieren eventuell sonst nicht erreichbarer energetischer Minima von supramolekularen Strukturen ermöglichen, andererseits können jene daraus hergestellten Schichten unter geänderten Bedingungen, wie zum Beispiel beim Wechsel der Grenzfläche bei der Abscheidung, in ihrer thermodynamischen Stabilität variieren.

Ein weiterer Ansatz zur Erzeugung thermodynamisch stabiler Schichten ohne Wechsel der Grenzfläche ist der der Selbstanordnung aus den sich in Lösungen befindlichen Amphiphilen an der Fest-Flüssig-Grenzfläche. Bei diesem Ansatz wird sich die gegensätzliche Polarität von Lösungsmittel und Substrat, oder die Affinität der Ankergruppe des Moleküls zum Substrat, als thermodynamische Triebkraft zur Selbstassemblierung, zu Nutze gemacht. In diesem Kapitel sollen daher die Bipolarität des 2-4-N,N-Dimethylaminophenyl-4-Hydroxy-5-2-Nitrophenyl-1,3-Thiazols (**7**) ausgenutzt werden, um selbiges an der Substratoberfläche *in situ* aus der gesättigten Lösung hochgeordnet selbst zu assemblieren. Neben den deutlichen spektralen Unterschieden verschiedener supramolekularer Strukturen und intra-, bzw. intermolekularer Interaktionen, zeichnen sich die Moleküle durch einen hohen Extinktionskoeffizienten und daher eine gute optische Charakterisierung monomolekularer Schichten aus. Die daraus gewonnen thermodynamischen stabilen Schichten amphiphiler Moleküle sollen anschließend hinsichtlich ihrer Fähigkeit zur Selbstheilung untersucht werden.

Bei diesem bereits im einleitenden Kapitel 1 erwähnten Prozesses der Selbstheilung durch Selbstassemblierung wird ausgenutzt, dass eine Degradation zum einem einen Wechsel der Polaritäten des Degradationsproduktes und zum anderen das Austreten dieses aus dem energetischen Minimum der supramolekularen Struktur führt. Dadurch kann das Degradationsprodukt aus der supramolekularen Struktur in die Lösung des Austauschvolumens gehen und von diesem ein neues Amphiphil in die supramolekulare Struktur assemblieren (siehe Abbildung 1.1). Dadurch können sowohl die supramolekulare Struktur als auch die Funktion der Schicht geheilt werden. Conti und Cecchini[42] zeigten durch quantenchemische Berechnungen, dass die Affinität der Selbstanordnung und thermodynamische Stabilität von Monolagen aus der Flüssigphase an der Flüssig-Fest-Grenzfläche mit der Konzentration des Adsorbers steigt. Der Konzentrationseffekt ist allerdings wiederum stark von der Temperatur (aufgrund messtechnischer Limitierungen in dieser Arbeit nicht betrachtet) und dem Lösungsmittel abhängig.[42, 201]

6.1 *In situ* Detektion der Selbstanordnung

Wie bereits erwähnt, kann die Bereitstellung einer Oberfläche, z.B. ein Quarzglas-Substrat, für oberflächenaktive Moleküle, z.B. ein mit einer hydrophilen COOH-Gruppe funktionalisiertes Amphiphil, eine Selbstanordnung letzterer veranlassen, falls ein Teil des Moleküls von der Substratoberfläche ausreichend angezogen wird. Der Prozesses der Selbstanordnung in speziellen Oberfläche-Amphiphile-Lösungsmittel Systemen wird typischerweise durch Rastertunnelmikroskopie[202-204] *in situ* an der Fest-Flüssig-Grenzfläche oder, im Falle starker chemischer Bindung des Amphiphil zum Substrat, mit einer Vielzahl an Charakterisierungsmethoden *ex situ* an der Fest-Luft-Grenzfläche[205-206] untersucht. In diesem Kapitel wird beschrieben wie die außergewöhnlich oberflächensensitive und für die Fest-Flüssig-Grenzfläche entwickelte photothermische Ablenkungsspektroskopie (*engl. photo-thermal deflection spectroscopy, PDS*) dafür benutzt werden kann die Bildung einer SAM amphiphiler Farbstoffe *in situ* spektroskopisch, wie in Abbildung 6.2 (A) schematisch dargestellt, zu untersucht.

Bei dem hier verwendeten transversalen *PDS*[207-208] erzeugt das einstrahlende, fokussierte Licht der Anregung (grün in Abbildung 6.2 (A)), durch Transformation von absorbiertem Licht in Wärme, einen oberflächennahen thermooptischen Gradienten (siehe thermische Linse in Abbildung 6.2 (A)). Dieser zeichnet sich durch eine lokale Änderung der Dichte und des Brechungsindexes des Lösungsmittels aus. Die hauptsächlich für die Detektion von Grenzflächen[209-210]- und Subbandlückenzuständen[27, 211] in Halbleitern entwickelte Methode ermöglicht bei der *in situ* Detektion an der Fest-Flüssig-Grenzfläche von (gesättigten) Lösungen eine hervorragende Differenzierbarkeit zwischen den selbstorganisierten und den in Lösung befindlichen Amphiphilen. Durch das seitliche Einstrahlen eines Messlasers in die thermische Linse wird dieser in Abhängigkeit des absorbierten Lichtes abgelenkt und detektiert. Ausführliche Arbeiten von Jackson[207] *et al.* zeigen, dass die aus dem Messsignals errechneten Intensität exponentiell vom Abstand des Lasers zur Substratoberfläche abhängig ist. Diese Abhängigkeit ist für die hier verwendeten Modifikationen der Messmethode, unter Verwendung einer gesättigten Lösung (Heptan) der *Push-Pull*-Thiazole (**7d**), in Abbildung 6.2 (B) demonstriert.

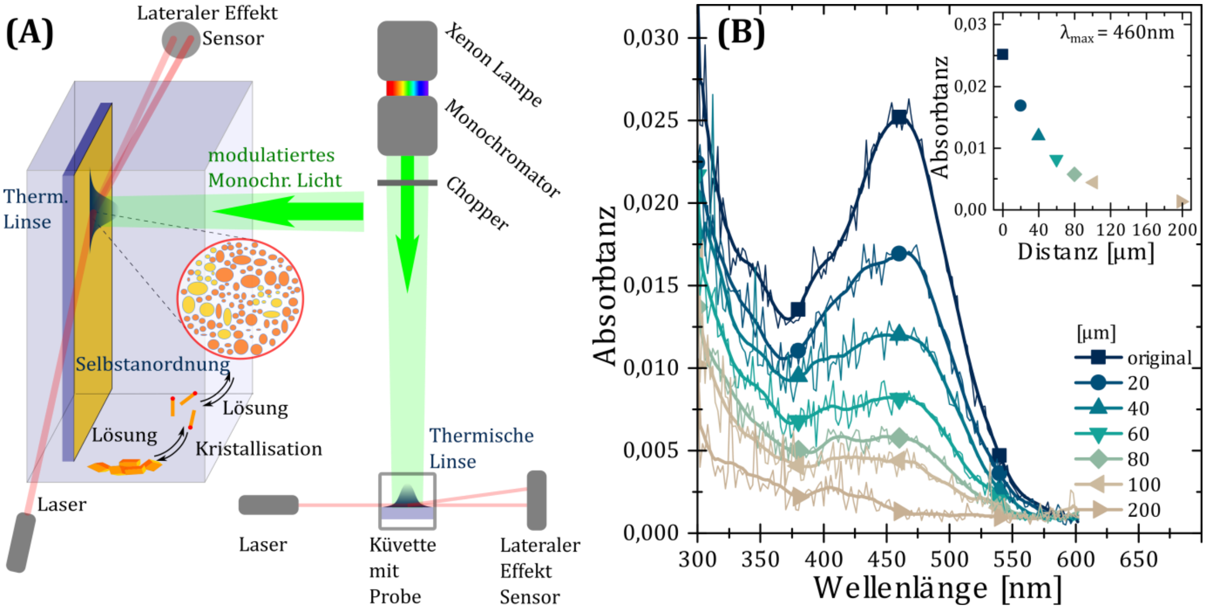

Abbildung 6.2: (A) Schematische Darstellung der photothermischen Ablenkungsspektroskopie und der Assemblierung einer selbstorganisierten Monolage (gelb) auf dem Substrat bei konstanter Farbstoffkonzentration der gesättigten Lösung und Austauschfarbstoff in einer Küvette. (B) Signal einer Monolage von **7d** in einer gesättigten Lösung mit Heptan in Abhängigkeit des Abstandes zwischen hydrophilen Quarzglas-Substrat und Messlaserstrahl. Der Einschub zeigt die Intensität λ_{max} = 460 nm aufgetragen über die Distanz des Messlasers vom Zentrum der thermischen Linse.

6.2 Einfluss der Lösungsmittelpolarität

Wie bereits erwähnt bildet die Affinität chemischer Ankergruppen zur Anbindung an das Substrat eine wesentliche thermodynamische Triebkraft der Selbstanordnung an der Flüssig-Fest-Grenzfläche. Es wurde gezeigt, dass das hier verwendete *Push-Pull*-Thiazol (**7**) eine Vielzahl einfach oder doppelt verankerter supramolekularen Strukturen erlaubt und diese stark abhängig von Länge und Art der zentral funktionalisierten Zwischenkette sind. Neben der supramolekularen Struktur bestimmt die unpolare $(CH_2)_n$-Kette zudem die Amphiphilie des stark bipolaren **7**. Diese ist wiederum ausschlaggebend für die Löslichkeit, Sättigungskonzentration und damit auch für die thermodynamische Triebkraft der Selbstassemblierung aus den gesättigten Lösungen verschiedener Lösungsmittelpolaritäten. Die Polarität[212] und die geometrische Struktur[213-214] des Lösungsmittel kann wiederum die supramolekulare Struktur der selbstorganisierten Schichten stark beeinflussen. Eine Restriktion der hier verwendeten modifizierten Messmethode bildet die Absorption des Anregungslichtes jener gesättigten

Lösung und die damit verbundene Abschwächung der Anregung der SAM. Das mit einer CH_2-Kette funktionalisierte **7d** zeigt im Gegensatz zu **7b**, **c** sowohl in unpolaren als auch polaren Lösungsmitteln eine ausreichend geringe Löslichkeit um optisch dünne, aber gesättigte Lösungen zu erzeugen. Daher wurde die supramolekulare Struktur der daraus gebildete SAM im Hinblick der Polarität des Substrates und Lösungsmittels bzw. dessen Geometrie näher untersucht.

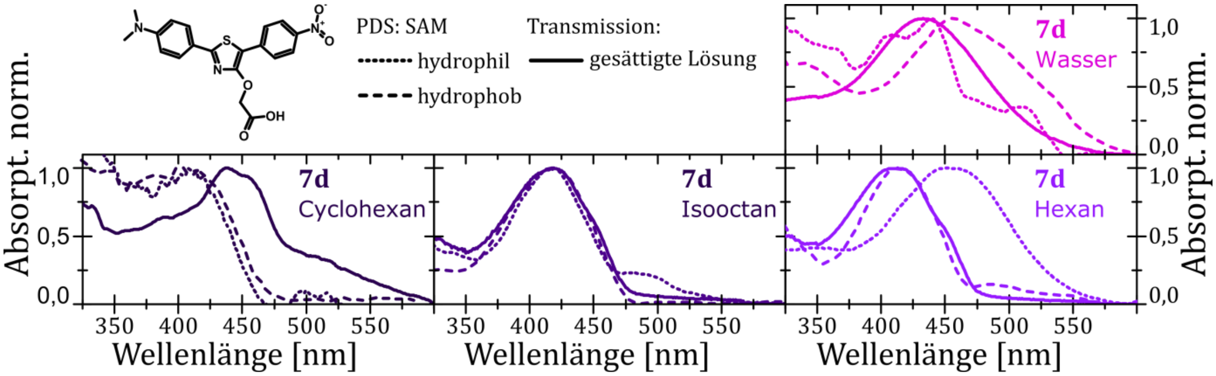

Abbildung 6.3: Absorptionsspektren der selbstorganisierten Monolagen des amphiphilen *Push-Pull*-Thiazols mit zentral substituierter alkylischer (CH_2-Gruppe) in einer gesättigten Lösung aus Cyclohexan, Isooctan, Hexan und Wasser (durchgezogen) auf einem hydrophilen (gepunktet) und hydrophoben (gestrichelt) Quarzglas-Substrat.

Alle für die gesättigten Lösungen mit **7d** verwendeten unpolaren, in Abbildung 6.3 mit Cyclohexan, Isooctan und Hexan repräsentativ dargestellten, Kohlenwasserstoffe zeigen aufgrund der geringen Amphiphilie des Farbstoffes sowohl auf hydrophilen als auch hydrophobierten Quarzglas eine Selbstorganisation. Die aus Cyclohexan resultierenden Monolagen weisen gegenüber dem stark vibronischen Lösungsmittelspektrum eine deutlich blauverschobene Absorptionsbande einer möglichen Aggregation parallel interagierender Chromophore auf. Die Änderung des spektralen Verhaltens wird somit einem Wechsel der Farbstoff-Farbstoff und/oder dem Verlieren der Farbstoff-Lösungsmittel Interaktion zugeordnet. Beim Wechsel der Lösungsmittelgeometrie von zyklischen (Cyclohexan) zu verzweigten (Isooctan) Kohlenwasserstoffen gleichen sich die Absorptionspektren von Monolage und gesättigter Lösung. Aufgrund der fehlenden spektralen Änderung wird für die SAM aus einer gesättigten Lösung von Isooctan eine niedermolekulare Ordnung erwartet, wenngleich lokal höhere Ordnung durch J-Aggregation gezeigt werden konnte (siehe rotverschobene Bande). In jener J-Aggregation, also einer aus den polaren Gruppen des Chromophors resultierenden gegenseitigen Verschiebung, assembliert sich **7d** durch den Wechsel zu linearen Kohlenwasserstoffen (Hexan) auf hydrophilen Substraten vorzugsweise selbst an. Monolagen von **7d** auf hydrophobierten Substraten in Hexan zeigen jedoch keinen Hinweis auf J-Aggregation.

Bei einem Wechsel der Lösungsmittelpolarität zum polaren Wasser ändern sich zugleich die für die Selbstanordnung zur Verfügung stehenden Gruppen (siehe supramolekularen Geometrien der Moleküle in Kapitel 2.2 und 5.2) und die daraus resultierenden supramolekularen Strukturen. Die für die Assemblierung aus Wasser bevorzugte unpolare, hydrophobierte Quarzglasoberfläche zeigt für die auf ihr assemblierten Monolage eine der J-Aggregation zugeordneten breit verschmierte, rotverschobene Absorption (Abbildung 6.3). Hingegen deutet die auf hydrophilem Quarzglas in Wasser assemblierte Monolage, mit ihrer geringen Intensität und stark vibronischen Struktur des Absorptionsspektrums, eine geringfügige Fähigkeit zur Assemblierung unter diesen Bedingungen an.

6.3 Einfluss der Amphiphilie

Neben der Polarität und geometrischen Struktur des Lösungsmittels bestimmt die molekulare Geometrie, also das Verhältnis von polaren sowie unpolaren Teilen und deren Trennung, die Möglichkeit der Selbstanordnung und die daraus resultierende supramolekulare Geometrie an der Fest-Flüssig-Grenzfläche.[215-217] Daher wird durch die Verlängerung der unpolaren $(CH_2)_n$-Kette neben der Steuerung der thermodynamischen Triebkraft der gesättigten Lösung, auch ein zusätzlicher Freiheitsgrad zur supramolekularen Assemblierung eingeführt,[193-194] was bereits in den vorrangegangenen Kapiteln näher untersucht wurde. Somit wurde, ähnlich wie bereits an der Flüssig-Gas-Grenzfläche (siehe L- und LB-Film Kapitel 4 und 5), der Einfluss der Länge (1, 5 und 10 CH_2-Gruppen) der unpolaren Zwischenkette auf die supramolekulare Assemblierung von **7d**, **7b** und **7c** an der Fest-Flüssig-Grenzfläche, am Beispiel des linearen Kohlenwasserstoffes (Heptan), untersucht.

Ähnlich wie für die zuvor gezeigten Kohlenwasserstoffe, assembliert **7d** von einer gesättigten Lösung aus Heptan sowohl auf hydrophilen als auch hydrophobierten Quarzglas an und zeigt dabei für beide Substratpolaritäten Anzeichen höherer molekularer Ordnung (siehe

Rotverschiebung gegenüber Lösungsmittelspektrum Abbildung 6.4). Auf hydrophoben Substraten kann eine Koexistenz von J-Aggregation und die von Hexan bekannte, ungeordnete Spezies gemessen werden.

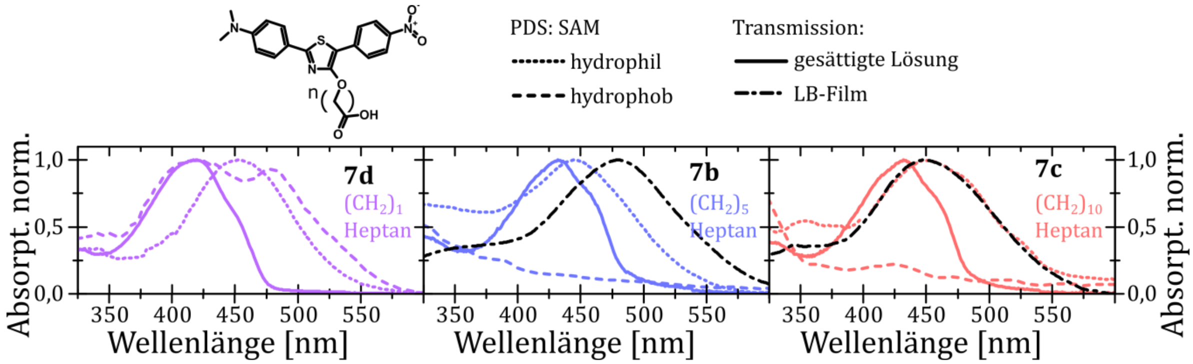

Abbildung 6.4: Absorptionsspektren der selbstorganisierten Monolagen der amphiphilen *Push-Pull*-Thiazole mit zentral substituierten alkylischen (CH_2 (**7d**), $(CH_2)_5$ (**7b**), $(CH_2)_{10}$ (**7c**)) Zwischenketten in einer gesättigten Lösung aus Heptan (durchgezogen) auf einem hydrophilen (gepunktet) und hydrophoben (gestrichelt) Quarzglas-Substrat im Vergleich zum LB-Film bei 10 mN/m (Strich Punkt).

Eine Verlängerung der Zwischenkette bei **7b** und **c** steigert die Amphiphilie des Moleküls, dessen Löslichkeit und die damit verbundene thermodynamische Triebkraft, hin zum Lösungsmittel. Folglich konnte keine Assemblierung aus unpolaren Lösungsmitteln an der unpolaren, hydrophobierten Substratoberfläche gemessen werden. Auf hydrophilen Substraten wird, ähnlich wie für **7d**, eine höhere molekulare Ordnung aus der spektralen Verschiebung gegenüber dem Lösungsmittelspektrum geschlussfolgert. Im Falle von **7b** zeigt der Vergleich der SAM mit dem LB-Film (schwarze strich-punkt Linie in Abbildung 6.4) von **7b *I***, eine gegenüber der gesättigten Lösung geringere Rotverschiebung und weist somit auf eine geringere molekulare Packungsdichte bzw. Ordnung hin (vgl. Kapitel 5.2 und 5.3). Hingegen zeigen SAM von **7c** mit den dazugehörigen LB-Filmen (**7c *I***) nahezu dasselbe Absorptionsspektrum, was Hinweise auf eine identische supramolekulare Struktur gibt.

6.4 Selbstheilung von selbstorganisierten Schichten

Durch das Bereitstellen einer thermodynamisch stabilen Monolage amphiphiler Moleküle in einem Reservoir wurde ein vereinfachtes Modell des in Abbildung 1.1 gezeigten selbstheilenden organischen Bauteils geschaffen. Daher kann anhand dieses Modellversuches das Prinzip des in dieser Arbeit beschriebenen Selbstheilungskonzeptes untersucht werden.

Die beschriebene Selbstanordnung und Selbstheilung einer Monolage amphiphiler Moleküle ist ein thermodynamischer, diffusionsgesteuerter Prozess.[201] Es muss daher in weiteren Arbeiten untersucht werden ob die durch die photothermische Messung induzierte thermische[218-219] Energie in Lösung und Monolage sowohl bei der erstmaligen als auch erneuten Assemblierung einen dazu notwendigen Impuls bildet. Zur Minimierung dieses Effektes und der Betrachtung der reinen, aus Amphiphilie resultierenden thermodynamischen Triebkraft zur Selbstanordnung, wurden sowohl Selbstanordnung als auch Selbstheilung unter Ausschluss von Licht bei RT vollzogen. Jedoch kann die Kinetik von Selbstassemblierung und Selbstheilung, mittels der hier verwendeten Messmethode, nur unter teilweise Beleuchtung, also Störung des ursprünglichen Prozesses, gemessen werden. Die für die Selbstheilung notwendige Zerstörung der Monolage wird durch die optoelektronische Stabilität des Moleküls bestimmt. Diese hängt stark von dem verwendeten Chromophor, der Art und Position der funktionalen Gruppen, sowie der Umgebung des Moleküls ab. Um ein selektives Zerstören sowie Assemblieren einzelner Spezies vorzubeugen wurde die Monolage durch fokussiertes ungefiltertes polychromatischen Lichts einer Xenonlampe bestrahlt.

Die Kinetik des Prozesses der Selbstanordnung und Selbstheilung der SAM wurde im Maximum der Absorbtanz ($\lambda_{max} = 450$ nm) gemessen und deren Verlauf unter Variation der Bestrahlzeiten der Zerstörung verglichen. Dafür wurde exemplarisch eine SAM von **7d**, gewachsen aus den zwei Fällen entgegengesetzter Polaritäten von Lösungsmittel (Heptan, Wasser) und Substrat (hydrophilen, hydrophobierten Quarzglas), untersucht. Die Assemblierung der ursprünglichen Monolage, gewachsen in einer unpolaren gesättigten Lösung auf polarem Substrat, weißt eine Langmuir-Typ Adsorbtionskinetik erster Ordnung[220-221] mit einer Sättigung nach durchschnittlich 3 h (siehe Abbildung 6.5 A) auf. Durch die Variation der Bestrahlzeiten mit fokussiertem ungefiltertem polychromatischem Licht konnte gezeigt werden, dass die Konzentration intakter Chromophore exponentiell mit dieser (siehe Abbildung 6.5 C, E, G) abnimmt. Die Kinetik des folgenden Prozesses der Selbstheilung ist durch die zusätzliche

Desorption der degradierten Farbstoffe gedämpft (Sättigung nach ≈ 21 h). Unter Beobachtung dieser Kinetik konnte keine vollständige Wiederherstellung der Absorbtanz (siehe Abbildung 6.5 B, D, F) gemessen werden. Folglich wird angenommen, dass die Degradationsprodukte, deren chemische Natur unbestimmt ist, unvollständig desorbieren. Die Kinetik zeigt, dass die Irreversibilität der Selbstheilung der SAM durch die Konzentration der Degradationsprodukte in ihr zunimmt. Es wird daher vermutet, dass kein vollständiger Wechsel der Polarität des Amphiphils bei Degradation einsetzt. Es wird somit ein wesentliches Kriterium des in Abbildung 1.1 beschriebenen selbstheilenden Systems nicht vollständig erfüllt. Die Untersuchung der Selbstanordnung von **7d** für die konträre Polarität, gewachsen aus Wasser auf hydrophobiertem Glas, konnte nur durch die von der Messung induzierten Wärme assemblieren und wurde daher nicht weiter betrachtet.

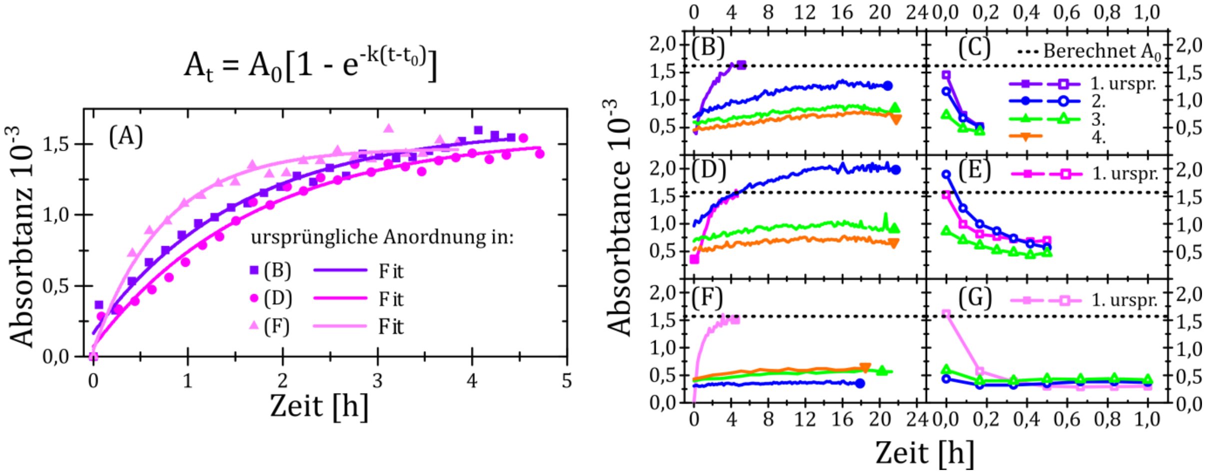

Abbildung 6.5: Absorbtanz (A_t) (λ_{max} = 450 nm) *versus* Zeit (t) Kinetik der ursprünglichen Assemblierung (A), zusammen mit der Heilung (B, D, F) und des Schadens (C, E, G) einer selbstorganisierten Monolage des amphiphilen *Push-Pull*-Thiazoles **7d** in einer gesättigten Lösung aus Heptan auf einem hydrophilen Quarzglas-Substrat. Die Langmuir-Typ Kinetik wird des Weiteren durch die maximale Absorbtanz (A_0), die Ratenkonstante (k) und die Offset-Zeit (t_0) bestimmt.

Die Absorptionsspektren der selbstassemblierten ursprünglichen sowie der selbstgeheilten Monolagen von **7d** (Heptan, hydrophiles Quarzglas) ist in Abbildung 6.6 (A) und die der Zerstörten in (B) dargestellt. Die Intensität der SAM-Hauptbande im Sichtbaren (450nm) wird innerhalb des ersten Zerstörungszyklus (Bestrahlzeit = 0,5 h) um 50 % vermindert. Wiederum innerhalb des folgenden Heilungszyklus konnte, anders als bei

Beobachtung des Prozesses zur Messung der Kinetik, mehr als 100 % des Ausgangssignals (vergleiche Maxima bei 450 nm in Abbildung 6.6 (C)) wieder hergestellt werden. Dieses Alterieren der Intensität wiederholt sich zudem für jeden weiteren Zerstörung-Heilungs-Zyklus, während zusätzlich eine Absorptionsbande ($\lambda_{abs} = 300$ nm) kontinuierlich wächst. Das Verhältnis zwischen der ursprünglichen Hauptabsorption und dieser zusätzlichen Bande (Abbildung 6.6 (D)) geht jedoch bereits nach 6 Zerstörung-Heilungs-Zyklen in eine Sättigung.

Durch die kurze Zwischenkette und den damit verbundenen geringeren Freiheitsgraden können intramolekulare Wechselwirkungen der funktionalen Gruppen von **7d**, wie sie in Kapitel 5 mittels quantenchemischer Berechnungen für **7a**, **b** gezeigt wurden, ausgeschlossen werden. Der Fakt, dass zusätzlich zur ersten, ursprünglichen Hauptbande eine zweite Absorptionsbande entsteht, deutet auf eine Zerstörung der Farbstoffschicht hin und dem Bilden von Degradationsprodukten hin. Diese können im hier verwendeten System nicht vollständig desorbieren. Diese überlagern die spektrale Form der Hauptabsorptionsbande, eine Heilungseffizienz kann somit nicht bestimmt werden.

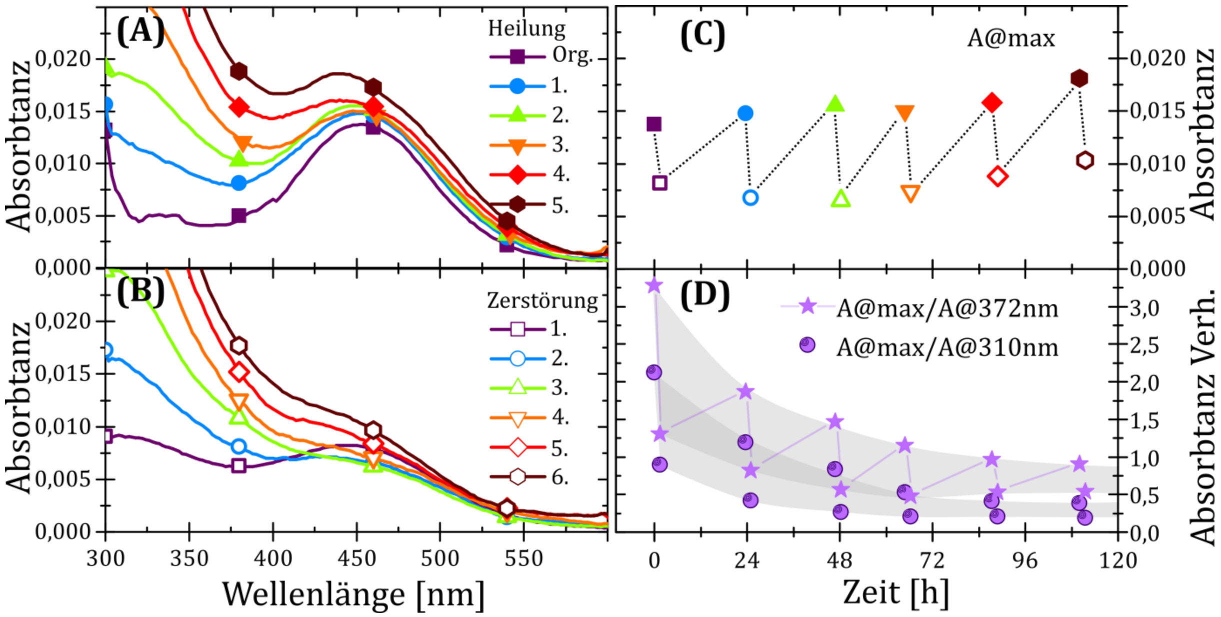

Abbildung 6.6: Absorptionsspektren der selbstorganisierten und selbstgeheilten Monolagen des amphiphilen *Push-Pull*-Thiazoles **7d** in einer gesättigten Lösung aus Heptan auf einem hydrophilen Quarzglas-Substrat nach verschiedenen Zerstörungs- (B) und Selbstheilungszyklen (A). Darstellung der Absorptionsintensität bei $\lambda_{max} = 450$ nm (C) und dem Verhältnis der Intensitäten bei 450 nm/374 nm (Sterne) and 450 nm/310 nm (Kugeln) über die Zeit (D).

In diesem Kapitel konnte erstmals durch den Einsatz von *PDS* die Selbstanordnung und Selbstheilung amphiphiler Moleküle aus der Flüssigphase an der Flüssig-Fest-Grenzfläche nachgewiesen werden. Dabei wurde die Selbstanordnung einer Monolage, des aus den vorangegangenen Kapiteln abgeleiteten T-förmigen Strukturmotivs der *Push-Pull*-Thiazole **7d, b** und **d**, in Abhängigkeit der Amphiphilie des Adsorbers, der Polarität und geometrischen Struktur des Lösungsmittels detektiert. Aus den spektralen Verschiebungen ($\Delta\lambda_{max}$ = 0, <0, >0) der Absorption konnte mittels des Vergleichs der Erkenntnisse aus dem L- und LB-Film ein detailliertes Bild der assemblierten supramolekularen Strukturen (isotrop, H-, J-Aggregation) gewonnen werden. Die Erkenntnisse einer thermodynamisch stabilen supramolekularen Struktur wurden folglich angewandt, um zum ersten Mal die Funktion (Absorption) einer, für eine optoelektronische Aktivschicht anwendbare, SAM *in situ* an der Flüssig-Fest-Grenzfläche mittels eines neuartigen Konzeptes selbstzuheilen. Dabei wurden sowohl die Absorptionsspektren als auch Adsorptionskinetik der Selbstassemblierung und Selbstheilung analysiert und die Bildung Degradationsprodukte, aber nicht deren chemische Natur, nachgewiesen.

7 Zusammenfassung

Diese Arbeit beschäftigt sich mit der spektroskopischen und elektrischen Charakterisierung monomolekularer Filme amphiphiler, T-förmiger 4-Hydroxythiazole. Im Hauptteil der Arbeit lag der Fokus auf der gezielten Steuerung der supramolekularen Geometrie, den daraus resultierenden optoelektronischen Eigenschaften und der thermodynamischen Stabilität unter Variation der molekularen Geometrie. Diese molekulare Geometrie wurde durch das vielseitig modifizierbare Strukturmotiv des Thiazols hinsichtlich der Art, Anzahl und Länge der Substitution an der 2-, 4-Hydroxy und 5-Positition (siehe Abbildung 7.1 I-V) des Chromophor, welches im Rahmen der Dissertation von Kaufmann[145] synthetisiert wurde, variiert. Die Steuerung der supramolekularen Geometrie wurde mittels des Langmuir-(L)-Blodgett-(B)-Verfahren an der flüssig-gasförmigen und fest-gasförmigen-Grenzfläche untersucht. Ziel dabei war es, durch das LB-Verfahren definierte zweidimensionale supramolekulare Strukturen zu erzeugen, um eine thermodynamische stabile Schicht organischer Farbstoffe für den Einsatz in einem neuartigen Konzept zur Selbstheilung eines optoelektronischen Bauteils zu finden. Die thermodynamische Stabilität dieser supramolekular geordneten Schichten der hier verwendeten amphiphilen Thiazole wurde zusätzlich zur LB-Technik über die Selbstassemblierung aus der Lösung an der flüssig-fest-Grenzfläche nachgewiesen. Diese selbstorganisierten Monolagen wurden hinsichtlich ihrer Fähigkeit zur Selbstheilung, innerhalb eines Models eines selbstheilenden organischen Bauteils, untersucht.

Der Fokus der Untersuchungen bzgl. des Einflusses einzelner oder Kombinationen von Substitutionen des Thiazolkerns auf die Assemblierung an der Luft-Wasser-Grenzfläche (LB-Verfahren) lag auf (i) photoaktiven Funktionalisierungen, (ii) polaren Ankergruppen oder (iii) unpolaren Zwischenketten. Dies hebt sich damit deutlich von oftmals limitierten Untersuchungen der Variation der Seitenkette von L- und LB-Filmen[86-90] ab. Durch die Variation der Substitution am Chromophor konnten zusätzliche, den Filmbildungsprozess stabilisierende, photoaktive Gruppen gefunden werden. Die Variation in Position, Anzahl und Art polarer Ankergruppen ermöglichte eine Vielzahl an supramolekularen Strukturen unterschiedlicher Freiheitsgrade. Die Variation in Art und Länge der Zwischenkette ermöglichte das gezielte Steuern supramolekularer Strukturen mit unterschiedlichen intra- und intermolekularen Wechselwirkungen. Mit der Demonstration der Übertragbarkeit der Schichten auf Substrate wurde entgegen der Meinung der Literatur die umfassende die Tauglichkeit des T-förmigen Strukturmotives für die LB-Methode gezeigt. Für die aus dem LB-Verfahren abgeleiteten Strukturmotive des T-förmig funktionalisierten Thiazols wurde die thermodynamische Stabilität zusätzlich erstmalig mittels Selbstassemblierung flüssig-fest-Grenzfläche nachgewiesen. Dabei konnte wiederum zum ersten Mal eine Selbstheilung dieser Schichten demonstriert werden. Die wichtigsten Ergebnisse der Arbeit wurden schematisch in Abbildung 7.2 dargestellt und werden im Folgenden kurz erläutert.

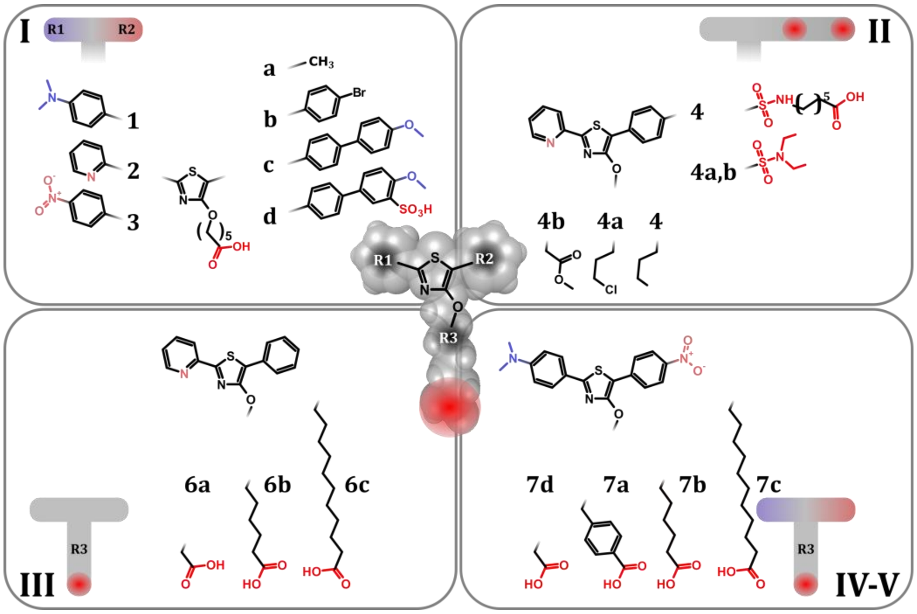

Abbildung 7.1: Schematische Übersicht der in dieser Arbeit verwendeten Variation des 4-Hydroxythiazol Kerns an der 2-(R1)-, 5-(R2)- und 4-Hydroxy-(R3)-Position.

Zuerst wurde in Kapitel 2 der Prozess der L-Filmbildung des 4-Hydroxythiazols an der Wasser-Luft-Grenzfläche durch Analyse der $\Pi(A)$-Isotherme charakterisiert. Die daraus abgeleiteten supramolekularen Strukturen des L-Films, schematisch dargestellt in Abbildung 7.2 I, wurden hinsichtlich ihrer spektralen Eigenschaften mit denen in Lösung verglichen. Das Strukturmotiv des 4-Hydroxythiazols wurde mit 2-(4-N,N-Dimethylaminophenyl (**1**), 2-Pyridyl (**2**), 4-Nitrophenyl (**3**)) an der 2-Position (R1), sowie mit Methyl (**a**), 4-Bromophenyl (**b**), 4-Methoxybiphenyl (**c**) und 4-Methoxyphenyl-3-Sulfonsäure (**d**) an der 5-Position (R2) (Abbildung 7.1 I) variiert. Das T-förmige Strukturmotiv wurde durch die unpolaren $(CH_2)_5$-Ketten (R3) und einer polaren Carbonsäure-(COOH)-Gruppe an der 4-Hydroxy-Position komplettiert. Es wurde bestätigt, dass die im LB-Verfahren notwendige Amphiphilie erst durch eine Phenylen-(Ph)-Gruppe (**b**, **c**, **d**) für R2 erzeugt wird. Weiterhin wurde ermittelt, dass neben dieser polaren COOH-Gruppe, sowohl die Pyridyl (Py) (**2**), aber vor allem die Dimethylamino-($N(CH_3)_2$)-(**1**)-Gruppe als zusätzlicher Anker zur Wassersubphase in der jeweiligen supramolekularen Struktur (**1b** ***I***; **1c** ***I,II***; **2c** ***I***) fungiert (siehe Abbildung 7.2 I). Die

Verlängerung des konjugierten π-Elektronensystems durch die Biphenyl-Gruppen (**c**) ermöglicht verstärkte intermolekulare ππ-Wechselwirkungen, welche den L-Film stabilisieren (**2c *II***). Eine weitere Stabilisierung wurde durch die bipolare Substitution, der zur 3D-Aggregation neigenden Nitro-(NO_2)-Derivate (**3**), mit einer Methoxybiphenyl-Substitution (**3c**) an der 5-Position, erreicht. Damit bilden die T-förmigen Strukturmotive, welche bipolare und ππ-Wechselwirkungen am Querbalken ermöglichen und um die Zwischenkette frei rotieren können, eine gute Grundlage für das Erreichen thermodynamisch stabiler Schichten. Dies bildet einen Vorteil gegenüber den nicht-kovalenten Wechselwirkungen der I-förmigen Strukturmotive, untersucht von Tang *et al.*[187], welche durch ihre Bipolarität zum monomolekularen Kollaps neigen.

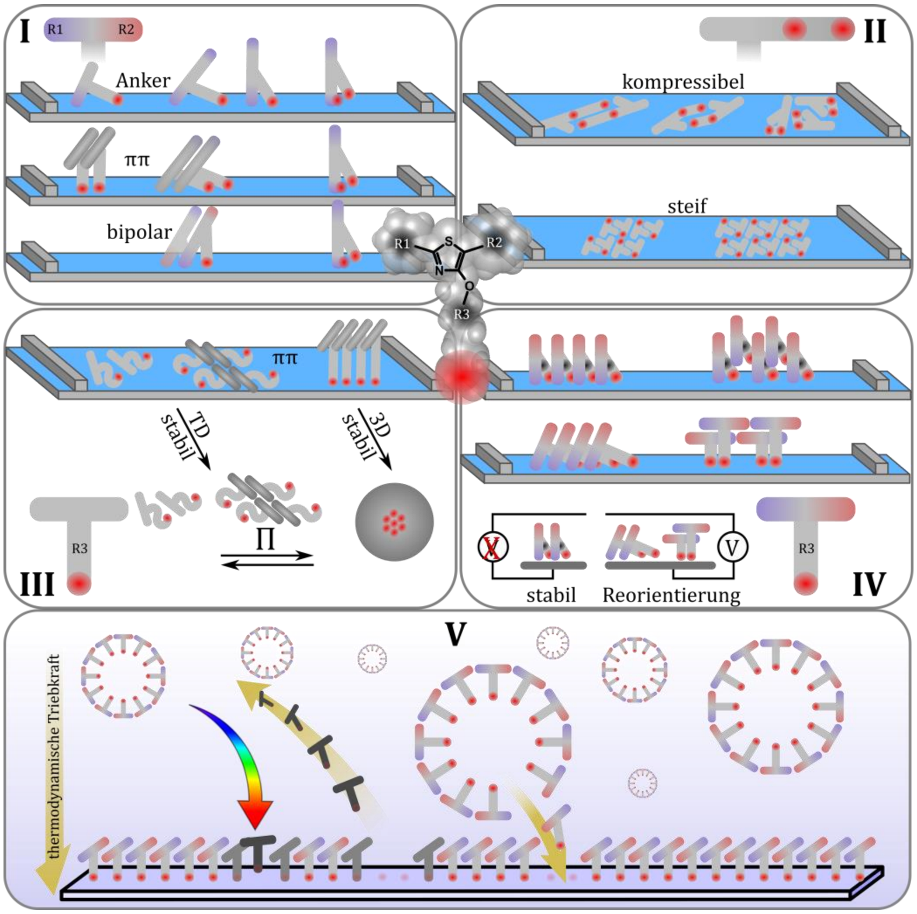

Abbildung 7.2: Schematische Darstellung der in dieser Dissertation behandelten Kapitel. Die Variation auxochromer Gruppen an der 2- und 5-Position des Strukturmotives (I), die Variation in Art, Anzahl und Position polarer Ankergruppen (II), die Variation der Länge (III) sowie Art (IV) zentral unpolar funktionalisierten Zwischenkette. Der Einsatz des aus I-IV abgeleiteten Strukturmotivs im Model eines selbstheilenden Bauteils (V).

Zur näheren Betrachtung der Auswirkung eines mehrfach mit Ankergruppen funktionalisierten Farbstoffes auf die Bildung von L-Filmen wurde das Strukturmotiv des Py-PhDerivates (vgl. **2b** und **5**) hinsichtlich Anzahl, Art und Position der polaren Ankergruppen, unpolarer Seiten- und Zwischenketten in Kapitel 3 (Abbildung 7.1 II) genauer untersucht. Die Einführung zweier polarer Ankergruppen (Sulfonamid (SO_2NH_2), COOH), getrennt durch eine $(CH_2)_{10}$-Kette an dem Py-Derivat (**4**), ermöglicht eine horizontal zur Wassersubphase orientierte supramolekulare Struktur (**4** ***I***), schematisch dargestellt in Abbildung 7.2 II. Diese zeigt gegenüber den literaturbekannten[146], molekular sehr steifen und einfach polar substituierten Molekülen (**4a**, **b**) einen höheren Freiheitsgrad der molekularer Assemblierung im L-Film. Anders als im vorangegangenen Absatz erzeugten die hier verwendeten Strukturen jedoch keine mehrphasigen Π(A)-Isothermen hoher Kompressibilität. Damit konnten, abgesehen von der Variation des Anstellwinkels und der damit verbundenen horizontalen Assemblierung von **4**, keine Veränderungen der supramolekularen Struktur, bzw. Hinweise auf starke intermolekulare Wechselwirkungen gefunden werden (vergleiche Abbildung 7.2 II). Diese Assemblierungen können aber gerade im Hinblick auf den optimalen Ladungsträgertransfer zwischen den Elektroden[222] und die vertikale Abstrahlcharakteristik[23] in optoelektronischen Bauteilen von großer Bedeutung sein. Zur Bestätigung der Annahme der supramolekularen Struktur wurden die L-Filme anschließend auf Substrate überführt und hinsichtlich ihrer supramolekularen Struktur mittels polarisationsabhängiger Fluoreszenzspektroskopie untersucht. Dabei konnte gezeigt werden, dass, unabhängig von molekularer Geometrie und verwendetem Abscheidedruck (Π_{LB}), eine Vorzugsorientierung vorherrscht, welche sich durch den Transfer von Wasser- zu Substratoberfläche ergibt. Neben dieser Vorzugsorientierung existiert eine Nebenorientierung deren supramolekulare Ordnung von molekularer Steifheit und Π_{LB} abhängig ist.

Aufgrund der eingeschränkten intermolekularer Wechselwirkung der horizontal zur Wasseroberfläche orientierten, doppelt verankerten 4-Hydroxythiazole (Kapitel 3) wurde, hinsichtlich weitere Betrachtung thermodynamisch stabiler Schichten, in Kapitel 4 zum zentral, mit einer $(CH_2)_n$-Kette und COOH-Gruppe substituierten Strukturmotiv (**2b**) zurückgekehrt. Dabei wurde unter Verwendung des Py-Ph-Derivates die Länge der $(CH_2)_{1,5,10}$-Kette (**6a**, **6b**, **6c**) variiert (Abbildung 7.1 III) und deren Einfluss auf die supramolekulare Struktur der L- und LB-Filme untersucht. Die Verlängerung der Zwischenkette ermöglicht dem Thiazol neben der für die $(CH_2)_5$-Kette bekannten einphasigen (vgl. **2b** ***I*** und **6b** ***I***), auch eine mehrphasige, deutlich separierte Π(A)-Isotherme des Thiazols mit $(CH_2)_{10}$-Kette (**6c** ***I, II, III***) zu erzeugen. Die Kombination aus Py-Ph-Derivat, welches zu starken intermolekularen ππ-Wechselwirkungen neigt und dem durch die $(CH_2)_{10}$-Kette induzierten Freiheitsgrad molekularer Assemblierung ermöglicht somit das gezielte Steuern supramolekularer Strukturen unterschiedlicher intermolekularer Wechselwirkungen (Abbildung 7.2 III). Letztere wurden mittels Kompressions-Expansions-Zyklen der Π(A)-Isotherme näher auf ihr Einwirken auf die thermodynamische Stabilität des L-Films untersucht. Dabei konnte erstmal und abhebend von der Literatur[187, 196-198] gezeigt werden, dass das gezielte Ansteuern kondensierter Phasen der Π(A)-Isotherme mit starken ππ-Wechselwirkungen (**6c** ***II, III***) schrittweise bei Raumtemperatur stabile dimere Strukturen erzeugt. Diese thermodynamisch stabilen supramolekularen Strukturen des L-Films wurden auf eine Substratoberfläche überführt und hinsichtlich ihrer Orientierung, mittels polarisationsabhängiger Fluoreszenzspektroskopie mit der aus der Π(A)-Isotherme abgeleiteten supramolekularen Strukturen, verglichen. Die LB-Filme zeigten, unabhängig von der supramolekularen Struktur von **6c**, eine durch die Absorptionswärme induzierte Reorientierung[209] oder ein Erhöhen der supramolekularen Ordnung an der Vorzugsorientierungen gemäß Rong *et al*[188]. Unabhängig davon konnte wiederum eine Vorzugs- und Nebenorientierung, wie zuvor für **4** ***I***, **4a** ***I*** und **4b** ***I***, aufgezeigt werden. Während beide Orientierungen in ihrer x-y-Ausrichtung durch Kompression beeinflusst werden, wurde nur in der Nebenorientierung ein Anstieg in der Anisotropie durch Kompression erreicht. Durch gezieltes thermisches Tempern der Schichten wurden die LB-Filme von **6c** auf ihre thermodynamische Stabilität, hinsichtlich ausbleibender Reorientierung der supramolekularen Struktur, untersucht. Es wurde gezeigt, dass sowohl die aus der Flüssigphase als auch die aus den verschiedenen kondensierten Phasen (**6c** ***I, II, III***) der Π(A)-Isotherme abgeschiedenen LB-Filme nur eine geringfügige Änderung der Orientierung durch Tempern aufweisen und somit thermodynamisch stabil sind. Dabei weisen die LB-Filme mit aufrecht stehender supramolekularer Struktur (**6b** ***III***) bei höchster Kompression die geringste Stabilität auf (siehe Abbildung 7.2 III). Währenddessen wird die höchste Stabilität mit starken Substrat-Molekül-Wechselwirkungen (**6b** ***I***) erreicht.

Anschließend wurde das Strukturmotiv des Thiazols hinsichtlich der Erkenntnisse der starken ππ-Wechselwirkungen der Ph-Gruppen (**1c**, **2c**) im L-Film mit bipolaren Wechselwirkungen (**3c**) in Kapitel 5 kombiniert. Dafür wurde das 4-Hydroxythiazol an der 2-Position mit einer 4-N,N-Dimethylaminophenyl und an der 5-Position eine Nitrophenyl-Gruppe (**7**) (Abbildung 7.1 IV) substituiert. Durch die Einführung einer arylischen (Ph) Zwischenkette (**7a**) soll überprüft werden, ob die elektrische Leitfähigkeit durch den damit erhöhten Anteil π-konjugierter Gruppen verstärkt werden kann. Daher wurde die Filmbildung und supramolekulare Struktur der L- und LB-Filme von **7a** mit den alkylischen $(CH_2)_{5,10}$ als Zwischenkette (**7b**, **c**) substituierten Thiazolen hinsichtlich optoelektronischer Eigenschaften verglichen. Die spektroskopische Charakterisierung der Lösungen von **7a** ergab, dass neben der Monomespezies eine zweite Spezies existiert, welche bei keinem der bisher literaturbekannten 4-Hydroxythiazole[140-141, 146, 165-166, 223] auftrat. Diese zweite Spezies ist von einer Kombination aus intramolekularen ππ-Wechselwirkungen der Ph-Zwischenkette mit dem Chromophor sowie intramolekularen Säure-Base-Wechselwirkungen der $N(CH_3)_2$- und COOH-Gruppe, geprägt. Wenngleich diese konformere Spezies die Filmbildung von **7a** ***I*** dominiert und zur Steigerung der Packungsdichte führt, konnte mit **7b** ***I*** eine ähnliche supramolekulare Struktur gefunden werden (vergleiche Abbildung 7.2 IV). Beide supramolekulare Strukturen sind mit $N(CH_3)_2$- und COOH-Gruppe doppelt verankert und vertikal gekippt. Unabhängig der Art der Zwischenkette konnte eine stabilisierende Wirkung der am Querbalken des T-förmigen Strukturmotives substituierten Bipolarität gegenüber **6b** (nur ππ-Wechselwirkungen) nachgewiesen werden. Im Gegensatz zur bipolaren Substitution I-förmiger Strukturmotive (Azobenzene bei Tang *et al.*[187]) ermöglicht die Substitution des T-förmigen Strukturmotivs somit nicht nur andere supramolekular Strukturen, sondern auch eine gesteigerte Stabilität im L-Film. Die spektroskopische Analyse der LB-Filme von **7a** ***I*** zeigte, dass die konformere Spezies auf das Substrat übertragen werden kann und bei steigenden Π_{LB} relaxiert. Die dazu vergleichbare Struktur von **7b** ***I*** zeigt beim Wechsel in **7b** ***II*** Anzeichen einer koexistierenden J-aggregierten Spezies, neben der bereits zu **7b** ***I*** zugeordneten Spezies. Diese drei supramolekularen Strukturen der beiden bipolaren Thiazole wurden anschließend mittels leitfähiger Rasterkraftmikroskopie vermessen (siehe Abbildung 7.2 IV). Dabei stellte sich heraus, dass die molekular dicht gepackten Strukturen von **7a** ***I*** gegenüber **7b** ***I*** deutlich elektrisch isolierender wirken, aber gegenüber der Änderung im elektrischen Feld stabil sind. Beide supramolekulare Strukturen von **7b** zeigen eine der Ausrichtung der bipolaren Chromophore zugeordnete Änderung der Leitfähigkeit durch mehrfaches Ansteuern innerhalb der Spannungszyklen. Aufgrund der durch Tunnelprozesse dominierten Leitung von Ladungsträgern der organischen Farbstoffe weichen insgesamt die Strom-Spannungs-Kennlinien beider Moleküle vom linearen, ohmschen Verlauf ab.[199-200, 224]

Es wurde ausführlich, durch eine Variation der molekularen Struktur und der aus ihr folgenden supramolekularen Struktur nach Assemblierung, die optoelektronischen Eigenschaften und thermodynamische Stabilität der L- und LB-Filme von Kapitel 2 bis 5 untersucht. Das daraus abgeleitete, als ideal identifizierte, Strukturmotiv eines bipolaren amphiphilen T-förmigen Thiazols wurde nun hinsichtlich des Einsatzes in dem, in der Einleitung beschriebenen, Modell eines selbstheilenden optoelektronischen Bauteil getestet. Eine wesentliche Voraussetzung dafür ist die thermodynamische Stabilität der aus amphiphilen Farbstoffen bestehenden organischen Aktivschicht des Bauteils gegenüber der (gesättigten) Lösung mit Austausch-Amphiphilen. Daher wurde der Beweis der thermodynamischen Stabilität dieser Aktivschicht über die freiwillige Selbstanordnung der Amphiphile aus der Lösung *in situ* an der flüssig-fest-Grenzfläche (siehe Abbildung 7.2 V) gezeigt. Zur *in situ* Charakterisierung jener Schichten wurde die bereits, hauptsächlich für die Detektion von Grenzflächen[209-210]- und Subbandlückenzuständen[27, 211] in Halbleitern, bekannte Messmethode der photothermischen Ablenkungsspektroskopie bezüglich der verwendeten Lösungsmittelumgebung mit der oben beschriebenen gesättigten Lösung modifiziert. Es wurde die Lösungsmittelumgebung hinsichtlich der strukturellen Geometrie (zyklische, verzweigte und lineare Kohlenwasserstoffe) und Polarität (unpolare Kohlenwasserstoffe und polares Wasser) variiert, da hierbei im Hinblick auf andere kleine Moleküle bereits in der Literatur eine deutliche Variation der supramolekularen Struktur[212-213] nachgewiesen werden konnte. Aufgrund messtechnischer Limitierungen konnte dabei der Einfluss der Temperatur[4042, 201] auf die Assemblierung im Rahmen dieser Arbeit nicht berücksichtigt werden. Nichtsdestotrotz konnten die gemessenen spektralen Verschiebungen der Absorptionsspektren gegenüber der gesättigten Lösung zeigen, dass durch die Selbstassemblierung ein Wechsel von Lösungsmittel-Farbstoff zu Farbstoff-Farbstoff-Wechselwirkungen an der flüssig-fest-Grenzfläche eintritt. So konnten für das mit der kürzesten CH_2-Kette funktionalisierte und damit LB-untaugliche *Push-Pull*-Thiazol **7d** Assemblierungen höherer Ordnung wie H-Aggregation in Cyclohexan (zyklisch) oder J-Aggregation in n-Hexan (linear) nachgewiesen werden. Durch die Variation der Amphiphilie, bzw. molekularen Geometrie des Thiazols mit Verlängerung der $(CH_2)_n$-Kette ($n = 1, 5, 10$), konnte bewiesen werden, dass diese die supramolekulare Geometrie an der flüssig-fest-Grenzfläche für selbstassemblierte Schichten bestimmt. Es wurde bestätigt, dass die Amphiphilie durch Variation der Zwischenkette maßgeblichen Einfluss auf die Bindungen der möglichen Assemblierung hat. Während das *Push-Pull*-Thiazol mit der geringsten Amphiphilie (**7d**) unabhängig von Substrat und Lösungsmittelumgebung assembliert, konnte dies bei gestiegener Amphiphilie (**7b**, **c**) nur unter idealen Bedingungen, also aus einer unpolaren Lösung auf einem polaren Substrat, nachgewiesen werden. Des Weiteren wurde durch den Vergleich der selbstorganisierten Monolagen der LB-tauglichen Moleküle **7b** und **c** mit deren LB-Filmen (**7b *I*** und **c *I***) eine ähnlich ausgeprägte spektrale Rotverschiebung höherer molekularer Ordnung nachgewiesen. Damit wurde gezeigt, dass eine hochgeordnete, thermodynamisch stabile Schicht amphiphiler Moleküle aus einem Überschussvolumen, gefüllt mit einer gesättigten Lösung von Austausch-Amphiphilen, gebildet werden kann. Somit wurde erstmals modellhaft die Bedingung für das in Abbildung 1.1 beschriebene selbstheilende, organische, optoelektronische Bauteil erfüllt. Im Zuge der Untersuchungen der Selbstheilung konnte exemplarisch für **7d** eine Langmuir-Typ Adsorption der ursprünglichen Monolage, gewachsen in einem unpolaren Lösungsmittel auf einem polaren Substrat nachgewiesen werden. Es konnte unter Verwendung von Photodegradation, induziert durch Bestrahlung der Anregungsquelle bei Weißlicht, eine vorrübergehende Schädigung in die selbstorganisierte Lage eingebracht werden. Es wurde gezeigt, dass dieser Schaden anschließend vollständig ausheilt und die volle spektrale Breite der Absorption der Monolage wiederhergestellt wird, aber zusätzlich Degradationsprodukte irreversible einlagert werden. Dabei hängt die Kinetik der

Selbstheilung stark von der Konzentration der Degradationsprodukte in der selbstorganisierten Monolage und der von der durch die Messung induzierten Wärme ab.

Durch diese Dissertation konnte gezeigt werden, wie anhand der systematischen Variation des T-förmigen Strukturmotivs des vielseitig funktionalisierbaren Thiazols die molekulare Geometrie, die Filmbildung und Eigenschaften der supramolekularen Geometrie gezielt beeinflusst werden können. Dafür wurden mittels LB-Technik und UV-vis Spektroskopie die Strukturmotive hinsichtlich ihrer thermodynamischen Stabilität an der gasförmig-flüssig- und gasförmig-fest-Grenzflächen sowie mittels Selbstanordnung an der flüssig-fest-Grenzfläche, abgeleitet. So konnte im Zuge der Dissertation und entgegen des Literaturstandes nicht nur die grundsätzliche Tauglichkeit eines ein-, zwei- und dreifach polar verankerten T-förmigen Strukturmotives in der LB-Technik gezeigt werden. Es wurden auch Vorarbeiten für dessen Einsatz in einem optoelektronischen Bauteil geliefert. In zukünftigen Arbeiten kann somit das optoelektronisch vielversprechende bipolare *Push-Pull*-Thiazol (**3c**, **7a-d**) in ein Bauteil eingearbeitet werden. Die daraus bestimmten Schichten bipolarer *Push-Pull*-Thiazole wurden innerhalb eines schematischen Aufbaus eines selbstheilenden organischen optoelektronischen Bauteils erfolgreich selbstgeheilt. Dies bildet dabei eines der wenigen Beispiele einer Selbstheilung unter Wiederherstellung einer Funktion der Schicht. Die dafür vorangestellten Untersuchungen der Kinetik des Prozesses der Selbstanordnung und nachfolgend der Selbstheilung muss von **7d** auf andere Derivate, wie z.B. **7c-d** und Lösungsmittel ausgeweitet werden. Zudem ist zu prüfen, ob der Prozess der Selbstheilung einer selbstorganisierten Monolage noch auf andere Farbstoffklassen oder verschiedene Zerstörungsmodi übertragbar ist. Dabei ist vor allem eine genaue Untersuchung hinsichtlich des Polaritätswechsels bei Degradation der Farbstoffe von entscheidender Bedeutung.

8 Summary

This thesis deals with the spectroscopic and electrical characterization of monomolecular films of amphiphilic, T-shaped 4-hydroxythiazoles. In the main part of the work, the focus lay on the targeted control of the supramolecular geometry, the resulting optoelectronic properties, and the influence of the molecular geometry on the thermodynamic stability. The molecular geometry was varied *via* the versatile thiazole motif with regards to type, number, and length of substitution at the 2-, 4-hydroxy, and 5-position (see Figure 7.1 I-V) of the chromophore. The control of the supramolecular geometry was studied by the Langmuir-(L)-Blodgett (B) technique at the liquid-gaseous and solid-gaseous interfaces, while the synthesis was performed by Kaufmann[145]. The aim was to generate two-dimensional supramolecular structures defined by the LB technique in order to find a thermodynamically stable layer of organic dyes that can be used as a novel self-healing concept of an optoelectronic device. The thermodynamic stability of these supramolecularly ordered layers of amphiphilic thiazoles employed in this study was, in addition to the LB technique, also demonstrated by self-assembly at the liquid-solid interface from a solution. These self-assembled monolayers were examined for their self-heal capability in a model representing an organic optoelectronic device.

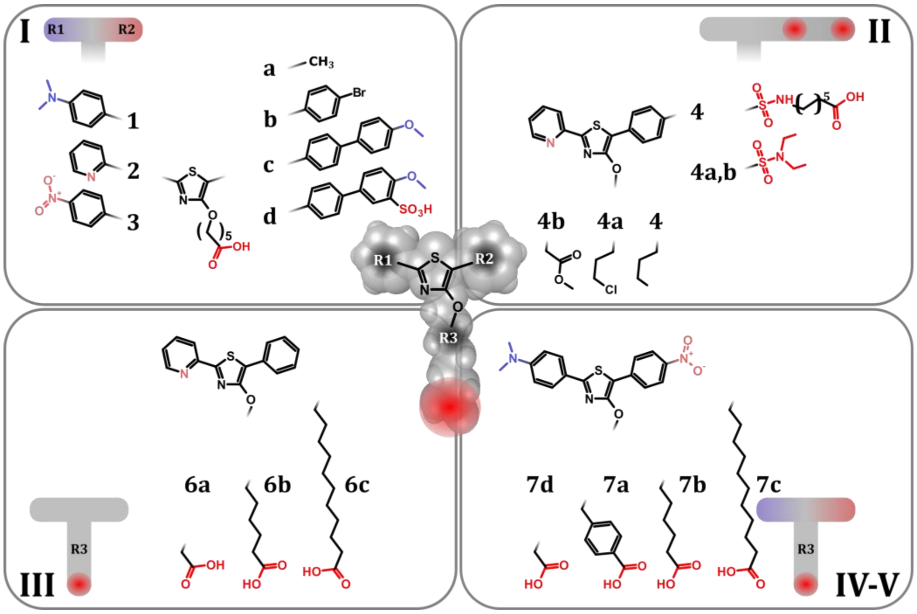

Figure 7.1: Schematic overview of the variation of the 4-hydroxythiazole core used in this work at the 2- (R1), 5- (R2) and 4-hydroxy (R3) positions.

The focus of the investigations regarding the influence of single or combinations of substitutions of the thiazole core on the assembly at the air-water interface (LB technique) was on (i) photoactive functionalizations, (ii) polar anchor groups, or (iii) non-polar intermediate chains. This is sets the work at hand apart from often limited studies of the variation in type, number, and length of the side chains of L- and LB-films[86-90]. By variation of substitution on the chromophore, additional photoactive groups that stabilize the film formation process were found. The variation in position, number, and type of polar anchor groups enabled a multitude of supramolecular structures with different degrees of freedom. The variation in type and length of the intermediate chain enabled the targeted control of supramolecular structures with different intra- and intermolecular interactions. By showing the transferability of the layers to substrates, the general suitability of the T-shaped structural motif for the LB method was demonstrated, contrary to the different opinions stated in literature. For the structural motifs of the T-shaped functionalized thiazole derived from the LB technique, thermodynamic stability was additionally demonstrated for the first time by self-assembly at the liquid-solid interface. Based on this a self-healing of these layers was demonstrated for the first time. The most important results of the work are shown schematically in Figure 7.2 and are briefly explained in the following.

First, in Chapter 2, the process of L-film formation of 4-hydroxythiazole at the air-water interface was characterized by analysis of the Π(A)-isotherm. The resulting supramolecular structures of the L-film, schematically shown in Figure 7.2 I, were compared to those in solution with respect to their spectral properties. The structural motif of 4-hydroxythiazole was varied with 2-(4-N,N-dimethylaminophenyl (**1**), 2-pyridyl (**2**), and 4-nitrophenyl (**3**)) at the 2-position (R1), and with methyl (**a**), 4-bromophenyl (**b**), 4-methoxybiphenyl (**c**), and 4-methoxyphenyl-3-sulfonic acid (**d**) at the 5-position (R2) (Figure 7.1 I). The T-shaped structural motif was completed by the nonpolar $(CH_2)_5$-chains (R3) and a polar carboxylic acid (COOH) group at the 4-hydroxy position. It was confirmed that the amphiphilicity required in the LB process is only obtained by a phenylene (Ph) group (**b**, **c**, **d**) for R2. In addition to this polar COOH-group, it was determined that both the pyridyl (Py) (**2**) and especially the dimethylamino $(N(CH_3)_2)$ (**1**) groups works as an additional anchor to the water subphase in the respective supramolecular structure (**1b** ***I***; **1c** ***I***,***II***; **2c** ***I***) (see Figure 7.2 I). The extension of the conjugated π-electron system by the biphenyl groups (**c**) enables enhanced intermolecular ππ-interactions which stabilize the L-film (**2c** ***II***). Further stabilization was achieved by bipolar substitution of nitro-(NO_2)-derivatives (**3**), which tend towards 3D aggregation, with methoxybiphenyl substitution (**3c**) at the 5-position. Thus, the T-shaped structural motifs, which allow bipolar and ππ-interactions at the crossbeam and can rotate freely around the intermediate chain, constitute a good basis for achieving thermodynamically stable layers. This is an advantage over the non-covalent interactions of the I-shaped structure motifs, studied by Tang et al.[187], which tend to monomolecular collapse due to their bipolarity.

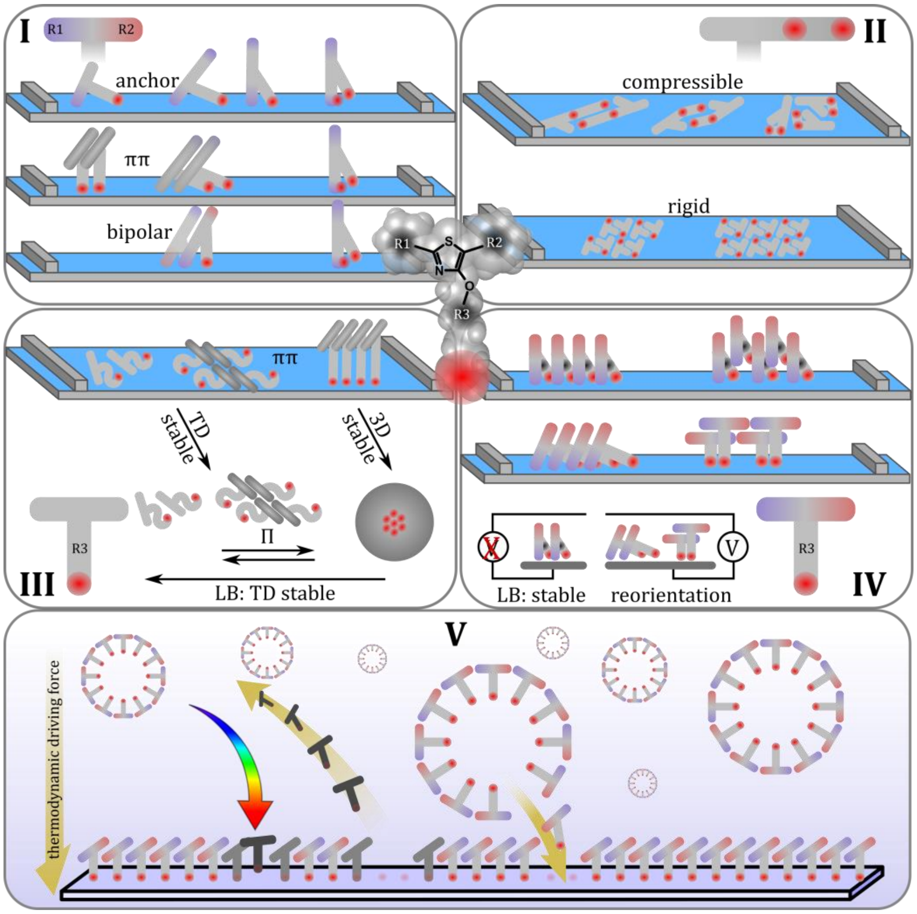

Figure 7.2: Schematic representation of the chapters covered in this dissertation. The variation of auxochromic groups at the 2- and 5-position of the structural motif (I), the variation in type, number and position of polar anchor groups (II), the variation of length (III) and type (IV) of centrally nonpolar functionalized intermediate chain. The use of the structural motif derived from I-IV in the model of a self-healing component (V).

For a closer examination of the effect of a dye functionalized several times with anchor groups on the formation of L-films, the structural motif of the Py-Ph-derivative (cf. **2b** and **5**) was examined more closely with regard to the number, type and position of the polar anchor groups, nonpolar side and intermediate chains in Chapter 3 (Figure 7.1 II). The introduction of two polar anchor groups (sulfonamide (SO_2NH_2), COOH), separated by a $(CH_2)_{10}$-chain on the Py derivative (**4**), allows a supramolecular structure (**4 *I***) oriented horizontally to the water subphase, schematically shown in Figure 7.2 II. This derivative shows a higher degree of freedom of molecular assembly in the L-film compared to the molecules (**4a**, **b**) known from literature[146], which are molecularly very stiff and monopolar substituted. In contrast to the previous paragraph, however, the structures used here did not produce multiphase Π(A)-isotherms of high compressibility. Thus, apart from the variation of the angle of attack and the associated horizontal assembly of **4**, no changes of the supramolecular structure or indications of strong intermolecular interactions were found (see Figure 7.2 II). However, these assemblies can be of great importance with regard to the optimal charge carrier transfer between the electrodes[222] and the vertical radiation characteristic[23] in optoelectronic devices. To confirm the assumption of the supra-molecular structure, the L-films were subsequently transferred to substrates and their supramolecular structure was examined by polarization dependent fluorescence spectroscopy. It was shown that, independent of molecular geometry or deposition pressure (Π_{LB}) employed, a preferential orientation prevails, which results from the transfer from water to substrate. Besides this preferred orientation, there is a side-orientation whose supramolecular order is dependent on molecular stiffness and Π_{LB}.

Due to the limited intermolecular interaction of the double-anchored 4-hydroxy-thiazoles oriented horizontally to the water surface (Chapter 3), the structural motif (**2b**) substituted with a $(CH_2)_n$-chain and COOH-group was again investigated in Chapter 4 for further consideration of thermodynamically stable layers. Using the Py-Ph-derivative, the length of the $(CH_2)_{1,5,10}$-chain (**6a**, **6b**, **6c**) was varied (Figure 7.1 III) and its influence on the supramolecular structure of the L and LB films was investigated. The extension of the intermediate chain enables the thiazole to generate a multiphase, clearly separated Π(A) isotherm of the thiazole with $(CH_2)_{10}$ chain-(**6c *I*, *II*, *III***) in addition to the single phase known for the $(CH_2)_5$-chain (cf. **2b *I*** and **6b *I***). The combination of Py-Ph-derivative, which tends to strong intermolecular ππ-interactions and the degree of freedom of molecular assembly induced by the $(CH_2)_{10}$-chain thus allows the targeted control of supramolecular structures of different intermolecular interactions (Figure 7.2 III). The latter have been investigated by compression-expansion-cycles of the Π(A)-isotherm to determine the effect of these interactions on the thermodynamic stability of the L-film. It was demonstrated for the first time – and in contrast to the literature[187, 196-198] – that the targeted control of condensed phases of the Π(A)-isotherm with strong ππ-interactions (**6c *II*, *III***) gradually produces stable dimeric structures at room temperature. These thermodynamically stable supramolecular structures of the L-film were transferred to a substrate and compared with the supramolecular structures derived from the Π(A)-isotherm by polarization-dependent fluorescence spectroscopy. For the LB films, irrespective of the supramolecular structure of **6c**, a reorientation[205] induced by the absorption heat or an increase of the supramolecular order at the preferred orientations according to Rong et al[188] was observed. Independently of this, a preferential and secondary orientation, as previously shown for **4 *I***,

4a ***I*** and **4b** ***I***, could again be demonstrated. While both orientations are influenced in their x-y-orientation by compression, an increase in anisotropy was only achieved in the side-orientation by compression. By targeted thermal annealing of the layers, the thermodynamic stability of the LB films of **6c** was investigated with respect to the lack of reorientation of the supramolecular structure. It was shown that the LB films deposited from the liquid phase as well as from the different condensed phases (**6c** ***I***, ***II***, ***III***) of the Π(A)-isotherm show only a slight change of orientation by annealing and are therefore thermodynamically stable. LB films with an upright supramolecular structure (**6b** ***III***) exhibit the lowest stability at highest compression (see Figure 7.2 III). Meanwhile, the highest stability is achieved with strong substrate-molecule interactions (**6b** ***I***).

Subsequently, the structural motif of thiazole was combined with bipolar interactions (**3c**) in Chapter 5 with regard to the findings of the strong interactions of the Ph-groups (**1c**, **2c**) in the L-film (ππ). Therefore the 4-hydroxythiazole was substituted at the 2-position with a 4-N,N-dimethylaminophenyl and at the 5-position with a nitrophenyl group (**7**) (Figure 7.1 IV). An arylic (Ph) intermediate chain (**7a**) was introduced to check whether the electrical conductivity can be increased by the increased proportion of conjugated groups (π). Therefore, the film formation and supramolecular structure of the L- and LB-films of **7a** were compared with the alkyl $(CH_2)_{5,\,10}$ as intermediate chain (**7b**, **c**) substituted thiazoles regarding optoelectronic properties. The spectroscopic characterization of the solutions of **7a** revealed that a second species exists alongside the monomer species, which did not occur in any of the 4-hydroxythiazoles[140-141, 146, 165-166, 223] previously known in literature. This second species is characterized by a combination of intramolecular ππ-interactions of the Ph intermediate chain with the chromophore and intramolecular acid-base interactions of the $N(CH_3)_2$- and COOH-groups. Although this conformers dominates the film formation of **7a** ***I*** and leads to an increase in packing density, a similar supramolecular structure was found with **7b** ***I*** (see Figure 7.2 IV). Both supramolecular structures are doubly anchored with $N(CH_3)_2$- and COOH-group and tilted vertically. Independently of the type of intermediate chain, a stabilizing effect of the bipolarity against **6b** substituted at the crossbar of the T-shaped structural motif (only ππ-interactions) was demonstrated. In contrast to the bipolar substitution of I-shaped structural motifs (azobenzene in Tang et al.[187]), the substitution of the T-shaped structural motif thus not only enables other supramolecular structures, but it also increased stability in the L-film. The spectroscopic analysis of the LB-films of **7a** ***I*** showed that the conformers can be transferred to the substrate and relaxes as the Π_{LB} rises. The comparable structure of **7b** ***I*** shows signs of a coexisting J-aggregated species when changing to **7b** ***II*** next to the species already assigned to **7b** ***I***. These three supramolecular structures of the two bipolar thiazoles were then measured by conductive atomic force microscopy (see Figure 7.2 IV). It was found that the molecularly densely packed structures of **7a *I*** are much more electrically insulating than those of **7b *I***, but are stable to changes in the electric field. Both supramolecular structures of **7b** show a change in conductivity associated with the orientation of the bipolar chromophores by multiple control within the voltage cycles. Due to the tunnel-dominated conduction of charge carriers of the organic dyes, the current-voltage characteristics of both molecules deviate from the linear, ohmic curve.[199-200, 224]

It was extensively studied, through a variation of the molecular structure and the resulting supramolecular structure after assembly, the optoelectronic properties and thermodynamic stability of the L and LB films from chapter 2 to 5. The resulting, as ideal identified structural motif of a bipolar amphiphilic T-shaped thiazole has now been tested for use in the model of a self-healing optoelectronic device described in the introduction. An essential prerequisite for this is the thermodynamic stability of the organic active layer of the component consisting of amphiphilic dyes against the (saturated) solution of exchange amphiphilic dyes. Therefore, the thermodynamic stability of this active layer was demonstrated *in situ* by the spontaneous self-assembly of the amphiphilic from the solution at the liquid-solid interface (see Figure 7.2 V). For the *in situ* characterization of these layers, the measurement method of photothermal deflection spectroscopy, already known in the context of the detection of interfaces[209-210] and subbandgap states[27, 211] in semiconductors, was modified with respect to the used solvent environment with the saturated solution described above. The solvent environment was varied with respect to structural geometry (cyclic, branched and linear hydrocarbons) and polarity (nonpolar hydrocarbons and polar water), since a clear variation of the supramolecular structure[212-213] was already be detected in the literature with respect to other small molecules. Due to limitations of the experimental setup, the influence of temperature[36, 42, 201] on the assembly was not considered in the context of this work. Nevertheless, the measured spectral shifts of the absorption spectra compared to the saturated solution could show that a change from solvent-dye to dye-dye interactions occurs at the liquid-solid interface due to self-assembly. Thus, for the push-pull thiazole **7d** functionalized with the shortest CH_2-chain and therefore unsuitable for LB, higher order assemblages such as H-aggregation in cyclohexane (cyclic) or J-aggregation in hexane (linear) was detected. By varying the amphiphilicity or molecular geometry of the thiazole with extension of the $(CH_2)_n$-chain ($n = 1, 5, 10$), it was proven that this determines the supramolecular geometry at the liquid-solid interface for self-assembled layers. It was confirmed that amphiphilicity by variation of the intermediate chain has a significant influence on the bonds of the possible assembly. While the push-pull thiazole with the lowest amphiphilicity (**7d**) assembles independently of substrate and solvent environment, this was only demonstrated under ideal conditions), i.e. from a nonpolar solution on a polar substrate, for the molecules with increased amphiphilicity (**7b**, **c**). Furthermore, comparison of the self-assembled monolayers of the LB-compatible molecules **7b** and **c** with their LB-films (**7b *I*** and **c *I***) revealed a similarly pronounced spectral red-shift of higher molecular order. This demonstrates that a highly ordered, thermodynamically stable layer of amphiphilic molecules was formed from an excess volume filled with a saturated solution of exchange amphiphiles. Thus the condition for the self-healing organic optoelectronic device described in Figure 1.1 was fulfilled for the first time. In the course of the investigations of self-healing, a Langmuir-type adsorption of the original monolayer, grown in a non-polar solvent on a polar substrate, was demonstrated exemplarily for **7d**. Upon white light irradiation, a temporary damage was induced in the self-organized layer. It was shown that this damage heals completely afterwards and the full spectral width of the monolayer is restored, but additional degradation products are irreversibly stored. The kinetics of self-healing strongly depends on the concentration of degradation products in the self-organized monolayer and on the heat induced by the measurement.

This dissertation shows how the molecular geometry, film formation and properties of supramolecular geometry can be influenced by the systematic variation of the T-shaped structural motif of the versatilely functionalizable thiazole. For this purpose, the structural motifs were derived by means of LB technology and UV-vis spectroscopy with regard to their thermodynamic stability at the gaseous-liquid and gaseous-solid interfaces and by means of self-assembly at the liquid-solid interface. Thus, in the course of this thesis and opposed to literature reports, it was not only possible to demonstrate the basic suitability of a single, double and triple polarly anchored T-shaped structural motif in the LB technique, but to also show preliminary work for its use in an optoelectronic component. In future work, the optoelectronically promising bipolar push-pull thiazole (**3c**, **7a-d**) can thus be incorporated into a component structure. The resulting layers of bipolar push-pull thiazoles were successfully self-healed within a schematic structure of a self-healing organic optoelectronic device. This is one of the few examples of self-healing by restoring a function of the layer. The preceding investigations of the kinetics of the process of self-arrangement and subsequent self-healing must be extended from **7d** to other derivatives such as **7c-d** and other solvents. In addition, it must be examined whether the process of self-healing of a self-organized monolayer can still be transferred to other dye classes or different modes of destruction. A precise investigation of the polarity change during degradation of the pigments is of decisive importance.

Literaturverzeichnis

1. Li, Y. W.; Xu, G. Y.; Cui, C. H.; Li, Y. F., Flexible and Semitransparent Organic Solar Cells. *Advanced Energy Materials* **2018,** *8* (7), 28.
2. Henning, S., 25th Anniversary Article: Organic Field-Effect Transistors: The Path Beyond Amorphous Silicon. *Advanced Materials* **2014,** *26* (9), 1319-1335.
3. Zhang, C.; Chen, P.; Hu, W., Organic field-effect transistor-based gas sensors. *Chemical Society Reviews* **2015,** *44* (8), 2087-2107.
4. Man-Keung, F.; Yan-Qing, L.; Liang-Sheng, L., Tandem Organic Light-Emitting Diodes. *Advanced Materials* **2016,** *28* (47), 10381-10408.
5. Ostroverkhova, O., Organic Optoelectronic Materials: Mechanisms and Applications. *Chemical Reviews* **2016,** *116* (22), 13279-13412.
6. Green, M. A.; Hishikawa, Y.; Dunlop, E. D.; Levi, D. H.; Hohl-Ebinger, J.; Ho-Baillie, A. W. Y., Solar cell efficiency tables (version 51). *Prog Photovoltaics* **2018,** *26* (1), 3-12.
7. Im, Y.; Byun, S. Y.; Kim, J. H.; Lee, D. R.; Oh, C. S.; Yook, K. S.; Lee, J. Y., Recent Progress in High-Efficiency Blue-Light-Emitting Materials for Organic Light-Emitting Diodes. *Advanced Functional Materials* **2017,** *27* (13), 24.
8. Yu, L.-S.; Tseng, H.-E.; Lu, H.-H.; Chen, S.-A., Effect of structure ordering on charge carrier mobilities in green-emitting poly(phenylene vinylene)s. *Applied Physics Letters* **2002,** *81* (11), 2014-2016.
9. Lee, E. K.; Lee, M. Y.; Park, C. H.; Lee, H. R.; Oh, J. H., Toward Environmentally Robust Organic Electronics: Approaches and Applications. *Advanced Materials* **2017,** *29* (44), 29.
10. Scholz, S.; Kondakov, D.; Lüssem, B.; Leo, K., Degradation Mechanisms and Reactions in Organic Light-Emitting Devices. *Chemical Reviews* **2015,** *115* (16), 8449-8503.
11. Cheng, P.; Zhan, X., Stability of organic solar cells: challenges and strategies. *Chemical Society Reviews* **2016,** *45* (9), 2544-2582.
12. Schaffer, C. J.; Palumbiny, C. M.; Niedermeier, M. A.; Jendrzejewski, C.; Santoro, G.; Roth, S. V.; Müller-Buschbaum, P., A Direct Evidence of Morphological Degradation on a Nanometer Scale in Polymer Solar Cells. *Advanced Materials* **2013,** *25* (46), 6760-6764.
13. Presselt, M.; Schnedermann, C.; Müller, M.; Schmitt, M.; Popp, J., Derivation of Correlation Functions to Predict Bond Properties of Phenyl-CH Bonds Based on Vibrational and H-1 NMR Spectroscopic Quantities. *Journal of Physical Chemistry A* **2010,** *114* (37), 10287-10296.
14. Fitzner, R.; Mena-Osteritz, E.; Mishra, A.; Schulz, G.; Reinold, E.; Weil, M.; Koerner, C.; Ziehlke, H.; Elschner, C.; Leo, K.; Riede, M.; Pfeiffer, M.; Uhrich, C.; Baeuerle, P., Correlation of pi-Conjugated Oligomer Structure with Film Morphology and Organic Solar Cell Performance. *Journal of the American Chemical Society* **2012,** *134* (27), 11064-11067.
15. Lo, W.-Y.; Zhang, N.; Cai, Z.; Li, L.; Yu, L., Beyond Molecular Wires: Design Molecular Electronic Functions Based on Dipolar Effect. *Accounts of Chemical Research* **2016,** *49* (9), 1852-1863.
16. Bayat, A.; Lacroix, J.-C.; McCreery, R. L., Control of Electronic Symmetry and Rectification through Energy Level Variations in Bilayer Molecular Junctions. *Journal of the American Chemical Society* **2016,** *138* (37), 12287-12296.
17. Das, S.; Herrmann-Westendorf, F.; Schacher, F. H.; Tauscher, E.; Ritter, U.; Dietzek, B.; Presselt, M., Controlling Electronic Transitions in Fullerene van der Waals Aggregates via Supramolecular Assembly. *ACS Applied Materials & Interfaces* **2016,** *8* (33), 21512-21521.

18. Herrmann, F.; Engmann, S.; Presselt, M.; Hoppe, H.; Shokhovets, S.; Gobsch, G., Correlation between near infrared-visible absorption, intrinsic local and global sheet resistance of poly(3,4-ethylenedioxy-thiophene) poly(styrene sulfonate) thin films. *Applied Physics Letters* **2012,** *100* (15), 153301-01 - 03.
19. Gampe, D. M.; Kaufmann, M.; Jakobi, D.; Sachse, T.; Presselt, M.; Beckert, R.; Gorls, H., Stable and easily accessible functional dyes: dihydrotetraazaanthracenes as versatile precursors for higher acenes. *Chemistry* **2015,** *21* (20), 7571-81.
20. Würthner, F.; Kaiser, T. E.; Saha-Möller, C. R., J-Aggregates: From Serendipitous Discovery to Supramolecular Engineering of Functional Dye Materials. *Angewandte Chemie International Edition* **2011,** *50* (15), 3376-3410.
21. Biesmans, G.; Verbeek, G.; Verschuere, B.; van der Auweraer, M.; De Schryver, F. C., On the fluorescence of anthracene chromophores in langmuir-blodgett films. *Thin Solid Films* **1989,** *169* (1), 127-142.
22. Li, Q.; Li, Z., The Strong Light-Emission Materials in the Aggregated State: What Happens from a Single Molecule to the Collective Group. *Advanced Science* **2017,** *4* (7), 1600484.
23. Flämmich, M.; Gather, M. C.; Danz, N.; Michaelis, D.; Bräuer, A. H.; Meerholz, K.; Tünnermann, A., Orientation of emissive dipoles in OLEDs: Quantitative in situ analysis. *Organic Electronics* **2010,** *11* (6), 1039-1046.
24. Mayr, C.; Schmidt, T. D.; Brütting, W., High-efficiency fluorescent organic light-emitting diodes enabled by triplet-triplet annihilation and horizontal emitter orientation. *Applied Physics Letters* **2014,** *105* (18), 183304-01 - 04.
25. Friederich, P.; Coehoorn, R.; Wenzel, W., Molecular Origin of the Anisotropic Dye Orientation in Emissive Layers of Organic Light Emitting Diodes. *Chemistry of Materials* **2017,** *29* (21), 9528-9535.
26. Presselt, M.; Herrmann, F.; Hoppe, H.; Shokhovets, S.; Runge, E.; Gobsch, G., Influence of Phonon Scattering on Exciton and Charge Diffusion in Polymer-Fullerene Solar Cells. *Advanced Energy Materials* **2012,** *2* (8), 999-1003.
27. Beenken, W. J. D.; Herrmann, F.; Presselt, M.; Hoppe, H.; Shokhovets, S.; Gobsch, G.; Runge, E., Sub-bandgap absorption in organic solar cells: experiment and theory. *Physical Chemistry Chemical Physics* **2013,** *15* (39), 16494-16502.
28. Presselt, M.; Bärenklau, M.; Rösch, R.; Beenken, W. J. D.; Runge, E.; Shokhovets, S.; Hoppe, H.; Gobsch, G., Sub-Bandgap Absorption in Polymer-Fullerene Solar Cells. *Applied Physics Letters* **2010,** *97* (25), 253302-01 - 02.
29. Shewmon, N. T.; Watkins, D. L.; Galindo, J. F.; Zerdan, R. B.; Chen, J.; Keum, J.; Roitberg, A. E.; Xue, J.; Castellano, R. K., Enhancement in Organic Photovoltaic Efficiency through the Synergistic Interplay of Molecular Donor Hydrogen Bonding and π-Stacking. *Advanced Functional Materials* **2015,** *25* (32), 5166-5177.
30. Li, Z.; Bian, J.; Wang, Y.; Jiang, F.; Liang, G.; He, P.; Hou, Q.; Tong, J.; Liang, Y.; Zhong, Z.; Zhou, Y.; Tian, W., Effect of Alkyl Chain Length on the Photovoltaic Performance of Oligothiophene-Based Small Molecules. *Solar Energy Materials and Solar Cells* **2014,** *130*, 336-346.
31. Poelking, C.; Tietze, M.; Elschner, C.; Olthof, S.; Hertel, D.; Baumeier, B.; Würthner, F.; Meerholz, K.; Leo, K.; Andrienko, D., Impact of mesoscale order on open-circuit voltage in organic solar cells. *Nature Materials* **2015,** *14* (4), 434-439.
32. Das, S.; Preiß, J.; Plentz, J.; Brückner, U.; von der Lühe, M.; Eckardt, O.; Dathe, A.; Schacher, F. H.; Täuscher, E.; Ritter, U.; Csáki, A.; Andrä, G.; Dietzek, B.; Presselt, M., Controlling Intermolecular Interactions at Interfaces: Case of Supramolecular Tuning of Fullerene's Electronic Structure. *Advanced Energy Materials* **2018,** *8* (32), 1801737.

33. Cai, Z.; Zhao, D.; Sharapov, V.; Awais, M. A.; Zhang, N.; Chen, W.; Yu, L., Enhancement in Open-Circuit Voltage in Organic Solar Cells by Using Ladder-Type Nonfullerene Acceptors. *ACS Applied Materials & Interfaces* **2018,** *10* (16), 13528-13533.
34. Chen, Y.; Feng, Y.; Gao, J.; Bouvet, M., Self-assembled aggregates of amphiphilic perylene diimide–based semiconductor molecules: Effect of morphology on conductivity. *Journal of colloid and interface science* **2012,** *368* (1), 387-394.
35. Grozema, F. C.; Siebbeles, L. D. A., Mechanism of charge transport in self-organizing organic materials. *Int. Rev. Phys. Chem.* **2008,** *27* (1), 87-138.
36. Presselt, M.; Herrmann, F.; Shokhovets, S.; Hoppe, H.; Runge, E.; Gobsch, G., Sub-bandgap absorption in polymer-fullerene solar cells studied by temperature-dependent external quantum efficiency and absorption spectroscopy. *Chemical Physics Letters* **2012,** *542*, 70-73.
37. Kar, H.; Gehrig, D. W.; Laquai, F.; Ghosh, S., J-Aggregation, its Impact on Excited State Dynamics and Unique Solvent Effects on Macroscopic Assembly of a Core-Substituted Naphthalenediimide. *Nanoscale* **2015,** *7* (15), 6729-6736.
38. De la Cadena, A.; Pascher, T.; Davydova, D. y.; Akimov, D.; Herrmann, F.; Presselt, M.; Wächtler, M.; Dietzek, B., Intermolecular exciton–exciton annihilation in phospholipid vesicles doped with [Ru(bpy)2dppz]2+. *Chemical Physics Letters* **2016,** *644*, 56-61.
39. Kitchen, B.; Awartani, O.; Kline, R. J.; McAfee, T.; Ade, H.; O'Connor, B. T., Tuning Open-Circuit Voltage in Organic Solar Cells with Molecular Orientation. *Acs Applied Materials & Interfaces* **2015,** *7* (24), 13208-13216.
40. Zhong, S.; Zhong, J. Q.; Wee, A. T. S.; Chen, W., Molecular orientation and electronic structure at organic heterojunction interfaces. *Journal of Electron Spectroscopy and Related Phenomena* **2015,** *204*, 12-22.
41. da Costa, V. C. P.; Hwang, B. J.; Eggen, S. E.; Wallace, M. J.; Annunziata, O., Formation and thermodynamic stability of (polymer+porphyrin) supramolecular structures in aqueous solutions. *The Journal of Chemical Thermodynamics* **2014,** *75*, 119-127.
42. Conti, S.; Cecchini, M., Predicting molecular self-assembly at surfaces: a statistical thermodynamics and modeling approach. *Physical Chemistry Chemical Physics* **2016,** *18* (46), 31480-31493.
43. Yang, Y.; Urban, M. W., Self-healing polymeric materials. *Chemical Society Reviews* **2013,** *42* (17), 7446-7467.
44. Ahner, J.; Bode, S.; Micheel, M.; Dietzek, B.; Hager, M. D., Self-Healing Functional Polymeric Materials. In *Self-healing Materials*, Hager, M. D.; van der Zwaag, S.; Schubert, U. S., Eds. Springer International Publishing: Cham, **2016**, pp 247-283.
45. Tan, Y. J.; Wu, J.; Li, H.; Tee, B. C. K., Self-Healing Electronic Materials for a Smart and Sustainable Future. *ACS Applied Materials & Interfaces* **2018,** *10* (18), 15331-15345.
46. Ahner, J.; Micheel, M.; Geitner, R.; Schmitt, M.; Popp, J.; Dietzek, B.; Hager, M. D., Self-healing Functional Polymers: Optical Property Recovery of Conjugated Polymer Films by Uncatalyzed Imine Metathesis. *Macromolecules* **2017,** *50* (10), 3789-3795.
47. Tumbleston, J. R.; Collins, B. A.; Yang, L. Q.; Stuart, A. C.; Gann, E.; Ma, W.; You, W.; Ade, H., The influence of molecular orientation on organic bulk heterojunction solar cells. *Nature Photonics* **2014,** *8* (5), 385-391.
48. Rivnay, J.; Jimison, L. H.; Northrup, J. E.; Toney, M. F.; Noriega, R.; Lu, S.; Marks, T. J.; Facchetti, A.; Salleo, A., Large modulation of carrier transport by grain-boundary molecular packing and microstructure in organic thin films. *Nat Mater* **2009,** *8* (12), 952-8.
49. Würthner, F., Dipole-Dipole Interaction Driven Self-Assembly of Merocyanine Dyes: From Dimers to Nanoscale Objects and Supramolecular Materials. *Accounts of Chemical Research* **2016,** *49* (5), 868-876.
50. Gutzler, R.; Sirtl, T.; Dienstmaier, J. F.; Mahata, K.; Heckl, W. M.; Schmittel, M.; Lackinger, M., Reversible Phase Transitions in Self-Assembled Monolayers at the Liquid−Solid Interface:

Temperature-Controlled Opening and Closing of Nanopores. *Journal of the American Chemical Society* **2010,** *132* (14), 5084-5090.
51. Kim, S.-Y.; Jeong, W.-I.; Mayr, C.; Park, Y.-S.; Kim, K.-H.; Lee, J.-H.; Moon, C.-K.; Brütting, W.; Kim, J.-J., Organic Light-Emitting Diodes with 30% External Quantum Efficiency Based on a Horizontally Oriented Emitter. *Advanced Functional Materials* **2013,** *23* (31), 3896-3900.
52. Chen, J.-D.; Cui, C.; Li, Y.-Q.; Zhou, L.; Ou, Q.-D.; Li, C.; Li, Y.; Tang, J.-X., Single-Junction Polymer Solar Cells Exceeding 10% Power Conversion Efficiency. *Advanced Materials* **2015,** *27* (6), 1035-1041.
53. Aziz, F.; Ismail, A. F., Spray coating methods for polymer solar cells fabrication: A review. *Materials Science in Semiconductor Processing* **2015,** *39*, 416-425.
54. Xu, J.; Wang, Y.; Shan, H.; Lin, Y.; Chen, Q.; Roy, V. A. L.; Xu, Z., Ultrasound-Induced Organogel Formation Followed by Thin Film Fabrication via Simple Doctor Blading Technique for Field-Effect Transistor Applications. *ACS Applied Materials & Interfaces* **2016,** *8* (29), 18991-18997.
55. Bürckstümmer, H.; Tulyakova, E. V.; Deppisch, M.; Lenze, M. R.; Kronenberg, N. M.; Gsänger, M.; Stolte, M.; Meerholz, K.; Würthner, F., Efficient Solution-Processed Bulk Heterojunction Solar Cells by Antiparallel Supramolecular Arrangement of Dipolar Donor–Acceptor Dyes. *Angewandte Chemie International Edition* **2011,** *50* (49), 11628-11632.
56. Würthner, F.; Chen, Z. J.; Hoeben, F. J. M.; Osswald, P.; You, C. C.; Jonkheijm, P.; von Herrikhuyzen, J.; Schenning, A.; van der Schoot, P.; Meijer, E. W.; Beckers, E. H. A.; Meskers, S. C. J.; Janssen, R. A. J., Supramolecular p-n-heterojunctions by co-self-organization of oligo(p-phenylene vinylene) and perylene bisimide dyes. *Journal Of The American Chemical Society* **2004,** *126* (34), 10611-10618.
57. Ariga, K.; Hill, J. P.; Ji, Q. M., Layer-by-layer assembly as a versatile bottom-up nanofabrication technique for exploratory research and realistic application. *Physical Chemistry Chemical Physics* **2007,** *9* (19), 2319-2340.
58. Wang, Y.; Angelatos, A. S.; Caruso, F., Template Synthesis of Nanostructured Materials via Layer-by-Layer Assembly. *Chemistry of Materials* **2008,** *20* (3), 848-858.
59. Würthner, F.; Yao, S.; Beginn, U., Highly Ordered Merocyanine Dye Assemblies by Supramolecular Polymerization and Hierarchical Self-Organization. *Angewandte Chemie International Edition* **2003,** *42* (28), 3247-3250.
60. Zhang, X.; Görl, D.; Stepanenko, V.; Würthner, F., Hierarchical Growth of Fluorescent Dye Aggregates in Water by Fusion of Segmented Nanostructures. *Angewandte Chemie International Edition* **2014,** *53* (5), 1270-1274.
61. Miyazawa, K.; Kuwasaki, Y.; Obayashi, A.; Kuwabara, M., C60 Nanowhiskers Formed by the Liquid–liquid Interfacial Precipitation Method. *Journal of Materials Research* **2002,** *17* (1), 83-88.
62. Ariga, K.; Yuki, H.; Kikuchi, J.-i.; Dannemuller, O.; Albrecht-Gary, A.-M.; Nakatani, Y.; Ourisson, G., Monolayer Studies of Single-Chain Polyprenyl Phosphates. *Langmuir* **2005,** *21* (10), 4578-4583.
63. Jin, J.; Li, L. S.; Li, Y.; Zhang, Y. J.; Chen, X.; Wang, D.; Jiang, S.; Li, T. J.; Gan, L. B.; Huang, C. H., Structural Characterizations of C60-Derivative Langmuir–Blodgett Films and Their Photovoltaic Behaviors. *Langmuir* **1999,** *15* (13), 4565-4569.
64. Angelova, A.; Ionov, R., Monolayer and Spectroscopic Studies of an Amphiphilic (Phenylethynyl)anthracene Probe in Pure and Mixed Films with Charged and Neutral Lipids. *Langmuir* **1999,** *15* (21), 7199-7207.
65. Modlińska, A.; Bauman, D., The Langmuir-Blodgett Technique as a Tool for Homeotropic Alignment of Fluorinated Liquid Crystals Mixed with Arachidic Acid. *International Journal of Molecular Sciences* **2011,** *12* (8), 4923-4945.

66. Ariga, K.; Yamauchi, Y.; Mori, T.; Hill, J. P., 25th Anniversary Article: What Can Be Done with the Langmuir-Blodgett Method? Recent Developments and its Critical Role in Materials Science. *Advanced Materials* **2013,** *25* (45), 6477-6512.
67. Langmuir, I., The Constitution and Fundamental Properties of Solids and Liquids. Ii. Liquids.1. *Journal of the American Chemical Society* **1917,** *39* (9), 1848-1906.
68. Blodgett, K. B., Films Built by Depositing Successive Monomolecular Layers on a Solid Surface. *Journal of the American Chemical Society* **1935,** *57* (6), 1007-1022.
69. Kato, N.; Sasaki, T.; Mukai, Y., Partially induced transition from horizontal to vertical orientation of helical peptides at the air–water interface and the structure of their monolayers transferred on the solid substrates. *Biochimica et Biophysica Acta (BBA) - Biomembranes* **2015,** *1848* (4), 967-975.
70. Schwarz, G.; Taylor, S. E., Peptide-lipid interactions in Langmuir monolayers. A novel approach toward structural and thermodynamic analyses. *Biophysical Journal* **1997,** *72* (2), TUAM1-TUAM1.
71. Cao, X. H.; Sui, G. D.; Huo, Q.; Leblanc, R. M., Langmuir and Langmuir-Blodgett films of a novel tryptophan peptide lipid. *Chemical Communications* **2002,** (8), 806-807.
72. Dennison, S. R.; Harris, F.; Phoenix, D. A., A Langmuir Approach Using Monolayer Interactions to Investigate Surface Active Peptides. *Protein and Peptide Letters* **2010,** *17* (11), 1363-1375.
73. Schmidt, T. F.; Salesse, C.; Riske, K. A., Effect of Dengue Fusion Peptide in Langmuir Monolayers. *Biophysical Journal* **2016,** *110* (3), 570A-570A.
74. Yang, J.; Kleijn, J. M., Order in Phospholipid Langmuir-Blodgett Layers and the Effect of the Electrical Potential of the Substrate. *Biophysical Journal* **1999,** *76* (1), 323-332.
75. Liljeroth, P.; Malkia, A.; Cunnane, V. J.; Kontturi, A. K.; Kontturi, K., Langmuir-Blodgett monolayers at a liquid-liquid interface. *Langmuir* **2000,** *16* (16), 6667-6673.
76. Saad, S. M. I.; Policova, Z.; Acosta, E. J.; Hair, M. L.; Neumann, A. W., Mixed DPPC/DPPG Monolayers at Very High Film Compression. *Langmuir* **2009,** *25* (18), 10907-10912.
77. Chen, X.; Huang, Z.; Hua, W.; Castada, H.; Allen, H. C., Reorganization and Caging of DPPC, DPPE, DPPG, and DPPS Monolayers Caused by Dimethylsulfoxide Observed Using Brewster Angle Microscopy. *Langmuir* **2010,** *26* (24), 18902-18908.
78. Kaganer, V. M.; Mohwald, H.; Dutta, P., Structure and phase transitions in Langmuir monolayers. *Reviews of Modern Physics* **1999,** *71* (3), 779-819.
79. Caruso, F.; Grieser, F.; Thistlethwaite, P. J.; Almgren, M., Lateral diffusion of amphiphiles in fatty acid monolayers at the air-water interface: a steady-state and time-resolved fluorescence quenching study. *Langmuir* **1993,** *9* (11), 3142-3148.
80. Rana, F. R.; Widayati, S.; Gregory, B. W.; Dluhy, R. A., Metastability in Monolayer Films Transferred onto Solid Substrates by the Langmuir-Blodgett Method: IR Evidence for Transfer-Induced Phase Transitions. *Applied Spectroscopy* **1994,** *48* (10), 1196-1203.
81. Roldan-Carmona, C.; Gonzalez-Delgado, A. M.; Guerrero-Martinez, A.; Cola, L. D.; Giner-Casares, J. J.; Perez-Morales, M.; Martin-Romero, M. T.; Camacho, L., Molecular organization and effective energy transfer in iridium metallosurfactant-porphyrin assemblies embedded in Langmuir-Schaefer films. *Physical Chemistry Chemical Physics* **2011,** *13* (7), 2834-2841.
82. Hertmanowski, R.; Martyński, T.; Bauman, D., Alignment of molecules in Langmuir and Langmuir-Blodgett films of binary mixtures of 3,4,9,10-tetra-(n-alkoxy-carbonyl)-perylenes with a liquid crystal. *Journal of Molecular Structure* **2005,** *741* (1), 201-211.
83. Makowiecki, J.; Piosik, E.; Neunert, G.; Stolarski, R.; Piecek, W.; Martynski, T., Molecular organization of perylene derivatives in Langmuir–Blodgett multilayers. *Optical Materials* **2015,** *46*, 555-560.

84. Piosik, E.; Kotkowiak, M.; Korbecka, I.; Galewski, Z.; Martynski, T., Photo-switching of a non-ionic azobenzene amphiphile in Langmuir and Langmuir-Blodgett films. *Physical Chemistry Chemical Physics* **2017,** *19* (34), 23386-23396.

85. Hertmanowski, R.; Biadasz, A.; Martyński, T.; Bauman, D., Optical spectroscopy study of some 3,4,9,10-tetra-(n-alkoxy-carbonyl)-perylenes in Langmuir–Blodgett films. *Journal of Molecular Structure* **2003,** *646* (1), 25-33.

86. Biadasz, A.; Hertmanowski, R.; Martyński, T.; Inglot, K.; Bauman, D., Langmuir films of dichroic dyes with fluorescent properties. *Dyes and Pigments* **2003,** *56* (3), 209-217.

87. Biadasz, A.; Martynski, T.; Stolarski, R.; Bauman, D., Molecular organization in binary mixtures of derivatives of naphthalenebicarboxylic acid and naphthoylenebenzimidazole with a liquid crystal in two-dimensional layers I. Langmuir films. *Liquid Crystals* **2004,** *31* (12), 1639-1648.

88. Zhang, L.; Cole, J. M., Anchoring Groups for Dye-Sensitized Solar Cells. *ACS Applied Materials & Interfaces* **2015,** *7* (6), 3427-3455.

89. Paluszkiewicz, J.; Stolarski, R.; Stanczyk, W. A.; Martynski, T.; Rutowicz, J., New perylene dyes, derivatives of 1,6,7,12-tetrachloroperylene-3,4,9,10-tetracarboxylic acid: synthesis and application. *Coloration Technology* **2016,** *132* (6), 449-459.

90. Bauman, D.; Hertmanowski, R.; Stefańska, K.; Stolarski, R., The synthesis of novel perylene-like dyes and their aggregation properties in Langmuir and Langmuir–Blodgett films. *Dyes Pigm.* **2011,** *91* (3), 474-480.

91. Debnath, C.; Shil, A.; Hussain, S. A.; Bhattacharjee, D., Effect of clay in controlling the non-fluorescence H-dimeric states of a cationic dye Nile Blue Chloride (NBC) in hybrid Langmuir–Blodgett (LB) film. *Chemical Physics Letters* **2018,** *691*, 298-306.

92. Banik, S.; Hussain, S. A.; Bhattacharjee, D., Modified aggregation pattern of cresyl violet acetate adsorbed on nano clay mineral layers in Langmuir Blodgett film. *Journal of Photochemistry and Photobiology A: Chemistry* **2018,** *353*, 570-580.

93. Debnath, C.; Shil, A.; Hussain, S. A.; Bhattacharjee, D., Metal ion-induced H-aggregation of a water-soluble anionic dye Congo red (CR) in Langmuir–Blodgett (LB) film. *Supramolecular Chemistry* **2017,** *29* (6), 401-410.

94. Bauman, D.; Plociennik, A.; Inglot, K., Molecular Interactions in Monolayers of Azo Dye/Liquid Crystal Mixtures at Interfaces. *Acta Physica Polonica A* **2009,** *116* (2), 203-210.

95. Nuckolls, C.; Katz, T. J.; Verbiest, T.; Elshocht, S. V.; Kuball, H.-G.; Kiesewalter, S.; Lovinger, A. J.; Persoons, A., Circular Dichroism and UV−Visible Absorption Spectra of the Langmuir−Blodgett Films of an Aggregating Helicene. *Journal of the American Chemical Society* **1998,** *120* (34), 8656-8660.

96. Miyata, A.; Heard, D.; Unuma, Y.; Higashigaki, Y., Three types of aggregates of spiropyran with long and short hydrophobic alkyl chains. *Thin Solid Films* **1992,** *210-211*, 175-177.

97. Łabuszewska, K.; Cegielski, R.; Niedbalska, M.; Martyński, T., Stilbazolium merocyanine systems in Langmuir and Langmuir–Blodgett molecular layers. *Colloids and Surfaces A: Physicochemical and Engineering Aspects* **2008,** *321* (1), 39-42.

98. Lodi, A.; Momicchioli, F.; Caselli, M.; Giancane, G.; Ponterini, G., A comparative study of two amphiphilic merocyanines: from monomers to aggregates in Langmuir and Langmuir-Blodgett mixed films. *RSC Advances* **2013,** *3* (5), 1468-1475.

99. Kędzierski, K.; Barszcz, B.; Kotkowiak, M.; Bursa, B.; Goc, J.; Dinçer, H.; Wróbel, D., Photophysics of an unsymmetrical Zn(II) phthalocyanine substituted with terminal alkynyl group. *Journal of Luminescence* **2016,** *180*, 132-139.

100. Mitsuru, Y.; Michio, S.; Mitsuyoshi, S.; Keiichi, I.; Shin-ichi, K.; Sigeru, I., Photoelectric Properties of Copper Phthalocyanine Langmuir-Blodgett Film. *Japanese Journal of Applied Physics* **1986,** *25* (7R), 961.

101. Biadasz, A.; Bursa, B.; Barszcz, B.; Bogucki, A.; Laskowska, B.; Graja, A.; Wróbel, D., Thermodynamics and in-situ absorption of Langmuir monolayers of selected copper phthalocyanine substituted with different peripheral groups. *Dyes and Pigments* **2011,** *89* (1), 86-92.

102. Lu, X. Z.; Ma, S. H.; Song, J.; Han, K.; Zheng, J. B.; Wang, W. C., Time Resolved Fluorescence investigations of Aggregation in LB Films. *Acta Phys.-Chim. Sin.* **1996,** *12* (5), 413-417.

103. Leray, A.; Rouede, D.; Odin, C.; Le Grand, Y.; Mongin, O.; Blanchard-Desce, M., Effect of the orientational disorder on the hyperpolarizability measurement of amphiphilic push-pull chromophores in Langmuir-Blodgett monolayers. *Optics Communications* **2005,** *247* (1-3), 213-223.

104. Selektor, S. L.; Shcherbina, M. A.; Bakirov, A. V.; Batat, P.; Grauby-Heywang, C.; Grigorian, S.; Arslanov, V. V.; Chvalun, S. N., Cation-Controlled Excimer Packing in Langmuir–Blodgett Films of Hemicyanine Amphiphilic Chromoionophores. *Langmuir* **2016,** *32* (2), 637-643.

105. Balaswamy, B.; Maganti, L.; Sharma, S.; Radhakrishnan, T. P., Mechanical Control of Molecular Aggregation and Fluorescence Switching/Enhancement in an Ultrathin Film. *Langmuir* **2012,** *28* (50), 17313-17321.

106. Debnath, P.; Chakraborty, S.; Deb, S.; Nath, J.; Dey, B.; Bhattacharjee, D.; Hussain, S. A., Stability of J-aggregated species in an indocarbocyanine dye in Langmuir–Blodgett Films. *Journal of Luminescence* **2016,** *179* (Supplement C), 287-296.

107. Debnath, P.; Chakraborty, S.; Deb, S.; Nath, J.; Bhattacharjee, D.; Hussain, S. A., Reversible Transition between Excimer and J-Aggregate of Indocarbocyanine Dye in Langmuir–Blodgett (LB) Films. *The Journal of Physical Chemistry C* **2015,** *119* (17), 9429-9441.

108. Hussain, S. A.; Dey, D.; Chakraborty, S.; Bhattacharjee, D., J-aggregates of thiacyanine dye organized in LB films: Effect of irradiation of light. *Journal of Luminescence* **2011,** *131* (8), 1655-1660.

109. Yamaguchi, A.; Kometani, N.; Yonezawa, Y., Luminescence properties of the mixed J-aggregate of oxacyanine dye and thiacyanine dye. Formation of a persistence-type aggregate. *Journal of Physical Chemistry B* **2005,** *109* (4), 1408-1414.

110. Ahmida, M.; Dufour, S.; Li, H.-S.; Kayal, H.; Schmidt, R.; DeWolf, C. E.; Eichhorn, S. H., Face- and edge-on orientations of octa-acid and -alcohol substituted tetraazaporphyrins in Langmuir and Langmuir-Blodgett monolayers. *Soft Matter* **2013,** *9* (3), 811-819.

111. Chou, H.; Chen, C. T.; Stork, K. F.; Bohn, P. W.; Suslick, K. S., LANGMUIR-BLODGETT-FILMS OF AMPHIPHILIC PUSH-PULL PORPHYRINS. *Journal of Physical Chemistry* **1994,** *98* (2), 383-385.

112. Matsui, J.; Shimada, T.; Miyashita, T., Electrochemical charging and photochemical discharging in heterodeposited polymer nanosheet assembly. *Journal of Materials Chemistry* **2011,** *21* (43), 17498-17504.

113. Matsui, J.; Kikuchi, R.; Miyashita, T., A Trilayer Film Approach to Multicolor Electrochromism. *Journal of the American Chemical Society* **2014,** *136* (3), 842-845.

114. Bursa, B.; Wróbel, D.; Lewandowska, K.; Graja, A.; Grzybowski, M.; Gryko, D. T., Spectral studies of molecular orientation in corrole-fullerene thin films. *Synthetic Metals* **2013,** *176*, 18-25.

115. Preiß, J.; Herrmann-Westendorf, F.; Ngo, T. H.; Martínez, T. J.; Dietzek, B.; Hill, J. P.; Ariga, K.; Kruk, M. M.; Maes, W.; Presselt, M., Absorption and Fluorescence Features of an Amphiphilic meso-Pyrimidinylcorrole: Experimental Study and Quantum Chemical Calculations. *The Journal of Physical Chemistry A* **2017,** *121* (45), 8614-8624.

116. Biadasz, A.; Martyński, T.; Bauman, D., Langmuir–Blodgett films of some fluorescent dichroic dyes as studied by optical spectroscopy methods. *Journal of Molecular Structure* **2005,** *744-747*, 973-978.

117. Bielejewska, N.; Chrzumnicka, E.; Stolarski, R.; Bauman, D., Spectral properties of naphthalimide dyes mixed with 4-heptyl-4′-cyanobiphenyl (7CB) in Langmuir-Blodgett films. *Opto-Electron. Rev.* **2010,** *18* (2), 197-207.
118. Zou, L.; You, A.; Song, J.; Li, X.; Bouvet, M.; Sui, W.; Chen, Y., Cation-induced self-assembly of an amphiphilic perylene diimide derivative in solution and Langmuir–Blodgett films. *Colloids and Surfaces A: Physicochemical and Engineering Aspects* **2015,** *465* (Supplement C), 39-46.
119. del Caño, T.; Parra, V.; Rodríguez-Méndez, M. L.; Aroca, R.; de Saja, J. A., Molecular stacking and emission properties in Langmuir–Blodgett films of two alkyl substituted perylene tetracarboxylic diimides. *Organic Electronics* **2004,** *5* (1), 107-114.
120. Vivo, P.; Vuorinen, T.; Chukharev, V.; Tolkki, A.; Kaunisto, K.; Ihalainen, P.; Peltonen, J.; Lemmetyinen, H., Multicomponent Molecularly Controlled Langmuir-Blodgett Systems for Organic Photovoltaic Applications. *The Journal of Physical Chemistry C* **2010,** *114* (18), 8559-8567.
121. Fernández-Hernández, J. M.; De Cola, L.; Bolink, H. J.; Clemente-León, M.; Coronado, E.; Forment-Aliaga, A.; López-Muñoz, A.; Repetto, D., White Light-Emitting Electrochemical Cells Based on the Langmuir–Blodgett Technique. *Langmuir* **2014,** *30* (46), 14021-14029.
122. Bolink, H. J.; Baranoff, E.; Clemente-León, M.; Coronado, E.; Lardiés, N.; López-Muñoz, A.; Repetto, D.; Nazeeruddin, M. K., Dual-Emitting Langmuir−Blodgett Film-Based Organic Light-Emitting Diodes. *Langmuir* **2010,** *26* (13), 11461-11468.
123. Hu, W.; Liu, Y.; Xu, Y.; Liu, S.; Zhou, S.; Zhu, D., The application of Langmuir–Blodgett films of a new asymmetrically substituted phthalocyanine, amino-tri-tert-butyl-phthalocyanine, in diodes and in all organic field-effect-transistors. *Synthetic Metals* **1999,** *104* (1), 19-26.
124. Wang, Y.; Chen, Y.; Li, R.; Wang, S.; Su, W.; Ma, P.; Wasielewski, M. R.; Li, X.; Jiang, J., Amphiphilic Perylenetretracarboxyl Diimide Dimer and Its Application in Field Effect Transistor. *Langmuir* **2007,** *23* (10), 5836-5842.
125. Baker, S.; Roberts, G. G.; Petty, M. C., Phthalocyanine Langmuir Blodgett-fiim gas detector. *IEE Proceedings I - Solid-State and Electron Devices* **1983,** *130* (5), 260-263.
126. Miller, L. S.; McRoberts, A. M.; Walton, D. J.; Peterson, I. R.; Parry, D. A.; Sykesud, C. G. D.; Newton, A. L.; Powell, B. D.; Jasper, C. A., Optical gas sensing using thin organic films. *Thin Solid Films* **1996,** *284*, 927-931.
127. Liang, B.; Yuan, C.; Wei, Y., Semiconducting, gas-sensing properties of Europium bisphthalocyanine Langmuir–Blodgett thin films. *Journal of Vacuum Science & Technology B* **1997,** *15* (4), 1432-1436.
128. Koo, J. R.; Kim, Y. K.; Kim, J. S., NO2 Gas Detection Characteristics of Octa-dodecyloxy Copper-phthalocyanine Langmuir-Blodgett(LB) Films. *Molecular Crystals and Liquid Crystals Science and Technology Section a-Molecular Crystals and Liquid Crystals* **1998,** *316*, 385-388.
129. Fischer, S.; Vestfrid, J.; Mahammed, A.; Herrmann-Westendorf, F.; Schulz, M.; Müller, J.; Kiesewetter, O.; Dietzek, B.; Gross, Z.; Presselt, M., Photometric Detection of Nitric Oxide Using a Dissolved Iron(III) Corrole as a Sensitizer. *ChemPlusChem* **2016,** *81* (7), 594-603.
130. Grummt, U.-W.; Weiss, D.; Birckner, E.; Beckert, R., Pyridylthiazoles: Highly Luminescent Heterocyclic Compounds. *The Journal of Physical Chemistry A* **2007,** *111* (6), 1104-1110.
131. Täuscher, E.; Weiß, D.; Beckert, R.; Görls, H., Synthesis and Characterization of New 4-Hydroxy-1,3-thiazoles. *Synthesis* **2010,** *2010* (10), 1603-1608.
132. Menzel, R.; Breul, A.; Pietsch, C.; Schäfer, J.; Friebe, C.; Täuscher, E.; Weiß, D.; Dietzek, B.; Popp, J.; Beckert, R.; Schubert, U. S., Blue-Emitting Polymers Based on 4-Hydroxythiazoles Incorporated in a Methacrylate Backbone. *Macromolecular Chemistry and Physics* **2011,** *212* (8), 840-848.
133. Breul, A. M.; Pietsch, C.; Menzel, R.; Schäfer, J.; Teichler, A.; Hager, M. D.; Popp, J.; Dietzek, B.; Beckert, R.; Schubert, U. S., Blue emitting side-chain pendant 4-hydroxy-1,3-thiazoles in

polystyrenes synthesized by RAFT polymerization. *European Polymer Journal* **2012,** *48* (7), 1339-1347.

134. Vollrath, A.; Pretzel, D.; Pietsch, C.; Perevyazko, I.; Schubert, S.; Pavlov, G. M.; Schubert, U. S., Preparation, cellular internalization, and biocompatibility of highly fluorescent PMMA nanoparticles. *Macromol Rapid Commun* **2012,** *33* (20), 1791-7.

135. Shi, Y.; Guo, H.; Qin, M.; Zhao, J.; Wang, Y.; Wang, H.; Wang, Y.; Facchetti, A.; Lu, X.; Guo, X., Thiazole Imide-Based All-Acceptor Homopolymer: Achieving High-Performance Unipolar Electron Transport in Organic Thin-Film Transistors. *Advanced Materials* **2018,** *30* (10), 1705745.

136. Shi, Y.; Guo, H.; Qin, M.; Wang, Y.; Zhao, J.; Sun, H.; Wang, H.; Wang, Y.; Zhou, X.; Facchetti, A.; Lu, X.; Zhou, M.; Guo, X., Imide-Functionalized Thiazole-Based Polymer Semiconductors: Synthesis, Structure–Property Correlations, Charge Carrier Polarity, and Thin-Film Transistor Performance. *Chemistry of Materials* **2018,** *30* (21), 7988-8001.

137. Stippich, K.; Weiss, D.; Guether, A.; Görls, H.; Beckert, R., Novel luminescence dyes and ligands based on 4-hydroxythiazole. *Journal of Sulfur Chemistry* **2009,** *30* (2), 109-118.

138. Menzel, R.; Täuscher, E.; Weiß, D.; Beckert, R.; Görls, H., The Combination of 4-Hydroxythiazoles with Azaheterocycles: Efficient Bidentate Ligands for Novel Ruthenium Complexes. *Zeitschrift für anorganische und allgemeine Chemie* **2010,** *636* (7), 1380-1385.

139. Menzel, R.; Weiß, D.; Täuscher, E.; Beckert, R.; Görls, H., Formation, X-ray structure and magnetic properties of two carboxy-bridged copper(II) complexes with tridentate bipyridine- and phenanthroline-based 1,3-thiazoles ligands. *Inorganic Chemistry Communications* **2012,** *18*, 65-68.

140. Habenicht, S. H.; Siegmann, M.; Kupfer, S.; Kübel, J.; Weiß, D.; Cherek, D.; Möller, U.; Dietzek, B.; Gräfe, S.; Beckert, R., And yet they glow: thiazole based push–pull fluorophores containing nitro groups and the influence of regioisomerism. *Methods and Applications in Fluorescence* **2015,** *3* (2), 025005.

141. Habenicht, S. H.; Schramm, S.; Zhu, M.; Freund, R. R.; Langenstuck, T.; Strathausen, R.; Weiss, D.; Biskup, C.; Beckert, R., pi-Extension of a 4-ethoxy-1,3-thiazole via aryl alkyne cross coupling: synthesis and exploration of the electronic structure. *Photochemical & photobiological sciences : Official journal of the European Photochemistry Association and the European Society for Photobiology* **2015,** *14* (11), 2097-107.

142. Gampe, D. M.; Nöller, F.; Hänsch, V. G.; Schramm, S.; Darsen, A.; Habenicht, S. H.; Ehrhardt, S.; Weiß, D.; Görls, H.; Beckert, R., Surprising characteristics of D–A-type functional dyes by introducing 4-alkoxythiazoles as the donor-unit. *Tetrahedron* **2016,** *72* (23), 3232-3239.

143. Gampe, D. M.; Schramm, S.; Noller, F.; Wei; Gorls, H.; Naumov, P.; Beckert, R., Pushing to the low limits: tetraazaanthracenes with very low-lying LUMO levels and near-infrared absorption. *Chemical Communications* **2017,** *53* (73), 10220-10223.

144. Gampe, D. M.; Hänsch, V. G.; Schramm, S.; Menzel, R.; Weiß, D.; Beckert, R., Mixing Chromophores: Donor–Acceptor Dyes with Low-Lying LUMOs and Narrow Band Gaps by Connecting 4-Alkoxythiazoles and Azaacenes. *European Journal of Organic Chemistry* **2017,** *2017* (10), 1369-1379.

145. Kaufmann, M. Entwicklung amphiphiler Thiazole zum Einsatz in der Langmuir-Blodgett Technik. Friedrich-Schiller-Universität Jena, Jena, **2018**.

146. Habenicht, S. H.; Schramm, S.; Fischer, S.; Sachse, T.; Herrmann-Westendorf, F.; Bellmann, A.; Dietzek, B.; Presselt, M.; Weiß, D.; Beckert, R.; Görls, H., Tuning the polarity and surface activity of hydroxythiazoles - extending the applicability of highly fluorescent self-assembling chromophores to supra-molecular photonic structures. *Journal of Materials Chemistry C* **2016,** *4* (5), 958-971.

147. Schwieger, C.; Chen, B.; Tschierske, C.; Kressler, J.; Blume, A., Organization of T-Shaped Facial Amphiphiles at the Air/Water Interface Studied by Infrared Reflection Absorption Spectroscopy. *The Journal of Physical Chemistry B* **2012,** *116* (40), 12245-12256.
148. Reuter, S.; Amado, E.; Busse, K.; Kraska, M.; Stühn, B.; Tschierske, C.; Kressler, J., Formation of 2D spherulites in Langmuir films of amphiphilic T-shaped liquid crystals. *Journal of colloid and interface science* **2012,** *372* (1), 192-201.
149. Ashwell, G. J.; Zhou, D. J.; Hamilton, R.; Skjonnemand, K.; Green, A., Molecular Lego: non-centrosymmetric Langmuir-Blodgett films for nonlinear optical applications. *Synthetic Metals* **2001,** *121* (1-3), 1455-1458.
150. Simonsen, J. B.; Westerlund, F.; Breiby, D. W.; Harrit, N.; Laursen, B. W., Columnar self-assembly and alignment of planar carbenium ions in Langmuir-Blodgett films. *Langmuir* **2011,** *27* (2), 792-9.
151. Plehnert, R.; Schröter, J.-A.; Tschierske, C., Influence of the Position of the Hydrophilic Group on the Monolayer Properties of Rigid Amphiphiles with Laterally Attached Headgroups. *Langmuir* **1999,** *15* (11), 3773-3781.
152. Davies, J. T.; Rideal, E. K., Chapter 5 - Properties of Monolayers. In *Interfacial Phenomena (Second Edition)*, Davies, J. T.; Rideal, E. K., Eds. Academic Press: **1961**, pp 217-281.
153. Wilhelmy, L., Ueber die Abhängigkeit der Capillaritäts-Constanten des Alkohols von Substanz und Gestalt des benetzten festen Körpers. *Annalen der Physik* **1863,** *195* (6), 177-217.
154. Ulman, A., *An Introduction to Ultrathin Organic Films: From Langmuir-Blodgett to Self-assembly*. Academic Press: **1991**.
155. Gaines, G. L., *Insoluble monolayers at liquid-gas interfaces*. Interscience Publishers: **1966**.
156. Latka, P. D.; Perez-Morales, M.; Munoz, E.; Broniatowski, M.; Martiin-Romero, M. T.; Camacho, L., Structural investigation of Langmuir and Langmuir-Blodgett monolayers of semifluorinated alkanes. *Journal of Physical Chemistry B* **2006,** *110* (12), 6095-6100.
157. Barzyk, W.; Lunkenheimer, K.; Pomianowski, A., Orientation phase transitions of undissociated n-decanoic acid at the air/solution interface revealed by surface pressure and electric potential. *Advances in colloid and interface science* **2018,** *259*, 1-20.
158. Fainerman, V. B.; Vollhardt, D., Equation of State for Monolayers with Additional Phase Transition between Condensed Phases of Different Compressibility. *The Journal of Physical Chemistry B* **2009,** *113* (18), 6311-6313.
159. Taniguchi, M.; Ueno, N.; Okamoto, K.; Karthaus, O.; Shimomura, M.; Yamagishi, A., Monolayer and Fluorescence Properties of a Chiral Amphiphilic Ruthenium(II) Complex at an Air−Water Interface. *Langmuir* **1999,** *15* (22), 7700-7707.
160. Dudkowiak, A.; Czapski, M.; Kotkowiak, M.; Miyake, J., The in situ characterization of bacteriochlorophyll c in Langmuir monolayers using polarized UV–vis spectroscopy. *Dyes and Pigments* **2010,** *86* (3), 227-232.
161. Ito, S.; Oki, S.; Hayashi, T.; Yamamoto, M., Fluorescence spectroscopy for a polymer monolayer at the air-water interface. *Thin Solid Films* **1994,** *244* (1), 1073-1077.
162. Zhang, L.; Cole, J. M., Dye aggregation in dye-sensitized solar cells. *Journal of Materials Chemistry A* **2017,** *5* (37), 19541-19559.
163. Kammel, R.; Tarabová, D.; Machalický, O.; Nepraš, M.; Frumarová, B.; Hanusek, J., Synthesis, characterization and spectral properties of new, highly fluorescent, 4-hydroxythiazoles. *Dyes and Pigments* **2016,** *128*, 101-110.
164. Reichardt, C., Solvatochromic Dyes as Solvent Polarity Indicators. *Chemical Reviews* **1994,** *94* (8), 2319-2358.
165. Schade, A.; Menzel, R.; Görls, H.; Spange, S.; Beckert, R., Negative Solvatochromism of an Anionic Thiazole-Based Dye. *Asian Journal of Organic Chemistry* **2013,** *2* (6), 498-503.

166. Menzel, R.; Kupfer, S.; Mede, R.; Görls, H.; González, L.; Beckert, R., Synthesis, properties and quantum chemical evaluation of solvatochromic pyridinium-phenyl-1,3-thiazol-4-olate betaine dyes. *Tetrahedron* **2013,** *69* (5), 1489-1498.
167. Scheibe, G., Über die Veränderlichkeit der Absorptionsspektren in Lösungen und die Nebenvalenzen als ihre Ursache. *Angewandte Chemie* **1937,** *50* (11), 212-219.
168. Sýkora, D.; Tesařová, E.; Popl, M., Interactions of basic compounds in reversed-phase high-performance liquid chromatography influence of sorbent character, mobile phase composition, and pH on retention of basic compounds. *Journal of Chromatography A* **1997,** *758* (1), 37-51.
169. Nachod, F. C.; Braude, E. A.; Phillips, W. D., *Determination of organic structures by physical methods / editors, E.A. Braude, F.C. Nachod*. Academic Press: New York, **1955**.
170. McFate, C.; Ward, D.; Olmsted, J., Organized collapse of fatty acid monolayers. *Langmuir* **1993,** *9* (4), 1036-1039.
171. Vaknin, D.; Bu, W.; Satija, S. K.; Travesset, A., Ordering by Collapse: Formation of Bilayer and Trilayer Crystals by Folding Langmuir Monolayers. *Langmuir* **2007,** *23* (4), 1888-1897.
172. Kundu, S.; Datta, A.; Hazra, S., Effect of Metal Ions on Monolayer Collapses. *Langmuir* **2005,** *21* (13), 5894-5900.
173. Inglot, K.; Martyński, T.; Bauman, D., Molecular organization and aggregation in Langmuir and Langmuir-Blodgett films of azo dye/liquid crystal mixtures. *Opto-Electron. Rev.* **2009,** *17* (2), 120-128.
174. Diep-Quang, H.; Ueberreiter, K., Monolayers of some liquid-crystal forming compounds. *Colloid and Polymer Science* **1980,** *258* (9), 1055-1061.
175. Ashwell, G. J.; Whittam, A. J.; Amiri, M. A.; Hamilton, R.; Green, A.; Grummt, U. W., An improved efficiency/transparency trade-off for second-harmonic generation by extending the pi-electron bridge of an optically nonlinear dye. *Journal of Materials Chemistry* **2001,** *11* (5), 1345-1350.
176. Kasha, M., Energy Transfer Mechanisms and the Molecular Exciton Model for Molecular Aggregates. *Radiation Research* **1963,** *20* (1), 55-70.
177. Gong, K.; Feng, S.-S.; Go, M. L.; Soew, P. H., Effects of pH on the stability and compressibility of DPPC/cholesterol monolayers at the air–water interface. *Colloids and Surfaces A: Physicochemical and Engineering Aspects* **2002,** *207* (1–3), 113-125.
178. Gew, L. T.; Misran, M., Albumin-fatty acid interactions at monolayer interface. *Nanoscale Research Letters* **2014,** *9* (1), 1-6.
179. Petaccia, M.; Giansanti, L.; Leonelli, F.; La Bella, A.; Villalva, D. G.; Mancini, G., Synthesis, characterization and inclusion into liposomes of a new cationic pyrenyl amphiphile. *Chemistry and Physics of Lipids* **2016,** *200*, 83-93.
180. Barnes, W. L., Fluorescence near interfaces: The role of photonic mode density. *Journal of Modern Optics* **1998,** *45* (4), 661-699.
181. Graf, A.; Liehm, P.; Murawski, C.; Hofmann, S.; Leo, K.; Gather, M. C., Correlating the transition dipole moment orientation of phosphorescent emitter molecules in OLEDs with basic material properties. *Journal of Materials Chemistry C* **2014,** *2* (48), 10298-10304.
182. N'Soukpoé-Kossi, C. N.; Sielewiesiuk, J.; Leblanc, R. M.; Bone, R. A.; Landrum, J. T., Linear dichroism and orientational studies of carotenoid Langmuir-Blodgett films. *Biochimica et Biophysica Acta (BBA) - Biomembranes* **1988,** *940* (2), 255-265.
183. Batat, P.; Bayar, M.; Pur, B.; Çoker, E.; Ahsen, V.; Yuksel, F.; Demirel, A. L., The optical characterization of metal-mediated aggregation behaviour of amphiphilic Zn(ii) phthalocyanines. *Physical Chemistry Chemical Physics* **2016,** *18* (23), 15574-15583.
184. Rajesh, K.; Balaswamy, B.; Yamamoto, K.; Yamaki, H.; Kawamata, J.; Radhakrishnan, T. P., Enhanced Optical and Nonlinear Optical Responses in a Polyelectrolyte Templated Langmuir–Blodgett Film. *Langmuir* **2011,** *27* (3), 1064-1069.

185. Hertmanowski, R.; Chudzinski, L.; Martynski, T.; Stempniewicz, P.; Wolarz, E.; Bauman, D., Spectroscopic studies of Langmuir-Blodgett films of 3,4,9,10-tetra(heptyloxycarbonyl)perylene and its mixtures with a liquid crystal. *Liquid Crystals* **2004,** *31* (6), 791-800.
186. Tao, T.; Ma, B.-B.; Peng, Y.-X.; Wang, X.-X.; Huang, W.; You, X.-Z., Asymmetrical/Symmetrical D−π−A/D−π−D Thiazole-Containing Aromatic Heterocyclic Fluorescent Compounds Having the Same Triphenylamino Chromophores. *The Journal of Organic Chemistry* **2013,** *78* (17), 8669-8679.
187. Tang, Z.; Johal, M. S.; Scudder, P.; Caculitan, N.; Magyar, R. J.; Tretiak, S.; Wang, H.-L., Study of the non-covalent interactions in Langmuir–Blodgett films: An interplay between π−π and dipole–dipole interactions. *Thin Solid Films* **2007,** *516* (1), 58-66.
188. Rong, Y.; Chen, P.; Wang, D.; Liu, M., Porphyrin Assemblies through the Air/Water Interface: Effect of Hydrogen Bond, Thermal Annealing, and Amplification of Supramolecular Chirality. *Langmuir* **2012,** *28* (15), 6356-6363.
189. Seo, Y.; Cho, C. Y.; Hwangbo, M.; Choi, H. J.; Hong, S. M., Effect of Temperature on the Interfacial Behavior of a Polystyrene-b-poly(methyl methacrylate) Diblock Copolymer at the Air/Water Interface. *Langmuir* **2008,** *24* (6), 2381-2386.
190. Wang, H.; Li, W.; Ding, H.; Zhang, Y.; Xi, S., A method to identify the collapse of monolayers at the air-water interface. *Thin Solid Films* **1996,** *284-285*, 119-121.
191. Bhullar, G. K.; Kaur, R.; Raina, K. K., Hybrid Polyaniline-TiO2 Nanocomposite Langmuir-Blodgett Thin Films: Self-Assembly and Their Characterization. *Journal of Applied Polymer Science* **2015,** *132* (5), 7.
192. Wang, X.; Ma, X.; Zang, D., Aggregation behavior of polystyrene-b-poly(acrylic acid) at the air-water interface. *Soft Matter* **2013,** *9* (2), 443-453.
193. Jäger, C. M.; Schmaltz, T.; Novak, M.; Khassanov, A.; Vorobiev, A.; Hennemann, M.; Krause, A.; Dietrich, H.; Zahn, D.; Hirsch, A.; Halik, M.; Clark, T., Improving the Charge Transport in Self-Assembled Monolayer Field-Effect Transistors: From Theory to Devices. *Journal of the American Chemical Society* **2013,** *135* (12), 4893-4900.
194. Khassanov, A.; Steinruck, H.-G.; Schmaltz, T.; Magerl, A.; Halik, M., Structural Investigations of Self-Assembled Monolayers for Organic Electronics: Results from X-ray Reflectivity. *Accounts of chemical research* **2015,** *48* (7), 1901-1908.
195. Gao, Y.; Tang, Z.; Watkins, E.; Majewski, J.; Wang, H.-L., Synthesis and Characterization of Amphiphilic Fullerenes and Their Langmuir−Blodgett Films. *Langmuir* **2005,** *21* (4), 1416-1423.
196. Theodoratou, A.; Jonas, U.; Loppinet, B.; Geue, T.; Stangenberg, R.; Li, D.; Berger, R.; Vlassopoulos, D., Photoswitching the mechanical properties in Langmuir layers of semifluorinated alkyl-azobenzenes at the air–water interface. *Physical Chemistry Chemical Physics* **2015,** *17* (43), 28844-28852.
197. Reda, T.; Hermel, H.; Holtje, H. D., Compression/expansion hysteresis of poly(L-glutamic acid) monolayers spread at the air/water interface. *Langmuir* **1996,** *12* (26), 6452-6458.
198. Jonas, U.; Cardullo, F.; Belik, P.; Diederich, F.; Gügel, A.; Harth, E.; Herrmann, A.; Isaacs, L.; Müllen, K.; Ringsdorf, H.; Thilgen, C.; Uhlmann, P.; Vasella, A.; Waldraff, C. A. A.; Walter, M., Synthesis of a Fullerene[60] Cryptate and Systematic Langmuir-Blodgett and Thin-Film Investigations of Amphiphilic Fullerene Derivatives. *Chemistry – A European Journal* **1995,** *1* (4), 243-251.
199. Gayathri, H. N.; Kumar, B.; Suresh, K. A.; Bisoyi, H. K.; Kumar, S., Charge transport in a liquid crystalline triphenylene polymer monolayer at air-solid interface. *Physical Chemistry Chemical Physics* **2016,** *18* (17), 12101-12107.
200. Xu, D.; Watt, G. D.; Harb, J. N.; Davis, R. C., Electrical Conductivity of Ferritin Proteins by Conductive AFM. *Nano Letters* **2005,** *5* (4), 571-577.

201. Hipps, K. W.; Mazur, U., Kinetic and Thermodynamic Control in Porphyrin and Phthalocyanine Self-Assembled Monolayers. *Langmuir* **2018,** *34* (1), 3-17.
202. Lee, W. H.; Park, Y. D., Tuning Electrical Properties of 2D Materials by Self-Assembled Monolayers. *Advanced Materials Interfaces* **2018,** *5* (1), 1700316.
203. Voïtchovsky, K.; Ashari-Astani, N.; Tavernelli, I.; Tétreault, N.; Rothlisberger, U.; Stellacci, F.; Grätzel, M.; Harms, H. A., In Situ Mapping of the Molecular Arrangement of Amphiphilic Dye Molecules at the TiO2 Surface of Dye-Sensitized Solar Cells. *ACS Applied Materials & Interfaces* **2015,** *7* (20), 10834-10842.
204. Resch, R.; Grasserbauer, M.; Friedbacher, G.; Vallant, T.; Brunner, H.; Mayer, U.; Hoffmann, H., In situ and ex situ AFM investigation of the formation of octadecylsiloxane monolayers. *Applied Surface Science* **1999,** *140* (1), 168-175.
205. Krekiehn, N. R.; Müller, M.; Jung, U.; Ulrich, S.; Herges, R.; Magnussen, O. M., UV/Vis Spectroscopy Studies of the Photoisomerization Kinetics in Self-Assembled Azobenzene-Containing Adlayers. *Langmuir* **2015,** *31* (30), 8362-8370.
206. Himmelhaus, M.; Eisert, F.; Buck, M.; Grunze, M., Self-Assembly of n-Alkanethiol Monolayers. A Study by IR−Visible Sum Frequency Spectroscopy (SFG). *The Journal of Physical Chemistry B* **2000,** *104* (3), 576-584.
207. Jackson, W. B.; Amer, N. M.; Boccara, A. C.; Fournier, D., Photothermal deflection spectroscopy and detection. *Applied Optics* **1981,** *20* (8), 1333-1344.
208. Boccara, A. C.; Fournier, D.; Jackson, W.; Amer, N. M., Sensitive photothermal deflection technique for measuring absorption in optically thin media. *Optics Letters* **1980,** *5* (9), 377-379.
209. Buchaca-Domingo, E.; Vandewal, K.; Fei, Z.; Watkins, S. E.; Scholes, F. H.; Bannock, J. H.; de Mello, J. C.; Richter, L. J.; DeLongchamp, D. M.; Amassian, A.; Heeney, M.; Salleo, A.; Stingelin, N., Direct Correlation of Charge Transfer Absorption with Molecular Donor:Acceptor Interfacial Area via Photothermal Deflection Spectroscopy. *Journal of the American Chemical Society* **2015,** *137* (16), 5256-5259.
210. Benson-Smith, J. J.; Goris, L.; Vandewal, K.; Haenen, K.; Manca, J. V.; Vanderzande, D.; Bradley, D. D. C.; Nelson, J., Formation of a ground-state charge-transfer complex in polyfluorene/[6,6]-phenyl-C-61 butyric acid methyl ester (PCBM) blend films and its role in the function of polymer/PCBM solar cells. *Advanced Functional Materials* **2007,** *17* (3), 451-457.
211. Ambacher, O.; Rieger, W.; Ansmann, P.; Angerer, H.; Moustakas, T. D.; Stutzmann, M., Sub-bandgap absorption of gallium nitride determined by Photothermal Deflection Spectroscopy. *Solid State Communications* **1996,** *97* (5), 365-370.
212. Kumar, K. S.; Patnaik, A., Solvent-Polarity-Tunable Dimeric Association of a Fullerene (C60)–N,N-Dimethylaminoazobenzene Dyad: Modulated Electronic Coupling of the Azo Chromophore with a Substituted 3D Fullerene. *Chemistry – A European Journal* **2011,** *17* (19), 5327-5343.
213. Park, C.; Song, H. J.; Choi, H. C., The critical effect of solvent geometry on the determination of fullerene (C60) self-assembly into dot, wire and disk structures. *Chemical Communications* **2009,** (32), 4803-4805.
214. Ambacher, O.; Brunner, D.; Dimitrov, R.; Stutzmann, M.; Sohmer, A.; Scholz, F., Absorption of InGaN Single Quantum Wells Determined by Photothermal Deflection Spectroscopy. *Japanese Journal of Applied Physics* **1998,** *37* (3R), 745.
215. Uemura, S.; Sengupta, S.; Würthner, F., Cyclic Self-Assembled Structures of Chlorophyll Dyes on HOPG by the Dendron Wedge Effect. *Angewandte Chemie International Edition* **2009,** *48* (42), 7825-7828.
216. Hoeben, F. J. M.; Zhang, J.; Lee, C. C.; Pouderoijen, M. J.; Wolffs, M.; Würthner, F.; Schenning, A. P. H. J.; Meijer, E. W.; De Feyter, S., Visualization of Various Supramolecular Assemblies of Oligo(para-phenylenevinylene)–Melamine and Perylene Bisimide. *Chemistry – A European Journal* **2008,** *14* (28), 8579-8589.

217. Kulkarni, C. V.; Wachter, W.; Iglesias-Salto, G.; Engelskirchen, S.; Ahualli, S., Monoolein: a magic lipid? *Physical Chemistry Chemical Physics* **2011,** *13* (8), 3004-3021.
218. Herrmann-Westendorf, F.; Sachse, T.; Schulz, M.; Kaufmann, M.; Sivakov, V.; Beckert, R.; Martinez, T. J.; Dietzek, B.; Presselt, M., Photo-Annealing of Merocyanine Aggregates. *The journal of physical chemistry. A* **2018,** *122* (51), 9821–9832.
219. Pasternack, R. F.; Fleming, C.; Herring, S.; Collings, P. J.; dePaula, J.; DeCastro, G.; Gibbs, E. J., Aggregation Kinetics of Extended Porphyrin and Cyanine Dye Assemblies. *Biophysical Journal* **2000,** *79* (1), 550-560.
220. Imae, T.; Torii, H., In Situ Investigation of Molecular Adsorption on Au Surface by Surface-Enhanced Infrared Absorption Spectroscopy. *The Journal of Physical Chemistry B* **2000,** *104* (39), 9218-9224.
221. Peterlinz, K. A.; Georgiadis, R., In Situ Kinetics of Self-Assembly by Surface Plasmon Resonance Spectroscopy. *Langmuir* **1996,** *12* (20), 4731-4740.
222. Tolkki, A.; Vuorimaa, E.; Chukharev, V.; Lemmetyinen, H.; Ihalainen, P.; Peltonen, J.; Dehm, V.; Würthner, F., Langmuir−Schaeffer Films from a π−π Stacking Perylenediimide Dye: Organization and Charge Transfer Properties. *Langmuir* **2010,** *26* (9), 6630-6637.
223. Menzel, R.; Ogermann, D.; Kupfer, S.; Weiß, D.; Görls, H.; Kleinermanns, K.; González, L.; Beckert, R., 4-Methoxy-1,3-thiazole based donor-acceptor dyes: Characterization, X-ray structure, DFT calculations and test as sensitizers for DSSC. *Dyes and Pigments* **2012,** *94* (3), 512-524.
224. Wold, D. J.; Haag, R.; Rampi, M. A.; Frisbie, C. D., Distance Dependence of Electron Tunneling through Self-Assembled Monolayers Measured by Conducting Probe Atomic Force Microscopy: Unsaturated versus Saturated Molecular Junctions. *The Journal of Physical Chemistry B* **2002,** *106* (11), 2813-2816.

Abkürzungsverzeichnis

4-Hydroxythiazol	4-Hydroxy-1,3-Thiazol
bPh	Biphenyl
$CHCl_3$	Chloroform
CH_3OH	Methanol
CH_3O	Methoxy
COOH	Carbonsäure
$N(CH_3)_2$	Dimethylamin
NO_2	Nitro
Ph	Phenyl
PMMA	Poly(Methyl Methacrylat)
Py	Pyridyl
SO_2NH_2	Sulfonamid
SO_3H	Sulfonsäure

%	Prozent
°	Grad
Å	Ångström
2D	Zweidimensional
3D	Dreidimensional
A	mittlere Fläche pro Molekül
A_0	extrapolierte Minimumfläche
c	Konzentration

C_s	Kompressibilität
C_S^{-1}	Kompressibilitätsmodulus
bzw.	beziehungsweise
E	Expansion
G	Gibbsenergie
HOMO	höchstes besetztes Molekülorbital
i, ii, iii	Konformere Spezies
I	Fluoreszenzintensität
I	Strom
ΔI	Fluoreszenzkontrast
K	Kompression
L	Langmuir
LB	Langmuir-Blodgett
LUMO	niedrigstes unbesetztes Molekülorbital
M	Molar
meV	Milielektronenvolt
nm	Nanometer
OFET	organischer Feldeffekt Transitor
OLED	organische Leuchtdiode
OS	organischer Sensor
OSZ	organische Solarzelle
PDS	*engl. photothermal deflection spectroscopy*; photothermische Ablenkungsspektroskopie
Push	*engl.;* Elektronen-schiebend
Pull	*Engl;.* Elektronen-ziehend

RT	Raumtemperatur
S_0	Singulett-Grundzustand
S_1	erster angeregter Singulett-Zustand
SAM	selbstassemblierte Monolage
TDV	*engl. transition dipole vector*; Übergangsdipolmoment
V	Spannung
Δ	Differenz
I, II, III	Kondensierte Phase des Langmuir-Films
α	Polarisationswinkel der Anregung
β	Polarisationswinkel der Detektion
γ	Grenzflächenspannung
ε	Extinktionskoeffizient
λ	Wellenlänge
λ_{exc}	Anregungswellenlänge
λ_{em}	Emissionswellenlänge
λ_{max}	Wellenlänge des Maximums
Π	Oberflächendruck
Π_{LB}	Abscheidedruck des LB-Films

Publikationen

Erklärung zu den Eigenanteilen des Promovenden sowie der weiteren Doktoranden/Doktorandinnen als Koautoren an den Publikationen und Zweitpublikationsrechten bei einer kumulativen Dissertation

Für alle in dieser kumulativen Dissertation verwendeten Manuskripte liegen die notwendigen Genehmigungen der Verlage („Reprint permissions“) für die Zweitpublikation vor.

Die Koautoren der in dieser kumulativen Dissertation verwendeten Manuskripte sind sowohl über die Nutzung, als auch über die oben angegebenen Eigenanteile der weiteren Doktoranden/Doktorandinnen als Koautoren an den Publikationen und Zweitpublikationsrechten bei einer kumulativen Dissertation informiert und stimmen dem zu.

Maximilian Lutz Hupfer Jena, den

Ich bin mit der Abfassung der Dissertation als publikationsbasiert, d.h. kumulativ, einverstanden und bestätige die vorstehenden Angaben. Eine entsprechend begründete Befürwortung mit Angabe des wissenschaftlichen Anteils des Doktoranden/der Doktorandin an den verwendeten Publikationen werde ich parallel an den Rat der Fakultät der Chemisch-Geowissenschaftlichen Fakultät richten.

Prof. Dr. Benjamin Dietzek Jena, den

[MLH1] Assembly of T-Shaped Amphiphilic Thiazoles on the Air-Water Interface: Impact of Polar Chromophore Moieties, as Well as Dipolarity and pi-Extension of the Chromophore on the Supramolecular Structure

Hupfer, M. L.; Kaufmann, M.; Preiß, L.; Weiß, D.; Beckert, R.; Dietzek, B.; Presselt, M., *Langmuir* **2019,** *35* (7), 2587-2600

Autor	1	2	3	4	5	6	7
Konzeption	x	x		x	x		x
Planung der Untersuchung	x	x					x
Datenerhebung	x	x	x				
Analyse und Interpretation	x	x					x
Schreiben des Manuskriptes	x	x				x	x
Publikationsäquivalente	1,0	n. a.	n. a.	n. a.	n. a.	n. a.	n. a.

LANGMUIR
Article
Cite This: Langmuir 2019, 35, 2587−2600
pubs.acs.org/Langmuir

Assembly of T-Shaped Amphiphilic Thiazoles on the Air−Water Interface: Impact of Polar Chromophore Moieties, as Well as Dipolarity and π-Extension of the Chromophore on the Supramolecular Structure

Maximilian L. Hupfer,[†,§] Martin Kaufmann,[†,‡] Julia Preiß,[†,§] Dieter Weiß,[‡] Rainer Beckert,[‡]
Benjamin Dietzek,[†,§] and Martin Presselt*[†,§,∥,⊥]

[†]Institute of Physical Chemistry, Friedrich Schiller University Jena, Helmholtzweg 4, 07743 Jena, Germany
[‡]Institute of Organic and Macromolecular Chemistry, Friedrich Schiller University Jena, Humboldtstraße 10, 07743 Jena, Germany
[§]Leibniz Institute of Photonic Technology (IPHT), Albert-Einstein-Str. 9, 07745 Jena, Germany
[∥]Center for Energy and Environmental Chemistry Jena (CEEC Jena), Friedrich Schiller University Jena, Philosophenweg 7a, 07743 Jena, Germany
[⊥]SciClus GmbH & Co. KG, Moritz-von-Rohr-Str. 1a, 07745 Jena, Germany

Supporting Information

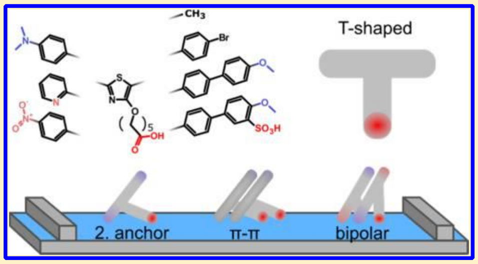

ABSTRACT: The supramolecular structure essentially determines the properties of organic thin films. In this work, we systematically investigate the influence of the chromophore on the supramolecular structure formation at air−water interfaces by means of the Langmuir−Blodgett technique. Therefore, we focus on the recently introduced class of double-anchor T-shaped amphiphilic dyes, namely, 4-hydroxy-thiazole chromophores that are centrally equipped with an amphiphilicity-inducing hexanoic acid. The thiazoles contain hydrophilic subphase-anchor groups in the 2-position (4-*N*,*N*-dimethylaminophenyl (**Am**), 2-pyridyl (**Py**), and 4-nitrophenyl (**Ni**)), whereas the chromophores are systematically extended in the 5-position with various substituents. The combination of the Langmuir technique with online fluorescence measurements revealed that the π−π interactions that are pronounced in the case of 4-methoxybiphenyl derivatives yield the most distinct supramolecular structures. Whereas in the case of **Py** and **Ni** derivatives ordered J-type supramolecular structures in microdomains are formed, the **Am** derivative forms ordered supramolecular structures that are more homogeneous, which are, however, not stabilized by J-type dipolar interactions. Because of the synergetic π−π and dipolar stabilizations, the **Ni** derivative bearing the 4-methoxybiphenyl unit forms exceptionally stable quasi-two-dimensional Langmuir monolayers reaching very high surface pressures beyond 60 mN/m without any sign of disturbance of the Langmuir monolayer.

■ INTRODUCTION

Organic (opto)electronic devices like solar cells,[1] light-emitting diodes,[2] and field effect transistors[3] are steadily gaining importance. The active layer and device properties, especially spectral[4−8] and radiative[9,10] characteristics, external quantum efficiency,[11−15] open circuit voltage,[16] conductivity,[17−20] excited-state dynamics,[21−23] and electrochemical potentials,[4,24,25] are tuned by engineering the molecular characteristics and the supramolecular structure. To control supramolecular structures, several techniques, like antiparallel supramolecular arrangement of dipolar donor−acceptor dyes,[26,27] co-self-organization,[28] layer-by-layer deposition,[29,30] and (self)assembly at heterointerfaces, have been developed. Another valuable technique that allows for advanced control of the supramolecular structure formation at liquid−gas interfaces is the Langmuir−Blodgett (LB) technique,[31−34] which enables supramolecular tuning of optical and optoelectronic properties of functional amphiphiles.[4,35,36]

The supramolecular geometries and their optoelectronic properties inherently depend on the molecular parameters,[37−40] such as the chromophore, chemical nature, number, and position of polar and nonpolar moieties in the amphiphile. It was shown that even the lengths and the types of spacers[41] between polar and nonpolar as well as the specific chemical nature of the polar moieties[41−43] heavily influence the geometries of supramolecular structures formed at the air−

Received: December 6, 2018
Revised: January 17, 2019
Published: January 28, 2019

DOI: 10.1021/acs.langmuir.8b04063

Scheme 1. Central Attachment of a Hydrophilic Head Group to a Thiazole Chromophore, Which is Systematically Varied on the 2- and 5-Positions, via an Alkylic Linker Yields a "T-Shaped" Amphiphile with Various Intra- and Intermolecular Interactions in a Langmuir Monolayer

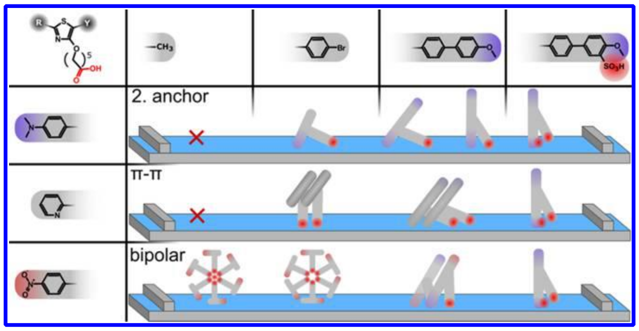

water interface. Recently, novel T-shaped amphiphilic dyes have been presented in which the amphiphilicity-introducing hexanoic acid is linked centrally to rather hydrophobic chromophores.[41,44−46] The flexibility of the hexanoic acid,[41] but also the tunable polarity of the chromophore, particularly introduction of second hydrophilic subphase-anchor groups and introduction of dipolarity,[45] makes this class of amphiphiles highly versatile and enables the formation of different supramolecular structures at the air−water interface.[41,44,45]

Basically, just two different types of chromophores from this type of T-shaped amphiphiles have been reported in the literature so far.[45] Here, we attempt to systematically study the influence of chemical variations of the chromophore (see Scheme 1) on the formation of supramolecular structures on air−water interfaces and the resulting optical properties. The large number of supramolecular structures that can form from the high number of investigated derivatives at varied Langmuir parameters is characterized via analysis of the $\Pi(A)$ isotherm and in situ fluorescence measurements.[47] UV−vis spectroscopy has been demonstrated to enable determination of interactions of the dye with the subphase[47] and thermodynamics in amphiphile mixtures[48] or changes of the supramolecular geometry.[43]

The T-shaped amphiphiles derived from 4-hydroxy-thiazoles are predestined for in situ fluorescence characterization as they often feature high fluorescence quantum yields (up to 95% in water[49]). Because of the corresponding slow nonradiative excited-state decay, 4-hydroxy-thiazoles have been tested for application in dye-sensitized solar cells,[50] as blue emitters in polymer backbones,[51,52] and as oligomers in organic field effect transistors.[53] In this work, the thiazole chromophore is varied by introducing three different hydrophilic subphase anchors in the 2-position of the thiazole, namely, 4-*N*,*N*-dimethylaminophenyl (**Am**), 2-pyridyl (**Py**), and 4-nitrophenyl (**Ni**).[54,55] Furthermore, the chromophore gets systematically π-extended in the 5-position for each of the anchor functions by substituting the methyl group (**Me**) by a 4-bromophenyl (**Br**) and 4-methoxybiphenyl (**Bi**). Finally, the chromophores are additionally equipped with a third hydrophilic anchor, a 4-methoxyphenyl-3-sulfonylphenyl (**BiSulf**) moiety. After presenting the synthesis, these systematically varied amphiphilic T-shaped thiazoles, along with their optical properties in solution and at an air−water interface, are determined and compared with mean molecular areas derived from Langmuir experiments to understand the film formation and to derive schemes of supramolecular structures formed at the air−water interface.

■ RESULTS AND DISCUSSION

To investigate a broad range of the effects of the chromophore, three different core units of the thiazoles were selected as target structures. An *N*,*N*-dimethylaminophenyl derivative was selected to represent electron-rich substituents, a nitrophenyl derivative was selected as the electron-deficient substituent, and a 2-pyridyl-derivative was selected as a "neutral", heterocyclic derivative. Based on the three core units, the electron-rich dimethylphenyl thiazole, the electron-deficient nitrophenyl thiazole, and the neutral, hetrocyclic pyridyl thiazole, three successive expansions (methyl group, bromphenyl group, methoxybiphenyl group, sulfonation) of the π-system are targeted. The synthetic route is depicted in Figure 1.

Starting from nitriles **1**, 5-methyl thiazoles **3** are accessible by the Erlenmeyer Route, in which the nitrile is condensed with thiolactic acid **2**, as shown in Figure 1. According to the method by Calderón-Ortiz,[56] the pyridyl derivative and the nitro derivative **Ni 3** were obtained in 76−81% yields. However, the amino thiazole could not be isolated because of degradation during the workup procedure. The alkylation with ethyl 6-bromo-hexanoate not only increases the solubility of the dye but also builds up the precursor for the amphiphilic anchor group. It was performed by a standard procedure, which is published for 4-hydroxy-thiazoles.[50,57,58] For the second π-expansion step, the thiazole core units have to be synthesized with the well-established Hantzsch thiazole synthesis.[59−61] Starting from thioamides (**Am**/**Py**/**Ni**) **5**, the condensation with **6** leads to 5-bromophenyl-4-hydroxy thiazoles **7**, which were obtained in very good yields from 60 to 87%. The following alkylation (iv) was carried out under the same conditions as in reaction step (ii), and alkoxy thiazoles **8** were obtained in 72−83% yields. A further expansion of the chromophore is possible by cross-coupling of the 5-(4-bromophenyl) substituent. Several different cross-coupling reactions, like Buchwald−Hartwig aminations,[58,62] Sonogashira cross-coupling,[63] or Stille cross-couplings, have already been

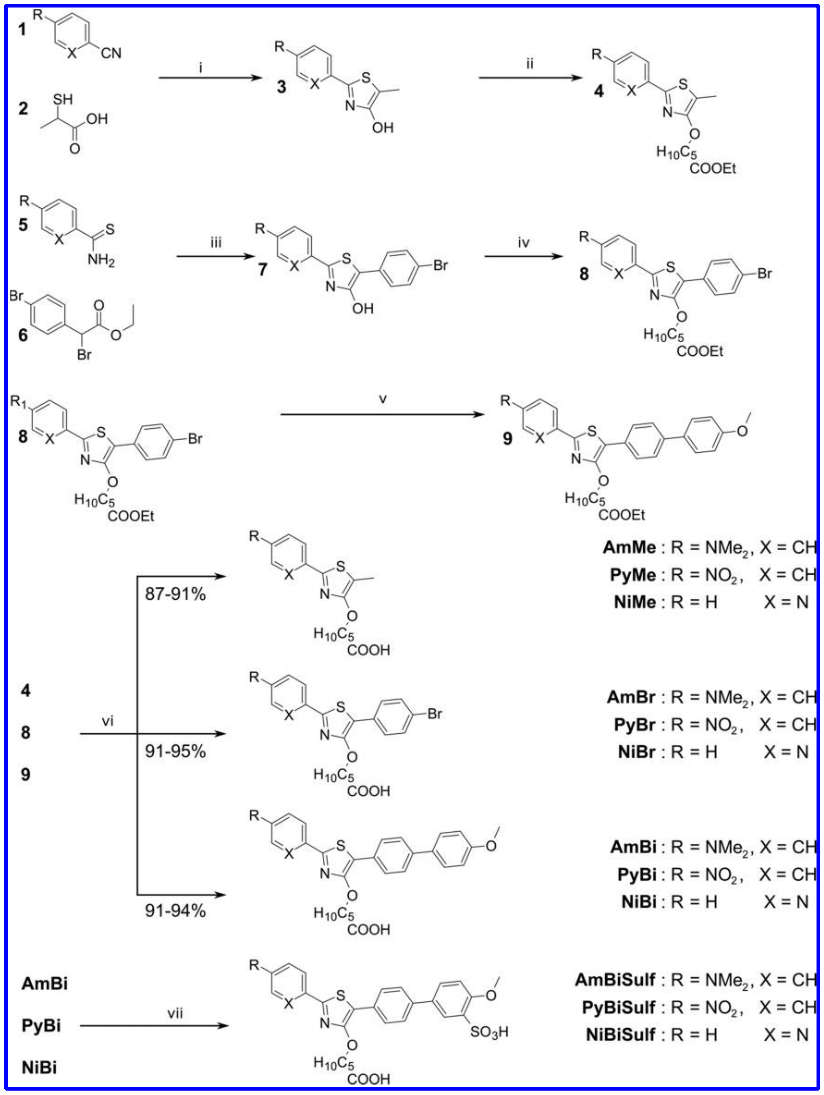

Figure 1. Synthetic route to the target compounds; (i) pyridin, Δ*T*, 0−81%; (ii) $BrC_5H_{10}CO_2Et$, $K_{PyBi}O_3$, acetone, Δ*T*, 64−73%; (iii) NaOAc, EtOH, Δ*T*, 60−87%; (iv) $BrC_5H_{10}CO_2Et$, $K_{PyBi}O_3$, acetone, Δ*T*, 72−83%; (v) *p*-OMePh-B(OH)$_2$, $K_{PyBi}O_3$, Pd(PPh$_3$)$_{PyBi}$I$_2$, thf, Δ*T*, 31−56%; (vi) KOH, EtOH (abs), 50 °C; and (vii) AcOH, H_2SO_4, room temperature—50 °C, 23−39%.

described for 5-bromophenyl thiazoles. Still, no Suzuki reactions on these dyes are known to date. However, Arcadi[64] et al. performed various Suzuki cross-couplings on 4-triflyl thiazoles, which are structurally comparable to our target molecules. With a slight variation of this method (changing the catalyst from Pd(PPh$_3$)$_4$ to Pd(PPh$_3$)$_{PyBi}$I$_2$), 5-(4-methoxybiphenyl)-thiazoles **9** were obtained in moderate 31−56% yields.

With the successful syntheses of **4**, **8**, and **9**, the ester group of the hexanoate side chain needs to be saponificated to yield the amphiphilic anchor group. Recently, the deprotection of such alkyl esters of 4-alkyoxy thiazoles was published using an anhydrous ethanolic potassium hydroxide solution.[41,42] Using this procedure, the aminothiazoles **AmBr** and **AmBi**, the pyridylthiazoles **PyMe**, **PyBr**, and **PyBi**, and the nitrothiazoles

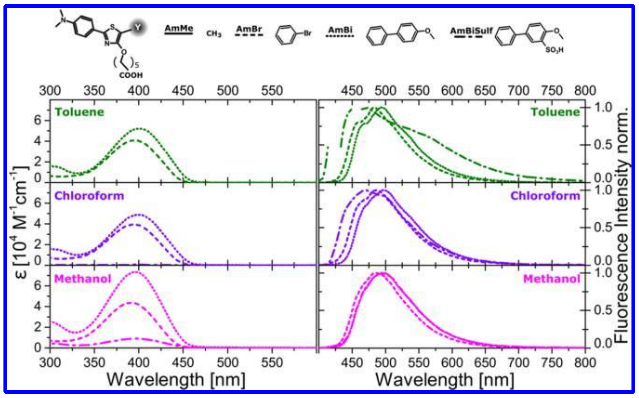

Figure 2. Extinction coefficients (ε) (left) and normalized emissions (right) of the 2-(4-*N*,*N*-dimethyl-aminophenyl)-4-hydroxy-5-Y-1,3-thiazole core (λ_{exc} = 405 nm) and the methyl (**AmMe**) (solid), phenyl-4-bromo (**AmBr**) (dotted), phenyl-4-methoxyphenyl (**AmBi**) (dashed), and 3-phenyl-4-methoxyphenyl-3-sulfonylphenyl (**AmBiSulf**) (dotted dashed) functionalizations in toluene (dark green, upper row), $CHCl_3$ (violet, middle row), and CH_3OH (pink, lower row) ($c < 10^{-6}$ M).

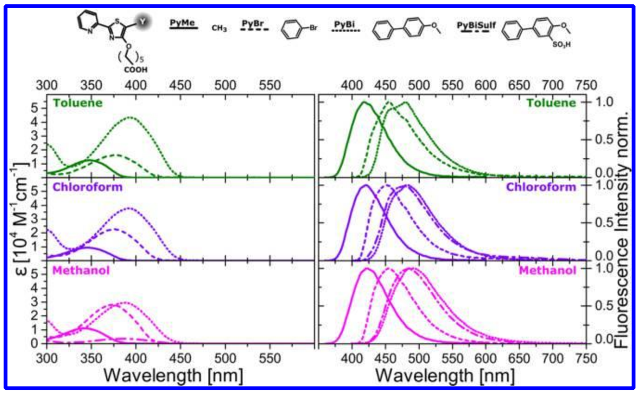

Figure 3. Extinction coefficients (ε) (left) and normalized emissions (right) of the 2-(2-pyridyl)-4-hydroxy-5-Y-1,3-thiazole core (405 nm) methyl (**PyMe**) (solid), phenyl-4-bromo (**PyBr**) (dotted), phenyl-4-methoxyphenyl (**PyBi**) (dashed), and 3-phenyl-4-methoxyphenyl-3-sulfonylphenyl (**PyBiSulf**) (dotted dashed) functionalizations in toluene (dark green, upper row), $CHCl_3$ (violet, middle row), and CH_3OH (pink, lower row) ($c < 10^{-6}$ M).

NiMe, **NiBr**, and **NiBi** were isolated in very good yields from 87 to 95%. Finally, the 5-(4-methoxybiphenyl)-thiazoles **AmBi**, **PyBi**, and **NiBi** were sulfonated by the method of Habenicht.[43] All target molecules except the sulfonated **AmBiSulf**, **PyBiSulf**, and **NiBiSulf** are well soluble in chloroform or dichloromethane, which are suitable solvents for the Langmuir technique. The sulfonic acid group increases the hydrophilicity; thus, the best solubility of these was observed in methanol. However, a mixture of chloroform and methanol can be used to achieve the necessary minimum solubility for the Langmuir technique.

UV−Vis Absorption and Fluorescence Spectroscopy. The influences of the above-introduced modifications to the thiazole chromophores are characterized by means of UV−vis absorption and fluorescence spectroscopy in solution. The variation in solvent polarity yields reference spectra for the thiazoles in different supramolecular environments studied in the subsequent Langmuir sections.

4-N,N-Dimethylaminophenyl Derivatives. The extinction coefficient ($\varepsilon(\lambda)$) spectra of **Am** (Figure 2) show a pronounced single absorption peak (cf. quantum chemical results shown in the Supporting Information (SI) Figure SI 37) with an increase of ε and a slight red shift upon extension of the π-electron system[63] from **AmBr** to **AmBi** (Figure 2). In **AmBi**, the CH_3O group adds a weak electron-donating (D) character[65] to the chromophore and complements its D−π−D character, which cause an additional red shift in the absorption. Introduction of an additional SO_3H group (**AmBiSulf**) significantly decreases the solubility in nonpolar and slightly polar solvents and does not notably shift the absorption maximum as compared to **AmBi**. In agreement with recent

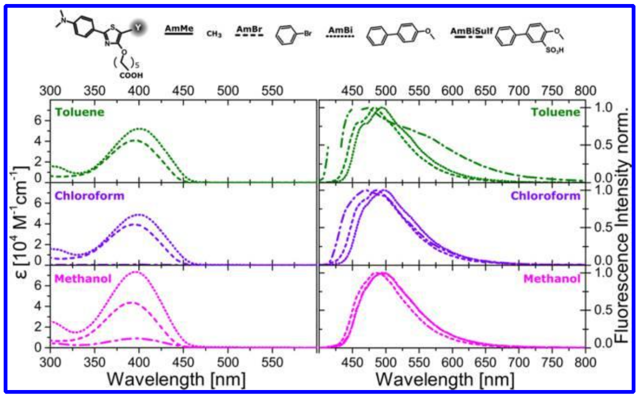

Figure 2. Extinction coefficients (ε) (left) and normalized emissions (right) of the 2-(4-*N*,*N*-dimethyl-aminophenyl)-4-hydroxy-5-Y-1,3-thiazole core (λ_{exc} = 405 nm) and the methyl (**AmMe**) (solid), phenyl-4-bromo (**AmBr**) (dotted), phenyl-4-methoxyphenyl (**AmBi**) (dashed), and 3-phenyl-4-methoxyphenyl-3-sulfonylphenyl (**AmBiSulf**) (dotted dashed) functionalizations in toluene (dark green, upper row), $CHCl_3$ (violet, middle row), and CH_3OH (pink, lower row) ($c < 10^{-6}$ M).

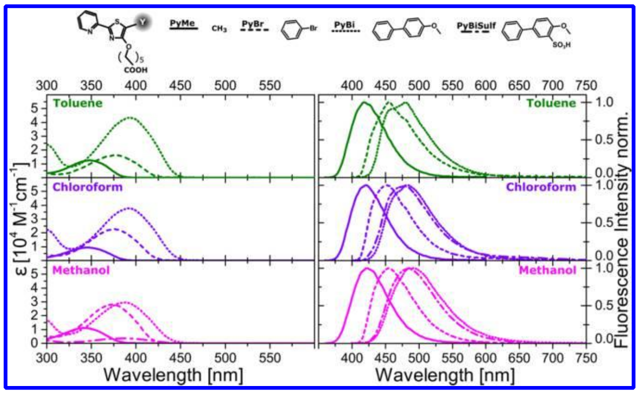

Figure 3. Extinction coefficients (ε) (left) and normalized emissions (right) of the 2-(2-pyridyl)-4-hydroxy-5-Y-1,3-thiazole core (405 nm) methyl (**PyMe**) (solid), phenyl-4-bromo (**PyBr**) (dotted), phenyl-4-methoxyphenyl (**PyBi**) (dashed), and 3-phenyl-4-methoxyphenyl-3-sulfonylphenyl (**PyBiSulf**) (dotted dashed) functionalizations in toluene (dark green, upper row), $CHCl_3$ (violet, middle row), and CH_3OH (pink, lower row) ($c < 10^{-6}$ M).

NiMe, **NiBr**, and **NiBi** were isolated in very good yields from 87 to 95%. Finally, the 5-(4-methoxybiphenyl)-thiazoles **AmBi**, **PyBi**, and **NiBi** were sulfonated by the method of Habenicht.[43] All target molecules except the sulfonated **AmBiSulf**, **PyBiSulf**, and **NiBiSulf** are well soluble in chloroform or dichloromethane, which are suitable solvents for the Langmuir technique. The sulfonic acid group increases the hydrophilicity; thus, the best solubility of these was observed in methanol. However, a mixture of chloroform and methanol can be used to achieve the necessary minimum solubility for the Langmuir technique.

UV−Vis Absorption and Fluorescence Spectroscopy. The influences of the above-introduced modifications to the thiazole chromophores are characterized by means of UV−vis absorption and fluorescence spectroscopy in solution. The variation in solvent polarity yields reference spectra for the thiazoles in different supramolecular environments studied in the subsequent Langmuir sections.

4-N,N-Dimethylaminophenyl Derivatives. The extinction coefficient ($\varepsilon(\lambda)$) spectra of **Am** (Figure 2) show a pronounced single absorption peak (cf. quantum chemical results shown in the Supporting Information (SI) Figure SI 37) with an increase of ε and a slight red shift upon extension of the π-electron system[63] from **AmBr** to **AmBi** (Figure 2). In **AmBi**, the CH_3O group adds a weak electron-donating (D) character[65] to the chromophore and complements its D−π−D character, which cause an additional red shift in the absorption. Introduction of an additional SO_3H group (**AmBiSulf**) significantly decreases the solubility in nonpolar and slightly polar solvents and does not notably shift the absorption maximum as compared to **AmBi**. In agreement with recent

DOI: 10.1021/acs.langmuir.8b04063
Langmuir 2019, 35, 2587−2600

Table 1. Extinction Coefficients ($\varepsilon(\lambda_{max})$) (Determined via Linear Regression for Concentrations Ranging from $c = 10^{-4}$ to 10^{-7} M; See the Supporting Information Figures SI 64−71), Spectral Positions of Absorption and Emission Maxima ($c < 10^{-6}$ M) of 2-(4-*N*,*N*-Dimethylaminophenyl/2-pyridyl/4-nitrophenyl)-4-hydroxy-5-Y-1,3-thiazoles with Different Functionalizations

		TD-DFT S_0 --> S_1	toluene dielectric constant: 2.4			$CHCl_3$ dielectric constant: 4.8			CH_3OH dielectric constant: 33		
R	Y	vac (nm)	ε (M/cm)	abs (nm)	em (nm)	ε (M/cm)	abs (nm)	em (nm)	ε (M/cm)	abs (nm)	em (nm)
Am	**Me**	355									
	Br	403	40 724	396	483	39 204	394	485	43 611	391	485
	Bi	415	51 712	400	494	48 833	400	497	75 764	396	496
	BiSulf	419			458		400	469		397	496
Py	**Me**	353	12 512	347	420	9127	345	420	11 145	342	422
	Br	400	12 274	376	452	22 696	375	454	27 882	375	455
	Bi	422	43 656	393	479	36 612	392	482	28 652	386	492
	BiSulf	408						478		386	484
Ni	**Me**	429	18 524	391	500	27 348	393	588	23 944	383	450
	Br	476	19 525	419	525	30 201	423	615	24 965	411	450
	Bi	519	26 037	436	562	36 091	439	689	44 795	426	484
	BiSulf	487		432	546		430	669		425	485

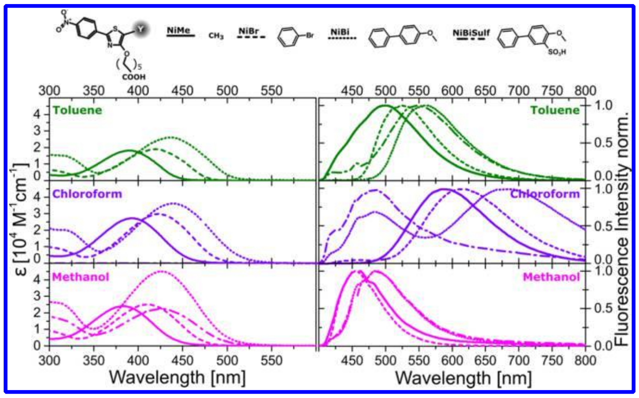

Figure 4. Extinction coefficients (ε) (left) and normalized emissions (right) of the 2-(4-nitrophenyl)-4-hydroxy-5-Y-1,3-thiazole core (λ_{exc} = 405 nm) methyl (**NiMe**) (solid), phenyl-4-bromo (**NiBr**) (dotted), phenyl-4-methoxyphenyl (**NiBi**) (dashed), and 3-phenyl-4-methoxyphenyl-3-sulfonylphenyl (**NiBiSulf**) (dotted dashed) functionalizations in toluene (dark green, upper row), $CHCl_3$ (violet, middle row), and CH_3OH (pink, lower row) ($c < 10^{-6}$ M).

reports on thiazole chromophores, their absorption spectra negligibly blue-shift upon increased solvent polarity.[44]

However, the extension of the π-electron system causes a red-shifted emission for the different Y functionalizations from **AmBr** to **AmBiSulf**. As an exception, the emission spectrum of **AmBiSulf** shows a slightly blue-shifted emission in nonpolar and aprotic polar solvents (toluene, $CHCl_3$) as compared to **AmBi**, which might be attributed to the presence of ground-state aggregates and a stabilization of excited states. Additionally, dipolar aggregation could cause a protonation of the $(CH_3)_2N$ group by the SO_3H moiety.

2-Pyridyl Derivatives. The extinction coefficient and emission spectra of the **Py** derivatives significantly red-shift upon extension of the π-system, as shown in Figure 3. Hence, whereas in the case of **Am** the absorption and emission properties were largely determined by the electron-pushing amine moiety, the pyridine moiety in **Py** enables enlarging the chromophoric unit upon attaching phenylene groups.

However, all spectra of the **Py** derivatives are blue-shifted as compared to their **Am** counterparts (compare Figure 2 with Figure 3; see Table 1), which is in agreement with reports on similar chromophores.[63] This difference in the spectral position increases with shortening of the π-system, that is, as most pronounced for the (**Am**/**Py**)**Me** derivatives. As mentioned for **AmBiSulf** above, an introduction of a SO_3H group at the 4-methoxybiphenyl moiety (**PyBiSulf**) significantly decreases solubility in nonpolar solvents and again the emission shifts slightly to blue due to aggregation in toluene and $CHCl_3$.

4-Nitrophenyl Derivatives. Similar to the **Py** thiazoles before, the **Ni** derivatives show red-shifted absorption (Figure 4) upon extension of the π-system through the different Y functionalizations. In contrast to **Am** and **Py**, the **Ni** derivatives show a pronounced solvent dependence of their fluorescence spectra, as shown in Figure 4. Although the fluorescence spectra of **Ni** dissolved in methanol are similar to those of **Am** and **Py** (λ_{max} = 450−500 nm, **Am** and **Py** in all solvents), they

DOI: 10.1021/acs.langmuir.8b04063
Langmuir 2019, 35, 2587−2600

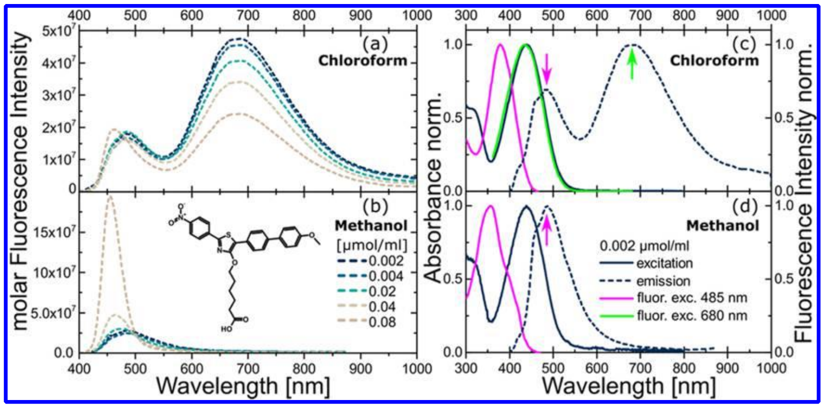

Figure 5. Molar and self-absorption corrected emission spectra of **NiBi** in $CHCl_3$ (a) and CH_3OH (b) (cf. 0.002 μmol/mL Figure 4) at five different concentrations. Excitation (dark blue, solid), emission (dark blue, dashed, λ_{ex} = 405 nm), and fluorescence excitation spectra at λ_{em} = 485 nm (green) and λ_{em} = 700 nm (pink) of **NiBi** in $CHCl_3$ (c) and CH_3OH (d) (0.002 μmol/mL).

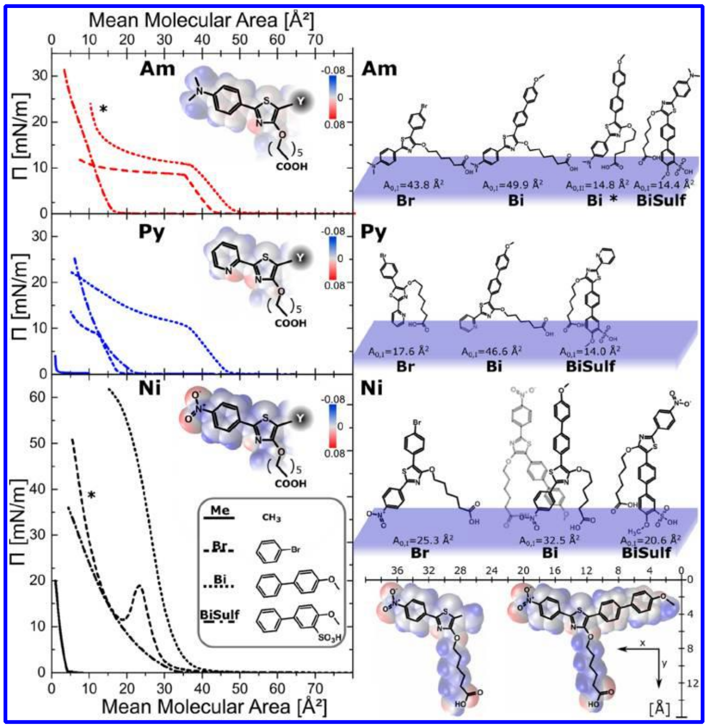

Figure 6. (Left) Averaged mean $\Pi(A)$ isotherms of (**Am**) 2-4-*N*,*N*-dimethylaminophenyl, (**Py**) 2-2-pyridyl, and (**Ni**) 2-4-nitrophenyl-4-hydroxy-5-Y-1,3-thiazoles and the methyl (**Me**, solid), phenyl-4-bromo (**Br**, dotted), phenyl-4-methoxyphenyl (**Bi**, dashed), and 3-phenyl-4-methoxyphenyl-3-sulfonylphenyl (**BiSulf**, dotted dashed) functionalizations. (Right) Molecular orientations of the different 4-hydroxy thiazoles in the Langmuir film derived from the extrapolated minimum molecular area (A_0) of the $\Pi(A)$ isotherm. Exemplarily, the representative molecular dimensions of **NiMe** and **NiBi** are given. Lewis structures are plotted on top of images of the electrostatic potential (φ) distribution at the van der Waals surface.

DOI: 10.1021/acs.langmuir.8b04063

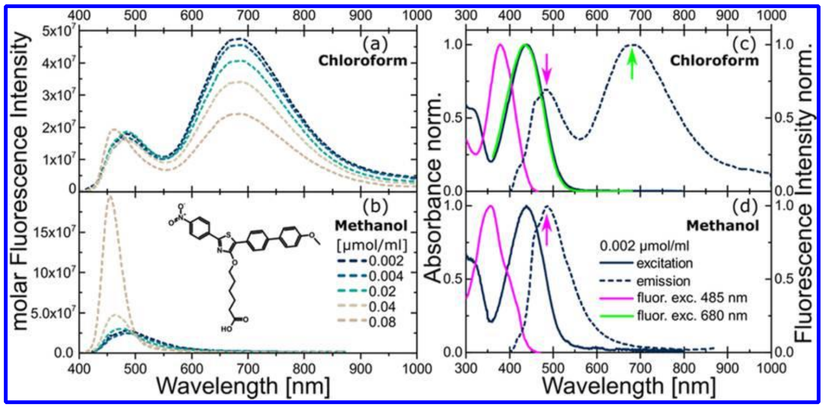

Figure 5. Molar and self-absorption corrected emission spectra of **NiBi** in CHCl$_3$ (a) and CH$_3$OH (b) (cf. 0.002 μmol/mL Figure 4) at five different concentrations. Excitation (dark blue, solid), emission (dark blue, dashed, λ_{ex} = 405 nm), and fluorescence excitation spectra at λ_{em} = 485 nm (green) and λ_{em} = 700 nm (pink) of **NiBi** in CHCl$_3$ (c) and CH$_3$OH (d) (0.002 μmol/mL).

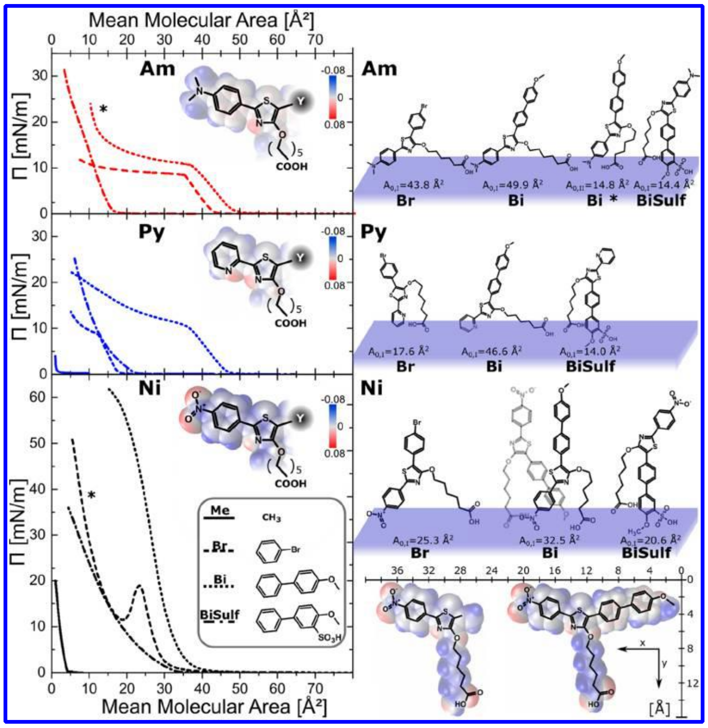

Figure 6. (Left) Averaged mean Π(A) isotherms of (**Am**) 2-4-*N*,*N*-dimethylaminophenyl, (**Py**) 2-2-pyridyl, and (**Ni**) 2-4-nitrophenyl-4-hydroxy-5-Y-1,3-thiazoles and the methyl (**Me**, solid), phenyl-4-bromo (**Br**, dotted), phenyl-4-methoxyphenyl (**Bi**, dashed), and 3-phenyl-4-methoxyphenyl-3-sulfonylphenyl (**BiSulf**, dotted dashed) functionalizations. (Right) Molecular orientations of the different 4-hydroxy thiazoles in the Langmuir film derived from the extrapolated minimum molecular area (A_0) of the Π(A) isotherm. Exemplarily, the representative molecular dimensions of **NiMe** and **NiBi** are given. Lewis structures are plotted on top of images of the electrostatic potential (φ) distribution at the van der Waals surface.

significantly red-shift to λ_{max} = 500−575 nm if the **Ni** derivatives are dissolved in toluene. A further red shift to λ_{max} = 575−700 nm is observed if the solvent is $CHCl_3$. In the case of **NiBi**, an additional peak between 450 and 500 nm is present in the $CHCl_3$ fluorescence spectrum. This peak, which features vibrational progression similar to the spectra of **NiBi** and **NiBiSulf** dissolved in CH_3OH, actually dominates the fluorescence spectra of the polar **NiBiSulf** derivatives when dissolved in $CHCl_3$.

To elucidate the origin of the dual emission of **NiBi** when dissolved in $CHCl_3$ (Figure 4), dilution studies have been performed to reveal the possible presence of molecular aggregates that might cause either of the fluorescence peaks. Variation of the concentration of **NiBi** in both solvents changes systematically the ratio between the dual emission peaks, as shown in Figure 5a,b. Because the fluorescence peak between 450 and 500 nm rises upon increasing concentration (Figure 5b), it is assigned to molecular aggregate fluorescence, whereas the 690 nm emission must originate from the monomer. The corresponding aggregate absorption, which is virtually invisible in the absorption spectra in Figure 4, peaks at 378 nm, as revealed by photoluminescence excitation spectroscopy in Figure 5c. Because of the blue shift and the dipolar chromophore character of the **Ni** derivatives, the aggregates are presumed to be of H type. Interestingly, when dissolved in methanol, the dimer emission dominates the fluorescence spectrum, whereas the monomer emission cannot be detected.

Finally, **Am** and **Py** show similar monomeric absorption and emission features and the same dependencies on molecular substitutions, namely, the **Me**, **Br**, **Bi**, and **BiSulf** substituents causing red shifts of the absorption and emission spectra with successive π-system extension (**Bi** always yielding the largest red shift). These results are in good agreement with the literature.[41−43,63] Whereas the **Am** and **Py** derivatives easily dissolve in the broad range of different polar solvents (except their **BiSulf** derivatives), the **Ni** derivatives show fluorescence peaks assigned to aggregates, even in the dilute solutions. Because of their spectral shifts as compared to the monomers, we deduce dipolar aggregation in the case of the **Ni** derivatives, which is expected to impact supramolecular structure formation at the air−water interface[45] as discussed next.

Π(*A*) Isotherms. In general, surface pressure (Π) vs mean molecular area (A) isotherms indicate the formation of two-dimensional (2D) monolayers featuring possibly different supramolecular structures, transitions between them, and their breakdown.[41,66] The supramolecular structures of these monomolecular Langmuir films are characterized by the molecular packing density or molecular orientations, which are deduced from the extrapolated minimum molecular area (A_0: derived from steep sections (cf. the compressibility modulus shown in Figure SI 64) of the $\Pi(A)$ isotherm). To assign distinct supramolecular structures to Langmuir monolayers, the experimentally determined A_0 areas are compared to theoretically derived A_0 areas of molecular conformations assumed to be possible at the air−water interface.[41] The molecular orientations in the individual condensed phases are then identified by the best fit between theoretical and experimental A_0 areas.

As shown in Figure 6, no $\Pi(A)$ isotherms rising at physically meaningful areas were detected for **Me** derivatives (Y = CH_3), which turn out to be water soluble and not sufficiently amphiphilic for use in the Langmuir technique. The isotherms further reveal that the largest A_0 areas observed do not exceed 50 Å^2. This small area shows that condensed phases are not formed from flat aligned amphiphiles (parallel to the water surface, thus necessitating areas significantly larger than the measured A_0 areas) but instead the chromophores must be partially dissolved in the aqueous subphase and vertically aligned or tilted when the Langmuir monolayers are formed. The maximum A_0 areas are obtained for the largest nonpolar Y substituents of type **Bi** for any of the thiazoles, that is, **AmBi**, **PyBi**, or **NiBi**.

4-N,N-Dimethylaminophenyl Derivatives. The $\Pi(A)$ isotherm of **AmBr** in Figure 6 (left) shows a stable and compressible monolayer between 44 and 35 Å^2 (A_0 = 44 Å^2, Table 2). A similar A_0 area $A_{0,theo}$ = 43 Å^2, shown in Figure 6 (**AmBr**), is also obtained when multiplying the molecular length between the COOH, which works as the anchor group to the water subphase, and **Am** (the $(CH_3)_2N$ group, 16.4 Å^2) with the sulfur van der Waals diameter (2.6 Å). As we have shown previously,[44] in this supramolecular orientation, the $(CH_3)_2N$ substituent works as a second anchor[67] because of its basicity (*N*,*N*-dimethylaniline, pK_a = 5.1;[68] cf. heptanoic acid, pK_a = 4.4[69]). Therefore, we conclude that the chromophore is slightly vertically tilted on the water surface and straightens up in the first phase of the stable and compressible monolayer, thus causing a reduction of the distance between the two anchors. Further compressions yield a transition phase of high compressibility, without a second rise of Π. Therefore, we conclude that the collapse point (Π_C) of the monolayer **AmBr** is reached at a surface pressure of Π_C > 8.5 mN/m.

Table 2. Extrapolated Minimum Molecular Area (A_0) Derived from the Π(*A*) Isotherm of Different 4-Hydroxy-5-1,3-thiazoles

	Am		Py		Ni	
	$A_0(A_0{*})$		$A_0(A_0{*})$		$A_0(A_0{*})$	
Y	exp (Å^2)	theo (Å^2)	exp (Å^2)	theo (Å^2)	exp (Å^2)	theo (Å^2)
Me			1		4 (4)	
Br	44	43	18	18	25 (15)	32
Bi	50 (15)	51 (18)	47	48	33	29
BiSulf	16	18	14	18	21	22

Extending Y to the still rather nonpolar 4-methoxybiphenyl moiety (**AmBi**) basically yields just a small shift of +6 Å^2 (even if now containing a sterically demanding twisted biphenyl moiety) of the isotherm (**AmBi**: A_0 = 50 Å^2), and an additional phase ($A_0{*}$ = 15 Å^2) is observed, as shown in Figure 6. Because this $A_0{*}$ area is very small, it might be assigned to upright aligned molecules with both anchors dissolved in the subphase, as shown in Figure 6 (**AmBi***), or to formation of three-dimensional aggregates. Further modification of Y by attaching a SO_3H group (**AmBiSulf**) significantly shifts the onset of the isotherm to smaller mean molecular areas. In accordance with the interpretation of the small $A_0{*}$ area of **AmBi***, the resulting small A_0 area (14 Å^2) of **AmBiSulf** is assigned to partially dissolved or three-dimensionally aggregated chromophores. However, because the SO_3H group is more hydrophilic than the $(CH_3)_2N$ group (cf. *p*-toluenesulfonic acid,[70] pK_a = −2.8[71]), the former is expected to function as a second anchor instead of the latter.

2-Pyridyl Derivatives. With the change to a 2-(2-pyridyl) substitution at the thiazole, the molecular amphiphilicity is significantly altered. The $\Pi(A)$ isotherm of **PyBr** starts rising at

22 Å^2 (A_0 = 17.6 Å^2; see Figure 6). A small A_0 area is obtained when multiplying the molecular y-lengths of **PyBr** (from the sulfur to the oxygen of the 4-hydroxy-5-Y-1,3-thiazoles y = 6.4 Å; see Figure 6) with the vdW diameter of sulfur. This A_0 area corresponds to a previously reported one for the same chromophore without the bromine.[41] Therefore, we expect a supramolecular structure where the chromophore is tilted with the Py group dissolved in the water subphase due to its polarity and acidity (pyridine, pK_a = 5.14[72]). Subsequently, the isotherm section being characteristic for **PyBr** is followed by a second rise of the $\Pi(A)$ isotherm after passing a pronounced bend.

Extending Y to a still rather nonpolar 4-methoxybiphenyl moiety increases the A_0 areas by 20 Å^2 (**PyBi**: A_0 = 46.6 Å^2), and again no second condensed phase is observed till the minimum trough area is reached. We assign the large A_0 area to a tilted molecule with both anchors dissolved in the subphase, as shown Figure 6 (**PyBi**). Similar to **AmBiSulf**, attaching of SO_3H (**PyBiSulf**) significantly shifts the A_0 area to smaller values and yields a liquid condensed phase. In accordance with the interpretation of the small A_0* area of **PyBi***, the resulting very small A_0 area (14 Å^2) of **PyBiSulf** is assigned to upright aligned and partially dissolved or three-dimensionally aggregated chromophores (Figure 6, **PyBiSulf**).

4-Nitrophenyl Derivatives. Introduction of nitrophenyl instead of aminophenyl or pyridine replaces the second strong anchor[73,74] by a less polar moiety. The $\Pi(A)$ isotherm for the molecule **NiBr** with a Y = bromophenyl functionalization shows a highly compressible liquid phase with increasing Π at A < 40 Å^2 that transforms to a condensed phase of lower compressibility at higher surface pressures and decreased areas (A_0 = 25 Å^2), cf. **AmBr** and **PyBr** above. A peak in the isotherm at A = 23 Å^2 (18 mN/m) indicates a collapse or strong reorganization of this first stable and compressible monolayer. At further compressions, the surface pressure steeply rises till Π > 50 mN/m, which indicates the formation of a second phase of a condensed **NiBr** monolayer with rather low compressibility[42] (compressibility modulus reaching 140 mN/m, as shown in Figure SI 64). The latter is similar to **AmBr** and **PyBr**, characterized by A_0* = 15 Å^2.

Extension of Y to a 4-methoxybiphenyl moiety (**NiBi**) also adds a third somewhat dipolar group (OCH_3) to the amphiphile, as shown by the electrostatic potential distribution at the van der Waals surface of **NiBi** in Figure 6. Instead of the NO_2 moiety, in certain cases the OCH_3 group might interact with the water subphase, thus causing an inverse orientation, as shown in Figure 6 for a dimer of **NiBi** with opposing molecular orientations. The structural motive of **NiBi** causes a single condensed phase (A_0 = 33 Å^2) that reaches exceptionally high surface pressures and relatively low compressibilities as compared to other thiazole amphiphiles[42] (compressibility modulus reaching ≈100 mN/m, as shown in Figure SI 64). As clearly visible from the sharp maximum in the compressibility modulus at 27 Å^2, the monolayer starts transforming into multilayers at 27 Å^2 (between 40 and 45 mN/m). Again, further modification of Y by attaching SO_3H (**NiBiSulf**) significantly shifts the onset of the isotherm to smaller areas (A_0 = 21 Å^2) and induces a liquid phase, as characterized by the small slope between 0 and 10 mN/m. Because of the additional strong anchor, the tendency of monolayer collapse decreases.

It was shown that the methyl (**Me**) functionalized thiazoles are not sufficiently amphiphilic for the Langmuir technique, whereas the extension of the π-system (**Br**, **Bi**) increases the weight of the nonpolar moiety and stabilizes the film formation. Here, the pyridyl (**Py**), but first and foremost the $(CH_3)_2N$ (**Am**) substituent, works as a second anchor to the water subphase and enables vertically tilted supramolecular structures. Though appearing to be a predestined second anchor as well, the NO_2 (**Ni**) changes the supramolecular structure distinctly, as such derivatives form dipolar aggregates, which have presumably H-type character, as deduced from the absorption and emission spectra above. Those interactions have been recently shown to significantly stabilize two-dimensional Langmuir layers.[45] Further insights into the supramolecular structure are gained directly during the Langmuir process via online fluorescence monitoring, as detailed below.

In Situ Steady-State Fluorescence Spectroscopy. Intermolecular interactions between the thiazoles will basically involve dipolar interactions, particularly in the case of the push−pull substitution pattern and π−π-quadrupole or London dispersion interactions in the case of the π-extended chromophores. Because the balance between these interactions depends on the polarity of the surrounding medium, we have chosen toluene, chloroform, and methanol as prototype nonpolar, medium, and highly polar solvents, respectively. These solvents might be suitable model media to mimic different molecular assemblies at heterointerfaces, as used in the Langmuir technique. In the following, we employ UV−vis transmission and emission spectroscopies to dissolved thiazoles to obtain reference spectra to be compared with those of typical H-, J-, or π-aggregates that possibly form at the air−water interface.

The supramolecular structure in the Langmuir layers of different types of 4-hydroxy-5-Y-1,3-thiazoles are characterized by their fluorescence spectra detected in situ upon compression. In the following, representative emission spectra of the quasi-gas (negligible molecular interactions) to condensed phases (strong molecular interactions) are compared with solution spectra to determine possible spectral changes arising from intermolecular interactions in the supramolecular assemblies.

4-N,N-Dimethylaminophenyl Derivatives. As compared to the fluorescence spectra of dissolved **AmBr**, the fluorescence spectra of the corresponding Langmuir layers are red-shifted and actually vibrationally not resolved at all investigated surface pressures (see Figure 7; for spectra of systematically varied Π, see Figure SI 51). The disappearance of the vibronic progression as compared to the solution is assigned to a superposition of fluorescence spectra from dyes in slightly varied environments in the Langmuir layer within the measurement spot. The red shift is assigned to the transition from solution to the condensed state. Upon increasing Π, that is, transition from the gas to the liquid phase, the emission maximum of **AmBr** shifts slightly to red (λ_{max} = 518 nm, Π = 0.1 mN/m), followed by a continuous blue shift (λ_{max} = 500 nm, Π = 12 mN/m) in the condensed phase without a change in spectral shape after the collapse point (Π_C > 11 mN/m; for in situ fluorescence isotherms, see SI). The above-discussed possible presence of acid−base equilibrium is not reflected in the in situ fluorescence spectra. No blue-shifted emission that can be assigned to a protonated species (Figure SI 49) is observed (see Figure SI 51).

In contrast to **AmBr**, Langmuir layers of **AmBi** can be compressed to higher surface pressures, assigned above to a

DOI: 10.1021/acs.langmuir.8b04063
Langmuir 2019, 35, 2587−2600

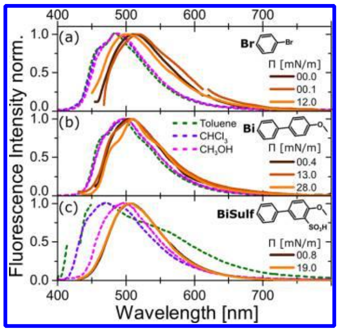

Figure 7. Normalized emission spectra of Langmuir layers at air—water interfaces (solid lines; quasi-2D phases varied from gas (Π = 0 mN/m) to condensed (Π > 0 mN/m)) of the 2-(4-*N*,*N*-dimethylaminophenyl)-4-hydroxy-5-Y-1,3-thiazole core (λ_{exc} = 405 nm) and the phenyl-4-bromo (**AmBr**), phenyl-4-methoxyphenyl (**AmBi**), and 3-phenyl-4-methoxyphenyl-3-sulfonylphenyl (**AmBiSulf**) functionalizations and solvent spectra (dashed line) for toluene (dark green), $CHCl_3$ (violet), and CH_3OH (pink).

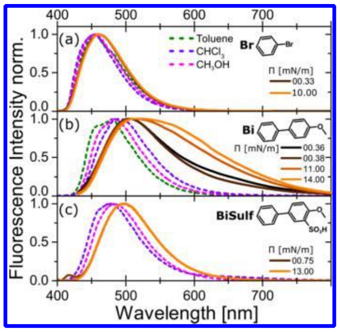

Figure 8. Normalized emission spectra of Langmuir layers at air—water interfaces (solid lines; quasi-2D phases varied from gas (Π = 0 mN/m) to condensed (Π > 0 mN/m)) of the 2-(2-pyridyl)-4-hydroxy-5-Y-1,3-thiazole core (λ_{exc} = 405 nm) and the phenyl-4-bromo (**Br**), phenyl-4-methoxyphenyl (**Bi**), and 3-phenyl-4-methoxyphenyl-3-sulfonylphenyl (**BiSulf**) functionalizations with the solvent spectra (dashed line) in toluene (dark green), $CHCl_3$ (violet), and CH_3OH (pink).

second condensed phase, which gives rise to better-resolved vibrational progression (Figures 7 and SI 52). The latter indicates improved supramolecular order favored through the extended π-electron system in **AmBi** as compared to **AmBr**. In contrast, the fluorescence spectra of **AmBiSulf** show no dependence on Π (Figure 7), hence pointing to a smaller supramolecular order than in the case of **AmBi** and possibly a preaggregation in solution or instantly at the air—water interface.

2-Pyridyl Derivatives. Similar to **Am**(**Br**,**BiSulf**), the fluorescence spectra of the Langmuir layers of **Py**(**Br**,**BiSulf**) are slightly red-shifted as compared to the corresponding solutions, show no vibrational progression, and are independent of Π. Again, no spectral sign of protonation (see Figure SI 50) of the basic anchoring group (now pyridine) by the COOH moiety is observed (see Figure 8; Figure SI 55). However, **PyBi** shows significant extension of the fluorescence spectra to red when reaching the condensed phase I, as shown in Figure 8.

Difference fluorescence spectra of the **PyBi** Langmuir layers (see Figure SI 56), where the quasi-gas-phase spectrum (A = 502 Å^2) was subtracted from the remaining spectra, reveal an initial fluorescence decrease for areas shrinking from 800 to 500 Å^2, followed by a steady fluorescence gain upon further compression into the condensed phases. Consequently, aggregation yields the extension of the fluorescence spectra to red upon increasing Π, as reported in Figure 8. As revealed by the evolution of the fluorescence difference spectra, aggregates have also formed initially on spreading the chloroform solution of **PyBi**, which dissociate in the course of the LB experiment during operation in the quasi-gas phase. Because of the red shift, aggregates are assigned as J-type.

As alternative origins of the red-shifted fluorescence peak, one might consider intra- or intermolecular protonation of the pyridine moiety by the COOH acid (λ_{em} = 492 nm (neutral), λ_{em} = 622 nm (protonated); see Figure SI 50), or excimer emission,[43,75] both of which might change with Π as the supramolecular structures change. However, it appears unlikely that such a process would be exclusively observed for **PyBi**, but not for all other **Py** derivatives.

Similar to **PyBr** (which also features similar A_0 areas), the fluorescence spectra of **PyBiSulf** are independent of Π, red-shifted, and show no vibronic progression as compared to the solution spectra. These equal results for distinctly different amphiphiles (two as compared to three anchors for **PyBr** and **PyBiSulf**) and the very small A_0 areas imply formation of amorphous rather than well-defined supramolecularly structured films that possibly extend to the third spatial dimension rather than being quasi-two-dimensional prototype Langmuir layers.

4-Nitrophenyl Derivatives. The fluorescence spectra of **Ni** derivatives on the LB trough are significantly broader than the spectra of the different solutions discussed above and shown for reference as dashed lines in Figure 9. Furthermore, their shape and spectral position typically depend more strongly on Π than in the case of the **Am** and **Py** derivatives discussed above, as surveyed in Figure 9.

In detail, the Langmuir layer of the CH_3-functionalized core (**NiMe**) shows a single emission feature (547 nm) located between the emission of maxima obtained for the rather nonpolar toluene and the polar $CHCl_3$ solutions (see Figure 9). The emission maximum shifts red (28 nm, Π = 9 mN/m; 10 nm, Π = 14 mN/m) when probing the compressible monolayer.

The opposite trend is observed for the Langmuir layer made from the Y = 4-bromophenyl functionalized molecule (**NiBr**). The main emission feature of the Langmuir layer disappears when probing the compressible monolayer, and an additional blue-shifted band rises upon increasing Π. Hence, the shape of emission switches from one representing the monomeric emission known from the $CHCl_3$ solution to an H-type aggregate emission (see CH_3OH solution, Figure 9). The latter (λ_{em} = 550 nm) features a pronounced vibrionic progression, which further supports the assumption of H-aggregate formation. For this aggregation, each second **NiBr** dye needs to switch orientation if they were uniquely aligned in the Langmuir gas phase. This reorganization likely causes the dip

DOI: 10.1021/acs.langmuir.8b04063
Langmuir 2019, 35, 2587−2600

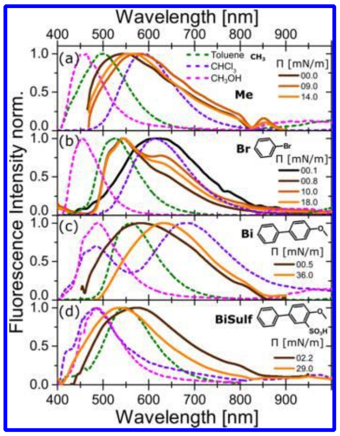

Figure 9. Normalized emission spectra of Langmuir layers at air−water interfaces (solid lines; quasi-2D phases varied from gas (Π = 0 mN/m) to condensed (Π > 0 mN/m)) of the 2-(4-nitrophenyl)-4-hydroxy-5-Y-1,3-thiazoles core (λ_{exc} = 405 nm) and the methyl (**Me**), phenyl-4-bromo (**Br**), phenyl-4-methoxyphenyl (**Bi**), and 3-phenyl-4-methoxyphenyl-3-sulfonylphenyl (**BiSulf**) functionalizations with the solvent spectra (dashed line) in toluene (dark green), $CHCl_3$ (violet), and CH_3OH (pink).

in the Π(*A*) isotherm discussed above. The accompanied complex supramolecular and morphological rearrangements during lateral compression of the Langmuir layer likely cause the nonmonotonous development of the ratio between monomer and aggregate fluorescence peaks, as seen in Figure 9 and in Figure SI 59. Formation of a layer over time without lateral compression apparently avoids reorganization in a dense layer and might be understood as crystallization as the fluorescence spectrum gets smoothly converted from the monomer spectrum to the aggregate spectrum within 40 min (see Figure SI 60). Such time is actually granted during the LB-online-fluorescence measurements. The Π(*A*) isotherms recorded during these fluorescence measurements ($\Pi(A)^{fluor}$) therefore differ from those discussed above (compare Figures 6 and SI 59). The $\Pi(A)^{fluor}$ isotherm in Figure SI 59 is shifted to an unphysically small A_0 area, thus indicating growth of H aggregates in three spatial dimensions, that is, losing the 2D-growth restriction typically enforced by the Langmuir technique in the case of **NiBr.**

In contrast to **NiBr**, **NiBi** shows just a red-shifted fluorescence (52 nm, 0.175 eV) upon lateral compression from the gas (0.5 mN/m) to the condensed phase (36 mN/m) without the appearance of new peaks. Hence, we deduce that the extension of the π-system in **NiBi**, as compared to **NiBr**, hampers reorganization because of increased π−π interactions, which stabilize a unique molecular orientation within the supramolecular structure. Within such structures, the molecules are apparently slightly tilted to additionally stabilize the supramolecular structure via J-type dipolar assembly of the D−π−A dyes, as revealed by the successive red shift upon increasing Π. The avoided reorganization due to stabilization of the two-dimensional layer upon enhanced π−π and dipolar interactions is presumably the major reason for reaching the exceptionally large surface pressures (Π ≈ 45 mN/m) before reorganization of the monolayer is observed, as discussed above. However, presumably the Langmuir layer consists of small domains as no vibrational progression can be observed in the Langmuir-layer fluorescence.

Contrary to **NiBi**, the fluorescence maximum of the Langmuir layer of **NiBiSulf** (λ_{max} = 574 nm) in the liquid phase (2.2 mN/m) shifts continuously to blue (38 nm, 0.149 eV, 29.00 mN/m), which is indicative of the formation of H aggregates. The reorganization involved in H-aggregate formation (discussed above for **NiBr**), the high compressibility deduced from the Π(*A*) isotherms in Figure 6, and the unphysically small A_0 areas indicate formation of three-dimensional aggregates upon lateral compression in the Langmuir experiment.

■ CONCLUSIONS

In the present work, we systematically investigate the influence of the chromophore within the recently introduced class of double-anchor T-shaped amphiphilic dyes[41] on the supramolecular structures they form on the air−water interface in Langmuir experiments. One hydrophilic subphase anchor is provided by a COOH moiety that is centrally linked via an alkylic flexible chain to the core of the chromophore, namely, a 4-hydroxy-thiazole. The second anchor is chosen to be an integral part of the chromophore to enable tuning of the molecular orientation upon lateral compression of Langmuir monolayers employed in this work. These R1 anchors in the 2-position of the thiazole have been chosen as 4-*N*,*N*-dimethylaminophenyl (**Am**), 2-pyridyl (**Py**), and 4-nitrophenyl (**Ni**).[54,55] For each of these derivatives, the chromophores have been systematically extended in the 5-position by replacing the methyl (**Me**) moiety with a 4-bromophenyl (**Br**), a 4-methoxybiphenyl (**Bi**), and a 4-methoxyphenyl-3-sulfonylphenyl (**BiSulf**) moiety.

As revealed by standard UV−vis transmission and fluorescence spectroscopies on solutions, the **Am** moiety dominates the electronic properties of all investigated **Am** derivatives. In contrast, the absorption and emission spectra systematically shift red upon extension of the π-system in the case of the **Py** and **Ni** derivatives.

For the given set of substituents in the 5-position of the thiazole, that is, **Me**, **Br**, **Bi**, and **BiSulf**, just the **Ni** derivatives, essentially **NiBr** and **NiBi**, feature dipolar chromophores that give rise to the formation of H and J aggregates at the air−water interface, respectively, as revealed by in situ fluorescence spectroscopy performed online during Langmuir experiments. From the Π(*A*) isotherms and the in situ detected fluorescence spectra, we deduce reorganization of the **NiBr** dyes and three-dimensional instead of 2D growth of their supramolecular structures. In contrast, we find that the diphenylene moiety in **NiBi** significantly stabilizes the compressible monolayer formed by the assembly at the air−water interface. Thus, reorientation is essentially hampered, and the dyes form J aggregates upon lateral compression of the Langmuir layer. The joint stabilization of this **NiBi** layer by π−π and dipolar interactions gives rise to considerably high surface pressures of ≈45 mN/m,[42,44,45,76−80] which are obtained without any signs of disturbance of the monolayer.

In summary, the combination of the Langmuir technique with online fluorescence measurements revealed that the π−π interactions, which are pronounced for the **Bi** derivatives, yield the most distinct supramolecular structures. Whereas in the cases of **PyBi** and **NiBi**, ordered J-type supramolecular

DOI: 10.1021/acs.langmuir.8b04063
Langmuir 2019, 35, 2587−2600

structures in microdomains are formed, as revealed by not vibrationally resolved, red-shifted fluorescence spectra, **AmBi** forms ordered supramolecular structures that are more homogeneous, as revealed by the resolved vibrational progression in the fluorescence spectra, which are, however, not stabilized by J-type dipolar interactions. Hence, the presented systematic study on the influence of the chromophore on the supramolecular structures that form at the air−water interface enables distinct choices of the substitution pattern to target distinct supramolecular structures desired in optoelectronically active materials.

UV−Vis Absorption and Fluorescence Spectroscopy. For the absorption spectroscopic measurements, a UV−vis (Varian: Cary 5000) spectrometer was used in the transmission mode. The fluorescence measurements using excitation wavelengths larger than 400 nm were performed on a custom-built setup (as detailed below); for excitation wavelengths smaller than 400 nm, a different spectrometer (Horiba Fluorolog) was used. The extinction coefficients ($\varepsilon(\lambda_{\max})$) of the absorption maxima were calculated via linear regression over the concentration range from $c = 10^{-4}$ to 10^{-7} M.

LB Isotherms and in Situ Fluorescence Spectroscopy of Langmuir Layers. For the basic $\Pi(A)$-isotherm characterizations, solutions of the dyes (1 and 0.1 μmol/mL in 80% $CHCl_3$/20% CH_3OH) were carefully spread onto the subphase (ultrapure water) of the LB trough (KSV 5000). For complete evaporation, a time of 10 min was granted before moving the barriers. Then, the barriers were compressed with a speed of 5 mm/min to record the isotherms.

For the in situ fluorescence spectroscopy studies, the same Langmuir parameters were applied at a KSV NIMA Alternate L 105 LB trough equipped with a custom-built fluorescence setup. This setup consists of an Isoplane 320 spectrograph with a cooled Pixis CCD-camera from Princeton Instruments. A fiber coupled 5 mW laser with a 405 nm output wavelength was used as the excitation source (incident under 55°), and the emissions were detected under 0° to the normal. Long-pass filters with low self-fluorescence (obtained from ITOS) were used to block scattered excitation light. The data were corrected by a self-written LabView and a C++ program. These programs remove the remaining scattered excitation light and cosmic rays. The maxima of the fluorescence spectra were analyzed by a self-written Mathematica program.

Density Functional Theory (DFT) Calculations. Quantum chemical structure optimizations and calculations of electrostatic potential and absorption spectra on **5_5** and **7** monomers were performed using the density functional theory (DFT) and its time-dependent derivative (TD-DFT) as implemented in Turbomole[81] and applying the generalized gradient approximation functional BP86 (preoptimization), followed by the hybrid functionals and B3LYP,[82] def2-SVP (preoptimization), and -TZVP basis sets,[83] and the MARI-J approximation in the case of BP86, which have been shown to yield reasonable electronic properties for a large variety of molecular motives, including push−pull systems and extended π-electron systems.[37,40,84−86]

■ ASSOCIATED CONTENT

Ⓢ Supporting Information

The Supporting Information is available free of charge on the ACS Publications website at DOI: 10.1021/acs.langmuir.8b04063.

Syntheses, used materials, quantum chemically calculated absorption spectra of various conformers, detailed fluorescence spectral series, protonation studies, and further details (PDF)

■ AUTHOR INFORMATION

Corresponding Author

*E-mail: martin.presselt@leibniz-ipht.de. Phone: +49 3641 206418.

ORCID

Maximilian L. Hupfer: 0000-0001-8890-0684
Julia Preiß: 0000-0002-7570-7305
Benjamin Dietzek: 0000-0002-2842-3537
Martin Presselt: 0000-0002-5579-0260

Notes

The authors declare no competing financial interest.

■ ACKNOWLEDGMENTS

The authors would like to thank the German Research Foundation (DFG PR 1415/2) and Bundesministerium für Bildung und Forschung (BMBF FKZ 03EK3507) for financial support. J.P. acknowledges funding from the Nagelschneider Stiftung.

■ REFERENCES

(1) Mishra, A.; Bäuerle, P. Small Molecule Organic Semiconductors on the Move: Promises for Future Solar Energy Technology. *Angew. Chem., Int. Ed.* **2012**, *51*, 2020−2067.

(2) Jou, J.-H.; Kumar, S.; Agrawal, A.; Li, T.-H.; Sahoo, S. Approaches for Fabricating High Efficiency Organic Light Emitting Diodes. *J. Mater. Chem. C* **2015**, *3*, 2974−3002.

(3) Sirringhaus, H. 25th Anniversary Article: Organic Field-Effect Transistors: The Path Beyond Amorphous Silicon. *Adv. Mater.* **2014**, *26*, 1319−1335.

(4) Das, S.; Herrmann-Westendorf, F.; Schacher, F. H.; Tauscher, E.; Ritter, U.; Dietzek, B.; Presselt, M. Controlling Electronic Transitions in Fullerene van der Waals Aggregates via Supramolecular Assembly. *ACS Appl. Mater. Interfaces* **2016**, *8*, 21512−21521.

(5) Herrmann, F.; Engmann, S.; Presselt, M.; Hoppe, H.; Shokhovets, S.; Gobsch, G. Correlation between near infrared-visible absorption, intrinsic local and global sheet resistance of poly(3,4-ethylenedioxy-thiophene) poly(styrene sulfonate) thin films. *Appl. Phys. Lett.* **2012**, *100*, No. 153301.

(6) Gampe, D. M.; Nöller, F.; Hänsch, V. G.; Schramm, S.; Darsen, A.; Habenicht, S. H.; Ehrhardt, S.; Weiß, D.; Görls, H.; Beckert, R. Surprising characteristics of D−A-type functional dyes by introducing 4-alkoxythiazoles as the donor-unit. *Tetrahedron* **2016**, *72*, 3232−3239.

(7) Würthner, F.; Kaiser, T. E.; Saha-Möller, C. R. J-Aggregates: From Serendipitous Discovery to Supramolecular Engineering of Functional Dye Materials. *Angew. Chem., Int. Ed.* **2011**, *50*, 3376−3410.

(8) Biesmans, G.; Verbeek, G.; Verschuere, B.; van der Auweraer, M.; De Schryver, F. C. On the fluorescence of anthracene chromophores in langmuir-blodgett films. *Thin Solid Films* **1989**, *169*, 127−142.

(9) Flämmich, M.; Gather, M. C.; Danz, N.; Michaelis, D.; Bräuer, A. H.; Meerholz, K.; Tünnermann, A. Orientation of Emissive Dipoles in OLEDs: Quantitative In Situ Analysis. *Org. Electron.* **2010**, *11*, 1039−1046.

(10) Mayr, C.; Schmidt, T. D.; Brütting, W. High-efficiency fluorescent organic light-emitting diodes enabled by triplet-triplet annihilation and horizontal emitter orientation. *Appl. Phys. Lett.* **2014**, *105*, No. 183304.

(11) Presselt, M.; Herrmann, F.; Hoppe, H.; Shokhovets, S.; Runge, E.; Gobsch, G. Influence of Phonon Scattering on Exciton and Charge Diffusion in Polymer-Fullerene Solar Cells. *Adv. Energy Mater.* **2012**, *2*, 999−1003.

(12) Beenken, W. J. D.; Herrmann, F.; Presselt, M.; Hoppe, H.; Shokhovets, S.; Gobsch, G.; Runge, E. Sub-bandgap absorption in organic solar cells: experiment and theory. *Phys. Chem. Chem. Phys.* **2013**, *15*, 16494−16502.

(13) Presselt, M.; Bärenklau, M.; Rösch, R.; Beenken, W. J. D.; Runge, E.; Shokhovets, S.; Hoppe, H.; Gobsch, G. Sub-Bandgap Absorption in Polymer-Fullerene Solar Cells. *Appl. Phys. Lett.* **2010**, *97*, No. 253302.

(14) Shewmon, N. T.; Watkins, D. L.; Galindo, J. F.; Zerdan, R. B.; Chen, J.; Keum, J.; Roitberg, A. E.; Xue, J.; Castellano, R. K. Enhancement in Organic Photovoltaic Efficiency Through the Synergistic Interplay of Molecular Donor Hydrogen Bonding and π-Stacking. *Adv. Funct. Mater.* **2015**, *25*, 5166−5177.

(15) Li, Z.; Bian, J.; Wang, Y.; Jiang, F.; Liang, G.; He, P.; Hou, Q.; Tong, J.; Liang, Y.; Zhong, Z.; Zhou, Y.; Tian, W. Effect of Alkyl Chain Length on the Photovoltaic Performance of Oligothiophene-Based Small Molecules. *Sol. Energy Mater. Sol. Cells* **2014**, *130*, 336−346.

(16) Poelking, C.; Tietze, M.; Elschner, C.; Olthof, S.; Hertel, D.; Baumeier, B.; Würthner, F.; Meerholz, K.; Leo, K.; Andrienko, D. Impact of mesoscale order on open-circuit voltage in organic solar cells. *Nat. Mater.* **2015**, *14*, 434−439.

(17) Chen, Y.; Feng, Y.; Gao, J.; Bouvet, M. Self-Assembled Aggregates of Amphiphilic Perylene Diimide−Based Semiconductor Molecules: Effect of Morphology on Conductivity. *J. Colloid Interface Sci.* **2012**, *368*, 387−394.

(18) Grozema, F. C.; Siebbeles, L. D. A. Mechanism of Charge Transport in Self-Organizing Organic Materials. *Int. Rev. Phys. Chem.* **2008**, *27*, 87−138.

(19) Wang, S.; Fabiano, S.; Himmelberger, S.; Puzinas, S.; Crispin, X.; Salleo, A.; Berggren, M. Experimental evidence that short-range intermolecular aggregation is sufficient for efficient charge transport in conjugated polymers. *Proc. Natl. Acad. Sci. U.S.A.* **2015**, *112*, 10599−10604.

(20) Presselt, M.; Herrmann, F.; Shokhovets, S.; Hoppe, H.; Runge, E.; Gobsch, G. Sub-bandgap absorption in polymer-fullerene solar cells studied by temperature-dependent external quantum efficiency and absorption spectroscopy. *Chem. Phys. Lett.* **2012**, *542*, 70−73.

(21) Kar, H.; Gehrig, D. W.; Laquai, F.; Ghosh, S. J-Aggregation, its Impact on Excited State Dynamics and Unique Solvent Effects on Macroscopic Assembly of a Core-Substituted Naphthalenediimide. *Nanoscale* **2015**, *7*, 6729−6736.

(22) Wong, C. Y.; Penwell, S. B.; Cotts, B. L.; Noriega, R.; Wu, H.; Ginsberg, N. S. Revealing Exciton Dynamics in a Small-Molecule Organic Semiconducting Film with Subdomain Transient Absorption Microscopy. *J. Phys. Chem. C* **2013**, *117*, 22111−22122.

(23) De la Cadena, A.; Pascher, T.; Davydova, D.; Akimov, D.; Herrmann, F.; Presselt, M.; Wächtler, M.; Dietzek, B. Intermolecular exciton−exciton annihilation in phospholipid vesicles doped with [Ru(bpy)2dppz]2+. *Chem. Phys. Lett.* **2016**, *644*, 56−61.

(24) Kitchen, B.; Awartani, O.; Kline, R. J.; McAfee, T.; Ade, H.; O'Connor, B. T. Tuning Open-Circuit Voltage in Organic Solar Cells with Molecular Orientation. *ACS Appl. Mater. Interfaces* **2015**, *7*, 13208−13216.

(25) Zhong, S.; Zhong, J. Q.; Wee, A. T. S.; Chen, W. Molecular Orientation and Electronic Structure at Organic Heterojunction Interfaces. *J. Electron Spectrosc. Relat. Phenom.* **2015**, *204*, 12−22.

(26) Bürckstümmer, H.; Tulyakova, E. V.; Deppisch, M.; Lenze, M. R.; Kronenberg, N. M.; Gsänger, M.; Stolte, M.; Meerholz, K.; Würthner, F. Efficient Solution-Processed Bulk Heterojunction Solar Cells by Antiparallel Supramolecular Arrangement of Dipolar Donor−Acceptor Dyes. *Angew. Chem., Int. Ed.* **2011**, *50*, 11628−11632.

(27) Herrmann-Westendorf, F.; Sachse, T.; Schulz, M.; Kaufmann, M.; Sivakov, V.; Beckert, R.; Martinez, T. J.; Dietzek, B.; Presselt, M. Photo-Annealing of Merocyanine Aggregates. *J. Phys. Chem. A* **2018**, 9821.

(28) Würthner, F.; Chen, Z. J.; Hoeben, F. J. M.; Osswald, P.; You, C. C.; Jonkheijm, P.; von Herrikhuyzen, J.; Schenning, A.; van der Schoot, P.; Meijer, E. W.; Beckers, E. H. A.; Meskers, S. C. J.; Janssen, R. A. J. Supramolecular p-n-heterojunctions by co-self-organization of oligo(p-phenylene vinylene) and perylene bisimide dyes. *J. Am. Chem. Soc.* **2004**, *126*, 10611−10618.

(29) Ariga, K.; Hill, J. P.; Ji, Q. Layer-By-Layer Assembly as a Versatile Bottom-Up Nanofabrication Technique for Exploratory Research and Realistic Application. *Phys. Chem. Chem. Phys.* **2007**, *9*, 2319−2340.

(30) Wang, Y.; Angelatos, A. S.; Caruso, F. Template Synthesis of Nanostructured Materials via Layer-by-Layer Assembly. *Chem. Mater.* **2008**, *20*, 848−858.

(31) Modlińska, A.; Piosik, E.; Paluszkiewicz, J.; Martyński, T. Aggregation properties of tetrachloroperylene-tetracarboxylic acid in binary Langmuir and Langmuir−Blodgett films. *J. Lumin.* **2014**, *148*, 44−54.

(32) Angelova, A.; Ionov, R. Monolayer and Spectroscopic Studies of an Amphiphilic (Phenylethynyl)anthracene Probe in Pure and Mixed Films with Charged and Neutral Lipids. *Langmuir* **1999**, *15*, 7199−7207.

(33) Modlińska, A.; Bauman, D. The Langmuir-Blodgett Technique as a Tool for Homeotropic Alignment of Fluorinated Liquid Crystals Mixed with Arachidic Acid. *Int. J. Mol. Sci.* **2011**, *12*, 4923−4945.

(34) Ariga, K.; Yamauchi, Y.; Mori, T.; Hill, J. P. 25th Anniversary Article: What Can Be Done with the Langmuir-Blodgett Method? Recent Developments and its Critical Role in Materials Science. *Adv. Mater.* **2013**, *25*, 6477−6512.

(35) Jin, J.; Li, L. S.; Li, Y.; Zhang, Y. J.; Chen, X.; Wang, D.; Jiang, S.; Li, T. J.; Gan, L. B.; Huang, C. H. Structural Characterizations of C60-Derivative Langmuir−Blodgett Films and Their Photovoltaic Behaviors. *Langmuir* **1999**, *15*, 4565−4569.

(36) Das, S.; Preiß, J.; Plentz, J.; Brückner, U.; von der Lühe, M.; Eckardt, O.; Dathe, A.; Schacher, F. H.; Täuscher, E.; Ritter, U.; Csáki, A.; Andrä, G.; Dietzek, B.; Presselt, M. Controlling Intermolecular Interactions at Interfaces: Case of Supramolecular Tuning of Fullerene's Electronic Structure. *Adv. Energy Mater.* **2018**, *8*, No. 1801737.

(37) Presselt, M.; Schnedermann, C.; Müller, M.; Schmitt, M.; Popp, J. Derivation of Correlation Functions to Predict Bond Properties of Phenyl-CH Bonds Based on Vibrational and H-1 NMR Spectroscopic Quantities. *J. Phys. Chem. A* **2010**, *114*, 10287−10296.

(38) Fitzner, R.; Mena-Osteritz, E.; Mishra, A.; Schulz, G.; Reinold, E.; Weil, M.; Koerner, C.; Ziehlke, H.; Elschner, C.; Leo, K.; Riede, M.; Pfeiffer, M.; Uhrich, C.; Baeuerle, P. Correlation of pi-Conjugated Oligomer Structure with Film Morphology and Organic Solar Cell Performance. *J. Am. Chem. Soc.* **2012**, *134*, 11064−11067.

(39) Szłapa, A.; Kula, S.; Błaszkiewicz, U.; Grucela, M.; Schab-Balcerzak, E.; Filapek, M. Simple Donor−π−Acceptor Derivatives Exhibiting Aggregation-Induced Emission Characteristics for Use as Emitting Layer in OLED. *Dyes Pigm.* **2016**, *129*, 80−89.

(40) Presselt, M.; Schnedermann, C.; Schmitt, M.; Popp, J. Prediction of electron densities, the respective laplacians, and ellipticities in bond-critical points of phenyl-CH-bonds via linear relations to parameters of inherently localized CD stretching vibrations and 1H NMR-shifts. *J. Phys. Chem. A* **2009**, *113*, 3210−3222.

(41) Hupfer, M. L.; Kaufmann, M.; Herrmann-Westendorf, F.; Sachse, T.; Roussille, L.; Feller, K. H.; Weiss, D.; Deckert, V.; Beckert, R.; Dietzek, B.; Presselt, M. On the Control of Chromophore Orientation, Supramolecular Structure, and Thermodynamic Stability of an Amphiphilic Pyridyl-Thiazol upon Lateral Compression and Spacer Length Variation. *ACS Appl. Mater. Interfaces* **2017**, *9*, 44181−44191.

(42) Kaufmann, M.; Hupfer, M. L.; Sachse, T.; Herrmann-Westendorf, F.; Weiß, D.; Dietzek, B.; Beckert, R.; Presselt, M. Introducing double polar heads to highly fluorescent Thiazoles:

DOI: 10.1021/acs.langmuir.8b04063
Langmuir 2019, 35, 2587−2600

Influence on supramolecular structures and photonic properties. *J. Colloid Interface Sci.* **2018**, *526*, 410−418.

(43) Habenicht, S. H.; Schramm, S.; Fischer, S.; Sachse, T.; Herrmann-Westendorf, F.; Bellmann, A.; Dietzek, B.; Presselt, M.; Weiß, D.; Beckert, R.; Görls, H. Tuning the polarity and surface activity of hydroxythiazoles - extending the applicability of highly fluorescent self-assembling chromophores to supra-molecular photonic structures. *J. Phys. Chem. C* **2016**, *4*, 958−971.

(44) Hupfer, M. L.; Kaufmann, M.; Roussille, L.; Preiß, J.; Weiß, D.; Hinrichs, K.; Deckert, V.; Dietzek, B.; Beckert, R.; Presselt, M. Arylic vs. Alkylic - Hydrophobic Linkers Determine Supramolecular Structure and Optoelectronic Properties of Tripodal Amphiphilic Push-Pull-Thiazoles. *Langmuir* **2019**, DOI: 10.1021/acs.langmuir.8b03893.

(45) Hupfer, M. L.; Kaufmann, M.; Preiß, J.; Weiß, D.; Dietzek, B.; Beckert, R.; Presselt, M. Combining Dipolar Aggregate Formation with Two-Dimensional Assembly at Air-Water-Interfaces: Case of Amphiphilic Push-Pull-Thiazoles. *Adv. Mater.* **2019**.

(46) Hupfer, M. L.; Herrmann-Westendorf, F.; Kaufmann, M.; Beckert, R.; Dietzek, B.; Presselt, M. Autonomous Interface Self-Healing: Monitored by Restoration of UV−vis Absorption Spectra of Self-Assembled Thiazole Layers. *Chem. - Eur. J.* **2019**.

(47) Ranyuk, E.; Ermakova, E. V.; Bovigny, L.; Meyer, M.; Bessmertnykh-Lemeune, A.; Guilard, R.; Rousselin, Y.; Tsivadze, A. Y.; Arslanov, V. V. Towards sensory Langmuir monolayers consisting of macrocyclic pentaaminoanthraquinone. *New J. Chem.* **2014**, *38*, 317−329.

(48) Caruso, F.; Grieser, F.; Thistlethwaite, P. J.; Almgren, M. Two-dimensional diffusion of amphiphiles in phospholipid monolayers at the air-water interface. *Biophys. J.* **1993**, *65*, 2493−2503.

(49) Grummt, U.-W.; Weiss, D.; Birckner, E.; Beckert, R. Pyridylthiazoles: Highly luminescent heterocyclic compounds. *J. Phys. Chem. A* **2007**, *111*, 1104−1110.

(50) Menzel, R.; Ogermann, D.; Kupfer, S.; Weiß, D.; Görls, H.; Kleinermanns, K.; González, L.; Beckert, R. 4-Methoxy-1,3-thiazole based donor-acceptor dyes: Characterization, X-ray structure, DFT calculations and test as sensitizers for DSSC. *Dyes Pigm.* **2012**, *94*, 512−524.

(51) Breul, A. M.; Pietsch, C.; Menzel, R.; Schäfer, J.; Teichler, A.; Hager, M. D.; Popp, J.; Dietzek, B.; Beckert, R.; Schubert, U. S. Blue Emitting Side-Chain Pendant 4-Hydroxy-1,3-Thiazoles in Polystyrenes Synthesized by RAFT Polymerization. *Eur. Polym. J.* **2012**, *48*, 1339−1347.

(52) Menzel, R.; Breul, A.; Pietsch, C.; Schäfer, J.; Friebe, C.; Täuscher, E.; Weiß, D.; Dietzek, B.; Popp, J.; Beckert, R.; Schubert, U. S. Blue-Emitting Polymers Based on 4-Hydroxythiazoles Incorporated in a Methacrylate Backbone. *Macromol. Chem. Phys.* **2011**, *212*, 840−848.

(53) Usta, H.; Sheets, W. C.; Denti, M.; Generali, G.; Capelli, R.; Lu, S.; Yu, X.; Muccini, M.; Facchetti, A. Perfluoroalkyl-Functionalized Thiazole−Thiophene Oligomers as N-Channel Semiconductors in Organic Field-Effect and Light-Emitting Transistors. *Chem. Mater.* **2014**, *26*, 6542−6556.

(54) Cong, J.; Yang, X.; Liu, J.; Zhao, J.; Hao, Y.; Wang, Y.; Sun, L. Nitro group as a new anchoring group for organic dyes in dye-sensitized solar cells. *Chem. Commun.* **2012**, *48*, 6663−6665.

(55) Zhang, L.; Cole, J. M. Anchoring Groups for Dye-Sensitized Solar Cells. *ACS Appl. Mater. Interfaces* **2015**, *7*, 3427−3455.

(56) Calderón-Ortiz, L. K.; Täuscher, E.; Leite Bastos, E.; Görls, H.; Weiß, D.; Beckert, R. Hydroxythiazole-Based Fluorescent Probes for Fluoride Ion Detection. *Eur. J. Org. Chem.* **2012**, *2012*, 2535−2541.

(57) Wolfram, S.; Wurfel, H.; Habenicht, S. H.; Lembke, C.; Richter, P.; Birckner, E.; Beckert, R.; Pohnert, G. A small azide-modified thiazole-based reporter molecule for fluorescence and mass spectrometric detection. *Beilstein J. Org. Chem.* **2014**, *10*, 2470−2479.

(58) Menzel, R.; Kupfer, S.; Mede, R.; Weiß, D.; Görls, H.; González, L.; Beckert, R. Arylamine-Modified Thiazoles as Donor−Acceptor Dyes: Quantum Chemical Evaluation of the Charge-Transfer Process and Testing as Ligands in Ruthenium(II) Complexes. *Eur. J. Org. Chem.* **2012**, *2012*, 5231−5247.

(59) Täuscher, E.; Weiß, D.; Beckert, R.; Fabian, J.; Assumpção, A.; Görls, H. Classical heterocycles with surprising properties: the 4-hydroxy-1,3-thiazoles. *Tetrahedron Lett.* **2011**, *52*, 2292−2294.

(60) Menzel, R.; Täuscher, E.; Weiß, D.; Beckert, R.; Görls, H. The Combination of 4-Hydroxythiazoles with Azaheterocycles: Efficient Bidentate Ligands for Novel Ruthenium Complexes. *Z. Anorg. Allg. Chem.* **2010**, *636*, 1380−1385.

(61) Kerdesky, F. A. J.; Holms, J. H.; Moore, J. L.; Bell, R. L.; Dyer, R. D.; Carter, G. W.; Brooks, D. W. 4-Hydroxythiazole inhibitors of 5-lipoxygenase. *J. Med. Chem.* **1991**, *34*, 2158−2165.

(62) Gampe, D. M.; Hänsch, V. G.; Schramm, S.; Menzel, R.; Weiß, D.; Beckert, R. Mixing Chromophores: Donor−Acceptor Dyes with Low-Lying LUMOs and Narrow Band Gaps by Connecting 4-Alkoxythiazoles and Azaacenes. *Eur. J. Org. Chem.* **2017**, *2017*, 1369−1379.

(63) Habenicht, S. H.; Schramm, S.; Zhu, M.; Freund, R. R.; Langenstuck, T.; Strathausen, R.; Weiss, D.; Biskup, C.; Beckert, R. pi-Extension of a 4-ethoxy-1,3-thiazole via aryl alkyne cross coupling: synthesis and exploration of the electronic structure. *Photochem. Photobiol. Sci.* **2015**, *14*, 2097−2107.

(64) Arcadi, A.; Attanasi, O. A.; Guidi, B.; Rossi, E.; Santeusanio, S. 2-Substituted 5-Acetyl-4-Thiazolyl Triflates as Useful Building Blocks for the Preparation of Functionalized Thiazoles. *Eur. J. Org. Chem.* **1999**, *1999*, 3117−3126.

(65) Habenicht, S. H.; Siegmann, M.; Kupfer, S.; Kübel, J.; Weiß, D.; Cherek, D.; Möller, U.; Dietzek, B.; Gräfe, S.; Beckert, R. And yet they glow: thiazole based push−pull fluorophores containing nitro groups and the influence of regioisomerism. *Methods Appl. Fluoresc.* **2015**, *3*, No. 025005.

(66) Kaganer, V. M.; Mohwald, H.; Dutta, P. Structure and phase transitions in Langmuir monolayers. *Rev. Mod. Phys.* **1999**, *71*, 779−819.

(67) Villares, A.; Lydon, D. P.; Low, P. J.; Robinson, B. J.; Ashwell, G. J.; Royo, F. M.; Cea, P. Characterization and Conductivity of Langmuir−Blodgett Films Prepared from an Amine-Substituted Oligo(phenylene ethynylene). *Chem. Mater.* **2008**, *20*, 258−264.

(68) Sýkora, D.; Tesařová, E.; Popl, M. Interactions of basic compounds in reversed-phase high-performance liquid chromatography influence of sorbent character, mobile phase composition, and pH on retention of basic compounds. *J. Chromatogr. A* **1997**, *758*, 37−51.

(69) (a) Williams, M. In *The Merck Index: An Encyclopedia of Chemicals, Drugs, and Biologicals*, 15th ed.; O'Neil, M. J., Ed.; PB - Royal Society of Chemistry: Cambridge, U.K., 2013; p 2708, 9781849736701. (b) Williams, M. *Drug Dev. Res.* **2013**, *74*, 339.

(70) Herrmann, F.; Muhsin, B.; Singh, C. R.; Shokhovets, S.; Gobsch, G.; Hoppe, H.; Presselt, M. Influence of Interface Doping on Charge-Carrier Mobilities and Sub-Bandgap Absorption in Organic Solar Cells. *J. Phys. Chem. C* **2015**, *119*, 9036−9040.

(71) Hartman, C. K.; Mezei, G. Mapping the Intricate Reactivity of Nanojars toward Molecules of Varying Acidity and Their Conjugate Bases Leading To Exchange of Pyrazolate Ligands. *Inorg. Chem.* **2017**, *56*, 10609−10624.

(72) Nachod, F. C.; Braude, E. A.; Phillips, W. D. In *Determination of Organic Structures by Physical Methods*; Braude, E. A., Nachod, F. C., Eds.; Academic Press: New York, 1955.

(73) Inglot, K.; Martyński, T.; Bauman, D. Surface potential measurements of Langmuir films of azo dye/liquid crystal mixtures. *Dyes Pigm.* **2009**, *80*, 106−114.

(74) Dynarowicz-Łatka, P.; Milart, P. Synthesis and Langmuir monolayer characterisation of some nitro derivatives of polyphenyl carboxylic acids. *J. Chem. Res.* **2009**, *2009*, 225−228.

(75) Biadasz, A.; Łabuszewska, K.; Chrzumnicka, E.; Michałowski, E.; Martyński, T.; Bauman, D. Spectral properties of some fluorescent dyes in two-dimensional films formed by means of Langmuir−Blodgett technique. *Dyes Pigm.* **2007**, *74*, 598−607.

(76) Schwieger, C.; Chen, B.; Tschierske, C.; Kressler, J.; Blume, A. Organization of T-Shaped Facial Amphiphiles at the Air/Water Interface Studied by Infrared Reflection Absorption Spectroscopy. *J. Phys. Chem. B* **2012**, *116*, 12245−12256.
(77) Das, S.; Preiß, J.; Plentz, J.; Brückner, U.; von der Lühe, M.; Eckardt, O.; Dathe, A.; Schacher, F. H.; Täuscher, E.; Ritter, U.; Csáki, A.; Andrä, G.; Dietzek, B.; Presselt, M. Controlling Intermolecular Interactions at Interfaces: Case of Supramolecular Tuning of Fullerene's Electronic Structure. *Adv. Energy Mater.* **2018**, *8*, No. 1801737.
(78) Bauman, D.; Hertmanowski, R.; Stefańska, K.; Stolarski, R. The synthesis of novel perylene-like dyes and their aggregation properties in Langmuir and Langmuir−Blodgett films. *Dyes Pigm.* **2011**, *91*, 474−480.
(79) del Caño, T.; Parra, V.; Rodríguez-Méndez, M. L.; Aroca, R.; de Saja, J. A. Molecular stacking and emission properties in Langmuir−Blodgett films of two alkyl substituted perylene tetracarboxylic diimides. *Org. Electron.* **2004**, *5*, 107−114.
(80) Zou, L.; You, A.; Song, J.; Li, X.; Bouvet, M.; Sui, W.; Chen, Y. Cation-induced self-assembly of an amphiphilic perylene diimide derivative in solution and Langmuir−Blodgett films. *Colloids Surf., A* **2015**, *465*, 39−46.
(81) Ahlrichs, R.; Bär, M.; Häser, M.; Horn, H.; Kölmel, C. Electronic structure calculations on workstation computers: The program system turbomole. *Chem. Phys. Lett.* **1989**, *162*, 165−169.
(82) Stephens, P. J.; Devlin, F. J.; Chabalowski, C. F.; Frisch, M. J. Ab-Initio Calculation of Vibrational Absorption and Circular-Dichroism Spectra Using Density-Functional Force-Fields. *J. Phys. Chem.* **1994**, *98*, 11623−11627.
(83) Weigend, F.; Ahlrichs, R. Balanced basis sets of split valence, triple zeta valence and quadruple zeta valence quality for H to Rn: Design and assessment of accuracy. *Phys. Chem. Chem. Phys.* **2005**, *7*, 3297−3305.
(84) Gampe, D. M.; Kaufmann, M.; Jakobi, D.; Sachse, T.; Presselt, M.; Beckert, R.; Gorls, H. Stable and easily accessible functional dyes: dihydrotetraazaanthracenes as versatile precursors for higher acenes. *Chem. - Eur. J.* **2015**, *21*, 7571−7581.
(85) Preiß, J.; Jäger, M.; Rau, S.; Dietzek, B.; Popp, J.; Martínez, T.; Presselt, M. How Does Peripheral Functionalization of Ruthenium-(II)−Terpyridine Complexes Affect Spatial Charge Redistribution after Photoexcitation at the Franck−Condon Point? *ChemPhysChem* **2015**, *16*, 1395−1404.
(86) Presselt, M.; Dehaen, W.; Maes, W.; Klamt, A.; Martínez, T.; Beenken, W. J. D.; Kruk, M. Quantum Chemical Insights into the Dependence of Porphyrin Basicity on the Meso-Aryl Substituents: Thermodynamics, Buckling, Reaction Sites and Molecular Flexibility. *Phys. Chem. Chem. Phys.* **2015**, *17*, 14096−14106.

DOI: 10.1021/acs.langmuir.8b04063
Langmuir 2019, 35, 2587−2600

Supplementary Information:

Assembly of T-Shaped Amphiphilic Thiazoles on the Air-Water Interface: Impact of Polar Chromophore-Moieties, as well as Dipolarity and π-Extension of the Chromophore on the Supramolecular Structure

Maximilian L. Hupfer[1,3], Martin Kaufmann[1,2], Julia Preiß[1,3], Dieter Weiß[2], Rainer Beckert[2], Benjamin Dietzek[1,3], Martin Presselt[1,3,4,5*]

[1] Institute of Physical Chemistry, Friedrich Schiller University Jena, Helmholtzweg 4, 07743 Jena, Germany, E-mail: martin.presselt@leibniz-ipht.de, Phone: +49 3641 206418

[2] Institute of Organic and Macromolecular Chemistry, Friedrich Schiller University Jena, Humboldstraße 10, 07743 Jena, Germany

[3] Leibniz Institute of Photonic Technology (IPHT), Albert-Einstein-Str. 9, 07745 Jena, Germany

[4] Center for Energy and Environmental Chemistry Jena (CEEC Jena), Friedrich Schiller University Jena, Philosophenweg 7a, 07743 Jena, Germany

[5] sciclus GmbH & Co. KG, Moritz-von-Rohr-Str. 1a, 07745 Jena, Germany

*Corresponding author: martin.presselt@leibniz-ipht.de

Number of pages: 44; Number of figures: 71; Number of tables: 0

Content

Materials

4-*N*,*N*-(dimethylamino)phenyl-carbothioamide, ethyl α-bromo-(4-nitrophenyl)acetate and methyl 11-bromoundecanoate were synthesized by literature procedures. All chemicals used were reagent grade and purchased from Sigma–Aldrich, TCI or Acros. Solvents were purified by standard procedures. Solvents for UV-Vis and emission spectroscopy were of analytical grade and bought from Sigma–Aldrich. Thin layer chromatography materials were from Merck (Polygram SIL G/ UV254, aluminum oxide 60 F254). The material for column chromatography was also obtained from Merck (silica gel 60; 0.04 – 0.063 mm). The synthesis of **1**, **2**, **3a**, **3b**, **3c, 5, 6** was described in the main text.

Experimental Characterization Methods

NMR-Spectroscopy

The NMR and the corresponding correlation spectra were recorded with Bruker AC-250 (250 MHz), AC-300 (300 MHz) and AC-400 (400 MHz) spectrometers. Chemical shifts (δ) are given relative to solvents.

Mass-Spectrometry

Mass spectra were measured either with a Finnigan MAT SSQ 710 (EI) or a MAZ 95 XL (ESI) system.

Synthesis

Ethyl 6-((5-methyl-2-(pyridine-2-yl)thiazole-4-yl)oxy)hexanoate (4 Py):

Synthesis from **Ni 3** and 6-bromo-hexaonic acid ethyl ether after route A; 73% yield. The product is yellowish oil.

^{1}H NMR (300 MHz, $CDCl_3$) δ 8.58 (d, *J* = 4.3 Hz, 1H), 8.07 (d, *J* = 7.9 Hz, 1H), 7.76 (t, *J* = 7.4 Hz, 1H), 7.26 (dd, *J* = 6.1, 4.2 Hz, 1H), 4.36 (t, *J* = 6.5 Hz, 2H), 2.48 – 2.37 (m, 2H), 2.33 (s, 3H), 1.93 – 1.69 (m, 4H), 1.65 – 1.49 (m, 2H).

^{13}C NMR (75 MHz, $CDCl_3$) δ 179.36, 160.28, 159.11, 151.31, 149.06, 137.11, 123.72, 118.95, 110.53, 70.25, 33.97, 29.21, 25.49, 24.45, 9.52.

EI-MS m/z: 334 [M^{+*}].

Ethyl 6-((5-methyl-2-(4-nitrophenyl)thiazole-4-yl)oxy)hexanoate (4-Ni):

Synthesis from **Ni 3** and 6-bromo-hexaonic acid ethyl ether after route A 64% yield. The product is an orange, amorphous powder.

^{1}H NMR (300 MHz, CDCl$_3$) δ 8.24 (d, *J* = 8.9 Hz, 2H), 7.98 (d, *J* = 8.9 Hz, 2H), 4.36 (t, *J* = 6.5 Hz, 2H), 4.13 (q, *J* = 7.1 Hz, 2H), 2.44 – 2.23 (m, 5H), 1.79 (dd, *J* = 14.7, 6.9 Hz, 2H), 1.71 (dd, *J* = 15.4, 7.6 Hz, 2H), 1.57 – 1.45 (m, 2H), 1.25 (t, *J* = 7.1 Hz, 3H).

^{13}C NMR (75 MHz, CDCl$_3$) δ 173.62, 161.00, 155.86, 147.73, 139.51, 125.64, 124.27, 110.01, 70.43, 60.23, 34.28, 29.22, 25.56, 24.72, 14.25, 9.45.

EI-MS m/z: 378 [M^{+*}].

5-(4-bromophenyl)-2-(4-(dimethylamino)phenyl)thiazole-4-ol (7 Am):

Synthesis from 4-N,N-dimethylaminophenyl-carbothioamide und α-bromo-(4-bromphenyl)-acetic acid ethyl ether after route C, 87% yield. The product is an orange, crystalline powder.

^{1}H NMR (300 MHz, DMSO) δ 7.70 (d, *J* = 9.0 Hz, 1H), 7.62 (d, *J* = 8.8 Hz, 1H), 7.54 (d, *J* = 8.8 Hz, 1H), 6.78 (d, *J* = 9.0 Hz, 1H), 2.99 (s, *J* = 9.7 Hz, 3H).

^{13}C NMR (75 MHz, DMSO) δ 161.37, 158.67, 151.59, 131.70, 131.53, 127.23, 126.56, 120.42, 117.71, 111.85, 103.11, 39.52.

EI-MS m/z: 376 [M^{+*} (^{81}Br)]; 374 [M^{+*} (^{79}Br)].

5-(4-bromophenyl)-2-(pyridine-2-yl)thiazole-4-ol (**7 Py**):

Synthesis from pyridine-2-carbothioamide and α-bromo-(4-bromophenyl)-acetic acid ethyl ether after route C, 60% yield. The product is a yellow, crystalline powder.

^{1}H NMR (300 MHz, DMSO) δ 11.85 (s, 1H), 8.76 – 8.55 (m, 1H), 8.08 – 7.88 (m, 2H), 7.80 – 7.67 (m, 2H), 7.66 – 7.54 (m, 2H), 7.54 – 7.43 (m, 1H).

^{13}C NMR (75 MHz, DMSO) δ 161.40, 159.61, 150.43, 150.25, 138.25, 132.17, 131.64, 128.39, 125.55, 119.51, 118.93, 109.62.

EI-MS m/z: 334 [M^{+*} (^{81}Br)]; 332 [M^{+*} (^{79}Br)].

5-(4-bromophenyl)-2-(4-nitrophenyl)thiazole-4-ol (7 Ni):

Synthesis from 4-nitrophenyl-carbothioamide und α-bromo-(4-bromophenyl)- acetic acid ethyl ether according route C, 81% yield. The product is an orange, amorphous powder.

^{1}H NMR (400 MHz, DMSO) δ 11.99 (s, 1H), 8.34 (d, J = 8.6 Hz, 2H), 8.11 (d, J = 8.4 Hz, 2H), 7.71 (d, J = 8.2 Hz, 2H), 7.61 (d, J = 8.2 Hz, 2H).

^{13}C NMR (101 MHz, DMSO) δ 168.80, 159.56, 156.87, 147.76, 138.06, 131.82, 131.69, 130.49, 127.88, 126.08, 124.54, 119.35, 109.53.

EI-MS m/z: 378 [M^{+*}(^{81}Br)]; 376 [M^{+*} (^{79}Br)].

Ethyl 6-((5-(4-bromophenyl)-2-(4-(dimethylamino)phenyl)thiazole-4-yl)oxy)hexanoate (8 Am):

Synthesis from **Am 7** und 6-brom-hexaonix acid ethylene ester after route A, 72% yield. The product is a yellow, amorphous powder.

^{1}H NMR (300 MHz, $CDCl_3$) δ 7.80 (d, *J* = 8.9 Hz, 1H), 7.60 (d, *J* = 8.5 Hz, 1H), 7.47 (d, *J* = 8.6 Hz, 1H), 6.74 (d, *J* = 8.0 Hz, 1H), 4.52 (t, *J* = 6.5 Hz, 1H), 4.15 (q, *J* = 7.1 Hz, 1H), 2.36 (t, *J* = 7.4 Hz, 1H), 1.97 – 1.82 (m, 1H), 1.82 – 1.68 (m, 1H), 1.62 – 1.49 (m, 1H).

^{13}C NMR (75 MHz, $CDCl_3$) δ 173.63, 159.07, 131.56, 127.81, 126.96, 119.09, 111.97, 70.23, 60.23, 40.36, 34.29, 29.31, 25.69, 24.72, 14.25.

EI-MS m/z: 518 [M^{+*}(^{81}Br)]; 516 [M^{+*} (^{79}Br)].

Ethyl 6-((5-(4-bromophenyl)-2-(pyridine-2-yl)thiazole-4-yl)oxy)hexanoate (8-Py):

Synthesis from **Py 7** und 6-brom-hexaonix acid ethylene ester after route A, 79% yield. The product is a yellow, amorphous powder.

^{1}H NMR (250 MHz, $CDCl_3$) δ 8.59 (d, *J* = 4.7 Hz, 1H), 8.10 (d, *J* = 7.9 Hz, 1H), 7.78 (td, *J* = 7.7, 1.6 Hz, 1H), 7.65 (d, *J* = 8.6 Hz, 2H), 7.49 (d, *J* = 8.6 Hz, 2H), 7.35 – 7.27 (m, 1H), 4.52 (t, *J* = 6.5 Hz, 2H), 4.12 (q, *J* = 7.1 Hz, 2H), 2.34 (t, *J* = 7.4 Hz, 2H), 1.97 – 1.82 (m, 2H), 1.81 – 1.65 (m, 2H), 1.62 – 1.46 (m, 2H), 1.25 (t, *J* = 7.1 Hz, 3H).

^{13}C NMR (63 MHz, $CDCl_3$) δ 174.52, 161.70, 160.46, 151.99, 150.37, 137.87, 132.68, 131.75, 129.19, 125.20, 121.21, 119.97, 114.07, 71.25, 61.18, 35.17, 30.13, 26.57, 25.59, 15.16.

EI-MS m/z: 476 [M^{+*}(^{81}Br)]; 474 [M^{+*} (^{79}Br)] 335 [M^{*}+H^{+} - $C_{14}H_{9}{}^{81}BrN_{2}O$]; 143[$C_8H_{15}O_2{}^{+*}$].

ethyl 6-((5-(4-bromophenyl)-2-(4-nitrophenyl)thiazole-4-yl)oxy)hexanoate (8-Ni):

Synthesis from **Ni 7** und 6-brom-hexaonix acid ethylene ester after route A, 83% yield. The product is a yellow, amorphous powder.

^{1}H NMR (300 MHz, $CDCl_3$) δ 8.30 (d, *J* = 9.0 Hz, 2H), 8.07 (d, *J* = 9.0 Hz, 2H), 7.64 (d, *J* = 8.7 Hz, 2H), 7.53 (d, *J* = 8.8 Hz, 2H), 4.56 (t, *J* = 6.5 Hz, 2H), 4.15 (q, *J* = 7.1 Hz, 2H), 2.37 (t, *J* = 7.4 Hz, 2H), 1.98 – 1.85 (m, 2H), 1.82 – 1.69 (m, 2H), 1.63 – 1.47 (m, 2H), 1.27 (t, *J* = 7.1 Hz, 3H).

^{13}C NMR (75 MHz, $CDCl_3$) δ 173.53, 160.05, 156.87, 148.16, 138.92, 131.91, 130.09, 128.32, 126.01, 124.37, 120.87, 113.19, 77.43, 77.21, 77.01, 76.58, 70.73, 60.28, 34.22, 29.18, 25.63, 24.65, 14.25.

EI-MS m/z: 520 [M^{+*}(^{81}Br)]; 518 [M^{+*} (^{79}Br)].

Ethyl 6-((2-(4-(dimethylamino)phenyl)-5-(4'-methoxy-[1,1'-biphenyl]-4-yl)thiazol-4-yl)oxy)hexanoate (9 Am):

Synthesis from **Am 8** und 4-methoxyphenylboronic acid, 31% yield. The product is a yellow powder.

^{1}H NMR (250 MHz, $CDCl_3$) δ 7.79 (t, *J* = 8.4 Hz, 4H), 7.62 – 7.51 (m, 4H), 6.98 (d, *J* = 8.5 Hz, 2H), 6.72 (d, *J* = 8.7 Hz, 2H), 4.52 (t, *J* = 6.5 Hz, 2H), 4.12 (q, *J* = 7.1 Hz, 2H), 3.86 (s, 3H), 3.04 (s, 6H), 2.34 (t, *J* = 7.4 Hz, 2H), 1.96 – 1.83 (m, 2H), 1.83 – 1.66 (m, 3H), 1.63 – 1.53 (m, 4H), 1.24 (t, *J* = 7.0 Hz, 5H).

EI-MS m/z: 544 [M^{+*}]

ethyl 6-((5-(4'-methoxy-[1,1'-biphenyl]-4-yl)-2-(pyridin-2-yl)thiazole-4-yl)oxy)hexanoate (9 Py):

Synthesis from **Py 8** und 4-methoxyphenylboronic acid, 48% yield. The product is a yellow powder.

^{1}H NMR (300 MHz, $CDCl_3$) δ 8.62 (d, *J* = 4.2 Hz, 1H), 8.14 (d, *J* = 7.9 Hz, 1H), 7.90 – 7.84 (m, 2H), 7.80 (td, *J* = 7.8, 1.7 Hz, 1H), 7.64 – 7.55 (m, 4H), 7.35 – 7.29 (m, 1H), 7.06 – 6.98 (m, 2H), 4.56 (t, *J* = 6.5 Hz, 2H), 4.14 (q, *J* = 7.1 Hz, 2H), 3.88 (s, 3H), 2.37 (t, *J* = 7.4 Hz, 2H), 2.03 – 1.86 (m, 2H), 1.83 – 1.70 (m, 2H), 1.67 – 1.53 (m, 3H), 1.26 (t, *J* = 7.1 Hz, 3H).

^{13}C NMR (101 MHz, $CDCl_3$) δ 173.82, 159.56, 159.36, 151.36, 149.50, 139.14, 137.16, 133.27, 130.36, 128.05, 127.37, 126.99, 124.24, 119.20, 114.65, 114.41, 77.16, 70.44, 60.40, 55.51, 34.45, 29.42, 25.85, 24.88, 14.40.

EI-MS m/z: 502 [M^{+*}]

Ethyl 6-((5-(4'-methoxy-[1,1'-biphenyl]-4-yl)-2-(4-nitrophenyl)thiazole-4-yl)oxy)hexanoate (9 Ni):

Synthesis from **Py 8** und 4-methoxyphenylboronic acid, 56% yield. The product is a red, crystalline acid

^{1}H NMR (300 MHz, CDCl$_3$) δ 8.32 (d, *J* = 8.8 Hz, 2H), 8.10 (d, *J* = 8.8 Hz, 2H), 7.84 (d, *J* = 8.4 Hz, 2H), 7.62 (t, *J* = 8.5 Hz, 4H), 7.03 (d, *J* = 8.7 Hz, 2H), 4.59 (t, *J* = 6.5 Hz, 2H), 4.15 (q, *J* = 7.1 Hz, 2H), 3.90 (s, 3H), 2.44 – 2.31 (m, 2H), 2.02 – 1.89 (m, 2H), 1.79 (dt, *J* = 15.0, 7.3 Hz, 2H), 1.60 (dd, *J* = 11.5, 3.4 Hz, 4H), 1.28 (dd, *J* = 9.6, 4.7 Hz, 3H).

^{13}C NMR (75 MHz, CDCl$_3$) δ 173.69, 156.32, 148.04, 139.22, 128.00, 127.36, 127.00, 125.98, 124.44, 114.40, 70.70, 55.45, 34.35, 29.31, 25.75, 24.78, 14.33.

EI-MS m/z: 546 [M^{+*}]

6-((5-methyl-2-(pyridine-2-yl)thiazole-4-yl)oxy)hexanoic acid (PyMe):

Synthesis from **Py 4** after route A, 91% yield. The product is a yellow powder. Melting point: 53°C

^{1}H NMR (300 MHz, CDCl$_3$) δ 8.61 (d, *J* = 4.5 Hz, 1H), 8.09 (d, *J* = 7.9 Hz, 1H), 7.82 (t, *J* = 7.5 Hz, 1H), 7.31 (dd, *J* = 11.3, 4.5 Hz, 1H), 2.47 – 2.35 (m, 2H), 2.33 (s, 3H), 1.89 – 1.69 (m, 4H), 1.61 – 1.49 (m, 2H).

^{13}C NMR (75 MHz, CDCl$_3$) δ 178.72, 160.53, 150.54, 148.27, 138.05, 123.82, 119.39, 111.35, 70.35, 40.64, 33.90, 29.17, 25.46, 24.44, 9.59.

EI-MS m/z: 306 [M^{+*}]

6-((5-methyl-2-(4-nitrophenyl)thiazole-4-yl)oxy)hexanoic acid (NiMe):

Synthesis from **Py 4** after route A, 87% yield. The product is a yellow-orange powder. Melting point: 98°C

^{1}H NMR (300 MHz, CDCl$_3$) δ 8.25 (d, *J* = 8.9 Hz, 2H), 7.99 (d, *J* = 8.9 Hz, 2H), 2.34 (s, 3H).

^{13}C NMR (75 MHz, CDCl$_3$) δ 178.97, 160.95, 155.88, 147.71, 139.48, 125.64, 124.29, 110.06, 70.33, 33.79, 29.17, 25.44, 24.39, 9.47.

EI-MS m/z: 350 [M^{+*}]

6-((5-(4-bromophenyl)-2-(4-(dimethylamino)phenyl)thiazole-4-yl)oxy)hexanoic acid (AmBr):

Synthesis from **Am 8** after Route A, 91% yield. The product is a yellow powder. Melting point: 214°C

^{1}H NMR (300 MHz, $CDCl_3$) δ 7.81 (d, *J* = 8.8 Hz, 2H), 7.60 (d, *J* = 7.9 Hz, 2H), 7.47 (d, *J* = 8.5 Hz, 2H), 6.77 (s, 2H), 4.53 (t, *J* = 6.3 Hz, 2H), 3.12 (d, *J* = 40.0 Hz, 5H), 2.42 (t, *J* = 7.4 Hz, 2H), 1.96 – 1.83 (m, 2H), 1.83 – 1.69 (m, 2H), 1.67 – 1.50 (m, 3H).

EI-MS m/z: 490 [M^{+*} (^{81}Br)]; 488 [M^{+*} (^{79}Br)].

6-((5-(4-bromophenyl)-2-(pyridine-2-yl)thiazole-4-yl)oxy)hexanoic acid (PyBr):

Synthesis from **Ni 8** after route A, 95% yield. The product is a yellow powder. Melting point: 164°C

^{1}H NMR (300 MHz, $CDCl_3$) δ 8.63 (d, *J* = 4.2 Hz, 1H), 8.13 (d, *J* = 7.9 Hz, 1H), 7.82 (td, *J* = 7.8, 1.7 Hz, 1H), 7.71 – 7.64 (m, 2H), 7.55 – 7.47 (m, 2H), 7.34 (ddd, *J* = 7.5, 4.9, 1.1 Hz, 1H), 4.55 (t, *J* = 6.5 Hz, 2H), 2.44 (t, *J* = 7.3 Hz, 2H), 1.98 – 1.87 (m, 2H), 1.87 – 1.73 (m, 2H), 1.66 – 1.57 (m, 3H).

EI-MS m/z: 448 [M^{+*} (^{81}Br)]; 446 [M^{+*} (^{79}Br)].

6-((5-(4-bromophenyl)-2-(4-nitrophenyl)thiazole-4-yl)oxy)hexanoic acid (NiBr):

Synthesis from **Py 8** after Route A, 92% yield. The product is a yellow-orange powder. Melting point: 205°C

^{1}H NMR (300 MHz, $CDCl_3$) δ 8.36 – 8.24 (m, 2H), 8.04 (dd, *J* = 13.6, 9.0 Hz, 2H), 7.59 (ddd, *J* = 22.8, 17.9, 9.5 Hz, 4H), 4.55 (t, *J* = 6.5 Hz, 2H), 2.42 (t, *J* = 7.3 Hz, 2H), 2.25 – 1.18 (m, 35H).

EI-MS m/z: 492 [M^{+*} (^{81}Br)]; 490 [M^{+*} (^{79}Br)].

2-(4-N,N-dimethylaminophenyl)-5-(4’-methoxybiphenyl)-1,3-thiazole-4-yl)-6-oxo-hexaonic acid (AmBi):

Synthesis from **Am 9** after Route A, 91% yield. The product is a yellow-greenish powder. Melting point: 178°C

^{1}H NMR (300 MHz, CDCl3) d 7.79 (dd, J = 10.9, 8.7 Hz, 4H), 7.57 (dd, J = 8.6, 2.9 Hz, 4H), 6.99 (d, J = 8.8 Hz, 2H), 6.73 (d, J = 8.9 Hz, 2H), 4.53 (t, J = 6.5 Hz, 2H), 3.87 (d, J =5.3 Hz, 3H), 3.04 (s, 6H), 2.41 (t, J = 7.4 Hz, 2H), 1.98 – 1.84 (m, 2H), 1.77 (dt, J = 14.9, 7.3 Hz, 2H), 1.69 – 1.53 (m, 3H).

^{13}C NMR (75 MHz, CDCl3) d 176.35, 159.05, 158.78, 151.46, 137.95, 133.33, 127.84, 126.88, 126.72, 114.22, 111.83, 108.68, 70.09, 55.34, 40.27, 29.32, 25.63, 24.44.

EI-MS m/z: 516 [M_+]

5-(4’-methoxybiphenyl)-2-(2-pyridyl)-1,3-thiazole-4-yl)-6-oxo- hexaonic acid (PyBi):

Synthesis from **Py 9** after Route A, 94% yield. The product is a yellow powder. Melting point: 164°C

^{1}H NMR (300 MHz, Aceton d6) d 8.62 (d, J = 4.4 Hz, 1H), 8.15 (d, J = 7.9 Hz, 1H), 8.02 – 7.86 (m, 3H), 7.68 (dd, J = 12.6, 5.6 Hz, 4H), 7.52 – 7.40 (m, 1H), 7.05 (d, J = 8.8 Hz, 2H), 4.60 (t, J = 6.5 Hz, 2H), 3.86 (s, 3H), 2.36 (t, J = 7.2 Hz, 2H), 1.78 – 1.59 (m, 4H), 1.41 – 1.30 (m, 3H).

^{13}C NMR (75 MHz, CDCl3) d 176.35, 159.21, 158.55, 151.50, 145.72, 137.56, 133.95, 127.84, 126.23, 126.72, 114.16, 112.83, 108.68, 70.09, 55.44, 40.27, 29.32, 25.63, 24.87.

EI-MS m/z: 474 [M_+]

5-(4’-methoxybiphenyl)-2-(4-nitrophenyl)-1,3-thiazole-4-yl)-6-oxo-hexaonic acid (NiBi):

Synthesis from **Ni 9** after Route A, 92% yield. The product is a red-brownish powder. Melting point: 170°C

^{1}H NMR (300 MHz, CDCl3) d 8.39 (d, J = 8.8 Hz, 2H), 8.17 (d, J = 8.8 Hz, 2H), 7.91 (d, J = 8.3 Hz, 2H), 7.75 – 7.64 (m, 4H), 7.10 (d, J = 8.7 Hz, 2H), 4.67 (t, J = 6.5 Hz, 2H), 3.97 (s, 3H), 2.62 – 2.45 (m, 2H), 2.12 – 1.96 (m, 2H), 1.88 (dt, J = 14.9, 7.3 Hz, 2H), 1.80 – 1.61 (m, 3H).

^{13}C NMR (75 MHz, CDCl3) d 178.75, 159.39, 139.51, 139.17, 132.91, 129.49, 127.97, 127.32, 126.96, 125.94, 124.41, 114.37, 70.58, 55.42, 33.77, 29.23, 25.61, 24.42.

EI-MS m/z: 518 [M_+]

2-(4-N,N-dimethylaminophenyl)-5-(3’-sulfonyl-4’-methoxybiphenyl)-1,3-thiazole-4-yl)-11-oxo-undecylic acid (AmBiSulf):

Synthesis from **AmBi** after Route A, 25% yield. The product is a green yellowish powder. Melting point: <300°C

^{1}H NMR (300 MHz, CDCl3) d 7.79 (dd, J = 10.9, 8.7 Hz, 4H), 7.57 (dd, J = 8.6, 2.9 Hz, 4H), 6.99 (d, J = 8.8 Hz, 2H), 6.73 (d, J = 8.9 Hz, 2H), 4.53 (t, J = 6.5 Hz, 2H), 3.87 (d, J = 5.3 Hz, 3H), 3.04 (s, 6H), 2.41 (t, J = 7.4 Hz, 2H), 1.98 – 1.84 (m, 2H), 1.77 (dt, J = 14.9, 7.3 Hz, 2H), 1.69 – 1.53 (m, 3H).

EI-MS m/z: 610 [M_+]

5-(3’-sulfonyl-4’-methoxybiphenyl)-2-(4-nitrophenyl)-1,3-thiazole-4-yl)-6-oxo-hexaonic acid (NiBiSulf):

Synthesis from **PyBi** after Route B, 39% yield. The product is a red-brownish powder. Melting point: <300°C

^{1}H NMR spectra (300 MHz, MeOD) d 8.39 (d, J = 8.8 Hz, 2H), 8.29 – 8.20 (m, 3H), 7.92 (d, J = 8.3 Hz, 2H), 7.81 (d, J = 8.3 Hz, 1H), 7.73 (d, J = 8.4 Hz, 2H), 7.24 (d, J = 8.6 Hz, 1H), 4.66 (t, J = 6.4 Hz, 2H), 4.03 (s, 3H), 2.47 – 2.35 (m, 2H), 2.06 – 1.91 (m, 2H), 1.88 – 1.59 (m, 6H).

EI-MS m/z: 598 [M_+]

5-(3’-sulfonyl-4’-methoxybiphenyl)-2-(2-pyridyl)-1,3-thiazole-4-yl)-6-oxo-hexaonic acid (PyBiSulf):

Synthesis from **NiBi** after route B, 23% yield. The product is a yellowish, microcrystalline powder. Melting point: <300°C

^{1}H NMR spectra(300 MHz, MeOD) d 8.71 (s, 1H), 8.28 (m, 3H), 7.99 – 7.89 (m, 2H), 7.81 (d, J = 8.2 Hz, 1H), 7.72 (d, J = 8.5 Hz, 2H), 7.22 (d, J = 8.6 Hz, 1H), 4.01 (s, 3H), 3.67 (m, 2H), 2.42 (t, J = 6.9 Hz, 2H), 2.02 (m, 2H), 1.80 (m, 2H), 1.67 (s, 2H).

EI-MS m/z: 554

^{1}H NMR

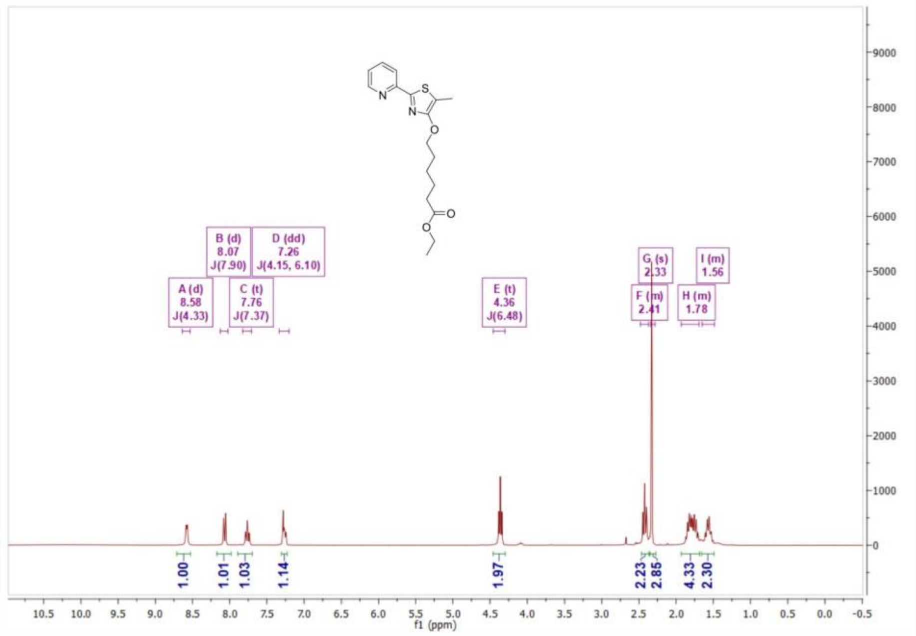

Figure SI 1: ^{1}H NMR spectrum of **4 Py**.

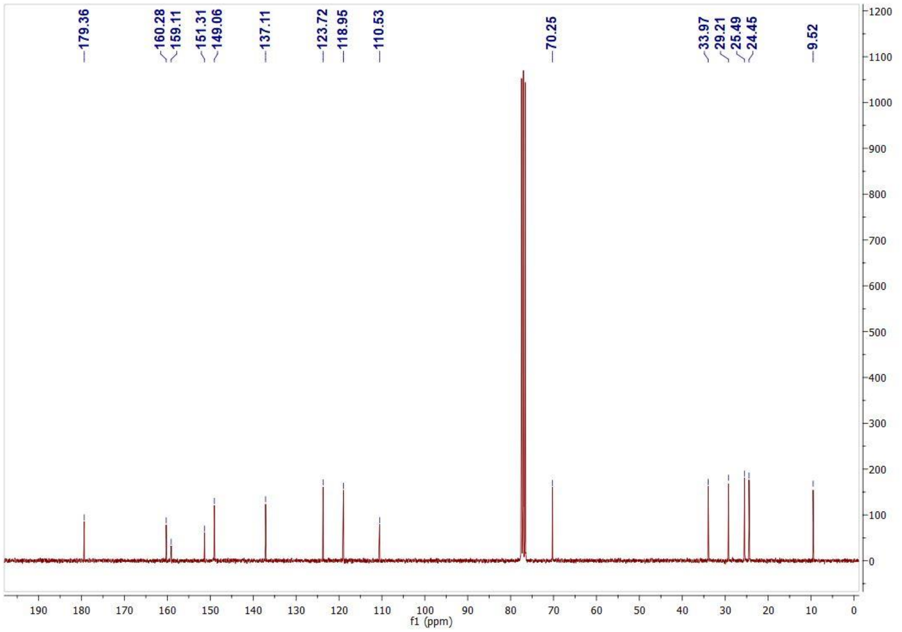

Figure SI 2: ^{1}H NMR spectrum of **4 Py**.

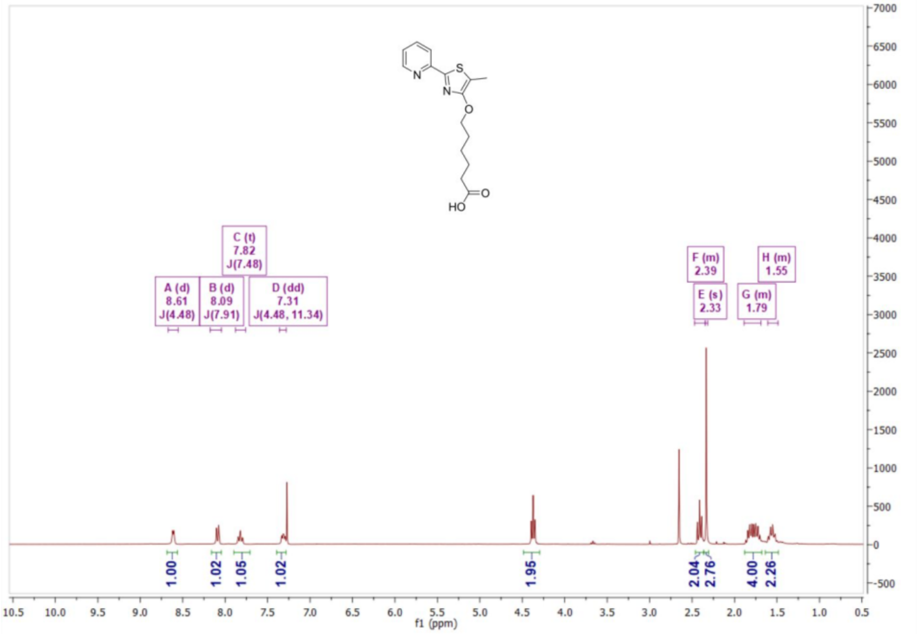

Figure SI 3: ^{1}H NMR spectrum of **PyMe**.

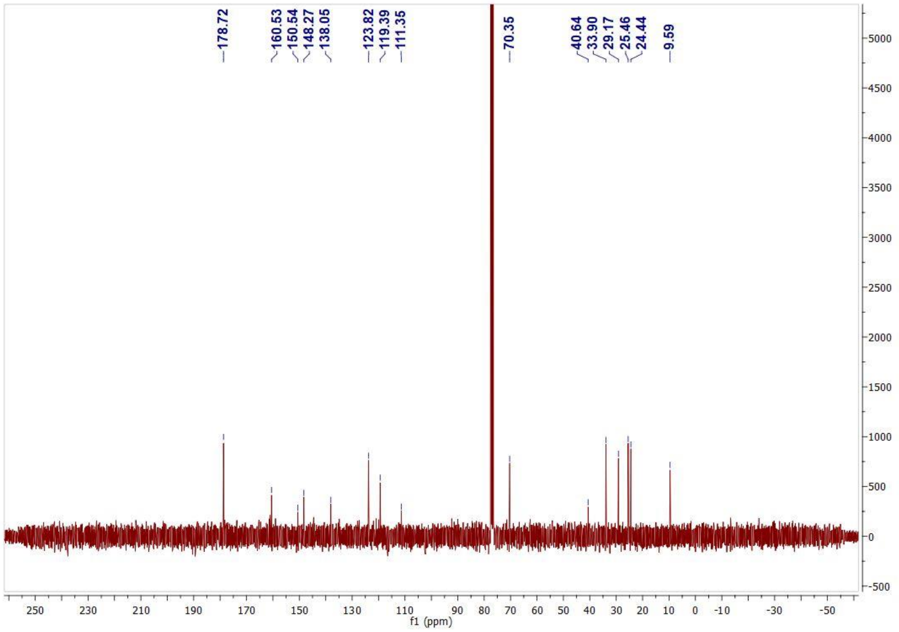

Figure SI 4: ^{13}C NMR spectrum of **PyMe**.

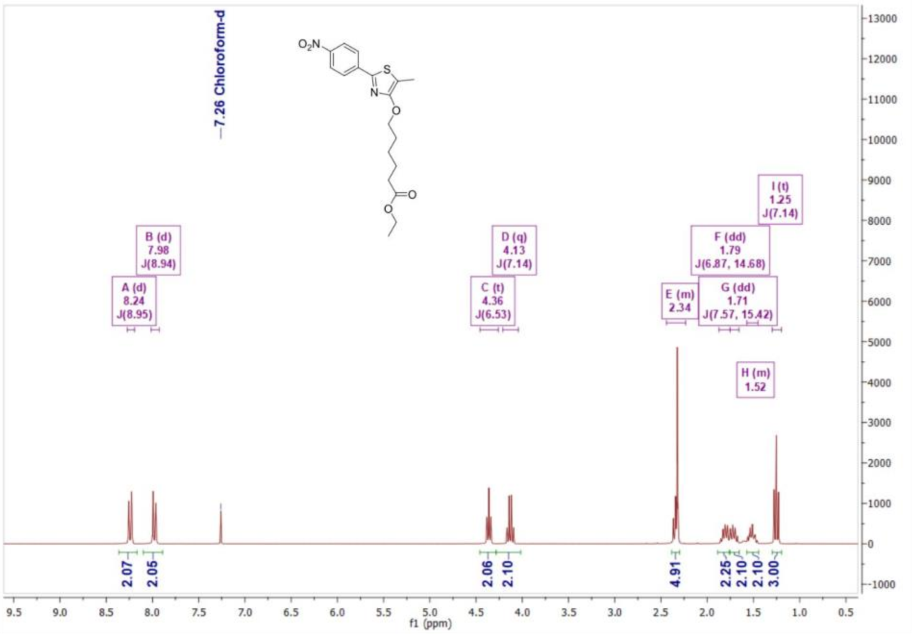

Figure SI 5: ^{1}H NMR spectrum of **4 Ni**.

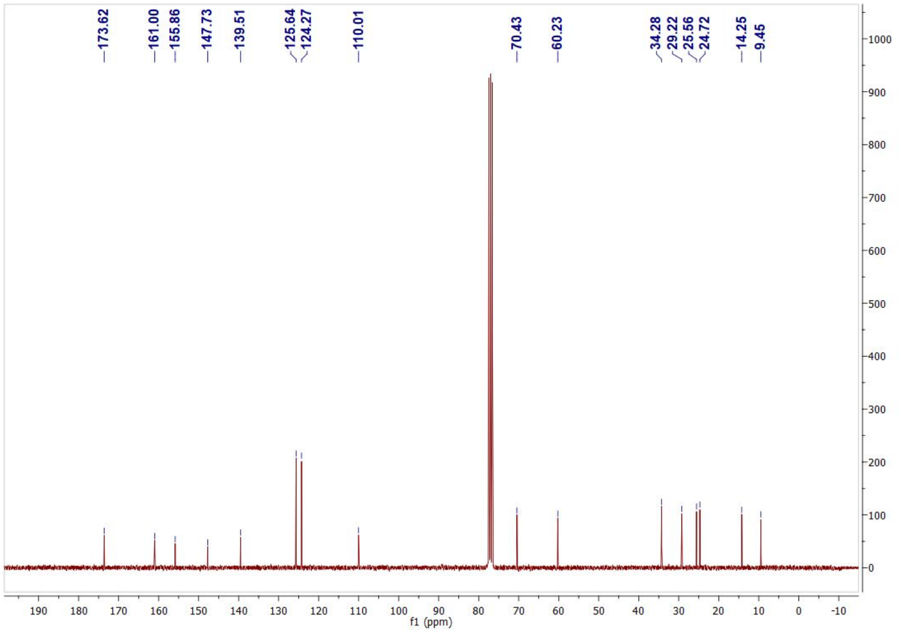

Figure SI 6: ^{13}C NMR spectrum of **4 Ni**.

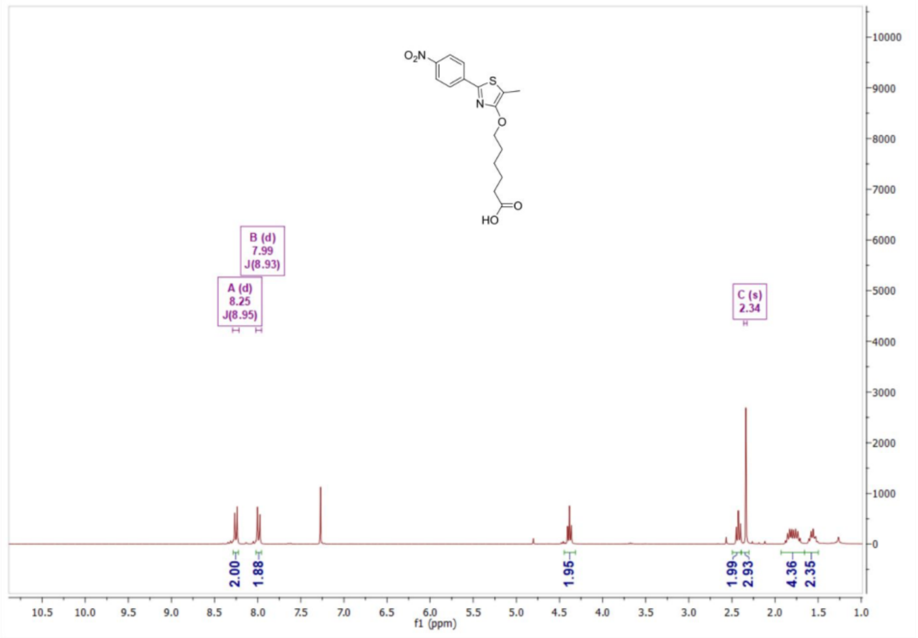

Figure SI 7: ^{1}H NMR spectrum of **NiMe**

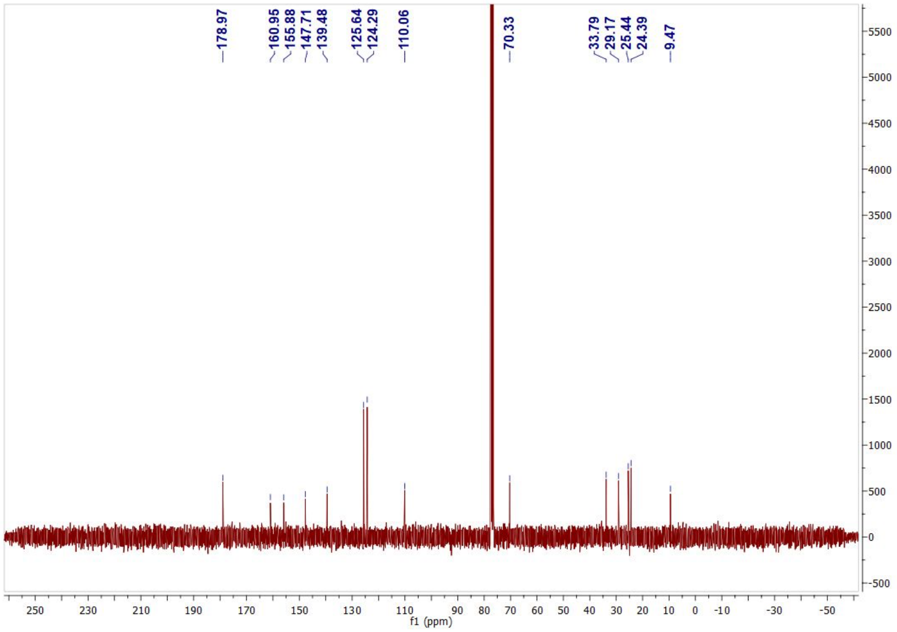

Figure SI 8: ^{13}C NMR spectrum of **NiMe**

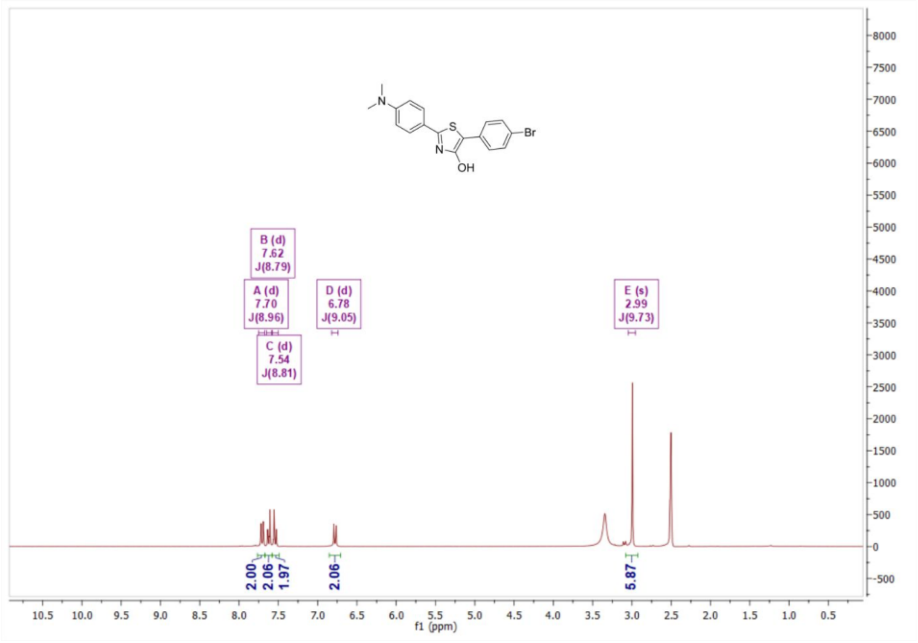

Figure SI 9: ^{1}H NMR spectrum of **7 Am**.

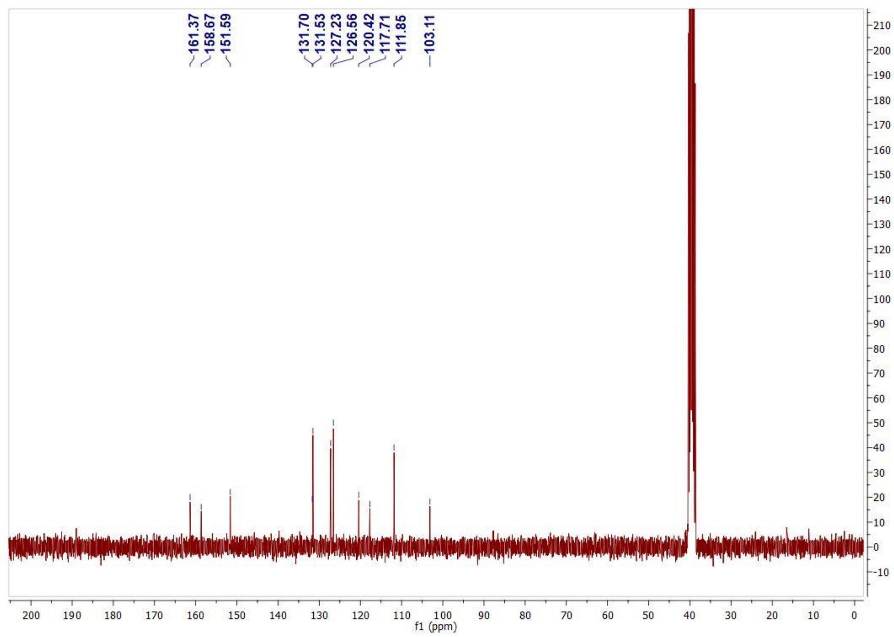

Figure SI 10: ^{13}C NMR spectrum of **7 Am**.

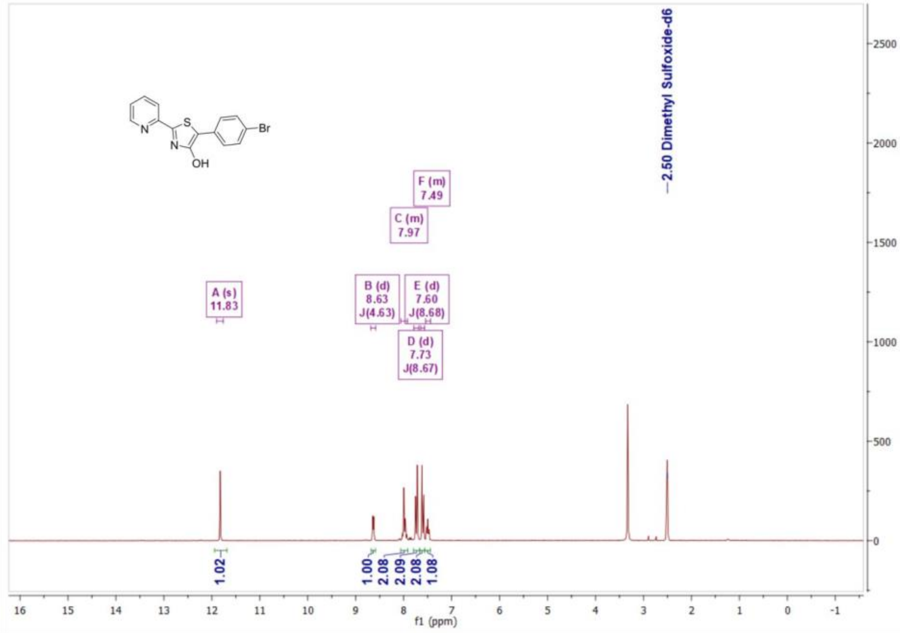

Figure SI 11: ^{1}H NMR spectrum of **7 Py**.

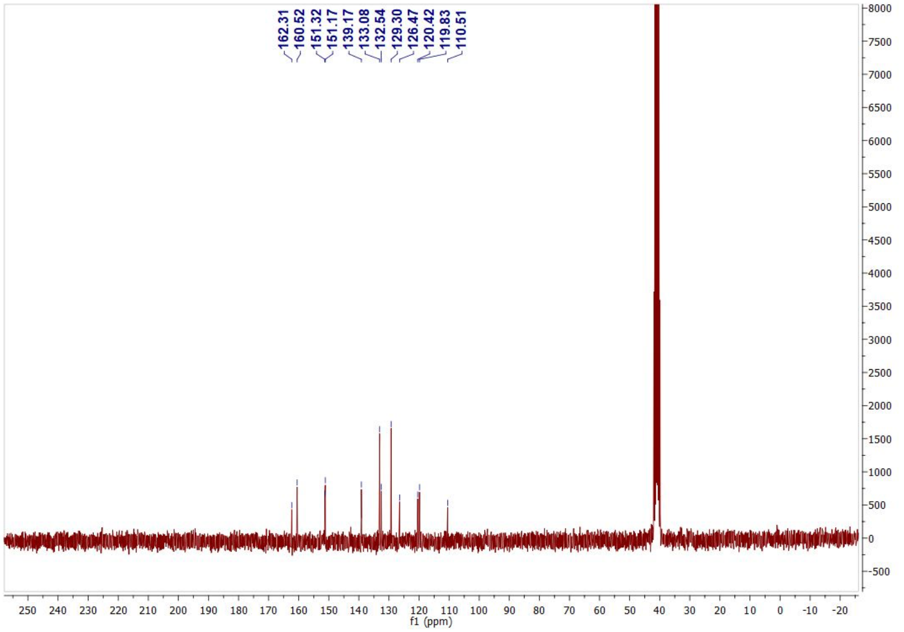

Figure SI 12: ^{13}C NMR spectrum of **7 Py**.

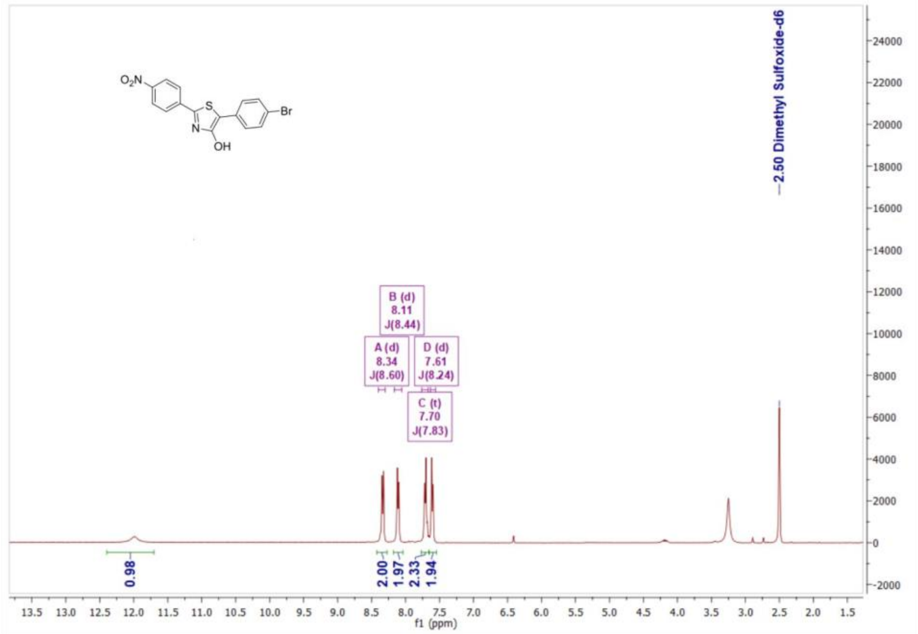

Figure SI 13: ^{1}H NMR spectrum of **7 Ni**.

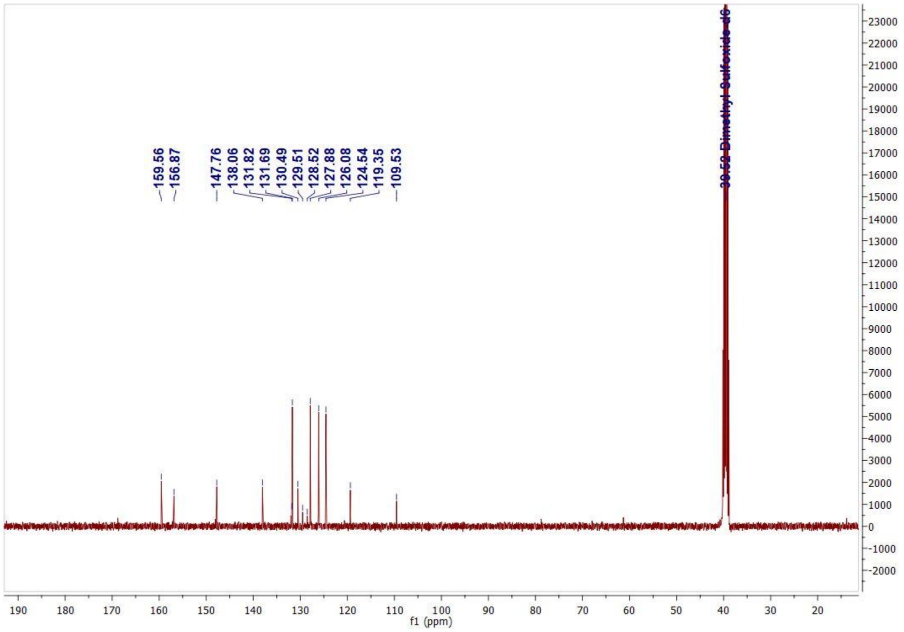

Figure SI 14: ^{13}C NMR spectrum of **7 Ni**.

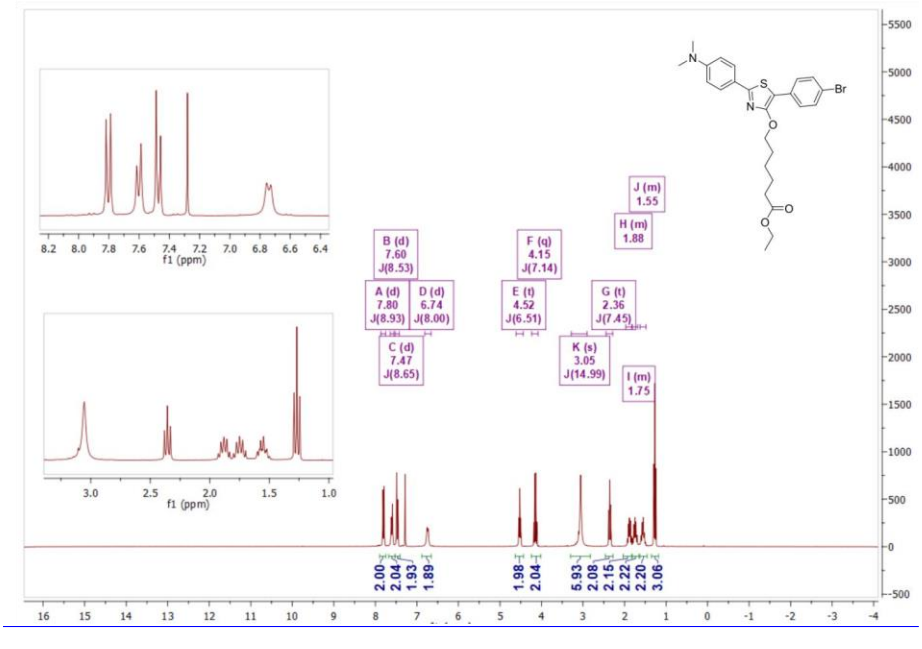

Figure SI 15: ^{1}H NMR spectrum of **8 Am**.

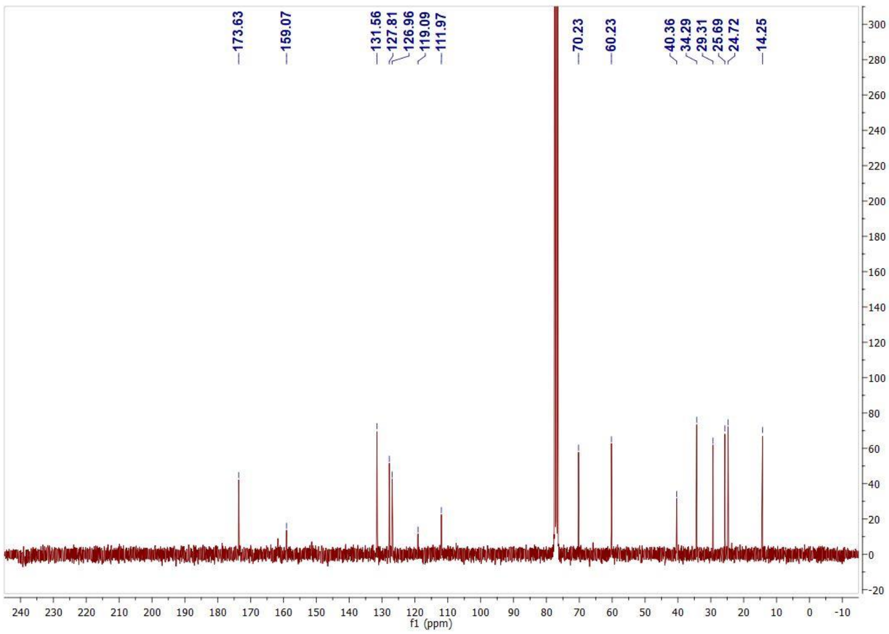

Figure SI 16: ^{13}C NMR spectrum of **8 Am**.

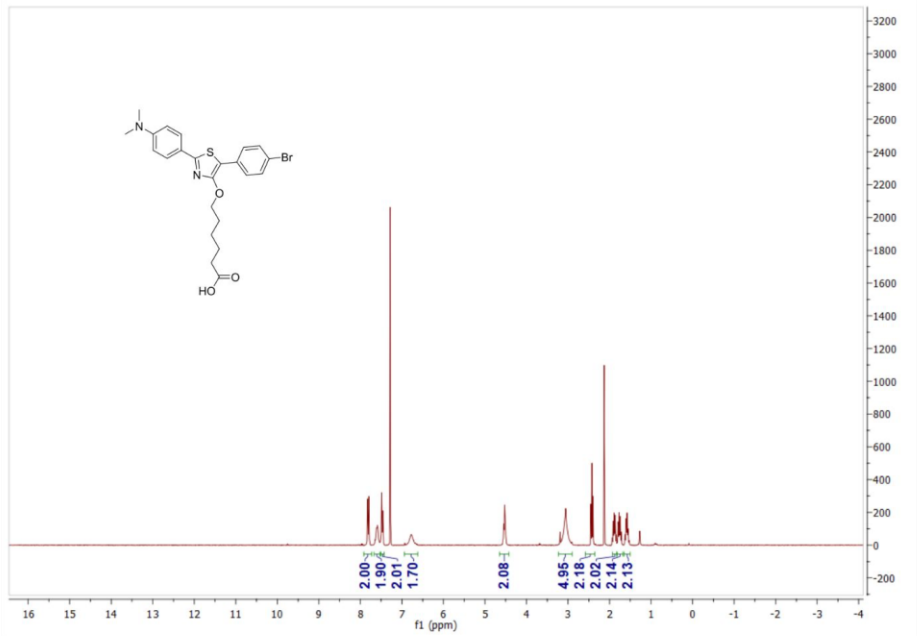

Figure SI 17: ^{13}C NMR spectrum of **AmBr** .

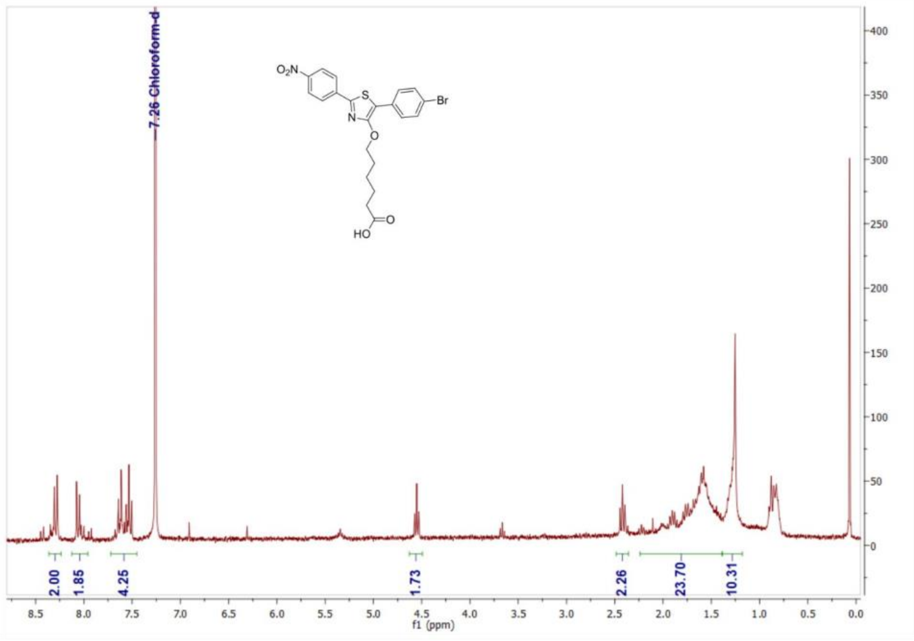

Figure SI 18: ^{1}H NMR spectrum of **NiBr**.

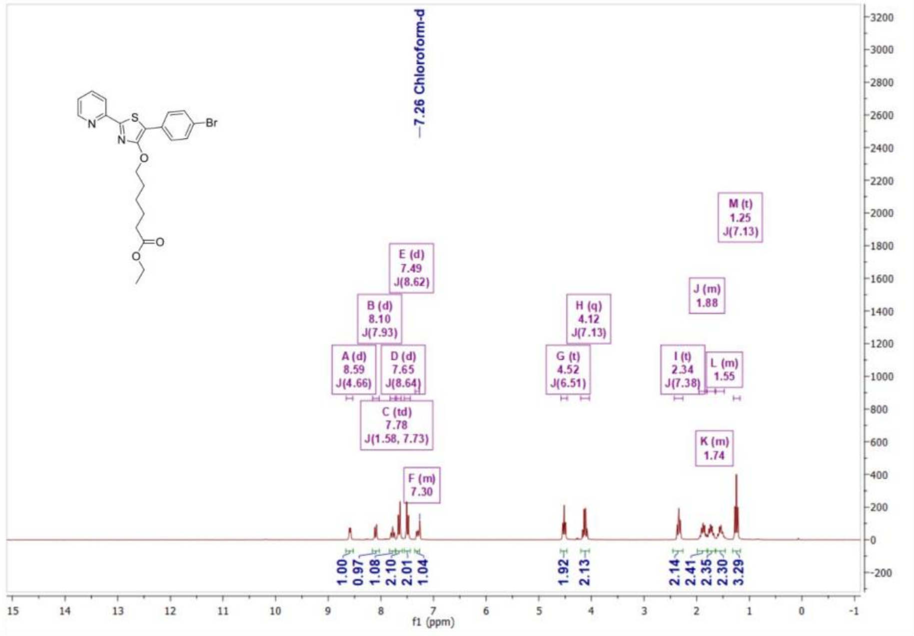

Figure SI 19: ^{1}H NMR spectrum of **8 Py**.

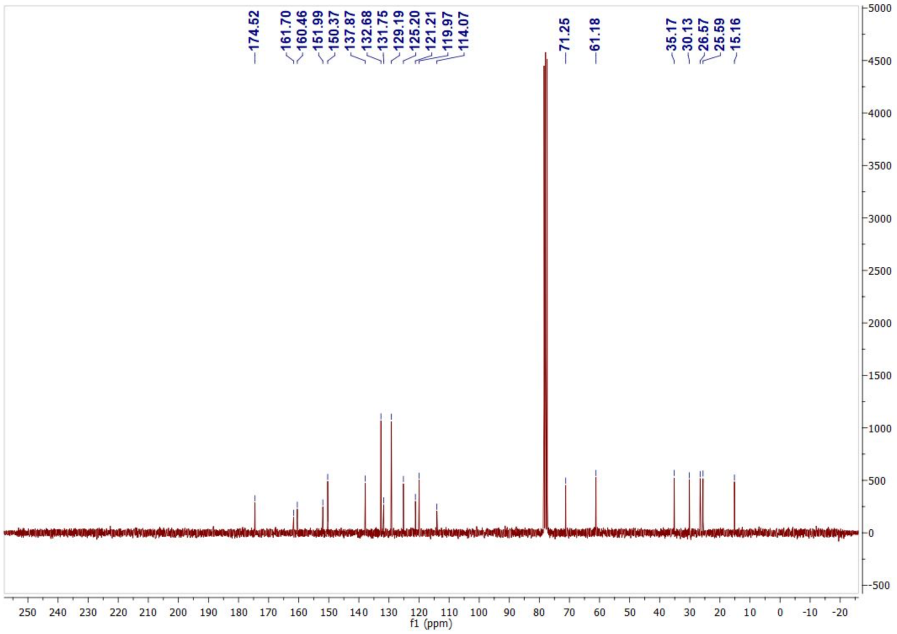

Figure SI 20: ^{13}C NMR spectrum of **8 Py**.

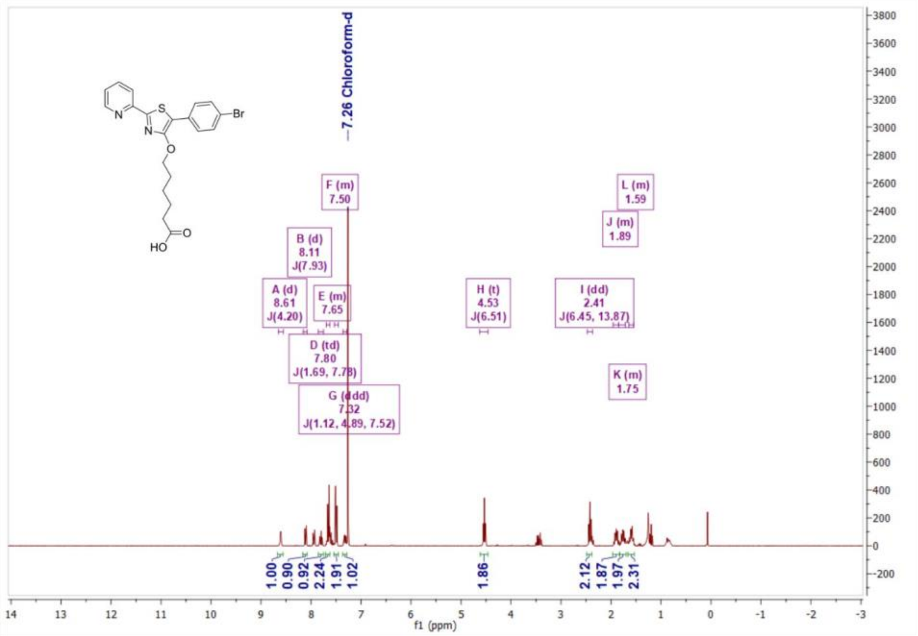

Figure SI 21: ^{1}H NMR spectrum of **PyBr**.

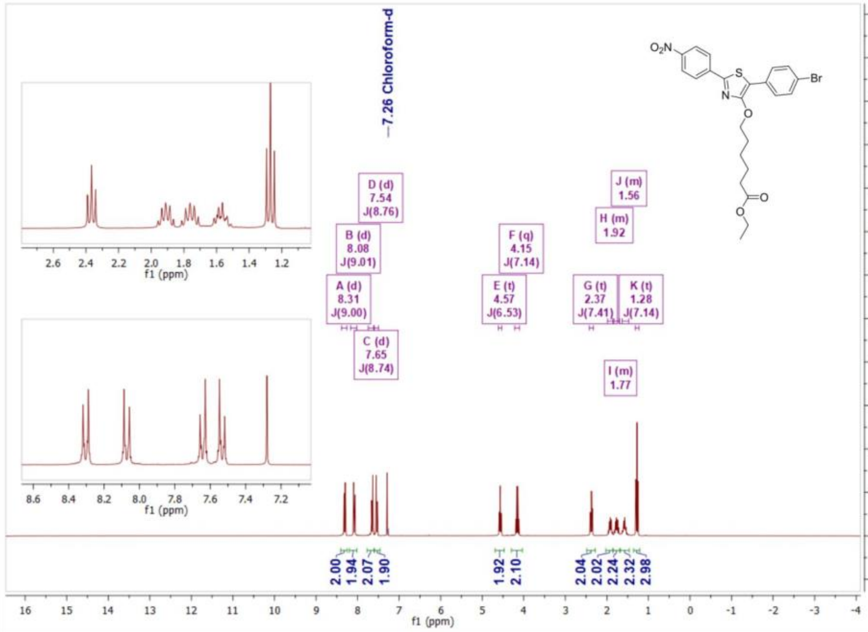

Figure SI 22: ^{1}H NMR spectrum of **8 Ni**.

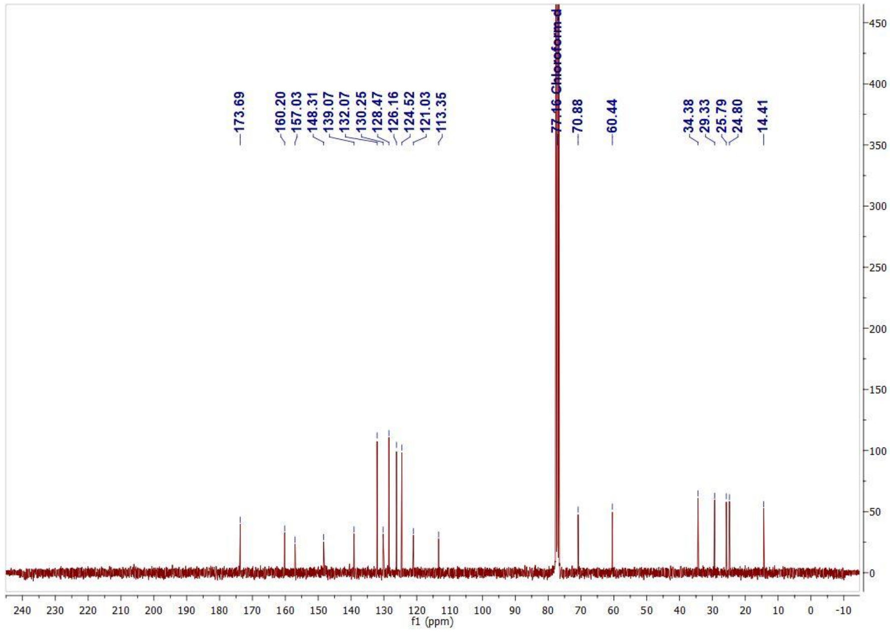

Figure SI 23: ^{13}C NMR spectrum of **8 Ni**.

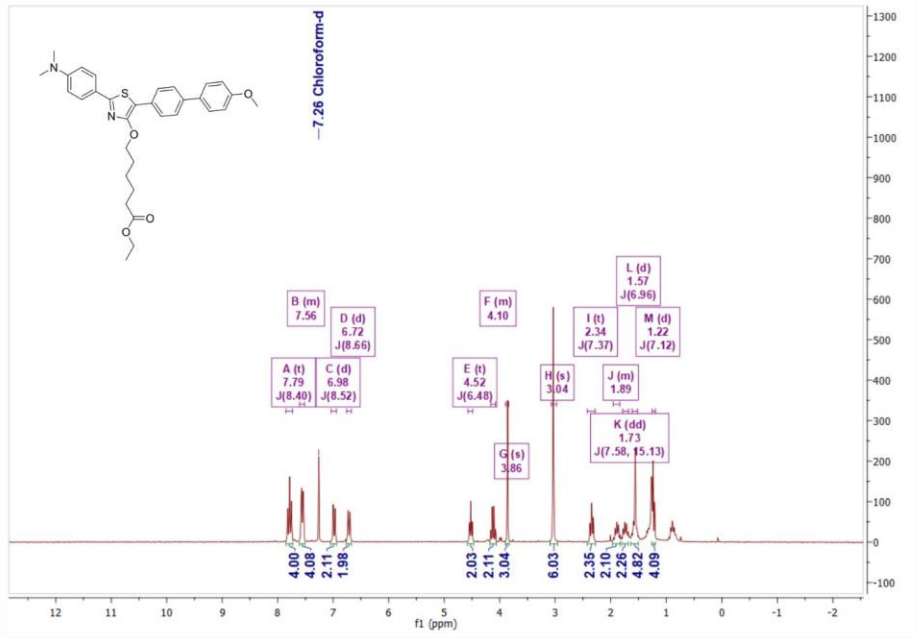

Figure SI 24: ^{1}H NMR spectrum of **9 Am**.

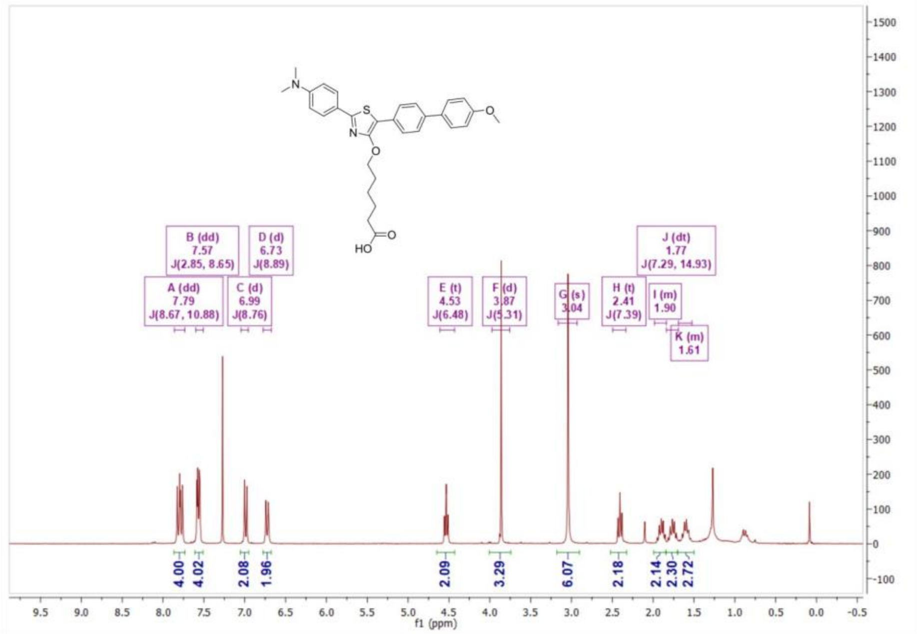

Figure SI 25: ^{1}H NMR spectrum of **AmBi**.

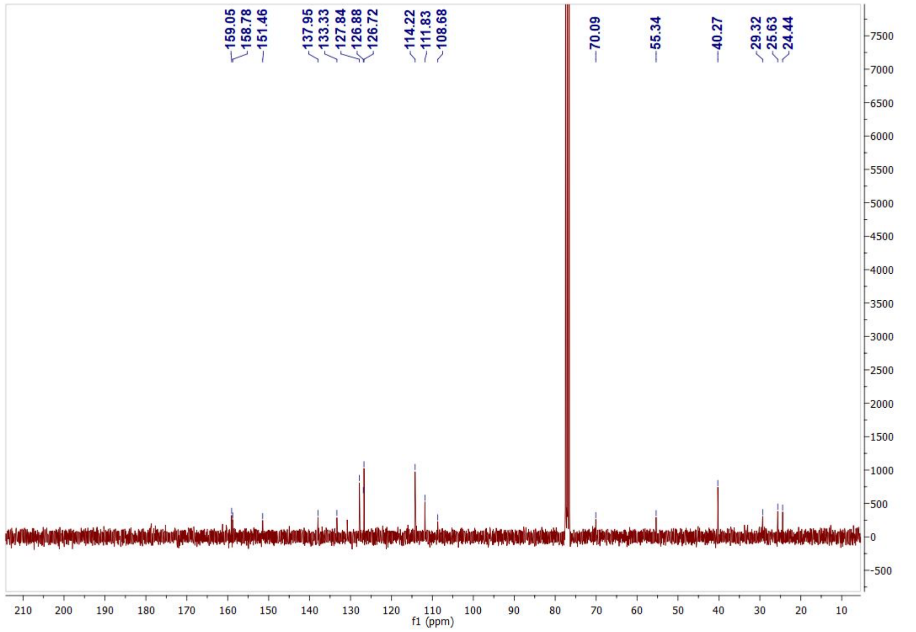

Figure SI 26: ^{13}C NMR spectrum of **AmBi**.

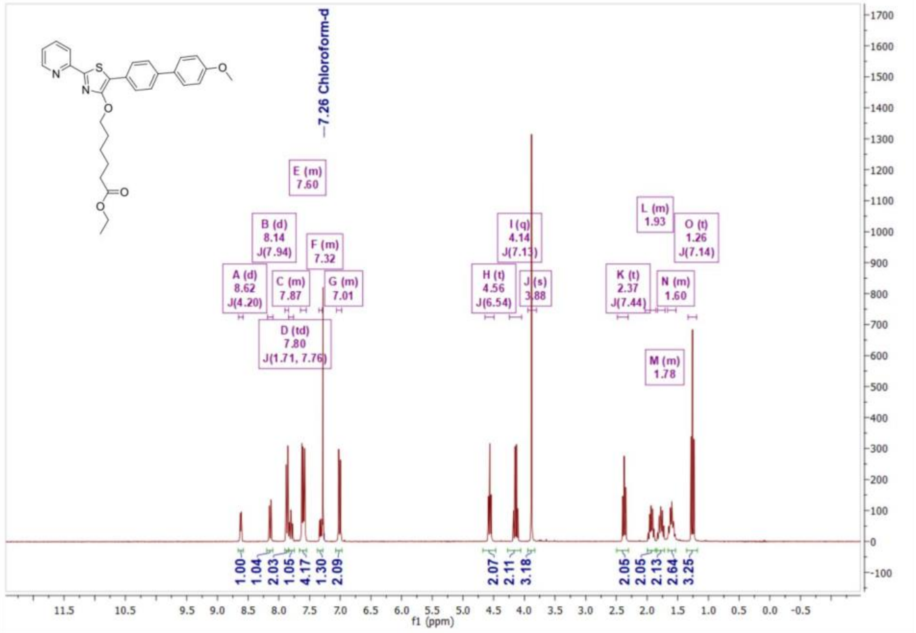

Figure SI 27: ^{1}H NMR spectrum of **9 Py**.

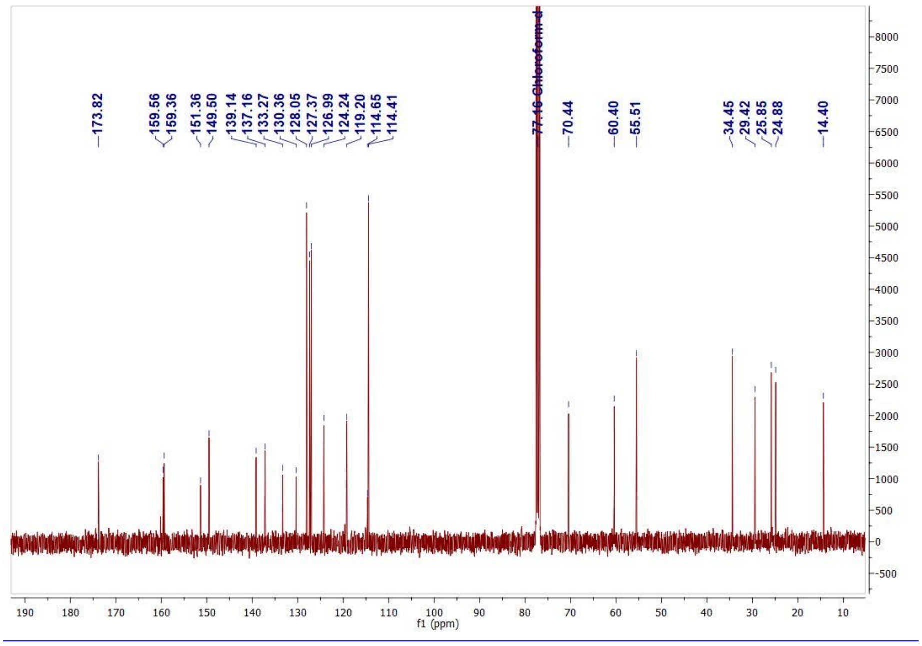

Figure SI 28: ^{13}C NMR spectrum of **9 Py**.

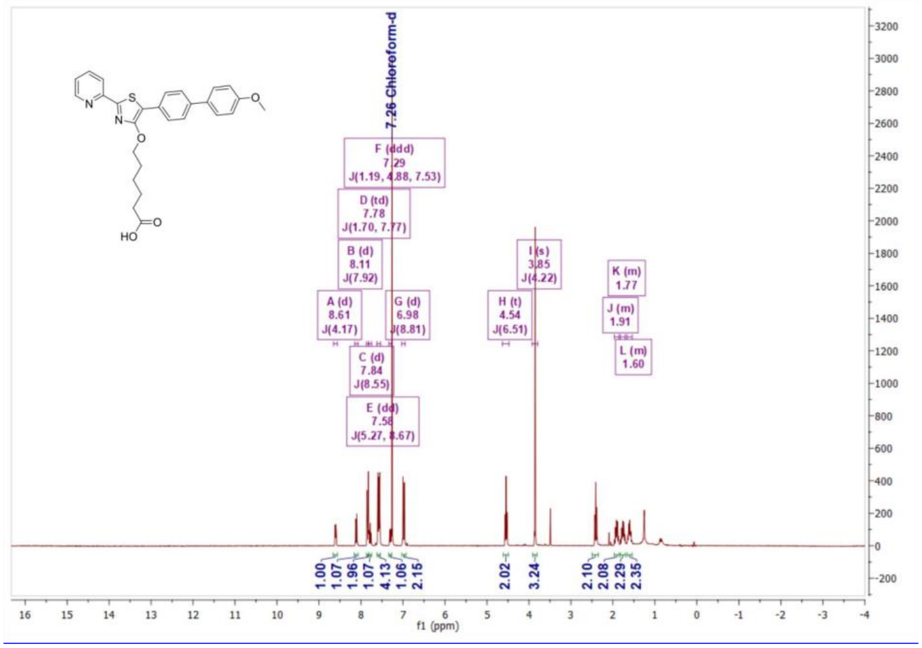

Figure SI 29: ^{13}C NMR spectrum of **PyBi**.

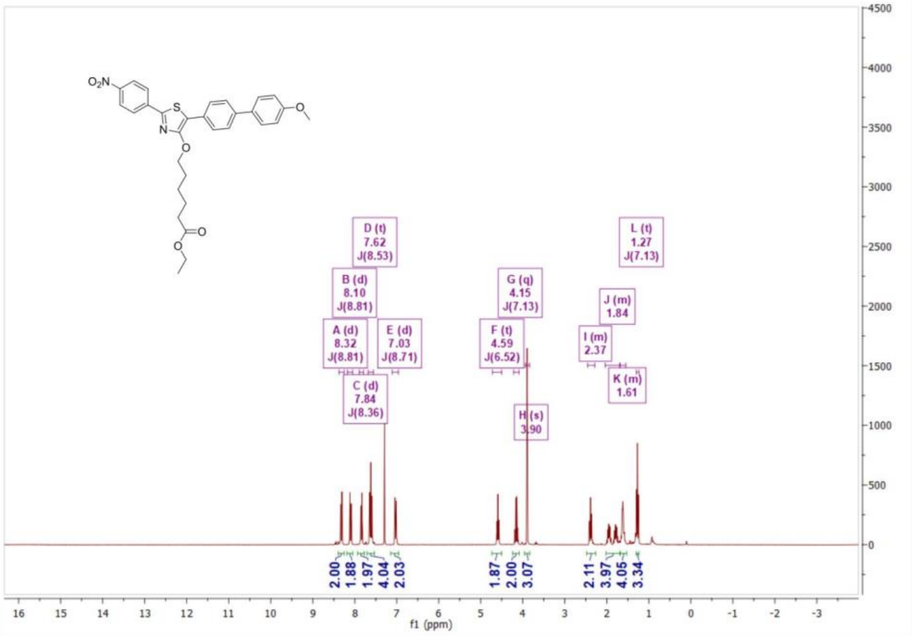

Figure SI 30: ^{1}H NMR spectrum of **9 Ni**.

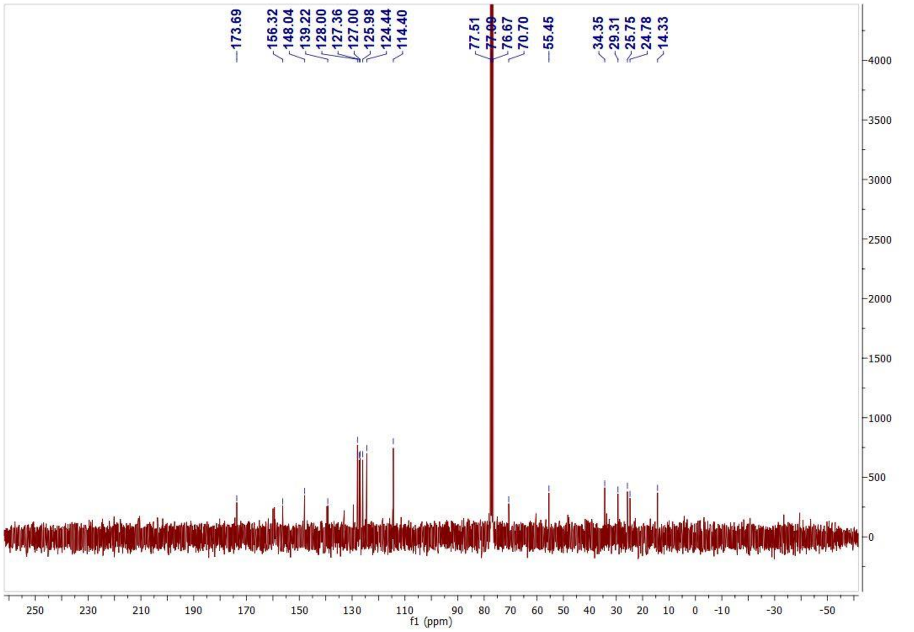

Figure SI 31: ^{13}C NMR spectrum of **9 Ni**.

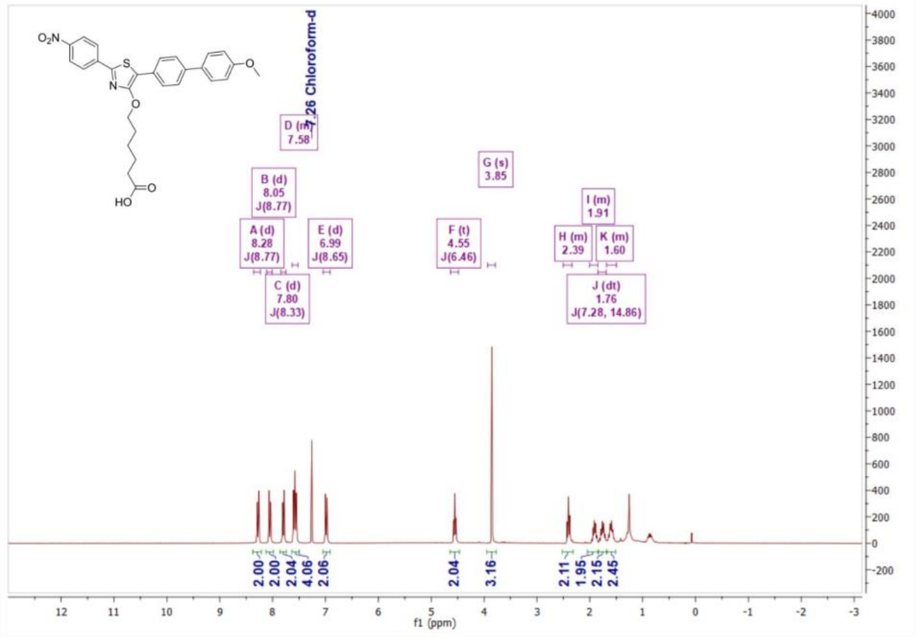

Figure SI 32: ^{1}H NMR spectrum of **NiBi**.

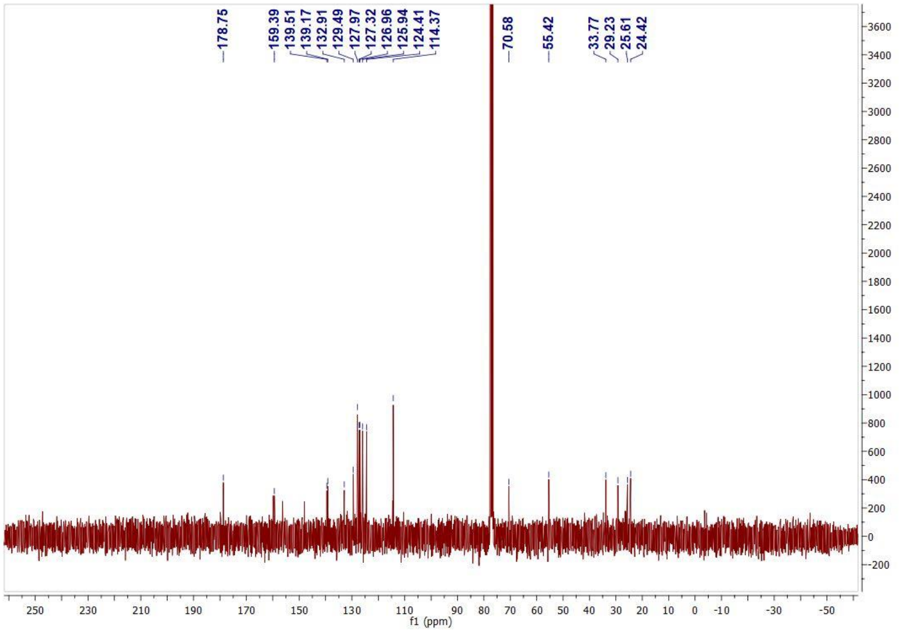

Figure SI 33: ^{13}C NMR spectrum of **NiBi**.

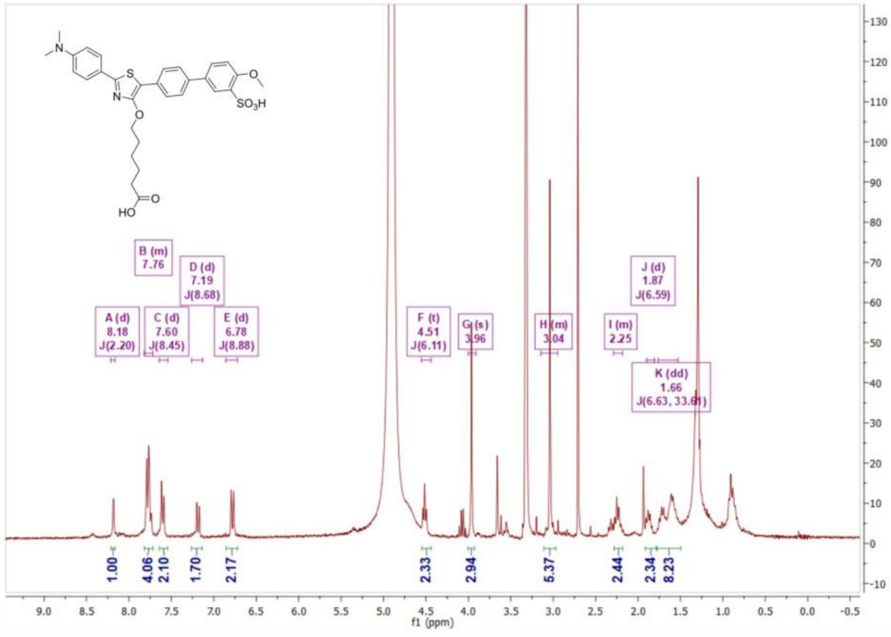

Figure SI 34: ^{1}H NMR spectrum of **AmBiSulf**.

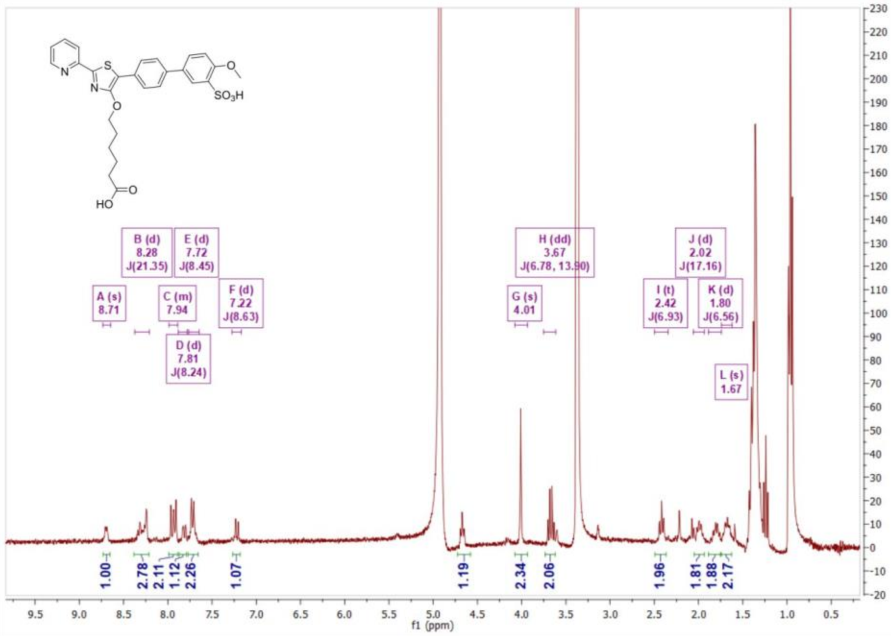

Figure SI 35: ^{1}H NMR spectrum of **PyBiSulf**.

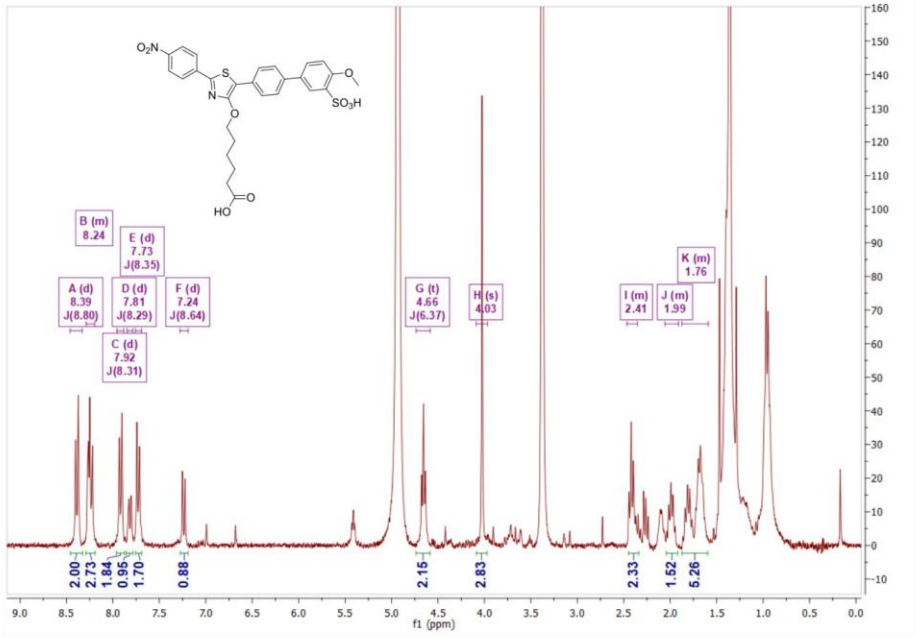

Figure SI 36: ^{1}H NMR spectrum of **NiBiSulf**.

Quantum Chemical Calculations

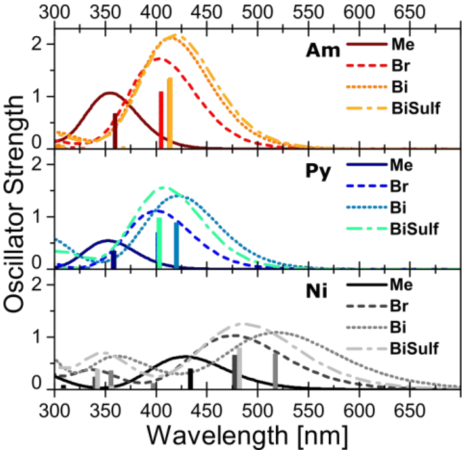

Figure SI 37: TD-DFT calculated (B3LYP, TZVP, vacuum) absorption spectra of **Am** (red), **Py** (blue), **Ni** (black) and the **Me** (solid), **Br** (dotted), **Bi** (dashed) and **BiSulf** (dotted dashed) functionalization.

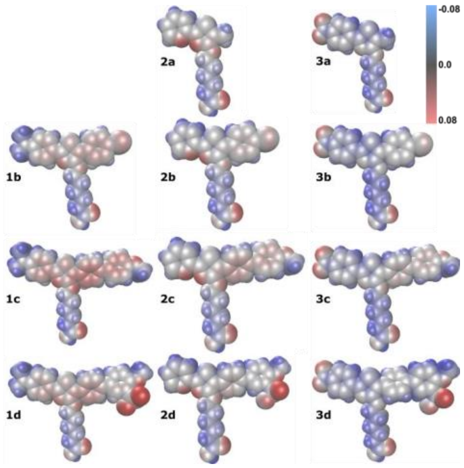

Figure SI 38: Electrostatic potential plotted over the Van-der-Waals surface of the DFT-calculated geometry optimized molecular structures in the COSMO conductor limit

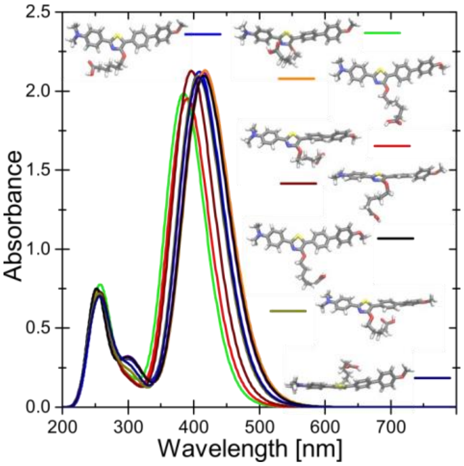

Figure SI 39: TD-DFT calculated (B3LYP, TZVP, vacuum) absorption spectra of **AmBi** with their different conformers

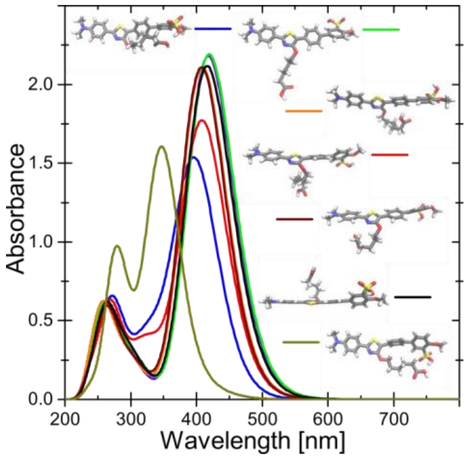

Figure SI 40: TD-DFT calculated (B3LYP, TZVP, vacuum) absorption spectra of **AmBiSulf** with their different conformers

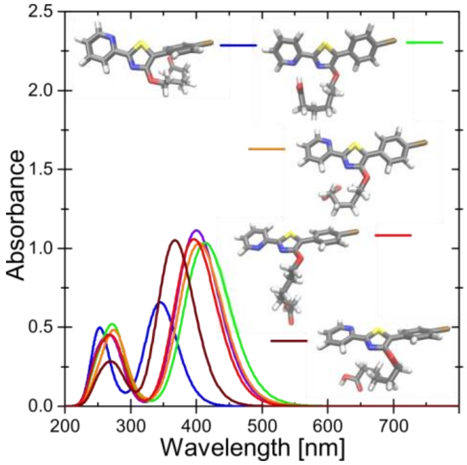

Figure SI 41: TD-DFT calculated (B3LYP, TZVP, vacuum) absorption spectra of **PyBr** with their different conformers

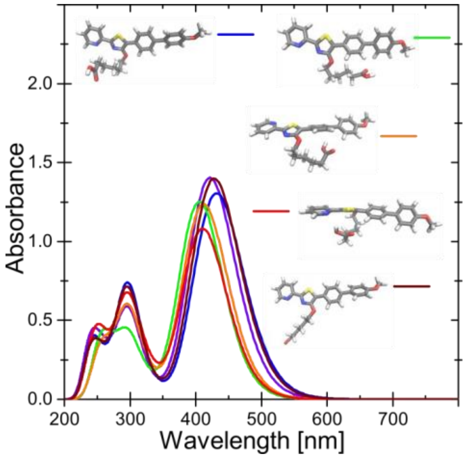

Figure SI 42: TD-DFT calculated (B3LYP, TZVP, vacuum) absorption spectra of **PyBi** with their different conformers

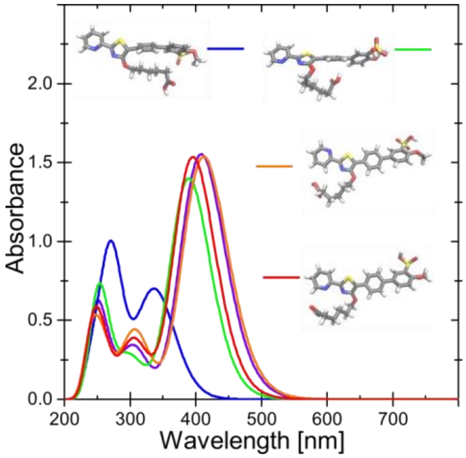

Figure SI 43: TD-DFT calculated (B3LYP, TZVP, vacuum) absorption spectra of **PyBiSulf** with their different conformers

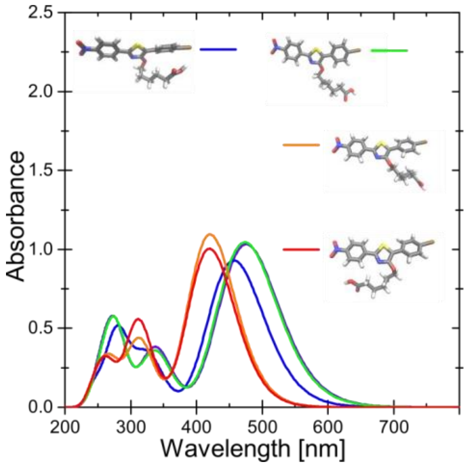

Figure SI 44: TD-DFT calculated (B3LYP, TZVP, vacuum) absorption spectra of **NiBi** with their different conformers

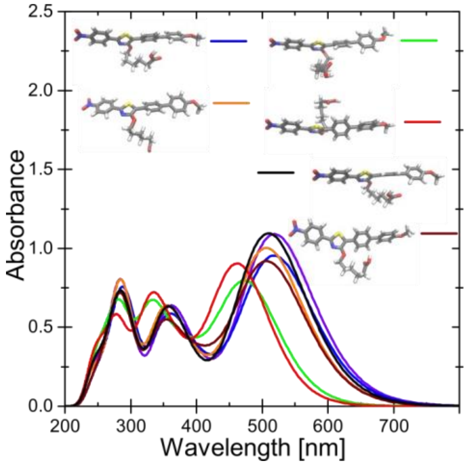

Figure SI 45: TD-DFT calculated (B3LYP, TZVP, vacuum) absorption spectra of **NiBi** with their different conformers

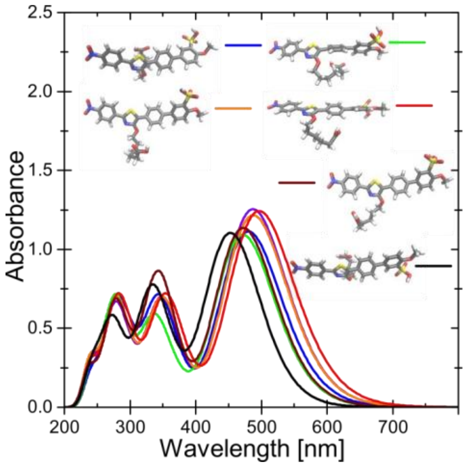

Figure SI 46: TD-DFT calculated (B3LYP, TZVP, vacuum) absorption spectra of **NiBiSulf** with their different conformers

UV-vis Absorption and Fluorescence Spectroscopy

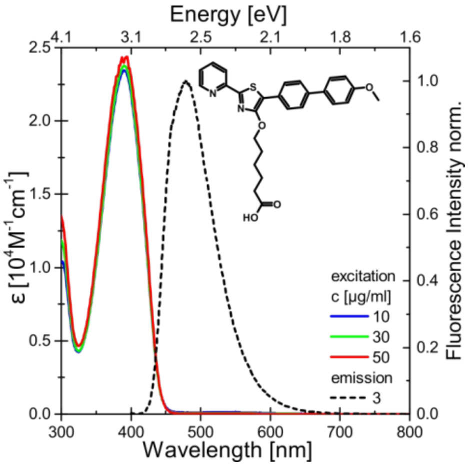

Figure SI 47: Extinction coefficient (ε) (solid line) and normalized emission (dotted line) of **PyBi** in THF

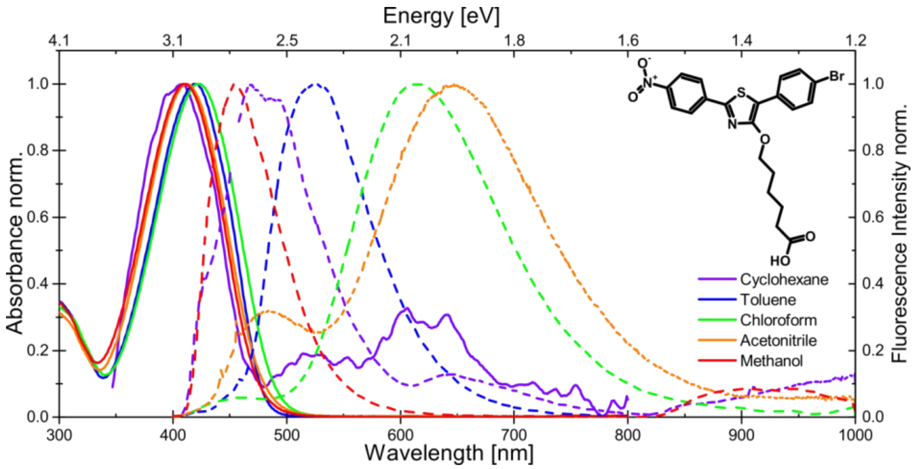

Figure SI 48: Extinction coefficient (ε) (solid line) and normalized emission (dotted line) of **NiBr** (405 nm) in cyclohexane (purple), toluene (blue), chloroform (green), acetonitrile (orange), methanol (red)

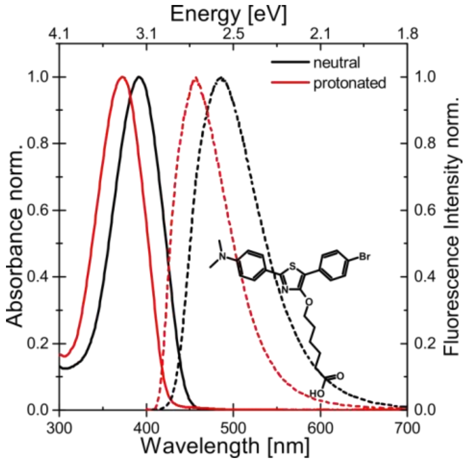

Figure SI 49: Normalized absorption (solid) and emission (dotted) spectra of the neutral (black) and protonated (red) species of **AmBr**.

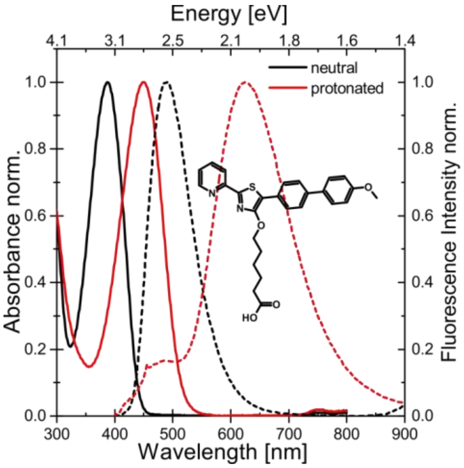

Figure SI 50: Normalized absorption (solid) and emission (dotted) spectra of the neutral (black) and protonated (red) species of **PyBi**.

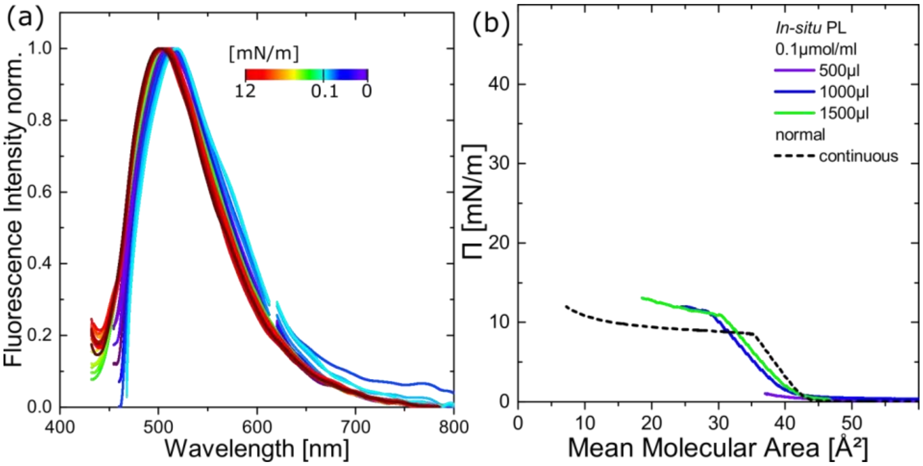

Figure SI 51: Normalized fluorescence spectra of a Langmuir layer at an air-water interface of the **AmBr** (a). Measured (solid) of the in-situ fluorescence measurements and averaged continuous recorded (dotted) mean value Π(A)-isotherm (b)

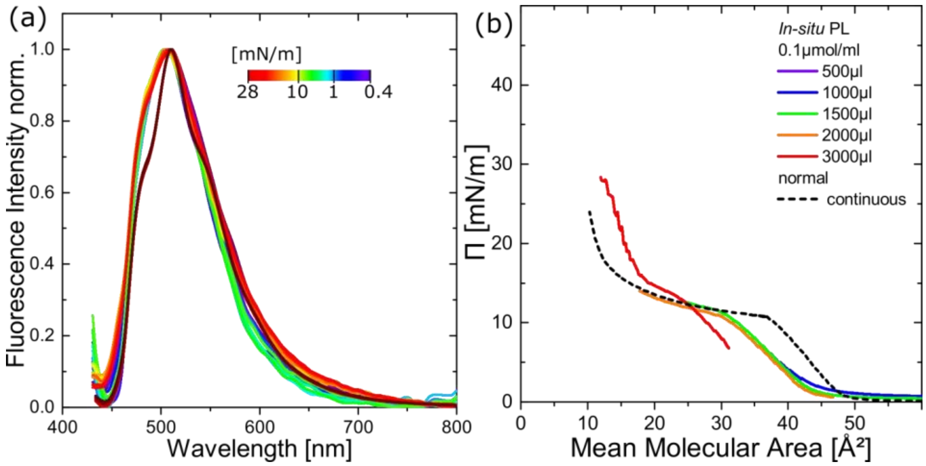

Figure SI 52: Normalized fluorescence spectra of a Langmuir layer at an air-water interface of the **AmBi** (a). Measured (solid) of the in-situ fluorescence measurements and averaged continuous recorded (dotted) mean value Π(A)-isotherm (b)

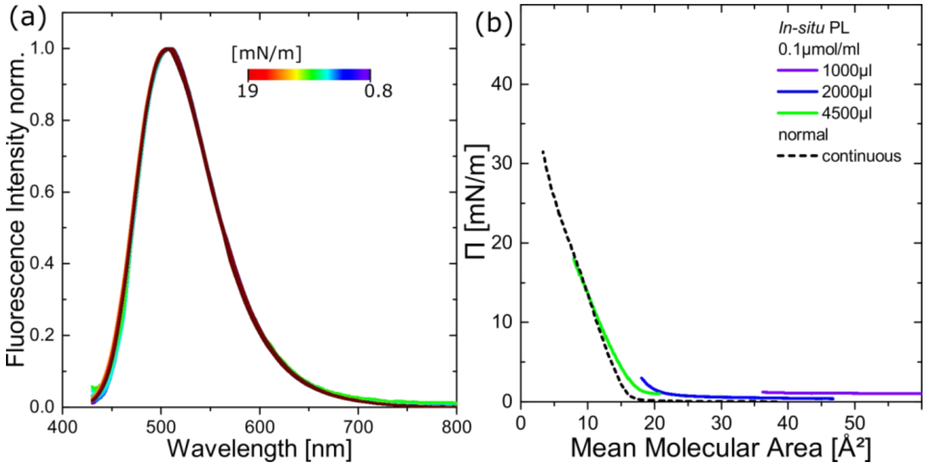

Figure SI 53: Normalized fluorescence spectra of a Langmuir layer at an air-water interface of the **AmBiSulf** (a). Measured (solid) of the in-situ fluorescence measurements and averaged continuous recorded (dotted) mean value Π(A)-isotherm (b)

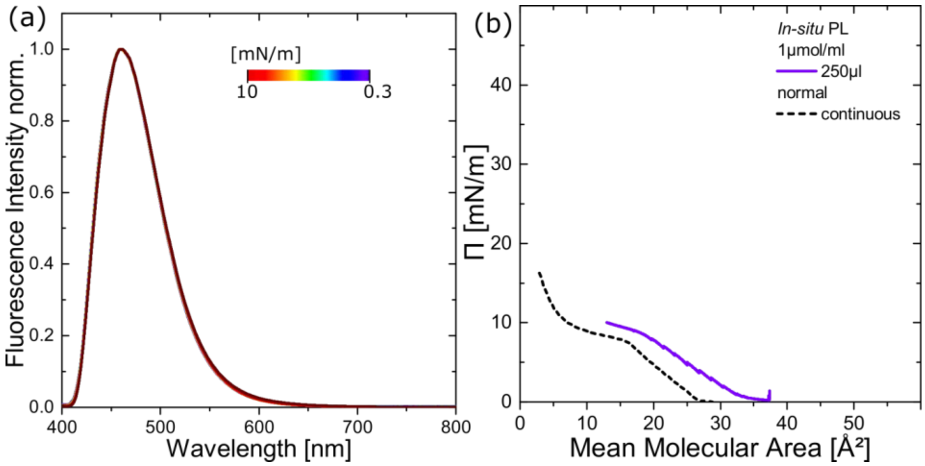

Figure SI 54: Normalized fluorescence spectra of a Langmuir layer at an air-water interface of the **PyBr** (a). Measured (solid) of the in-situ fluorescence measurements and averaged continuous recorded (dotted) mean value Π(A)-isotherm (b)

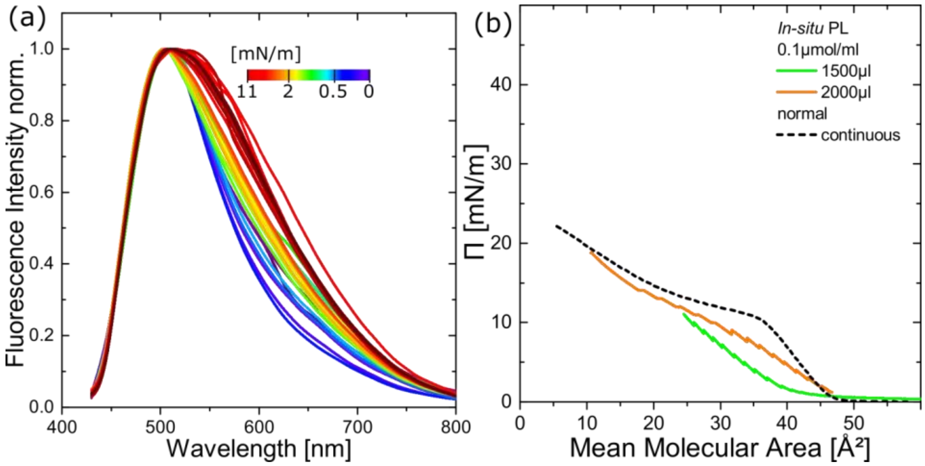

Figure SI 55: Normalized fluorescence spectra of a Langmuir layer at an air-water interface of the **PyBi** (a). Measured (solid) of the in-situ fluorescence measurements and averaged continuous recorded (dotted) mean value Π(A)-isotherm (b)

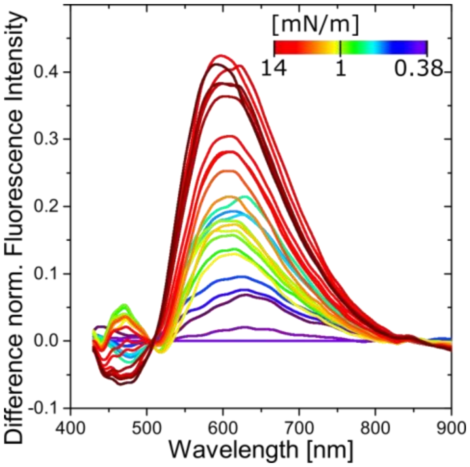

Figure SI 56: Difference spectra of the Langmuir layer at an air-water interface (solid line) **PyBi**

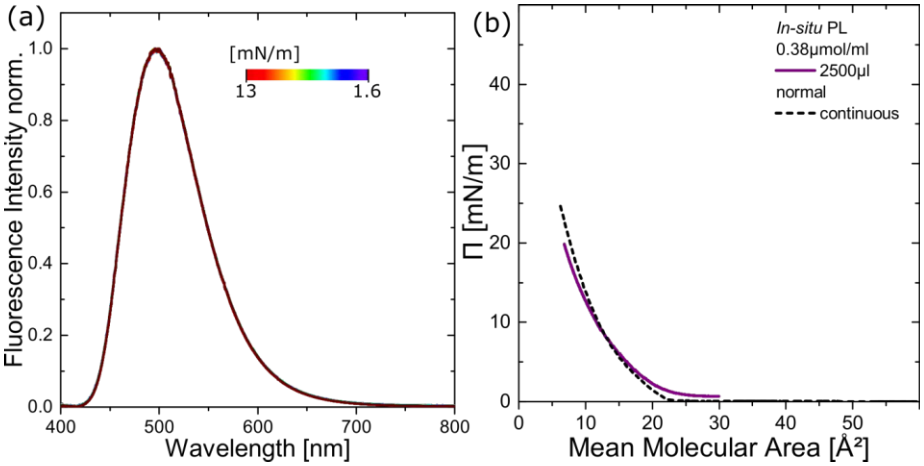

Figure SI 57: Normalized fluorescence spectra of a Langmuir layer at an air-water interface of the **PyBiSulf** (a). Measured (solid) of the in-situ fluorescence measurements and averaged continuous recorded (dotted) mean value Π(A)-isotherm (b)

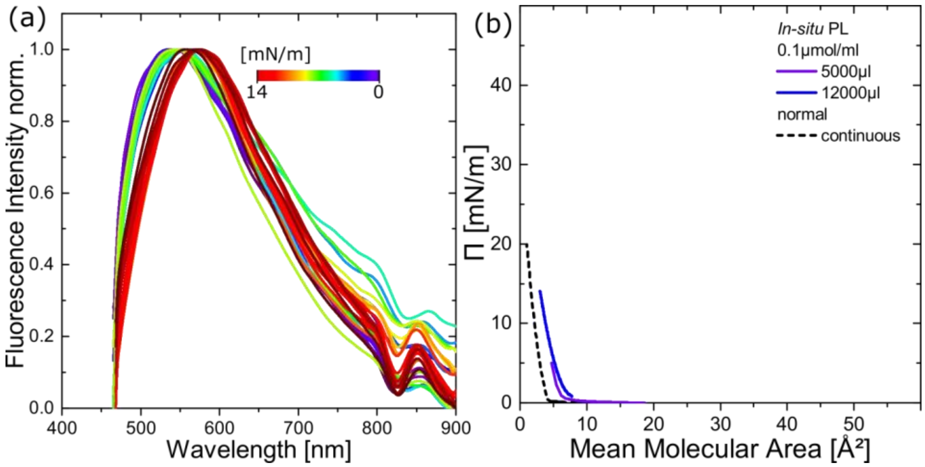

Figure SI 58: Normalized fluorescence spectra of a Langmuir layer at an air-water interface of the **NiMe** (a). Measured (solid) of the in-situ fluorescence measurements and averaged continuous recorded (dotted) mean value Π(A)-isotherm (b)

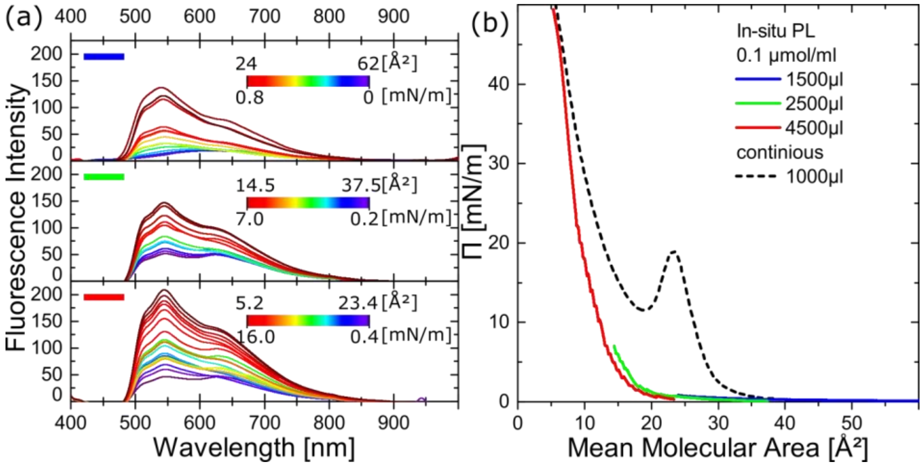

Figure SI 59: Normalized fluorescence spectra of a Langmuir layer at an air-water interface of the **NiBr** (a). Measured (solid) of the in-situ fluorescence measurements and averaged continuous recorded (dotted) mean value Π(A)-isotherm (b)

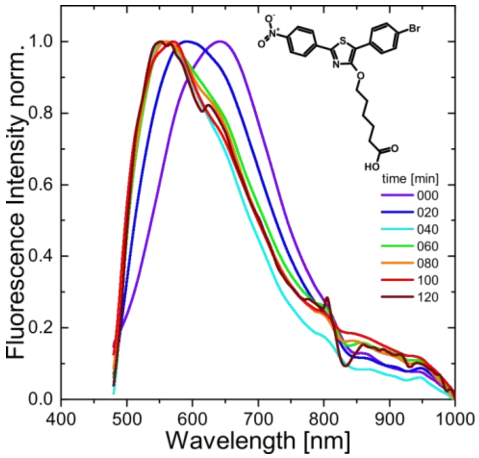

Figure SI 60: Normalized emission spectra a Langmuir layer at an air-water interface with time (solid line) of **NiBr**.

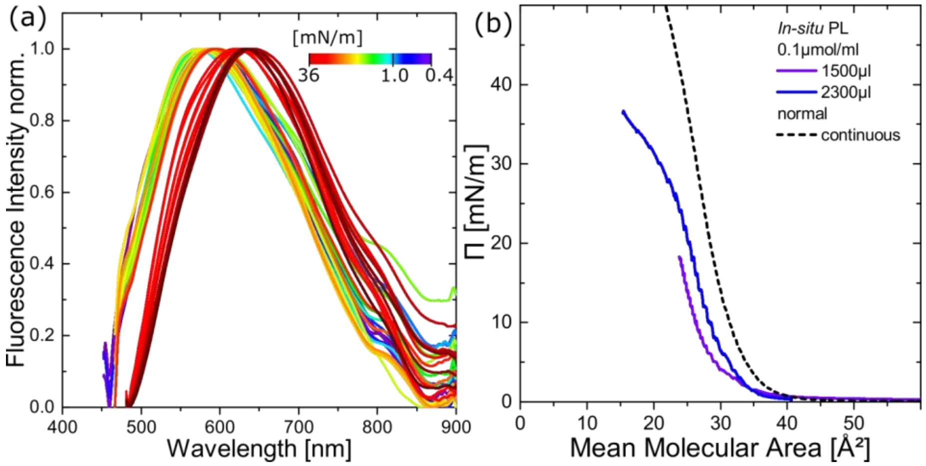

Figure SI 61: Normalized fluorescence spectra of a Langmuir layer at an air-water interface of the **NiBi** (a). Measured (solid) of the in-situ fluorescence measurements and averaged continuous recorded (dotted) mean value Π(A)-isotherm (b)

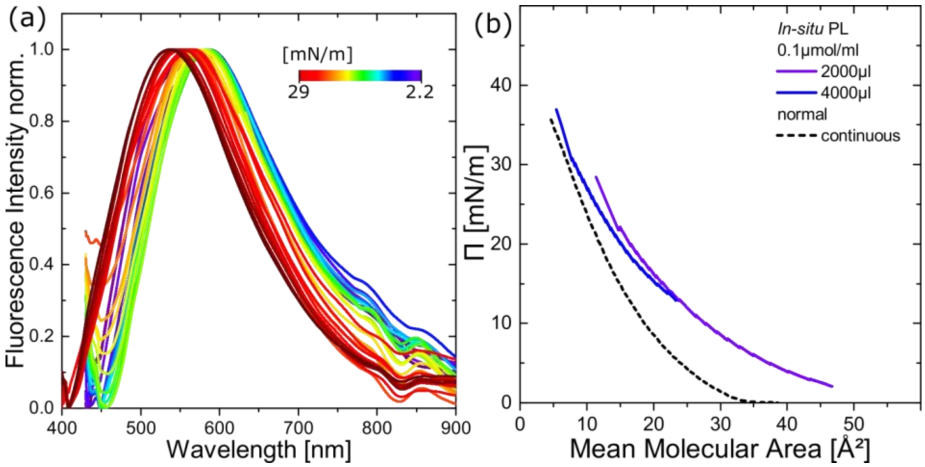

Figure SI 62: Normalized fluorescence spectra of a Langmuir layer at an air-water interface of the **NiBiSulf** (a). Measured (solid) of the in-situ fluorescence measurements and averaged continuous recorded (dotted) mean value Π(A)-isotherm (b)

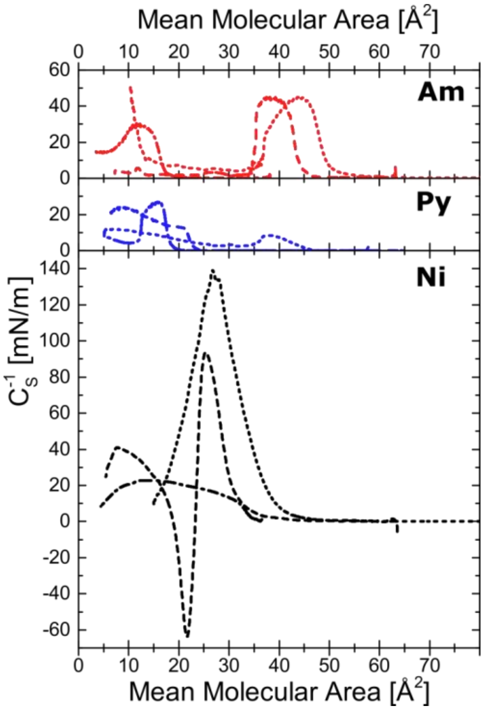

Figure SI 63: Compressibility modulus $C_S^{-1} = -A\, d\Pi/dA$ of (**Am**) 2-4-N,N-dimethylaminophenyl-; (**Py**) 2-2-pyridyl; (**Ni**) 2-4-nitrophenyl-4-hydroxy-5-Y-1,3 thiazoles and the methyl (**Me**, solid), phenyl-4-bromo (**Br**, dotted), phenyl-4-methoxyphenyl (**Bi**, dashed) and 3-phenyl-4-methoxyphenyl-3-sulfonylphenyl (**BiSulf**, dotted dashed) functionalization.

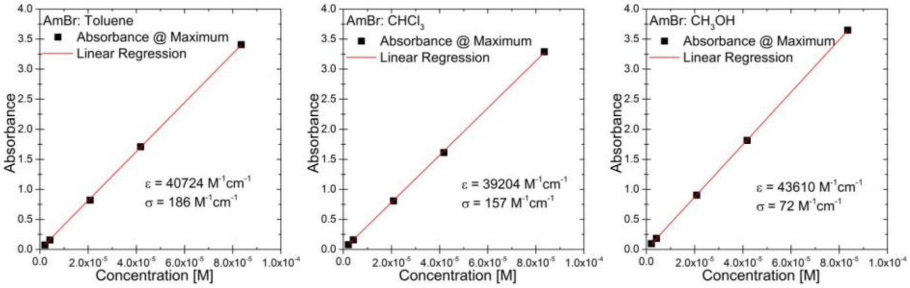

Figure SI 64: Extinction coefficients (ε(λ_{max})) (determined *via* linear regression for **AmBr** in Toluene, CHCl$_3$ and CH$_3$OH

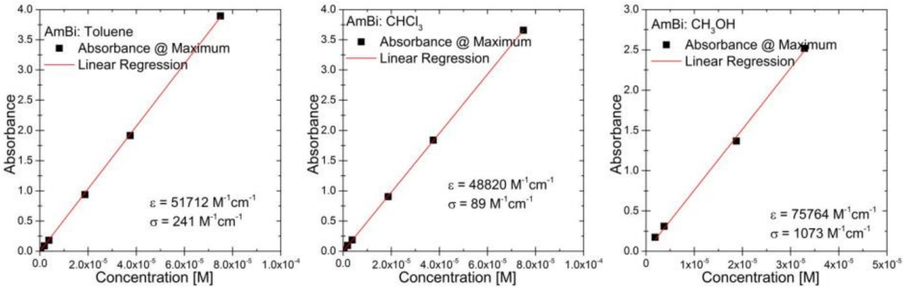

Figure SI 65: Extinction coefficients (ε(λ_{max})) (determined *via* linear regression for **AmBi** in Toluene, CHCl$_3$ and CH$_3$OH

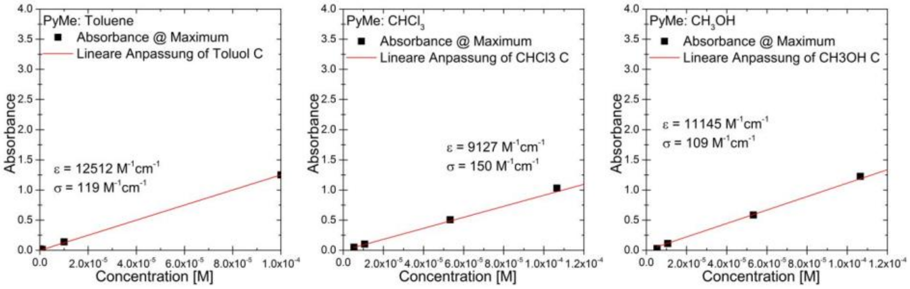

Figure SI 66: Extinction coefficients (ε(λ_{max})) (determined *via* linear regression for **PyMe** in Toluene, CHCl$_3$ and CH$_3$OH

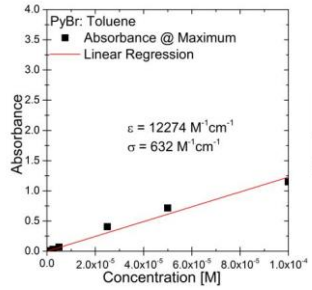

Figure SI 67: Extinction coefficients (ε(λ_{max})) (determined *via* linear regression for **PyBr** in Toluene, $CHCl_3$ and CH_3OH

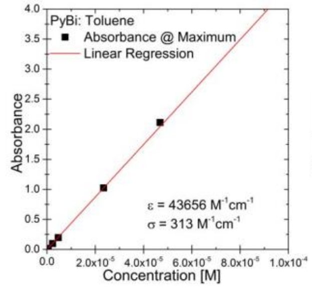

Figure SI 68: Extinction coefficients (ε(λ_{max})) (determined *via* linear regression for **PyBi** in Toluene, $CHCl_3$ and CH_3OH

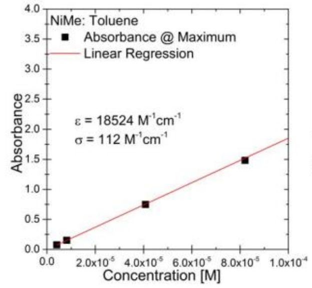

Figure SI 69: Extinction coefficients (ε(λ_{max})) (determined *via* linear regression for **NiMe** in Toluene, $CHCl_3$ and CH_3OH

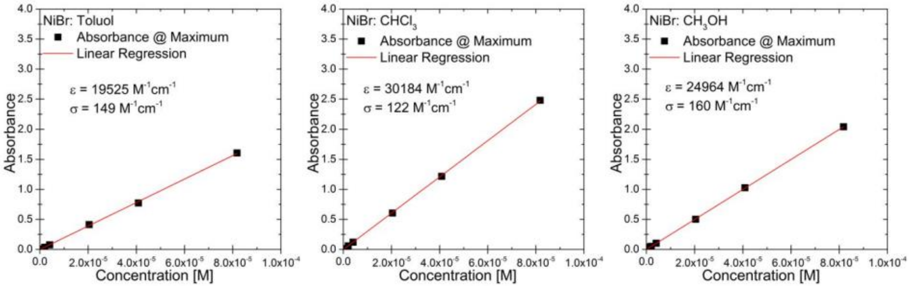

Figure SI 70: Extinction coefficients ($\varepsilon(\lambda_{max})$) (determined *via* linear regression for **NiBr** in Toluene, $CHCl_3$ and CH_3OH

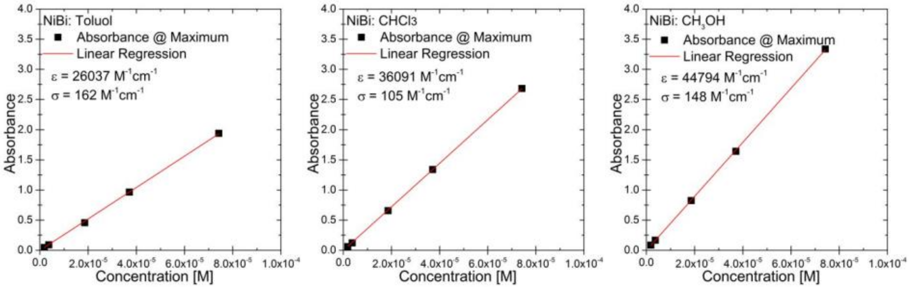

Figure SI 71: Extinction coefficients ($\varepsilon(\lambda_{max})$) (determined *via* linear regression for **NiBr** in Toluene, $CHCl_3$ and CH_3OH

[MLH2] Introducing double polar heads to highly fluorescent Thiazoles: Influence on supramolecular structures and photonic properties

Kaufmann, M.; Hupfer, M. L.; Sachse, T.; Herrmann-Westendorf, F.; Weiß, D.; Dietzek, B.; Beckert,R.; Presselt, M., Journal of Colloids and Interface Science, **2018**, 526:410-418.

Autor	1	2	3	4	5	6	7	8
Konzeption	x	x					x	x
Planung der Untersuchung	x	x						x
Datenerhebung	x	x	x	x				
Analyse und Interpretation	x	x	x					x
Schreiben des Manuskriptes	x	x				x		x
Publikationsäquivalente	0.5	0.5	n. a.	n. a.	n. a.	n. a.	n. a.	n. a.

Journal of Colloid and Interface Science 526 (2018) 410–418

Contents lists available at ScienceDirect

Journal of Colloid and Interface Science

journal homepage: www.elsevier.com/locate/jcis

Regular Article

Introducing double polar heads to highly fluorescent Thiazoles: Influence on supramolecular structures and photonic properties

M. Kaufmann [a,b], M.L. Hupfer [b], T. Sachse [b,c], F. Herrmann-Westendorf [b], D. Weiß [a], B. Dietzek [b,c], R. Beckert [a,*], M. Presselt [b,c,d,e,*]

[a] Institute of Organic and Macromolecular Chemistry, Friedrich Schiller University Jena, Humboldtstraße 10, Jena 07743, Germany
[b] Institute of Physical Chemistry, Friedrich Schiller University Jena, Helmholtzweg 4, 07743 Jena, Germany
[c] Leibniz Institute of Photonic Technology (IPHT), Albert-Einstein-Str. 9, 07745 Jena, Germany
[d] Center for Energy and Environmental Chemistry Jena (CEEC Jena), Friedrich Schiller University Jena, Philosophenweg 7a, 07743 Jena, Germany
[e] SciClus GmbH & Co. KG, Moritz-von-Rohr Str. 1a, 07745 Jena, Germany

GRAPHICAL ABSTRACT

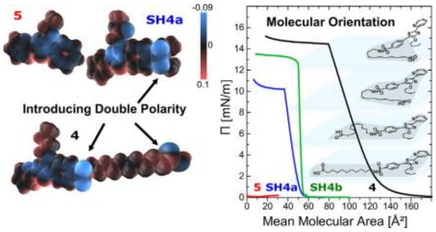

ARTICLE INFO

Article history:
Received 21 March 2018
Revised 27 April 2018
Accepted 27 April 2018
Available online 30 April 2018

Keywords:
Thiazole
Fluorophore
Self-assembly
Molecular orientation
Langmuir Blodgett technique

ABSTRACT

Hypothesis: Supramolecular structures determine properties of optoelectronically active materials and can be tailored *via* the Langmuir-Blodgett (LB) technique. Interactions between dyes can cause high crystallinities of Langmuir monolayers, thus rendering retaining their integrity during the LB-deposition challenging. However, increasing degrees of freedom exclusively at the polar anchoring moieties of dyes might improve processability without perturbing the dye's optoelectronic properties nor the function-determining crystallinity of the layer.

Experiments: (Amphiphilic) thiazole dyes without, with a mono-polar, and with a double-polar anchor were synthesized, whereas the two constituting polar moieties of the latter derivate are separated by a flexible alkyl chain. The supramolecular structures and crystallinities of Langmuir and LB monolayers were characterized by means of LB isotherms, atomic force microscopy and polarization-resolved fluorescence spectroscopy.

Findings: As compared to the mono-polar reference the introduction of a flexible double-polar head did not deteriorate UV-vis absorption, emission or electrochemical properties of the thiazole but significantly extended the range of constant compressibility modulus, thus indicating improved processability of the Langmuir monolayers. Indeed, AFM studies revealed that the integrity of the monolayers could be retained during LB-deposition. Additionally, also the underlying supramolecular structure of the chromophore moieties is largely identical to those obtained from the mono-polar reference thiazoles.

---

[*] Corresponding authors at: Leibniz Institute of Photonic Technology (IPHT), Albert-Einstein-Str. 9, 07745 Jena, Germany (M. Presselt).
E-mail addresses: rainer.beckert@t-online.de (R. Beckert), martin.presselt@leibniz-ipht.de (M. Presselt).

https://doi.org/10.1016/j.jcis.2018.04.105

1. Introduction

Supramolecular structures, particularly molecular packing density and molecular orientation [1], constitute the morphology of active layers in organic (opto)electronic devices, such as organic solar cells [2–5] (OSCs) and organic light-emitting diodes [6,7] (OLEDs). In the case of OLEDs, the morphology of the active layer needs to be engineered for optimal directional emission characteristics while, in the case of OSCs, the morphology of the active layer needs to be elaborately tuned for optimal power conversion efficiency [8–10]. Thus, control of morphologies is of utmost importance for the optimal function of organic (opto)electronic devices.

Although morphologies heavily depend on molecular properties, it is difficult to target morphologies by molecular design, even if supported by molecular modelling [11], because various solid state phases of the same material might coexist [12], blend ratios might vary locally [13,14], different additives yield different supramolecular structures [15,16], and interfaces to other layers influence the morphology [10,17]. Therefore, various approaches have been developed to control the morphology of molecular films [18–22]. The most frequently applied approach for morphology control is the empirical variation of the (post-) processing parameters, particularly for annealing [23–25]. In contrast to such laborious and time-consuming approaches, control over the formation of supramolecular structures is possible with the Langmuir-Blodgett (LB) technique, which utilizes the assembly of amphiphiles at the water-air interface [26–28]. We have recently shown that the LB technique allows the targeted deposition of distinct solid phases, with a distinct influence of the molecular shape and the type of polar anchors on the supramolecular structures [29–32].

Furthermore, the LB technique allows the deposition of thin films with directional anisotropy of their UV-vis transmission and fluorescence [29], a feature that might be employed in, *e.g.*, light-emitting devices. For the latter application, highly fluorescent dyes are beneficial, such as 4-hydroxy-1,3-thiazoles (fluorescence quantum yields up to 95% in water [33]). It was recently shown that those thiazoles form very rigid Langmuir-monolayers with exceptionally low compressibilities C_S down to 0.004 m/mN if the thiazoles are equipped with sulfonamide moieties [32]. To improve processing, conformational flexibility might be introduced to the polar head, *cf.* the review of Eastoe and Vesperinas [34] and the work of Shang et al. [35]. Therefore, we focus in the present paper on equipping thiazoles with flexible double polar heads that are constituted by a sulfonamide moiety linked to a carboxylic acid by a long alkyl-spacer. We investigate how this flexible double polar head influences formation of Langmuir- and LB films and their morphological properties. The latter are characterized by means of atomic force microscopy (AFM) and polarization-dependent fluorescence. To enable assessment of suitability for optoelectronic applications, we present basic electrochemical and UV-vis absorption and emission characteristics of the bare thiazoles fluorophore and it derivative equipped with the double polar head.

2. Experimental and theoretical details

2.1. Electrochemistry

The cyclovoltammetric measurements (oxidation and reduction side investigated separately) were performed with a Metrohm Autolab PGSTAT30 potentiostat in 0.1 M solution of $TBAPF_6$ in THF (concentration of compounds: 1×10^{-5} M) on a graphite working electrode with a scanning speed of 50 mV s^{-1}; platinum was used as counter and Ag/AgCl as the reference electrode. The data were calibrated externally *vs.* ferrocen/ferrocenium oxidation half-cell potential $E^0_{1/2}$ ($E^0_{1/2}(Fc/Fc^+) = 0.476$ V). The onset-potentials were determined by calculating the crossing between lines fitted to the onset and to the corresponding background of the cyclovoltammogramm for each oxidation and reduction.

2.2. UV–vis absorption and emission spectroscopy

UV-vis absorption spectra of solutions were measured with a Lambda 45 spectrometer from Perkin–Elmer and emission spectra of solutions were measured with a Jasco FP 6500 instrument.

Standard fluorescence measurements of the LB films were made on a custom built setup. This consists of an Isoplane 320 spectrograph with a cooled Pixis CCD-camera from Princeton Instruments. A fiber coupled 5 mW laser with a 405 nm output wavelength was used as excitation source (incident under 55°) and the emission were detected under 35° with respect to the substrate normal. Long pass filters with low self-fluorescence from ITOS were used to block scattered excitation light.

For the polarized fluorescence measurements a polarizer was placed in front of the excitation and an analyzer in front of the spectrometer. Here, the sample was excited under an angle of 70° and the emission was detected under an angle of 5° with respect to the substrate normal. A notch filter (Thorlabs NF405-13) was placed in front of the spectrograph to block scattered excitation light and a better filter correction for low signals. The polarizers were rotated in 10° steps. The data were corrected by a self-written LabView and C++ program. These programs remove last scattered excitation light and cosmic rays. The maxima of the fluorescence spectra were analyzed by a self-written Mathematica program.

2.3. Langmuir and Langmuir-Blodgett (LB) films

Solutions of the dyes (1 mg/ml in $CHCl_3$) were carefully spread onto the subphase (ultra-pure water) of the LB trough (KSV NIMA Alternate L 105 and KSV 5000). The chloroform was allowed to evaporate for 10 min. Then, the barriers were moved with 5 mm/min to record the isotherms. Quartz glass substrates were treated with acetone and iso-propanol in the ultrasonic bath for each solvent 3 times and the substrates were stored in isopropanol. The deposition of LB films on the quartz-glass (30 mm × 5 mm × 1 mm) was done using an upstroke, while a constant pressure was maintained at a dipping speed of 5 mm min^{-1}. All fabricated LB samples contain one monolayer.

2.4. Scanning force microscopy

Atomic force microscopy (AFM) was carried out using a Veeco Digital Instruments AFM Nanoscope IIIa, with a head Dimension 3100 in tapping mode on air with a silicon tip (radius < 8 nm) at 300 kHz with a force constant of E40 N m^{-1} (Budget Sensors Tap 300-G). The AFM histograms include the height distribution of the background only. Background detection was performed by Otsu's method [75] using Gwyddion [76] and the appropriateness of the result was verified by visual inspection. Background data points, which all lay well within −5 nm to +5 nm around each background's mean height, were then sorted into 100 bins of constant width using routines provided within the NumPy and SciPy program packages [77]. All histograms were scaled so that their curves enclose an area of 1 nm. To the histograms thus obtained, we fit Gaussian functions, whose standard deviations followed to all be less than $\sigma = 0.565$ nm. Furthermore, at least 91.6% of all data points lay within a range of -2σ to $+2\sigma$ around each Gaussian's center h_c. Almost all data points that lay far below $h_c - 2\sigma$ are due to scratches on the surfaces.

2.5. Theoretical details

Density functional theory (DFT) and time-dependent (TD) DFT calculations were performed with a developer version of the *TeraChem* [78,79] quantum chemistry software using Ahlrich's polarizable double-ζ valence basis set [80]. We chose the hybrid version of the long-range corrected Perdew-Burke-Ernzerhof density functional [81] as implemented in *TeraChem* at a range-separation parameter of $\omega = 0.15$ reciprocal Bohr radii. Solvent effects were taken into account by means of the conductor-like screening model (COSMO) both, in time-independent [82] and time-dependent [83] calculations where the inclusion of solvent effects is mentioned. The computed stick spectra were broadened by a Gaussian distribution with a full-width at half-maximum of 0.5 eV and shifted bathochromically by 0.36 eV.

3. Results and discussion

3.1. Synthesis

The thiazole **1** was synthesized *via* Hantzsch thiazole cyclisation of pyridine-2-thioamide with ethyl α-bromo-phenylacetate [36,37]. The corresponding thioamide and phenylacetate were synthesized according to the literature [38,39]. To improve solubility in organic solvents, the hydroxygroup was alkylated with butyl iodide *via* Williamson-type etherification as shown in Scheme 1. We used methyl 11-aminoundecanoate as amine to introduce a second polar group that is connected to the polar sulfonamide moiety with a long and flexible alkyl spacer. That way, the 4-butoxythiazole **2** was successively chlorosulfonated and aminated in a two-step process to get the sulfonamide **3**; *cf.* Scheme 1. Finally, the carboxylic acid was deprotected *via* ester hydrolysis with ethanolic potassium hydroxide [40]. The sulfonamide group is stable against hydrolysis over a wide pH range, thus being a good linking group between the chromophore and the amphiphilic precursor. After an acidic work-up, the amphiphilic dye **4** was obtained in very good yields. The thiazole **4** can be isolated as a yellow crystalline solid with a turquoise to green solid state fluorescence. The compound is soluble in a wide range of solvents from polar protic ones, such as methanol, to non-polar aprotic ones, like toluene. This solubility is due to the butoxy and the undecanoic acid groups. The best solubility was observed in chloroform, with more than 15 mg/ml. A second dye **5** was synthesized *via* Williamson-type etherification with ethyl iodide to yield a non-amphiphilic reference compound of the chromophore, see Scheme 1. The new dyes were fully characterized by means of NMR, MS, melting point and photophysical methods (see supporting information).

3.2. UV-vis absorption and fluorescence spectra of solutions

The UV-vis absorption spectrum of **4**, dissolved in acetonitrile (see Fig. 1), is dominated by an intense vibrationally broadened absorption band between 320 and 430 nm. This transition can be characterized as π-π^* transition as indicated by charge difference densities [41–43] derived from electron density distributions [44,45] (see Fig. 1). The thiazole **5**, which has the same chromophore except the sulfonamide group, shows a virtually identical major absorption band, which is only slightly hypsochromically shifted as compared to **4**. The time-dependent density functional theory calculations, from which the charge difference densities were derived, perfectly reproduce this shift (see stick spectra in Fig. 1). The experimental fluorescence spectrum of **4** shows no notable shift compared to **5** ($\lambda_{max} = 451$ nm) but an additional bathochromic shoulder at 470 nm that is attributed to different vibrational progressions. Therefore, we conclude that the installation of the sulfonamide group does not change the absorption and emission features of the underlying chromophore. Hence, the morphology of resultant molecular films can be tailored independently from the optical properties of the molecular entity, which is important for the function of dye layers in light absorbing or emitting devices.

The influence of the surrounding medium on the absorption and emission properties was investigated by varying the solvent polarity as well as the acidity of the solution. The solvent polarity has a very weak influence on the optical properties, *i.e.* weak solvatochromism and weak changes in the fluorescence quantum yields (70–77%) as detailed in the supporting information (see Fig. SI 11). As shown in Fig. 1, protonation of the pyridine moiety of **4** causes strong bathochromic shifts of the absorption and fluorescence spectra, *cf.* $pK_A = 2.1$ of a 2,2′-pyridylthiazol as determined by Grummt et al. [33]. This shift is caused by the stronger electron withdrawing effect of the cationic pyridinium species as compared to the non-protonated pyridyl moiety. Consequently more charge is transferred from the π-donor to the pyridinium acceptor moiety upon photoexcitation than in case of the neutral pyridine acceptor. Accordingly, the fluorescence band of **4H⁺** shows a green emission at 513 nm instead of the deep blue emission at 451 nm of **4**. Upon

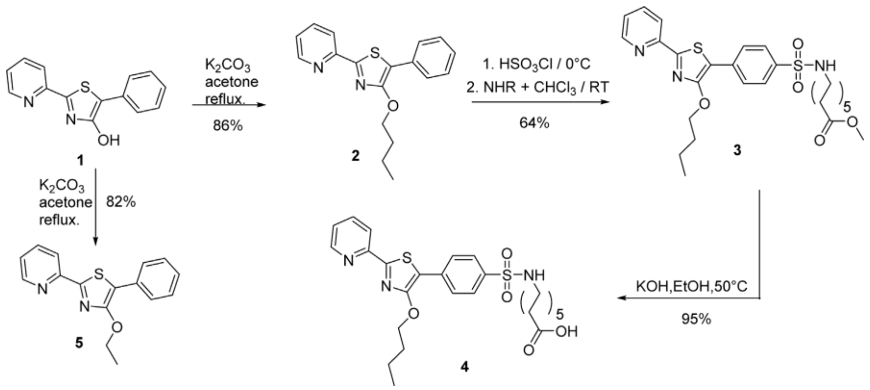

Scheme 1. Synthesis of the thiazole dyes **4** and **5**.

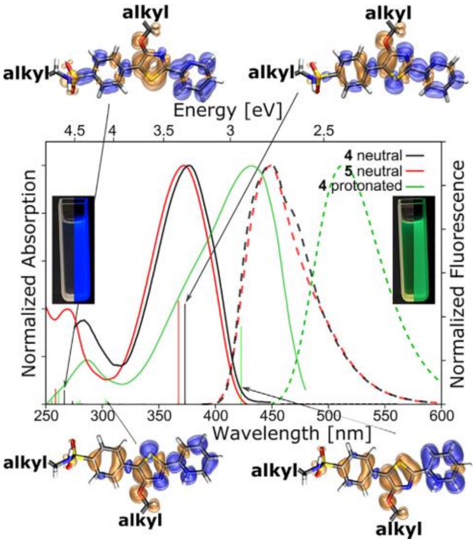

Fig. 1. Comparison between experimental absorption and fluorescence spectra of 2-pyridyl-5-phenyl-4-alkoxythiazole without (**5**) and with (**4**) a sulfonamide group (solvent: methanol, thiazole concentration $c = 10^{-5}$ M) and its protonated state (2 drops of methanolic sulfuric acid) together with pictures of the measured solutions under daylight (left) and UV-radiation (right); Quantum chemically derived stick spectra of **4** and **5** are shown together with charge difference densities (CDDs) for the respective two lowest lying absorption bands. CDDs resulting from increased (decreased) electron density upon photoexcitation are marked blue (orange). (For interpretation of the references to colour in this figure legend, the reader is referred to the web version of this article.)

pyridine protonation the Stokes shift slightly increases from 3601 to 4303 cm^{-1}. The large bathochromic shifts between the absorption as well as emission spectra of **4** and **4H⁺** might be utilized as markers for interface interactions when layers of **4** are in contact or mixed with acidic materials, such as PEDOT:PSS (poly(3,4-ethylenedioxythiophene) polystyrene sulfonate) as used in organic solar cells [10,46]. Furthermore, comparison between the spectra of the neutral and the protonated species reveals that pyridine protonation by the carboxylic acid moiety does virtually not happen in solution.

3.3. Electrochemical characterization of the thiazoles in solution

To determine the redox properties of **4** and **5**, particularly the energies of the highest occupied and lowest unoccupied molecular orbitals (HOMO and LUMO), cyclic voltammetry measurements were performed (for details see methods section). As depicted in Fig. 2, the amphiphilic dye **4** shows one oxidation wave at $E_{ox} = 1.14$ V and two reduction waves ($E_{red1} = -2.25$ V, $E_{red2} = -2.46$ V), which seem to be reversible. **5** shows one oxidation wave at $E_{ox} = 1.5$ V and just one reduction wave at $E_{red} = -2.3$ V. Following the work of Gampe et al. [47] the oxidation potential is assigned to the thiazole moiety and, according to Menzel et al. [48], the reduction to the pyridine moiety.

The HOMO and LUMO energies were derived from the onset potentials of oxidation and reduction [49] (**4:** $E_{HOMO/LUMO} = -5.68/-2.91$ eV; **5:** $E_{HOMO/LUMO} = -5.53/-2.65$ eV, see Table 1) and prove the here investigated thiazoles as suitable candidates for optoelectronic materials when employed in standard optoelectronic device structures with respect to charge injection and extraction [50–53]. Additionally, the amphiphilicity of **4** is expected to enable self-organization, thus possibly enabling formation of smooth model layers, *e.g.*, model layers for organic optoelectronic devices, as discussed in the subsequent section.

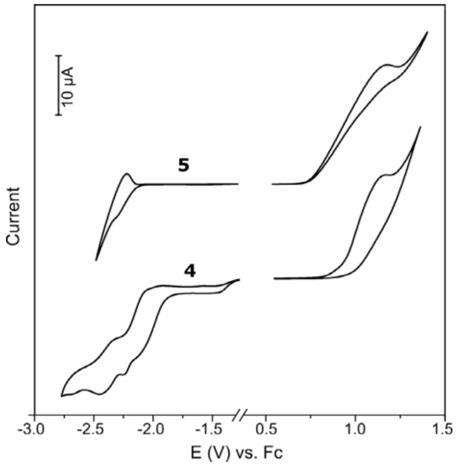

Fig. 2. Cyclic voltammograms of **5** and **4** in THF; the data show oxidation and reduction.

3.4. Assembly and characterization of Langmuir-Blodgett (LB) films

After the basic characterization of the thiazoles in solution, we focus on the formation of molecularly thin films of the amphiphilic derivative **4** by means of the LB technique. First, we discuss the influence of the double polar substituent on the amphiphilicity of **4**. Therefore, the electrostatic potential distribution at the van der Waals surface of **4** is compared to that of the non-amphiphilic reference **5** and to the pyridyl-thiazoles **SH4a,b** from Habenicht et al. (*4a* and *4b* in [32]), which contains just the sulfonamide single polar group instead of the double polar head in **4**.

As shown in Fig. 3 the non-polar reference compound **5** shows a rather homogenous electrostatic potential [55–58] over the entire molecule, thus no amphiphilicity is expected. In contrast, in **4** and **SH4a** sulfonamide sites are pronounced negatively charged spots, while the additional carboxylic acid in **4** is less polar and separated from the sulfonamide moiety by the long, flexible, non-polar alkyl chain, which is shown in a straight, relaxed geometry Fig. 3. However, the alkyl chain might coil or bend to adopt the relative position of the two polar groups in **4** according to environmental conditions, *e.g.* hetero-polar interfaces.

For **5**, which served as non-polar reference compound in spectroscopic and electrochemical solution experiments and lacks amphiphilicity, no self-assembly on the air-water interface on the LB trough is expected. Accordingly, the surface pressure Π does not increase when shrinking the air-water interface in LB experiments (see Fig. 3), *i.e.* **5** is not suitable for LB studies and will not be discussed in the following.

In Fig. 3 the Π(A)-isotherms of **4**, containing the double polar head, is compared with two mono polar derivatives of the same chromophore **SH4a** (methyl acetate side chain) and **SH4b** (chloropropyl side chain) [32]. The isotherms differ in their mean molecular areas A of the solid phases and their slopes, as already reported

Table 1
UV-vis spectroscopic and electrochemical properties of **4** and **5**.

	λ_{abs} (ε)[a]	λ_{em} (Φ_{max})[a,b]	E_{ox}^{onset}[c]	E_{red}^{onset}[c]	E_{HOMO}[d]	E_{LUMO}[d]	E_{gap}^{CV}[e]	E_{gap}^{opt}[f]
	[nm] ([10^4 $M^{-1}cm^{-1}$])	[nm] ([%])	[V]	[V]	[eV]	[eV]	[eV]	[eV]
4	288 (0.77), 383 (2.6)	451 (76)	0.89	−1.92	−5.99	−3.18	2.81	2.92
5	273 (0.76), 379 (2.1)	451 (∼95)	0.73	−2.15	−5.83	−2.95	2.88	2.94

[a] Measured in toluene.
[b] Measured in toluene, relative to quinine sulfate (Φ = 0.52).
[c] Recorded by cyclic voltammetry in 0.1 M solution of $TBAPF_6$ in THF, *versus* $E_{onset}(Fc/Fc^+)$.
[d] Calculated *via* $E_{HOMO} = -[E_{onset}(Ox) - E^0_{1/2}(Fc/Fc^+)] - 5.1$ eV and $E_{Lumo} = -[E_{onset}(Red) - E^0_{1/2}(Fc/Fc^+)] - 5.1$ eV [54].
[e] $E_{Gap}^{CV} = E_{LUMO} - E_{HOMO}$, measured in THF.
[f] Calculated from the onset (10%) of the absorption spectra, measured in methanol.

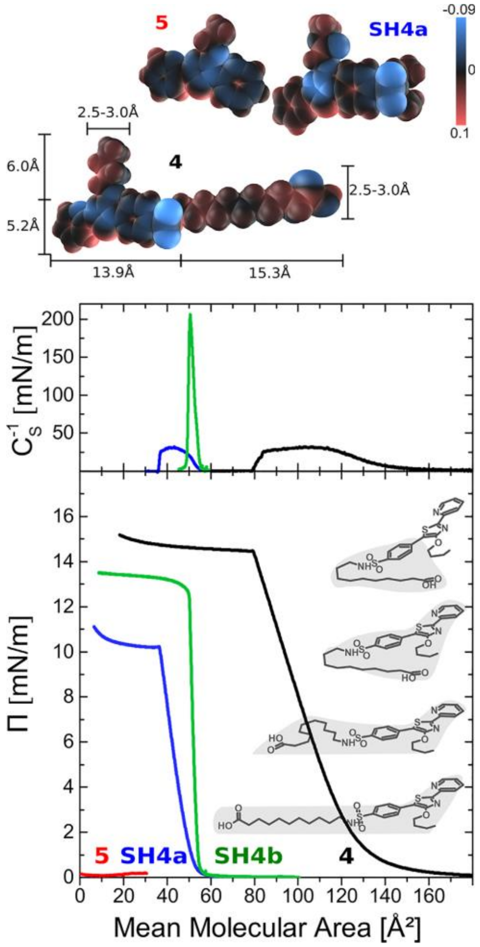

Fig. 3. Top: Electrostatic potentials on van der Waals surfaces of the dyes **4**, **5**, and **SH4a**. Bottom: C_S^{-1}(A) curves and Π(A) isotherms of **4** (double polar head groups), **5** (non-amphiphilic), **SH4a** (methyl acetate side chain) and **SH4b** (chloropropyl side chain). Right: Cartoons of the orientation of **4** with varied degrees of spacer coiling and chromophore tilts. The shades represent the assumed spatial demands on the subphase surface, *i.e.* estimates of mean molecular areas.

in Ref. [32]. Due to the large double polar head involving the alkyl spacer the isotherm of **4** starts at significantly larger mean molecular areas as compared to the ones of **SH4a** and **SH4b** (A_0 (linear section of Π(A) extrapolated to Π = 0) of **SH4a,b, 4**: 51, 54 and 126 Å^2), but features a smaller slope, *i.e.* a higher compressibility of the Langmuir monolayer, than **SH4a,b** what is attributed to the flexibility of the alkyl spacer in the double polar head in **4**. Particularly, the Π(A)-slope of **SH4b** implies that its Langmuir monolayer has the least degree of freedom for supramolecular packing, *i.e.* **SH4b** readily forms densely packed layers that are virtually not compressible and are presumably characterized by a high molecular order. The exceptionally low compressibility C_S of **SH4b** is connected to an extremely high compressibility modulus $C_S^{-1} = -A\, d\Pi/dA$ [59–61], as shown in Fig. 3. The analysis of the compressibility modulus supports the above interpretation, that Langmuir monolayers of **4** are more compressible ($(C_S^{-1})^{max}$ = 31 mN/m), *i.e.* less rigid, than those made from **SH4b** ($(C_S^{-1})^{max}$ = 206 mN/m), but feature a similar maximum compressibility modulus as **SH4a** ($(C_S^{-1})^{max}$ = 32 mN/m). The region of maximum compressibility modulus C_S^{-1}, *i.e.* least compressibility, extends over a significantly broader mean molecular area range for **4** as compared to **SH4a**. Thus, the introduction of flexibility and double polarity to the head of **4** enables a slower formation of the Langmuir layer (in terms of dΠ/dA) and, therefore, likely fewer tendencies for local aggregation but presumably reaches similar molecular order as **SH4a**.

The mean molecular area of the chromophore, visualized by the shades in Fig. 3, might be approx. 80 Å^2, depending on the packing in the Langmuir monolayer. Thus, the smaller A_0-areas of **SH4a,b** indicate that the molecules readily tilt upwards around either the long or short molecular axis (both might be possible, depending on the molecular packing) upon formation of the most densely packed Langmuir layer. From the molecular dimensions of **4** we estimate a mean molecular area between 126 and 137 Å^2 for chromophores oriented parallel to the subphase surface and a straight and non-coiled spacer in the double polar group as schematically shown in Fig. 3. Since this area matches the experimentally determined one (126 Å^2, see above), we deduce that, in contrast to **SH4a, b**, molecules of **4** are oriented flat at the subphase surface at the beginning of formation of the solid phase Langmuir layer. This phase is characterized by virtually perfect linearity of the Π(A)-isotherm between 120 and 80 Å^2 and ends at Π(80 Å^2) = 15 mN/m. Upon further shrinking the available surface area a highly compressible transition phase, involving molecular reorientations, is formed.

To investigate the homogeneity and smoothness of the molecular monolayers atomic force microscopic (AFM) investigations were performed on LB films deposited at surface pressures between 2 and 12 mN/m. Basically, all topology images in Fig. 4 show homogenous films with very smooth backgrounds as quantified *via* histograms of the height distribution of the full background only (see Fig. 4 at the very right, for details on histogram construction see the methods section).

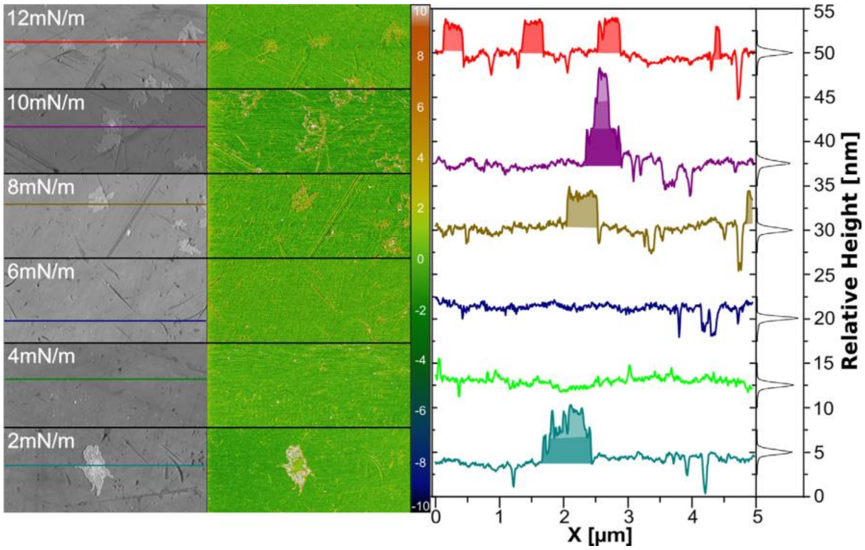

Fig. 4. AFM images of the LB films of **4** at different deposition pressures. The topography image (left), the phase picture (middle) and cross-section analysis of topography (right) are shown. All films contain one monolayer of **4**. The deposition pressures are 2, 4, 6, 8, 10 and 12 mN/m.

However, possibly due to increasing mechanical strain at LB deposition with increasing Π_{LB}, flake-like structures seem to appear progressively. The height of the flakes is about 3 nm or multiples thereof, as indicated by the shaded areas in the exemplary line profiles in Fig. 4, right. This height approximately matches twice the length of **4**. Thus, the flakes are assigned to three-dimensional aggregate structures that probably form upon local supramolecular rearrangement during vertical deposition of the Langmuir monolayers.

Furthermore, the absorption spectra of LB-monolayers that are shown in Fig. SI 12 do not shift significantly in wavelength as compared the solution spectra and also not when surface pressure at deposition is varied (1, 7, 12 mN/m). Thus, pyridine protonation by the carboxylic acid moiety is also not observed in the solid phase, *cf.* solution spectra discussed above. Thus, the newly introduced double polar functionalization, which involves the carboxylic acid moiety, does not disturb the absorption and electronic properties of the thiazoles fluorophore, cf. non-amphiphilic reference **5** and the mono-polar amphiphiles **SH4a** and **SH4b** published recently.

3.5. Polarized steady state fluorescence and fluorescence anisotropy of thin films

The AFM-images discussed above show largely homogeneous films of **4**. This is in line with the clear Π(A)-isotherm showing a single phase of **4** in the pressure range used for deposition. However, the molecular orientations of **4**, **SH4a**,**b**, differ within the Langmuir layer as discussed above. This difference involves varied orientation of the transition dipole moments (TDV) of these thiazoles [62–65]. To investigate the possibly different orientation of the TDVs of **4**, **SH4a**,**b** the Langmuir monolayers of these derivatives were deposited *via* the LB technique onto quartz-glass and investigated by means of polarization-resolved fluorescence [29]. Therefore, both the polarization of the incident and the emitted light were varied as illustrated in Fig. 5.

The results of these experiments are shown in the first column "I(α)" of Fig. 5. Each of the LB films shows a pronounced dependence of the fluorescence intensity on the polarization of the incident light. Such behavior is not observed for isotropic drop-casted reference samples of thiazoles embedded into poly(methyl methacrylate) matrices (PMMA, see gray crosses in Fig. 5). Thus, we deduce that in the PMMA films the chromophores are oriented randomly, whereas they are preferentially oriented in LB films. In the films the TDV are oriented predominantly in the α=70°-polarization direction of the incident light, see Fig. 5. Since the TDVs are oriented along the major molecular axis, as illustrated in Fig. 5, one can deduce that the chromophores of **4**, **SH4a**,**b** are mainly tilted slightly (20°) away from the substrate surface.

As shown in Fig. 5, the dominant molecular orientation, as deduced from the polarization angle for maximum fluorescence, just weakly depends on the surface pressure at deposition Π_{LB} for all studied thiazoles. Therefore, we conclude on a significant influence of the LB deposition process and the substrate-molecule interaction on the molecular orientation [29].

The small influence of Π_{LB} on the difference between maximal (normalized to 100%) and minimal (varying between 65 and 75%) fluorescence intensity shown in Fig. 5, *i.e.* the fluorescence contrast ΔI, is largest for **4** (35%), followed by **SH4a** (30%), and **SH4b** (25%). However, for uniformly oriented TDVs the minimum of the fluorescence must be zero at a polarization of light that is perpendicular to the TDVs where no light is absorbed [29]. Thus, the large minimum fluorescence intensities (65–75%) show that the molecular orientations are clearly not uniform, even if a certain preferential orientation was deduced above.

Alternatively or possibly adding to the non-uniformity of the TDV-orientation, *i.e.* the orientational distribution of chromophores, the large minimal fluorescence intensities might be explained by superposition of two molecular sets with different TDV-orientations such as given in the case of the presence of two different LB phases [29]. To test for the existence of two different solid LB phases with distinct chromophore orientation the polarizer is fixed

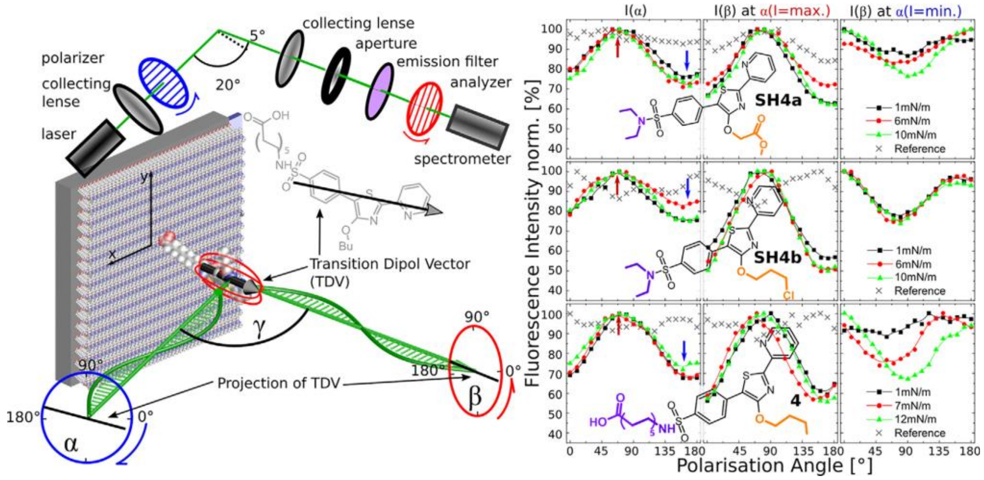

Fig. 5. Steady state fluorescence anisotropic measurements of LB films from **SH4a**, **SH4b**, **4** at different deposition pressures.

at the position of maximum or minimum fluorescence and the polarization of the emitted light[1] I(β) is analyzed as shown in the middle "I(β) at α(I = max.)" and right "I(β) at α(I = min.)" column of Fig. 5, respectively.

When fixing α so that I(α) = max. the resulting ΔI (**SH4b**: 50%, **4**: 45%, **SH4a**: 40%) is higher than in the experiments discussed above, while excitation at α(I = min.) yields I(β)-dependencies that are phase shifted by ~90° as compared to the aforementioned I(β) excited at α(I = max.) (compare central "I(β) at α(I = max.)" and right "I(β) at α(I = min.)" column in Fig. 5). Finding these two phase-shifted I(β)-dependencies clearly indicates the presence of two different solid phases with TDVs tilted by 90° accordingly. However, within these solid phases the TDVs are still not oriented uniformly, but are rather characterized by a certain orientational distribution as deduced from the non-vanishing fluorescence intensities in the I(β)-minima.

For the major solid phases, which are probed at α(I = max.) (central "I(β) at α(I = max.)" column in Fig. 5), still no dependencies of I(β), *i.e.* of the molecular orientations, on Π_{LB} can be observed. In contrast the minor phases excited at α(I = min.) of **4** and **SH4a** show dependencies of ΔI on Π_{LB}. While for **SH4a** ΔI is systematically slightly enhanced with increasing Π_{LB} from 10 to 25%, virtually no ΔI is present for **4** at Π_{LB} = 1 mN/m, thus implying isotropic molecular orientation in the liquid phase of **4**. With increasing Π_{LB}, ΔI of **4** gets systematically improved to 35% (at Π_{LB} = 12 mN/m). Additionally, the fluorescence minimum and maximum shift by 30°. Since this shift is exclusive for the minor LB phase it might be assigned to the flake-like structures seen in the AFM-pictures in Fig. 4.

Finally, the polarization resolved fluorescence data show that the investigated thiazoles differ little in the molecular orientations of the major solid phases, but the double polarity of **4** induces sufficient flexibility to allow for controlling the molecular orientation in the minor solid phase by means of the LB deposition pressure. This behavior is in agreement with the larger compressibility of the Langmuir monolayers of **4** as compared to the mono-polar thiazoles (**SH4a,b**) deduced from the Π(A)-isotherms above.

4. Conclusions

On the basis of recently reported research on supramolecular control in small molecule semiconductor layers by means of amphiphilic functionalization and interface assembly [29,32], this work has demonstrated that utilization of flexible double-polar heads improves Langmuir-Blodgett (LB) processing as compared to the mono-polar reference [32] without deteriorating the monolayer's supramolecular structure. The LB isotherm reveals that the *terminal* functionalization of the here investigated thiazoles implicates formation of a single, well-defined solid phase that gets disrupted at a mean molecular area A < 80 $Å^2$, rather than transition to distinct solid phases observed for similar but *centrally* functionalized – T-shaped – amphiphilic thiazoles [29] and other chromophores [66]. Importantly, the terminal introduction of the flexible double polar head enables formation of smooth and homogeneous monolayers with a steady, well-defined transition between liquid and solid phase. The latter features a moderate compressibility modulus of C_S^{-1} = 31 mN/m, *i.e.* indicating formation of soft films that can be continuously deposited as homogeneous LB monolayers. This compressibility modulus is similar to the one of a recently reported amphiphilic thiazole with a mono-polar head [32], but is virtually constant over a significantly larger range of the mean molecular area (120–85 $Å^2$ as compared to 50–35 $Å^2$), thus supporting the hypothesis of improving processability by introducing additional degrees of motional freedom upon installing a flexible double-polar head. Additionally, the double polarity improved anchoring of the molecules at polar surfaces and subphases as shown by the increased achievable maximum surface pressure in the first solid phase as compared to the mono-polar reference amphiphiles [32]. Detailed UV-vis absorption and fluorescence spectroscopy revealed that the additional polar COOH moiety constituting the double-polar anchor can be considered as inert polar group that does not deteriorate the optical or electronic properties of the hydrophobic chromophore upon acid-base reactions [10], being key to application of COOH

---

[1] From the small Stokes-shift discussed above we deduce that just small molecular geometry changes happen after photoexcitation and the TDV is approximated to have identical orientations for excitation and light emission.

to virtually any organic semiconductor containing hetero-aromatic cycles [1,67]. Thus, the presented thiazoles, which are excellent fluorophores, show promising electronic and photonic properties and their processability could be significantly improved by the introduction of the flexible, double polar, hydrophilic anchor presented in this work, thus rendering these thiazoles attractive for use in optoelectronic devices. Particularly, the flexible double polar anchors was proven to be an excellent structural motif for advanced control of monolayer formation and deposition by means of the LB technique. Subsequent studies shall reveal whether the additional degrees of motional freedom as compared to mono-polar references cause entropic stabilization of the derived two-dimensional model layers. Further development on homogeneous and well-defined semiconductor monolayers will enable establishment of model interfaces between electron donor and acceptor layers for advanced studies on photo-driven charge separation that significantly improve over the state of the art model layers [68–74].

Conflicts of interests

There are no conflicts to declare.

Acknowledgements

The authors thank the Bundesministerium für Bildung und Forschung (BMBF FKZ 03EK3507) and the Deutsche Forschungsgemeinschaft (DFG Grant No. PR 1415/2-1) for financial support. T. Sachse acknowledges the German Federal Environmental Foundation for his fellowship. The authors would like to thank Karin Kobow for support in the lab and Prof. Todd Martínez (Stanford University, USA) for quantum chemical support.

Appendix A. Supplementary material

Supplementary data associated with this article can be found, in the online version, at https://doi.org/10.1016/j.jcis.2018.04.105.

References

[1] K.R. Graham, C. Cabanetos, J.P. Jahnke, M.N. Idso, A. El Labban, G.O.N. Ndjawa, T. Heumueller, K. Vandewal, A. Salleo, B.F. Chmelka, A. Amassian, P.M. Beaujuge, M.D. McGehee, J. Am. Chem. Soc. 136 (2014) 9608.
[2] Y. Liu, C.-C. Chen, Z. Hong, J. Gao, Y. Yang, H. Zhou, L. Dou, G. Li, Y. Yang, Sci. Rep. 3 (2013).
[3] C. Brabec, V. Dyakonov, U. Scherf, Organic Photovoltaics: Materials, Device Physics, and Manufacturing Technologies, Wiley-VCH, 2008.
[4] M. Presselt, M. Bärenklau, R. Rösch, W.J.D. Beenken, E. Runge, S. Shokhovets, H. Hoppe, G. Gobsch, Appl. Phys. Lett. 97 (2010) 253302.
[5] M. Presselt, F. Herrmann, S. Shokhovets, H. Hoppe, E. Runge, G. Gobsch, Chem. Phys. Lett. 542 (2012) 70.
[6] S.Y. Lee, C. Adachi, T. Yasuda, Adv. Mater. 28 (2016) 4626.
[7] X. Yang, X. Xu, G. Zhou, J. Mater. Chem. C 3 (2015) 913.
[8] H. Hoppe, M. Niggemann, C. Winder, J. Kraut, R. Hiesgen, A. Hinsch, D. Meissner, N.S. Sariciftci, Adv. Funct. Mater. 14 (2004) 1005.
[9] R.M. Beal, A. Stavrinadis, J.H. Warner, J.M. Smith, H.E. Assender, A.A.R. Watt, Macromolecules 43 (2010) 2343.
[10] F. Herrmann, B. Muhsin, C.R. Singh, S. Shokhovets, G. Gobsch, H. Hoppe, M. Presselt, J. Phys. Chem. C 119 (2015) 9036.
[11] T. Sachse, T.J. Martinez, B. Dietzek, M. Presselt, J. Comput. Chem. 39 (2018) 763.
[12] R. Noriega, J. Rivnay, K. Vandewal, F.P.V. Koch, N. Stingelin, P. Smith, M.F. Toney, A. Salleo, Nat. Mater. 12 (2013) 1038.
[13] T.P. Le, Z. Shang, L. Wang, N. Li, S. Vajjala Kesava, J.W. O'Connor, Y. Chang, C. Bae, C. Zhu, A. Hexemer, E.W. Gomez, A. Salleo, M.A. Hickner, E.D. Gomez, Macromolecules 48 (2015) 5162.
[14] M. Presselt, F. Herrmann, H. Hoppe, S. Shokhovets, E. Runge, G. Gobsch, Adv. Energy Mater. 2 (2012) 999.
[15] M.J. Hollamby, M. Karny, P.H.H. Bomans, N.A.J.M. Sommerdjik, A. Saeki, S. Seki, H. Minamikawa, I. Grillo, B.R. Pauw, P. Brown, J. Eastoe, H. Möhwald, T. Nakanishi, Nat. Chem. 6 (2014) 690.
[16] C. Park, H.J. Song, H.C. Choi, Chem. Commun. (2009) 4803.
[17] B. Meredig, A. Salleo, R. Gee, ACS Nano 3 (2009) 2881.
[18] Y. Diao, L. Shaw, Z. Bao, S.C.B. Mannsfeld, Energy Environ. Sci. 7 (2014) 2145.
[19] L.F. Doessel, V. Kamm, I.A. Howard, F. Laquai, W. Pisula, X. Feng, C. Li, M. Takase, T. Kudernac, S. De Feyter, K. Muellen, J. Am. Chem. Soc. 134 (2012) 5876.
[20] H. Bürckstümmer, E.V. Tulyakova, M. Deppisch, M.R. Lenze, N.M. Kronenberg, M. Gsänger, M. Stolte, K. Meerholz, F. Würthner, Angew. Chem. Int. Ed. 123 (2011) 11832.
[21] F. Würthner, Z.J. Chen, F.J.M. Hoeben, P. Osswald, C.C. You, P. Jonkheijm, J. von Herrikhuyzen, A. Schenning, P. van der Schoot, E.W. Meijer, E.H.A. Beckers, S.C. J. Meskers, R.A.J. Janssen, J. Am. Chem. Soc. 126 (2004) 10611.
[22] V.L. Gunderson, A.L. Smeigh, C.H. Kim, D.T. Co, M.R. Wasielewski, J. Am. Chem. Soc. 134 (2012) 4363.
[23] J.A. Renz, T. Keller, M. Schneider, S. Shokhovets, K.D. Jandt, G. Gobsch, H. Hoppe, Sol. Energy Mater. Sol. Cells 93 (2009) 508.
[24] D. Minh Trung, L. Hirsch, G. Wantz, J.D. Wuest, Chem. Rev. 113 (2013) 3734.
[25] D. Minh Trung, L. Hirsch, G. Wantz, Adv. Mater. 23 (2011) 3597.
[26] K. Ariga, Y. Yamauchi, T. Mori, J.P. Hill, Adv. Mater. 25 (2013) 6477.
[27] P. Dynarowicz-Łątka, A. Dhanabalan, O.N. Oliveira Jr, Adv. Colloid Interface Sci. 91 (2001) 221.
[28] S. Das, F. Herrmann-Westendorf, F.H. Schacher, E. Tauscher, U. Ritter, B. Dietzek, M. Presselt, ACS Appl. Mater. Interfaces 8 (2016) 21512.
[29] M.L. Hupfer, M. Kaufmann, F. Herrmann-Westendorf, T. Sachse, L. Roussille, K.-H. Feller, D. Weiß, V. Deckert, R. Beckert, B. Dietzek, M. Presselt, ACS Appl. Mater. Interfaces 9 (2017) 44181.
[30] C. Huang, K. Wang, G. Xu, X. Zhao, X. Xie, Y. Xu, Y. Liu, L. Xu, T. Li, J. Phys. Chem. 99 (1995) 14397.
[31] U. Hartnagel, A. Hirsch, D. Felder-Flesch, J.-L. Gallani, C. Bourgogne, J. Exp. Nanosci. 3 (2008) 229.
[32] S.H. Habenicht, S. Schramm, S. Fischer, T. Sachse, F. Herrmann-Westendorf, A. Bellmann, B. Dietzek, M. Presselt, D. Weiß, R. Beckert, H. Görls, J. Mater. Chem. C 4 (2016) 958.
[33] U.-W. Grummt, D. Weiss, E. Birckner, R. Beckert, J. Phys. Chem. A 111 (2007) 1104.
[34] J. Eastoe, A. Vesperinas, Soft Matter 1 (2005) 338.
[35] T. Shang, K.A. Smith, T.A. Hatton, Langmuir 19 (2003) 10764.
[36] E. Täuscher, D. Weiß, R. Beckert, H. Görls, Synthesis 2010 (2010) 1603.
[37] S.H. Habenicht, M. Siegmann, S. Kupfer, J. Kübel, D. Weiß, D. Cherek, U. Möller, B. Dietzek, S. Gräfe, R. Beckert, Meth. Appl. Fluoresc. 3 (2015) 025005.
[38] V. Sharma, J.J. Tepe, Org. Lett. 7 (2005) 5091.
[39] Marco H. Klingele, S. Brooker, Eur. J. Org. Chem. 2004 (2004) 3422.
[40] A.H.G.O. Becker, Autorenkollektiv: *Organikum.* 23. Auflage. Wiley-VCH Weinheim (2009).
[41] M.T. Sun, P. Kjellberg, W.J.D. Beenken, T. Pullerits, Chem. Phys. 327 (2006) 474.
[42] W.J.D. Beenken, F. Herrmann, M. Presselt, H. Hoppe, S. Shokhovets, G. Gobsch, E. Runge, Phys. Chem. Chem. Phys. 15 (2013) 16494.
[43] J. Preiß, M. Jäger, S. Rau, B. Dietzek, J. Popp, T. Martínez, M. Presselt, ChemPhysChem 16 (2015) 1395.
[44] M. Presselt, B. Dietzek, M. Schmitt, S. Rau, A. Winter, M. Jäger, U.S. Schubert, J. Popp, J. Phys. Chem. A 114 (2010) 13163.
[45] M. Presselt, C. Schnedermann, M. Müller, M. Schmitt, J. Popp, J. Phys. Chem. A 114 (2010) 10287.
[46] F. Herrmann, S. Engmann, M. Presselt, H. Hoppe, S. Shokhovets, G. Gobsch, Appl. Phys. Lett. 100 (2012) 153301.
[47] D.M. Gampe, F. Nöller, V.G. Hänsch, S. Schramm, A. Darsen, S.H. Habenicht, S. Ehrhardt, D. Weiß, H. Görls, R. Beckert, Tetrahedron 72 (2016) 3232.
[48] R. Menzel, S. Kupfer, R. Mede, D. Weiß, H. Görls, L. González, R. Beckert, Eur. J. Org. Chem. 2012 (2012) 5231.
[49] C.M. Cardona, W. Li, A.E. Kaifer, D. Stockdale, G.C. Bazan, Adv. Mater. 23 (2011) 2367.
[50] Q. Zhang, B. Li, S. Huang, H. Nomura, H. Tanaka, C. Adachi, Nat. Photonics 8 (2014) 326.
[51] H. Yoshida, K. Yoshizaki, Org. Electron. 20 (2015) 24.
[52] Y. Luo, H. Aziz, Adv. Funct. Mater. 20 (2010) 1285.
[53] T. Zhang, B. Chu, W. Li, Z. Su, Q.M. Peng, B. Zhao, Y. Luo, F. Jin, X. Yan, Y. Gao, H. Wu, F. Zhang, D. Fan, J. Wang, ACS Appl. Mater. Interfaces 6 (2014) 11907.
[54] S. Trasatti, Pure Appl. Chem. 58 (1986) 955.
[55] J. Preiß, F. Herrmann-Westendorf, T.H. Ngo, T.J. Martínez, B. Dietzek, J.P. Hill, K. Ariga, M.M. Kruk, W. Maes, M. Presselt, J. Phys. Chem. A 121 (2017) 8614.
[56] W. Beenken, W. Maes, M. Kruk, T. Martínez, M. Presselt, J. Phys. Chem. A 119 (2015) 6875.
[57] M. Presselt, W. Dehaen, W. Maes, A. Klamt, T. Martínez, W.J.D. Beenken, M. Kruk, Phys. Chem. Chem. Phys. 17 (2015) 14096.
[58] M. Presselt, M. Wojdyr, W.J.D. Beenken, M. Kruk, T.J. Martinez, Chem. Phys. Lett. 603 (2014) 21.
[59] K. Gong, S.-S. Feng, M.L. Go, P.H. Soew, Colloids Surf., A 207 (2002) 113.
[60] L.T. Gew, M. Misran, Nanoscale Res. Lett. 9 (2014) 1.
[61] M. Petaccia, L. Giansanti, F. Leonelli, A. La Bella, D.G. Villalva, G. Mancini, Chem. Phys. Lipids 200 (2016) 83.
[62] L. Penninck, F. Steinbacher, R. Krause, K. Neyts, Org. Electron. 13 (2012) 3079.
[63] M. Flämmich, M.C. Gather, N. Danz, D. Michaelis, A.H. Bräuer, K. Meerholz, A. Tünnermann, Org. Electron. 11 (2010) 1039.
[64] W.L. Barnes, J. Mod. Opt. 45 (1998) 661.
[65] A. Graf, P. Liehm, C. Murawski, S. Hofmann, K. Leo, M.C. Gather, J. Mater. Chem. C 2 (2014) 10298.
[66] C. Schwieger, B. Chen, C. Tschierske, J. Kressler, A. Blume, J. Phys. Chem. B 116 (2012) 12245.

[67] D.M. Gampe, M. Kaufmann, D. Jakobi, T. Sachse, M. Presselt, R. Beckert, H. Görls, Chem. – A Eur. J. 21 (2015) 7571.
[68] C. Uhrich, D. Wynands, S. Olthof, M.K. Riede, K. Leo, S. Sonntag, B. Maennig, M. Pfeiffer, J. Appl. Phys. 104 (2008) 6.
[69] A. Aoki, S. Fukayama, Electrochemistry 78 (2010) 178.
[70] Y. Shimata, M. Ide, M. Tashiro, M. Katouda, Y. Imamura, A. Saeki, J. Phys. Chem. C 120 (2016) 17887.
[71] N. Joseph, J. Thomas, P. Ahmadiannamini, H. Van Gorp, R. Bernstein, S. De Feyter, M. Smet, W. Dehaen, R. Hoogenboom, I.F.J. Vankelecom, Adv. Funct. Mater. 27 (2017).
[72] J.S. Mattu, G.W. Leach, J. Am. Chem. Soc. 132 (2010) 3204.
[73] A.L. Ayzner, C.J. Tassone, S.H. Tolbert, B.J. Schwartz, J. Phys. Chem. C 113 (2009) 20050.
[74] D.M. Stevens, Y. Qin, M.A. Hillmyer, C.D. Frisbie, J. Phys. Chem. C 113 (2009) 11408.
[75] N. Otsu, IEEE SMC 9 (1979) 62.
[76] D. Nečas, P. Klapetek, Cent. Eur. J. Phys. 10 (2012) 181.
[77] S.v.d. Walt, S.C. Colbert, G. Varoquaux, Comput. Sci. Eng. 13 (2011).
[78] I.S. Ufimtsev, T.J. Martinez, J. Chem. Theory Comput. 5 (2009) 2619.
[79] J. Kästner, J.M. Carr, T.W. Keal, W. Thiel, A. Wander, P. Sherwood, J. Phys. Chem. A 113 (2009) 11856.
[80] A. Schäfer, H. Horn, R. Ahlrichs, J. Chem. Phys. 97 (1992) 2571.
[81] M.A. Rohrdanz, K.M. Martins, J.M. Herbert, J. Chem. Phys. 130 (2009) 054112.
[82] A. Klamt, G. Schuurmann, J. Chem. Soc. Perkin Trans. 2 (1993) 799.
[83] M. Cossi, V. Barone, J. Chem. Phys. 112 (2000) 2427.

Supporting Information

Introducing Double Polar Heads to Highly Fluorescent Thiazoles: Influence on Supramolecular Structures and Photonic Properties

M. Kaufmann[a,b], M. L. Hupfer[b], T. Sachse[b,c], F. Herrmann-Westendorf[b], D. Weiß[a], B. Dietzek[b,c], R. Beckert[a]*, M. Presselt[b,c,d,e]*

[a] Institute of Organic and Macromolecular Chemistry, Friedrich-Schiller-University Jena, Humboldtstraße 10, Jena, 07743, Germany

[b] Institute of Physical Chemistry, Friedrich Schiller University Jena, Helmholtzweg 4, 07743 Jena, Germany

[c] Leibniz Institute of Photonic Technology (IPHT), Albert-Einstein-Str. 9, 07745 Jena, Germany

[d] Center for Energy and Environmental Chemistry Jena (CEEC Jena), Friedrich Schiller University Jena, Jena, Germany

[e] sciclus GmbH & Co. KG, Moritz-von-Rohr Str. 1a, 07745 Jena, Germany

**corresponding authors: Synthesis: rainer.beckert@uni-jena.de ; Thin films: martin.presselt@leibniz-ipht.de*

CONTENT

MATERIALS

Pyridin-2-thioamide, ethyl α-bromo-phenylacetate and Methyl 11-aminoundecanoate were synthesized by literature procedures.[1-3]All chemicals used were reagent grade and purchased from Sigma–Aldrich, TCI or Acros. Solvents were purified by standard procedures. Solvents for UV-Vis and emission spectroscopy were of analytical grade and bought from Sigma–Aldrich. TLC materials were from Merck (Polygram SIL G/ UV254, aluminum oxide 60 F254). The material for column chromatography was also obtained from Merck (silica gel 60; 0.04 – 0.063 mm).

EXPERIMENTAL CHARACTERIZATION METHODS

NMR-SPECTROSCOPY

^{1}H and ^{13}C NMR and the corresponding correlation spectra were recorded with Bruker AC-250 (250 MHz), AC-300 (300 MHz) and AC-400 (400 MHz) spectrometers. Chemical shifts (δ) are given relative to solvents.

MASS-SPECTROMETRY

Mass spectra were measured either with a Finnigan MAT SSQ 710 (EI) or a MAZ 95 XL (ESI) system.

SYNTHESES

4-HYDROXY-5-PHENYL-2-(PYRIDIN-2-YL)-THIAZOLE 1

The compound was synthesized by a slightly modified method of Habenicht et al. [4]

8 g (57.9 mmol) pyridine-2-thioamide, 19.7 g (81.05 mmol) ethyl α-bromo-phenylacetate and 11.9 g (145 mmol) sodium acetate were suspended in 50 mL ethanol and refluxed for 5 hours. The progress of the reaction was monitored *via* TLC. After the reaction was finished, the mixture was cooled down to room temperature and poured into 100 mL water, whereby a yellow solid precipitate. The crude product was filtered off and washed successive with water, cold ethanol and pentane. The solid recrystallized from ethanol/chloroform and dried *in vacuo* to give the title compound as yellow crystals (10.5 g, 41.3 mmol, 71%).The spectroscopic data were in agreement with those reported in literature.

^{1}H NMR (250 MHz, DMSO) δ 11.61 (s, 1H), 8.61 (d, J = 4.7 Hz, 1H), 8.02 – 7.89 (m, 2H), 7.77 (d, J = 7.4 Hz, 2H), 7.52 – 7.35 (m, 3H), 7.22 (t, J = 7.4 Hz, 1H).^{13}C NMR (63 MHz, DMSO) δ 160.85, 159.14, 150.54, 150.19, 138.19, 132.28, 129.27, 126.83, 126.57, 125.37, 118.80, 110.82.); EI-MS *m/z* (%): 254 [M^{*+}].

4-BUTHOXY-5-PHENYL-2-(PYRIDIN-2-YL)-THIAZOLE 2

2 g (7.86 mmol) **1**, 2.2 g potassium carbonate (15.92 mmol) were suspended in 50 mL acetone. The mixture was stirred for 30 min. at 50°C until an orange slurry is formed from the deprotonated thiazole. 1.30 mL 1-iodobutane was added and the mixture was heated to reflux for 18 hours. The progress of the

reaction was monitored *via* TLC. The reaction is finished, when all deprotonated thiazole is consumed. Otherwise 0.6 mL additional 1-iodobutanewere added and the mixture was refluxed for 6 hours again. After cooling down to room temperature the solution was poured into 50 mL water and extracted three times with ethyl acetate. The organic layer was successively washed with saturated sodium carbonate solution, water and brine. The solution was dried over manganese sulfate and the solvent was distilled off. The crude product was purified by column chromatography (silica, $CHCl_3$/heptane 2:1) to yield the title compound as bright yellow solid (2.1 g, 6.77 mmol, 86 %)

^{1}H NMR (400 MHz, $CDCl_3$) δ 8.61 (ddd, J = 4.8, 1.5, 0.9 Hz, 1H), 8.14 (d, J = 7.9 Hz, 1H), 7.84 (dd, J = 8.4, 1.1 Hz, 2H), 7.79 (td, J = 7.7, 1.7 Hz, 1H), 7.41 (t, J = 7.8 Hz, 2H), 7.33 – 7.24 (m, 2H), 4.55 (t, J = 6.6 Hz, 2H), 1.88 (dt, J = 14.4, 6.6 Hz, 2H), 1.63 – 1.51 (m, 2H), 1.04 (t, J = 7.4 Hz, 3H). ^{13}C NMR (101 MHz, 04_CDCl3) δ 160.37, 159.50, 151.36, 149.44, 136.87, 131.93, 128.69, 126.90, 126.66, 124.07, 118.99, 114.43, 70.34, 31.70, 19.35, 13.92.; EI-MS *m/z* (%): 310 [M^{*+}]

METHYL 11-((4-(4-BUTOXY-2-(PYRIDIN-2-YL)-THIAZOL-5-YL)-PHENYL)-SULFONAMIDO)-UNDECANOATE 3

10 mL chlorosulfonic acid were cooled down to 0°C with an ice bath and 500 mg (1.16 mmol) **2** were added in one step. The mixture was stirred for 30 minutes, than the ice bath was removed and the mixture was allowed to warm to room temperature and stirred for additional two hours. Afterwards the reaction mixture was dropped very slowly to 100 mL ice water and stand for 10 minutes without stirring. The yellow precipitate was filtered off and dried *in vacuo*. The solid was used for the next step without further purification.

The solid was dissolved in 50 mL dichloromethane and 860 mg (2.32 mmol) methyl 11-aminoundecanoatewere added. 1.2 mL triethylamine in 50 mL dichloromethane were added dropwise over a period of 15 minutes to the mixture. After the complete addition of triethylamine the mixture was stirred for 5 hours at room temperature. Than the reaction mixture was treated with 100 mL water and extracted with dichloromethane. The organic layer was washed with water and brine and dried over manganese sulfate. The solvent was distilled off and after a column chromatography (silica, $CHCl_3$) the title compound was obtained as yellow oil, which solidifies after cooling in a fridge. (621 mg, 1.03mmol, 64%).

^{1}H NMR (250 MHz, DMSO-d_6) δ 8.61 (d, J = 4.5 Hz, 1H), 8.13 (d, J = 7.9 Hz, 1H), 7.92 (d, J = 8.6 Hz, 2H), 7.87 – 7.76 (m, 3H), 7.33 (dd, J = 7.3, 5.1 Hz, 1H), 4.57 (t, J = 6.6 Hz, 2H), 4.46 (t, J = 6.0 Hz, 1H), 3.65 (s, 3H), 2.96 (q, J = 6.7 Hz, 2H), 2.27 (t, J = 7.5 Hz, 2H), 1.94 – 1.78 (m, 2H), 1.64 – 1.40 (m, 6H), 1.24 (dd, J =

12.3, 5.0 Hz, 12H), 1.02 (t, J = 7.3 Hz, 3H). ^{13}C NMR (63 MHz, CDCl3) δ 174.27, 162.16, 160.85, 150.79, 149.43, 148.22, 137.15, 137.08, 136.50, 127.52, 126.79, 124.61, 119.31, 112.32, 77.51, 77.00, 76.49, 70.67, 60.36, 51.39, 43.28, 34.07, 31.61, 29.64, 29.30, 29.24, 29.14, 29.07, 29.01, 26.49, 24.90, 21.00, 19.32, 14.18, 13.85; EI-MS *m/z* (%): 587 [M^{*+}], 309 (M^{*+} - $C_{12}H_{24}NO_4S$), 254 (M^{*+} - $C_{16}H_{31}NO_4S$).

11-((4-(4-BUTOXY-2-(PYRIDIN-2-YL)-THIAZOL-5-YL)-PHENYL)-SULFONAMIDO)-UNDECANOIC ACID 4

190 mg (3.4 mmol) potassium hydroxide were suspended in 5 mL anhydrous ethanol and stirred at room temperature capped with a calcium chloride tube, until all solid is diluted. 500 mg (850 µmol) **3** were added and the mixture was stirred for additional 18 hours at room temperature. The mixture was poured into 50 mL water, neutralized with acetic acid and extracted with dichloromethane. The organic layer was washed with water and brine and dried over manganese sulfate. After removing the solvent and drying in *in vacuo* the title compound was obtained as yellow powder (465 mg, 810 µmol, 95%).

^{1}H NMR (250 MHz, CDCl3) δ 8.61 (d, J = 4.7 Hz, 1H), 8.12 (d, J = 7.9 Hz, 1H), 7.91 (d, J = 8.7 Hz, 1H), 7.87 – 7.75 (m, 2H), 7.39 – 7.28 (m, 1H), 4.76 (t, J = 6.1 Hz, 1H), 4.57 (t, J = 6.6 Hz, 1H), 2.96 (dd, J = 13.2, 6.7 Hz, 1H), 2.32 (t, J = 7.4 Hz, 1H), 1.95 – 1.76 (m, 1H), 1.66 – 1.38 (m, 3H), 1.23 (d, J = 11.2 Hz, 6H), 1.01 (t, J = 7.3 Hz, 2H). ^{13}C NMR (63 MHz, CDCl3) δ 178.80, 162.19, 160.80, 150.79, 149.46, 137.07, 137.02, 136.47, 127.49, 126.75, 124.60, 119.31, 112.24, 70.64, 43.17, 33.86, 31.58, 29.51, 29.22, 29.15, 29.04, 28.92, 26.40, 24.61, 19.29, 13.82. ; ESI (pos.)-MS *m/z* (%):574,2 $[M+H]^+$, 596,3 $[M+Na]^+$, UV-vis nm (log ε) 288 (3.95), 383 (4.40). fluorescence nm (λex, Φ_{Fl}) 451 (375, 0,76).

4-ETHOXY-5-PHENYL-2-(PYRIDIN-2-YL)-THIAZOLE 5

The procedure was similar to that used for **2** except that instead of 1-iodobutane, 0.95 mL iodoethane was used. For a further purification a column chromatography (silica, $CHCl_3$) was used yielding a yellow solid (1.83 g, 7.86 mmol, 82%).

^{1}H NMR (250 MHz, $CDCl_3$) δ 8.64 (d, *J* = 4.7 Hz, 1H), 8.16 (d, *J* = 7.9 Hz, 1H), 7.94 – 7.70 (m, 3H), 7.44 (t, *J* = 7.6 Hz, 2H), 7.32 (t, *J* = 6.9 Hz, 2H), 4.63 (q, *J* = 7.0 Hz, 2H), 1.54 (t, *J* = 7.0 Hz, 3H); ^{13}C NMR (63 MHz, $CDCl_3$) δ 161.33, 160.19, 152.24, 150.35, 137.78, 132.79, 129.60, 127.84, 127.61, 125.00, 119.88, 115.46, 78.47, 77.96, 77.45, 67.22, 16.21. EI-MS *m/z* (%): 282 [M^{*+}], UV-vis nm (log ε) 273 (3.92), 379 (4.32). fluorescence nm (λex, Φ_{Fl}) 451 (375, 0.95).

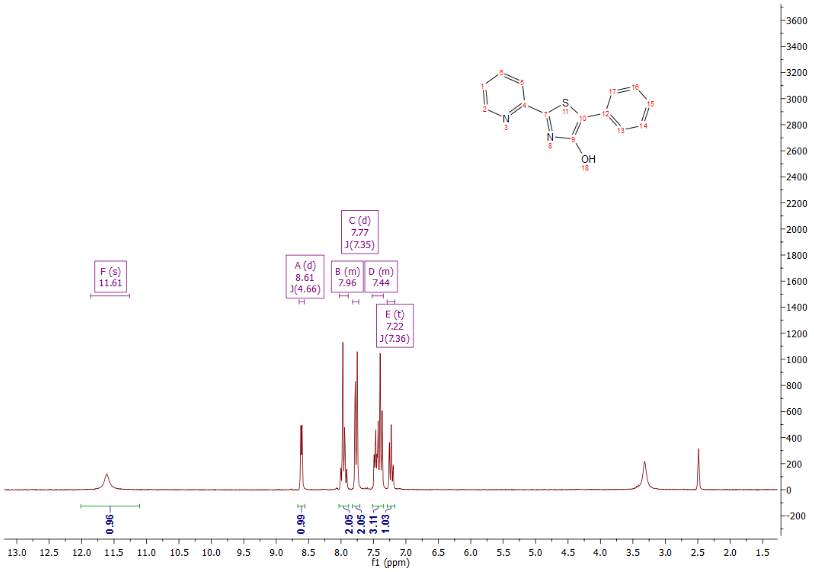

Figure SI 1:^{1}H-NMR spectrum of **1**

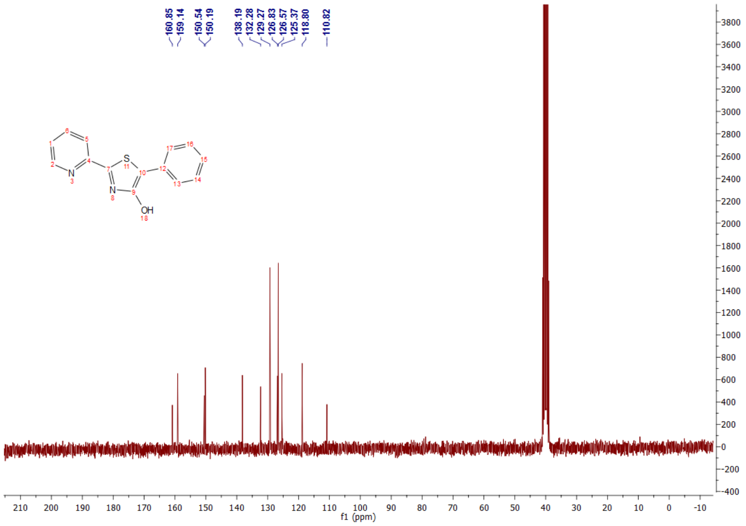

Figure SI 2:^{13}C-NMR spectrum of **1**

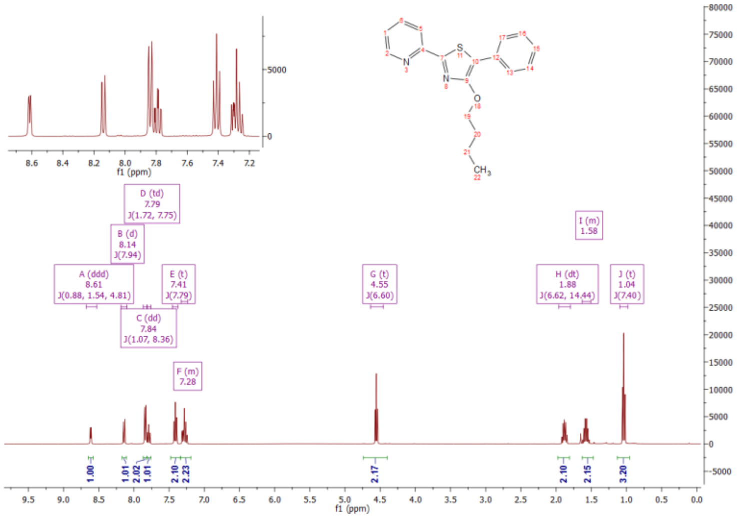

Figure SI 3: ^{1}H-NMR spectrum of **2**

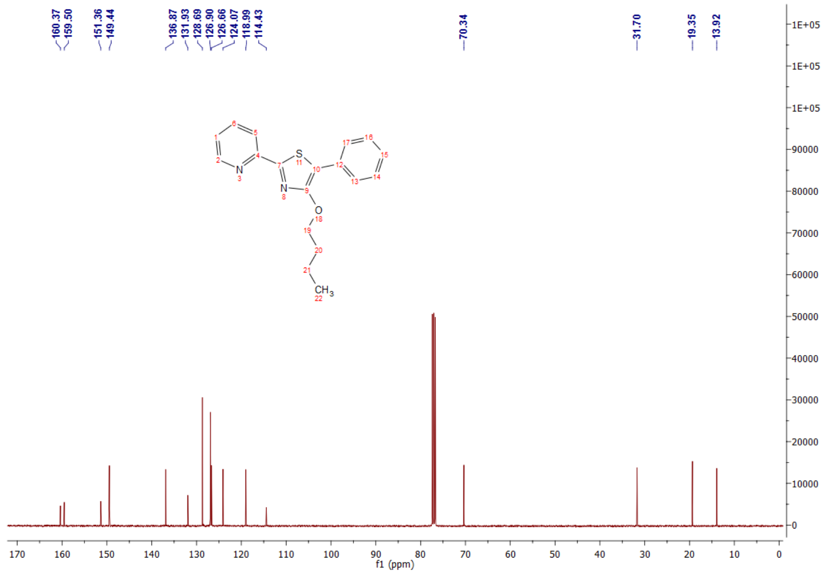

Figure SI 4: ^{13}C-NMR spectrum of **2**

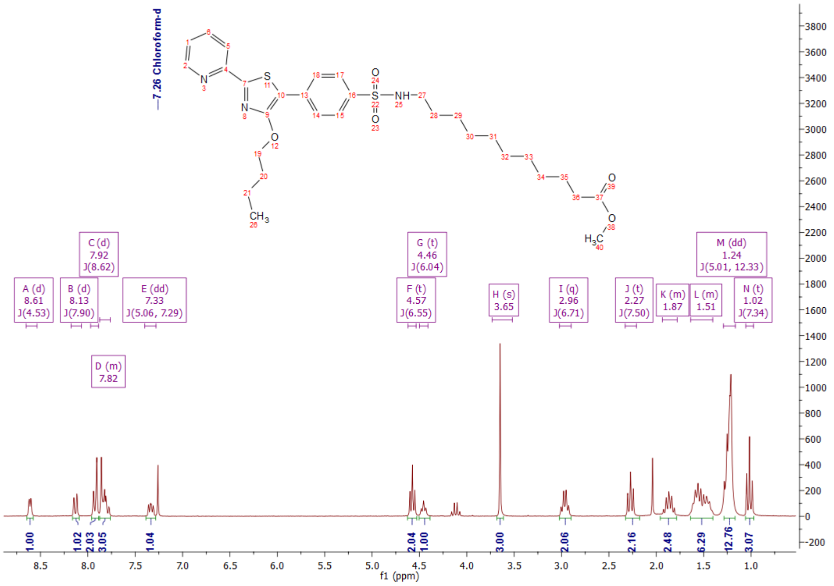

Figure SI 5: ^{1}H-NMR spectrum of **3**

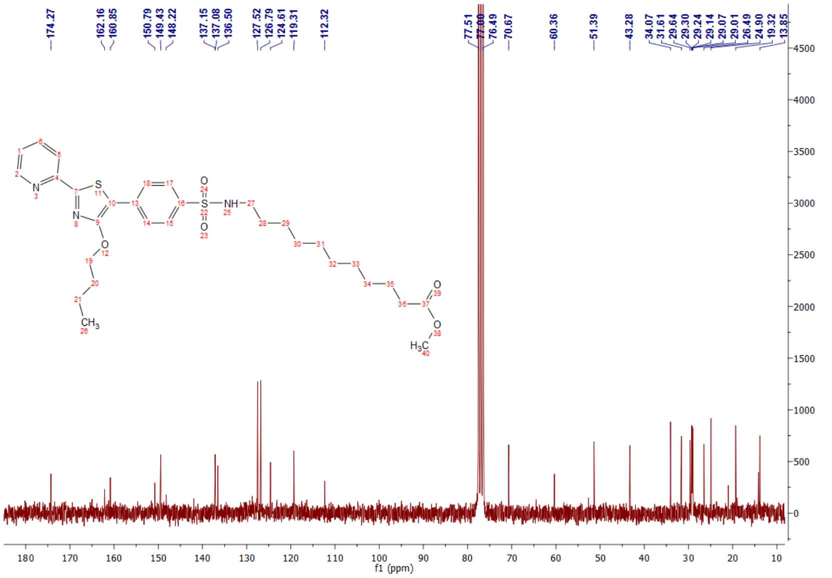

Figure SI 6: ^{13}C-NMR spectrum of **3**

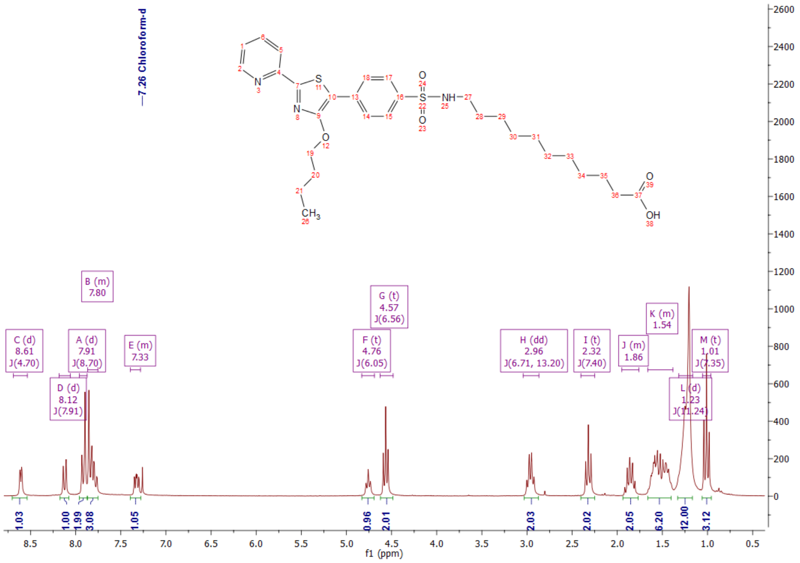

Figure SI 7: ^{1}H-NMR spectrum of **4**

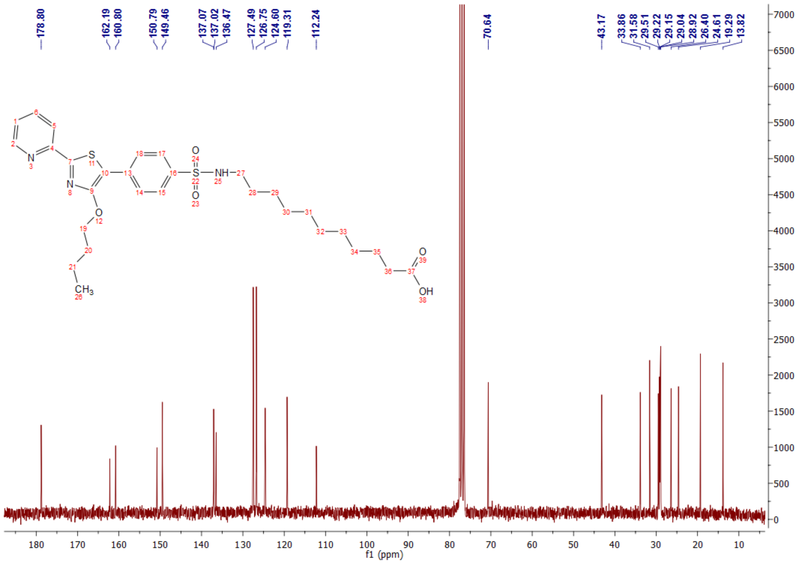

Figure SI 8: ^{13}C-NMR spectrum of **4**

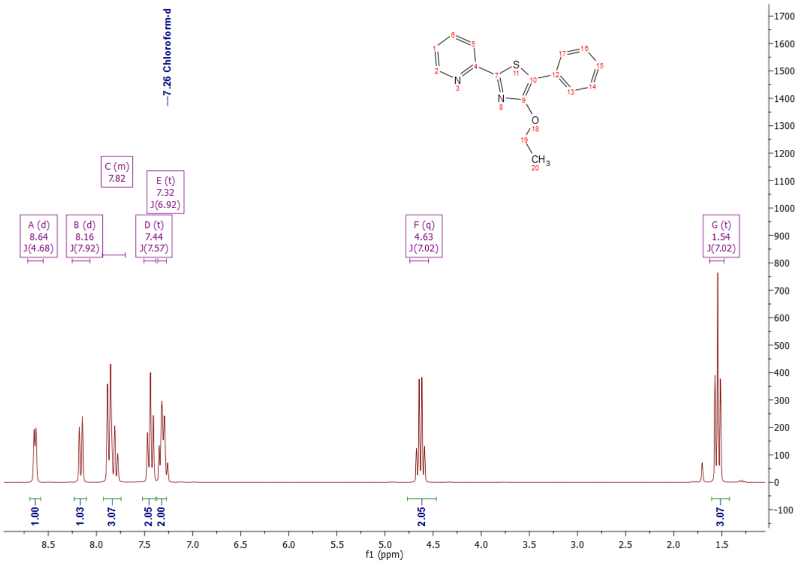

Figure SI 9: 1H NMR spectrum of **5**.

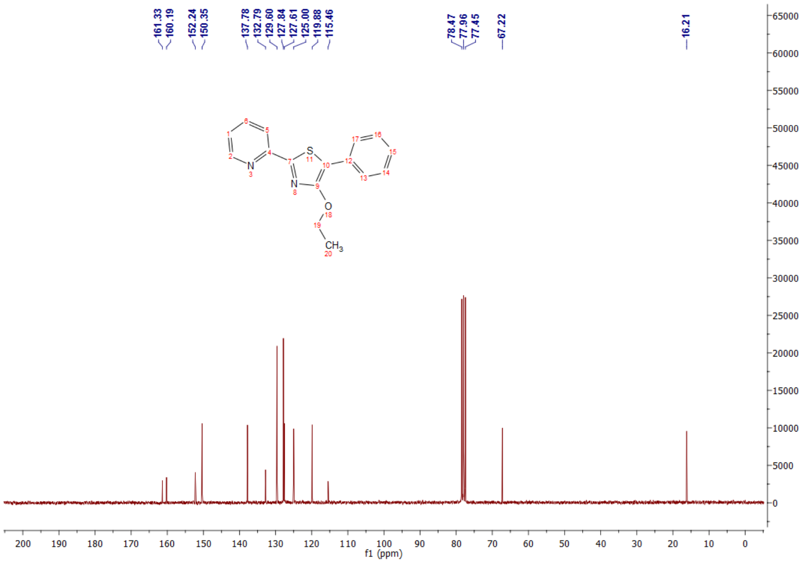

Figure SI 10: 13C NMR spectrum of **5**.

ABSORPTION UND FLUORESCENCE SPECTRA

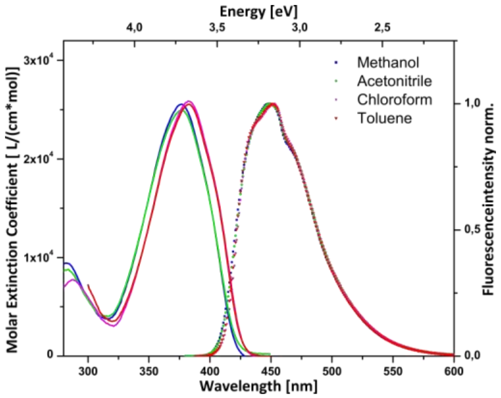

Figure SI 11: Absorption and emission spectra of **4** in various solvents.

The Langmuir monolayers of **4** were deposited onto quartz glass at three different surface pressures (Π_{LB}=1, 7, 12 mN/m) and characterized by means of UV-vis transmission spectroscopy. The obtained absorption spectra, shown in **Fehler! Verweisquelle konnte nicht gefunden werden.**, feature constant wavelengths at maximum absorption (λ_{max}=375 nm) for the varied surface pressure at deposition that are virtually identical to those of the dissolved thiazoles shown in the main text.

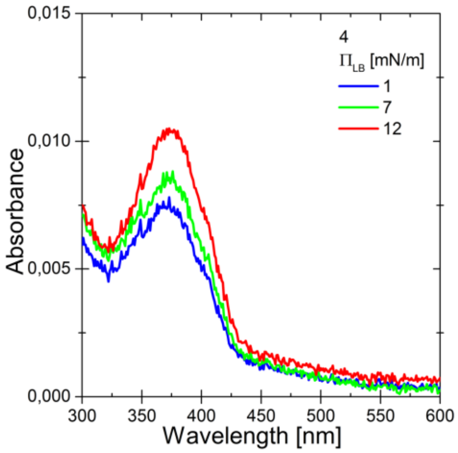

Figure SI 12: Absorption spectra of LB films of **4** deposited at different surface pressures

REFERENCES

[1] Marco H. Klingele, S. Brooker, European Journal of Organic Chemistry 2004 (2004) 3422.

[2] V. Sharma, J.J. Tepe, Organic Letters 7 (2005) 5091.
[3] E. Huerta, Macromolecular rapid communications. 35 (2014) 1320.
[4] S.H. Habenicht, M. Siegmann, S. Kupfer, J. Kübel, D. Weiß, D. Cherek, U. Möller, B. Dietzek, S. Gräfe, R. Beckert, Methods and Applications in Fluorescence 3 (2015) 025005.

[MLH3] On the Control of Chromophore Orientation, Supra-Molecular Structure and Thermodynamic Stability of an Amphiphilic Pyridyl-Thiazol upon Lateral Compression and Spacer Length Variation

Hupfer, M. L.; Kaufmann, M.; Herrmann-Westendorf, F.; Sachse, T.; Roussille, L.; Feller, K.; Weiß, D.; Deckert, V.; Beckert,R.; Dietzek, B.; Presselt, M., ACS Applied Materials and Interfaces , **2017**, 9: 44181-44191

Autor	1	2	3	4	5	6	7	8	9	10	11
Konzeption	x	x					x		x		x
Planung der Untersuchung	x	x			x					x	x
Datenerhebung	x	x			x	x					
Analyse und Interpretation	x	x	x	x	x			x		x	x
Schreiben des Manuskriptes	x	x								x	x
Publikationsäquivalente	1,0	n. a.	n. a.	n. a.	n. a.	n. a.	n. a.	n. a.	n. a.	n. a.	n. a.

ACS APPLIED MATERIALS & INTERFACES
Research Article
Cite This: ACS Appl. Mater. Interfaces 2017, 9, 44181−44191
www.acsami.org

On the Control of Chromophore Orientation, Supramolecular Structure, and Thermodynamic Stability of an Amphiphilic Pyridyl-Thiazol upon Lateral Compression and Spacer Length Variation

Maximilian L. Hupfer,[†,§] Martin Kaufmann,[†,‡] Felix Herrmann-Westendorf,[†,§] Torsten Sachse,[†,§] Ludovic Roussille,[†,§] Karl-Heinz Feller,[∥] Dieter Weiß,[‡] Volker Deckert,[†,§] Rainer Beckert,[‡] Benjamin Dietzek,[†,§] and Martin Presselt*[,†,§,⊥,#]

[†]Institute of Physical Chemistry, Friedrich Schiller University Jena, Helmholtzweg 4, 07743 Jena, Germany
[‡]Institute of Organic and Macromolecular Chemistry, Friedrich Schiller University Jena, Humboldstraße 10, 07743 Jena, Germany
[§]Leibniz Institute of Photonic Technology (IPHT), Albert-Einstein-Str. 9, 07745 Jena, Germany
[∥]FB Med Tech & Biotechnol, University of Applied Sciences Jena, 07745 Jena, Germany
[⊥]Center for Energy and Environmental Chemistry Jena (CEEC Jena), Friedrich Schiller University Jena, Philosophenweg 7a, 07743 Jena, Germany
[#]SciClus GmbH & Co. KG, Moritz-von-Rohr-Str. 1a, 07745 Jena, Germany

Supporting Information

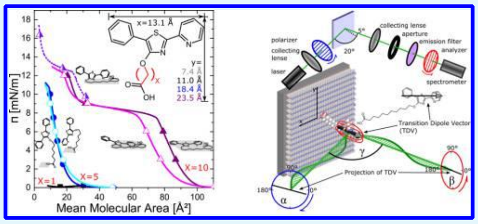

ABSTRACT: The supramolecular structure essentially determines the properties of organic thin films. Therefore, it is of utmost importance to understand the influence of molecular structure modifications on supramolecular structure formation. In this article, we demonstrate how to tune molecular orientations of amphiphilic 4-hydroxy thiazole derivatives by means of the Langmuir−Blodgett (LB) technique and how this depends on the length of an alkylic spacer between the thiazole chromophore and the polar anchor group. Therefore, we characterize their corresponding supramolecular structures, thermodynamic, absorption, and fluorescence properties. Particularly, the polarization-dependence of the fluorescence is analyzed to deduce molecular orientations and their possible changes after annealing, i.e., to characterize the thermodynamic stability of the individual solid state phases. Because the investigated thiazoles are amphiphilic, the different solid state phases can be formed and be controlled by means of the Langmuir−Blodgett (LB) technique. This technique also allows to deduce atomistic supramolecular structure motives of the individual solid phases and to characterize their thermodynamic stabilities. Utilizing the LB technique, we demonstrate that subtle molecular changes, like the variation in spacer length, can yield entirely different solid state phases with distinct supramolecular structures and properties.

KEYWORDS: *Langmuir−Blodgett, Langmuir−Blodgett isotherms, Langmuir−Blodgett hysteresis, thiazoles, OLED, thermodynamic stability, molecular orientation, supramolecular structure*

■ INTRODUCTION

Organic thin films are basic components in organic (opto)-electronic devices like solar cells,[1] light-emitting diodes (OLEDs),[2] and field effect transistors.[3] Besides the molecular characteristics,[4−6] the supramolecular structure essentially determines the thin film and device properties, particularly absorption[7−9] and emission spectra,[10,11] radiation characteristics,[12,13] quantum efficiency,[14−18] open circuit voltage,[19] conductivity,[20−22] excited state dynamics,[23,24] and electrochemical potentials.[7,25,26] Therefore, several techniques have been developed to control the supramolecular structure of organic molecules, such as antiparallel supramolecular arrangement of dipolar donor−acceptor dyes,[27] co-self-organization,[28] layer-by-layer deposition,[29,30] and (self)assembly at hetero-interfaces. The latter involves film formation at liquid−gas interfaces, such as in the Langmuir−Blodgett (LB) technique,[31−35] or precipitation at liquid−liquid interfaces,[36] or self-assembling (monolayers) at solid−liquid interfaces[37,38]

Particularly, the LB technique allows for advanced control of the supramolecular structure formation if the molecules spread onto the LB trough surface are amphiphilic.[35,39] Additionally, supramolecular geometries and their optoelectronic properties

Received: September 14, 2017
Accepted: November 29, 2017
Published: November 29, 2017

ACS Publications

DOI: 10.1021/acsami.7b13042
ACS Appl. Mater. Interfaces 2017, 9, 44181−44191

Scheme 1. Syntheses and Structure of the Compounds

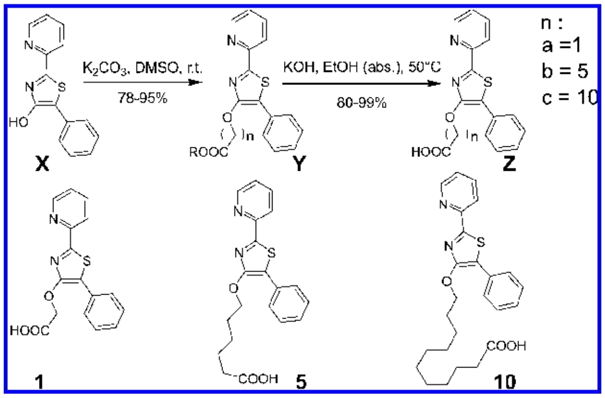

inherently depend on the molecular parameters, such as the chromophore, chemical nature, number, and position of polar and nonpolar moieties in the amphiphile.[40−42] Recently, it was shown that even the lengths of spacers between polar and nonpolar moieties heavily influence the geometries of supramolecular structures.[43]

In the present article, we vary a single parameter, namely the length of the alkylic spacer between a rather nonpolar 2-pyridyl-4-hydroxy-5-phenyl-1,3-thiazole and the polar head (COOH), and use the Langmuir technique to tune the orientation of the thiazole chromophores in the Langmuir layers. Such a control of molecular orientation is of particular importance for the development of active materials to be used in OLEDs.[2] Therefore, we employ thiazoles, which are structurally similar to firefly luciferin,[44−46] as one example of highly fluorescent dyes. These dyes can be versatilely functionalized to yield various extents of amphiphilicity.[47] First studies about the fluorescence of 2-pyridyl-thiazoles by Grummt et al. showed that these compounds offer fluorescence quantum yields up to 95% in water, depending on the pH value.[48] Because of their slow nonradiative deactivation and the resulting high fluorescence quantum yields, they were used in dye-sensitized solar cells[49] and as blue emitters in polymer backbones.[50,51] The employed structural motive of linking a functional moiety, in this case the chromophore, with an anchor group for surface adhesion via spacers is well established in surface science,[52] e.g., for functionalizing various nanoparticles from metallic[53] to oxidic ones.[54]

Here, we present the synthesis of the above-mentioned thiazoles with alkylic spacers of different lengths, i.e., the number of CH$_2$-groups be, 1, 5, or 10, and characterize the structure and thermodynamic properties of their supramolecular assemblies in Langmuir- and LB layers.[55,56] Therefore, LB isotherms are analyzed and LB hysteresis experiments and polarization-dependent absorption and fluorescence spectroscopy were performed. Polarization-dependent fluorescence spectroscopy is used to characterize molecular orientation before and after annealing the deposited LB layers. Thus, we investigate whether the supramolecular structures are in a thermodynamic favorable geometry right after LB deposition or not and instead reorient due to annealing to arrive in a thermodynamic favorable geometry.

RESULTS AND DISCUSSION

The starting 4-hydroxy-1,3-thiazole X was obtained via Hantzsch cyclization reaction from 2-pyridinecarbothioamide with ethyl α-bromo-phenylacetate, with pyridine as base, as described by Täuscher et al.[57] The hydroxyl group was alkylated with a ω-bromoalkanoic ester to both increase the solubility and install the amphiphilic precursor with different spacer lengths, as shown in Scheme 1. First attempts of Williamson type etherification with potassium carbonate in acetone leads to good yields for the methyl acetate derivative,[47] but only poor to moderate yields are obtained for longer halogenalkanes. Therefore, the reaction conditions were changed to potassium carbonate in dimethyl sulfoxide at room temperature whereby all ethers could be isolated in good to excellent yields.[58] The last reaction step is the saponification of the ester groups. The standard procedure in ethanol with aqueous potassium hydroxide solution at room temperature[47] works well for the methyl acetate derivative, whereas with the hexanoic ester and the undecanoic ester, no conversions were observed. Different approaches with variation of temperature and base did not improve the yields. Finally, the conversions with dried potassium hydroxide in absolute ethanol and exclusion of moisture gave the desired products 1, 5, and 10 in very good yields (80−99%, NMR- and mass-spectrometric characterizations of the products are shown in Supporting Information (SI)).

Because of the amphiphilic character, the dyes have a good solubility in a broad range of solvents. 1 shows the best solubility for protic polar solvents like water and even nonpolar solvents like toluene. In contrast, 5 and 10 are only water soluble in alkaline or strong acidic solutions due to the deprotonation of the carboxylic group or the protonation of the pyridine moiety,[44] respectively, with the highest solubility in chloroform and tetrahydrofuran.

Π(A)-Isotherms. The surface pressure (Π) vs mean molecular area (A), isotherms of the 4-hydroxy-1,3-thiazole, are shown in Figure 1. The Π(A)-isotherm of 1 is flat even at small areas per molecule. Hence, 1 is not sufficiently amphiphilic to form stable Langmuir monolayers on the LB trough but rather dissolves in the water subphase.

For 5, the isotherm shows a steep rise after the liquid phase (20−40 Å^2) that indicates a solid phase with an extrapolated

DOI: 10.1021/acsami.7b13042
ACS Appl. Mater. Interfaces 2017, 9, 44181−44191

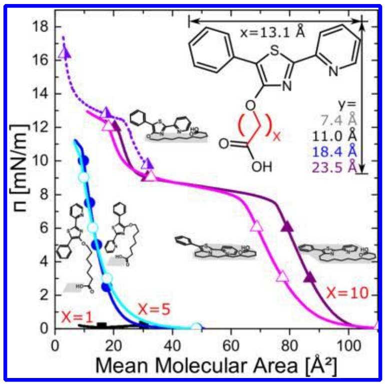

Figure 1. Average Π(A) isotherm (typically three individual isotherms as shown in detail in the SI) of the thiazole (solid line) with three different spacer lengths, **1** (black), **5** (blue), and **10** (violet), recorded at a water phase (filled symbols) and 1% citric acid (CA) water phase (open symbols). Dotted line: nonaveraged Π(A) isotherm of **10** at lower mean molecular areas. The mean molecular areas for the possible molecular orientations are schematically visualized by gray shades beneath the Lewis structures.

minimum molecular area (A_0) of 18.0 Å^2 (Figure 1, blue). In the case of monomolecular Langmuir films with uniform molecular orientations, the latter can be deduced from the molecular packing density in the Langmuir layer or the A_0 areas that are inversely proportional to the packing density. Therefore, for different molecular orientations, the theoretical geometric molecular area requirements on the subphase surface are compared with the measured A_0 areas. The molecular orientations are then identified by the best fit between the theoretical areas and the single experimental A_0 area. In the case of **5**, a small area of 19.2 Å^2 is obtained when multiplying the molecular y length of **5** (7.4 Å, see Figure 1) with the sulfur van der Waals diameter (2.6 Å). Because this area approximately fits the determined A_0 area of 18.0 Å^2, we conclude that the chromophore is vertically oriented on the water surface in the solid phase. At a surface pressure of Π = 10.5 mN/m, the isotherm shows a characteristic bend that could be due to a supramolecular phase change of the solid phase.[59] The influence of subphase acidity (1% citric acid in subphase: pH = 2.4) on the isotherm is weak, as shown in Figure 1 (default (deionized ultrapure water): pH = 6). Therefore, for both subphases, we deduce orientations of **5** with the pyridine, which would change the Π(A) isotherm if it could be pulled into the subphase by increasing acidity, distant from the subphase, i.e., the left-hand side structure in Figure 1 with a large pyridine-subphase distance.

The molecule **10**, with the longest spacer, shows multiple phases. The isotherm starts rising at larger molecular areas (Figure 1, purple), as compared with **5**, leading to a first solid phase I between 75 and 100 Å^2 and a characteristic $A_{0,\mathrm{I}}$ value of 94.0 Å^2. If we divide $A_{0,\mathrm{I}}$ by the long molecular axis (x in Figure 1) length (13.1 Å) the resulting width (y in Figure 1) is 7.2 Å, similar to the y length determined for the same chromophore in **5**. Therefore, we conclude that the molecule is oriented horizontally at the water surface in the first solid phase of **10**. The flexible alkyl chains are expected to fit the interstitial spaces. Increasing the acidity of the subphase lowers $A_{0,\mathrm{I}}$ significantly to 85.4 Å^2. This decrease is attributed to a tilted orientation of the chromophore on the water surface due to enhanced interactions between the pyridine moiety and the water subphase. This tilt of the chromophore allows for partial overlapping of the chromophores, yielding a denser packing and the lowered $A_{0,\mathrm{I}}$ value.

After reaching a surface pressure of Π ≈ 7.5 mN/m, the isotherm of **10** shows a phase transition at which the monolayer is easily compressible, as indicated by the small slope of the Π(A) isotherm. This transition phase is compressible because local molecular reorientations release lateral stress from the densely packed phase I Langmuir layer. At 35 Å^2, a second solid phase starts to form (default pH = 6 subphase) and features an $A_{0,\mathrm{II}}$ area of 42.8 Å^2. This area is a little larger than what we would expect from turning the molecule around its long axis to a vertical orientation on the water surface (34.0 Å^2, as deduced from the sulfur van der Waals diameter (2.6 Å), and the molecular x length (13.1 Å)) if just the chromophore geometry is considered. The difference between these areas is assigned to the alkyl spacer. Because of the tilt of the chromophore, the interaction with the subphase changes from facial, including the polarizable π system and all heteroatoms, to binding just via two heteroatoms, as shown in Figure 1. This binding might be enhanced by decreasing the pH value, but that apparently does not influence the isotherm and presumably not the supramolecular geometry significantly in the second solid phase, as shown in Figure 1. The supramolecular structure in this densely packed second solid phase is additionally influenced by π−π interactions between the chromophores.

At Π = 12.5 mN/m, a second phase transition starts but the experimental setup limits the minimal molecular area per run. Therefore, a second Π(A) isotherm was measured with a starting point at the onset of the second solid phase (dashed line in Figure 1), i.e., higher thiazole concentrations are used in the solution to spread onto the subphase surface. At the resulting increased surface concentration, assembly into the two-dimensional (2D) structures of the second solid phase described before might be hindered and locally different supramolecular assemblies such as micelles might be formed. However, this second isotherm is just slightly shifted to larger mean molecular areas in the second solid phase as compared with the first isotherm starting at low surface concentrations. This second isotherm shows that after the second transition phase, a third solid phase with even denser packing is formed, which is characterized by an $A_{0,\mathrm{III}}$ area of 12.1 Å^2.

This $A_{0,\mathrm{III}}$ area of **10** is even smaller than the value determined for the first solid phase of **5** (18.0 Å^2). Nevertheless, we assign a vertical chromophore orientation to the third solid phase of **10** according to the discussion of **5**. The difference between the A_0 values of **5** and **10** at similar molecular orientations is inherently linked to the spacer length. Although we expect a regular packing for **5**, the spacer in **10** exceeds the chromophore lengths, which probably causes interstitial gaps. If these gaps are filled with horizontally oriented thiazoles, the effective packing density for **10** is higher than in the case of **5**, thus explaining the difference in the A_0 values. Consequently, for the maximum molecular order, spacers should not be too long to avoid formation of interstitial gaps, cf. the work on fullerene self-assembled monolayers by Halik and co-workers.[43,60] In summary, we find that the spacer length has a dramatic influence on the supramolecular structures that are accessible in Langmuir films. The discussed

DOI: 10.1021/acsami.7b13042
ACS Appl. Mater. Interfaces 2017, 9, 44181−44191

supramolecular structures differ in their molecular orientation, their interaction with the subphase, and their intermolecular interactions. The latter were studied in more detail by means of hysteresis experiments and are discussed in the next section.

Hysteresis. The intermolecular interactions between the amphiphiles in the individual solid state phases are probed by compression to target surface pressures that are characteristic for the individual phases. Subsequent expansion of the film and further compression−expansion (CE) cycles will cause hysteresis of the $\Pi(A)$ isotherm if thermodynamically stable aggregates are formed in the probed phase.[61] In this case, their binding energy is larger than the thermal energy at the given experimental conditions (25.18−25.44 meV). The energy that is stored in a Langmuir layer at compression can be directly determined from the area between two subsequently determined $\Pi(A)$ isotherms.

*Thiazole **5**.* In the case of **5**, the A_0 areas strongly decrease from 18.1 to 4 Å^2 with the first two CE cycles and converges at approximately 3 Å^2 for more CE cycles, as shown in Figure 2. These tiny areas, in particular compared to the molecular dimensions, cannot be assigned to single molecules in a two-dimensional packing pattern but rather indicate the facile formation of three-dimensional (3D) aggregates, such as micelles. Thus, because no stable 2D layers can be obtained from **5**, it is not further considered in detail in what follows.

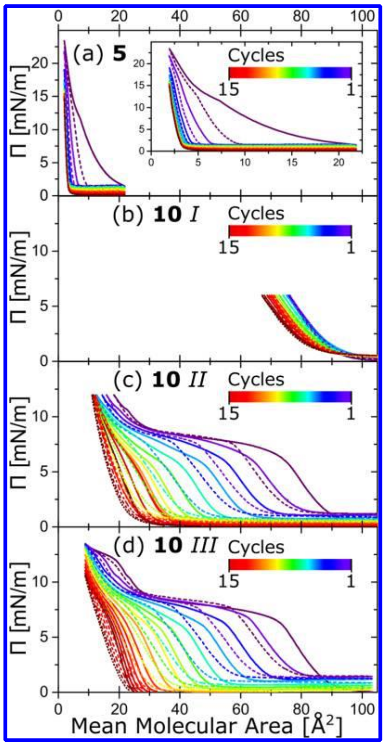

Figure 2. Compression−expansion hysteresis of a $\Pi(A)$ isotherm of **5** (a) and **10** (b−d) with 15 compression and expansion cycles.

*Thiazole **10**.* In the case of **10**, no stable aggregates are expected to form in the first solid phase because just edge-to-edge interactions between the molecules shall be possible. Nevertheless, a small decrease of the A_0 values (from 95 to 85 Å^2 at 15 CE cycles) can be found at subsequent CE cycles, as shown in Figure 2b, whereas the change between $\Pi(A)$ isotherms within a single CE cycle is negligible.

In stark contrast, when probing the second solid phase (Π_{target} = 12 mN/m), the $A_{0,\text{II}}$ areas significantly decrease within each CE cycle (see Figure 2), thus indicating the formation of aggregates that are stable at room temperature. These aggregates are bound by π−π interactions between the chromophores.[59] The necessary face-to-face chromophore orientations are enabled by the tilts around the molecular edges when forming phase II, as derived above from the A_0 areas. In phase II of **10**, we consider the aggregation energy to equal a dimerization energy. Because the phase I characteristics have virtually vanished from the $\Pi(A)$ isotherm after 15 CE cycles, the dimerization energy was determined by calculating the difference between the first compression and the last compression, last expansion, respectively, thus yielding ΔG_{II} = 30−32 meV. Note that the $A_{0,\text{II}}$ areas of the second phase shift with repeated CE cycles to areas lower than the one determined in the previous section (see Table 1), possibly due to improved packing upon repeated CE cycles.

Table 1. Extrapolated Minimum Molecular Area A_0 of the Different Phases of the Thiazol with a Spacer Length of 5 and 10 at a Water- and 1% Citric Acid (CA) Phase[a]

substance (subphase)	phase 1: A_0 [Å^2]	phase 2: A_0 [Å^2]	phase 3: A_0 [Å^2]
5	n/a	n/a	18.0
5 (1% CA)	n/a	n/a	18.1
10	94.0	42.8	*12.1*
10 (1% CA)	85.4	45.0	*12.1*

[a] Values in italic represent A_0 areas extrapolated from $\Pi(A)$ isotherms, with a starting point at the onset of the second solid phase.

When targeting phase III of **10**, the evolution of the $\Pi(A)$ isotherms with the CE cycles is very similar to the one when targeting the second solid phase, as shown in Figure 2. The deduced dimerization energy (ΔG_{III} = 31.25 meV) does virtually not differ from the one in phase II, as π−π interactions constantly dominate the intermolecular interactions[59] with altered molecular orientation. Thus, although the short spacer in **5** does not allow for the formation of thermodynamically stable 2D Langmuir layers, the longer spacer in **10** enables stable 2D Langmuir layers for the second and third solid phase. However, the determined intermolecular binding energies for **10** are just slightly above the thermal energy at room temperature.

Atomic Force Microscopy (AFM). For morphological characterization by means of atomic force microscopy (AFM), Langmuir layers of **10** were deposited onto quartz glass substrates. The resulting Langmuir−Blodgett (LB) layers show a smooth topography when deposited at surface pressures Π_{LB} within or below the first solid phase, as shown in Figure 3. The corresponding phase images, which are sensitive to the chemical interaction between the molecules in the layer and the AFM tip, show a random orientation of small aggregates for

DOI: 10.1021/acsami.7b13042
ACS Appl. Mater. Interfaces 2017, 9, 44181−44191

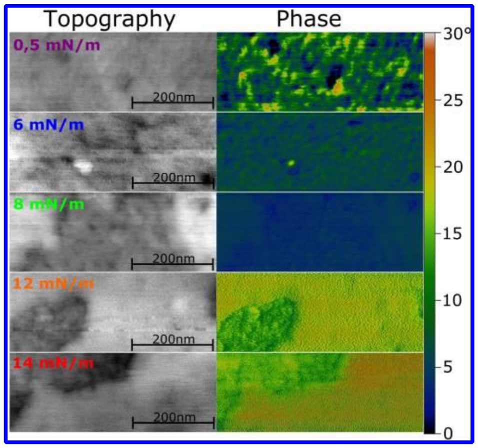

Figure 3. Atomic force microscopy (AFM) images of LB films of **10** at five different deposition pressures; left: topography images; and right: phase images. The height profiles, indicated by the straight lines in the left column, are given in the SI (Figure S6).

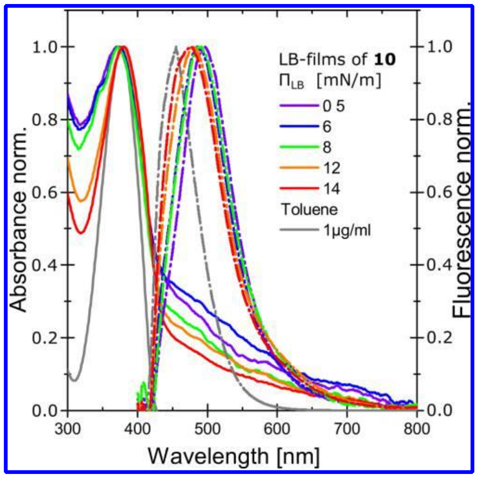

Figure 4. Normalized absorbance (solid lines) and fluorescence emission (dotted lines) of LB films of **10** at five different Π_{LB} pressures (0.5, 6, 8, 12, and 14 mN/m) and solution (toluene 1 μg/mL).

the liquid phase (deposition pressure Π_{LB} = 0.5 mN/m) that becomes more uniform with higher surface pressure at deposition (Π_{LB}: 6, 8 mN/m), i.e., increasing supramolecular order in phase I.

When increasing Π_{LB} to 12 mN/m (phase II), the AFM phase image shows the coexistence of two individual solid phases. The border between them can also be seen in the topography image and is characterized by a step of approx. 2 nm, see Supporting Information. We assign these phases to phases I and II, as identified from the $\Pi(A)$ isotherms. A similar pattern is found for Π_{LB} = 14 mN/m. Because at Π_{LB} = 14 mN/m, the Langmuir layer is at the edge between the second transition phase and the third solid phase, we might tentatively assign the two phases in the AFM images at Π_{LB} = 14 mN/m to phases II and III of **10**. However, because of the phase coexistence and the limited scanned area in AFM, an unambiguous assignment of the different phases is not possible in the framework of the herein reported research, except for phase I of **10**, as discussed above. Within few days, supramolecular rearrangement changes the morphology, as shown in Supporting Information.

Absorption and Fluorescence Spectra of Solutions and LB Films. To identify the influence of the molecular order, which can be varied between different solid phases just in the case of **10**, on optical properties of **10**, UV−vis absorption and fluorescence spectra of LB films deposited at different surface pressures were measured and compared with spectra of **10** dissolved in toluene. The absorption spectra essentially feature single absorption peaks with maxima at ∼375 nm, as shown in Figure 4, which can be assigned to the $S_0 \rightarrow S_1$ transition. This maximum slightly shifts to higher wavelengths with an increasing molecular order at higher deposition pressures, Π_{LB} (372 nm at 0.5 mN/m to 379 nm at 14 mN/m). Accordingly, the fluorescence maxima shifts from 495 to 476 nm with an increasing molecular order, with slight changes of the spectral shape. This change is assigned to alterations in the vibrational progression with raising intensity of the 0−0 transition upon denser packing with increasing deposition pressures, cf. changed vibrational progression with varied morphologies of small molecule chromophores[62−66] and polymers.[67−69] However, the fluorescence maximum of the toluene solution is at even shorter wavelengths (455 nm).

Polarization-Dependent Fluorescence of LB Layers. Finally, the thermodynamic stabilities of deposited individual phases of **5** and **10**, i.e., Langmuir−Blodgett rather than the Langmuir layers characterized by hysteresis experiments above, are evaluated by analysis of possible changes of their molecular orientation upon thermal annealing. Therefore, the molecular orientation of LB films that were deposited on the quartz glass is investigated by means of polarization-dependent fluorescence spectroscopy.

In the polarization-dependent fluorescence measurements, the LB film is irradiated in grazing incidence (20° to the substrate normal vector) and the emitted light is collected in a back-scattering geometry 5° to the substrate normal, as visualized in Figure 5. In the case of upright standing molecules (transition dipole vector, TDV, parallel to the substrate normal), maximum absorption and therefore maximum emission $I(\alpha)$ would be obtained at $\alpha = 0°$ polarization and no absorption and emission would be detected at $\alpha = 90°$. Consequently, a periodic change of the fluorescence intensity $I(\alpha)$ will be obtained for systematic tuning of the polarization angle α of the incident light if the TDVs are oriented uniformly.

Isotropic Molecule Orientations. In contrast to uniformly oriented chromophores, no periodic $I(\alpha)$ relation is obtained for isotropically oriented chromophores, as in the case of chromophores embedded in an isotropic matrix, like drop-cast poly(methyl methacrylate) (PMMA) represented by the gray line in Figure 6A. Particularly, $I(\alpha)$ of **10** in PMMA monotonically decreases with larger polarization angles of the incident light, as shown in Figure 6A. We attribute this decrease in the fluorescence intensity to static quenching upon reorientation of the chromophores during fluorescence

DOI: 10.1021/acsami.7b13042
ACS Appl. Mater. Interfaces 2017, 9, 44181−44191

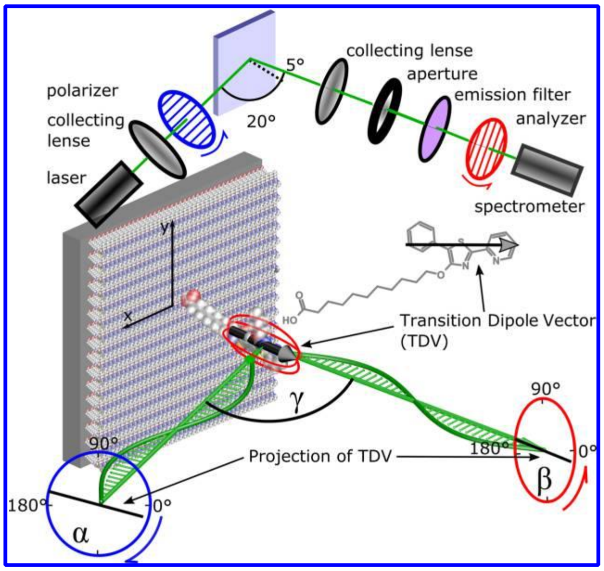

Figure 5. Scheme of the setup for detection of polarization-dependent fluorescence.

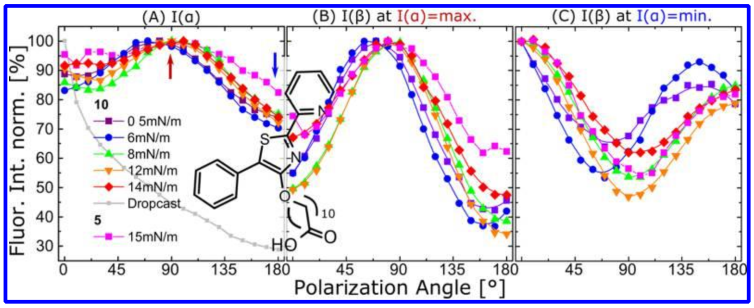

Figure 6. Polarization-dependent fluorescence of LB films of **5** and **10** at five different Π_{LB}-pressures (0.5, 6, 8, 12, and 14 mN/m) in comparison with a drop-casted sample (**10** in a PMMA matrix; gray line). The measurements were performed without analyzer (panel A), excitation at 90° (panel B) and 0° polarization (panel C), and rotation of the analyzer (panels B and C).

detection. This reorientation from random molecule orientations after drop casting to energetically more favorable supramolecular geometries is supposed to be driven by thermalized absorbed energy, i.e., by photoannealing.[70] The quenching might be due to self-quenching or unfavorable rotation of the TDVs.

Thiazole 5. In the case of **5**, nonuniform chromophore orientation is expected if the Langmuir layer is deposited at Π_{LB} = 15 mN/m, as discussed above in the hysteresis section. However, in contrast to the drop-cast PMMA film (c(**10**) = 5 wt %) discussed before, the fluorescence is not monotonically decreasing but rather slightly varies between 100 and 90% normalized fluorescence intensity ($\alpha < 90°$). At ~90° polarization of the incident light, the fluorescence is most intense and decreases to 83% at 180°, as shown in Figure 6A.

The fact that the fluorescence quenching upon photoannealing is significantly weaker than in the case of the PMMA drop-cast film is attributed to the energetically favorable LB assembly of **5**. Furthermore, the above discussed formation of stable 3D aggregates, such as micelles, in the Langmuir layer of **5** would result in isotropic chromophore orientation and constant $I(\alpha)$ if photoannealing could be neglected. The fact that $I(\alpha)$ passes a maximum at 90° indicates a slight preferred chromophore orientation in the direction the substrate was pulled out of the LB trough (direction of y-axis in Figure 5).

Thiazole 10. In the case of **10**, $I(\alpha)$ of all LB films show a pronounced maxima $I(\alpha)_{max}$ between 75 and 95° polarization and slight photoannealing. Notably, the difference between $I(\alpha)_{max}$ and $I(\alpha)_{min}$, i.e., the fluorescence contrast, $\Delta I = I(\alpha)_{max} - I(\alpha)_{min}$, is virtually independent of Π_{LB}, instead of increasing for more ordered films, as expected for increasing Π_{LB}. For perfectly uniform chromophore orientations, we would expect ΔI = 100%, as discussed above, but instead detect ΔI values between 25 and 30% for all LB films of **10**. Possible reasons for this low fluorescence contrast are convolution of the sinoidal $I(\alpha)$ dependence with a Gaussian distribution of chromophore orientations, as shown in Figure 7A, or superposition of two distinct phases with different chromophore orientations and distinct, phase-shifted sinoidal $I(\alpha)$-dependencies, as shown in Figure 7B, or a combination of both.

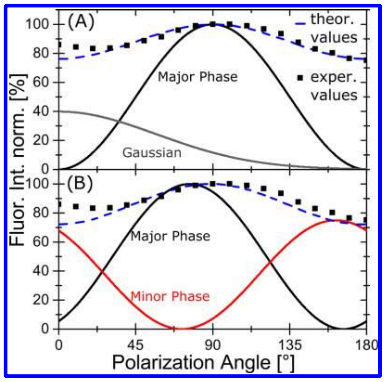

Figure 7. Modeling of the dependence of the experimental fluorescence of LB films on the polarization angle of the excitation light. $I(\alpha)$ is broadened (A) by convolving $I(\alpha)$ of a uniform chromophore orientation with a Gaussian distribution and (B) by superposition of two distinct phases with shifted individual $I(\alpha)$ dependencies.

Considering the individual phases of **10**, we find that $I(\alpha)_{max}$ is constant at 75° polarization when increasing Π_{LB} from pressures corresponding to the liquid till those of the first solid phase (0.5, 6 mN/m). When targeting the first transition and solid phases II and III (8, 12, and 14 mN/m), $I(\alpha)_{max}$ shifts to α = 95°. This shift again might be explained by two different models: either the more densely packed films at Π_{LB} > 6 mN/m, i.e., beyond solid phase I, involve chromophores that are not parallel to the substrate surface but slightly rotated toward the substrate normal or the ratio between two solid phases with phase-shifted $I(\alpha)$-dependencies changes. The latter model is in full accordance with the AFM-derived coexistence of at least two phases after deposition beyond Π_{LB} values characteristic for phase I.

In the case of two distinct phases, upon fixing the polarizer in the position of the maximum, the minimum fluorescence at 90, 0°, predominantly the phase with the larger, smaller weight is probed, respectively, see Figure 6. For both cases, the polarization of the light emitted by the LB layers is measured by means of an analyzer, as shown in Figure 5. Probing of the major phase ($I(\beta,\alpha = 90°)$) essentially yields maxima between 70 and 80°, and the significantly enhanced fluorescence contrasts between ΔI = 55 and 65%, as shown in Figure 6B. Thus, the predominant chromophore orientation is close to 90° (parallel to the y-axis in Figure 5), i.e., chromophores are laying rather flat on the substrate surface. The coincidence between the dominant chromophore orientation at $\alpha \approx 90°$ and the LB deposition direction for basically all investigated LB films indicates a distinct influence of the deposition on the chromophore orientation. However, the fluorescence contrast $\Delta I(\beta)$ is still rather independent from Π_{LB}, thus indicating that the molecular order in the major phase is already high at low Π_{LB}, presumably due to self-assembly, and cannot be increased significantly by increasing Π_{LB} in the major solid phase.

As shown in Figure 6, probing the minor phase ($I(\beta,\alpha = 0°)$) yields increased fluorescence contrasts as well and maxima at 0 and 180° for Π_{LB} > 6 mN/m, i.e. chromophores and TDVs within the x, z-plane in Figure 5. In the case of phase I (Π_{LB} = 0.5, 6 mN/m), the maximum and minimum is shifted to lower polarization angles by ~23°, as compared with $I(\beta)$ of the other phases. Furthermore and in contrast to $I(\alpha)$, the fluorescence contrast $\Delta I(\beta)$ in the minor phase systematically increases with larger Π_{LB} values, except for Π_{LB} = 14 mN/m where the 2D layers might be already disrupted, cf. **5**.

Annealing of LB Films. After having identified that deposition of phase III of **10** (Π_{LB} = 14 mN/m) involves perturbation of the 2D layer, the thermodynamic stability of the individual phases of **10** is tested by means of thermal annealing to yield thermodynamic characteristics of deposited LB layers, cf. thermodynamic characterization of nondeposited Langmuir layers by means of hysteresis experiments above. Therefore, $I(\beta)$ at fixed α (90, 180°) were compared before and after short thermal annealing (50 °C, 15 min). Variations in $I(\beta)$ upon thermal annealing would indicate reorganization to thermodynamically more favorable supramolecular structures.

As shown in Figure 8, rather small changes of $I(\beta)$ upon thermal annealing can be observed for any of the investigated LB films, except slightly weakening the photoannealing discussed above. For the liquid phase (Π_{LB} = 0.5 mN/m, $\Delta I(\beta)^{major}$ = 60%, $\Delta I(\beta)^{minor}$ < 35%), thermal annealing reduces photoannealing just in the minor phase, whereas for the even less ordered disturbed phase III LB film (Π_{LB} = 14 mN/m, $\Delta I(\beta)^{major}$ = 50%, $\Delta I(\beta)^{minor}$ < 35%), thermal annealing reduced photoannealing in both the major and minor phase. For the relatively highly ordered phase II LB film (Π_{LB} = 12 mN/m, $\Delta I(\beta)^{major}$ = 65%, $\Delta I(\beta)^{minor}$ < 50%), where

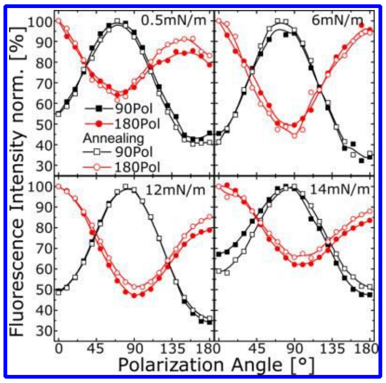

Figure 8. Polarization-dependent fluorescence of LB films of **10** at four different surface pressures; 90° (black) and 180° (red) polarization of the excitation light, before (filled symbols) and after annealing (50 °C, 15 min.; open symbols).

DOI: 10.1021/acsami.7b13042
ACS Appl. Mater. Interfaces 2017, 9, 44181−44191

we deduced coexistence with a second phase (presumably phase I), thermal annealing influences just the minor phase. The latter shows already a high degree of molecular ordering, as deduced from the large $\Delta I(\beta)^{\mathrm{minor}}$ fluorescence contrast above. With respect to the given annealing parameters, the most stable LB film is the one deposited at Π_{LB} = 6 mN/m (phase I, $\Delta I(\beta)^{\mathrm{major}}$ = 65%, $\Delta I(\beta)^{\mathrm{minor}} < 55\%$), where photoannealing is almost negligible and $I(\beta)$ is basically not changed upon thermal annealing. In phase I, the molecular orientation in the Langmuir and the LB film coincide with thermodynamically favorable molecular orientations for interactions with the substrate, thus yielding stable layers after deposition onto the quartz glass.

SUMMARY AND CONCLUSIONS

In the present work, we demonstrate that the molecular orientation of a centrally functionalized amphiphilic 4-hydroxythiazole fluorophore can be tuned by means of the Langmuir technique. We provide evidence that these molecular orientations can be deduced from the LB isotherms, which were differently interpreted for other "T-shaped" molecules in former reports. However, whether or not the molecular orientation can be tuned heavily depends on the length of the alkyl spacer between lipophilic fluorophore and hydrophilic anchor.

To systematically investigate this influence of the spacer length on molecular orientation, three different amphiphilic thiazoles were synthesized, **1**, **5**, and **10**, which possess C_1H_2, C_5H_{10}, and $C_{10}H_{20}$ alkyl spacers, respectively. From $\Pi(A)$ isotherms, we deduced that **1** is not suited for Langmuir−Blodgett (LB) experiments because of water solubility, **5** forms a single solid Langmuir phase, and the long alkyl spacer in **10** allows for the formation of three distinct solid Langmuir phases, with flat, tilted, and upright (same as **5**) oriented chromophores.

However, LB hysteresis experiments readily reveal that the 2D Langmuir layer of **5** is not stable but rather forms 3D assemblies, presumably micelles. In contrast, the long flexible spacer in **10** enables adaption of molecular shapes so that all three phases of **10** appear stable as Langmuir layers on the subphase surface. The deduced aggregate formation energies indicate that phases II and III shall be significantly more stable than phase I because of the stronger intermolecular interactions in these phases as compared to that in phase I. The aggregations in phases II and III are driven by $\pi-\pi$ interactions between the planar thiazole chromophores, which are stronger than those in tilted T-shaped amphiphilic terphenylenes reported in the literature. Accordingly, the mean molecular areas phases I, II, and III of **10** are characterized by different molecular orientations.

The stabilities of the films and their molecular orders after deposition onto solid substrates (formation of LB layers) are evaluated by means of atomic force microscopy (AFM) and analysis of the polarization-dependence of the LB layer fluorescence. The AFM pictures of LB layers of **10** reveal the coexistence of at least two distinct phases when LB films were deposited at surface pressures that are characteristic for phases II and III. Thus, the AFM results clearly support the hypothesis of accessing different thin-film phases when compressing the Langmuir layer, as deduced from the LB isotherms.

The coexistence of two sets with distinct molecular orientation after deposition was revealed as well from the polarization-dependence of the fluorescence of particular LB layers. The dominant chromophore orientation in the LB layers is that of phases I and II determined for the Langmuir layers in the direction of the deposition. The largest fluorescence contrast of 65% for polarized incident light is found for LB films deposited at surface pressures characteristic for phase I and II of **10**. The altered phase III LB film and the one deposited at the liquid phase show less molecular order, which can be slightly improved due to both thermal and photoannealing. In contrast, phase II and particularly phase I LB films show almost no change in the polarization dependence of the fluorescence upon both types of annealing, which is attributed to the impact of chromophore−substrate interaction in the case of phase I. The latter is also presumed to cause phase II existing rather locally embedded in phase I in the LB films after deposition, which fits with the phase differences seen in the AFM pictures. The weak influence of annealing on the fluorescence contrast points to thermodynamically stable films upon LB fabrication, particularly for phase I of **10**.

Finally, we demonstrated in the herein presented work that the chromophore orientations of centrally functionalized thiazoles, in contrast to those of other reported T-shaped amphiphiles, can be tuned by means of lateral compression of their Langmuir layers. These highly fluorescent thiazoles, whose thin-film properties were studied the first time in this work, show strong intermolecular $\pi-\pi$ interactions favored by the planarity of the chromophores. This planarity is enabled by the heteroatoms in the thiazole. However, our research shows that the accessibility of the different molecular orientations in the corresponding thin-film phases heavily depends on subtle molecular changes, such as the length of spacers between chromophores and polar heads. The suitability of distinct molecular structures for the formation of those layers can be easily investigated by means of LB hysteresis experiments. However, the supramolecular structures present in the Langmuir layers and their thermodynamic stability might be altered when deposited to solid substrates as LB layers because of substrate−chromophore interactions. Thus, our study highlights that the first Langmuir layer shall be possibly deposited at different parameters than subsequent layers. In this respect, the results of the present work are essential for the general design of layer architectures from organic amphiphiles. Further studies need to reveal how molecular orientations can be controlled in successively deposited Langmuir layers.

EXPERIMENTAL DETAILS

Langmuir−Blodgett (LB) Films. Solutions of the dyes (1 mg/mL in $CHCl_3$) were carefully spread onto the subphase (ultrapure water) of the LB trough (KSV NIMA Alternate L 105 and LB Trough). For complete evaporation of $CHCl_3$, a time of 10 min was given before moving the barriers. Then, the barriers were compressed with 5 mm/min to record the isotherms. The compression and expansion were performed with the same speed and without dwell time at the reversal points. Quartz glass substrates were treated with acetone and isopropanol in the ultrasonic bath for each solvent three times, and the substrates were stored in isopropanol. The deposition of LB films on the quartz glass (30 mm × 5 mm × 1 mm) was done using Z-type dipping with constant pressure and a dipping speed of 5 mm/min.

Scanning Force Microscopy. Atomic force microscopy (AFM) was carried out using a Veeco Digital Instruments AFM Nanoscope IIIa, with a head Dimension 3100 in tapping mode on air with a silicon tip (radius < 8 nm) at 300 kHz, with a force constant of E40 N/m (Budget Sensors Tap 300-G). Aged samples have been measured using a JPK Nanowizard III (NT-MDT tip NSG10), see Supporting Information.

DOI: 10.1021/acsami.7b13042
ACS Appl. Mater. Interfaces 2017, 9, 44181−44191

UV–Vis Absorption and Fluorescence Spectroscopy. For the absorption spectroscopic measurements, we used a UV–vis (Varian: Cary 5000) spectrometer in transmission mode. The fluorescence measurements were made on a custom-built setup. This consists of an Isoplane 320 Spectrograph with a cooled Pixis CCD Camera from Princeton Instruments. A fiber-coupled 5 mW laser with a 405 nm output wavelength was used as the excitation source (incident under 55°), and the emissions were detected under 35° to the normal. Long pass filters with low self-fluorescence from ITOS were used to block scattered excitation light. For the polarized fluorescence measurements, a polarizer was placed in front of the excitation and an analyzer was placed in front of the spectrometer. Here, the sample was excited under an angle of 20° and the emission was detected under an angle of 5° with respect to the substrate normal. A notch filter (Thorlabs NF405-13) was placed in front of the spectrograph to block scattered excitation light and for a better filter correction for low signals. The polarizers were rotated in 10° steps. The data were corrected by a self-written LabView and C++ program. These programs remove last scattered excitation light and cosmic rays. The maxima of the fluorescence spectra were analyzed by a self-written Mathematica program.

■ ASSOCIATED CONTENT

Ⓢ Supporting Information

The Supporting Information is available free of charge on the ACS Publications website at DOI: 10.1021/acsami.7b13042.

2-Pyridyl-4-hydroxy-5-phenyl-1,3-thiazole synthesis, materials, Figures S1–S8 (PDF)

■ AUTHOR INFORMATION

Corresponding Author

*E-mail: martin.presselt@leibniz-ipht.de. Phone: +49 3641 206418.

ORCID

Maximilian L. Hupfer: 0000-0001-8890-0684
Felix Herrmann-Westendorf: 0000-0003-0471-1902
Torsten Sachse: 0000-0002-2205-5024
Volker Deckert: 0000-0002-0173-7974
Benjamin Dietzek: 0000-0002-2842-3537
Martin Presselt: 0000-0002-5579-0260

Notes

The authors declare no competing financial interest.

■ ACKNOWLEDGMENTS

The authors are grateful to the Deutsche Forschungsgemeinschaft DFG (PR 1415/2) and Bundesministerium für Bildung und Forschung (BMBF FKZ 03EK3507) for financial support. T. Sachse acknowledges the German Federal Environmental Foundation for his fellowship. We thank Andrea Csáki for support in collection and analysis of atomic force microscopy data.

■ REFERENCES

(1) Mishra, A.; Bäuerle, P. Small Molecule Organic Semiconductors on the Move: Promises for Future Solar Energy Technology. *Angew. Chem., Int. Ed.* **2012**, *51*, 2020–2067.

(2) Jou, J.-H.; Kumar, S.; Agrawal, A.; Li, T.-H.; Sahoo, S. Approaches for Fabricating High Efficiency Organic Light Emitting Diodes. *J. Mater. Chem. C* **2015**, *3*, 2974–3002.

(3) Sirringhaus, H. 25th Anniversary Article: Organic Field-Effect Transistors: The Path Beyond Amorphous Silicon. *Adv. Mater.* **2014**, *26*, 1319–1335.

(4) Presselt, M.; Schnedermann, C.; Schmitt, M.; Popp, J. Prediction of Electron Densities, the Respective Laplacians and Ellipticities in Bond-Critical Points of Phenyl-CH-Bonds via Linear Relations to Parameters of Inherently Localized CD Stretching Vibrations and 1H-NMR-Shifts. *J. Phys. Chem. A* **2009**, *113*, 3210–3222.

(5) Presselt, M.; Schnedermann, C.; Müller, M.; Schmitt, M.; Popp, J. Derivation of Correlation Functions to Predict Bond Properties of Phenyl-CH Bonds Based on Vibrational and H-1 NMR Spectroscopic Quantities. *J. Phys. Chem. A* **2010**, *114*, 10287–10296.

(6) Fitzner, R.; Mena-Osteritz, E.; Mishra, A.; Schulz, G.; Reinold, E.; Weil, M.; Koerner, C.; Ziehlke, H.; Elschner, C.; Leo, K.; Riede, M.; Pfeiffer, M.; Uhrich, C.; Baeuerle, P. Correlation of pi-Conjugated Oligomer Structure with Film Morphology and Organic Solar Cell Performance. *J. Am. Chem. Soc.* **2012**, *134*, 11064–11067.

(7) Das, S.; Herrmann-Westendorf, F.; Schacher, F. H.; Täuscher, E.; Ritter, U.; Dietzek, B.; Presselt, M. Controlling Electronic Transitions in Fullerene van der Waals Aggregates via Supramolecular Assembly. *ACS Appl. Mater. Interfaces* **2016**, *8*, 21512–21521.

(8) Herrmann, F.; Engmann, S.; Presselt, M.; Hoppe, H.; Shokhovets, S.; Gobsch, G. Correlation Between Near Infrared-Visible Absorption, Intrinsic Local and Global Sheet Resistance of Poly(3,4-Ethylenedioxy-Thiophene) Poly(Styrene Sulfonate) Thin Films. *Appl. Phys. Lett.* **2012**, *100*, No. 153301.

(9) Gampe, D. M.; Kaufmann, M.; Jakobi, D.; Sachse, T.; Presselt, M.; Beckert, R.; Görls, H. Stable and Easily Accessible Functional Dyes: Dihydrotetraazaanthracenes as Versatile Precursors for Higher Acenes. *Chem. - Eur. J.* **2015**, *21*, 7571–7581.

(10) Würthner, F.; Kaiser, T. E.; Saha-Möller, C. R. J-Aggregates: From Serendipitous Discovery to Supramolecular Engineering of Functional Dye Materials. *Angew. Chem., Int. Ed.* **2011**, *50*, 3376–3410.

(11) Biesmans, G.; Verbeek, G.; Verschuere, B.; van der Auweraer, M.; De Schryver, F. C. On the fluorescence of anthracene chromophores in langmuir-blodgett films. *Thin Solid Films* **1989**, *169*, 127–142.

(12) Flämmich, M.; Gather, M. C.; Danz, N.; Michaelis, D.; Bräuer, A. H.; Meerholz, K.; Tünnermann, A. Orientation of Emissive Dipoles in OLEDs: Quantitative In Situ Analysis. *Org. Electron.* **2010**, *11*, 1039–1046.

(13) Mayr, C.; Schmidt, T. D.; Brütting, W. High-Efficiency Fluorescent Organic Light-Emitting Diodes Enabled by Triplet-Triplet Annihilation and Horizontal Emitter Orientation. *Appl. Phys. Lett.* **2014**, *105*, No. 183304.

(14) Presselt, M.; Herrmann, F.; Hoppe, H.; Shokhovets, S.; Runge, E.; Gobsch, G. Influence of Phonon Scattering on Exciton and Charge Diffusion in Polymer-Fullerene Solar Cells. *Adv. Energy Mater.* **2012**, *2*, 999–1003.

(15) Beenken, W. J. D.; Herrmann, F.; Presselt, M.; Hoppe, H.; Shokhovets, S.; Gobsch, G.; Runge, E. Sub-Bandgap Absorption in Organic Solar Cells: Experiment and Theory. *Phys. Chem. Chem. Phys.* **2013**, *15*, 16494–16502.

(16) Presselt, M.; Bärenklau, M.; Rösch, R.; Beenken, W. J. D.; Runge, E.; Shokhovets, S.; Hoppe, H.; Gobsch, G. Sub-Bandgap Absorption in Polymer-Fullerene Solar Cells. *Appl. Phys. Lett.* **2010**, *97*, No. 253302.

(17) Shewmon, N. T.; Watkins, D. L.; Galindo, J. F.; Zerdan, R. B.; Chen, J.; Keum, J.; Roitberg, A. E.; Xue, J.; Castellano, R. K. Enhancement in Organic Photovoltaic Efficiency Through the Synergistic Interplay of Molecular Donor Hydrogen Bonding and π-Stacking. *Adv. Funct. Mater.* **2015**, *25*, 5166–5177.

(18) Li, Z.; Bian, J.; Wang, Y.; Jiang, F.; Liang, G.; He, P.; Hou, Q.; Tong, J.; Liang, Y.; Zhong, Z.; Zhou, Y.; Tian, W. Effect of Alkyl Chain Length on the Photovoltaic Performance of Oligothiophene-Based Small Molecules. *Sol. Energy Mater. Sol. Cells* **2014**, *130*, 336–346.

(19) Poelking, C.; Tietze, M.; Elschner, C.; Olthof, S.; Hertel, D.; Baumeier, B.; Würthner, F.; Meerholz, K.; Leo, K.; Andrienko, D. Impact of Mesoscale Order on Open-Circuit Voltage in Organic Solar Cells. *Nat. Mater.* **2015**, *14*, 434–439.

(20) Chen, Y.; Feng, Y.; Gao, J.; Bouvet, M. Self-Assembled Aggregates of Amphiphilic Perylene Diimide–Based Semiconductor

Molecules: Effect of Morphology on Conductivity. *J. Colloid Interface Sci.* **2012**, *368*, 387−394.

(21) Grozema, F. C.; Siebbeles, L. D. A. Mechanism of Charge Transport in Self-Organizing Organic Materials. *Int. Rev. Phys. Chem.* **2008**, *27*, 87−138.

(22) Presselt, M.; Herrmann, F.; Shokhovets, S.; Hoppe, H.; Runge, E.; Gobsch, G. Sub-Bandgap Absorption in Polymer-Fullerene Solar Cells Studied by Temperature-Dependent External Quantum Efficiency and Absorption Spectroscopy. *Chem. Phys. Lett.* **2012**, *542*, 70−73.

(23) Kar, H.; Gehrig, D. W.; Laquai, F.; Ghosh, S. J-Aggregation, its Impact on Excited State Dynamics and Unique Solvent Effects on Macroscopic Assembly of a Core-Substituted Naphthalenediimide. *Nanoscale* **2015**, *7*, 6729−6736.

(24) De la Cadena, A.; Pascher, T.; Davydova, D.; Akimov, D.; Herrmann, F.; Presselt, M.; Wächtler, M.; Dietzek, B. Intermolecular Exciton−Exciton Annihilation in Phospholipid Vesicles Doped with [Ru(bpy)2dppz]2+. *Chem. Phys. Lett.* **2016**, *644*, 56−61.

(25) Kitchen, B.; Awartani, O.; Kline, R. J.; McAfee, T.; Ade, H.; O'Connor, B. T. Tuning Open-Circuit Voltage in Organic Solar Cells with Molecular Orientation. *ACS Appl. Mater. Interfaces* **2015**, *7*, 13208−13216.

(26) Zhong, S.; Zhong, J. Q.; Wee, A. T. S.; Chen, W. Molecular Orientation and Electronic Structure at Organic Heterojunction Interfaces. *J. Electron Spectrosc. Relat. Phenom.* **2015**, *204*, 12−22.

(27) Bürckstümmer, H.; Tulyakova, E. V.; Deppisch, M.; Lenze, M. R.; Kronenberg, N. M.; Gsänger, M.; Stolte, M.; Meerholz, K.; Würthner, F. Efficient Solution-Processed Bulk Heterojunction Solar Cells by Antiparallel Supramolecular Arrangement of Dipolar Donor−Acceptor Dyes. *Angew. Chem., Int. Ed.* **2011**, *50*, 11628−11632.

(28) Würthner, F.; Chen, Z. J.; Hoeben, F. J. M.; Osswald, P.; You, C. C.; Jonkheijm, P.; von Herrikhuyzen, J.; Schenning, A.; van der Schoot, P.; Meijer, E. W.; Beckers, E. H. A.; Meskers, S. C. J.; Janssen, R. A. J. Supramolecular p-n-Heterojunctions by Co-Self-Organization of Oligo(P-Phenylene Vinylene) and Perylene Bisimide Dyes. *J. Am. Chem. Soc.* **2004**, *126*, 10611−10618.

(29) Ariga, K.; Hill, J. P.; Ji, Q. Layer-By-Layer Assembly as a Versatile Bottom-Up Nanofabrication Technique for Exploratory Research and Realistic Application. *Phys. Chem. Chem. Phys.* **2007**, *9*, 2319−2340.

(30) Wang, Y.; Angelatos, A. S.; Caruso, F. Template Synthesis of Nanostructured Materials via Layer-by-Layer Assembly. *Chem. Mater.* **2008**, *20*, 848−858.

(31) Ariga, K.; Yuki, H.; Kikuchi, J.-I.; Dannemuller, O.; Albrecht-Gary, A.-M.; Nakatani, Y.; Ourisson, G. Monolayer Studies of Single-Chain Polyprenyl Phosphates. *Langmuir* **2005**, *21*, 4578−4583.

(32) Jin, J.; Li, L. S.; Li, Y.; Zhang, Y. J.; Chen, X.; Wang, D.; Jiang, S.; Li, T. J.; Gan, L. B.; Huang, C. H. Structural Characterizations of C60-Derivative Langmuir−Blodgett Films and Their Photovoltaic Behaviors. *Langmuir* **1999**, *15*, 4565−4569.

(33) Angelova, A.; Ionov, R. Monolayer and Spectroscopic Studies of an Amphiphilic (Phenylethynyl)anthracene Probe in Pure and Mixed Films with Charged and Neutral Lipids. *Langmuir* **1999**, *15*, 7199−7207.

(34) Modlińska, A.; Bauman, D. The Langmuir-Blodgett Technique as a Tool for Homeotropic Alignment of Fluorinated Liquid Crystals Mixed with Arachidic Acid. *Int. J. Mol. Sci.* **2011**, *12*, 4923−4945.

(35) Ariga, K.; Yamauchi, Y.; Mori, T.; Hill, J. P. 25th Anniversary Article: What Can Be Done with the Langmuir-Blodgett Method? Recent Developments and its Critical Role in Materials Science. *Adv. Mater.* **2013**, *25*, 6477−6512.

(36) Miyazawa, K.; Kuwasaki, Y.; Obayashi, A.; Kuwabara, M. C60 Nanowhiskers Formed by the Liquid−liquid Interfacial Precipitation Method. *J. Mater. Res.* **2002**, *17*, 83−88.

(37) Würthner, F.; Yao, S.; Beginn, U. Highly Ordered Merocyanine Dye Assemblies by Supramolecular Polymerization and Hierarchical Self-Organization. *Angew. Chem., Int. Ed.* **2003**, *42*, 3247−3250.

(38) Zhang, X.; Görl, D.; Stepanenko, V.; Würthner, F. Hierarchical Growth of Fluorescent Dye Aggregates in Water by Fusion of Segmented Nanostructures. *Angew. Chem., Int. Ed.* **2014**, *53*, 1270−1274.

(39) Langmuir, I. The Constitution and Fundamental Properties of Solids and Liquids. Ii. Liquids.1. *J. Am. Chem. Soc.* **1917**, *39*, 1848−1906.

(40) Novak, M.; Jäger, C. M.; Rumpel, A.; Kropp, H.; Peukert, W.; Clark, T.; Halik, M. The Morphology of Integrated Self-Assembled Monolayers and their Impact on Devices − a Computational and Experimental Approach. *Org. Electron.* **2010**, *11*, 1476−1482.

(41) Yao, Y.; Xue, M.; Chen, J.; Zhang, M.; Huang, F. An Amphiphilic Pillar[5]arene: Synthesis, Controllable Self-Assembly in Water, and Application in Calcein Release and TNT Adsorption. *J. Am. Chem. Soc.* **2012**, *134*, 15712−15715.

(42) Yu, G.; Jie, K.; Huang, F. Supramolecular Amphiphiles Based on Host−Guest Molecular Recognition Motifs. *Chem. Rev.* **2015**, *115*, 7240−7303.

(43) Jäger, C. M.; Schmaltz, T.; Novak, M.; Khassanov, A.; Vorobiev, A.; Hennemann, M.; Krause, A.; Dietrich, H.; Zahn, D.; Hirsch, A.; Halik, M.; Clark, T. Improving the Charge Transport in Self-Assembled Monolayer Field-Effect Transistors: From Theory to Devices. *J. Am. Chem. Soc.* **2013**, *135*, 4893−4900.

(44) Grummt, U.-W.; Weiss, D.; Birckner, E.; Beckert, R. Pyridylthiazoles: Highly Luminescent Heterocyclic Compounds. *J. Phys. Chem. A* **2007**, *111*, 1104−1110.

(45) Täuscher, E.; Weiß, D.; Beckert, R.; Fabian, J.; Assumpção, A.; Görls, H. Classical heterocycles with surprising properties: the 4-hydroxy-1,3-thiazoles. *Tetrahedron Lett.* **2011**, *52*, 2292−2294.

(46) Dodson, R. M.; Turner, H. W. α-Cyanoalkyl Sulfonates. I. The Reactions of α-Cyanobenzyl Benzenesulfonate. *J. Am. Chem. Soc.* **1951**, *73*, 4517−4519.

(47) Habenicht, S. H.; Schramm, S.; Fischer, S.; Sachse, T.; Herrmann-Westendorf, F.; Bellmann, A.; Dietzek, B.; Presselt, M.; Weiß, D.; Beckert, R.; Görls, H. Tuning the Polarity and Surface Activity of Hydroxythiazoles - Extending the Applicability of Highly Fluorescent Self-Assembling Chromophores to Supra-Molecular Photonic Structures. *J. Mater. Chem. C* **2016**, *4*, 958−971.

(48) Grummt, U.-W.; Weiss, D.; Birckner, E.; Beckert, R. Pyridylthiazoles: Highly Luminescent Heterocyclic Compounds. *J. Phys. Chem. A* **2007**, *111*, 1104−1110.

(49) Menzel, R.; Ogermann, D.; Kupfer, S.; Weiß, D.; Görls, H.; Kleinermanns, K.; González, L.; Beckert, R. 4-Methoxy-1,3-thiazole based donor-acceptor dyes: Characterization, X-ray structure, DFT calculations and test as sensitizers for DSSC. *Dyes Pigm.* **2012**, *94*, 512−524.

(50) Breul, A. M.; Pietsch, C.; Menzel, R.; Schäfer, J.; Teichler, A.; Hager, M. D.; Popp, J.; Dietzek, B.; Beckert, R.; Schubert, U. S. Blue Emitting Side-Chain Pendant 4-Hydroxy-1,3-Thiazoles in Polystyrenes Synthesized by RAFT Polymerization. *Eur. Polym. J.* **2012**, *48*, 1339−1347.

(51) Menzel, R.; Breul, A.; Pietsch, C.; Schäfer, J.; Friebe, C.; Täuscher, E.; Weiß, D.; Dietzek, B.; Popp, J.; Beckert, R.; Schubert, U. S. Blue-Emitting Polymers Based on 4-Hydroxythiazoles Incorporated in a Methacrylate Backbone. *Macromol. Chem. Phys.* **2011**, *212*, 840−848.

(52) Khassanov, A.; Steinruck, H.-G.; Schmaltz, T.; Magerl, A.; Halik, M. Structural Investigations of Self-Assembled Monolayers for Organic Electronics: Results from X-ray Reflectivity. *Acc. Chem. Res.* **2015**, *48*, 1901−1908.

(53) Imahori, H.; Norieda, H.; Ozawa, S.; Ushida, K.; Yamada, H.; Azuma, T.; Tamaki, K.; Sakata, Y. Chain Length Effect on Photocurrent from Polymethylene-Linked Porphyrins in Self-Assembled Monolayers. *Langmuir* **1998**, *14*, 5335−5338.

(54) Jaehne, E.; Oberoi, S.; Adler, H.-J. P. Ultra Thin Layers as New Concepts for Corrosion Inhibition and Adhesion Promotion. *Prog. Org. Coat.* **2008**, *61*, 211−223.

(55) Blodgett, K. B. Monomolecular Films of Fatty Acids on Glass. *J. Am. Chem. Soc.* **1934**, *56*, 495.

(56) Blodgett, K. B. Films Built by Depositing Successive Monomolecular Layers on a Solid Surface. *J. Am. Chem. Soc.* **1935**, *57*, 1007−1022.

(57) Täuscher, E.; Weiß, D.; Beckert, R.; Görls, H. Synthesis and Characterization of New 4-Hydroxy-1,3-thiazoles. *Synthesis* **2010**, *2010*, 1603−1608.

(58) Gampe, D. M.; Nöller, F.; Hänsch, V. G.; Schramm, S.; Darsen, A.; Habenicht, S. H.; Ehrhardt, S.; Weiß, D.; Görls, H.; Beckert, R. Surprising Characteristics of D−A-Type Functional Dyes by Introducing 4-Alkoxythiazoles as the Donor-Unit. *Tetrahedron* **2016**, *72*, 3232−3239.

(59) Antunes, P. A.; Constantino, C. J. L.; Aroca, R. F.; Duff, J. Langmuir and Langmuir−Blodgett Films of Perylene Tetracarboxylic Derivatives with Varying Alkyl Chain Length: Film Packing and Surface-Enhanced Fluorescence Studies. *Langmuir* **2001**, *17*, 2958−2964.

(60) Khassanov, A.; Steinruck, H.-G.; Schmaltz, T.; Magerl, A.; Halik, M. Structural Investigations of Self-Assembled Monolayers for Organic Electronics: Results from X-ray Reflectivity. *Acc. Chem. Res.* **2015**, *48*, 1901−8.

(61) Gao, Y.; Tang, Z.; Watkins, E.; Majewski, J.; Wang, H.-L. Synthesis and Characterization of Amphiphilic Fullerenes and Their Langmuir−Blodgett Films. *Langmuir* **2005**, *21*, 1416−1423.

(62) Spano, F. C. Analysis of the UV/Vis and CD Spectral Line Shapes of Carotenoid Assemblies: Spectral Signatures of Chiral H-Aggregates. *J. Am. Chem. Soc.* **2009**, *131*, 4267−4278.

(63) Spano, F. C. The Spectral Signatures of Frenkel Polarons in H- and J-Aggregates. *Acc. Chem. Res.* **2010**, *43*, 429−439.

(64) Preiß, J.; Jäger, M.; Rau, S.; Dietzek, B.; Popp, J.; Martínez, T.; Presselt, M. How Does Peripheral Functionalization of Ruthenium-(II)−Terpyridine Complexes Affect Spatial Charge Redistribution after Photoexcitation at the Franck−Condon Point? *ChemPhysChem* **2015**, *16*, 1395−1404.

(65) Preiß, J.; Sachse, T.; Herrmann-Westendorf, F.; Ngo, T. H.; Martínez, T. J.; Hill, J. P.; Ariga, K.; Kruk, M. M.; Maes, W.; Presselt, M. Absorption and Fluorescence Features of an Amphiphilic meso-Pyrimidinylcorrole: Experimental Study and Quantum Chemical Calculations. *J. Phys. Chem. A* **2017**, *121*, 8614−8624.

(66) Beenken, W.; Presselt, M.; Ngo, T. H.; Dehaen, W.; Maes, W.; Kruk, M. Molecular Structures and Absorption Spectra Assignment of Corrole NH Tautomers. *J. Phys. Chem. A* **2014**, *118*, 862−871.

(67) Spano, F. C.; Silva, C. H- and J-Aggregate Behavior in Polymeric Semiconductors. *Annu. Rev. Phys. Chem.* **2014**, *65*, 477−500.

(68) Hoffmann, S. T.; Bässler, H.; Köhler, A. What Determines Inhomogeneous Broadening of Electronic Transitions in Conjugated Polymers? *J. Phys. Chem. B* **2010**, *114*, 17037−17048.

(69) Reinspach, J. A.; Diao, Y.; Giri, G.; Sachse, T.; England, K.; Zhou, Y.; Tassone, C.; Worfolk, B. J.; Presselt, M.; Toney, M. F.; Mannsfeld, S.; Bao, Z. Tuning the Morphology of Solution-Sheared P3HT:PCBM Films. *ACS Appl. Mater. Interfaces* **2016**, *8*, 1742−1751.

(70) Lafalce, E.; Toglia, P.; Lewis, J. E.; Jiang, X. Photo Annealing Effect on p-Doped Inverted Organic Solar Cell. *J. Appl. Phys.* **2014**, *115*, No. 244511.

Supporting Information

On the Control of Chromophore Orientation, Supra-Molecular Structure and Thermodynamic Stability of an Amphiphilic Pyridyl-Thiazol upon Lateral Compression and Spacer Length Variation

Maximilian L. Hupfer[1,3], Martin Kaufmann[1,2], Felix Herrmann-Westendorf[1,3],Torsten Sachse[1,3], Ludovic Roussille[1,3], Karl-Heinz Feller[4], Dieter Weiß[2] , Volker Deckert[1,3], Rainer Beckert[2], Benjamin Dietzek[1,3], Martin Presselt[1,3,5,6,*]

[1] Institute of Physical Chemistry, Friedrich Schiller University Jena, Helmholtzweg 4, 07743 Jena, Germany, E-mail: martin.presselt@leibniz-ipht.de, Phone: +49 3641 206418

[2] Institute of Organic and Macromolecular Chemistry, Friedrich Schiller University Jena, Humboldstraße 10, 07743 Jena, Germany,

[3] Leibniz Institute of Photonic Technology (IPHT), Albert-Einstein-Str. 9, 07745 Jena, Germany

[4]University of Applied Sciences, FB Med Tech & Biotechnol, Jena, Germany

[5] Center for Energy and Environmental Chemistry Jena (CEEC Jena), Friedrich Schiller University Jena, Philosophenweg 7a, 07743 Jena, Germany

[6] sciclus GmbH & Co. KG, Moritz-von-Rohr-Str. 1a, 07745 Jena, Germany

*Corresponding author: martin.presselt@leibniz-ipht.de

Syntheses of the materials

General Methods

The starting material 2-Pyridyl-5-phenyl-4-hydroxy-1.3-thiazole **X** was synthesized by literature procedures.[1] All chemicals used were reagent grade and purchased from Sigma–Aldrich, TCI or Acros. Solvents were purified by standard procedures. ^{1}H and ^{13}C NMR and the corresponding correlation spectra were recorded with Bruker AC-250 (250 MHz), AC-300 (300 MHz) and AC-400 (400 MHz) spectrometers. Chemical shifts (δ) are given relative to solvents. Mass spectra were measured either with a Finnigan MAT SSQ 710 (EI) or a MAZ 95 XL (ESI) system. TLC materials were from Merck (Polygram SIL G/ UV254, aluminum oxide 60 F254). The material for column chromatography was also obtained from Merck (silica gel 60. 0.04 – 0.063 mm).

Methyl 2-(5-phenyl-2-(2-pyridyl)-thiazol-4-yloxy)acetate 1a:

2 g (8 mmol) **X**, 1.4 g (10 mmol) potassium carbonate were suspended in 30 mL acetone. The Mixture was stirred for 30 min. at 50°C until an orange slurry is formed from the deprotonated thiazole. 10 mmol alkylhalogenide was added and the mixture was heated to reflux for 18 hours. The progress of the reaction was controlled via TLC. The reaction is finished, when all deprotonated thiazole is consumed. Otherwise 3 mmol additional alkylhalogenide were added and the mixture was refluxed for 6 hours again. After cooling down to room temperature the solution was poured into 50 mL water and extracted three times with ethyl acetate. The organic layer was successive washed with saturated sodium carbonate solution, water and brine. The solution was dry over manganese sulfate and the solvent was distilled off. The crude product was purified by column chromatography (silica, $CHCl_3$/heptane 2:1) to yield the title compound as yellow solid (2.95 g 95% Yield).

^{1}H NMR (400 MHz, $CDCl_3$) δ 8.78 (d, *J* = 4.3 Hz, 1H), 8.32 (d, *J* = 7.9 Hz, 1H), 8.16 – 8.03 (m, 3H), 7.64 (t, *J* = 7.5 Hz, 3H), 7.51 (t, *J* = 7.4 Hz, 1H), 5.33 (s, 2H) 3.51 (s, 3H), DEI-MS *m/z* (%): 326 [M^{*+}].

Ethyl 2-(5-phenyl-2-(2-pyridyl)-thiazol-4-yloxy)hexanoate 1b:

2 g (8 mmol) **X**, 1.4 g (10 mmol) potassium carbonate were suspended in 20 mL DMSO. The Mixture was stirred for 30 min. until an orange solution is formed from the deprotonated thiazole. 10 mmol alkylhalogenide was added and the mixture was stired for 18 hours. The progress of the reaction was controlled via TLC. The reaction is finished, when all deprotonated thiazole is consumed. The solution was poured into 50 mL water and extracted three times with diethylether. The organic layer was successive washed with saturated sodium carbonate solution, water and brine. The solution was dry over manganese sulfate and the solvent was distilled off. The crude product was purified by column chromatography (silica, $CHCl_3$/heptane 2:1) to yield the title compound as yellow solid (2.5 g , 80% Yield).

^{1}H NMR (400 MHz, $CDCl_3$) δ 8.78 (d, *J* = 4.3 Hz, 1H), 8.32 (d, *J* = 7.9 Hz, 1H), 8.16 – 8.03 (m, 3H), 7.64 (t, *J* = 7.5 Hz, 3H), 7.51 (t, *J* = 7.4 Hz, 1H), 5.33 (s, 2H), 4.14 (q, 2H), 1.26 (td, 3H), DEI-MS *m/z* (%): 396 [M^{*+}].

Methyl 2-(5-phenyl-2-(2-pyridyl)-thiazol-4-yloxy)undecanoate 1c:

The reaction was carried out according to the procedure of **1b**. After the described workup procedure the desired product were obtained as yellow solid (2.8 g , 78% Yield).

^{1}H NMR (400 MHz, $CDCl_3$) δ 8.78 (d, *J* = 4.3 Hz, 1H), 8.32 (d, *J* = 7.9 Hz, 1H), 8.16 – 8.03 (m, 3H), 7.64 (t, *J* = 7.5 Hz, 3H), 7.51 (t, *J* = 7.4 Hz, 1H), 5.33 (s, 2H), 3,65 (s, 3H) DEI-MS *m/z* (%): 452 [M^{*+}],

General procedure of saponification of the alkylester 2:

4 eq. potassium hydroxide were suspended in 5 mL water free ethanol and stirred at room temperature capped with a calcium chloride tube, until all solid is diluted. 1 eq. **3** were added and the mixture was stirred for additional 18 hours at room temperature. The mixture was poured into 50 mL water, neutralized with acetic acid and extracted with dichloromethane. The

organic layer was washed with water and brine and dried over manganese sulfate. After removing the solvent and drying in *in vacuo* the title compound was obtained as yellow powder.

2-(5-phenyl-2-(2-pyridyl)-thiazol-4-yloxy)acetic acid 2a:

The reaction was carried out according to the general procedure **2** with 100mg (0.3 mmol) educt **1a**. After the described workup procedure 95 mg (99% Yield) of the desired product were obtained as yellow solid.

^{1}H NMR (400 MHz, MeOD) δ 8.78 (d, *J* = 4.3 Hz, 1H), 8.32 (d, *J* = 7.9 Hz, 1H), 8.16 – 8.03 (m, 3H), 7.64 (t, *J* = 7.5 Hz, 3H), 7.51 (t, *J* = 7.4 Hz, 1H), 5.33 (s, 2H), DEI-MS *m/z* (%): 312 [M^{*+}], 254 [M^{*+}]-$C_2H_3O_2$, 121 [M^{*+}]-$C_{10}H_8NO_3$, UV/vis (MeOH): λ_{max} (log ε): 377nm (4,34), Fluorescence (MeOH): λ_{max} (λ_{exc}): 450nm (377nm).

2-(5-phenyl-2-(2-pyridyl)-thiazol-4-yloxy)hexanoic acid 2b:

The reaction was carried out according to the general procedure **2** with 100mg (0.3 mmol) educt **1b**. After the described workup procedure 88 mg (95% Yield) of the desired product were obtained as yellow solid.

^{1}H NMR (400 MHz, $CDCl_3$) δ 8.59 (d, *J* = 4.3 Hz, 1H), 8.10 (d, *J* = 7.9 Hz, 1H), 7.84 – 7.68 (m, 3H), 7.37 (t, *J* = 7.7 Hz, 2H), 7.33 – 7.14 (m, 3H), 4.53 (t, *J* = 6.5 Hz, 2H), 2.40 (t, *J* = 7.4 Hz, 2H), 1.96 – 1.84 (m, 2H), 1.82 – 1.72 (m, 2H), 1.65 – 1.54 (m, 2H), DEI-MS *m/z* (%): 368 [M^{*+}], 254 [M^{*+}]-$C_6H_{11}O_2$, 121 [M^{*+}]-$C_{14}H_{16}NO_3$, UV/vis (MeOH): λ_{max} (log ε): 377nm (4,30), Fluorescence (MeOH): λ_{max} (λ_{exc}): 450nm (377nm).

2-(5-phenyl-2-(2-pyridyl)-thiazol-4-yloxy)undecanoic acid 2c:

The reaction was carried out according to the general procedure **2** with 100mg (0.22 mmol) educt **1c**. After the described workup procedure 78 mg (80% Yield) of the desired product were obtained as yellow solid.

^{1}H NMR (400 MHz, $CDCl_3$) δ 8.59 (ddd, *J* = 4.7, 1.5, 0.8 Hz, 1H), 8.11 (d, *J* = 7.9 Hz, 1H), 7.84 – 7.73 (m, 3H), 7.38 (dd, *J* = 10.6, 4.9 Hz, 2H), 7.31 – 7.21 (m, 3H), 4.51 (t, *J* = 6.6 Hz, 2H), 2.39 – 2.29 (m, 2H), 1.92 – 1.77 (m, 2H), 1.67 – 1.56 (m, 2H), 1.56 – 1.43 (m, 2H), 1.43 – 1.18 (m, 13H), DEI-MS *m*/*z* (%): 438 [M^{*+}], 254 [M^{*+}]-$C_{11}H_{21}O_2$, 121 [M^{*+}]-$C_{19}H_{26}NO_3$, UV/vis (MeOH): λ_{max} (log ε): 377nm (4,26), Fluorescence (MeOH): λ_{max} (λ_{exc}): 450nm (377nm).

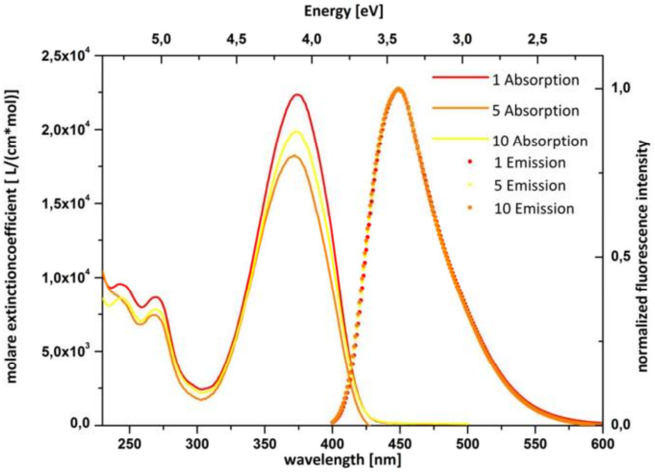

S 1: UV/vis absorption and fluorescence emission spectra of the thiazoles **1**, **5**, **10** in methanol.

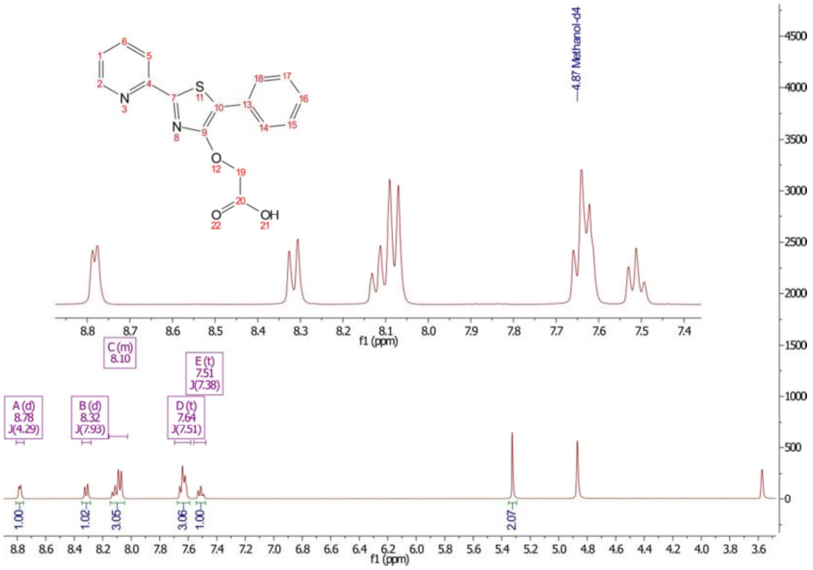

S 2: ^{1}H NMR of **1**.

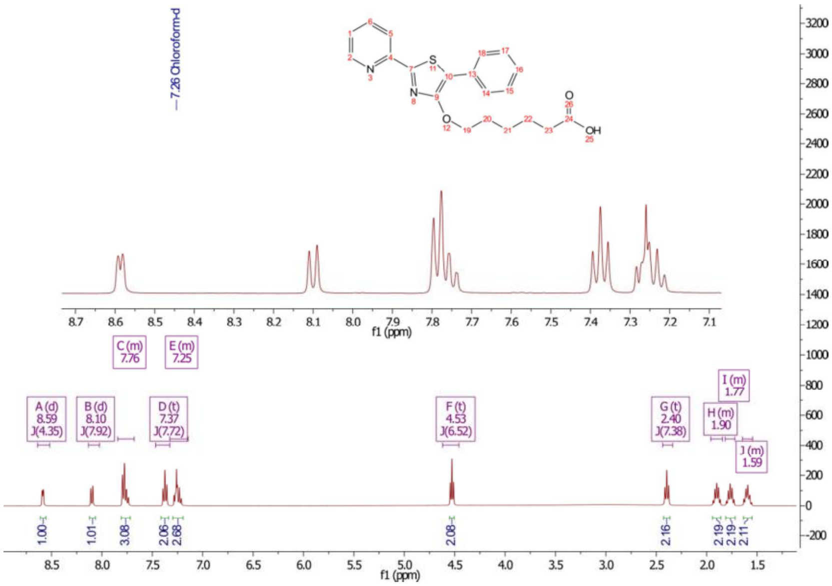

S 3: ^{1}H NMR of **5**.

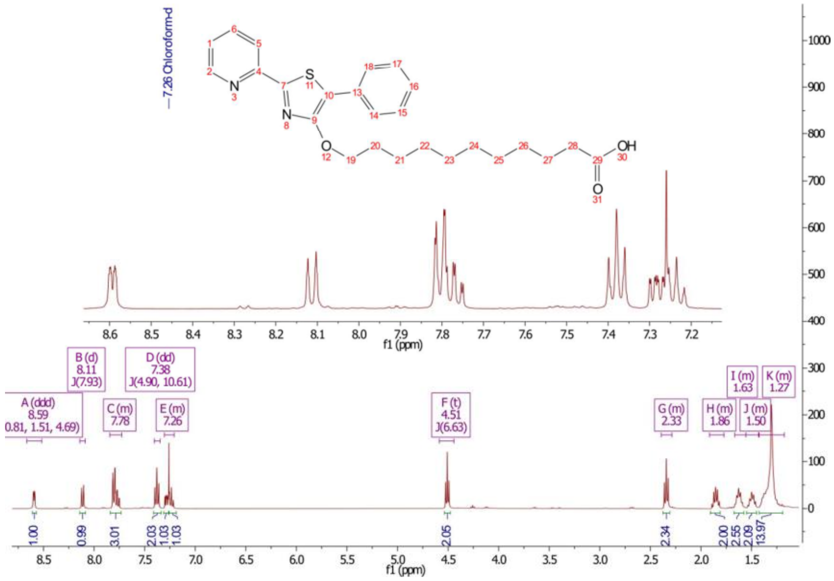

S 4: 1H NMR of **10**.

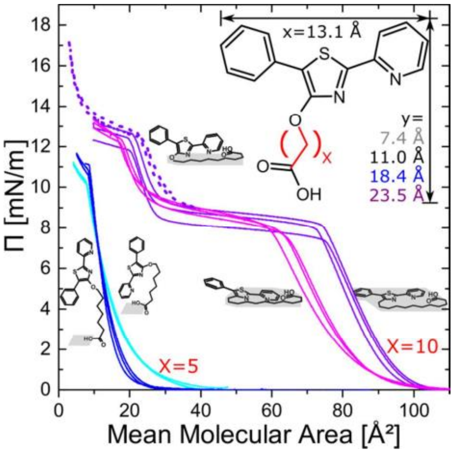

S 5: 3 individual Π(A)-isotherm of the thiazole (solid line) with 2 different spacer lengths, **5** (blue) and **10** (violet) recorded at a water phase (darker line) and 1% citric acid water phase (brighter line). Dotted line: Non averaged Π(A)-isotherm of **10** at lower mean molecular areas

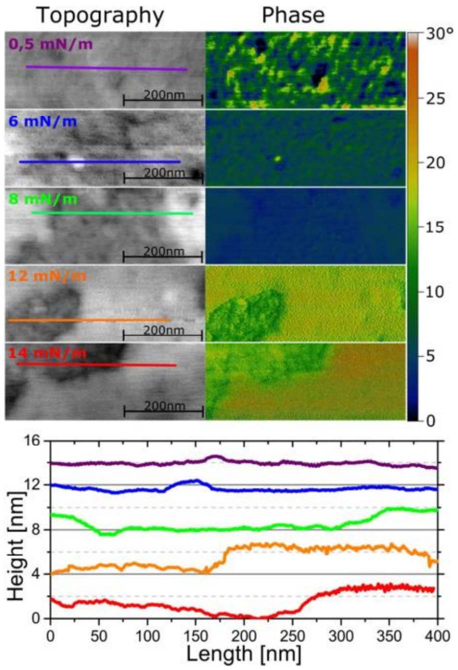

S 6: AFM line profiles

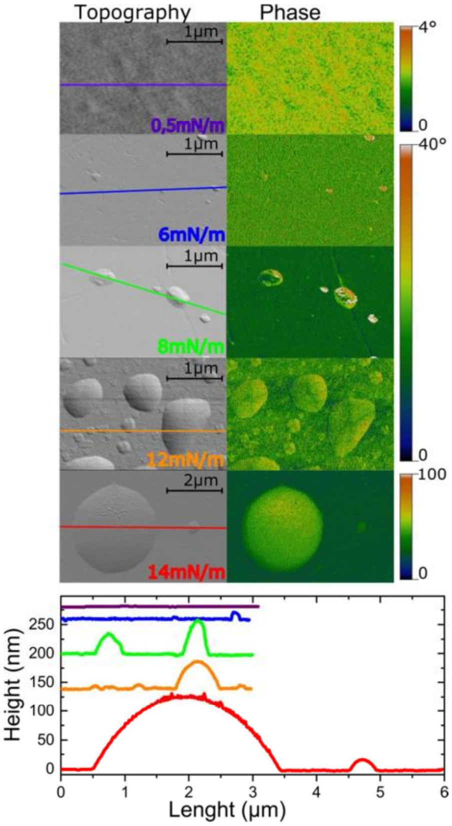

S 7: AFM: aging of LB-films of **10** with AFM line profiles

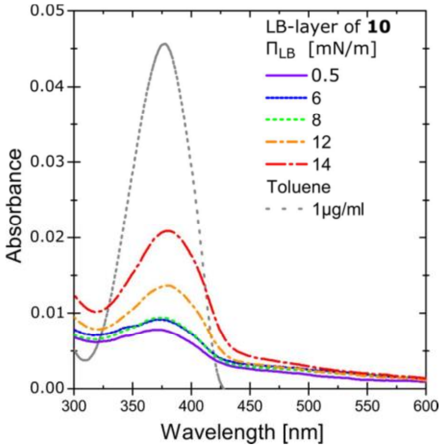

S 8: Absorption spectra of LB-films of **10** at five different Π_{LB}-pressures (0.5, 6, 8, 12, 14 mN/m) and solution (toluene 1µg/ml)

[MLH4] Enhancing Supramolecular Stability of Monolayers by Combining Dipolar with Amphiphilic Motifs: Case of Amphiphilic Push-Pull-Thiazole

Hupfer, M. L.; Kaufmann, M.; May, S.; Preiß, J.; Weiß, D.; Dietzek, B.; Beckert,R.; Presselt, M., Physical Chemistry Chemical Physics **2019,** *submitted*,

Autor	1	2	3	4	5	6	7	8
Konzeption	x	x			x		x	x
Planung der Untersuchung	x							x
Datenerhebung	x			x				
Analyse und Interpretation	x		x			x	x	x
Schreiben des Manuskriptes	x		x			x		x
Publikationsäquivalente	1,0	n. a.	n. a.	n. a.	n. a.	n. a.	n. a.	n. a.

Physical Chemistry Chemical Physics

Enhancing Supramolecular Stability of Monolayers by Combining Dipolar with Amphiphilic Motifs: Case of Amphiphilic Push-Pull-Thiazole

Journal:	*Physical Chemistry Chemical Physics*
Manuscript ID	CP-ART-04-2019-002013
Article Type:	Paper
Date Submitted by the Author:	10-Apr-2019
Complete List of Authors:	Hupfer, Maximilian; Friedrich Schiller University Jena, Institute for Physical Chemistry; Leibniz Institute of Photonic Technology (IPHT) Kaufmann, Martin; Friedrich-Schiller-University, Institute for Organic Chemistry and Macromolecular Chemistry, Faculty for Chemistry and Earth Sciences May, Sylvio; North Dakota State University, Department of Physics Preiß, Julia; Friedrich-Schiller-Universitat Jena, Institute of Physical Chemistry; Leibniz-Institut fur Photonische Technologien, Weiss, Dieter; Friedrich-Schiller Universitaet, Institut fuer Organische Chemie und Makromolekulare Chemie Dietzek, Benjamin; Friedrich-Schiller-University Jena, Institute for Physical Chemistry; Leibniz Institute of Photonic Technology Jena, Functional Interfaces Beckert, Rainer; Friedrich-Schiller-University, Institute for Organic Chemistry and Macromolecular Chemistry Presselt, Martin; Institute for Physical Chemistry, Friedrich Schiller University Jena

ARTICLE

Enhancing Supramolecular Stability of Monolayers by Combining Dipolar with Amphiphilic Motifs: Case of Amphiphilic Push-Pull-Thiazole

Received 00th January 20xx,
Accepted 00th January 20xx

DOI: 10.1039/x0xx00000x

M. L. Hupfer[a,b], M. Kaufmann[a,c], S. May[d], J. Preiß[a,b], D. Weiß[c], B. Dietzek[a,b], R. Beckert[b]*, M. Presselt[a,b,e,f]*

Equipping a thiazole dye with push and pull moieties adds dipolar intermolecular interactions and two hydrophilic anchors to a centrally anchored π-stacking and otherwise mono-amphiphilic dye. We show that, despite the resulting irregular shape of the tripodal amphiphile, the enhanced intermolecular interactions and amphiphilicity yields smooth and stable thin films. Further, we present a first approach for deriving supramolecular binding energies from Langmuir-Blodgett hysteresis data.

Introduction

In addition to molecular[1], supramolecular structures essentially determine active layer properties, such as spectral[2-4] characteristics, external quantum efficiency[5-7], open circuit voltage[8], conductivity[9-11], and electrochemical potentials[12], both in the bulk and at interfaces[13]. Among the comprehensive tools of supramolecular chemistry, assembly based on ππ-[14, 15] or dipolar interactions[16, 17], and assembly at interfaces[18] might be the most prominent techniques for controlling supramolecular structure formation. While aggregates formed from dipolar dyes can vary substantially depending on the molecular substitution pattern[3], those formed at interfaces are typically restricted to two-dimensional (2D) growth and can be tuned *via* the Langmuir-Blodgett (LB) technique[18].

The essential structural motif for such interface assembly is amphiphilicity, *i.e.* the combination of a hydrophilic and a lipophilic moiety. Interactions between the latter, typically non-polar, moieties are governed by dispersion interactions that can yield up to few hundreds millielectronvolt binding energy (up to 40 kJ/mol).[19] Energies similar to these reported for dispersion interaction-dominated binding are considered the lower boundary in case of dipolar intermolecular binding[20]. For push-pull dyes combining both types of intermolecular binding, 1.78 eV (172 kJ/mol = 41 kcal/mol) exceptionally high binding energy have been reported.[21] Hence, implementation of push-pull moieties into chromophores constituting the hydrophobic, *i.e.* lipophilic, part of amphiphilic dyes presumably enhances the stability of supramolecular layers formed from those dyes at interfaces significantly.

To fully exploit the advanced control of 2D-supramolecular structure formation and thin film production of the LB technique in this work, the investigated dyes are equipped with a hydrophilic anchor that is centrally linked to the chromophore *via* a flexible hydrophobic linker.[22] This central and orthogonal functionalization of the chromophore (Figure 1) is supposed to yield a minimal disturbance of the electronic structure of the dipolar chromophore, *cf*. the work of Tang *et al*.[23] where dipole-dipole repulsion is energetically not favourable in the parallel LB-assembly of linear dipolar amphiphilic dyes. Instead, the orthogonal combination between dipolar chromophore and linker-anchor moiety yields “T-shaped” amphiphiles[22, 24], which finally feature three hydrophilic moieties because of the dipolarity of the chromophore (see Figure 1). The resulting versatile tripodal amphiphile is expected to enable formation of different thermodynamically stable supramolecular structures, which can be controlled by means of the LB technique.[22] Such stable layers with tuneable molecular orientations are of large interest in organic optoelectronics, particularly as interlayers between contacts and active materials, where a high thermo-dynamic stability might also enable self-healing of such layers.[25]

[a] Institute of Physical Chemistry, Friedrich Schiller University Jena, Jena, Germany

[b] Leibniz Institute of Photonic Technology (IPHT), Jena, Germany

[c] Institute of Organic and Macromolecular Chemistry, Friedrich Schiller University Jena, Jena, Germany

[d] Department of Physics, North Dakota State University, Fargo, United States of America

[e] Center for Energy and Environmental Chemistry Jena (CEEC Jena), Friedrich Schiller University Jena, Jena, Germany

[f] sciclus GmbH & Co. KG, Jena, Germany

**corresponding authors: Synthesis:* rainer.beckert@uni-jena.de *; Thin films:* martin.presselt@leibniz-ipht.de

Electronic Supplementary Information (ESI) available: See DOI: 10.1039/x0xx00000x

In this work, we employ the class of 4-hydroxy-1,3 thiazoles that can be functionalized to yield various degrees of amphiphilicity[26, 27]. Here, the 4-hydroxy moiety is used to attach an alkylic chain that separates a polar carboxylic acid group from the chromophore, finally resulting in a water insoluble amphiphile. An electron donating dimethylamine and an electron accepting nitro group attached to the thiazole form the dipolar push-pull chromophore, as shown in Figure 1 and described in detail in the supporting information, section "Synthesis"

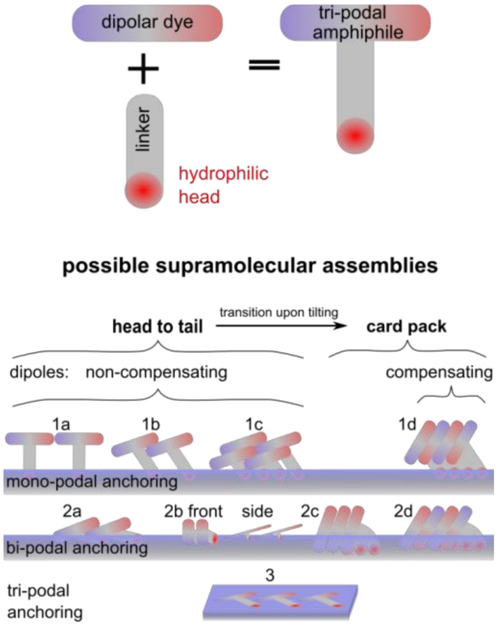

Figure 1: Central attachment of a hydrophilic head to a dipolar chromophore *via* a hydrophobic linker yields a "T-shaped" amphiphile that can be anchored just *via* the hydrophilic head (mono-podal structures 1a-d), additionally *via* one hydrophilic moiety of the dipolar chromophore (di-podal structures 2a-d, 2c represents an energetically unfavourable case shown for reference), or *via* all three hydrophilic moieties (tri-podal structure 3).

Results and discussion

The LB isotherms in Figure 2b show that the dipolar amphiphile (**B**) forms Langmuir layers featuring four-fold increased maximum surface pressure Π as compared to the reference amphiphile **A** (Π_{max}(**B**)≥40 mN/m, Π_{max}(**A**)≤12 mN/m).[28] Thus, the LB isotherms readily reveal that the push-pull motif significantly stabilizes the Langmuir layer of **B**. However, both the push and the pull moieties are hydrophilic (see Figure 2c), thus providing additional anchors in the aqueous subphase[29], which are presumed to contribute to enhanced maximum surface pressures. To investigate how possible anchoring schemes, as depicted in Figure 1 contribute to Langmuir layer formation, the LB Π(A)-isotherm of **B** is analyzed in detail. Figure 2b reveals a non-monotonous evolution of the Π(A)-isotherm's slope. The latter is smallest between 40 and 20 Å², what corresponds to an increased compressibility. The compressibility modulus C_S^{-1} shown in Figure 2a shows a minimum at 30 Å², thus indicating transitions between distinct solid phases[30]. Consequently, at A_I>30 Å² (corresponding to Π_I<20 mN/m, labeled phase I in the following) a different supramolecular structure is supposed to dominate the Langmuir layer as compared to A_{II}<30 Å² (corresponding to Π_{II}>20 mN/m, labeled phase II in the following). However, note that the change in the slope of the Π(A)-isotherm is rather small as compared to Π(A)-isotherms indicating substantial supramolecular rearrangement[22, 24].

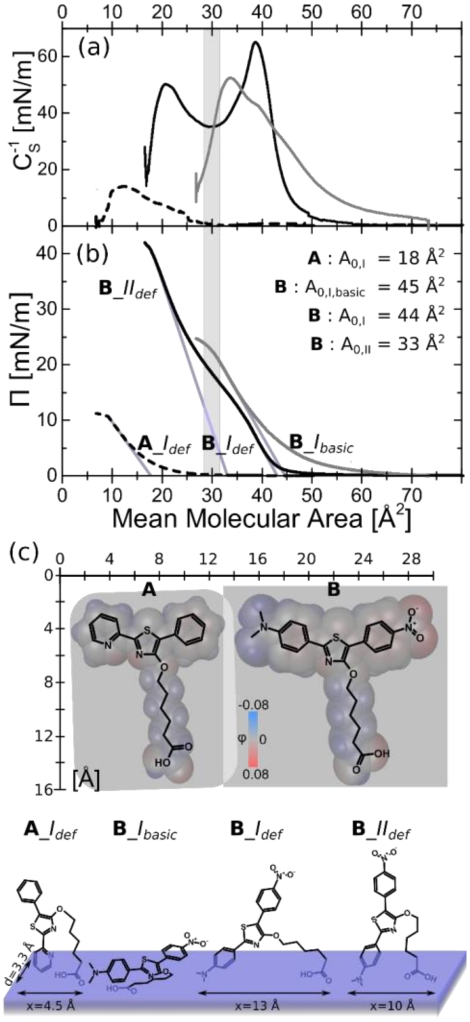

Figure 2: (a) Compressibility modulus [illegible]= -A dΠ/dA and (b) Π(A) isotherm of the two thiazoles with a pyridyl-phenyl- (A, dashed) and dimethylaminophenyl-nitro-

phenyl-substitution (B, solid) on ultra-pure water (black) and 1% Na_2HPO_4 (grey). (c) Electrostatic potentials (φ) on van der Waals surfaces of A and B and their proposed orientations (bottom) in the Langmuir layers that show lateral spatial demands (x · d) fitting the A_0-areas derived from the Π(A)-isotherms for the individual solid state phases of the Langmuir layers.

To deduce supramolecular geometrical features of the Langmuir layer, we compare the extrapolated A_0-areas[31-36] of phase I and II, $A_{0,I}$=43 Å² and $A_{0,II}$=34 Å², respectively, with those of the supramolecular models shown in Figure 1. If all three hydrophilic groups, COOH, $N(CH_3)_2$, NO_2, would anchor in the subphase an A_0 area of 95 Å² for dense packing to ≈ 150 Å² = 10 Å · 15 Å, could be expected. Those large areas corresponding to flat molecular orientations have been observed for other T-shaped amphiphiles of similar size, but with fewer hydrophilic moieties.[22, 24] In contrast, the isotherm of **B** does not feature notable surface pressures at high (>100 Å²) mean molecular areas, thus indicating that the chromophore is partially dissolved in the subphase and already slightly tilted before lateral compression, see scheme of molecular orientation "I_{def}" in Figure 2c. Consequently, **B** is initially anchored *via* two polar groups in the subphase, one being the dipolar group COOH group and the other the aniline-derived $N(CH_3)_2$-group, which is more hydrophilic than the NO_2-moiety, particularly in its protonated form. The assumption that the $N(CH_3)_2$- and not the NO_2-group is the second anchor is supported by a shift of the Π(A)-isotherm to larger areas and an increase in compressibility (see Figure 2a) when making the subphase basic (1% Na_2HPO_4 in subphase: pH = 8.98; default (deionized ultra-pure water): pH = 6). This subphase-change shifts the Π(A)-isotherm to larger values as one anchor becomes less hydrophilic upon increasing basicity. Such behavior is not expected for the NO_2- or the COOH-group, but rather for $N(CH_3)_2$. Here, a more basic subphase shifts the acid-base equilibrium to the non-protonated and less polar free-base $N(CH_3)_2$-form giving rise to the experimentally observed shift of the isotherm.

Finally, the spatial demand of the tilted chromophore shown schematically in Figure 1 and Figure 2c are estimated to 43 Å², if the anchoring COOH- and $N(CH_3)_2$-groups are separated by x = 13 Å and the chromophores intermolecular ππ-distance of d=3.3 Å[26, 37] ($A_{0,I}^{theo}$ = 3.3 Å · 13.0 Å ≈ 43 Å²). This $A_{0,I}^{theo}$ area fits the measured $A_{0,I}$ = 44 Å² area of phase I of **B**. With further lateral compression towards phase II the **B** chromophores are expected to tilt more vertically or rearrange to supramolecular structures with compensating dipole moments, such as structural motives 2a-d in Figure 1.

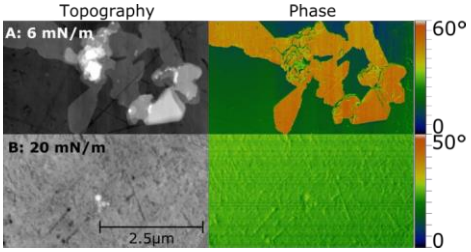

Figure 3: AFM images of LB films of **A** (Π_{LB} = 6mN/m) and **B** (Π_{LB} = 20mN/m)

In the latter case, the combination of amphiphilic and dipolar assembly induced by the LB technique might cause stabilized 2D-films in case of phase II as compared to phase I. The influence of such stabilization on the morphology is investigated by means of atomic force microscopy (AFM). As shown by the AFM images in Figure 3 (detailed in Figure SI 10), LB films deposited at surface pressures Π_{LB} within phase I (Π_{LB}≤20 mN/m) feature grainy and fibrous structures within the 2D-LB films, hence indicating supramolecular rearrangement during LB deposition onto quartz glass. In contrast, deposition of phase II, *i.e.* Π_{LB} > 20 mN/m, yields LB layers that are exceptionally flat, particularly when compared to those produced from phase I and from the non-dipolar reference amphiphile **A**, as shown by the topography images in Figure 3. Consequently, the supramolecular structure in phase II is distinctly stabilized as compared to phase I. However, the AFM phase of the flat LB monolayers deposited at Π_{LB} ≥ 35 mN/m show a heterogeneous phase distribution, thus revealing that phase **B_*II*** is constituted of different supramolecular structures, which might be assigned to a co-existence of phase I and II at Π_{LB} ≥ 35 mN/m.

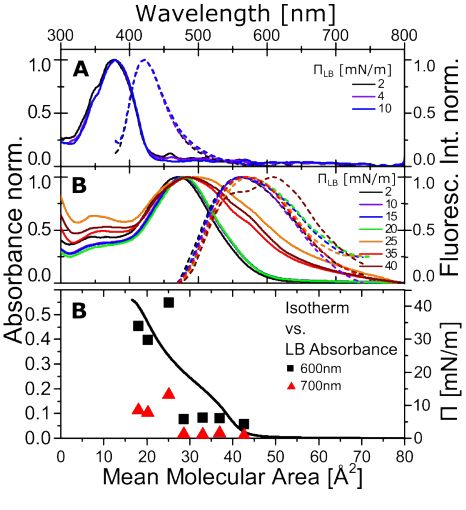

Figure 4: Absorption and emission spectra of **B** (450 nm excitation) and **A** (420 nm excitation) at certain LB deposition pressures Π_{LB} and correlation between J-aggregate

absorption at λ≥600 nm and changes between phases **B_*I*** and **B_*II*** that are assigned to distinct sections of the LB isotherm (A_{B_I}>30 Å², A_{B_II}<30 Å²)

The hypothesis introduced above that in phase II a combination between interface and dipolar assembly was induced is tested by means of UV-vis absorption spectroscopy, which allows for identification of dipolar H- or J-type aggregates possibly formed from **B**. The UV-vis absorption spectra shown in Figure 4B reveal a distinct extension to lower energies in case of phase II (λ_{II}(A=10%)=707-735 nm, Figure 4B) as compared to phase I (λ_I(A=10%)=590 nm), while the spectral changes between the samples within the same phase differ negligibly. The extension of the phase II absorption spectrum to the red is assigned to solid state extended J-aggregates.[38, 39] The fact that the spectrum is extended instead of shifted reveals the coexistence of phase I and II when Π_{LB} > 20 mN/m, as already observed in the AFM phase images in Figure 3. Such formation of J-aggregates with reduced optical gap is a distinct feature of the dipolarity of the chromophore, hence not occurring for the non-dipolar reference chromophore **A**, as shown in Figure 4A. Hence, the dipolar assembly induced at higher surface pressures, *i.e*. at phase **B_*II*** as shown in Figure 4B, is unambiguously revealed by UV-vis absorption spectroscopy. From the di-podal supramolecular models introduced in Figure 1, structures 2a-c might represent the observed red-shifted J-aggregates, whereas 2cseems to be energetically less favourable as compared to 2a and 2b but might be realized due to the lateral LB pressure. Hence, the two different observed phases of **B** might be assigned to structures 2a and 2b.

The energetic stabilization due to the dipolar interactions are quantified by LB hysteresis experiments shown in Figure 5. Due to the dipolar interactions the energy that is stored in the Langmuir layer **B_II** upon successive compression expansion cycles, interpreted as intermolecular binding energy, is increased from 9 to 35 meV (0.9 to 3.4 kJ/mol) if compared to **A**[22]. We assume that this intermolecular binding hampers dissociation at layer expansion rather than kinetic trapping as no constraints, like adsorption on solid substrates or lateral pressure, are present at expansion.

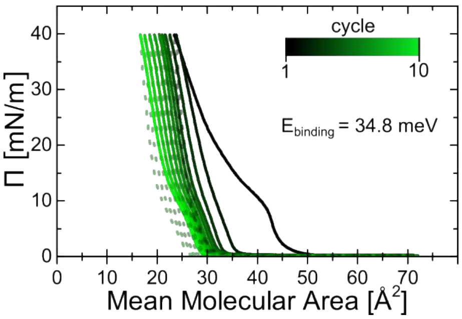

Figure 5: Langmuir hysteresis experiment used to derive the energy stored in the Langmuir layer at repeated compression-expansion cycles. This energy is assigned to an intermolecular binding energy $E_{binding}$ per molecule.

Identifying the area enclosed by a hysteresis cycle in the Π-A diagram with the intermolecular binding energy is an approximation that we motivate by an accurate calculation for the specific example of a two-dimensional binary lattice gas with nearest neighbour interactions, treated on the level of the random mixing approximation[40, 41]. This model is often referred to as Bragg-Williams model. We identify one component as amphiphile and the other as a void. While the lattice gas model certainly oversimplifies the actual system of a tripodal amphiphile investigated in our work, it can be analyzed rigorously and illustrates the salient features of passing through a hysteresis cycle.

Denoting the intermolecular interaction strength between two amphiphiles as ω (with ω>0 for repulsion and ω<0 for attraction) and the lattice coordination number by z, the lateral pressure of the lattice gas Π=Π(A) as function of the mean molecular area A amounts to

$$\Pi = \frac{z}{2}\omega\frac{A_0}{A^2} - \frac{k_BT}{A_0}\ln\left(1-\frac{A_0}{A}\right) \qquad (1)$$

where A_0 is the minimal cross-sectional area per amphiphile as determined by its steric size. Also, k_B is Boltzmann's constant and T the absolute temperature. Of the two terms on the right-hand side of Eq. 1, the second one describes the pressure due to a non-interacting lattice gas, and the first corresponds to an increase (for ω>0) or a decrease (for ω<0) of the pressure due to, respectively, repulsive or attractive intermolecular interactions. Eq. 1 predicts a critical point $\omega=\omega_c=-4/z\ k_BT$ and $A=A_c=2\ A_0$ and thus phases separation for $\omega<\omega_c$. For sufficiently large values of the mean molecular area A the system behaves as an ideal gas. Upon decreasing A, first the binodal line $A=A_b$ and then the spinodal line $A=A_s$ are crossed. The binodal, which follows from the familiar Maxwell construction, fulfills the relation

$$\omega = \frac{2}{z}k_BT\frac{A_b}{A_b-2A_0}\ln\left(\frac{A_0}{A_b-A_0}\right) \qquad (2)$$

whereas the spinodal, which demands a vanishing slope of Π(A), satisfies

$$\omega = -\frac{k_BT}{z}\frac{A_s^2}{A_0(A_s-A_0)} \qquad (3)$$

The region $A_s<A<A_b$ is metastable, thus allowing for hysteresis cycles. The isothermal hysteresis cycle that encloses a maximal area in the Π-A diagram compresses a homogeneous system from A_b to A_s and then expands the phase separated system back from A_s to A_b. This is displayed in the main diagram of Fig. SI-1 for one specific isotherm with z=6 and ω=-11/15 k_BT=-0.73 k_BT. Cross sections with the binodal and spinodal are marked by the two open circles and the two bullets, respectively. For each pair the larger mean molecular area is A_s=2.86 A_0 and A_b =4.02 A_0. The area

$$\alpha = \int_{A_s}^{A_b} dA\left[\Pi(A)-\Pi(A_b)\right] \qquad (4)$$

enclosed in the Π(A) diagram by the isotherm that passes through a hysteresis cycle bounded by As and Ab is displayed in the inset of Figure 6 as function of the negative excess intermolecular interaction strength (ω-$ω_c$)/(k_BT), expressed in units of the thermal energy. Note that α has the unit of energy. For example, (ω-$ω_c$)/(k_BT)=0.3 implies that the attraction strength between two amphiphiles is 0.3 k_BT stronger than the critical value $ω_c$=-4/z k_BT =-2/3 k_BT =-0.66 k_BT, needed to induce phase separation. Note that both the main diagram and the inset of Figure 6 are computed for a lattice coordination number z=6, which is typical for a two-dimensional system. No other parameter enters into our model, implying that the inset of Figure 6 characterizes the generic behavior of a hysteresis cycle carried out between binodal and spinodal of a two-dimensional lattice gas on the level of Bragg-Williams theory. For large intermolecular interaction strengths (that is, far away from the critical point) the two quantities α/(k_BT) and (ω-$ω_c$)/(k_BT) are indeed of the same order of magnitude. This provides qualitative justification to identify the enclosed area with the order of magnitude of the interaction strength relative to that of a critical system.

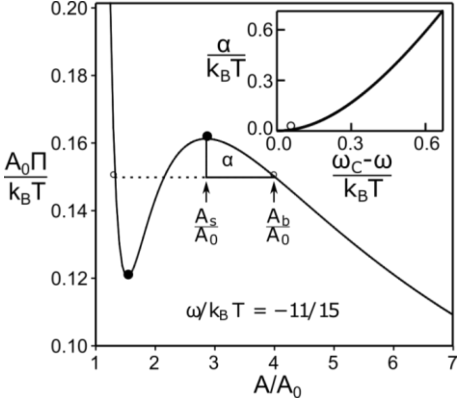

Figure 6: Dimensionless lateral pressure *Π A_0/(k_BT)* according to Eq. 1 for *z*=6 and *ω*=-11/15 k_BT=-0.73 k_BT, plotted as function of the scaled mean molecular area *A*/A_0, where A_0 denotes the minimal cross-sectional area per amphiphile and k_BT the thermal energy unit. The two open circles and two bullets mark the binodal and spinodal, respectively. The corresponding molecular areas A_s=2.86 A_0 and A_b = 4.02 A_0 are indicated. The area enclosed by the hysteresis cycle of decreasing *A* for a homogeneous system from the binodal line (marked by the right vertical arrow) to the spinodal (marked by the left vertical arrow), and then back – phase separated – from the spinodal to the binodal, is denoted by α. The inset shows α as a function of the negative excess intermolecular interaction strength (*ω*-$ω_c$)/(k_BT), where $ω_c$=-4/*z* k_BT=-2/3 k_BT=-0.667 k_BT marks the critical point, the onset of phase separation. The open circle in the inset labels the system shown in the main diagram, corresponding to *ω*=-11/15 k_BT and hence $ω_c$-*ω*=1/15 k_BT=0.067 k_BT. This gives rise to α=0.0082 k_BT.

Conclusions

Finally, the novel design principle of orthogonal combination of T-shape amphiphilicity and dipolar chromophores yielded an assembly-motif with the electron-pushing moiety of the chromophore in addition to the carboxylic acid group anchoring in the aqueous subphase. The resulting supramolecular structure arises from interface-assembly, while dipolar intermolecular interactions are negligible. The latter can be enforced at higher lateral compression of Langmuir layers as revealed by evolution of J-type absorption peaks. Apparently, these additional dipolar interactions stabilize the two-dimensional Langmuir layers, as they feature exceptionally flat topographies.

Experimental

UV-vis Absorption and Emission Spectroscopy

The absorption spectroscopic measurements we used a UV-vis (Varian: Cary 5000) spectrometer in transmission mode. Standard fluorescence measurements of the LB-films were made on a costume built setup. This consists of an Isoplane 320 Spectrograph with a cooled Pixis CCD-Camera from Princeton Instruments. A fiber coupled 5 mW laser with a 405 nm output wavelength was used as excitation source (incident under 55°) and the emission were detected under 35° with respect to the substrate normal. Long pass filters with low self-fluorescence from ITOS were used to block scattered excitation light.

Langmuir-Blodgett (LB) Films

Solutions of the dyes (0.05 µmol/ml in $CHCl_3$) were carefully spread onto the subphase (ultra-pure water) of the LB-trough (KSV NIMA Alternate L 105 and KSV 5000). For complete evaporation of $CHCl_3$ a time of 10 min were waited before moving the barriers. Then, the barriers were compressed with 5 mm/min to record the isotherms. Quartz glass substrates were treated with acetone and iso-propanol in the ultrasonic bath for each solvent 3 times and the substrates were stored in isopropanol. The deposition of LB-films on the quartz-glass (30 mm x 5 mm x 1mm) was done using uptroke dipping with constant pressure and a dipping speed of 5 mm min^{-1}

Scanning Force Microscopy

Atomic force microscopy (AFM) was carried out using a Veeco Digital Instruments AFM Nanoscope IIIa, with a head Dimension 3100 in tapping mode on air with a silicon tip (radius < 8 nm) at 300 kHz with a force constant of E40 N m^{-1} (Budget Sensors Tap 300-G).

Density functional theory calculations

Quantum chemical structure optimizations and calculations of electrostatic potentials on **A** and **B** monomers were performed using density functional theory (DFT) implemented in Turbomole[42] and applying the GGA (generalized gradient approximation) functional BP86 (preoptimization), followed by the hybrid functionals and B3LYP[43], the def2-SVP (preoptimization) and -TZVP basis sets[44], and the MARI-J approximation in case of BP86, which have been shown to yield reasonable electronic properties for a large variety of molecular motives, including push-pull systems and extended π-electron systems[45-50].

Conflicts of interest

There are no conflicts to declare

Acknowledgements

The acknowledgements come at the end of an article after the conclusions and before the notes and references.

References

1. R. Fitzner, C. Elschner, M. Weil, C. Uhrich, C. Koerner, M. Riede, K. Leo, M. Pfeiffer, E. Reinold, E. Mena-Osteritz and P. Baeuerle, *Advanced Materials*, 2012, **24**, 675-+.
2. S. Das, F. Herrmann-Westendorf, F. H. Schacher, E. Täuscher, U. Ritter, B. Dietzek and M. Presselt, *ACS Appl Mater Interfaces*, 2016, **8**, 21512-21521.
3. F. Würthner, T. E. Kaiser and C. R. Saha-Möller, *Angewandte Chemie International Edition*, 2011, **50**, 3376-3410.
4. M. Presselt, F. Herrmann, S. Shokhovets, H. Hoppe, E. Runge and G. Gobsch, *Chemical Physics Letters*, 2012, **542**, 70-73.
5. M. Presselt, F. Herrmann, H. Hoppe, S. Shokhovets, E. Runge and G. Gobsch, *Advanced Energy Materials*, 2012, **2**, 999-1003.
6. W. J. D. Beenken, F. Herrmann, M. Presselt, H. Hoppe, S. Shokhovets, G. Gobsch and E. Runge, *Physical Chemistry Chemical Physics*, 2013, **15**, 16494-16502.
7. N. T. Shewmon, D. L. Watkins, J. F. Galindo, R. B. Zerdan, J. Chen, J. Keum, A. E. Roitberg, J. Xue and R. K. Castellano, *Advanced Functional Materials*, 2015, **25**, 5166-5177.
8. C. Poelking, M. Tietze, C. Elschner, S. Olthof, D. Hertel, B. Baumeier, F. Würthner, K. Meerholz, K. Leo and D. Andrienko, *Nat Mater*, 2015, **14**, 434-439.
9. Y. Chen, Y. Feng, J. Gao and M. Bouvet, *Journal of colloid and interface science*, 2012, **368**, 387-394.
10. F. C. Grozema and L. D. A. Siebbeles, *Int. Rev. Phys. Chem.*, 2008, **27**, 87-138.
11. F. Herrmann, S. Engmann, M. Presselt, H. Hoppe, S. Shokhovets and G. Gobsch, *Applied Physics Letters*, 2012, **100**, 153301-153301 - 153303.
12. B. Kitchen, O. Awartani, R. J. Kline, T. McAfee, H. Ade and B. T. O'Connor, *Acs Applied Materials & Interfaces*, 2015, **7**, 13208-13216.
13. F. Herrmann, B. Muhsin, C. R. Singh, S. Shokhovets, G. Gobsch, H. Hoppe and M. Presselt, *The Journal of Physical Chemistry C*, 2015, **119**, 9036-9040.
14. F. Wurthner, C. R. Saha-Moller, B. Fimmel, S. Ogi, P. Leowanawat and D. Schmidt, *Chemical Reviews*, 2016, **116**, 962-1052.
15. M. R. Molla and S. Ghosh, *Physical Chemistry Chemical Physics*, 2014, **16**, 26672-26683.
16. F. Würthner, *Accounts of Chemical Research*, 2016, **49**, 868-876.
17. T. Ikeda and T. Haino, *Polymer*, 2017, **128**, 243-256.
18. K. Ariga, Y. Yamauchi, T. Mori and J. P. Hill, *Advanced Materials*, 2013, **25**, 6477-6512.
19. T. E. Shubina, D. I. Sharapa, C. Schubert, D. Zahn, M. Halik, P. A. Keller, S. G. Pyne, S. Jennepalli, D. M. Guldi and T. Clark, *Journal of the American Chemical Society*, 2014, **136**, 10890-10893.
20. F. Würthner and S. Yao, *Angewandte Chemie-International Edition*, 2000, **39**, 1978-1981.
21. S. Grimme, J. Antony, T. Schwabe and C. Muck-Lichtenfeld, *Organic & Biomolecular Chemistry*, 2007, **5**, 741-758.
22. M. L. Hupfer, M. Kaufmann, F. Herrmann-Westendorf, T. Sachse, L. Roussille, K. H. Feller, D. Weiss, V. Deckert, R. Beckert, B. Dietzek and M. Presselt, *ACS Appl Mater Interfaces*, 2017, **9**, 44181-44191.
23. Z. Tang, M. S. Johal, P. Scudder, N. Caculitan, R. J. Magyar, S. Tretiak and H.-L. Wang, *Thin Solid Films*, 2007, **516**, 58-66.
24. C. Schwieger, B. Chen, C. Tschierske, J. Kressler and A. Blume, *The Journal of Physical Chemistry B*, 2012, **116**, 12245-12256.
25. M. L. Hupfer, F. Herrmann-Westendorf, M. Kaufmann, R. Beckert, B. Dietzek and M. Presselt, *Chemistry - A European Journal*, 2019, **to be submitted**.
26. S. H. Habenicht, S. Schramm, S. Fischer, T. Sachse, F. Herrmann-Westendorf, A. Bellmann, B. Dietzek, M. Presselt, D. Weiß, R. Beckert and H. Görls, *Journal of Materials Chemistry C*, 2016, **4**, 958-971.
27. M. L. Hupfer, M. Kaufmann, J. Preiss, D. Weiss, R. Beckert, B. Dietzek and M. Presselt, *Langmuir*, 2019, **35**, 2587-2600.
28. M. L. Hupfer, M. Kaufmann, L. Roussille, J. Preiss, D. Weiss, K. Hinrichs, V. Deckert, B. Dietzek, R. Beckert and M. Presselt, *Langmuir*, 2019, **35**, 2561-2570.
29. L. Zhang and J. M. Cole, *ACS Applied Materials & Interfaces*, 2015, **7**, 3427-3455.
30. J. Y. Josefowicz, N. C. Maliszewskyj, S. H. J. Idziak, P. A. Heiney, J. P. McCauley and A. B. Smith, *Science*, 1993, **260**, 323.
31. P. Debnath, S. Chakraborty, S. Deb, J. Nath, D. Bhattacharjee and S. A. Hussain, *The Journal of Physical Chemistry C*, 2015, **119**, 9429-9441.
32. A. Ulman, *An Introduction to Ultrathin Organic Films: From Langmuir-Blodgett to Self-assembly*, Academic Press1991.
33. G. L. Gaines, *Insoluble monolayers at liquid-gas interfaces*, Interscience Publishers1966.
34. A. J. Erwin, W. Xu, H. He, K. Matyjaszewski and V. V. Tsukruk, *Langmuir*, 2017, **33**, 3187-3199.
35. H. Chou, C. T. Chen, K. F. Stork, P. W. Bohn and K. S. Suslick, *Journal of Physical Chemistry*, 1994, **98**, 383-385.
36. C. J. L. Constantino, L. P. Juliani, V. R. Botaro, D. T. Balogh, M. R. Pereira, E. A. Ticianelli, A. A. S. Curvelo and O. N. Oliveira, *Thin Solid Films*, 1996, **284-285**, 191-194.
37. M. Kaufmann, Dr. rer. nat., Friedrich-Schiller-Universität Jena, 2018.
38. A. Modlińska, K. Inglot, T. Martyński, R. Dąbrowski, J. Jadżyn and D. Bauman, *Liquid Crystals*, 2009, **36**, 197-208.
39. A. Miyata, D. Heard, Y. Unuma and Y. Higashigaki, *Thin Solid Films*, 1992, **210-211**, 175-177.
40. T. L. Hill, *An introduction to statistical thermodynamics*, Dover Publications, New York, 1986.
41. S. Safran, *Statistical Thermodynamics Of Surfaces, Interfaces, And Membranes*, Westview Press2003.
42. F. Furche, R. Ahlrichs, C. Hattig, W. Klopper, M. Sierka and F. Weigend, *Wiley Interdisciplinary Reviews-Computational Molecular Science*, 2014, **4**, 91-100.

43. P. J. Stephens, F. J. Devlin, C. F. Chabalowski and M. J. Frisch, *The Journal of Physical Chemistry*, 1994, **98**, 11623-11627.
44. F. Weigend and R. Ahlrichs, *Physical Chemistry Chemical Physics*, 2005, **7**, 3297-3305.
45. M. Presselt, C. Schnedermann, M. Schmitt and J. Popp, *The journal of physical chemistry. A*, 2009, **113**, 3210-3222.
46. M. Presselt, C. Schnedermann, M. Müller, M. Schmitt and J. Popp, *Journal of Physical Chemistry A*, 2010, **114**, 10287-10296.
47. W. Beenken, W. Maes, M. Kruk, T. Martínez and M. Presselt, *The Journal of Physical Chemistry A*, 2015, **119**, 6875-6883.
48. D. M. Gampe, M. Kaufmann, D. Jakobi, T. Sachse, M. Presselt, R. Beckert and H. Gorls, *Chemistry*, 2015, **21**, 7571-7581.
49. J. Preiß, M. Jäger, S. Rau, B. Dietzek, J. Popp, T. Martínez and M. Presselt, *ChemPhysChem*, 2015, **16**, 1395-1404.
50. M. Presselt, W. Dehaen, W. Maes, A. Klamt, T. Martínez, W. J. D. Beenken and M. Kruk, *Physical Chemistry Chemical Physics*, 2015, **17**, 14096-14106.

Supporting Information

Enhancing Supramolecular Stability of Monolayers by Combining Dipolar with Amphiphilic Motifs: Case of Amphiphilic Push-Pull-Thiazole

M. L. Hupfer[a,b], M. Kaufmann[a,c], S. May[d], J. Preiß[a,b], D. Weiß[c], B. Dietzek[a,b], R. Beckert[b]*, M. Presselt[a,b,e,f]*

[a] Institute of Physical Chemistry, Friedrich Schiller University Jena, Helmholtzweg 4, 07743 Jena, Germany

[b] Leibniz Institute of Photonic Technology (IPHT), Albert-Einstein-Str. 9, 07745 Jena, Germany

[c] Institute of Organic and Macromolecular Chemistry, Friedrich-Schiller-University Jena, Humboldtstraße 10, Jena, 07743, Germany

[d] Department of Physics, North Dakota State University, Fargo, United States of America

[e] Center for Energy and Environmental Chemistry Jena (CEEC Jena), Friedrich Schiller University Jena, Jena, Germany

[f] sciclus GmbH & Co. KG, Moritz-von-Rohr Str. 1a, 07745 Jena, Germany

**corresponding authors: Synthesis: rainer.beckert@uni-jena.de ; Thin films: martin.presselt@leibniz-ipht.de*

Π(A)-Isotherm

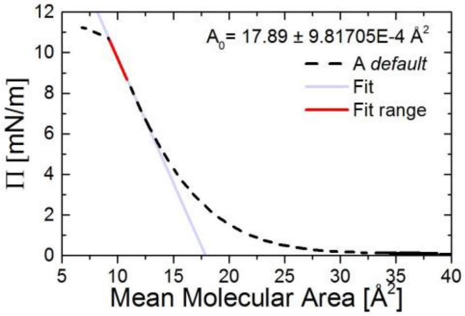

Figure SI 1: Averaged mean Π(A) isotherms of A on ultra-pure water (dotted black) and the fitted A_0-area derived from the Π(A)-isotherms for the individual solid state phase of the Langmuir layer

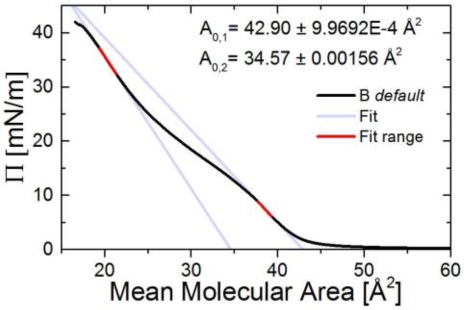

Figure SI 2: Averaged mean Π(A) isotherms of B on ultra-pure water (solid black) and the fitted A_0-area derived from the Π(A)-isotherms for the individual solid state phase of the Langmuir layer

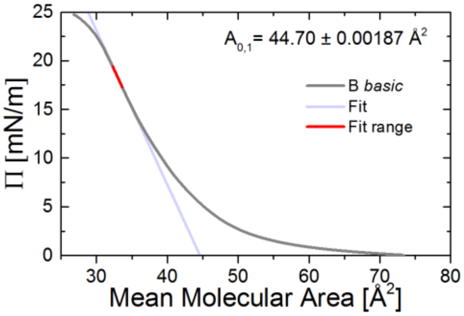

Figure SI 3: Averaged mean Π(A) isotherms of B on 1% Na_2HPO_4 water (solid grey) and the fitted A_0-area derived from the Π(A)-isotherms for the individual solid state phase of the Langmuir layer

ATOMIC FORCE MICROSCOPY

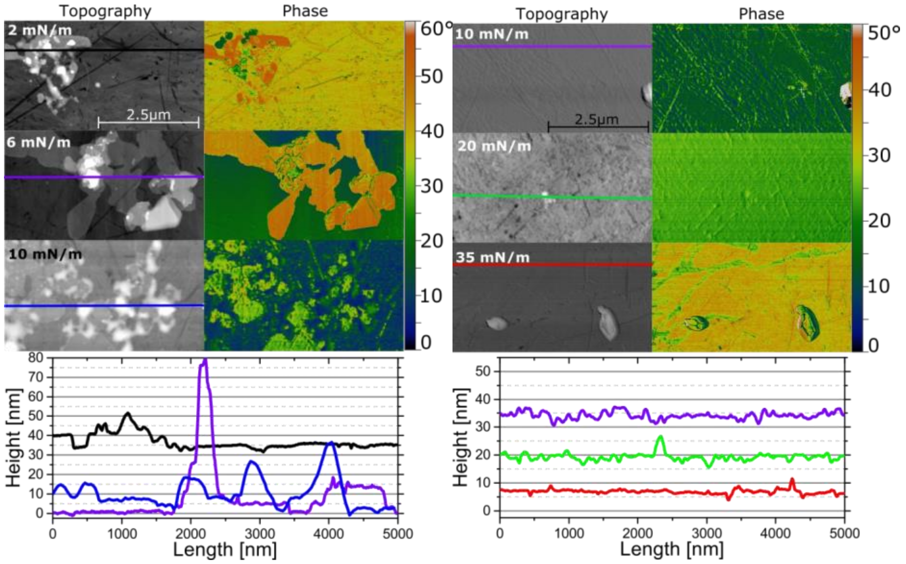

Figure SI 4: Atomic force microscopy images of LB-films of **A** (left) and **B** (right) at different deposition pressures; Left row: topography images; Right row: phase images

REFERENCES

1. T. L. Hill, *An introduction to statistical thermodynamics*, Dover Publications, New York, 1986.
2. S. Safran, *Statistical Thermodynamics Of Surfaces, Interfaces, And Membranes*, Westview Press2003.
3. F. Furche, R. Ahlrichs, C. Hattig, W. Klopper, M. Sierka and F. Weigend, *Wiley Interdisciplinary Reviews-Computational Molecular Science*, 2014, **4**, 91-100.
4. P. J. Stephens, F. J. Devlin, C. F. Chabalowski and M. J. Frisch, *The Journal of Physical Chemistry*, 1994, **98**, 11623-11627.
5. F. Weigend and R. Ahlrichs, *Physical Chemistry Chemical Physics*, 2005, **7**, 3297-3305.
6. M. Presselt, C. Schnedermann, M. Schmitt and J. Popp, *The journal of physical chemistry. A*, 2009, **113**, 3210-3222.
7. M. Presselt, C. Schnedermann, M. Müller, M. Schmitt and J. Popp, *Journal of Physical Chemistry A*, 2010, **114**, 10287-10296.
8. W. Beenken, W. Maes, M. Kruk, T. Martínez and M. Presselt, *The Journal of Physical Chemistry A*, 2015, **119**, 6875-6883.
9. D. M. Gampe, M. Kaufmann, D. Jakobi, T. Sachse, M. Presselt, R. Beckert and H. Gorls, *Chemistry*, 2015, **21**, 7571-7581.

10. J. Preiß, M. Jäger, S. Rau, B. Dietzek, J. Popp, T. Martínez and M. Presselt, *ChemPhysChem*, 2015, **16**, 1395-1404.
11. M. Presselt, W. Dehaen, W. Maes, A. Klamt, T. Martínez, W. J. D. Beenken and M. Kruk, *Physical Chemistry Chemical Physics*, 2015, **17**, 14096-14106.
12. D. Cież and J. Svetlik, *Synlett*, 2011, **2011**, 315-318.
13. V. Sharma and J. J. Tepe, *Organic Letters*, 2005, **7**, 5091-5094.
14. S. R. Yasa, S. S. Kaki, Y. Poornachandra, C. G. Kumar and V. Penumarthy, *Bioorganic & Medicinal Chemistry Letters*, 2016, **26**, 1978-1982.

[MLH5] Arylic *vs.* Alkylic - Hydrophobic Linkers Determine Supramolecular Structure and Optoelectronic Properties of Tripodal Amphiphilic Push-Pull-Thiazoles

Hupfer, M. L.; Kaufmann, M.; Roussille, L.; Preiß, J.; Weiß, D.; Hinrichs, K.; Deckert, V.; Dietzek, B.; Beckert,R.; Presselt, M., Langmuir **2019,** *35* (7), 2561-2570

Autor	1	2	3	4	5	6	7	8	9	10
Konzeption	x	x			x				x	x
Planung der Untersuchung	x	x	x			x				x
Datenerhebung	x	x	x			x				
Analyse und Interpretation	x	x	x	x		x	x	x		x
Schreiben des Manuskriptes	x	X						x		x
Publikationsäquivalente	1,0	n. a.	n. a.	n. a.	n. a.	n. a.	n. a.	n. a.	n. a.	n. a.

LANGMUIR
Article
Cite This: Langmuir 2019, 35, 2561−2570
pubs.acs.org/Langmuir

Arylic versus Alkylic—Hydrophobic Linkers Determine the Supramolecular Structure and Optoelectronic Properties of Tripodal Amphiphilic Push−Pull Thiazoles

M. L. Hupfer,[†,‡] M. Kaufmann,[†,§] L. Roussille,[†,‡] J. Preiß,[†,‡] D. Weiß,[‡] K. Hinrichs,[∥] V. Deckert,[†,‡] B. Dietzek,[†,‡] R. Beckert,*[‡] and M. Presselt*[†,‡,⊥,#]

[†]Institute of Physical Chemistry, Friedrich Schiller University Jena, Helmholtzweg 4, 07743 Jena, Germany
[‡]Leibniz Institute of Photonic Technology (IPHT), Albert-Einstein-Str. 9, 07745 Jena, Germany
[§]Institute of Organic and Macromolecular Chemistry, Friedrich-Schiller-University Jena, Humboldtstraße 10, Jena 07743, Germany
[∥]Leibniz-Institut für Analytische Wissenschaften—ISAS—e.V., Schwarzschildstr. 8, 12489 Berlin, Germany
[⊥]Center for Energy and Environmental Chemistry Jena (CEEC Jena), Friedrich Schiller University Jena, Jena 07743, Germany
[#]Sciclus GmbH & Co. KG, Moritz-von-Rohr Str. 1a, 07745 Jena, Germany

Ⓢ *Supporting Information*

ABSTRACT: The supramolecular structures and their constituents essentially determine the optoelectronic properties of thin films. The introduction of amphiphilicity to the constituents and interface assembly is one established technique to control supramolecular structures and resulting material properties. To yield amphiphilicity, rather hydrophobic chromophores are linked to hydrophilic head groups via flexible alkyl chains. In the present work, we investigate whether replacement of the alkyl linkers by a phenylene linker, that is, replacing an electrically isolating moiety with a potentially semiconducting one, increases the conductivity through the resulting layers. After investigating the influence of the linker on molecular properties of the 2-(4-*N*,*N*-dimethylaminophenyl)-4-hydroxy-5-nitrophenyl-1,3 thiazoles exemplarily used in this work, we produce supramolecular structures by means of the Langmuir−Blodgett (LB) technique. Atomic force microscopy (AFM) and UV−vis absorption spectroscopy reveal that thin films made from the more rigid thiazole bearing the arylic linker feature a more homogeneous and stable supramolecular structure as compared to those made from the thiazole dye containing the flexible alkylic linker. Finally, conductive AFM (cAFM) results disclose that the LB films made from the thiazole bearing the π-conjugated arylic linker are less conductive than their counterparts based on the alkylic linkers. In the latter layers, the alkylic linkers provide sufficient motional degrees of freedom to allow for supramolecular rearrangement upon electrical operation during cAFM measurements, hence yielding supramolecular structures featuring increased conductivity with successive cAFM measurements. This work highlights the importance of supramolecular structures for optoelectronic properties by presenting a case where supramolecular effects excel the property changes introduced by molecular modifications.

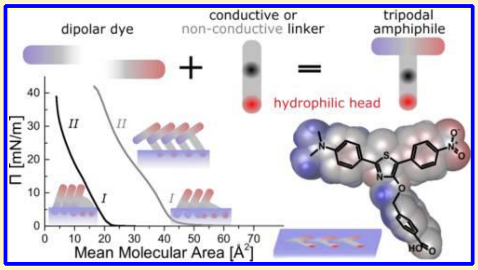

INTRODUCTION

In addition to molecular structures,[1−3] particularly supramolecular structures essentially determine active layer properties relevant in organic (opto)electronic devices,[4−7] such as spectral characteristics,[8−11] quantum efficiency,[12−14] open-circuit voltage,[15] conductivity,[16−18] excited-state dynamics,[19−21] and electrochemical potentials of electrons and holes.[22,23] The techniques to control and tune supramolecular structures involve antiparallel arrangement of dipolar donor−acceptor dyes,[24] layer-by-layer deposition,[25,26] and (self)assembly at heterointerfaces.[27,28] In the case of the latter, amphiphilicity is the central chemical motif, which is utilized in the Langmuir−Blodgett (LB) technique for advanced interface assembly.[27,28] Recently, dipolar and interface assemblies have been successfully combined by central functionalization of a push−pull-substituted thiazole.[29] In this and similar amphiphilic dyes, hydrophobic chromophores are connected with hydrophilic groups via typically flexible linkers,[30] such as alkyl chains.[31] These alkyl chains are frequently used to improve processing and morphologies of organic semiconducting films, like in the case of the polymer poly(3-hexylthiophene),[32,33] but do not contribute to conductivity because of the lacking π-electron

Received: November 21, 2018
Revised: January 25, 2019
Published: January 29, 2019

DOI: 10.1021/acs.langmuir.8b03893
Langmuir 2019, 35, 2561−2570

system. Hence, replacing these alkylic linkers by arylic linkers increases the ratio of potentially conducting and isolating moieties, which might increase the conductivity of the corresponding layers.[34] However, it is known that these linkers actually determine the supramolecular structure formed at interfaces,[31] thus influencing the conductivity of thin films indirectly. Consequently, it is not a priori clear whether the replacement of alkylic by arylic linkers improves conductivity.

To investigate the influence of the linkers on the supramolecular structure, its UV−vis absorption and emission properties, and finally on the conductivity, we stick in the present work to the above introduced motif of a dipolar dye centrally functionalized with linkers connecting to a hydrophilic group.[29] The dipolar dye is based on 4-hydroxy-1,3-thiazole that can be versatilely functionalized to yield various extents of amphiphilicity.[29,31,35,36] The introduction of the electron-donating dimethylamine and the electron-accepting nitro group to the thiazole creates a dipolar push−pull chromophore that is water insoluble and, hence, suitable for the LB technique. After presenting the synthetic routes for introduction of arylic and alkylic linkers to the hydrophilic carboxylic acid group and characterizing their optical and electronic properties in solution, we investigate the influence of the linker on the supramolecular structures obtained via the LB technique and characterize their UV−vis absorption spectra and conductivity.

■ RESULTS AND DISCUSSION

Syntheses. The target structure **7**, which contains the arylic linker as introduced in Scheme 1, can be synthesized partially according to routes described[29] for the reference structure **5** featuring the alkylic linker: From the thioamide **1** and the α-bromophenylacetic acid **2**, the thiazole moiety **3** was obtained via Hantzsch' thiazole synthesis (see Scheme 2). Alkylation of the 4-hydroxy group via Williamson-type etherification with ω-bromoacetic acid, ω-bromohexanoic acid, and ω-bromoundecanoic acid, respectively, leads to well-soluble precursors of the amphiphilic thiazoles **4** with three different linker lengths. Additionally, the arylation of **3** with ethyl 4-(bromomethyl)-benzoate leads to the benzylated derivative **6**, where the phenyl ring works as a conjugated rigid linker with approximately the same distance between the polar anchor group and the chromophore as in **4_5**. The deprotections of the alkylic carboxy groups of **4** were carried out with potassium hydroxide in anhydrous ethanol in good to excellent yields to get **5_*n*** (with *n* as the number of the CH_2 groups). When applying the latter procedure to the benzylic derivate **6**, the benzylic ether instead of the methyl ester was cleaved and 4-hydroxythiazole **3** was isolated. Thus, another benzylation of **3** with *tert*-butyl 4-(bromomethyl)benzoate to **8** was performed. Because *tert*-butylesters are stabile under alkaline conditions but labile under acidic conditions, the cleavage of **8** was carried out in trifluoroacetic acid and **7** was isolated in excellent yields.

Scheme 1. Central Attachment of a Hydrophilic Head Group to a Dipolar Chromophore via a Hydrophobic Conductive Arylic and Nonconductive Alkylic Linker Yields a "T-Shaped" Amphiphile That Orthogonally Combines Dipolar with Interface Assembly

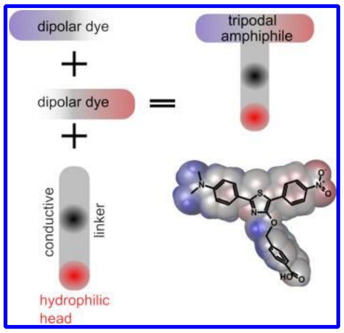

UV−Vis Spectroscopy in Solutions. In order to determine the influence of intra- and possible intermolecular interactions in solution, UV−vis absorption and steady-state emission spectra of the chromophores with the two different linkers, alkylic (**5**) and arylic (**7**), were recorded in solvents of different polarities.

The extinction coefficient ($\varepsilon(\lambda)$) spectra of **5_5** (Figure 1) show pronounced single absorption peaks with a 60% higher extinction coefficient ($\varepsilon \approx 3.5 \times 10^4$ M^{-1} cm^{-1}) than reported for a similar class of thiazoles without the push−pull character.[31] The absorption maximum slightly shifts from 448 nm in toluene to 464 nm in dimethyl sulfoxide (DMSO). This red shift upon increasing the solvent polarity from toluene to DMSO (see Table 1) points to an increased dipole moment in the first excited state (S_1 state) as compared to the ground state,[37] as also corroborated by the increasing Stokes shift shown in Figure 1. The amplitude of the maximum of the extinction coefficients does not change significantly upon varying solvent polarity.

The absorption spectrum of **7**, which differs from **5_5** just in the linker that is electronically not connected with the chromophore in either case, again features a peak at 450 nm and in addition a major peak located at 405 nm. In addition to this peak, a further difference between the absorption spectra of **5_5** and **7** exhibits the extinction coefficients that are an order of magnitude lower for **7** as compared to **5_5** (see Figure 1).

Intuitively and according to the quantum chemical calculations in Figure 2, **5_5** and **7** shall feature virtually identical extinction coefficients and oscillator strengths if the linker and the COOH group would not interact with the chromophore. Fluorescence excitation spectra shown in Figure 3A reveal that the additional peak that is blue-shifted from the major absorption peak originates from a different species. Such a different, blue-shifted, species of **7**, which are not observed for **5**, might be (a) H-aggregates that are stabilized by the arylic linker, (b) additional conformers that are energetically stabilized by interactions between the arylic linker and the chromophore, and (c) a protonated form of **7** because the arylic linker causes an increased acidity of the COOH moiety, thus causing protonation of the chromophore.

Origin (a) is ruled out because the absorption spectra do not depend on the concentration of **7**, as shown in Figure 3B. The decrease of the fluorescence of the major species at 570 nm for higher concentrations of **7** ($c > 5 \times 10^{-5}$ M) is attributed to dynamic quenching. The development of absorption spectra in course of an acid−base titration (Figure 3C) shows hypsochromic shifts of both the absorption and emission spectra upon protonation of the chromophore. The position of the absorption maximum of the protonated form matches with one of the peaks exclusively observed for **7** at 400 nm. However, neither the reduction of extinction coefficients by 1 order of magnitude nor the extremely small Stokes shift (λ_{max}(Abs) = 400 nm, λ_{max}(Em) = 430 nm) when replacing the alkylic with the

DOI: 10.1021/acs.langmuir.8b03893
Langmuir 2019, 35, 2561−2570

Scheme 2. Synthesis of the Amphiphilic Dyes[a]

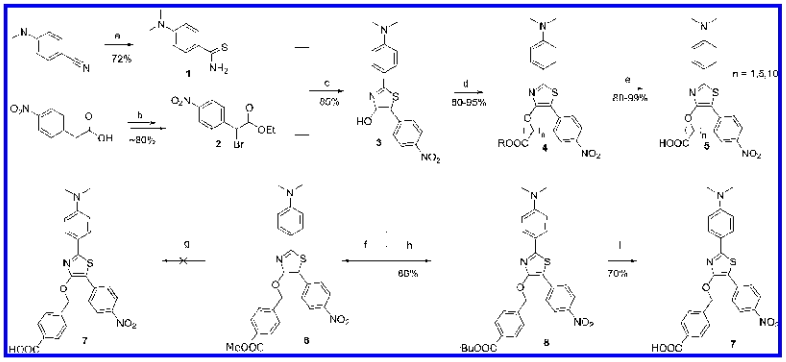

[a]Details: (a) O,O′-diethyl-dithiophosphate (1.1 equiv), water (1 equiv), rt 50 °C, (b) 1. TsOH (cat.), EtOH, reflux, 2. NBS (1.3 equiv), CCl_4, hν, reflux, (c) NaOAc (2.5 equiv), EtOH, reflux, (d) K_2CO_3 (1.5 equiv), NaI (cat.), acetone, reflux, (e) KOH (4 equiv), EtOH (anhydrous), 50 °C, (h) K_2CO_3 (1.5 equiv), NaI (cat.), acetone, reflux, (i) TFA, 50 °C.

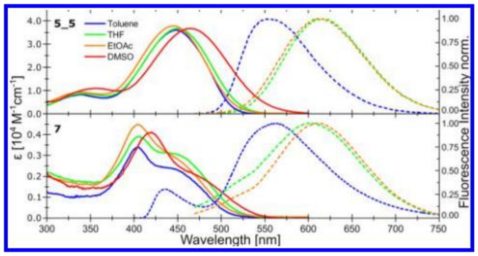

Figure 1. Extinction coefficient (ε) (solid line) and normalized emission (dotted line) spectra of 5_5 and 7 in toluene (Tol, blue), tetrahydrofuran (THF, green), ethyl acetate (EtOAc, orange), and DMSO (red).

Table 1. Absorption and Emission Maximum as Well as Extinction Coefficients of 5_5 and 7 Dissolved in Tol, THF, EtOAc, and DMSO

	5_5			7		
	λ_{Abs} [nm]	ε(λ) [M^{-1} cm^{-1}]	λ_{Em} [nm]	λ_{Abs} [nm]	ε(λ) [M^{-1} cm^{-1}]	λ_{Em} [nm]
DMSO	464	36 710		420	4100	
EtOAc	445	37 910	612	403	4450	600
THF	450	36 680	615	405	3930	612
Tol	448	36 030	554	405	3270	563

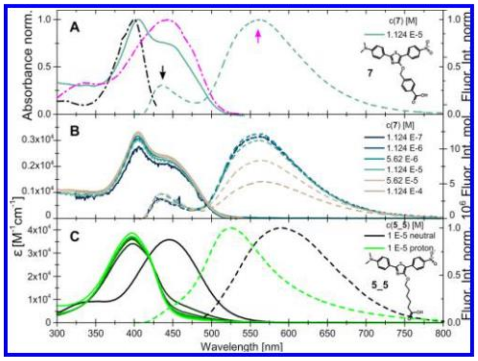

Figure 3. (A) Normalized emission excitation spectra (dashed–dotted) at λ_{em} = 430 (black) and 560 nm (pink) with normalized absorbance (solid) and emission (dashed) of 7 with c = 1.124 × 10^{-5} M in toluene. (B) Extinction coefficient (ε) (solid line) and molar emission (dotted line) spectra of 7 in toluene for different concentrations (from 1 × 10^{-7} M: dark blue to 1 × 10^{-4} M: gray). (C) Extinction coefficient (ε) and normalized emission of the neutral (black) and protonated species (green) and the different intermediate states of 5_5 in methanol.

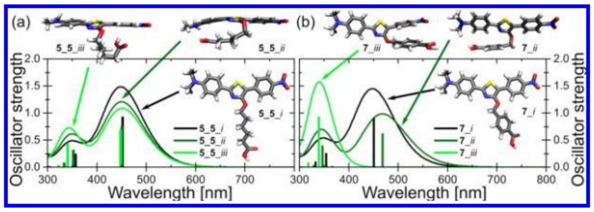

Figure 2. TD-DFT-derived absorption spectra of different conformers of 5_5 and 7.

DOI: 10.1021/acs.langmuir.8b03993
Langmuir 2019, 35, 2561−2570

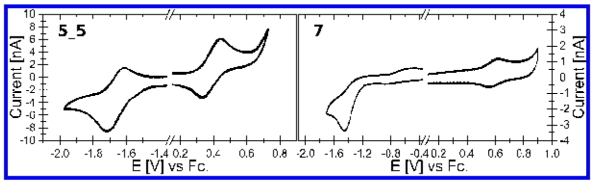

Figure 4. Cyclic voltammograms of 5_5 (left) and 7 (right) in THF.

arylic spacer is reproduced upon protonation. The small Stokes shift of the species absorbing at 400 nm hints to a rigidification of the chromophore, likely due to interaction between the arylic spacer and the chromophore in 7 (equals (c), see above). The influence of conformers of 7, particularly those with interactions between the linker and chromophore, on the absorption spectra is investigated in the following.

A conformer analysis for 7 yielded three distinct types of conformers shown in Figure 2b, which are as follows: (i) noninteracting and a (ii) ph-COOH−N(CH$_3$)$_2$-ph acid−base-type conformer and (iii) a ph-COOH−π-system interacting conformer. In the latter, 7_iii, the ph-NO$_2$ moiety is decoupled from the remaining chromophore (tilted perpendicular). This energetically unfavorable conformation (see Supporting Information, Table S1) is stabilized by π−π interactions between the ph-NO$_2$ moiety and the aryl linker. The time-dependent-density functional theory (TD-DFT)-derived absorption spectra of these three conformers distinctly differ as shown in Figure 2b: as compared to the noninteracting conformers (7_i), the ph-COOH−N(CH$_3$)$_2$-ph intramolecular acid−base interaction (7_ii) considerably decreases the oscillator strength of the energetically lowest bright electronic transition, while the UV peak at ≈350 nm gains oscillator strength. In contrast, no bright peak is present at wavelengths longer than 400 nm in the case of the ph-COOH−π-system interacting conformer 7_iii but rather one prominent peak in the UV spectral range (at ≈350 nm in Figure 2b). Considering the possible errors of TD-DFT in predicting electronic excitation energies, the absorption of 7_iii might be assigned to the 400 nm peak in question. The large total energies of 7_ii and 7_iii as compared to 7_i reported in Table S1 might be reduced to energies thermally available at room temperature if explicit solvent molecules stabilize 7_ii and 7_iii. Finally, we deduce from the conformer analysis that the experimental absorption spectra of 7 in all solvents might be basically considered as an approximately balanced superposition of 7_iii and 7_i/_ii. Thus, the 400 nm absorption peak and the overall decreased extinction coefficients of 7 as compared to 5_5 are finally attributed to intramolecular interaction in 7, which involve the aryl spacer and are hence not present in 5_5.

Electrochemical Characterization of the Thiazoles in Solution. To determine the energies of the highest occupied molecular orbital (HOMO) and lowest unoccupied molecular orbital (LUMO), cyclic voltammetry measurements were performed (for details, see experimental details). As depicted in Figure 4, 5_5 shows one reversible oxidation wave at E_{ox} = 0.44 V and one reversible reduction wave at E_{red} = −1.72 V. 7 shows one reversible oxidation wave at E_{ox} = 0.45 V and one irreversible reduction wave at E_{red} = −1.62 V. According to Menzel et al.,[38] both oxidations are assigned to the amino moiety.

In contrast to 5_5, the reduction wave of 7 is not reversible and is shifted by +0.1 V. Because 5_5 and 7 feature identical push−pull-type chromophores that stabilize the RNO_2^{-*} radical anion formed upon reduction, reversibility of the reduction has been expected for both thiazole derivatives, as known from aprotic solutions in THF.[39] However, in presence of a proton source, an irreversible pathway opens through protonation of the radical anion.[40] This difference in reduction reversibility between 5_5 and 7 is again attributed to the linker, as discussed above. In the case of conformer 7_iii, the carboxylic acid of the benzylic moiety can interact with the nitro group because of the proximity between these moieties. Such interaction may lead to an auto protonation and the irreversibility of the reduction of 7.[41,42]

The HOMO and LUMO energies were derived from the onset potentials of oxidation and reduction signals of the cyclic voltammograms[43] (5_5: $E_{HOMO/LUMO}$ = −4.92/−2.85 eV; 7: $E_{HOMO/LUMO}$ = −4.97/−3.02 eV, see Table 2). These frontier molecular orbital energies prove the here investigated thiazoles as suitable candidates for optoelectronic materials when employed in standard optoelectronic device structures with respect to charge injection and extraction.[44−49] The fact that the electrochemical gap is larger than the optical gap is attributed to strong molecular and solvent shell reorganization with reduction or oxidation. Furthermore, in contrast to solids, the additional charge cannot be delocalized over neighboring molecules. In total, these differences between dissolved molecules and solids yield an electrochemical gap of the dissolved molecule that can be significantly smaller than the polaronic gap in corresponding solids (cf. the work of Deibel et al.[50]) and also smaller than the optical gap.

Table 2. UV−Vis Spectroscopic and Electrochemical Properties of 5_5 and 7

	E_{ox}^{onset} [a] [V]	E_{red}^{onset} [a] [V]	E_{HOMO} [b] [eV]	E_{LUMO} [b] [eV]	E_{gap}^{CV} [c] [eV]	E_{gap}^{opt} [d] [eV]
5_5	0.31	−1.56	−4.92	−2.85	2.07	2.38
7	0.34	−1.39	−4.97	−3.02	1.95	2.37

[a] Recorded by cyclic voltammetry in 0.1 M solution of $TBAPF_6$ in THF vs $E_{onset}(Fc/Fc^+)$. [b] Calculated via $E_{HOMO} = -[E_{onset}(Ox) - E^0_{1/2}(Fc/Fc^+)] - 5.1$ eV and $E_{LUMO} = -[E_{onset}(red) - E^0_{1/2}(Fc/Fc^+)] - 5.1$ eV.[51] [c] $E_{gap}^{CV} = E_{LUMO} - E_{HOMO}$, measured in THF. [d] Calculated from the onset (10%) of the absorption spectra, measured in THF.

Supramolecular Structure of Layers at the Air−Water Interface. The supramolecular structures of thin films of the reference amphiphile 5_5 produced by means of the LB technique have been detailed recently.[29] It was found that the combination between dipolarity and amphiphilicity in 5_5 yields two solid phases, as revealed by the minimum in the compressibility modulus $C_S^{-1} = -A\,d\Pi/dA$[52−54] at 30 Å^2 (see Figure 5A).[29] In the first phase (A_{0I} > 30 Å^2), 5_5 is anchored in the subphase via the carboxylic acid and the amino groups, as revealed by weakening the anchor strength of the latter upon

DOI: 10.1021/acs.langmuir.8b03993
Langmuir 2019, 35, 2561−2570

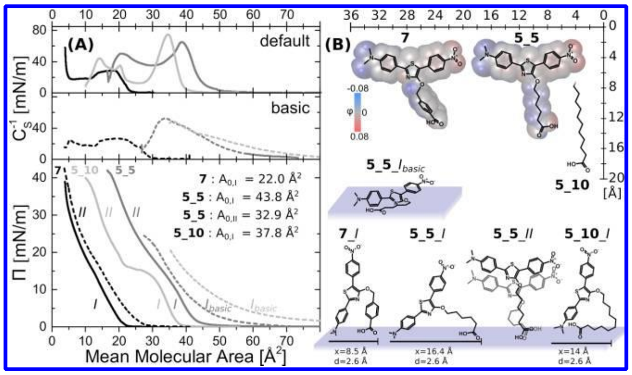

Figure 5. (A) Π(*A*)-isotherm and compressibility modulus C_S^{-1} of the 2-(4-*N*,*N*-dimethylaminophenyl)-4-hydroxy-5-nitrophenyl-1,3-thiazoles with a conjugated linker 7 (black), the alkylic linker with 5 CH_2 groups **5_5** (gray, reported in ref 29), and 10 CH_2 groups **5_10** (light gray) in ultrapure water (solid) and water with 1% Na_2HPO_4 added (dashed). (B) Lewis structure and the electrostatic potentials on van der Waals surfaces of **7** (left) and **5_5** (right) and the supramolecular structures of **7**, **5_5**, and **5_10** derived from the individual solid-state phases of the Π(*A*)-isotherm.

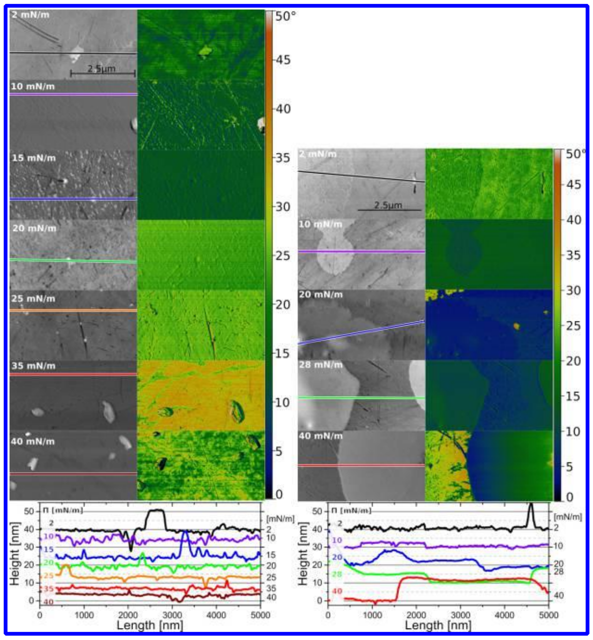

Figure 6. AFM images of LB films of **5_5** (left) and **7** (right) at different deposition pressures; left row: topography images and right row: phase images.

increasing the subphase basicity (see isotherm shifts in Figure 5).[29] With further lateral compression, phase II ($A_{0,II}$ < 30 Å²) forms in addition to phase I upon J-type dipolar arrangement as revealed by absorption extensions to the red region in UV−vis spectra (see Figure 7).[29]

Such dipolar reassembly seems to be facilitated by a more flexible linker, as shown by the pronounced transition phase of **5_10** (see Figure 5), which features a twice as long alkylic linker than **5_5**. However, rigidification by replacing the alkylic chain by the phenylene linker might hamper this dipolar reassembly in the case of **7**. The Π(*A*)-isotherm of **7** is notably shifted to smaller areas and features a shallower minimum of the compressibility modulus (at *A* = 5−12 Å²), as compared to **5_5**. The first solid phase of **7** might be structurally related to phase I or II of **5_5**, but, as deduced from the small mean molecular area ($A_{0,I}$ = 21 Å²), it apparently features a denser packing because of the more rigid molecular structure (see Figure 5 for the geometrical motif). Beyond rigidification, the phenylene linker in **7** likely π-interacts with the adjacent chromophores intra- or intermolecularly, which further contributes to the differences in the supramolecular structures. The second phase features an area that is unphysically small for a two-dimensional Langmuir layer ($A_{0,II}$ = 7 Å^2). Hence, **7** reassembles into three-dimensional structures in the second solid phase that features three-time higher packing density than the Langmuir layer in phase I.

These three-dimensional structures of phase II of **7** are multilayered films as revealed by the atomic force microscopy (AFM) data in Figure 6 for LB layers deposited at Π_{LB} = 2, 10, 20, 28, and 40 mN/m. The corresponding plateaus are exceptionally flat and homogeneous, thus indicating a uniform distinct supramolecular structure in the constituting layers. Also, the flat areas surrounding the plateaus are exceptionally smooth and homogeneous for all the deposition pressures, except for Π_{LB} = 2 and 40 mN/m, as revealed by the topography and AFM phase images. In addition, the base and plateau regions show the same AFM phase, that is, chemical surface. Therefore and because the plateau height h_P of 2−3 nm (for Π_{LB} = 2 and 10 mN/m) approximately is equal to twice the molecular lengths of ≈1.5 nm (see Figure 5B), the plateaus are assigned to LB double layers on top of the monolayer. The step size of the plateau increases from h_P = 2−3 nm (Π_{LB} = 2 and 10 mN/m) to $2h_P$ (Π_{LB} = 20 mN/m), $2-3h_P$ (Π_{LB} = 28 mN/m), and $4h_P$ (Π_{LB} = 28 mN/m), thus showing that multilayers are locally present. The LB-transfer ratios vary between 0.7 and 1.6, thus indicating that the local multilayer formation additionally happens during the deposition process. The AFM data of **7** show no changes in the supramolecular structure on the quartz glass upon increased surface pressure at deposition.

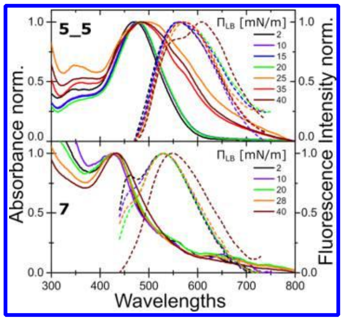

Figure 7. Absorption and emission spectra of **5_5** (450 nm excitation) (reported in ref 29) and **7** (420 nm excitation) at certain LB deposition pressures Π_{LB} and in solution (gray).

Furthermore, the UV−vis absorption spectra of LB films of **7** deposited at various surface pressures shown in Figure 7 reveal that dipolar reorganization does not occur during lateral compression in the LB process as no red-shifted J-aggregate absorption is observed, cf. the UV−vis absorption spectra of **5_5**. In contrast, the UV−vis absorption spectra of LB films of **7** (Figure 7) basically resemble those of the solutions but with the double peak structure smeared, enhanced UV absorption, and tails till 800 nm, which are due to reflection of the quartz glass substrate. Upon increasing the surface pressure at the deposition of **7**, the low-energy absorption edge and the fluorescence main peak are virtually constant, except at Π_{LB} = 40 mN/m where a small red shift ($\Delta\lambda_{max}$ = 6 nm) is observed. Hence, as extended absorption features at the low-energy absorption edge are only observed for **5_5** but not for **7**. Thus, the alkyl spacer enables dipolar assembly, whereas the arylic spacer hampers dipolar assembly.

Compared to **5_5**, which features a grainy morphology in phase I and where phase II coexists with phase I, LB films at phase II of **7**, which shows constant absorption spectra and exceptionally smooth morphological features, are expected to have a uniform homogeneous supramolecular structure. Surprisingly, the IR-ellipsometric spectra shown in Figure 8 feature anisotropic signals neither for LB film made from **5_5** nor from **7**. Thus, in the case of **5_5**, the apparently smooth and homogeneous films (Π_{LB} = 25 mN/m, Figure 6) are constituted by sub-microdomains with different supramolecular structures (due to partial dipolar reassembly as deduced from the UV−vis absorption spectra). Similarly, in the case of **7**, the presumably distinct molecular orientations in the individual crystalline domains seen in the AFM topography images are averaged in the IR-ellipsometric measurements.

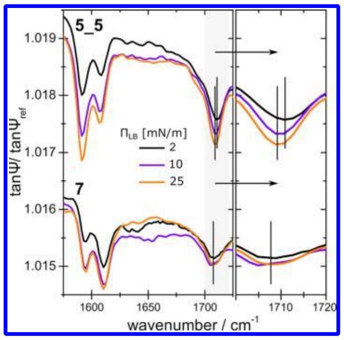

Figure 8. IR ellipsometry of the different types of linkers with the push−pull thiazole on silicon (left) and detailed C═O part (right).

However, the IR-ellipsometric spectra show C═O absorption bands (ca. 1710 cm^{-1}) that slightly shift to smaller energies upon increasing Π_{LB}. This shift is interpreted as increasing interaction of the COOH moiety with its environment, particularly with the amine function, as shown for the supramolecular structure in the first solid phase of the $\Pi(A)$-isotherm. In detail, the C═O-band of **5_5** changes its shape and shifts by about 2 cm^{-1} upon transition from the liquid to the first solid phase (Π_{LB}: 2 → 10 mN/m), which involves increasing interactions between the amine and the COOH function that are both dissolved in the aqueous subphase beneath the Langmuir layer (see the scheme in Figure 5), thus being expected to be in proximity in the resulting LB layers deposited onto silicon. This C═O absorption band does not further shift by increasing Π_{LB} to 25 mN/m. In the case of **7**, the C═O band slightly splits (composed of a peak at 1705 and 1712 cm^{-1}) upon changing from the liquid phase to the first solid phase (Π_{LB}: 2 → 10 mN/m). The supramolecular structures giving rise to the double peak structure at Π_{LB} = 10 mN/m are assigned to the background layer and the plateaus shown in the AFM pictures in Figure 6, respectively.

DOI: 10.1021/acs.langmuir.8b03893
Langmuir 2019, 35, 2561−2570

Electric Properties. After having identified the distinct supramolecular structures in phases I and II of **5_5** and the stabilization of phase I via the rigid spacer in **7** that hampers dipolar supramolecular reorganization, we apply conductive AFM (cAFM) to investigate whether the higher fraction of π-conjugated moieties in **7** finally increases the conductivity as compared to **5_5** or not.[34] Therefore, LB films of **5_5**, phases I and II, and **7**, phase I, were deposited on gold-coated quartz glass and current (I)−voltage (V) curves were measured at specific points of the LB layers.

All I−V curves of the LB films of **5_5** (first and second solid phases, Π_{LB} = 10, 25 mN/m) shown in Figure 9 represent shapes that are typical for semiconductor resistors.[55] The initial voltage increase yields exponentially rising currents at voltages larger than 1 V, thus indicating activated transport involving a potential barrier[56] between the electrodes and molecules. However, the onset voltage of current rise, that is, the potential barrier,[57] varies in dependence on the direction of the applied voltage (2 to −2 V and −2 to 2 V), which can be explained by two basic mechanisms: thermionic emission (Schottky emission) and electron tunneling. The linear increase of dI/dU with I (see Figures S10−S12) indicates a tunneling process through the monolayer.[56]

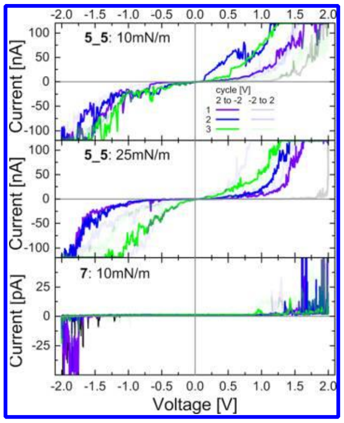

Figure 9. I−V curves of point-contact measurements via cAFM of LB films of **5_5** (Π_{LB} = 10, 25 mN/m) and **7** (Π_{LB} = 10 mN/m) with three full cycles (purple, blue, green) separated into 2 to −2 V (solid) and −2 to 2 V (pale) and a starting cycle (black) from 0 to 2 V. Note the different scaling of the current axes between **5_5** and **7**.

Interestingly, all I−V curves of **5_5** shift about 1 V to lower voltages upon repeated I−V cycles, which is assigned to decreasing potential barriers, that is, higher conductivity, during cAFM measurements. In the case of **5_5**, phase I, the I−V curves change only little (≈0.5 V) between the three full cycles (starting from −2 to +2 V and back to −2 V) for negative voltages, whereas larger shifts (≈1 V) are observed for positive voltages (see Figure 9). These shifts in the I−V characteristics are assigned to supramolecular reorganization upon electric operation enabled by the flexibility of the alkylic linker in phase I of **5_5**. In the second solid-state phase of **5_5** (Π_{LB} = 25 mN/m), which is stabilized by dipolar interactions, the turn-on voltage of the I−V curve in the starting cycle (0−2 V) increases by (≈0.6 V). However, for the following three full cycles, the I−V curves develop similar as those of phase I described above but reach slightly larger currents. Hence, supramolecular rearrangement upon electric operations occurs in all solid LB phases of **5_5**.

In stark contrast, virtually no current (pA-scale, cf. with nA-scale of **5_5**) was measured between −2 and 2 V for the LB films deposited in the first solid phase of **7** (Π_{LB} = 10 mN/m). Furthermore, the supramolecular structures rigidified by the arylic linker, as discussed above, do not rearrange upon electric operation as no changes in the I−V curves upon repeated I−V cycles are observed. Hence, though the supramolecular structure is stabilized and the fraction of π-conjugated moieties is increased upon replacing the alkylic with the arylic linker, the resulting LB films are not conductive.

CONCLUSIONS

In this work, we investigated whether an increase in the fraction of π-conjugated molecular moieties causes supramolecular structures featuring increased conductivity. Therefore, we have focused on thiazole dyes that are expected to form stable supramolecular structures because of cooperative dipolar and amphiphilic assembly and binding.[29] In this class of T-shaped dipolar amphiphiles, a hydrophilic head is centrally linked to a hydrophobic, though dipolar, chromophore.[29] Although in previous works nonconductive alkyl chains have been used as linkers,[29,31,35,36] they are replaced by phenylene linkers in the present work. Replacing a linker might appear as subtle molecular structure modification that does not deteriorate the supramolecular structure. In stark contrast, our work shows that even the molecular properties are significantly altered, which is ascribed to intramolecular π−π interactions between the phenylene spacer and the thiazole dye and acid−base interactions between the carboxylic acid and the amine moieties that are changed because of the increase in acidity upon replacing the alkylic with the arylic linker. This change affects both electric and photonic molecular properties: the arylic linker stabilizes the reduced form of the dipolar chromophore, thus hampering reversibility of the reduction, and decreases the extinction coefficients in the UV−vis spectra, as compared to the alkylic linker.

The molecular rigidification of the dipolar amphiphiles upon replacing the alkylic by the arylic linker also alters the supramolecular structure: namely, a denser packing of the Langmuir layer and hampered dipolar reassembly upon increasing lateral pressure applied during the LB process. The denser packing is deduced from the LB isotherm and the hampered dipolar assembly is revealed by the UV−vis absorption spectra, which feature J-aggregate-type red-shifted absorption features only for the LB films made from the amphiphilic thiazole bearing the alkylic linker and not from the derivative bearing the arylic linker. Instead of the dipolar reassembly upon increasing the surface pressure, the thiazole bearing the arylic linker forms smooth and homogeneous multilayers, as revealed by AFM. Finally, cAFM revealed that actually the supramolecular structures involving the alkylic and not the arylic linker show conductivity and additionally reorganize toward higher conductivity upon electric operation. Hence, we could show in this work that the actual supramolecular structure clearly determines optoelectronic properties. In the case of the here investigated dipolar and amphiphilic thiazoles, the flexibility of the alkylic linker yields high extinction coefficients, reversibility of reduction, and conductive LB layers,

DOI: 10.1021/acs.langmuir.8b03893
Langmuir 2019, 35, 2561−2570

whereas the rigid, electron-pulling, and π-interacting arylic linker deteriorates these properties. Finally, the implementation of additional π-conjugated molecular moieties alters the supramolecular structure that becomes less conductive instead of providing additional paths for charge carrier migration.

■ EXPERIMENTAL AND THEORETICAL DETAILS

Electrochemistry. The cyclovoltammetric measurements (oxidation and reduction side investigated separately) were performed with a Metrohm Autolab PGSTAT30 potentiostat in 0.1 M solution of $TBAPF_6$ in THF (concentration of compounds: 1×10^{-5} M) on a graphite working electrode with a scanning speed of 50 mV s^{-1}; platinum was used as the counter electrode and Ag/AgCl as the reference electrode. The data were calibrated externally versus ferrocene/ferrocenium oxidation half-cell potential $E^0_{1/2}$ ($E^0_{1/2}$(Fc/Fc^+) = 0.476 V). The onset potentials were determined by calculating the crossing between lines fitted to the onset and to the corresponding background of the cyclovoltammogram for each oxidation and reduction.

UV−Vis Absorption and Emission Spectroscopy. UV−vis absorption spectra of solutions were measured with a Lambda 45 spectrometer from PerkinElmer, and emission spectra of solutions were measured with a Jasco FP 6500 instrument.

Standard fluorescence measurements of the LB films were made on a costume built setup. This consists of an IsoPlane 320 Spectrograph with a cooled Pixis CCD-Camera from Princeton Instruments. A fiber-coupled 5 mW laser with a 405 nm output wavelength was used as the excitation source (incident under 55°), and the emission was detected under 35° with respect to the substrate normal. Long-pass filters with low self-fluorescence from ITOS were used to block scattered excitation light.

LB Films. Solutions of the dyes (1 mg/mL in $CHCl_3$) were carefully spread onto the subphase (ultrapure water) of the LB trough (KSV NIMA Alternate L 105 and KSV 5000). For complete evaporation of $CHCl_3$, we waited for 10 min before moving the barriers. Then, the barriers were compressed with 5 mm/min to record the isotherms. Quartz glass substrates were treated with acetone and isopropanol in an ultrasonic bath for each solvent three times, and the substrates were stored in isopropanol. The deposition of LB films on the quartz glass (30 mm × 5 mm × 1 mm) was done using Z-type dipping with constant pressure and a dipping speed of 5 mm min^{-1}.

Scanning Force Microscopy. AFM was carried out using a Veeco Digital Instruments AFM Nanoscope IIIa, with a head Dimension 3100 in tapping mode on air with a silicon tip (radius < 8 nm) at 300 kHz with a force constant of E40 N/m (BudgetSensors Tap 300-G).

Conductive-Scanning Force Microscopy. cAFM measurements have been carried out on a NanoWizard 3 from JPK. ContE-G tips (BudgetSensors, k = 0.2 N/m) mounted on the JPK C-AFM module have been used in contact mode with the lowest force possible to map and record I−V measurements. The electrical contact between the sample and the sample holder has been checked before each measurement with a multimeter.

IR Ellipsometry. For IR-ellipsometric investigations, thiazoles **5_5** and **7** were deposited at varied surface pressures (Π_{LB} = 2, 10, 25 mN/m) on silicon substrates, which have a similar chemical surface as the quartz glass used for the preparation of AFM samples because of an oxide surface layer on silicon.

The samples were measured in a dry air-purged environment. The used IRSE setup is a custom-built infrared spectroscopic ellipsometer attached to a Fourier transform infrared (Vertex 70 from Bruker, Germany) spectrometer equipped with a liquid nitrogen-cooled photovoltaic mercury−cadmium−telluride detector. The ellipsometric tan Ψ spectra (corresponding to the amplitude ratio of reflected p- and s-polarized components) were taken at a spectral resolution of 4 cm^{-1} and an incidence angle of 65°. Further details on the ellipsometric method can be found in ref 58.

DFT Calculations. Quantum chemical structure optimizations and calculations of electrostatic potential and absorption spectra on **5_5** and **7** monomers were performed using DFT and its time-dependent derivative (TD-DFT) as implemented in Turbomole[59] and applying the generalized gradient approximation functional BP86 (preoptimization), followed by the hybrid functionals and B3LYP,[60] the def2-SVP (preoptimization) and -TZVP basis sets,[61] and the MARI-J approximation in the case of BP86, which have been shown to yield reasonable electronic properties for a large variety of molecular motives, including push−pull systems and extended π-electron systems.[3,62−65]

■ ASSOCIATED CONTENT

Supporting Information

The Supporting Information is available free of charge on the ACS Publications website at DOI: 10.1021/acs.langmuir.8b03893.

> 2-((2-(4-(Dimethylamino)phenyl)-5-(4-nitrophenyl)-thiazol-4-yl)oxy)acetic acid, -hexaonic acid, and -undecanoic acid synthesis; materials; NMR spectra; DFT-derived total energies; and dI/dU versus I plot of a LB film (PDF)

■ AUTHOR INFORMATION

Corresponding Authors
*E-mail: rainer.beckert@uni-jena.de (R.B.).
*E-mail: martin.presselt@leibniz-ipht.de (M.P.).

ORCID
M. L. Hupfer: 0000-0001-8890-0684
J. Preiß: 0000-0002-7570-7305
K. Hinrichs: 0000-0002-6580-7791
V. Deckert: 0000-0002-0173-7974
B. Dietzek: 0000-0002-2842-3537
M. Presselt: 0000-0002-5579-0260

Notes

The authors declare no competing financial interest.

■ ACKNOWLEDGMENTS

The authors would like to thank the Bundesministerium für Bildung und Forschung (BMBF FKZ 03EK3507) and the Deutsche Forschungsgemeinschaft (DFG grant no. PR 1415/2-1) for financial support. J.P. acknowledges funding from the Nagelschneider Stiftung. L.R. acknowledges funding from the German Science Foundation (DFG) under TRR 166 ReceptorLight, project A2. V.D. acknowledges funding from the German Science Foundation (DFG) under TRR 234 Catalight, project A4. The authors would like to thank K. Kobow and I. Engler for support in the lab. K.H. additionally acknowledges support by the Ministerium für Innovation, Wissenschaft und Forschung des Landes Nordrhein-Westfalen, the Regierende Bürgermeister von Berlin—Senatskanzlei Wissenschaft und Forschung, and the European Union through EFRE 1.8/13.

■ REFERENCES

(1) Fitzner, R.; Elschner, C.; Weil, M.; Uhrich, C.; Körner, C.; Riede, M.; Leo, K.; Pfeiffer, M.; Reinold, E.; Mena-Osteritz, E.; Bäuerle, P. Interrelation between Crystal Packing and Small-Molecule Organic Solar Cell Performance. *Adv. Mater.* **2012**, *24*, 675−680.

(2) Szlapa, A.; Kula, S.; Blaszkiewicz, U.; Grucela, M.; Schab-Balcerzak, E.; Filapek, M. Simple donor−π−acceptor derivatives exhibiting aggregation-induced emission characteristics for use as emitting layer in OLED. *Dyes Pigm.* **2016**, *129*, 80−89.

(3) Presselt, M.; Schnedermann, C.; Schmitt, M.; Popp, J. Prediction of Electron Densities, the Respective Laplacians, and Ellipticities in Bond-Critical Points of Phenyl−CH−Bonds via Linear Relations to Parameters of Inherently Localized CD Stretching Vibrations and1H NMR-Shifts. *J. Phys. Chem. A* **2009**, *113*, 3210−3222.

(4) Mishra, A.; Bäuerle, P. Small Molecule Organic Semiconductors on the Move: Promises for Future Solar Energy Technology. *Angew. Chem., Int. Ed.* **2012**, *51*, 2020−2067.

(5) Sirringhaus, H. 25th Anniversary Article: Organic Field-Effect Transistors: The Path Beyond Amorphous Silicon. *Adv. Mater.* **2014**, *26*, 1319−1335.

(6) Presselt, M.; Bärenklau, M.; Rösch, R.; Beenken, W. J. D.; Runge, E.; Shokhovets, S.; Hoppe, H.; Gobsch, G. Subbandgap absorption in polymer-fullerene solar cells. *Appl. Phys. Lett.* **2010**, *97*, 253302.

(7) Herrmann, F.; Engmann, S.; Presselt, M.; Hoppe, H.; Shokhovets, S.; Gobsch, G. Correlation between near infrared-visible absorption, intrinsic local and global sheet resistance of poly(3,4-ethylenedioxythiophene) poly(styrene sulfonate) thin films. *Appl. Phys. Lett.* **2012**, *100*, 153301.

(8) Würthner, F.; Kaiser, T. E.; Saha-Möller, C. R. J-Aggregates: From Serendipitous Discovery to Supramolecular Engineering of Functional Dye Materials. *Angew. Chem., Int. Ed.* **2011**, *50*, 3376−3410.

(9) Gampe, D. M.; Nöller, F.; Hänsch, V. G.; Schramm, S.; Darsen, A.; Habenicht, S. H.; Ehrhardt, S.; Weiß, D.; Görls, H.; Beckert, R. Surprising characteristics of D-A-type functional dyes by introducing 4-alkoxythiazoles as the donor-unit. *Tetrahedron* **2016**, *72*, 3232−3239.

(10) Biesmans, G.; Verbeek, G.; Verschuere, B.; van der Auweraer, M.; De Schryver, F. C. On the fluorescence of anthracene chromophores in langmuir-blodgett films. *Thin Solid Films* **1989**, *169*, 127−142.

(11) Das, S.; Herrmann-Westendorf, F.; Schacher, F. H.; Täuscher, E.; Ritter, U.; Dietzek, B.; Presselt, M. Controlling Electronic Transitions in Fullerene van der Waals Aggregates via Supramolecular Assembly. *ACS Appl. Mater. Interfaces* **2016**, *8*, 21512−21521.

(12) Shewmon, N. T.; Watkins, D. L.; Galindo, J. F.; Zerdan, R. B.; Chen, J.; Keum, J.; Roitberg, A. E.; Xue, J.; Castellano, R. K. Enhancement in Organic Photovoltaic Efficiency through the Synergistic Interplay of Molecular Donor Hydrogen Bonding and π-Stacking. *Adv. Funct. Mater.* **2015**, *25*, 5166−5177.

(13) Li, Z.; Bian, J.; Wang, Y.; Jiang, F.; Liang, G.; He, P.; Hou, Q.; Tong, J.; Liang, Y.; Zhong, Z.; Zhou, Y.; Tian, W. Effect of Alkyl Chain Length on the Photovoltaic Performance of Oligothiophene-Based Small Molecules. *Sol. Energy Mater. Sol. Cells* **2014**, *130*, 336−346.

(14) Presselt, M.; Herrmann, F.; Shokhovets, S.; Hoppe, H.; Runge, E.; Gobsch, G. Sub-bandgap absorption in polymer-fullerene solar cells studied by temperature-dependent external quantum efficiency and absorption spectroscopy. *Chem. Phys. Lett.* **2012**, *542*, 70−73.

(15) Poelking, C.; Tietze, M.; Elschner, C.; Olthof, S.; Hertel, D.; Baumeier, B.; Würthner, F.; Meerholz, K.; Leo, K.; Andrienko, D. Impact of mesoscale order on open-circuit voltage in organic solar cells. *Nat. Mater.* **2014**, *14*, 434−439.

(16) Chen, Y.; Feng, Y.; Gao, J.; Bouvet, M. Self-assembled aggregates of amphiphilic perylene diimide-based semiconductor molecules: Effect of morphology on conductivity. *J. Colloid Interface Sci.* **2012**, *368*, 387−394.

(17) Grozema, F. C.; Siebbeles, L. D. A. Mechanism of Charge Transport in Self-Organizing Organic Materials. *Int. Rev. Phys. Chem.* **2008**, *27*, 87−138.

(18) Presselt, M.; Herrmann, F.; Hoppe, H.; Shokhovets, S.; Runge, E.; Gobsch, G. Influence of Phonon Scattering on Exciton and Charge Diffusion in Polymer-Fullerene Solar Cells. *Adv. Energy Mater.* **2012**, *2*, 999−1003.

(19) Kar, H.; Gehrig, D. W.; Laquai, F.; Ghosh, S. J-Aggregation, its Impact on Excited State Dynamics and Unique Solvent Effects on Macroscopic Assembly of a Core-Substituted Naphthalenediimide. *Nanoscale* **2015**, *7*, 6729−6736.

(20) Wong, C. Y.; Penwell, S. B.; Cotts, B. L.; Noriega, R.; Wu, H.; Ginsberg, N. S. Revealing Exciton Dynamics in a Small-Molecule Organic Semiconducting Film with Subdomain Transient Absorption Microscopy. *J. Phys. Chem. C* **2013**, *117*, 22111−22122.

(21) De la Cadena, A.; Pascher, T.; Davydova, D.; Akimov, D.; Herrmann, F.; Presselt, M.; Wächtler, M.; Dietzek, B. Intermolecular exciton-exciton annihilation in phospholipid vesicles doped with [Ru(bpy) 2 dppz] 2+. *Chem. Phys. Lett.* **2016**, *644*, 56−61.

(22) Kitchen, B.; Awartani, O.; Kline, R. J.; McAfee, T.; Ade, H.; O'Connor, B. T. Tuning Open-Circuit Voltage in Organic Solar Cells with Molecular Orientation. *ACS Appl. Mater. Interfaces* **2015**, *7*, 13208−13216.

(23) Zhong, S.; Zhong, J. Q.; Wee, A. T. S.; Chen, W. Molecular Orientation and Electronic Structure at Organic Heterojunction Interfaces. *J. Electron Spectrosc. Relat. Phenom.* **2015**, *204*, 12−22.

(24) Bürckstümmer, H.; Tulyakova, E. V.; Deppisch, M.; Lenze, M. R.; Kronenberg, N. M.; Gsänger, M.; Stolte, M.; Meerholz, K.; Würthner, F. Efficient Solution-Processed Bulk Heterojunction Solar Cells by Antiparallel Supramolecular Arrangement of Dipolar Donor-Acceptor Dyes. *Angew. Chem., Int. Ed.* **2011**, *50*, 11628−11632.

(25) Ariga, K.; Hill, J. P.; Ji, Q. Layer-By-Layer Assembly as a Versatile Bottom-Up Nanofabrication Technique for Exploratory Research and Realistic Application. *Phys. Chem. Chem. Phys.* **2007**, *9*, 2319−2340.

(26) Wang, Y.; Angelatos, A. S.; Caruso, F. Template Synthesis of Nanostructured Materials via Layer-by-Layer Assembly†. *Chem. Mater.* **2008**, *20*, 848−858.

(27) Ariga, K.; Yamauchi, Y.; Mori, T.; Hill, J. P. 25th Anniversary Article: What Can Be Done with the Langmuir-Blodgett Method? Recent Developments and its Critical Role in Materials Science. *Adv. Mater.* **2013**, *25*, 6477−6512.

(28) Langmuir, I. The Constitution and Fundamental Properties of Solids and Liquids. Ii. Liquids.1. *J. Am. Chem. Soc.* **1917**, *39*, 1848−1906.

(29) Hupfer, M. L.; Kaufmann, M.; Preiß, J.; Weiß, D.; Dietzek, B.; Beckert, R.; Presselt, M. Combining Dipolar Aggregate Formation with Two-Dimensional Assembly at Air-Water-Interfaces: Case of Amphiphilic Push-Pull-Thiazoles. *Adv. Mater.* **2019**, submitted.

(30) Schwieger, C.; Chen, B.; Tschierske, C.; Kressler, J.; Blume, A. Organization of T-Shaped Facial Amphiphiles at the Air/Water Interface Studied by Infrared Reflection Absorption Spectroscopy. *J. Phys. Chem. B* **2012**, *116*, 12245−12256.

(31) Hupfer, M. L.; Kaufmann, M.; Herrmann-Westendorf, F.; Sachse, T.; Roussille, L.; Feller, K.-H.; Weiß, D.; Deckert, V.; Beckert, R.; Dietzek, B.; Presselt, M. On the Control of Chromophore Orientation, Supramolecular Structure, and Thermodynamic Stability of an Amphiphilic Pyridyl-Thiazol upon Lateral Compression and Spacer Length Variation. *ACS Appl. Mater. Interfaces* **2017**, *9*, 44181−44191.

(32) Dang, M. T.; Hirsch, L.; Wantz, G. P3HT:PCBM, Best Seller in Polymer Photovoltaic Research. *Adv. Mater.* **2011**, *23*, 3597−3602.

(33) Beenken, W. J. D.; Herrmann, F.; Presselt, M.; Hoppe, H.; Shokhovets, S.; Gobsch, G.; Runge, E. Sub-bandgap absorption in organic solar cells: experiment and theory. *Phys. Chem. Chem. Phys.* **2013**, *15*, 16494−16502.

(34) Wang, Y.; Guo, H.; Harbuzaru, A.; Uddin, M. A.; Arrechea-Marcos, I.; Ling, S.; Yu, J.; Tang, Y.; Sun, H.; López Navarrete, J. T.; Ortiz, R. P.; Woo, H. Y.; Guo, X. (Semi)ladder-Type Bithiophene Imide-Based All-Acceptor Semiconductors: Synthesis, Structure-Property Correlations, and Unipolar n-Type Transistor Performance. *J. Am. Chem. Soc.* **2018**, *140*, 6095−6108.

(35) Habenicht, S. H.; Schramm, S.; Fischer, S.; Sachse, T.; Herrmann-Westendorf, F.; Bellmann, A.; Dietzek, B.; Presselt, M.; Weiß, D.; Beckert, R.; Görls, H. Tuning the polarity and surface activity of hydroxythiazoles - extending the applicability of highly fluorescent self-assembling chromophores to supra-molecular photonic structures. *J. Mater. Chem. C* **2016**, *4*, 958−971.

(36) Kaufmann, M.; Hupfer, M. L.; Sachse, T.; Herrmann-Westendorf, F.; Weiß, D.; Dietzek, B.; Beckert, R.; Presselt, M. Introducing double polar heads to highly fluorescent Thiazoles: Influence on supramolecular structures and photonic properties. *J. Colloid Interface Sci.* **2018**, *526*, 410−418.

(37) Preiß, J.; Herrmann-Westendorf, F.; Ngo, T. H.; Martínez, T.; Dietzek, B.; Hill, J. P.; Ariga, K.; Kruk, M. M.; Maes, W.; Presselt, M. Absorption and Fluorescence Features of an Amphiphilic meso-Pyrimidinylcorrole: Experimental Study and Quantum Chemical Calculations. *J. Phys. Chem. A* **2017**, *121*, 8614−8624.

(38) Menzel, R.; Kupfer, S.; Mede, R.; Weiß, D.; Görls, H.; González, L.; Beckert, R. Arylamine-Modified Thiazoles as Donor-Acceptor Dyes: Quantum Chemical Evaluation of the Charge-Transfer Process and Testing as Ligands in Ruthenium(II) Complexes. *Eur. J. Org. Chem.* **2012**, 5231−5247.

(39) Shalev, H.; Evans, D. H. Solvation of anion radicals: gas-phase versus solution. *J. Am. Chem. Soc.* **1989**, *111*, 2667−2674.

(40) Cadle, S. H.; Tice, P. R.; Chambers, J. Q. Electrochemical reduction of aromatic nitro compounds in the presence of proton donors. *J. Phys. Chem.* **1967**, *71*, 3517−3522.

(41) Koopmann, R.; Gerischer, H. Untersuchung der elektrochemischen Reduktion von Nitrobenzol durch Kombination von ESR-Messungen mit elektroanalytischen Methoden. *Ber. Bunsenges. Phys. Chem.* **1966**, *70*, 127−138.

(42) Kastening, B. Zur theorie der polarographischin ströme bei dismutation des elektrodenreaktionsprodukts. *J. Electroanal. Chem. Interfacial Electrochem.* **1970**, *24*, 417−426.

(43) Cardona, C. M.; Li, W.; Kaifer, A. E.; Stockdale, D.; Bazan, G. C. Electrochemical Considerations for Determining Absolute Frontier Orbital Energy Levels of Conjugated Polymers for Solar Cell Applications. *Adv. Mater.* **2011**, *23*, 2367−2371.

(44) Zhang, Q.; Li, B.; Huang, S.; Nomura, H.; Tanaka, H.; Adachi, C. Efficient blue organic light-emitting diodes employing thermally activated delayed fluorescence. *Nat. Photonics* **2014**, *8*, 326−332.

(45) Yoshida, H.; Yoshizaki, K. Electron affinities of organic materials used for organic light-emitting diodes: A low-energy inverse photoemission study. *Org. Electron.* **2015**, *20*, 24−30.

(46) Luo, Y.; Aziz, H. Correlation Between Triplet-Triplet Annihilation and Electroluminescence Efficiency in Doped Fluorescent Organic Light-Emitting Devices. *Adv. Funct. Mater.* **2010**, *20*, 1285−1293.

(47) Zhang, T.; Chu, B.; Li, W.; Su, Z.; Peng, Q. M.; Zhao, B.; Luo, Y.; Jin, F.; Yan, X.; Gao, Y.; Wu, H.; Zhang, F.; Fan, D.; Wang, J. Efficient Triplet Application in Exciplex Delayed-Fluorescence OLEDs Using a Reverse Intersystem Crossing Mechanism Based on a ΔES-T of around Zero. *ACS Appl. Mater. Interfaces* **2014**, *6*, 11907−11914.

(48) Shi, Y.; Guo, H.; Qin, M.; Zhao, J.; Wang, Y.; Wang, H.; Wang, Y.; Facchetti, A.; Lu, X.; Guo, X. Thiazole Imide-Based All-Acceptor Homopolymer: Achieving High-Performance Unipolar Electron Transport in Organic Thin-Film Transistors. *Adv. Mater.* **2018**, *30*, 1705745.

(49) Shi, Y.; Guo, H.; Qin, M.; Wang, Y.; Zhao, J.; Sun, H.; Wang, H.; Wang, Y.; Zhou, X.; Facchetti, A.; Lu, X.; Zhou, M.; Guo, X. Imide-Functionalized Thiazole-Based Polymer Semiconductors: Synthesis, Structure-Property Correlations, Charge Carrier Polarity, and Thin-Film Transistor Performance. *Chem. Mater.* **2018**, *30*, 7988−8001.

(50) Deibel, C.; Mack, D.; Gorenflot, J.; Scholl, A.; Krause, S.; Reinert, F.; Rauh, D.; Dyakonov, V. Energetics of excited states in the conjugated polymer poly(3-hexylthiophene). *Phys. Rev. B: Condens. Matter Mater. Phys.* **2010**, *81*, 085202.

(51) Trasatti, S. The absolute electrode potential: an explanatory note (Recommendations 1986). *Pure Appl. Chem.* **1986**, *58*, 955−966.

(52) Gong, K.; Feng, S.-S.; Go, M. L.; Soew, P. H. Effects of pH on the stability and compressibility of DPPC/cholesterol monolayers at the air-water interface. *Colloids Surf., A* **2002**, *207*, 113−125.

(53) Gew, L. T.; Misran, M. Albumin-fatty acid interactions at monolayer interface. *Nanoscale Res. Lett.* **2014**, *9*, 218.

(54) Petaccia, M.; Giansanti, L.; Leonelli, F.; Bella, A. L.; Gradella Villalva, D.; Mancini, G. Synthesis, characterization and inclusion into liposomes of a new cationic pyrenyl amphiphile. *Chem. Phys. Lipids* **2016**, *200*, 83−93.

(55) Bayat, A.; Lacroix, J.-C.; McCreery, R. L. Control of Electronic Symmetry and Rectification through Energy Level Variations in Bilayer Molecular Junctions. *J. Am. Chem. Soc.* **2016**, *138*, 12287−12296.

(56) Xu, D.; Watt, G. D.; Harb, J. N.; Davis, R. C. Electrical Conductivity of Ferritin Proteins by Conductive AFM. *Nano Lett.* **2005**, *5*, 571−577.

(57) Gayathri, H. N.; Kumar, B.; Suresh, K. A.; Bisoyi, H. K.; Kumar, S. Charge transport in a liquid crystalline triphenylene polymer monolayer at air-solid interface. *Phys. Chem. Chem. Phys.* **2016**, *18*, 12101−12107.

(58) Hinrichs, K.; Eichhorn, K.-J. *Ellipsometry of Functional Organic Surfaces and Films*, 2nd ed.; Springer International Publishing, 2018.

(59) Ahlrichs, R.; Bär, M.; Häser, M.; Horn, H.; Kölmel, C. Electronic structure calculations on workstation computers: The program system turbomole. *Chem. Phys. Lett.* **1989**, *162*, 165−169.

(60) Stephens, P. J.; Devlin, F. J.; Chabalowski, C. F.; Frisch, M. J. Ab Initio Calculation of Vibrational Absorption and Circular Dichroism Spectra Using Density Functional Force Fields. *J. Phys. Chem.* **1994**, *98*, 11623−11627.

(61) Weigend, F.; Ahlrichs, R. Balanced basis sets of split valence, triple zeta valence and quadruple zeta valence quality for H to Rn: Design and assessment of accuracy. *Phys. Chem. Chem. Phys.* **2005**, *7*, 3297−3305.

(62) Presselt, M.; Schnedermann, C.; Müller, M.; Schmitt, M.; Popp, J. Derivation of Correlation Functions to Predict Bond Properties of Phenyl−CH Bonds Based on Vibrational and1H NMR Spectroscopic Quantities. *J. Phys. Chem. A* **2010**, *114*, 10287−10296.

(63) Gampe, D. M.; Kaufmann, M.; Jakobi, D.; Sachse, T.; Presselt, M.; Beckert, R.; Görls, H. Stable and Easily Accessible Functional Dyes: Dihydrotetraazaanthracenes as Versatile Precursors for Higher Acenes. *Chem.—Eur. J.* **2015**, *21*, 7571−7581.

(64) Preiß, J.; Jäger, M.; Rau, S.; Dietzek, B.; Popp, J.; Martínez, T.; Presselt, M. How Does Peripheral Functionalization of Ruthenium(II)-Terpyridine Complexes Affect Spatial Charge Redistribution after Photoexcitation at the Franck-Condon Point? *ChemPhysChem* **2015**, *16*, 1395−1404.

(65) Presselt, M.; Dehaen, W.; Maes, W.; Klamt, A.; Martínez, T.; Beenken, W. J. D.; Kruk, M. Quantum Chemical Insights into the Dependence of Porphyrin Basicity on the Meso-Aryl Substituents: Thermodynamics, Buckling, Reaction Sites and Molecular Flexibility. *Phys. Chem. Chem. Phys.* **2015**, *17*, 14096−14106.

Supporting Information:

Arylic *vs*. Alkylic - Hydrophobic Linkers Determine Supramolecular Structure and Optoelectronic Properties of Tripodal Amphiphilic Push-Pull-Thiazoles

M. L. Hupfer[a,b], M. Kaufmann[a,c], L. Roussille[a,b], J. Preiss[a,b, D. Weiß[b], K. Hinrichs[d], V. Deckert[a,b], B. Dietzek[a,b], R. Beckert[b]*, M. Presselt[a,b,e,f]*

[a] Institute of Physical Chemistry, Friedrich Schiller University Jena, Helmholtzweg 4, 07743 Jena, Germany

[b] Leibniz Institute of Photonic Technology (IPHT), Albert-Einstein-Str. 9, 07745 Jena, Germany

[c] Institute of Organic and Macromolecular Chemistry, Friedrich-Schiller-University Jena, Humboldtstraße 10, Jena, 07743, Germany

[d] Leibniz-Institut für Analytische Wissenschaften – ISAS – e.V., Schwarzschildstr. 8, 12489 Berlin, Germany

[e] Center for Energy and Environmental Chemistry Jena (CEEC Jena), Friedrich Schiller University Jena, Jena, Germany

[f] sciclus GmbH & Co. KG, Moritz-von-Rohr Str. 1a, 07745 Jena, Germany

**corresponding outhors: Sythesis: rainer.beckert@uni-jena.de ; Thin films: martin.presselt@leibniz-ipht.de*

Content

Materials

4-*N*,*N*-(dimethylamino)phenyl-carbothioamide, Ethyl α-bromo-(4-nitrophenyl)acetate and methyl 11-bromoundecanoate were synthesized by literature procedures.[1] All chemicals used were reagent grade and purchased from Sigma–Aldrich, TCI or Acros. Solvents were purified by standard procedures. Solvents for UV-Vis and emission spectroscopy were of analytical grade and bought from Sigma–Aldrich. TLC materials were from Merck (Polygram SIL G/ UV254, aluminum oxide 60 F254). The material for column chromatography was also obtained from Merck (silica gel 60; 0.04 – 0.063 mm).

Experimental Characterization Methods

NMR-Spectroscopy

The NMR and the corresponding correlation spectra were recorded with Bruker AC-250 (250 MHz), AC-300 (300 MHz) and AC-400 (400 MHz) spectrometers. Chemical shifts (δ) are given relative to solvents.

Mass-Spectrometry

Mass spectra were measured either with a Finnigan MAT SSQ 710 (EI) or a MAZ 95 XL (ESI) system.

Synthesis

2-(4-*N*,*N*-Dimethylaminophenyl)-4-hydroxy-5-(4-nitrophenyl)-1,3-thiazol (3):

30 mmol of **1** (1,0 eq.) and 40 mmol **2** (1,3 eq.) und 75 mmol sodium acetate (2,5 eq.) were placed in a round flask and were suspended in 80 mL ethanol. The mixture was heated to reflux for 8 hours. The progress of the reaction was monitored by TLC. After the complete consumption of **1**, the reaction mixture and cooled down to room temperature and poured into 60 mL of water, whereby the product starts to participate. After 10 minutes of stirring at room temperature the mixture was filtrated and the solid was washed successively with water, ethanol and pentane. The raw product was dried in vacuo and can be used for following reactions without further purification.

For analytically approaches the product can be recrystallized from DMF. Yield: 85%, mp.: >300°C.

^{1}H NMR (250 MHz, $CDCl_3$) δ 8.28 (d, *J* = 8.8 Hz, 1H), 7.75 (dd, *J* = 8.7, 6.2 Hz, 2H), 6.70 (d, *J* = 8.9 Hz, 1H), 3.07 (s, 3H).

DEI-MS m/z: 341 [M^{*+}].

General Procedure for Alkylation of 4-Hydroxy-thiazoles:

8 mmol of **3** (1 eq.) and 16 mmol K_2CO_3 (2 eq.) were placed and suspended in 50 mL of acetone. The mixture was heated to 50°C for 30 min until all of **3** was deprotonated, indicated by colour change and TLC. Than 12 mmol (1.5 eq) of the alkyl halide were added and the solution was refluxed for 18 hours. The progress of the reaction was monitored by TLC (silica, $CHCl_3$/Hept, 2:1). If the educt wasn't completely consumed after 18 hours, additional 4 mmol (0.5 eq.) were added and the mixture was heated for additional 8 hours. After the reaction was cooled down to room temperature, it was poured into 50 mL water and was extracted 3 times by ethyl acetate. The combined organic phase was washed with a saturated $NaCO_3$ solution, water and brine and was dried with $MgSO_4$. The solvent was distilled of and the raw product was purified by the column chromatography (silica, CHCl3/Hept, 2:1) to supply the product as a red solid.

methyl 2-((2-(4-(dimethylamino)phenyl)-5-(4-nitrophenyl)thiazol-4-yl)oxy)acetate (4a):

According to the general procedure for alkylation, from **3** and methyl bromoacetate, yield: 95%.

The product was obtained as small red needles.

^{1}H NMR (250 MHz, $CDCl_3$) δ 8.30 – 8.11 (m, 2H), 7.93 – 7.81 (m, 2H), 7.75 (d, *J* = 9.0 Hz, 2H), 6.69 (d, *J* = 9.0 Hz, 2H), 5.12 (s, 2H), 3.82 (s, 3H), 3.05 (s, 6H).

EI-MS m/z: 413 [M^{*+}].

ethyl 6-((2-(4-(dimethylamino)phenyl)-5-(4-nitrophenyl)thiazol-4-yl)oxy)hexanoate (4b):

According to the general procedure for alkylation, from **3** and ethyl bromohexanoate, yield: 90%.

The product was obtained as deep/black red needles.

^{1}H NMR (300 MHz, CDCl$_3$) δ 8.18 (d, *J* = 9.1 Hz, 2H), 7.80 (dd, *J* = 9.0, 1.0 Hz, 4H), 6.71 (d, *J* = 8.9 Hz, 2H), 4.57 (t, *J* = 6.5 Hz, 2H), 4.13 (q, *J* = 7.1 Hz, 2H), 3.05 (s, *J* = 6.2 Hz, 6H), 2.35 (t, *J* = 7.4 Hz, 2H), 1.96 – 1.82 (m, 2H), 1.81 – 1.69 (m, 2H), 1.62 – 1.52 (m, 2H), 1.25 (t, *J* = 7.1 Hz, 3H).

EI-MS m/z: 483 $[M^{+*}]$

ethyl 6-((2-(4-(dimethylamino)phenyl)-5-(4-nitrophenyl)thiazol-4-yl)oxy)undecanoate (4c):

According to the general procedure for alkylation, from **3** and ethyl bromoundecanoate, Yield: 60%.

The product was obtained as deep/black red needles.

^{1}H NMR (250 MHz, CDCl$_3$) δ 8.18 (d, *J* = 9.0 Hz, 2H), 7.82 (dd, *J* = 9.0, 2.0 Hz, 4H), 7.19 (t, *J* = 9.0 Hz, 2H), 6.72 (d, *J* = 8.9 Hz, 2H), 4.57 (t, *J* = 6.6 Hz, 2H), 3.66 (s, 1H), 3.06 (s, 6H), 2.30 (t, *J* = 7.5 Hz, 2H), 1.94 – 1.80 (m, 2H), 1.56 (dd, *J* = 20.5, 6.8 Hz, 4H), 1.30 (s, 10H).

EI-MS m/z: 539 $[M^{*+}]$.

tert-butyl 4-(((2-(4-(dimethylamino)phenyl)-5-(4-nitrophenyl)thiazol-4-yl)oxy)methyl)benzoate (8):

According to the general procedure for alkylation, from **3** and tert-butyl 4-(bromomethyl)benzoate, with a catalytic amount of sodium iodide. The purification was performed on silica with chloroform as eluent. Yield: 63%. The product was obtained as red/brown powder.

^{1}H NMR (250 MHz, CDCl$_3$) δ 8.12 (d, *J* = 9.28 Hz, 2H), 7.91 (d, *J* = 8.14, 2H), 7.75 (m, 4H), 7.48 (d, *J* = 8.31 Hz, 2H), 7.36 (d, *J* = 8.06 Hz, 2H), 6.68 (d, *J* = 8.8 Hz, 2H), 4.54 (s, 2H), 3.06 (s, 6H), 1.53 (s, 3H).

EI-MS m/z: 531 $[M^{+*}]$

General Procedure for Saponification of alkyl esters:

4 eq. potassium hydroxide were suspended in 5 mL anhydrous ethanol and stirred at room temperature capped with a calcium chloride tube for 30 minutes. 1 eq. of the alkyl ester was added and the mixture was stirred for additional 18 hours at room temperature. The mixture was poured into 50 mL water, neutralized with acetic acid and extracted with dichloromethane. The organic layer was washed with water and brine and dried over manganese sulfate. After removing the solvent, the compound was recrystalized in the given solvent and dried *in vacuo* to supply the desired product.

2-((2-(4-(dimethylamino)phenyl)-5-(4-nitrophenyl)thiazol-4-yl)oxy)acetic acid (5_1):

According to the general procedure for saponification, from **4a**, yield: 96%

The product was recrystallized from cyclohexane/chloroform and was obtained as red powder.

^{1}H NMR (250 MHz, DMSO) δ 8.23 (d, *J* = 9.0 Hz, 2H), 7.89 (d, *J* = 9.0 Hz, 2H), 7.71 (d, *J* = 8.9 Hz, 2H), 6.77 (d, *J* = 9.0 Hz, 2H), 5.08 (s, 2H), 3.00 (s, 6H).

EI-MS m/z: 399 $[M^{+*}]$

6-((2-(4-(dimethylamino)phenyl)-5-(4-nitrophenyl)thiazol-4-yl)oxy)hexanoic acid (5_5):

According to the general procedure for saponification, from **4b**, yield: 99%

The product was recrystallized from toluene and was obtained as dark red crystals with green luster.

1H NMR (250 MHz, DMSO) δ 12.19 – 11.76 (m, 1H), 8.22 (d, J = 9.0 Hz, 2H), 7.84 (d, J = 9.0 Hz, 2H), 7.76 (d, J = 8.9 Hz, 2H), 6.78 (d, J = 9.0 Hz, 2H), 4.53 (t, J = 6.4 Hz, 2H), 3.01 (s, 6H), 2.26 (t, J = 7.1 Hz, 2H), 1.93 – 1.73 (m, 2H), 1.69 – 1.42 (m, 4H).

EI-MS m/z: 455 $[M^{+*}]$

11-((2-(4-(dimethylamino)phenyl)-5-(4-nitrophenyl)thiazol-4-yl)oxy)undecanoic acid (5_11):

According to the general procedure for saponification, from **4c**, yield: 80%

The product was recrystallized from toluene and was obtained as red powder.

^{1}H NMR (250 MHz, $CDCl_3$) δ 8.18 (d, *J* = 9.0 Hz, 2H), 7.82 (dd, *J* = 9.0, 2.0 Hz, 4H), 7.19 (t, *J* = 9.0 Hz, 2H), 6.72 (d, *J* = 8.9 Hz, 2H), 4.57 (t, *J* = 6.6 Hz, 2H), 3.66 (s, 1H), 3.06 (s, 6H), 2.30 (t, *J* = 7.5 Hz, 2H), 1.94 – 1.80 (m, 2H), 1.56 (dd, *J* = 20.5, 6.8 Hz, 4H), 1.30 (s, 10H).

EI-MS m/z: 525 $[M^{+*}]$

4-(((2-(4-(dimethylamino)phenyl)-5-(4-nitrophenyl)thiazol-4-yl)oxy)methyl)benzoic acid (7):

50 mg **8** were dissolved in 4 mL dichloromethane and 2 mL of trifluoroacetic acid were added. The reaction vessel was capped with a bubble counter and was stirred for 24 hours at room temperature.

Afterwards the solvent was distilled of and the residue was dissolved in 40 mL dichloromethane. The solution was washed several times with water and brine and was dried over manganese sulfate. The solvent was distilled of and the raw product was purified by column chromatography (silica, $CHCl_3$/MeOH, 5/1) to obtain the title compound as a red/brown powder. Yield: 90%

^{1}H NMR (400 MHz, $CDCl_3$) δ 8.17 (d, *J* = 8.8 Hz, 1H), 7.82 (dd, *J* = 8.6, 3.9 Hz, 2H), 7.52 (d, *J* = 8.2 Hz, 1H), 7.38 (d, *J* = 8.1 Hz, 1H), 6.80 (d, *J* = 8.7 Hz, 1H), 5.58 (s, 1H), 3.07 (s, 3H).

EI-MS m/z: 461 [M^{+*}]

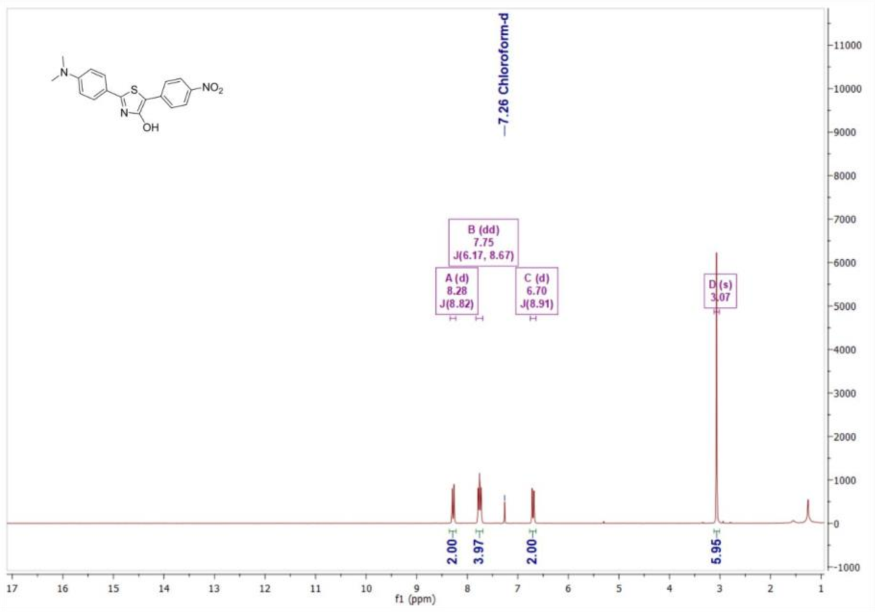

Figure SI 1: ^{1}H-NMR spectrum of **3**.

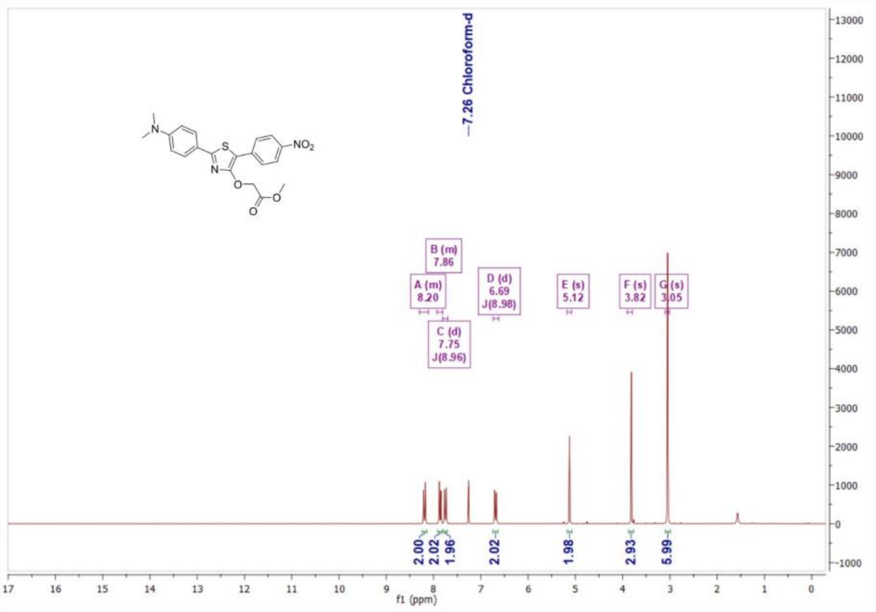

Figure SI 2: ^{1}H-NMR spectrum of **4a**.

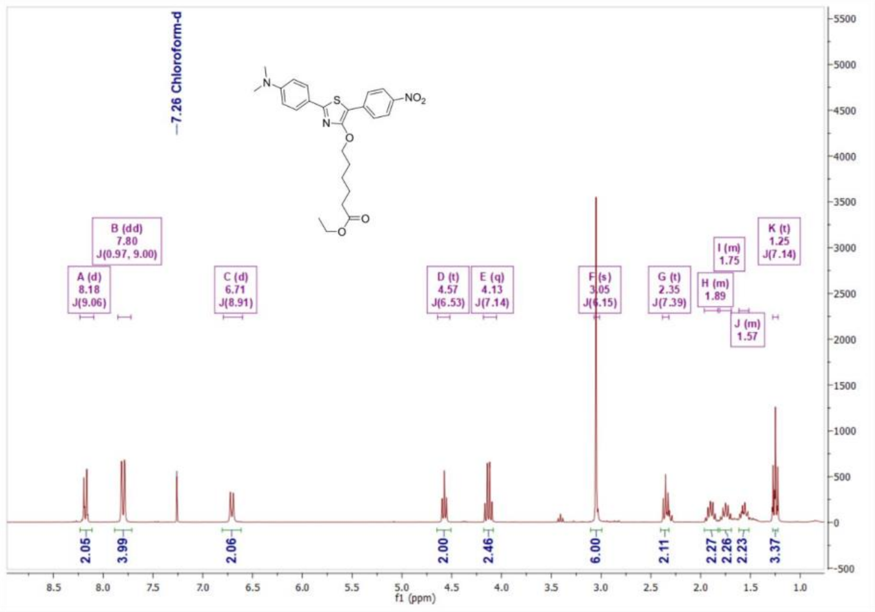

Figure SI 3: ^{1}H-NMR spectrum of **4b**.

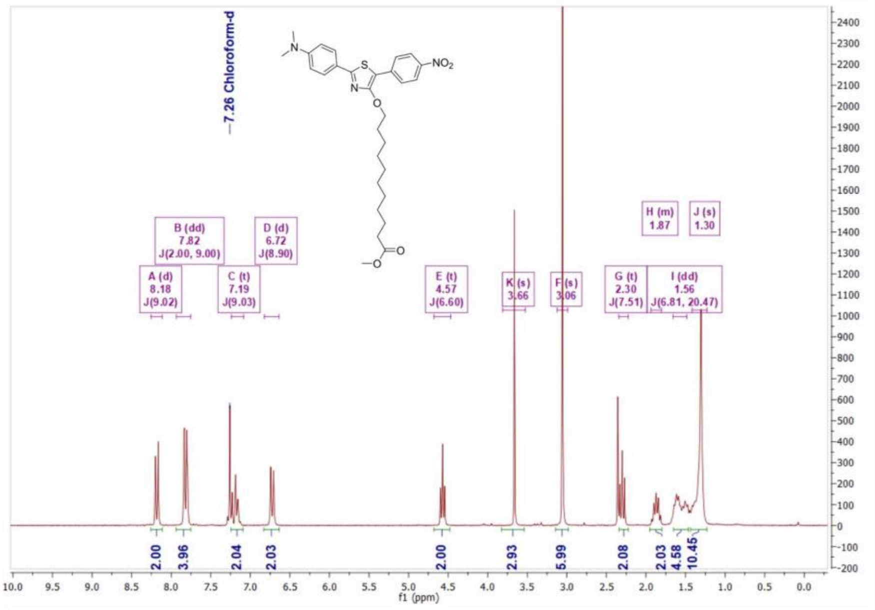

Figure SI 4: ^{1}H-NMR spectrum of **4c**.

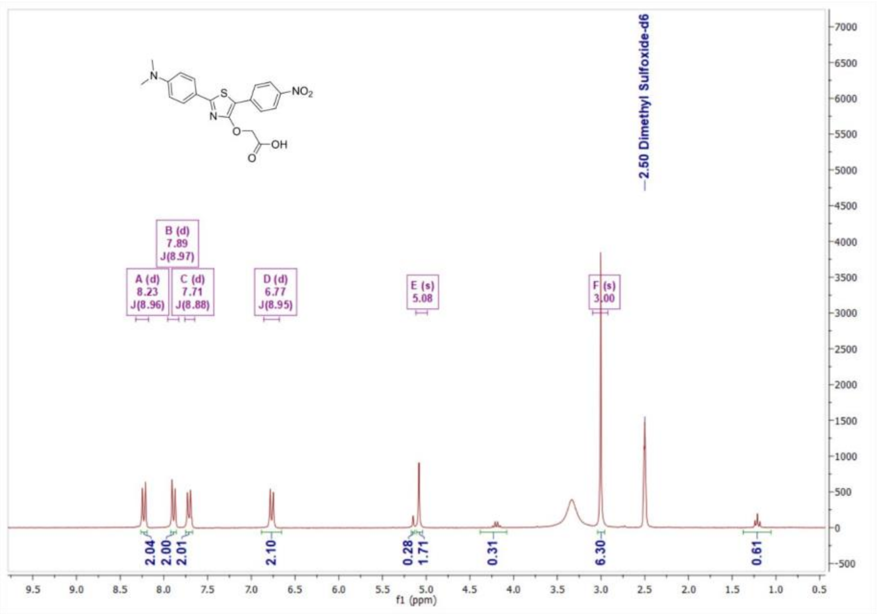

Figure SI 5: ^{1}H-NMR spectrum of **5_1**.

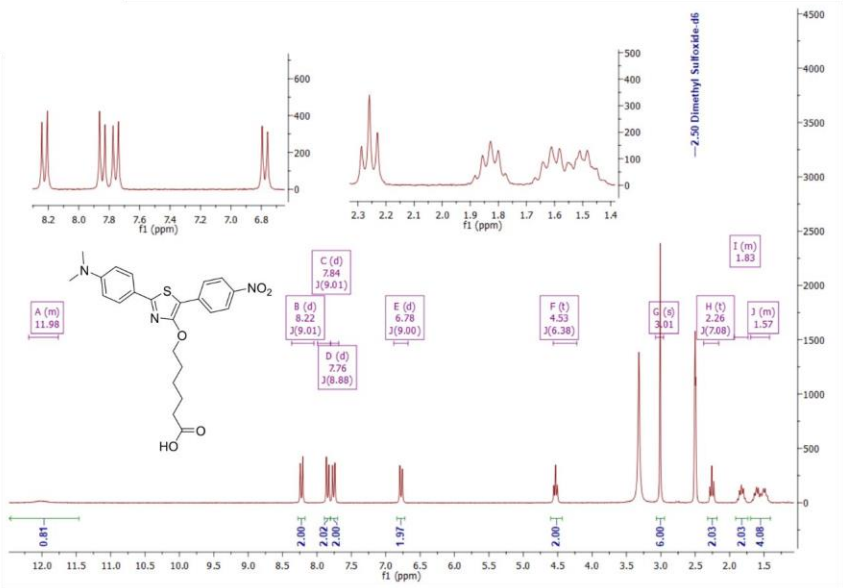

Figure SI 6: ^{1}H-NMR spectrum of **5_5**.

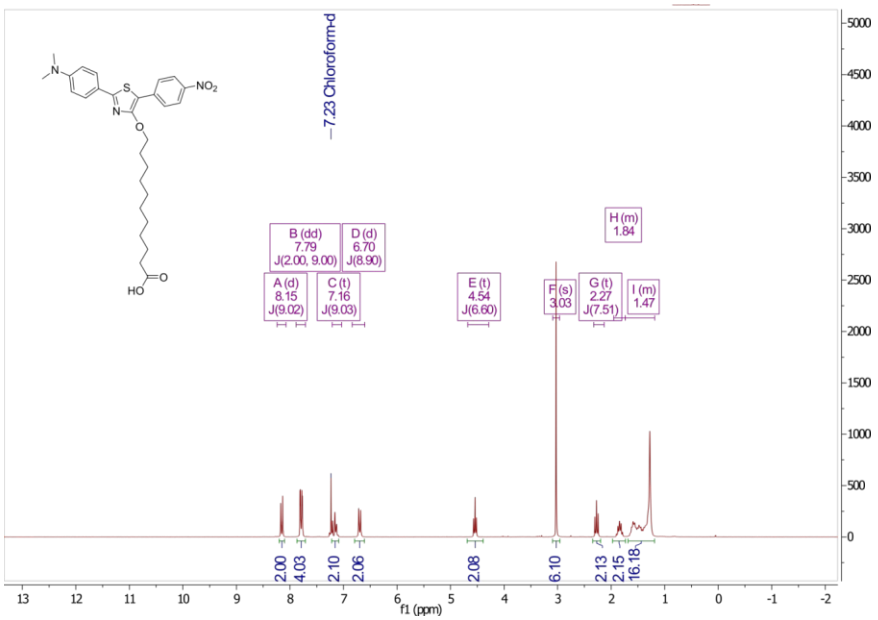

Figure SI 7: ^{1}H-NMR spectrum of **5_10**.

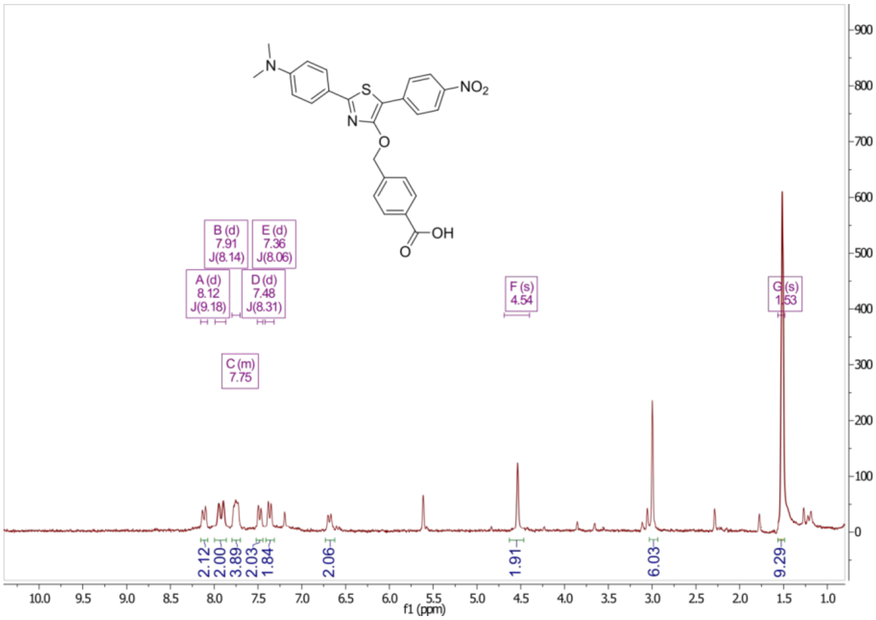

Figure SI 8: ^{1}H-NMR spectrum of **7**.

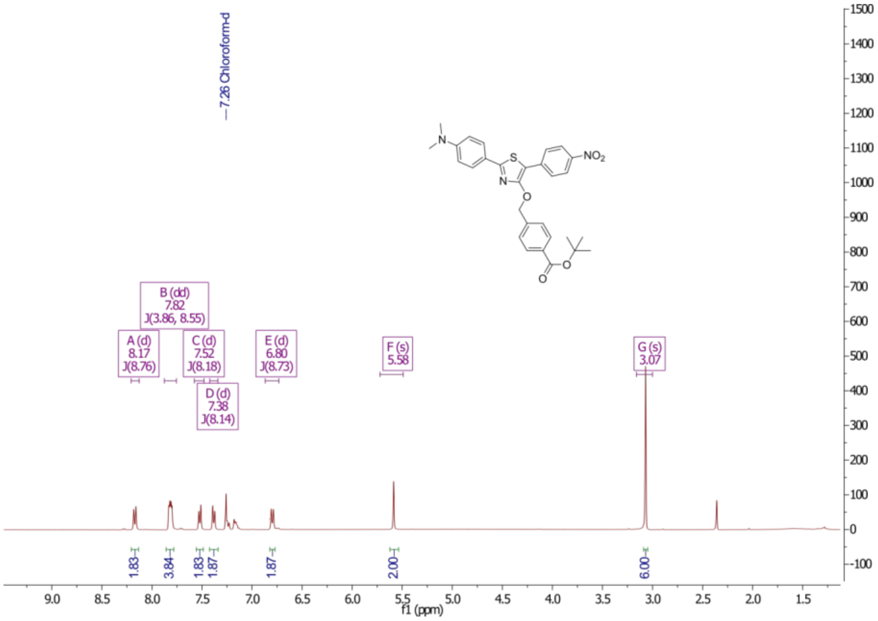

Figure SI 9: ^{1}H-NMR spectrum of **8**.

Quantum Chemical Calculation

Table SI 1: DFT derived () total energies of different conformers of **5_5** and **7**

Conformer	**5_5** Total Energy		**7** Total Energy	
	Vac [meV]	Inf [meV]]	Vac [meV]	Inf [meV]]
i	97.4	0	44.8	0
ii	0	40.7	108.5	128.8
iii	137.3	158.2	251.3	189.6

Electronic Properties

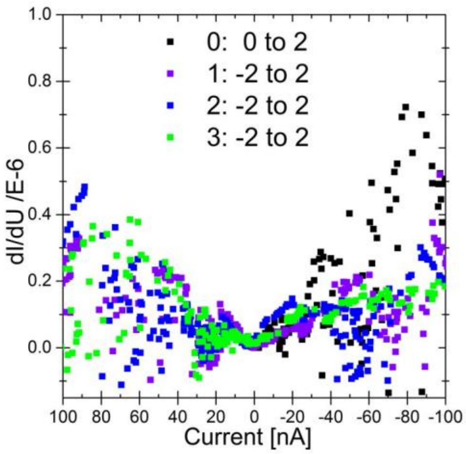

Figure SI 10: dI/dU vs. I plot of a LB-film molecule **5_5** at Π_{LB} = 10 mN/m measured by conductive AFM.

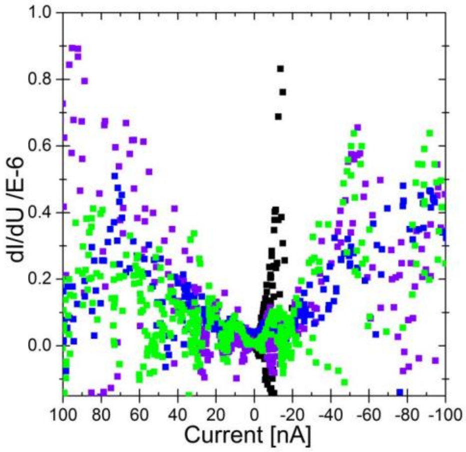

Figure SI 11: dI/dU vs. I plot of a LB-film molecule **5_5** at Π_{LB} = 25 mN/m measured by conductive AFM.

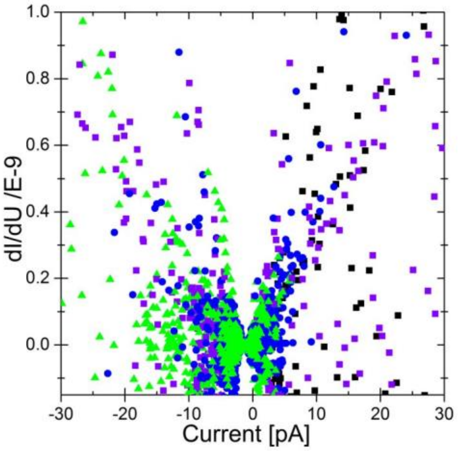

Figure SI 12: dI/dU vs. I plot of a LB-film molecule **7** at ΠLB = 10 mN/m measured by conductive AFM.

REFERENCES

1. (a) Cież, D.; Svetlik, J. A One-Pot Preparation of 5-Oxo 2,4-Disubstituted 2,5-Dihydro-1H-imidazol-2-carboxylates from α-Bromo Esters. *Synlett* **2011,** *2011* (03), 315-318; (b) Sharma, V.; Tepe, J. J. Diastereochemical Diversity of Imidazoline Scaffolds via Substrate Controlled TMSCl Mediated Cycloaddition of Azlactones. *Organic Letters* **2005,** *7* (22), 5091-5094; (c) Yasa, S. R.; Kaki, S. S.; Poornachandra, Y.; Kumar, C. G.; Penumarthy, V. Synthesis, characterization, antimicrobial and biofilm inhibitory studies of new esterquats. *Bioorganic & Medicinal Chemistry Letters* **2016,** *26* (8), 1978-1982.

[MLH6] Autonomous Supramolecular Interface Self-Healing Monitored by Restoration of UV-vis Absorption Spectra of Self-Assembled Thiazole Layers

Hupfer, M. L.; Herrmann-Westendorf, F.; Kaufmann, M.; Weiß, D.; Dietzek, B.; Beckert,R.; Presselt, M., Chemistry - A European Journal **2019**, submitted

Autor	1	2	3	4	5	6	7
Konzeption	x	x	x	x	x	x	x
Planung der Untersuchung	x				x		x
Datenerhebung	x						
Analyse und Interpretation	x	x			x		x
Schreiben des Manuskriptes	x	x			x		x
Publikationsäquivalente	1,0	n. a.	n. a.	n. a.	n. a.	n. a.	n. a.

Chemistry - A European Journal

Autonomous Supramolecular Interface Self-Healing Monitored by Restoration of UV-vis Absorption Spectra of Self-Assembled Thiazole Layers

--Manuscript Draft--

Manuscript Number:	chem.201901549
Article Type:	Full Paper
Corresponding Author:	Martin Presselt Friedrich-Schiller-University Jena Jena, GERMANY
Corresponding Author E-Mail:	martin.presselt@gmail.com
Order of Authors (with Contributor Roles):	Maximilian Lutz Hupfer
	Felix Herrmann-Westendorf
	Martin Kaufmann
	Dieter Weiß
	Rainer Beckert
	Benjamin Dietzek
	Martin Presselt
Keywords:	self-healing; self-assembly; push-pull-chromophore; organic electronic; amphiphilic dye
Manuscript Classifications:	Kinetics; Organic electronics; Self-assembly
Suggested Reviewers:	
Opposed Reviewers:	
Abstract:	Longevity of complex organic devices critically depends on the supramolecular integrity of the constituting layers and interfaces. Because the latter are soft matter they can structurally respond to perturbation of their supramolecular structure by relaxing back to a thermodynamically favorable state. To employ this response for self-healing optoelectronically active layers and particularly interfaces the degraded dyes in these layers need to be exchanged with non-degraded ones. Here, we present a dye-layer interfaced between a solid surface and a dye-reservoir that autonomously self-heals after photo-degradation of single molecules to restore its optical function. Surface sensitive in situ photothermal deflection spectroscopy reveals that this supramolecular self-healing approach critically depends on the thermodynamic stability of the layer, the chemical change of the dye upon degradation, and the medium dissolving the degraded dye and providing the reservoir dyes. Hence, the interplay of these parameters is key to successfully employ this supramolecular self-healing approach to thin layers and interfaces in organic device for increased sustainability of organic optoelectronics and related fields.
Author Comments:	Dear Dr. Dr. Leana Travaglini and Dr. Elisabeth von Roedern, We would like to submit the revised manuscript named “Autonomous Supramolecular Interface Self-Healing by Restoration of UV-vis Absorption Spectra of Self-Assembled Thiazole Layers ” to Chemistry – A European Journal. In compliance to reviewers and editorial responses, we have thoroughly revised the paper and the supporting information.
Section/Category:	
Additional Information:	
Question	Response
Submitted solely to this journal?	Yes
Has there been a previous version?	Yes

Please state previous 1) Manuscript ID and 2) journal. 3) If the paper was reviewed, please include a point-by-point response to the reviewer comments. as follow-up to "Has there been a previous version?"	1) chem.201900043 2) Chemistry - A European Journal 3) see uploaded files
Do you or any of your co-authors have a conflict of interest to declare?	No. The authors declare no conflict of interest.
Animal/tissue experiments?	No

Autonomous Supramolecular Interface Self-Healing Monitored by Restoration of UV-vis Absorption Spectra of Self-Assembled Thiazole Layers

Maximilian L. Hupfer[1,3], Felix Herrmann-Westendorf[1,3], Martin Kaufmann[1,2], Dieter Weiß[2], Rainer Beckert[2], Benjamin Dietzek[1,3], Martin Presselt[1,3,4,5,*]

[1] Institute of Physical Chemistry, Friedrich Schiller University Jena, Helmholtzweg 4, 07743 Jena, Germany, E-mail: martin.presselt@leibniz-ipht.de, Phone: +49 3641 206418

[2] Institute of Organic and Macromolecular Chemistry, Friedrich Schiller University Jena, Humboldstraße 10, 07743 Jena, Germany

[3] Leibniz Institute of Photonic Technology (IPHT), Albert-Einstein-Str. 9, 07745 Jena, Germany

[4] Center for Energy and Environmental Chemistry Jena (CEEC Jena), Friedrich Schiller University Jena, Philosophenweg 7a, 07743 Jena, Germany

[5] sciclus GmbH & Co. KG, Moritz-von-Rohr-Str. 1a, 07745 Jena, Germany

*Corresponding author: martin.presselt@leibniz-ipht.de

ABSTRACT

Longevity of complex organic devices critically depends on the supramolecular integrity of the constituting layers and interfaces. Because the latter are soft matter they can structurally respond to perturbation of their supramolecular structure by relaxing back to a thermodynamically favorable state. To employ this response for self-healing optoelectronically active layers and particularly interfaces the degraded dyes in these layers need to be exchanged with non-degraded ones. Here, we present a dye-layer interfaced between a solid surface and a dye-reservoir that autonomously self-heals after photo-degradation of single molecules to restore its optical function. Surface sensitive *in situ* photothermal deflection spectroscopy reveals that this supramolecular self-healing approach critically depends on the thermodynamic stability of the layer, the chemical change of the dye upon degradation, and the medium dissolving the degraded dye and providing the reservoir dyes. Hence, the interplay of these parameters is key to successfully employ this supramolecular self-healing approach to thin layers and interfaces in organic device for increased sustainability of organic optoelectronics and related fields.

Impressive progress has been achieved in self-healing mechanical properties of polymers, as *e.g.* reviewed by Yang *et al.*[1] and Ahner *et al.*[2] Recently, also self-healing concepts to restore electronic[3] or optical[4] properties of polymeric bulk materials have been introduced that enable extending the lifetime of organic optoelectronic devices. However, the latter essentially depends on the integrity of the carefully designed interfaces between the functional materials[5], which need to self-heal as well to achieve prolonged lifetimes of any optoelectronic and electronic device. Such interface self-healing has not yet been addressed by self-healing on the essential supramolecular scale[6].

Mechanisms that restore supramolecular structures might rely on thermodynamic stability of the underlying structures to naturally cause return to the thermodynamically favorable supramolecular structure after perturbation.[7] Inherent thermodynamically stable supramolecular structures are yielded by classic crystallization[8] and self-assembly[9]. However, if the constituting molecules degrade they need to be exchanged or overgrown to restore the supramolecular structure and function of optoelectronically active layers. Such a supramolecular self-healing necessitates the active molecules being integrated into the function-determining supramolecular structure and being in contact with a reservoir, which ideally dissolves the degraded dyes and provides pristine dyes that self-assemble into the supramolecular structure. Because the exchange between degraded and non-degraded dyes involves molecular diffusion this supramolecular self-healing would be slow in crystallites and other bulk-materials. Instead such mechanism appears to be predestined for self-healing the essential interfaces and interlayers in optoelectronic devices[5, 10]. The merge of pristine molecules or even of small supramolecular assemblies into interfacial membranes might be viewed as analog to the natural exocytosis working in living cells and is illustrated in Figure 1A.

However, even the simpler process of self-assembly – as compared to self-healing – is already considerably complex[11] and depends on a large variety of parameters, involving properties of the amphiphile (surface activity[12], hydrophilic to lipophilic balance[13], amphiphilicity[14], solubility, shape[15] and many more, see *e.g*. the review by Tschierske and Ungar *et al*.[16]), the substrate surface, the solvent (polarity[17], but even the shape of similarly polar solvents[18]), and physical parameters (essentially temperature[11, 19]). Therefore, detailed studies on self-assembly rely on surface-sensitive *in situ* techniques, such as elaborate atomic force[20] or scanning tunneling microscopy[9, 20a, 21]. These techniques can be even applied to investigate self-healing of mechanically induced damage, such as scratches[22], but studying photo- or other damage at molecular scales appears challenging. An alternative, optical operating technique to study interfaces or ultra-thin layers (down to 1 nm) of dyes is photothermal deflection spectroscopy (PDS[23]). In the following we use PDS to *in situ* investigate self-healing, according the above introduced supramolecular self-healing scheme, of self-assembled monolayers (SAMs). Utilizing PDS inherently yields exclusive information on self-assembled monolayers (SAMs), what corresponds to a depth resolution of about 1 nm, not reached in any other surface-related self-healing research.[24]

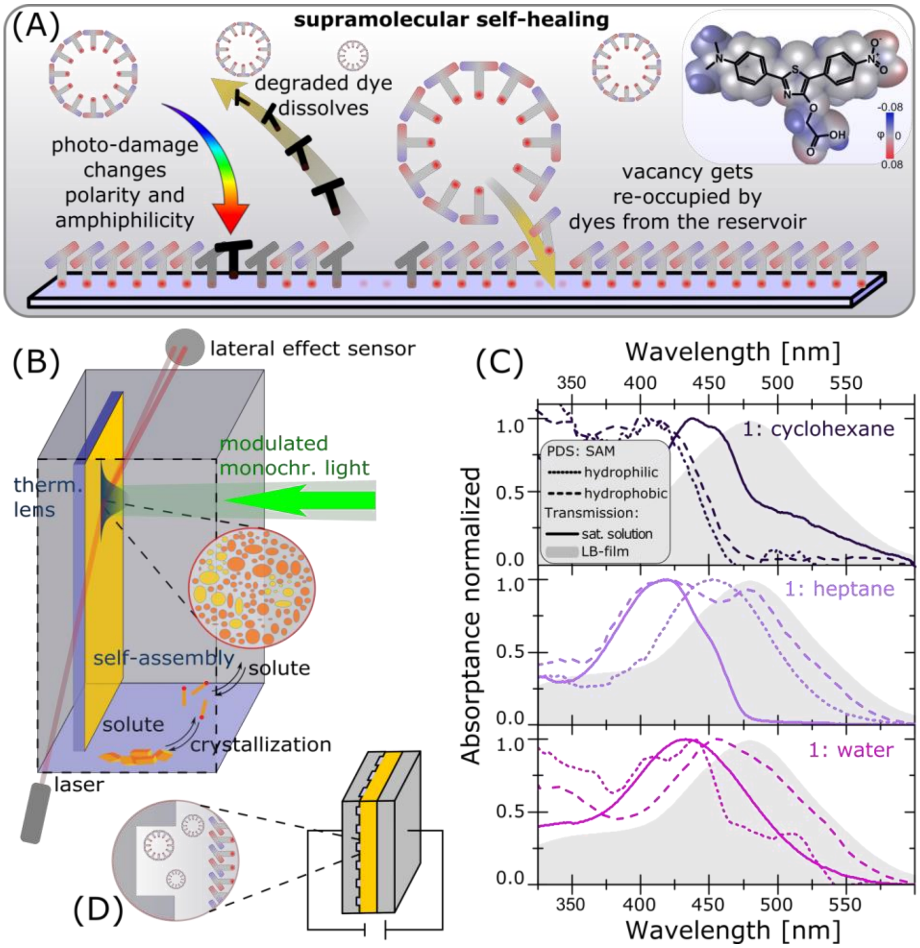

Figure 1: (A) Scheme of supramolecular self-healing of an optoelectronically active membrane that is in contact with a reservoir for to exchange degraded and pristine dyes. Inset on the right shows the actual chemical structure of the used amphiphilic thiazole with dipolar chromophore. The electrostatic potential φ is plotted at the van der Waals surface. (B) Scheme of setup to detect self-healing of self-assembled structures *in situ* by means of photothermal deflection spectroscopy (PDS). (C) Absorption spectra of self-assembled monolayer of the amphiphilic push-pull-thiazole **1** in saturated solutions (solid) with different nonpolar (heptane, cyclohexane) and polar (water) solvents on hydrophilic (dotted) and hydrophobized (dashed) quartz glass substrate in comparison to the spectrum of the LB film of **1** reported in Ref. [25]. (D) Sketch of device-implementation of the model system shown in (B).

To proof the principle of the above introduced supramolecular self-healing, the setting schematically illustrated in Figure 1A is experimentally realized. Therefore, a cuvette containing the dye-reservoir solution and a model substrate are used as shown in Figure 1B. In case the dissolved dyes self-assemble at the substrate's surface an absorption spectrum of the resulting thin SAM can be measured by PDS[23b, 26]. If no SAMs are formed, *e.g.* on inappropriate surfaces, no PDS-signals are detected. Hence, the applied PDS is surface-sensitive and exclusively detects the absorption of the SAM and not of the solution. Thus PDS is an invaluable tool for *in situ* detection of self-assembly and self-healing (also see Figure SI 1 in the supporting information (SI)).

For dyes constituting the SAMs we focus on amphiphilic thiazoles because their supramolecular structures, surface activities, and optical properties have been extensively studied in literature[25, 27]. The amphiphilicity und weak solubility of thiazole **1** in water (see Figure 1A, electrostatic potential (φ) distribution) renders **1** predestined for SAM formation and self-healing to restore both, structure and function of the SAM.

The dependence of the SAM formation, particularly its supramolecular structure, on the solvent is revealed by comparing the PDS absorptance spectra of SAMs grown from cyclohexane, heptane, water, and further solvents, as shown in Figure 1C and Figure SI 2. The SAM grown from the heptane solution on hydrophilic quartz glass features a PDS absorptance spectrum shifted uniformly to the red as compared to its solution (λ_{max}(solution)=420 nm $\rightarrow$ λ_{max}(SAM)=450 nm). This red-shift indicates a supramolecular structure constituted by J-aggregates, *cf*. spectrum of the corresponding Langmuir Blodgett (LB) film in Figure 1C (λ_{max}(LB)=450 nm)[25, 27d].

In contrast, the SAMs grown from water or cyclohexane solutions on hydrophilic quartz glass show no absorption of J-type supramolecular structures (Figure 1C). Instead, their absorption spectra peak at the maximum absorption of the heptane solution. Because of this spectral similarity, we deduce the presence of rather amorphous SAMs when grown from cyclohexane or water on hydrophilic quartz glass. Furthermore, the low signal-to-noise ratio of the absorptance spectra of the latter (Figures SI 3 and 7) indicate that the latter SAMs are rather sparse distribution of molecules on the surfaces than densely packed SAMs.

To study supramolecular self-healing, we first focus on the SAM with the highest molecular order, namely the one grown on a hydrophilic quartz glass from the saturated heptane solution. The photo-degradation of the SAM is provoked by irradiation with white-light provided by the Xenon lamp of the PDS setup, see Figure 1B. This irradiation reduces the major absorption of a SAM at 450 nm to half of the initial intensity within the damage time (d = 30 min), as shown in Figure 2a-c and detailed in the section SI 2.4. To demonstrate self-healing, the SAM is kept in the dark for t = 22 hours after irradiation, during which time the sample recovers its absorption entirely as shown in Figure 2a-c. This damage-healing cycle can be successfully repeated multiple times, as shown in Figure 2c.

However, the absorption spectra in Figure 2a reveal that with each damage-healing cycle a broad absorption in the UV rises, which must be due to photo-degradation products that adhere to the surface as well. To account for the superposition of the UV and the major 460 nm absorption, the ratios between the absorptions at 460 nm and 374 nm as well as 310 nm (both of the latter being indicative for the concentration of photo-degradation products), respectively, are plotted in Figure 2d. These absorption ratios reveal a decreasing healing efficiency with repeated cycles, obviously because the photo-degradation products occupy supramolecular sites, thus successively prohibiting dye exchange. Ignoring the spectral superposition of original and degraded dyes yields a false, opposing trend of the self-healing efficiency η when calculated classically, as detailed in SI section 2.3.

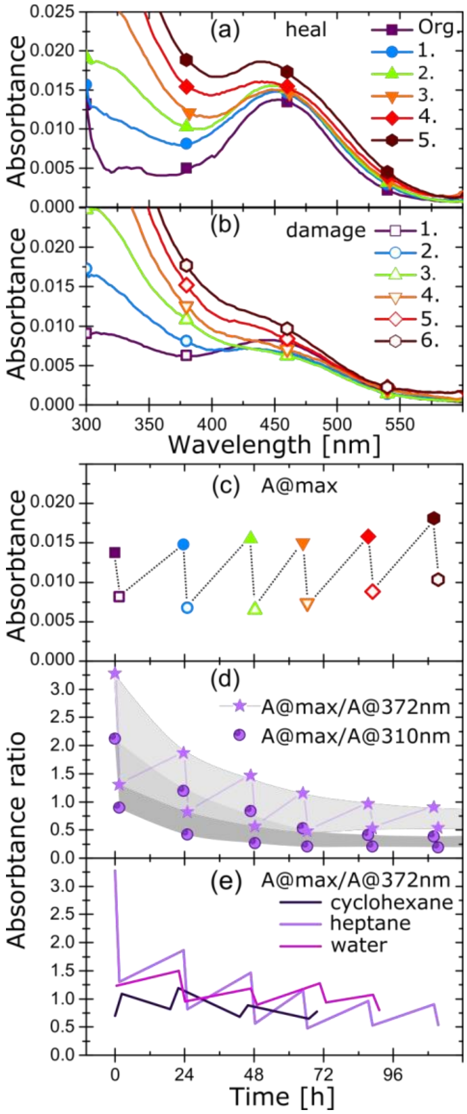

Figure 2: Absorption spectra of self-assembled and self-healed monolayer of the amphiphilic push-pull-thiazoles **1** in a saturated solution of heptane at hydrophilic quartz-glass after different damage (b) and self-healing (a) cycles. Absorption at λ_{max} = 460 nm (c) and the absorption ratio A@460 nm/A@374 nm (stars) and A@460 nm/@310 nm (discs) *vs.* time (d), the A@460 nm/A@374 nm absorption ratios for cyclohexane, heptane and water (e).

The availability of free binding sites for healing depends on the surface concentration of adhered degraded dyes. Therefore, we varied the duration of irradiation to investigate how the concentration of degraded dyes influences the healing. After the initial self-assembly, which follows a basic first order Langmuir[29] kinetic (see Table 1, Eq. 1, and SI section 2.4) and converges after approx. 3 h to an absorptance of A_0=1.5, we have chosen three different damage times of 10, 30, and 60 min.

[illegible] Equation 1

As shown in Figure 3c,e,g, the absorptance decays exponentially upon white light illumination with rate constants of 0.5±0.2 min^{-1} (see Table 1 and Section SI 2.4 for details). While the self-assembly (adsorption combined with rising intermolecu[illegible] happens with rate constants of k=k_{ad}[illegible]10^{-3} min^{-1} (except one sample with apparently numerous predestined seed [illegible]10^{-3} min^{-1}) the rate constants of self-healing are significantly smaller (k=k_{ad} + k_{de}=3±1$\cdot10^{-3}$ min^{-1}), as they additionally involve desorption (k_{de}). Furthermore, the self-healing rate constats are virtually independent on the irradiation time d, *i.e.* surface concentration of degraded dyes. However, the latter significantly influences the maximum restored absorptance A_0, which slowly decreases from A_0(d=10 min)=1.3$\cdot10^{-3}$, to 1.0$\cdot10^{-3}$, to 0.9$\cdot10^{-3}$ upon repeated 10 mins of photo-degradation. At prolonged photo-degradation of d=30 min A_0 decreases stronger from A_0(d=30 min)=2.0$\cdot10^{-3}$, to 0.9$\cdot10^{-3}$, to 0.7$\cdot10^{-3}$. In contrast, the longest photo-degradation (d=60 min) yields an A_0-increase upon successive degradation cycles (A_0(d=10 min)=0.4$\cdot10^{-3}$, to 0.6$\cdot10^{-3}$, to 0.6$\cdot10^{-3}$). Apparently, the prolonged degradation yields different products that desorb faster than those formed at shorter irradiation times.

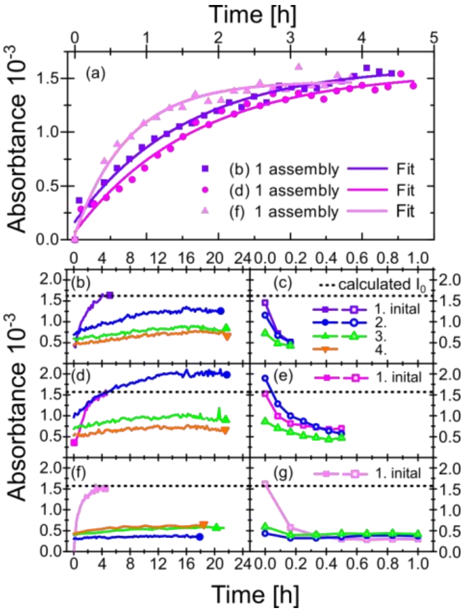

Figure 3: Absorbtance *versus* time kinetic of the assembly of the initial assembly (a), together with the healing (left, b, d, f) and damage (right; c, e, g) of self-assembled monolayer of the amphiphilic push-pull-thiazoles **1** on hydrophilic quartz-glass from a saturated solution of heptane determined at λ_{max} = 450 nm.

Table 1: Langmuir-type absorptance (A_t) versus time (t) kinetic of the assembly with the maximum absorptance (A_0), the rate constant (k) and damage (d) and offset time (t_0)

Assembly $A_t = A_o[1-e^{-k(t-t_o)}]$				Damage	
	$A_0 \cdot 10^{-3}$	t_0	$k \cdot 10^{-3}$	d	$A_D \cdot 10^{-3}$
		[min]	[min^{-1}]	[min]	
1	1.62	10	10.8	10	0.52
2	1.27	287	2.3		0.50
3	1.00	725	1.0		0.42
4	0.94	657	0.8		/
1	1.57	5	9.9	30	0.70
2	2.00	205	2.9		0.57
3	0.91	325	3.4		0.47
4	0.68	404	2.5		/
1	1.47	1	22.2	60	0.30
2	0.37	553	3.2		0.37
3	0.59	540	2.1		0.42
4	0.61	297	4.0		/

To highlight the role of the solvent in self-assembly and supramolecular self-healing, we replaced heptane by cyclohexane and water, retaining all other experimental conditions except the differing saturation concentrations (see methods section detailed in the SI). These two alternative solvents yield ideal polar and non-polar reference systems that both do not show formation of J-aggregated films, as discussed above, but rather sparsely distributed dyes at the substrate surface that are challenging to detect.

In the case of opposite polarities, *i.e*. self-assembly and –healing from polar water solutions at non-polar hydrophobized quartz glass, **1** shows no self-assembly for at least five hours in the dark at room temperature (Figure SI 14c). However, after PDS-detection of an absorptance spectrum the absorptance at 460 nm converges at the double intensity as before. The following initial damage-healing cycle causes constantly increasing absorptance at 460 nm. Hence, the initial damage-healing cycle yields a surface that favors self-assembly and self-healing as compared to the pristine hydrophobized quartz glass surface (Figure SI 14). We assign this activated assembly to photoassisted assembly either because of increased dipole moments in the excited states, similar to the known photo-annealing of dipolar dyes[28], or to a temperature activation enabled by excited state deactivation. After this initial photo-enhanced assembly, the supramolecular self-healing operates similar as reported for heptane above. In case of cyclohexane, the SAM absorptance spectra are very weak and show very small changes.

In summary, we introduced a new concept for supramolecular self-healing of organic interfaces. We demonstrated that the self-assembly at interfaces and the formation of distinct supramolecular structures of a thiazole dye, which combines dipolarity and amphiphilicity, critically depends on the solvent. The autonomous and spontaneous self-healing worked best for layers that formed the densest (as deduced from the high absorptance) self-assembled layers that also showed supramolecular stabilization and ordering upon J-aggregation (as deduced from the absorption red-shifts), in this case heptane, but also for other solvents, such as water. In the latter case, we observed photo-annealing that finally protected the SAM largely from photo-degradation. For this research we developed an *in situ* detection of self-assembly and self-healing *via* photothermal deflection spectroscopy.

ACHNOWLEDGEMENT

The authors thank the Deutsche Forschungsgemeinschaft DFG (PR 1415/2) and Bundesministerium für Bildung und Forschung (BMBF FKZ 03EK3507) for financial support.

REFERENCES

[1] Y. Yang and M. W. Urban, *Chemical Society Reviews* **2013**, *42*, 7446-7467.

[2] J. Ahner, S. Bode, M. Micheel, B. Dietzek and M. D. Hager in *Self-Healing Functional Polymeric Materials*, Eds.: M. D. Hager, S. van der Zwaag and U. S. Schubert), Springer International Publishing, Cham, **2016**, pp. 247-283.

[3] Y. J. Tan, J. Wu, H. Li and B. C. K. Tee, *ACS Applied Materials & Interfaces* **2018**, *10*, 15331-15345.

[4] J. Ahner, M. Micheel, R. Geitner, M. Schmitt, J. Popp, B. Dietzek and M. D. Hager, *Macromolecules* **2017**, *50*, 3789-3795.

[5] a) H.-L. Yip, S. K. Hau, N. S. Baek, H. Ma and A. K.-Y. Jen, *Advanced Materials* **2008**, *20*, 2376-2382; b) S. Khodabakhsh, B. M. Sanderson, J. Nelson and T. S. Jones, *Advanced Functional Materials* **2006**, *16*, 95-100.

[6] a) J. R. Tumbleston, B. A. Collins, L. Q. Yang, A. C. Stuart, E. Gann, W. Ma, W. You and H. Ade, *Nature Photonics* **2014**, *8*, 385-391; b) J. Rivnay, L. H. Jimison, J. E. Northrup, M. F. Toney, R. Noriega, S. Lu, T. J. Marks, A. Facchetti and A. Salleo, *Nat Mater* **2009**, *8*, 952-958; c) C. Poelking, M. Tietze, C. Elschner, S. Olthof, D. Hertel, B. Baumeier, F. Würthner, K. Meerholz, K. Leo and D. Andrienko, *Nature*

Materials **2015**, *14*, 434-439; d) S. Das, F. Herrmann-Westendorf, F. H. Schacher, E. Täuscher, U. Ritter, B. Dietzek and M. Presselt, *ACS Appl Mater Interfaces* **2016**, *8*, 21512-21521; e) S. Das, J. Preiß, J. Plentz, U. Brückner, M. von der Lühe, O. Eckardt, A. Dathe, F. H. Schacher, E. Täuscher, U. Ritter, A. Csáki, G. Andrä, B. Dietzek and M. Presselt, *Advanced Energy Materials* **2018**, *0*, 1801737.

[7] a) K. W. Hipps and U. Mazur, *Langmuir* **2018**, *34*, 3-17; b) F. Würthner, *Nature Chemistry* **2014**, *6*, 171-173.

[8] F. Würthner, *Accounts of Chemical Research* **2016**, *49*, 868-876.

[9] R. Gutzler, T. Sirtl, J. F. Dienstmaier, K. Mahata, W. M. Heckl, M. Schmittel and M. Lackinger, *Journal of the American Chemical Society* **2010**, *132*, 5084-5090.

[10] F. Herrmann, B. Muhsin, C. R. Singh, S. Shokhovets, G. Gobsch, H. Hoppe and M. Presselt, *The Journal of Physical Chemistry C* **2015**, *119*, 9036-9040.

[11] S. Conti and M. Cecchini, *Physical Chemistry Chemical Physics* **2016**, *18*, 31480-31493.

[12] M. Mastrangeli in *Surface tension-driven self-assembly*, (Ed. P. Lambert), Springer, pp. 227-253-227-253.

[13] a) V. Yesilyurt, R. Ramireddy, M. A. Azagarsamy and S. Thayumanavan, *Chemistry – A European Journal* **2012**, *18*, 223-229; b) M. R. Molla, P. Prasad and S. Thayumanavan, *Journal of the American Chemical Society* **2015**, *137*, 7286-7289; c) P.-P. Yang, X.-X. Zhao, A.-P. Xu, L. Wang and H. Wang, *Journal of Materials Chemistry B* **2016**, *4*, 2662-2668.

[14] P. A. Hassan and S. L. Gawali, *Langmuir* **2018**.

[15] C. V. Kulkarni, W. Wachter, G. Iglesias-Salto, S. Engelskirchen and S. Ahualli, *Physical Chemistry Chemical Physics* **2011**, *13*, 3004-3021.

[16] G. Ungar, C. Tschierske, V. Abetz, R. Holyst, M. A. Bates, F. Liu, M. Prehm, R. Kieffer, X. Zeng, M. Walker, B. Glettner and A. Zywocinski, *Advanced Functional Materials* **2011**, *21*, 1296-1323.

[17] Y. Yang and C. Wang, *Current Opinion in Colloid & Interface Science* **2009**, *14*, 135-147.

[18] a) W. Mamdouh, H. Uji-i, J. S. Ladislaw, A. E. Dulcey, V. Percec, F. C. De Schryver and S. De Feyter, *Journal of the American Chemical Society* **2006**, *128*, 317-325; b) C. Park, H. J. Song and H. C. Choi, *Chemical Communications* **2009**, 4803-4805.

[19] a) R. Yamada, H. Wano and K. Uosaki, *Langmuir* **2000**, *16*, 5523-5525; b) D. Gorl and F. Wurthner, *Angewandte Chemie-International Edition* **2016**, *55*, 12094-12098; c) S. Ogi, V. Stepanenko, K. Sugiyasu, M. Takeuchi and F. Würthner, *Journal of the American Chemical Society* **2015**, *137*, 3300-3307.

[20] a) R. Resch, M. Grasserbauer, G. Friedbacher, T. Vallant, H. Brunner, U. Mayer and H. Hoffmann, *Applied Surface Science* **1999**, *140*, 168-175; b) S. Campen, J. H. Green, G. D. Lamb and H. A. Spikes, *Tribology Letters* **2015**, *58*, 1-15; c) I. Doudevski, W. A. Hayes and D. K. Schwartz, *Physical Review Letters* **1998**, *81*, 4927-4930.

[21] a) W. H. Lee and Y. D. Park, *Advanced Materials Interfaces* **2018**, *5*, 1700316; b) K. Voïtchovsky, N. Ashari-Astani, I. Tavernelli, N. Tétreault, U. Rothlisberger, F. Stellacci, M. Grätzel and H. A. Harms, *ACS Applied Materials & Interfaces* **2015**, *7*, 10834-10842.

[22] a) B. R. A. Neves, M. E. Salmon, J. E. B. Troughton and P. E. Russell, *Nanotechnology* **2001**, *12*, 285; b) C. Meltzer, J. Paul, H. Dietrich, C. M. Jäger, T. Clark, D. Zahn, B. Braunschweig and W. Peukert, *Journal of the American Chemical Society* **2014**, *136*, 10718-10727; c) J. J. Benítez, J. A. Heredia-Guerrero, M. A. San-Miguel and H. C. Galloway, *The Journal of Physical Chemistry B* **2018**, *122*, 493-499.

[23] a) W. B. Jackson, N. M. Amer, A. C. Boccara and D. Fournier, *Applied Optics* **1981**, *20*, 1333-1344; b) A. C. Boccara, D. Fournier, W. Jackson and N. M. Amer, *Optics Letters* **1980**, *5*, 377-379; c) E. Buchaca-Domingo, K. Vandewal, Z. Fei, S. E. Watkins, F. H. Scholes, J. H. Bannock, J. C. de Mello, L. J. Richter, D. M. DeLongchamp, A. Amassian, M. Heeney, A. Salleo and N. Stingelin, *Journal of the American Chemical Society* **2015**, *137*, 5256-5259; d) B.-S. J. J., G. L., V. K., H. K., M. J. V., V. D., B. D. D. C. and N. J., *Advanced Functional Materials* **2007**, *17*, 451-457.

[24] a) J. Cui, D. Daniel, A. Grinthal, K. Lin and J. Aizenberg, *Nature Materials* **2015**, *14*, 790; b) Y. Li, L. Li and J. Sun, *Angewandte Chemie International Edition* **2010**, *49*, 6129-6133.

[25] M. L. Hupfer, M. Kaufmann, L. Roussille, J. Preiss, D. Weiss, K. Hinrichs, V. Deckert, B. Dietzek, R. Beckert and M. Presselt, *Langmuir* **2019**, *35*, 2561-2570.

[26] a) M. Presselt, F. Herrmann, S. Shokhovets, H. Hoppe, E. Runge and G. Gobsch, *Chemical Physics Letters* **2012**, *542*, 70-73; b) F. Herrmann, S. Engmann, M. Presselt, H. Hoppe, S. Shokhovets and G. Gobsch, *Applied Physics Letters* **2012**, *100*, 153301-153301 - 153303.

[27] a) S. H. Habenicht, S. Schramm, S. Fischer, T. Sachse, F. Herrmann-Westendorf, A. Bellmann, B. Dietzek, M. Presselt, D. Weiß, R. Beckert and H. Görls, *Journal of Materials Chemistry C* **2016**, *4*, 958-971; b) M. L. Hupfer, M. Kaufmann, F. Herrmann-Westendorf, T. Sachse, L. Roussille, K.-H. Feller, D. Weiss, V. Deckert, R. Beckert, B. Dietzek and M. Presselt, *ACS Appl Mater Interfaces* **2017**, *9*, 44181-44191; c) M. Kaufmann, M. L. Hupfer, T. Sachse, F. Herrmann-Westendorf, D. Weiß, B. Dietzek, R. Beckert and M. Presselt, *Journal of Colloid and Interface Science* **2018**, *526*, 410-418; d) M. L. Hupfer, M. Kaufmann, J. Preiß, D. Weiß, S. May, B. Dietzek, R. Beckert and M. Presselt, *Physical Chemistry Chemical Physics* **2019**, *submitted*.

[28] a) F. Herrmann-Westendorf, T. Sachse, M. Schulz, M. Kaufmann, V. Sivakov, R. Beckert, T. J. Martinez, B. Dietzek and M. Presselt, *J Phys Chem A* **2018**; b) S. A. Hussain, D. Dey, S. Chakraborty and D. Bhattacharjee, *Journal of Luminescence* **2011**, *131*, 1655-1660.

[29] a) T. Imae and H. Torii, *The Journal of Physical Chemistry B* **2000**, *104*, 9218-9224; b) K. A. Peterlinz and R. Georgiadis, *Langmuir* **1996**, *12*, 4731-4740.

Autonomous Supramolecular Interface Self-Healing Monitored by Restoration of UV-vis Absorption Spectra of Self-Assembled Thiazole Layers

Supporting Information

Maximilian L. Hupfer[1,3], Felix Herrmann-Westendorf[1,3], Martin Kaufmann[1,2], Dieter Weiß[2], Rainer Beckert[2], Benjamin Dietzek[1,3], Martin Presselt[1,3,4,5,*]

[1] Institute of Physical Chemistry, Friedrich Schiller University Jena, Helmholtzweg 4, 07743 Jena, Germany, E-mail: martin.presselt@leibniz-ipht.de, Phone: +49 3641 206418

[2] Institute of Organic and Macromolecular Chemistry, Friedrich Schiller University Jena, Humboldstraße 10, 07743 Jena, Germany

[3] Leibniz Institute of Photonic Technology (IPHT), Albert-Einstein-Str. 9, 07745 Jena, Germany

[4] Center for Energy and Environmental Chemistry Jena (CEEC Jena), Friedrich Schiller University Jena, Philosophenweg 7a, 07743 Jena, Germany

[5] sciclus GmbH & Co. KG, Moritz-von-Rohr-Str. 1a, 07745 Jena, Germany

*Corresponding author: martin.presselt@leibniz-ipht.de

1. METHODS

1.1. Photothermal Deflection Spectroscopy

For the SAM it is necessary to use saturated solutions to support the assembling on a substrate. The dye concentration and therefore the thermodynamic driving force can be indirect measured by the UV-vis absorbance spectra. The absorbance of the solution should be lower than 0.2 to ensure that the intensity of the incident light on the SAM is still sufficiently high to yield a good signal to noise ratio, after passing the saturated solution. Too high dye concentrations heat up the solution and produce heat stream and therefore a low signal to noise ratio. Too low dye concentration causes a lower thermodynamic driving force to ensure self-assembly and therefore a low signal to noise ratio. The SAM were measured immeadiately after immersion of the clean substrates into the solution at room temperature.

The here used PDS setup consists of the following parts: As light source a system obtained from LOT-QD was used. This system contains of a 1000W Xe-high pressure lamp and a 260mm monochromator optimized to deliver maximum intensity from 200nm up to 2500nm. The light is than modulated by a chopper from Thorlabs and afterwards focused on the sample by a f=75mm lens. The intensity of the incident light is monitored using a quartz glass plate as beam splitter, placed between focusing lens and sample, and a UV-optimized trans-impedance amplified silicon detector obtained from Thorlabs. The deflection of a 0.5mW HeNe-laser is measured using a lateral effect sensor PDA90 from Thorlabs. To decrease electronic noise the detector was not connected to a standard current source. The standard source was replaced by two $LiFePO_4$ motorcycle batteries (Shido Lithium LTX4L-BS) delivering the plus and minus 12V to drive the detector. The deflection and reference signal was read out by using two Lock-In amplifiers (SRS-830) from Stanford research systems. The whole system is controlled using a self-written Labview program, which collects all the data and also corrects the PDS signal in accordance to the incident intensity. As reference sample a 5x30mm glassy carbon sample was used.

Figure SI 1 shows that the measured absorption exponentially decays when increasing the distance between surface and probe-laser focus from the optimum, *i.e*. closest, distance. Hence, the applied PDS is surface sensitive and exclusively detects the absorption of the SAM and not of the solution, thus being an invaluable tool for *in situ* detection of self-assembly and self-healing.

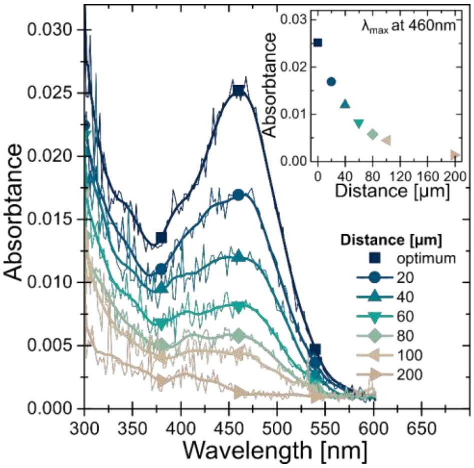

Figure SI 1: Exponentially decaying absorptance upon increasing the distance between the HeNe-laser focus and the self-assembled layer demonstrates the surface sensitivity of the here used PDS-setup. The layer is formed on a hydrophilic quartz-glass substrate from the amphiphilic push-pull thiazole **1** that was dissolved in heptane (saturated solution to keep the dye concentration constant)

1.2. Transmission spectroscopy

For the absorbance measurements in solution, we used an UV−vis (Varian: Cary 5000) spectrometer in transmission mode.

1.3. Density functional theory calculations

Quantum chemical structure optimizations and calculations of electrostatic potentials were performed using density functional theory (DFT) implemented in Turbomole(*1*) and applying the GGA (generalized gradient approximation) functional BP86 (preoptimization), followed by the hybrid functionals and B3LYP(*2*), the def2-SVP (preoptimization) and -TZVP basis sets(*3*), and the MARI-J approximation in case of BP86, which have been shown to yield reasonable electronic properties for a large variety of molecular motives, including push-pull systems and extended π-electron systems(*4-9*).

2. RESULTS

2.1. Comparison between UV-vis spectra of SAMs and solutions

1 was dissolved in solvents of varied polarity because the essential driving forces for self-healing, namely thermodynamic stability of the SAM and the energy difference between dissolved degraded and pristine dyes, critically depend on the substrate's surface polarity and the solvent polarity. To reduce attenuation of the incident light travelling through the cuvette (see Figure 1B of the main text) the solutions of **1** shall be saturated at rather low optical densities. To realize corresponding low saturation concentration, which ensure constant concentrations of **1** in long-term experiments, non-polar alkanes and the highly polar water were used as solvents. The alkanes were varied (cyclohexane, isooctane, n-heptane, n-hexane) to additionally account for possibly different supramolecular structures that form because of different solvent geometries(*10, 11*).

Figure SI 2 shows that in cases **1** is dissolved till saturation in n-hexane, n-heptane, or isooctane the UV-vis absorption spectrum of the solution, as measured by means of UV-vis transmission spectroscopy, features a single, vibronically structured major absorption peak at λ_{max}=420 nm that levels off at 475 nm. In case of water and cyclohexane, in which **1** is hardly soluble, the UV-vis spectra are red-shifted, what is assigned to absorption of J-aggregates(*12*) that apparently formed in solution.

As revealed by Figure SI 2, UV-vis (PDS) absorption spectra of SAMs could be measured for all above listed solutions and both hydrophilic and hydrophobized quartz glass surfaces. In case of cyclohexane and isooctane the absorption spectra of the SAMs basically resemble those of **1** dissolved in the linear hydrocarbons. This similarity reveals the presence of amorphous SAMs or rather sparsely distributed dyes that adsorbed at the hydrophilic or hydrophobic quartz glass. However, in the system containing isooctane, an additional weak red-shifted absorption between 475 and 525 nm is observed for the SAM formed at the hydrophilic surface, which is assigned to J-aggregates.

Interestingly, formation of the latter is notably supported by n-hexane as revealed by the absorption spectrum of the SAM at hydrophilic quartz glass in Figure SI 2, which is red-shifted and dominated by J-aggregate absorptions. Weak J-like absorptions are even detected on hydrophobic quartz glass if the solvent is hexane. Extending the hydrocarbon chain to heptane changes not the absorption spectrum of the SAM at hydrophilic, but on hydrophobic quartz glass. At the latter, the spectrum features two pronounced maxima, one corresponding to the solution spectrum and one to J-aggregate absorption. In case of water, J-aggregate absorption dominates the UV-vis spectrum of SAMs at hydrophobic surfaces, while on hydrophilic ones the absorption spectra comprise features of sparsely distributed or dissolved as well as few J-aggregated dyes. Note that in case of the latter, similarly to hydrophilic and hydrophobic surfaces when cyclohexane is used, the PDS-determined absorption spectra are very weak and approach the sensitivity-limit of the PDS setup, as revealed by the small signal to noise ratios of the non-smoothened data shown in the supporting information (SI), Figures SI 3, 7. Finally, when using heptane dipolar supramolecular assemblies easily form on either surface and give rise to intense PDS-spectra, thus apparently yielding the thermodynamically most favorable SAMs.

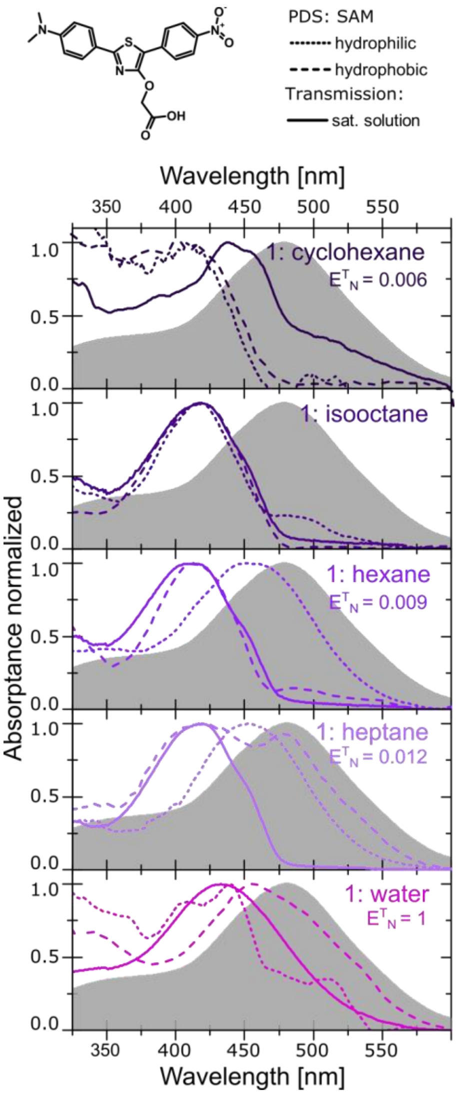

Figure SI 2: Absorption spectra of self-assembled monolayer of the amphiphilic push-pull-thiazoles **1**, **5** and **10** in saturated solutions (solid) with different nonpolar (isooctane, n-hexane, n-heptane, cyclohexane) and polar (water) solvent on hydrophilic (dotted) and hydrophobized (dashed) quartz-glass substrate; The E^T_N values given in the figure refer to Reichardt's polaritiy scale(*13*) (cyclohexane E^T_N = 0,006; hexane E^T_N = 0,009; heptane E^T_N = 0,012).

2.2. PDS absorptance measurements of SAMs with raw data

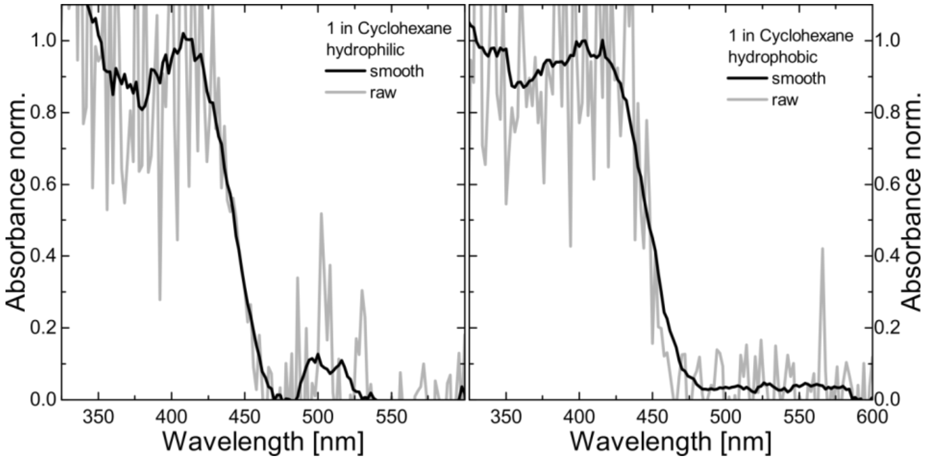

Figure SI 3: Normalized raw and smoothed absorption spectra of self-assembled monolayer of the amphiphilic push-pull-thiazoles **1** in saturated solutions of cyclohexane on hydrophilic (left) and hydrophobized (right) quartz-glass substrate

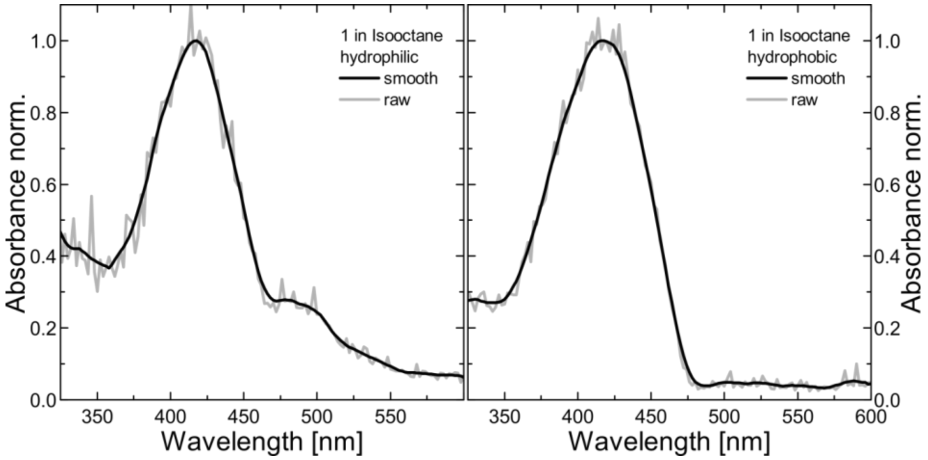

Figure SI 4: Normalized raw and smoothed absorption spectra of self-assembled monolayer of the amphiphilic push-pull-thiazoles **1** in saturated solutions of isooctane on hydrophilic (left) and hydrophobized (right) quartz-glass substrate

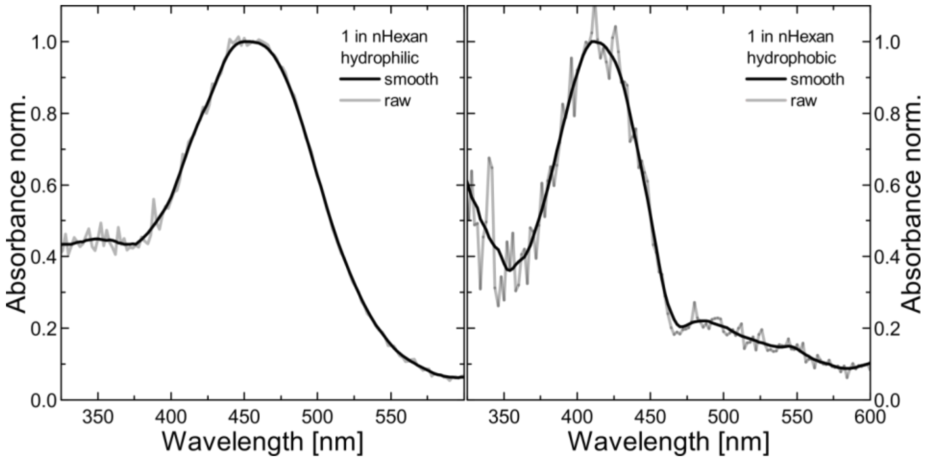

Figure SI 5: Normalized raw and smoothed absorption spectra of self-assembled monolayer of the amphiphilic push-pull-thiazoles **1** in saturated solutions of n-hexane on hydrophilic (left) and hydrophobized (right) quartz-glass substrate

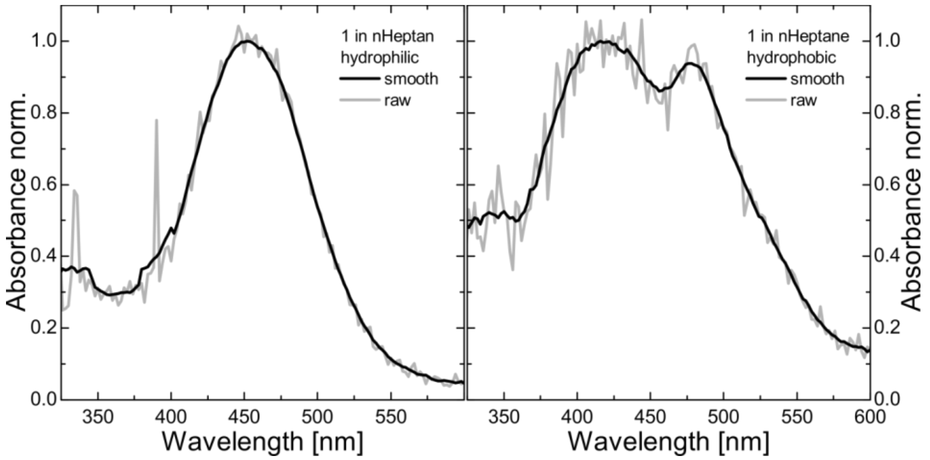

Figure SI 6: Normalized raw and smoothed absorption spectra of self-assembled monolayer of the amphiphilic push-pull-thiazoles **1** in saturated solutions of n-heptane on hydrophilic (left) and hydrophobized (right) quartz-glass substrate

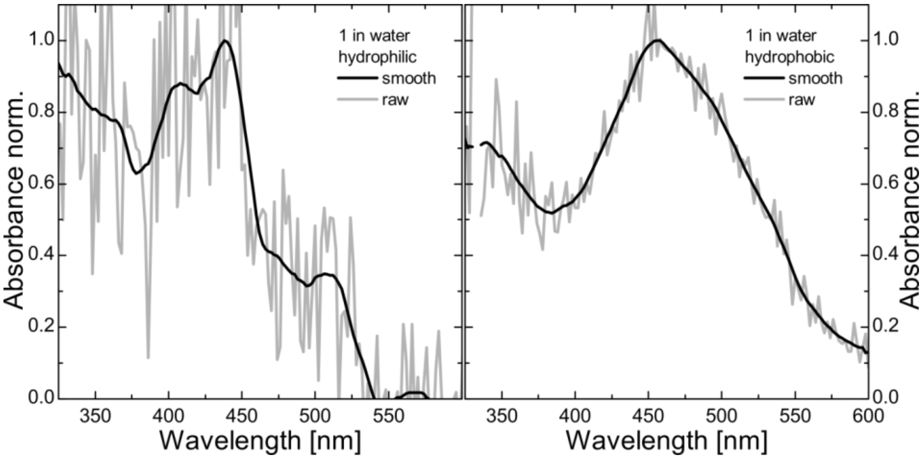

Figure SI 7: Normalized raw and smoothed absorption spectra of self-assembled monolayer of the amphiphilic push-pull-thiazoles **1** in saturated solutions of water on hydrophilic (left) and hydrophobized (right) quartz-glass substrate

2.3. Self-healing

Usage of the absorption as self-healed function in the classic definition of self-healing efficiency η yields the following expression:

η = (A(healed) - A(damaged)) / (A(pristine) - A(damaged))

Because this expression does not account for the superposition of absorption peaks, the growth of the UV-absorption upon successive self-healing cycles raises the healing-efficiency from One towards Two in case of n-heptane, as shown in Figure SI 8. The unphysical values of the self-healing efficiency also highlights the difficulties of self-healing in cyclohexane and water, as shown in Figure SI 8.

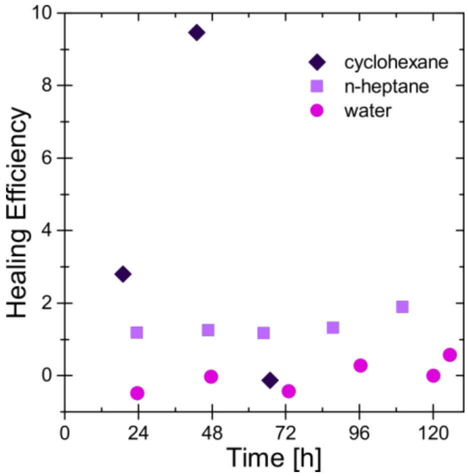

Figure SI 8: Self-healing efficiency of self-assembled and self-healed monolayer of the amphiphilic push-pull-thiazoles **1** in a saturated solution of cyclohexane, heptane and water

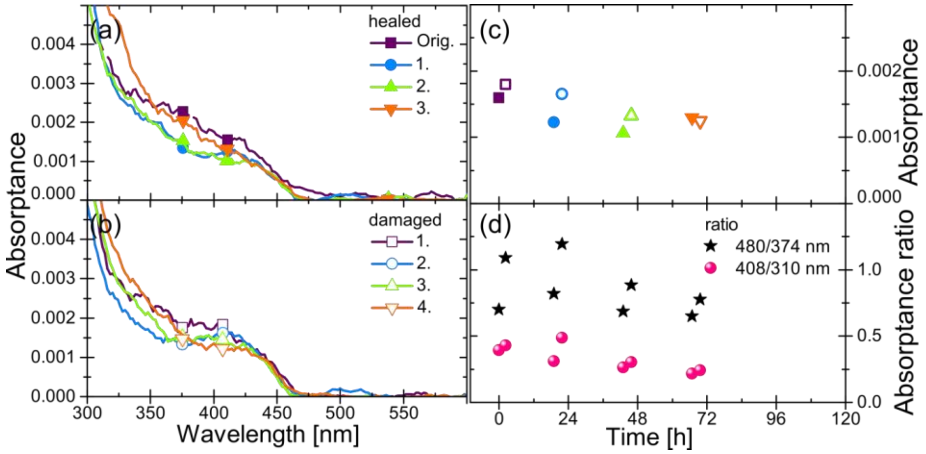

Figure SI 9: Absorption spectra of self-assembled and self-healed monolayer of the amphiphilic push-pull-thiazoles **1** in a saturated solution of water at hydrophilic quartz-glass after different damage (b) and self-healing (a) cycles. Absorption intensity at λ_{max} = 460 nm (c) and the ratio of intensity at 460 nm/374 nm (stars) and 460 nm/310 nm (balls) vs. time (d)

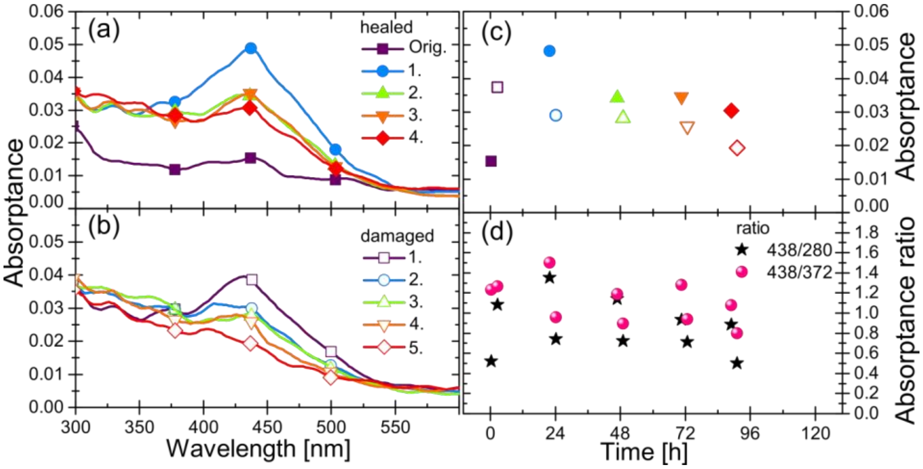

Figure SI 10: Absorption spectra of self-assembled and self-healed monolayer of the amphiphilic push-pull-thiazoles **1** in a saturated solution of water at hydrophilic quartz-glass after different damage (b) and self-healing (a) cycles. Absorption intensity at λ_{max} = 460 nm (c) and the ratio of intensity at 460 nm/374 nm (stars) and 460 nm/310 nm (balls) vs. time (d)

2.4. Self-healing kinetics

For specification of the mechanism of assembly, damage and healing of the SAMs, the kinetics derived from intensity *vs*. time curves (see manuscript Figure 3) was measured exemplary for the species where highest molecular order is expected (**1** λ_{max} = 450 nm from n-heptane) *via* PDS. However, few critical aspects have to be mentioned in connection with the measuring setup. Adsorption and its kinetic strongly depend of the chemical conditions of the substrate surface and anchor group of the dye. Moreover, for each measurement of an assembly-damage-healing cycle (see manuscript Figure 3b-c, d-e, f-g) the sample needs to be manually adjusted (typically ranges of about 200 µm, see Figure SI 1) in the beginning of the measurement. In accordance to that, the excitation during measurement induces different temperatures for the different focused spots, which obviously influences the thermodynamically driven process of the adsorption. Therefore, as shown in manuscript Figure 3a, the kinetics of the initial assembly in a full assembly-damage cycle slightly deviates.

To reduce the thermal influence on assembly and healing, UV-vis absorption during self-assembly and –healing must be largely avoided. Therefore, we changed the wavelength of the irradiation from λ_{max}=450 nm used for probing the absorptance (data acquisition time: 20 s) of the SAMs to λ_{rest}=2500 nm, where electronic excitation cannot happen, in our automated measurement protocols to determine assembly and healing kinetics. The time interval between the absorptance measurement, *i.e*. the rest-time at λ_{rest}=2500 nm provided for either assembly or healing, amounts 10 mins. This repeated measure-rest routine was running for 4 h in case of studying self-healing, as shown in Figure SI 11Figure SI 12Figure SI 13c

The damage kinetic is measured similarly. The kinetic is also characterized by the time-evolution of the absorptance A_t at λ_{max}, which is the averaged intensity over 3 mins after each damage time step. These damage time steps last 5 mins for total damage times D<30 min and 10 mins for D>30 mins, see Fig. 3c,e,g of the main text and Figure SI 11Figure SI 12Figure SI 13d. This damage of the layer is induced by nonfiltered and focused polychromatic white light of the excitation source by changing the monochromator to zero order.

After each assembly, heal or damage kinetic a spectra was measured as shown in Figure SI 11Figure SI 12Figure SI 13 a (heal) and b (damage).

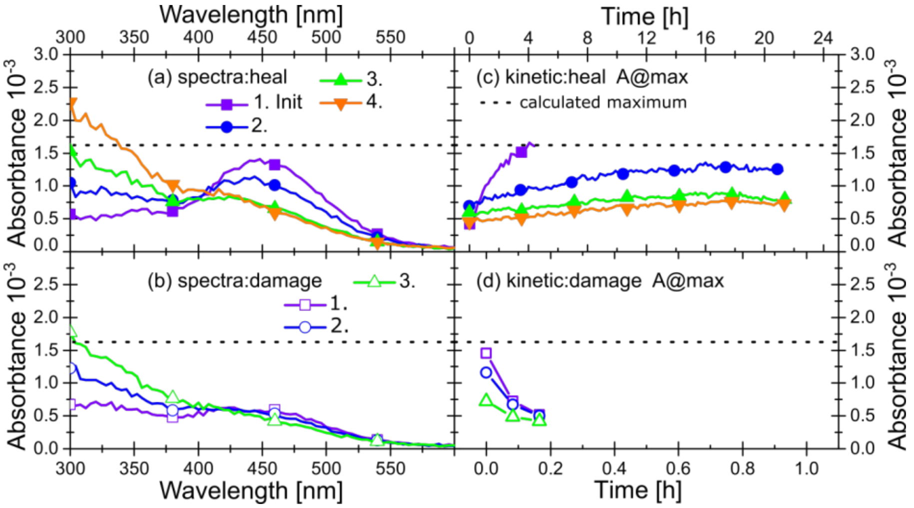

Figure SI 11: Absorption spectra of self-assembled and self-healed monolayer of the amphiphilic push-pull-thiazoles **1** in a saturated solution of heptane at hydrophilic quartz-glass after different damage (b) and self-healing (a) cycles. Kinetic of self-assembly/self-healing (c) of the same monolayer at the absorption maximum at λ_{max} = 450 nm and kinetic of damage *via* concentrated white light illumination

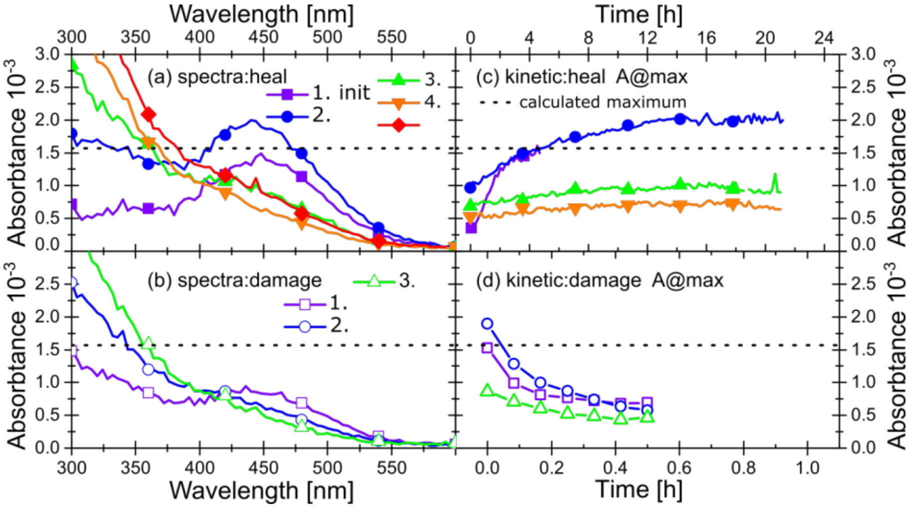

Figure SI 12: Absorption spectra of self-assembled and self-healed monolayer of the amphiphilic push-pull-thiazoles **1** in a saturated solution of heptane at hydrophilic quartz-glass after different damage (b) and self-healing (a) cycles. Kinetic of self-assembly/self-healing (c) of the same monolayer at the absorption maximum at $\lambda_{max} = 450$ nm and kinetic of damage *via* concentrated white light illumination

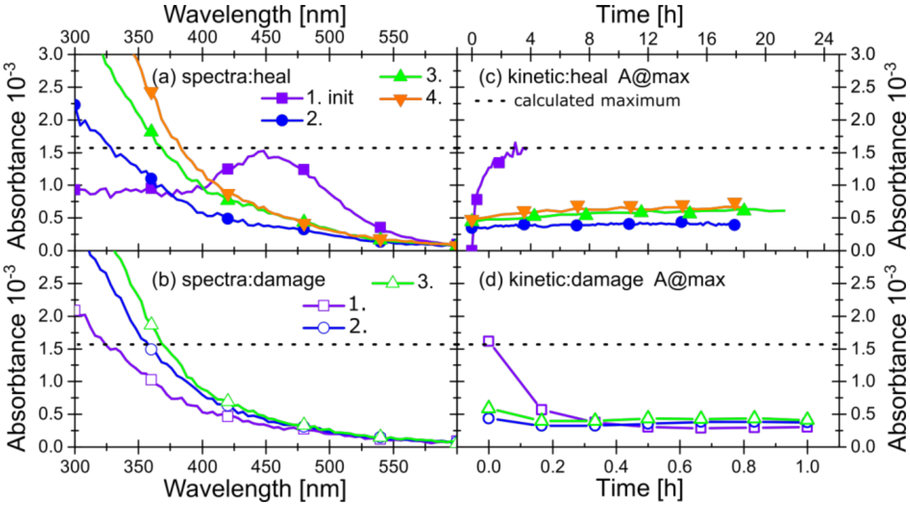

Figure SI 13: Absorption spectra of self-assembled and self-healed monolayer of the amphiphilic push-pull-thiazoles **1** in a saturated solution of heptane at hydrophilic quartz-glass after different damage (b) and self-healing (a) cycles. Kinetic of self-assembly/self-healing (c) of the same monolayer at the absorption maximum at λ_{max} = 450 nm and kinetic of damage *via* concentrated white light illumination

	Assembly $A_t = A_0[1 - e^{-k(t-t_0)}]$			Damage	
	$A_0 \cdot 10^{-3}$	t_0 [min]	K [min^{-1}]	D [min]	$A_D \cdot 10^{-3}$
1	1.62	10	0.0108	10	0.52
2	1.27	287	0.0023		0.50
3	1.00	725	0.0010		0.42
4	0.94	657	0.0008		/
1	1.57	5	0.0099	30	0.70
2	2.00	205	0.0029		0.57
3	0.91	325	0.0034		0.47
4	0.68	404	0.0025		/
1	1.47	1	0.0222	60	0.30
2	0.37	553	0.0032		0.37
3	0.59	540	0.0021		0.42
4	0.61	297	0.0040		/

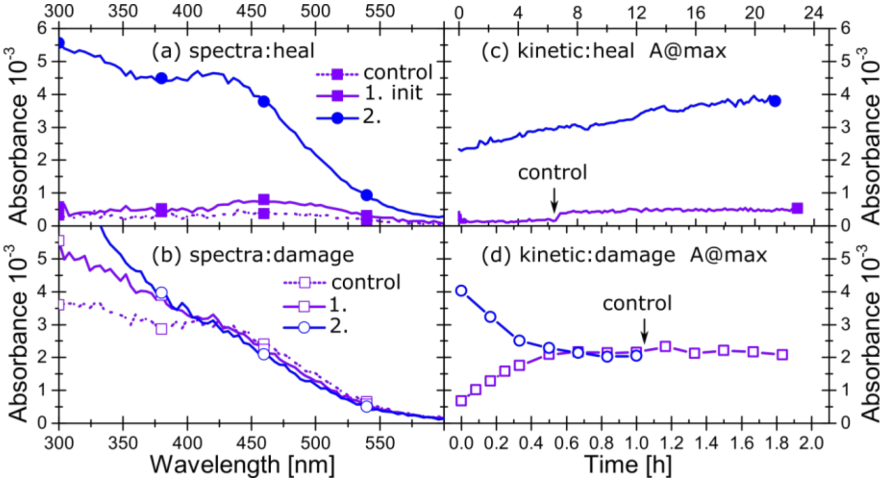

Figure SI 14: Absorption spectra of self-assembled and self-healed monolayer of the amphiphilic push-pull-thiazoles **1** in a saturated solution of water at hydrophobic quartz-glass after different damage (b) and self-healing (a) cycles. Kinetic of self-assembly/self-healing (c) of the same monolayer at the absorption maximum at λ_{max} = 460 nm and kinetic of damage *via* concentrated white light illumination

REFERENCES

1. F. Furche *et al.*, Turbomole. *Wiley Interdisciplinary Reviews-Computational Molecular Science* **4**, 91-100 (2014).
2. P. J. Stephens, F. J. Devlin, C. F. Chabalowski, M. J. Frisch, Ab-Initio Calculation of Vibrational Absorption and Circular-Dichroism Spectra Using Density-Functional Force-Fields. *The Journal of Physical Chemistry* **98**, 11623-11627 (1994).
3. F. Weigend, R. Ahlrichs, Balanced basis sets of split valence, triple zeta valence and quadruple zeta valence quality for H to Rn: Design and assessment of accuracy. *Physical Chemistry Chemical Physics* **7**, 3297-3305 (2005).
4. M. Presselt, C. Schnedermann, M. Schmitt, J. Popp, Prediction of electron densities, the respective laplacians, and ellipticities in bond-critical points of phenyl-CH-bonds via linear relations to parameters of inherently localized CD stretching vibrations and 1H NMR-shifts. *The journal of physical chemistry. A* **113**, 3210-3222 (2009).
5. M. Presselt, C. Schnedermann, M. Müller, M. Schmitt, J. Popp, Derivation of Correlation Functions to Predict Bond Properties of Phenyl-CH Bonds Based on Vibrational and H-1 NMR Spectroscopic Quantities. *Journal of Physical Chemistry A* **114**, 10287-10296 (2010).
6. W. Beenken, W. Maes, M. Kruk, T. Martínez, M. Presselt, Origin of the Individual Basicity of Corrole NH-Tautomers: A Quantum Chemical Study on Molecular Structure and Dynamics, Kinetics, and Thermodynamics. *The Journal of Physical Chemistry A* **119**, 6875-6883 (2015).
7. D. M. Gampe *et al.*, Stable and easily accessible functional dyes: dihydrotetraazaanthracenes as versatile precursors for higher acenes. *Chemistry* **21**, 7571-7581 (2015).
8. J. Preiß *et al.*, How Does Peripheral Functionalization of Ruthenium(II)–Terpyridine Complexes Affect Spatial Charge Redistribution after Photoexcitation at the Franck–Condon Point? *ChemPhysChem* **16**, 1395-1404 (2015).
9. M. Presselt *et al.*, Quantum Chemical Insights into the Dependence of Porphyrin Basicity on the Meso-Aryl Substituents: Thermodynamics, Buckling, Reaction Sites and Molecular Flexibility. *Physical Chemistry Chemical Physics* **17**, 14096-14106 (2015).
10. C. Park, H. J. Song, H. C. Choi, The critical effect of solvent geometry on the determination of fullerene (C60) self-assembly into dot, wire and disk structures. *Chemical Communications*, 4803-4805 (2009).
11. S. S. Babu, H. Mohwald, T. Nakanishi, Recent progress in morphology control of supramolecular fullerene assemblies and its applications. *Chemical Society Reviews* **39**, 4021-4035 (2010).
12. M. L. Hupfer *et al.*, Combining Dipolar Aggregate Formation with Two-Dimensional Assembly at Air-Water-Interfaces: Case of Amphiphilic Push-Pull-Thiazoles. *Advanced Materials* **to be published**, (2018).
13. C. Reichardt, Solvatochromic Dyes as Solvent Polarity Indicators. *Chemical Reviews* **94**, 2319-2358 (1994).

1. F. Furche *et al.*, Turbomole. *Wiley Interdisciplinary Reviews-Computational Molecular Science* **4**, 91-100 (2014).
2. P. J. Stephens, F. J. Devlin, C. F. Chabalowski, M. J. Frisch, Ab-Initio Calculation of Vibrational Absorption and Circular-Dichroism Spectra Using Density-Functional Force-Fields. *The Journal of Physical Chemistry* **98**, 11623-11627 (1994).
3. F. Weigend, R. Ahlrichs, Balanced basis sets of split valence, triple zeta valence and quadruple zeta valence quality for H to Rn: Design and assessment of accuracy. *Physical Chemistry Chemical Physics* **7**, 3297-3305 (2005).
4. M. Presselt, C. Schnedermann, M. Schmitt, J. Popp, Prediction of electron densities, the respective laplacians, and ellipticities in bond-critical points of phenyl-CH-bonds via linear relations to parameters of inherently localized CD stretching vibrations and 1H NMR-shifts. *The journal of physical chemistry. A* **113**, 3210-3222 (2009).

5. M. Presselt, C. Schnedermann, M. Müller, M. Schmitt, J. Popp, Derivation of Correlation Functions to Predict Bond Properties of Phenyl-CH Bonds Based on Vibrational and H-1 NMR Spectroscopic Quantities. *Journal of Physical Chemistry A* **114**, 10287-10296 (2010).
6. W. Beenken, W. Maes, M. Kruk, T. Martínez, M. Presselt, Origin of the Individual Basicity of Corrole NH-Tautomers: A Quantum Chemical Study on Molecular Structure and Dynamics, Kinetics, and Thermodynamics. *The Journal of Physical Chemistry A* **119**, 6875-6883 (2015).
7. D. M. Gampe *et al.*, Stable and Easily Accessible Functional Dyes: Dihydrotetraazaanthracenes as Versatile Precursors for Higher Acenes. *Chemistry – A European Journal* **21**, 7571-7581 (2015).
8. J. Preiß *et al.*, How Does Peripheral Functionalization of Ruthenium(II)–Terpyridine Complexes Affect Spatial Charge Redistribution after Photoexcitation at the Franck–Condon Point? *ChemPhysChem* **16**, 1395-1404 (2015).
9. M. Presselt *et al.*, Quantum Chemical Insights into the Dependence of Porphyrin Basicity on the Meso-Aryl Substituents: Thermodynamics, Buckling, Reaction Sites and Molecular Flexibility. *Physical Chemistry Chemical Physics* **17**, 14096-14106 (2015).
10. C. Park, H. J. Song, H. C. Choi, The critical effect of solvent geometry on the determination of fullerene (C60) self-assembly into dot, wire and disk structures. *Chemical Communications*, 4803-4805 (2009).
11. S. S. Babu, H. Mohwald, T. Nakanishi, Recent progress in morphology control of supramolecular fullerene assemblies and its applications. *Chemical Society Reviews* **39**, 4021-4035 (2010).
12. M. L. Hupfer *et al.*, Combining Dipolar Aggregate Formation with Two-Dimensional Assembly at Air-Water-Interfaces: Case of Amphiphilic Push-Pull-Thiazoles. *Advanced Materials* **to be published**, (2018).

Liste der Veröffentlichungen

Referierte Publikationen in wissenschaftlichen Journalen

Hupfer, M. L.; Kaufmann, M.; Preiss, J.; Weiss, D.; Beckert, R.; Dietzek, B.; Presselt, M., Assembly of T-Shaped Amphiphilic Thiazoles on the Air-Water Interface: Impact of Polar Chromophore Moieties, as Well as Dipolarity and pi-Extension of the Chromophore on the Supramolecular Structure. *Langmuir* **2019,** *35* (7), 2587-2600.

Kaufmann, M.; Hupfer, M. L.; Sachse, T.; Herrmann-Westendorf, F.; Weiß, D.; Dietzek, B.; Beckert, R.; Presselt, M., Introducing double polar heads to highly fluorescent Thiazoles: Influence on supramolecular structures and photonic properties. *Journal of colloid and interface science* **2018,** *526*, 410-418.

Hupfer, M. L.; Kaufmann, M.; Herrmann-Westendorf, F.; Sachse, T.; Roussille, L.; Feller, K. H.; Weiss, D.; Deckert, V.; Beckert, R.; Dietzek, B.; Presselt, M., On the Control of Chromophore Orientation, Supramolecular Structure, and Thermodynamic Stability of an Amphiphilic Pyridyl-Thiazol upon Lateral Compression and Spacer Length Variation. *ACS Appl Mater Interfaces* **2017,** *9* (50), 44181-44191.

Hupfer, M. L.; Kaufmann, M.; Preiß, J.; Weiß, D.; May, S.; Dietzek, B.; Beckert, R.; Presselt, M., Enhancing Supramolecular Stability of Monolayers by Combining Dipolar with Amphiphilic Motifs: Case of Amphiphilic Push-Pull-Thiazole. *Physical Chemistry Chemical Physics* **2019,** *submitted*.

Hupfer, M. L.; Kaufmann, M.; Roussille, L.; Preiss, J.; Weiss, D.; Hinrichs, K.; Deckert, V.; Dietzek, B.; Beckert, R.; Presselt, M., Arylic versus Alkylic-Hydrophobic Linkers Determine the Supramolecular Structure and Optoelectronic Properties of Tripodal Amphiphilic Push-Pull Thiazoles. *Langmuir* **2019,** *35* (7), 2561-2570.

Hupfer, M. L.; Herrmann-Westendorf, F.; Kaufmann, M.; Beckert, R.; Dietzek, B.; Presselt, M., Autonomous Interface Self-Healing: Monitored by Restoration of UV-vis Absorption Spectra of Self-Assembled Thiazole Layers. *Chemistry - A European Journal* **2019,** *submitted*.

Poster

Self-Assembling Amphiphilic Fluorophores: In-Situ Monitoring and Photonic Characterization, *MRS Spring Meeting*, **2016**, Phoenix, Vereinigte Staaten von Amerika

Orientation and Thermodynamic Stability of Self-Assembled Amphiphilic Thiazoles, *115th General Assembly of the German Bunsen Society for Physical Chemistry*, **2016**, Rostock, Deutschland

Orientation and Thermodynamic Stability of Self-Assembled Amphiphilic Thiazoles, *25. Lecture Conference on Photochemistry*, **2016**, Jena, Deutschland

Controlling Supra-Molecular Structures and Thermodynamic Properties of Langmuir-(Blodgett) Films of Amphiphilic Thiazole Dyes as Prerequisites for Self-Healing Photonic Membranes, 6th *International Conference on Self-healing Materials*, **2017**, Friedrichshafen, Deutschland

Jena, den

Maximilian Lutz Hupfer

Selbstständigkeitserklärung

Ich erkläre, dass ich die vorliegende Arbeit selbständig und unter Verwendung der angegebenen Hilfsmittel, persönlichen Mitteilungen und Quellen angefertigt habe.

Jena, den

Maximilian Lutz Hupfer

Danksagung

Diese Doktorarbeit wäre in ihrem Umfang und ihrer Qualität nicht ohne meine Arbeitsgruppe und meine beiden Betreuern möglich gewesen, welche mich vor allem nach meinem Fachwechsel von der angewandten Physik in die physikalische Chemie unterstützten. Daher gilt allen, insbesondere Prof. Dr. Benjamin Dietzek und Dr. Martin Presselt, mein ausdrücklicher Dank, für die mir gegebene, unschätzbare Chance mich auf diesem Gebiet zu etablieren. Dies schaffte ein sicheres Fundament zur Entwicklung dieser Dissertation. Ein besonderer Dank gilt Dr. Martin Presselt, welcher mich in unzähligen Korrekturrunden und einer Vielzahl an Testvorträgen zu einem vollständigen Wissenschaftler reifen ließ.

Jeder physikalische Chemiker, ist von der Qualität der zu charakterisierenden Moleküle abhängig. Über den Zugriff auf maßgeschneiderter Thiazole von Dr. Martin Kaufmann schätze ich mich daher in besonderem Maße glücklich. Wir konnten so gemeinsam an dem Ziel arbeiten, eine neuartige Farbstoffklasse in der Langmuir-Blodgett-Technik zu etablieren. Jeder zweifach linkshändige Wissenschaftler ist froh einen Kollegen wie Felix Herrmann-Westendorf zu haben, der mit seinem „Händchen“ jedes Labogerät instand hält. Mit der Planung und Konstruktion vieler Geräte trug er maßgeblich zum Gelingen vieler Projekte bei. Die Möglichkeiten quantenchemischer Berechnungen sind für eine moderne Dissertation des Fachgebietes ein Obligatorium. Umso wertvoller waren komplexe Skripte meiner Kollegen Dr. Martin Presselt, Dr. Julia Preiß und Dr. Torsten Sachse die unbedarften Experimentatoren wie mir Zugriff auf quantenchemische Erkenntnisse ermöglichten und welchen diesbezüglich mein ausdrücklicher Dank zu Teil wird. Es gilt des Weiteren den vielen Kollegen wie Dr. Fischer, Dr. Mathias Micheel, Dr. Christian Reichardt, Karin Kobow, Saunak Das, und Jasmin Finkelmeyer für ihre fachliche und nicht fachliche Begleitung während der letzten 4 Jahre herzlich zu danken.

Meinen Eltern, die mich immer unterstützten und Geduld mit mir bewiesen, gilt ein besonderer persönlicher Dank. Nur durch ihre aufopfernde Erziehung und Unterstützung konnte ich privat und akademisch reifen. Nicht zuletzt möchte ich meiner Isabel danken, die mir in den letzten 4 Jahren durch ihre Liebe die notwendige Kraft und Motivation spendete.